Long bone morphological adaptation to graviportality in Rhinocerotoidea

Christophe Mallet

MUSÉUM NATIONAL D'HISTOIRE NATURELLE

École Doctorale 227
Sciences de la nature et de l'Homme : évolution et écologie

Année 2020 **N° attribué par la bibliothèque**
|_|_|_|_|_|_|_|_|_|_|_|_|_|

THÈSE

pour obtenir le grade de

DOCTEUR DU MUSÉUM NATIONAL D'HISTOIRE NATURELLE

Spécialité : Biologie Évolutive

présentée et soutenue publiquement par

Christophe MALLET

le 20 novembre 2020

Adaptation morphologique des os longs à la graviportalité chez les Rhinocerotoidea

---

sous la direction de :	**Dr Alexandra HOUSSAYE**	**Directrice de recherche, CNRS**	**Directrice**
	Dr Raphaël CORNETTE	**Assistant ingénieur, CNRS**	**Co-directeur**
	Dr Guillaume BILLET	**Maître de conférences, MNHN**	**Co-directeur**
devant le jury :	**Dr Stephanie E. PIERCE**	**Professeure associée, Harvard University**	**Rapportrice**
	Pr Peter AERTS	**Professeur, Universiteit Antwerpen**	**Rapporteur**
	Dr Ursula B. GÖHLICH	**Docteure Privat-docent, Naturhistorisches Museum Wien**	**Examinatrice**
	Pr Pierre-Olivier ANTOINE	**Professeur, Université de Montpellier**	**Examinateur**

À mon père

The human factor in classification is nowhere more evident than in dealing with this superfamily [Rhinocerotoidea]*. It is, as mammalian superfamilies go, well known, but what is "known" about it is so inconsistent in places that much of it must be wrong.*

George G. Simpson 1945, The principles of classification and a classification of mammals

Bulletin of the American Museum of Natural History, 45

Table of contents

List of figures

List of tables

Remerciements / Acknowledgements

« Les remerciements, c'est la seule chose que les gens lisent alors que c'est toujours ce qu'on écrit en dernier. »

Source anonyme

Suivant cet adage plein de sagesse, la rédaction du manuscrit final a ainsi débuté par la partie la plus essentielle à mes yeux. Le seul moyen de remercier à leur juste valeur toutes les personnes sans qui ce travail n'aurait pu aboutir sous cette forme.

Mes trois encadrant·e·s, tout d'abord. Alexandra, merci d'avoir donné sa chance au « vieux » que je suis, malgré mon parcours atypique et ma grande capacité à toujours tout remettre en question (d'aucuns diraient « râler »). Une fois habitué à ton rythme de travail « un peu » élevé ou tes mails constitués uniquement d'un titre, j'ai pu mesurer la chance d'avoir une encadrante si investie au quotidien. Merci pour tes connaissances, ta rigueur, ta confiance, tes critiques toujours constructives et toutes tes autres qualités que je n'ai pas la place de lister.

Raphaël, la pratique de la morphométrie aurait été sans doute bien plus fastidieuse et frustrante sans toi. Toujours questionner ce que l'on fait, remettre en question les évidences, adapter l'analyse à la question : autant de choses, et bien d'autres encore, que j'ai développées grâce à ta disponibilité et ta patience. Merci pour tout cela.

Guillaume, merci pour ta capacité, toi aussi, à toujours aller chercher le détail qui change tout, à me faire me poser les bonnes questions et organiser mes propres idées. Merci également de m'avoir permis de réaliser ce rêve de gosse que de travailler dans la Galerie de Paléontologie : toute la poussière remuée durant les nombreuses sessions de scan, seul au milieu des fossiles, valait la peine d'être remuée.

All my gratitude goes to Stephanie Pierce, Ursula Göhlich, Peter Aerts and Pierre-Olivier Antoine who accepted to be part of my thesis jury and evaluate my work. I hope that this work will meet your expectations. Thanks also to Sandra Nauwelaerts, Pierre-Olivier Antoine and Eric Guilbert for being part of my thesis committee and helping me to focus and reorient my research when needed.

I would also like to thank the European Research Council (ERC) for funding this work through the project GRAVIBONE carried by Alexandra.

Collecting more than 1,600 scans of rhino bones would have been impossible without the precious help of all the curators of the numerous institutions I have visited during these three years. For your

kindness and your warm welcome despite my curious “flashing hairdryer scanner” and my will to scan “all the rhinos that you have in there”, many thanks to:

- E. Hoeger, S. Ketelsen, R. O’Leary, J. Meng, J. Galkin (American Museum of Natural History, New York, USA);
- J.-M. Pouillon, C. Bouix (Association Rhinopolis, Gannat, France);
- D. Berthet (Centre de Conservation et d’Étude des Collections, Musée des Confluences, Lyon, France);
- E. Robert (Collections de Géologie de Lyon, Université Lyon 1 Claude Bernard, Lyon, France);
- M. Landreau (Muséum d’Histoire Naturelle de Bordeaux, Bordeaux, France);
- Y. Laurent (Muséum d’Histoire Naturelle de Toulouse, Toulouse, France);
- J. Lesur, A. Verguin, S. Bailon (Muséum National d’Histoire Naturelle, Paris, France);
- P. Brewer, R. Pappa and R. Portela-Miguez (Natural History Museum, London, UK);
- C. West, R. Jennings, M. Cobb (Powell Cotton Museum, Birchington-on-Sea, UK);
- A. Folie, C. Cousin, O. Pauwels and S. Bruaux (Royal Belgian Institute of Natural Sciences, Brussels, Belgium);
- E. Gilissen (Royal Museum for Central Africa, Tervuren, Belgium);
- D. Brinkman (Yale Peabody Museum, New Haven, USA);
- A. H. van Heteren (Zoologische Staatssammlung München, Munich, Germany).

I would also like to thank people that I did not met in person but who gave access to specimens to Alexandra or provided me 3D scans directly: G. Rößner (Bayerische Staatssammlung für Paläontologie und Geologie, Munich, Germany), L. Costeur and F. Dammeyer (Naturhistorisches Museum Basel, Basel, Switzerland), F. Zachos, A. Bibl (Naturhistorisches Museum Wien, Vienna, Austria), W. Liu (Institute of Vertebrate Paleontology and Paleoanthropology, Beijing, China), T. Ingicco (Musée de l’Homme, MNHN, Paris, France) and M. C. Reyes (National Museum of the Philippines, Manila, Philippines). A special thanks also to J. Hutchinson for providing CT-scan data and for organizing together with Alexandra the “GraviDawn” meeting – to date, the biggest crossover in the ERC history!

Trois ans à trainer dans les couloirs des musées permettent de rencontrer beaucoup de « rhinophiles » avec qui j’ai eu des discussions souvent éclairantes et passionnantes. Merci à Pierre-Olivier Antoine pour les informations fournies directement par mail ou lors des comités de thèse, et pour son omniprésence indirecte dans les réserves de musées : rares sont les collections de rhinocéros fossiles à ne pas contenir une réattribution spécifique lui étant due. Merci à Jérémy Tissier pour les conseils avisés concernant la phylogénie des rhinocéros, rapidement concrétisés à travers des articles qui m’ont été fortement utiles sur la fin. Merci à Olivier Maridet de m’avoir proposé de l’accompagner, ainsi que

Jérémy, en Chine, même si cette « non-mission » est tombée à l'eau de mon côté… Une autre fois, peut-être ! Un grand merci à Constance Bronnert pour m'avoir notamment permis de scanner les restes de *Propachynolophus*, et de m'avoir même servi de pare-soleil pour réussir à les numériser ! Même s'il est plus « hippophile » que « rhinophile », un grand merci à Florian Martin pour les échanges de données ou de scans, et les discussions sur nos grosses bêtes respectives. De même, merci à Pauline Hanot pour les échanges à propos des périssodactyles, de l'intégration et de la morphométrie en général.

A very special thanks to Dr. Kees Rookmaaker (Director and Chief Editor) and to all the staff of the online database Rhino Resource Center, a priceless goldmine of studies about modern and fossil rhinos. RRC contains almost 25,000 bibliographic references about rhinos in open access, many of which cannot be found elsewhere on the Internet and are sometimes even missing from physical libraries. Needless to say, it is an invaluable resource that I used and overused for 3 years. Thank you for your dedication to this lifetime task. I am very proud to see my own works now joining this immense collection.

Un grand merci également aux gens croisés en congrès pour les discussions que nous avons pu avoir, en direct ou par mail : Loïc Costeur, Manon Hullot, Miranta Kouvari, Bastien Mennecart, Maéva Orliac et bien d'autres. Un petit coucou à Antoine Zazzo, que je ne pensais pas retrouver au Muséum après l'avoir rencontré dans les steppes mongoles. Un merci également à Thomas Cucchi pour avoir remis des pétreux sur mon chemin quand je pensais en avoir fini avec eux (on n'en est jamais débarrassé, et puis je les aime bien quand même). Et pardon à celles et ceux que j'oublie certainement.

Another very special thanks for Jamie MacLaren, first met in a dark basement of the Galerie de Paléontologie, but soon became a recurrent interlocutor when talking about fossil tapirs and rhinos. Many thanks for your help, the numerous exchanged mails and the passionate discussions about metacarpals, centre of mass and other functional stuff. I hope that, despite your newfound passion for mosasaur skulls, we will be able to talk about Perissodactyla and collaborate again!

En plus de l'encadrement quasi-idéal (n'exagérons rien) dont j'ai bénéficié pendant trois ans, j'ai également eu la chance d'être accueilli dans un laboratoire rempli de personnes d'une grande qualité scientifique et humaine. Merci donc à Fabienne, Anick, Emmanuelle, Anthony, Marc et à toutes celles et ceux que j'oublie et qui m'ont permis de me sentir moins déraciné au milieu de la capitale. Un merci particulier à Pauline pour les discussions scientifiques et sociétales, ainsi que quelques belles manifestations ensemble ! Merci également à Christine pour les nombreux fous rires tous ensemble à la cantine, entrecoupés de discussions myologiques ou de passages en allemand quand Alex ne voulait pas que les « petits » entendent ce qu'elle avait à dire… Un grand merci aux « ancien·ne·s » thésard·e·s qui

partaient quand j'arrivais : Ameline qui m'a permis de trouver un appartement sans même chercher (un bien précieux à Paris !), Marion pour m'avoir fait visiter quelques coulisses du Muséum à New York, Léo pour les précieux conseils sur R et ses travaux qui m'ont beaucoup trop servi de modèle.

À plus petite échelle, je ne peux bien sûr pas oublier l'équipe dans l'équipe que forme le groupe GRAVIBONE autour d'Alexandra. Que de bons moments à parler de graviportalité, de dinosaures et de grosses bêtes, ou juste à partager une galette des rois ou un verre bien mérité. Ronan, le grand dinosaurologue, merci pour ta sympathie et ta bonne humeur contagieuse. Un immense merci également à Arnaud pour tous les coups de main sur les outils 3D, ainsi que les nombreux fous rires avec Raphaël. Sans oublier bien sûr Andréa et le camarade Alexis, parmi les premiers arrivés et à essuyer les plâtres sur le scanner et la photogrammétrie, ainsi que Clémentin et Kinga qui ont passé quelques heures à reconstruire des modèles 3D. Une pensée aussi pour les M1 et M2 croisé·e·s pendant 3 ans : Manon, Lou, Adrien, Kévin, Morgane, Charlène, Guillaume. Et bien sûr Camille, la seule autre personne que je connaisse à avoir fait son M2 sur les pétreux de mouton : rien que pour ça, nous sommes liés, désormais ! Merci pour tous les coups de main réciproques sur R, les manifs et les fermetures de bars avec Colline !

Le Muséum est une grande fourmilière dans laquelle j'ai pu croiser quantité de gens adorables avec qui discuter et/ou blaguer a toujours été un plaisir. Tour d'horizon non-exhaustif (que les personnes oubliées ici me pardonnent) : Kévin, intarissable sur l'allométrie, la morphométrie et le pommeau, Morgane « la gauchiste », Jordan, avec qui j'ai virtuellement partagé un bureau pendant 5 mois, Anne-Sophie que j'ai retrouvé dans le bureau voisin après une première rencontre en 2010 en fouille dans le Vaucluse (le monde est petit), Mathilde et Valentine qui ont supporté mes crises de rage sur R au bâtiment 139, Léa et Margot pour les bons moments à l'ICVM et dans les brasseries tchèques. Sans oublier les autres thésard·e·s de l'ED 227 pour la super semaine passée à Concarneau. Une pensée bien sûr aux camarades en lutte contre la LPPR que j'ai pu croiser dans les AG du muséum : on commençait à tenir quelque chose avant que la pandémie ne nous coupe l'herbe sous le pied, mais le combat continue !

Enfin, les collègues de fortune et d'infortune, la clique de thésard·e·s de FUNEVOL, toujours là pour débugger un script, boire une bière ou juste se plaindre et râler tous ensemble (notre pêché mignon). Fanny et ses oiseaux, coincée entre les « anciens » et les « nouveaux » thésards, avec qui on s'est trop souvent lamenté sur l'efficacité de nos ordinateurs ; Colline et ses renards, la transfuge d'archéozoo et son milliard de têtes de chiens dans une poubelle ; Maxime et ses vomis de lézard, toujours présent pour déconner et réciter les répliques de Kaamelott ou du Palmashow en boucle ; Rohan et son poisson à pattes, constamment à l'affût d'une nouvelle occasion de se blesser ou de sortir par une fenêtre. On

a râlé et stressé mais c'était quand même 3 belles années, non ? Bien sûr, un grand merci et beaucoup de courage à la génération d'après : Ana, Marjorie, Julie, Priscilla, et Laurie tout récemment, ça va bien se passer. Bien se passer. Un énorme merci également à Cyril et Romain, à qui ça n'a visiblement pas servi de leçon de nous voir galérer et qui ont quand même décidé d'aller en thèse. C'est audacieux. L'entraide permanente autour des pauses-café, il n'y a rien de mieux, merci à vous. Et enfin, un merci tout particulier au camarade Rémi, pour ces échanges infinis sur tous les sujets ou presque, jusqu'à en arriver à la conclusion que « en fait, tout ce qu'on fait est faux ». Promis, j'irai une dernière fois aux Korrigans avant de partir, je te dois bien ça pour toute l'aide fournie pendant 3 ans !

Et maintenant, la vie d'avant la thèse. Pour toutes les personnes à qui j'ai dit « là, je cherche une thèse » pendant environ 5 ans, souvent sans trop y croire moi-même. Merci d'y avoir cru (ou fait semblant d'y croire). Un grand merci à l'équipe du Musée du Grand-Pressigny, avec qui j'ai passé 2 saisons formidables et où j'ai tant appris. Michel, Frédéric, Laure-Anne, Valérianne et toute l'équipe, mille mercis. De même, une pensée pour l'équipe de la Maison de la Dame de Brassempouy, pour cette autre année riche (et intense) au pays de l'armagnac. Lionel, Estéle, Coralie, Ophélie, Johanne, Christophe, Ludivine, Mathieu, David et celles et ceux que j'oublie, à très vite en Chalosse.

Une pensée toute particulière va à Jean-Luc Guadelli, mon mentor en anatomie comparée, en réflexion et rigueur scientifique. Que de bons moments à parler anatomie crânienne, os pétreux, Préhistoire, puis à dériver sur les guerres napoléoniennes, la géopolitique mondiale et l'eau-de-vie de prune maison. Que de galères à Pradayrol, que de bases de données et mails perdus, que de pannes de voiture. Mais que de bons souvenirs et de leçons apprises. Merci pour tout.

De même, mon passage à Lyon m'a permis de rencontrer Gildas Merceron, que je remercie pour son soutien et son enthousiasme qui n'ont pas diminué depuis 2012. Comment ne pas évoquer également Jean-Baptiste Fourvel, qui m'a quasiment tout appris du squelette postcrânien à l'été 2010 lorsque l'on triait les milliers de restes de lièvre du Coulet des Roches ? Et tant que j'en suis à évoquer le sud de la France, un grand merci à Evelyne Crégut pour son soutien et sa gentillesse, ainsi qu'à Jean-Philip Brugal, qui a tant essayé de me trouver un sujet de thèse (en vain). Je n'oublie pas non plus Antigone Uzunidis, rhinophile du Pléistocène avec qui nous aurons beaucoup à échanger maintenant que cette thèse est finie !

Dix années à Bordeaux laissent des traces et des amitiés. Merci donc à Antoine « le suidologue » et Sohee pour le soutien et l'enthousiasme sans faille, et les discussions concernant les pétreux pendant que Lucien et Lise hurlaient autour (pas merci pour les pertes auditives, cela dit). Mathieu, camarade parmi les camarades, merci de continuer la lutte ! Pierre, le binôme de toujours, merci pour ton amitié et tous ces quizz remportés grâce à ta culture musicale infinie. Guillaume, Harry, Gwenn, les potes de

lycée qui se retrouvent tous à Paris 15 ans plus tard, ça ferait vraiment un très mauvais scénario de film français mais dans la vraie vie, c'est une situation plutôt sympa !

Comment ne pas évoquer les copains du net rencontrés sur NDM et devenus pour certains des copains dans la vraie vie ? Merci à vous tous pour ces 15 ans de vie virtuelle et pourtant bien réelle, et pour tous les délires et les dramas vécus. Le lécheur de cailloux a enfin fini sa thèse, ilménite à tous. Et un merci particulier à Keryan « Xeto(s) » Didier et à Arnaud « Nens » Paris respectivement pour l'hébergement lors de mon entretien pour l'obtention de la thèse et lors de ma mission à Toulouse. De même, un immense merci à Raphaël Pezet et toute l'équipe de Pix'n Love de me permettre d'écrire des bouquins sur les jeux vidéo, et me changer les idées quand je sature des rhinocéros.

Cyrielle et Cyril, mon couple de lithiciens préféré, quelle chance et quel plaisir de pouvoir compter sur votre amitié depuis toutes ces années. Axelle et Corentin, mon couple de paléontologues préféré, quelle chance et quel plaisir de… Mince, je me répète. Reprendre un M1 après un M2 n'était pas la meilleure décision de ma vie, sauf sur un point : je ne vous aurais sans doute jamais rencontrés et la vie aurait été bien moins riche sans cela. Je n'oublie pas non plus Jean-Michel, mon binôme lyonnais toujours là pour se taper des barres ou soutenir quand ça va mal. À vous cinq, enfin, merci d'avoir fait une thèse avant moi : la mienne aurait été bien plus douloureuse à réaliser sans modèles à suivre !

Monique et Gérard, Audrey et Max, Elodie et François (et désormais Anatole), quel bonheur de vous avoir comme belle-famille. Merci à vous tous pour votre soutien depuis toutes ces années.

Daniela, Antoine, Lucile, les meilleurs. Je ne sais même pas quoi écrire tellement on s'est tout dit depuis plus de 10 ans. Les mots sont trop limités pour exprimer ces choses-là. Merci d'avoir été là dans les instants les plus joyeux comme les plus tristes. Vous êtes irremplaçables.

À ma famille enfin. Tout a commencé par cet os de poulet déterré dans le jardin quand j'étais gamin. Il doit toujours être quelque part dans un carton. Depuis, une seule idée en tête : devenir paléontologue. Maman, merci d'y avoir toujours cru même si tout ça doit te sembler un peu abstrait. Cyril, je suis tellement fier de toi. Tu as tenu bon dans les pires moments. Tu vas tout déchirer.

Et Lysianna, bien entendu. Tu as déjà tout dit dans ta propre thèse. Tu sais déjà tout. Une fois n'est pas coutume, je vais juste me taire.

Bonus : un extrait de la bande-son de cette thèse. Car les longs voyages, les sessions de scans, de reconstruction 3D, de pose de points et de débuggage sous R auraient été un calvaire sans tous ces artistes dans les oreilles. Merci donc à Beirut, Ben Harper, Bérurier Noir, Chicago, Dooz Kawa, Eminem, Gringe, Jean Ferrat, Kenji Yamamoto, Kikesa, Koji Kondo, Lomepal, Lorenzo, Megadeth, Michael Jackson, Mick Gordon, Nekfeu, Orelsan, Pantera, Radiohead, Slayer, Soundgarden, Stupeflip, Tenacious D, The Hu, The Smashing Pumpkins, Tool, Yes et bien d'autres… Sans oublier The Stagnants, le meilleur groupe du monde.

Résumé étendu

Chez les vertébrés terrestres, les os des membres sont des organes d'une importance primordiale qui assurent le soutien du corps et sa locomotion. Leur forme est influencée par des facteurs structurels et historiques, ainsi que des contraintes fonctionnelles, notamment la nécessité de résister aux forces dues à la gravité. Cette contrainte de poids est très élevée chez les mammifères quadrupèdes pesant plusieurs tonnes, ce qui entraîne des modifications morphologiques des membres afin d'éviter l'écrasement des os. Les mammifères quadrupèdes présentant de telles modifications architecturales de leurs membres dues à une masse élevée ont été appelés « graviporteurs » (par opposition à « coureurs »). La graviportalité telle que définie historiquement est marquée par un allongement du stylopode et un raccourcissement de l'autopode, une masse corporelle de plusieurs centaines de kilos, des membres verticaux redressés (en colonne), des os larges et robustes, des pieds larges avec des coussins adipeux épais, des foulées longues et une incapacité à galoper. Cependant, de nombreux groupes de quadrupèdes ne présentent pas l'ensemble de ces critères et soulignent la difficulté de donner à la graviportalité une définition précise qui pourrait être utilisée de manière générale sur n'importe quel taxon. De nombreuses lignées d'amniotes présentent une tendance évolutive vers une augmentation de la masse et de la taille du corps au cours du temps, notamment la superfamille des Rhinocerotoidea appartenant à l'ordre des Perissodactyla. Bien que seulement représentés de nos jours par 5 espèces, les Rhinocerotoidea formaient un groupe à l'évolution florissante au cours du Cénozoïque, représenté par des dizaines de genres fossiles parfois documentés par des centaines d'individus. Les Rhinocerotoidea variaient de moins de 100 kg chez *Hyrachyus*, le plus ancien représentant de la superfamille, à plus de 10 tonnes chez les Paraceratheriidae géants. Entre ces deux extrêmes, plusieurs lignées ont montré des augmentations convergentes de la masse corporelle, avec de nombreuses espèces dépassant une tonne ou plus. En plus de cette variation de masse, les Rhinocerotoidea présentent des fluctuations de leur organisation corporelle générale (de « coureur » à « graviporteur »), de leur degré de brachypodie (ou gracilité, c'est-à-dire une réduction de la longueur relative de leurs membres), de leurs affinités écologiques (milieux ouverts, fermés ou modes de vie présumés semi-aquatiques), de leur nombre de doigts du membre antérieur (main tétradactyle ou tridactyle), ou de la présence de cornes. Pour toutes ces raisons, les Rhinocerotoidea apparaissent donc comme un groupe pertinent pour étudier les relations entre la masse corporelle et la forme des os des membres, et comment une même masse corporelle peut être associée à différentes formes corporelles. Ce travail propose donc d'explorer la variation de forme des os longs des membres chez les Rhinocerotoidea par rapport à la masse et aux proportions du corps au cours de leur histoire évolutive afin de mieux comprendre comment le squelette se modifie pour répondre aux exigences fonctionnelles d'une locomotion coordonnée et au soutien d'une forte masse. Pour ce faire, j'ai étudié les six os du stylopode et du zeugopode (humérus,

radius, ulna, fémur, tibia, fibula) en sélectionnant plusieurs centaines d'ossements de rhinocéros modernes et fossiles dans une vingtaine de collections. Ces ossements ont été numérisés en 3D afin de procéder à l'analyse de leurs variations de forme via la morphométrie géométrique 3D, une approche permettant de quantifier et visualiser les différences morphologiques entre des objets à l'aide des coordonnées de points-repères (landmarks) placés à leur surface. Après une analyse Procrustes permettant de supprimer les effets d'échelle, de rotation et de translation, les coordonnées des landmarks ont été utilisées comme base pour les différentes analyses menées au cours de ce travail (analyses en composantes principales, régression multivariée, test d'intégration et « Two-Block Partial Least Squares », ANOVA Procruste).

La forme des os des rhinocéros ayant été peu explorée jusqu'à présent dans une optique morpho-fonctionnelle, j'ai tout d'abord étudié les os longs des cinq espèces actuelles afin de comprendre comment la forme varie entre ces taxons en fonction de la taille, de la masse corporelle et de la phylogénie. Mes résultats indiquent que les cinq espèces présentent des différences morphologiques importantes en fonction des os considérés. L'humérus et le fémur présentent des différences interspécifiques notables entre les rhinocéros africains et asiatiques. La masse corporelle a un effet significatif sur la forme de ces deux os. Le radius et le cubitus sont plus fortement corrélés à la masse corporelle également. Alors que le tibia présente une variation de forme liée à la phylogénie et à la masse corporelle, la fibula présente une très grande variation intraspécifique. J'ai pu mettre en évidence trois morphotypes distincts de forme osseuse, qui apparaissent en fonction de la phylogénie : un morphotype africain (rhinocéros blanc [*Ceratotherium simum*] et rhinocéros noir [*Diceros bicornis*]), un morphotype « *Rhinoceros* » (rhinocéros indien [*Rhinoceros unicornis*] et rhinocéros de Java [*Rhinoceros sondaicus*]) et un morphotype « *Dicerorhinus* (rhinocéros de Sumatra [*Dicerorhinus sumatrensis*]). L'augmentation de la masse corporelle chez les cinq espèces existantes est marquée par une augmentation de la robustesse générale des os, des épiphyses d'apparence plus larges et robustes, des attaches plus prononcées pour les muscles extenseurs et un développement des diaphyses. L'influence de la masse corporelle semble également s'exprimer de manière inégale sur les différents os : la variation de forme du zeugopode, notamment pour le membre avant, suit davantage la variation de masse que le stylopode. Cette première étude souligne que les caractéristiques morphologiques liées à l'augmentation de la masse corporelle ne sont pas similaires entre les rhinocéros et les autres mammifères lourds tels que les éléphants et les hippopotames, ce qui suggère que la contrainte de poids peut entraîner des réponses morphologiques différentes selon les taxons.

Ce premier volet de mon travail ayant mis en avant les variations observables os par os, j'ai souhaité compléter ces résultats par une approche plus globale de la covariation de forme des os entre eux. En

effet, le squelette appendiculaire des tétrapodes est une structure particulièrement intégrée (c'est-à-dire présentant des covariations entre ces différentes parties) en raison de l'origine commune du développement ou de contraintes fonctionnelles similaires exercées sur ses éléments. Parmi ces contraintes, la masse corporelle influence fortement son intégration, mais son effet sur la covariation des formes a rarement été abordé chez les mammifères, en particulier chez les taxons lourds. Ce deuxième volet de ma thèse explore donc les schémas de covariation des os longs chez les rhinocéros actuels et leur lien avec la masse corporelle. J'ai étudié la covariation de la forme des os des membres à la fois entre les espèces et au sein de celles-ci. Mes résultats indiquent que le squelette appendiculaire des rhinocéros forme une structure fortement intégrée. Au niveau interspécifique, la covariation de forme est à peu près similaire entre toutes les paires d'os. Les zones anatomiques covariantes sont principalement les insertions musculaires liées aux mouvements de flexion et d'extension. L'intégration du membre antérieur semble plus élevée et plus liée à la masse corporelle que celle du membre postérieur, ce qui suggère une spécialisation pour le soutien du poids. L'intégration des éléments du stylopode (humérus et fémur) ne semble pas liée à la masse corporelle, ce qui suggère un effet plus important des facteurs de développement communs sur leur degré de covariation. À l'inverse, la covariation des os du zeugopode semble davantage associée à la masse corporelle, en particulier pour la paire radius-ulna. La fibula covarie faiblement avec les autres os, en particulier chez les espèces n'appartenant pas au genre *Rhinoceros*, ce qui pourrait représenter un cas de parcellisation due à une dissociation fonctionnelle entre les os des membres postérieurs. L'exploration des patrons d'intégration au niveau intraspécifique met également en évidence un effet plus important de l'âge que de la masse corporelle individuelle sur la covariation des formes au sein de *C. simum*. Ce second volet de mon étude vient donc appuyer les observations faites sur les os individuels, mais également l'hypothèse d'un lien marqué entre une forte masse corporelle et un niveau d'intégration élevé.

Les deux premiers volets de cette étude m'ont permis d'appréhender la variation de forme des os longs chez les rhinocéros actuels. Cependant, ces cinq espèces modernes ne reflètent que très partiellement la diversité de forme, de taille et de poids rencontrées parmi les Rhinocerotoidea fossiles. Les membres de la superfamille des Rhinocerotoidea présentent une grande variété de masse corporelle, de taille et de proportions, allant de petites formes coureuses proches des tapirs à des espèces géantes ou à pattes courtes (c'est-à-dire brachypodes). J'ai donc étendu mon approche à l'ensemble de la superfamille, afin d'explorer la variation de forme des os des membres au sein des Rhinocerotoidea et sa relation avec la masse, la taille et les proportions du corps. Compte tenu des altérations taphonomiques présentées par certains fossiles (cassures, déformations), l'approche de morphométrie géométrique jusqu'ici appliquée sur des os complets a été étendue à des portions d'os afin d'inclure le maximum de taxons présentant une masse élevée.

La variation de forme des trois os du membre antérieur (humérus, radius et ulna) a été comparée avec la taille centroïde, la masse corporelle moyenne et l'indice de gracilité calculé sur le troisième métapode (largeur divisée par longueur). Mes résultats indiquent une augmentation générale de la robustesse et un développement des insertions musculaires en association avec une masse corporelle et une taille élevées. La taille centroïde apparaît comme un indicateur pertinent pour estimer la masse corporelle. La taille centroïde et la gracilité ne sont, en revanche, pas toujours corrélées avec la forme selon l'os considéré. J'ai ainsi observé de fortes différences entre la variation de forme du stylopode et du zeugopode. La forme de l'humérus est influencée à la fois par la masse, la taille et la gracilité tout en restant fortement contrainte par l'histoire évolutive des Rhinocerotoidea. Inversement, les formes du radius et de l'ulna sont principalement liées à la gracilité, soulignant un effet plus important de la répartition de la masse dans le corps que de la masse elle-même. En outre, la partie proximale de l'ulna varie de la même manière que l'humérus, ce qui semble indiquer que l'articulation du coude pourrait constituer une structure fortement covariante. Ces résultats confirment également le caractère unique des Paraceratheriidae géants parmi les Rhinocerotoidea, présentant un mélange peu commun de variation de forme liée à une masse corporelle élevée tout en conservant une construction coureuse des membres antérieurs, remettant en question l'opposition classique entre ces deux extrêmes.

Le même cadre analytique a été appliqué sur les os du membre arrière (fémur, tibia, fibula), dont le rôle fonctionnel diffère du membre avant (ce dernier étant davantage impliqué dans le support du poids et le ralentissement de l'allure lors de la locomotion, alors que le membre arrière a un rôle propulseur). Des résultats similaires à ceux du membre avant ont été obtenus sur le membre arrière. Au-delà d'une augmentation commune de la robustesse et du renforcement des insertions musculaires chez les espèces lourdes, la forme du stylopode et du zeugopode ne suit pas les mêmes patrons de variation. Tout comme l'humérus, la forme du fémur est intimement liée à la fois à la masse, la taille et la gracilité, tout en restant contrainte par l'histoire évolutive de la superfamille. À l'inverse, la forme du tibia est davantage associée aux variations de gracilité, dans une moindre mesure que sur le membre avant. La forme de la fibula, en revanche, semble là encore dominée par de fortes variations intraspécifiques malgré une influence du degré de gracilité. En outre, il apparait que la partie distale du fémur présente des patrons de variations similaires à ceux observés sur le tibia, indiquant une probable covariation marquée des éléments de l'articulation du genou.

À l'issue de ces différents volets, l'étude des patrons de variation de la forme des os longs chez les Rhinocerotoidea révèle un signal complexe, et souvent double, lié à la masse corporelle et aux proportions du corps en général. D'une part, il apparaît clairement que la forme varie en partie en fonction de la masse corporelle chez les Rhinocerotoidea. Des patrons communs très nets apparaissent, tel que

l’augmentation de robustesse des os, ainsi que le renforcement des insertions pour les muscles extenseurs. Ces deux modifications visent à résister aux contraintes de masse, particulièrement en l’absence de membres columnaires au sein de ce groupe. D'autre part, la diversité de la forme des os par rapport aux proportions du corps met en évidence plusieurs façons de soutenir une masse corporelle élevée au sein de la superfamille. Des différences existent entre le membre avant et le membre arrière, probablement liées à leurs rôles fonctionnels distincts. Cependant, les différences de variation de forme sont bien plus prononcées entre les éléments du stylopode et du zeugopode. Alors que la forme du stylopode semble directement associée à la masse corporelle, celle du zeugopode semble davantage liée à la répartition de cette masse dans le corps et à la position du centre de gravité de l’animal. Ainsi, une même masse corporelle peut être associée à différentes formes d'os et, à une échelle plus large, à différentes constructions de membres selon le groupe considéré. Inversement, on peut observer une similitude de forme chez les taxons présentant une construction distincte. Toutes ces observations au sein des Rhinocerotoidea questionnent ainsi le concept même de graviportalité, dont la définition ne permet pas de couvrir la diversité morphologique de ce groupe. Les rhinocéros apparaissent comme un compromis entre la nécessité de soutenir une forte masse corporelle et le maintien d’une locomotion relativement rapide. En dehors de leur forte masse, ils ne présentent quasiment aucun autre caractère associé traditionnel aux animaux graviporteurs. La graviportalité ayant été définie principalement sur la base du plan architectural des éléphants, lequel semble être une exception au sein des mammifères lourds, elle ne peut embrasser toute la diversité morphologique présente dans d’autres groupes présentant une forte masse comme les rhinocéros. Il apparait donc plus pertinent de rechercher quelles sont les caractéristiques rencontrées de manière répétée au sein de divers taxons présentant une masse corporelle élevée avant de définir un concept général tel que la graviportalité.

Chapter 1

Introduction and objectives

Bones are undoubtedly the most emblematic organs of vertebrate animals, and the ones that confer them most of their biological specificities. These mineralized organs fulfil numerous vital functions both at microscopic and macroscopic scales. At the microscopic scale, bones constitute a stock of minerals constantly renewed throughout life and their marrow produces essential blood components like erythrocytes and leukocytes (Currey, 2006; Barone, 2010a). At the macroscopic scale, bones provide protection for inner vital organs (e.g. brain, heart or lungs) and structure the whole body allowing notably weight support and active locomotion (Currey, 2006; Barone, 2010a). Together with muscles, tendons, cartilages and ligaments, they form a complex musculoskeletal system of paramount importance for the subsistence of vertebrates (Hildebrand, 1974). Because of their mineral composition, they are, with teeth, among the organs that are best preserved over long-time periods through the fossilization process, making them essential clues for reconstructing the biology and evolutionary history of vertebrates in deep time.

Like for all other organs, bone shape results from the combination of three categories of factors that constrain and drive its variation (Seilacher, 1970, 1991; Gould, 2002; Cubo, 2004). First, bones being submitted to physical and chemical principles, their shape is necessarily constrained by **structural factors**. These factors, first explored by Thompson (1917) and enhanced latter by Gould et al. (1979) can be defined as "*processes of direct physical causation during development and their morphological expression*" and "*physically or geometrically necessary consequences (by-products, spandrels) of other changes*" (Cubo, 2004). Structural factors act as a physical bound limiting the range of morphological variation. Second, bone shape is constrained by **historical factors**. Members of a same taxonomic group will be affected by "phylogenetic inertia" (Blomberg & Garland, 2002), i.e. the fact that they share inherited genetic processes making the shape variation dependant of their evolutionary history. As stated by Blomberg & Garland (2002), "*once organisms begin to evolve in a particular direction, they tend to keep evolving in the same direction*". Historical factors therefore act as another limit of the range of morphological variation. Finally, bone shape is also submitted to **functional factors**. Bones are involved in one or more essential functions in the organism, like feeding, support of body weight or locomotion in different environments (terrestrial, arboreal, aquatic, aerial, subterranean. Moreover, bone itself is a living tissue that undergoes constant remodelling across lifetime under environmental constraints to keep ensuring these required functions (Lanyon et al., 1982; Hadjidakis & Androulakis, 2006; Currey, 2006). Functional factors constitute therefore a third limit to bone morphological variation.

In tetrapods, bones constituting limb elements (forming, with girdles, the appendicular skeleton) play three main roles in shaping and supporting the body, as well as providing an efficient locomotion in a given environment. Furthermore, limb bones are intimately related to each other through joint caps

firmly maintained by strong ligaments, but also related to muscles attached to them with tendons and ensuring movements (Hildebrand, 1974; Polly, 2007). Limbs constitute a system of joints and levers that must resist the stresses exerted by static and dynamic loads during standing and locomotion phases (Hildebrand, 1974; Biewener, 1990). Contrary to flying or swimming vertebrates that undergo different external forces (respectively, air lift and buoyancy), exclusive terrestrial quadrupeds are subject to one dominant external constraint: gravity (Ross, 1984). In this context, the heavier a terrestrial quadruped, the greater the strain on its bones (Ross, 1984; Lanyon, 1992). Therefore, the shape of the limb bones in terrestrial quadrupeds is necessarily highly related to body mass and locomotor constraints (Hildebrand, 1974; Polly, 2007; Biewener & Patek, 2018).

On the concept of graviportality

Repeated modifications of the body plan and of the musculoskeletal system related to an increase in body mass among mammalian quadrupeds have been studied and described by authors for more than a century. These observations led them to characterize tall and heavy mammals as "graviportal" (Hildebrand, 1974; Polly, 2007). However, as obvious and intuitive as it may seem, the concept of "**graviportality**" proved to be difficult to define precisely and objectively. This term was first introduced a century ago by Gregory (1912), based on an idea of Osborn (1900). The very first definition of graviportality was broad and mainly based on limb segment proportions, graviportal taxa being defined as "*heavy-bodied animals with long proximal and short distal limb segments*" (Gregory, 1912) (Figure 1). Although the term "animal" was quite unprecise, Gregory and Osborn only considered mammals in their framework. Together with limb ratios, other anatomical and locomotor criteria were also involved in this definition: body mass of several hundreds of kilograms, straightened vertical limbs (i.e. columnar), large and strong bones, large feet with enlarged adipose cushions, reduced phalanges, long strides associated with the inability to gallop. The archetypal group fulfilling all these criteria – and on which the definition was mainly constructed – is proboscideans, and particularly modern elephants.

Gregory considered graviportality as opposed to "**cursoriality**", which characterizes lightly-build mammalian quadrupeds with long and thin limbs associated with the ability to run or gallop, a category of which horses and many ungulates are the most emblematic representatives. Gregory used a functional and biomechanical approach to discriminate the limb bones of cursorial and graviportal taxa, elaborating his definition both on the general construction of the limbs and on the shape of its components, i.e. long bones and metapodials. Using different ratios between limb segments, Gregory sharpened his classification introducing two intermediate categories named "**mediportal**" and "**subcursorial**", defined *a posteriori* following the different ranges of ratio he obtained rather than on precise anatomical features. A subcursorial mammal should be understood as possessing moderate cursorial adaptations

with good running performances (e.g. felids and canids), whereas mediportal animals show conformations meeting both the heavy weight bearing aspect and running capacities (e.g. suids, tapirs). Osborn (1929) further developed these locomotor categories in his monography on American brontotherids, using this morphofunctional and anatomical framework to make locomotor inferences, not only on these heavy Eocene-Oligocene perissodactyls but also on various other quadrupeds.

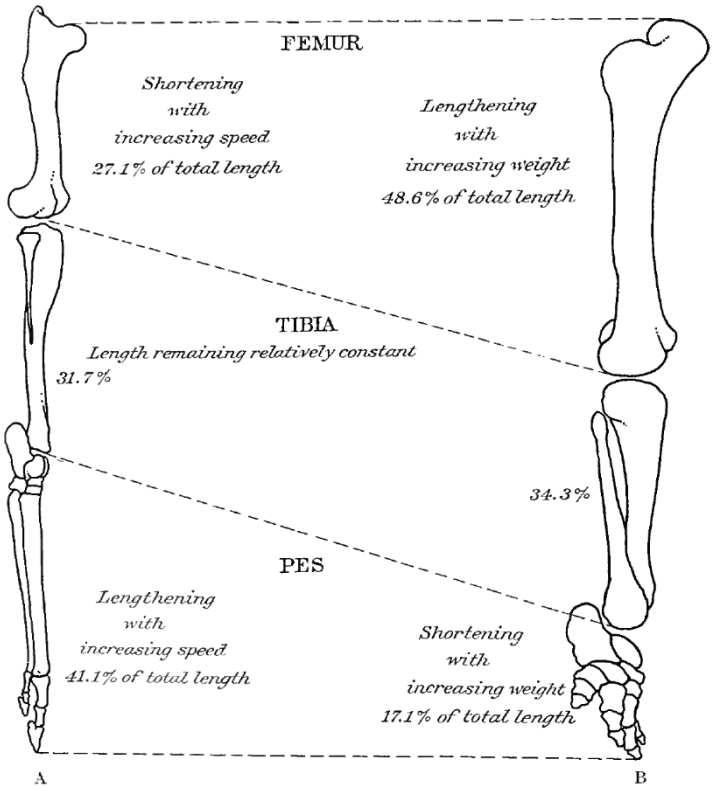

Figure 1: Theoretical changes in the relative length of hind limb segments between cursorial (A, *Neohipparion*) and graviportal taxa (B, *Mastodon*). After Osborn (1929), p. 734.

However, these pioneer works, despite their huge impact on subsequent morphofunctional considerations, were based on a reduced taxonomic diversity among mammals and mixed heterogeneous considerations to define these categories. Graviportality – and, similarly, cursoriality – was defined simultaneously on body proportions, limb construction, body weight, gait and some additional anatomical features. If some archetypal animals like elephants and horses obviously fall in one of these categories, most mammalian quadrupeds challenge this classification by displaying only part of the features associated with each category.

Despite some limits, these locomotor categories have largely been used in anatomical, functional and morphological works on mammalian quadrupeds, with few criticisms or attempts to clarify their definition and their bounds. Maynard Smith and Savage (1956) refined this framework by considering only two main criteria to explain the variation observed in mammalian skeletons: the mechanical advantage of a muscle (i.e. the lever arm on which it attaches) and the gait of an animal. This apparent

simplification led to terminological changes, like with the category “semi-graviportal”, in which were placed groups previously considered as mediportals (like tapirs). Later, Hildebrand (1974) introduced an arbitrary body mass of 900 kg beyond which species should be considered graviportal, although without justifying this threshold by any functional or anatomical criterion. This framework developed on mammals was then transferred to the study of Dinosauria by Coombs (1978). Some dinosaurs, like sauropods, display gigantic proportions unrivalled among terrestrial animals and, consequently, are extreme examples of graviportality. Coombs therefore used cursorial and graviportal categories to study Dinosauria, trying to classify these animals without really questioning the categories themselves or their accuracy outside Mammalia.

More recently, Carrano (1999) tackled this problem and tried to rethink those categories to overcome the differences between clades and the difficulty to precisely define intermediate conformations. He therefore replaced the classic discrete categories by a multivariate continuum of locomotor habits, ranging from graviportal to cursorial and based on bone and muscular insertion measurements (Figure 2). These measurements were chosen to be “*biomechanically relevant*” and performed on both mammals and dinosaurs. However, given the high disparity in body construction between these clades, this questions the pertinence of mixing such different groups. Measurements were restricted to hind limb elements, which display a very different organisation and role between mammals and dinosaurs. They do not support the same proportion of the global mass and the presence of a long tail in most Dinosauria involves major architectural changes in the appendicular skeleton (Henderson, 2006). This approach, despite its novelty and originality, did not manage to bring a conclusive answer to the concept of graviportality and its definition. One of the most recent progresses relative to this aspect has been brought by Goussard (2009) in his unpublished study of the autopodium of sauropodomorphs. Goussard proposed a new definition of graviportality based on three criteria: 1) columnar limbs (i.e. *sensu* Osborn) with mandatory quadrupedy; 2) a reduction of the distal segments of the limbs relatively to the proximal ones; 3) a deep modification of the morphology of the anterior and/or posterior autopodium relatively to the plesiomorphic condition of the considered group (Goussard, 2009). This enhanced definition, developed mainly on the observation of Sauropodomorpha, may, however, be subject to exceptions when applied to other clades not directly related to Dinosauria.

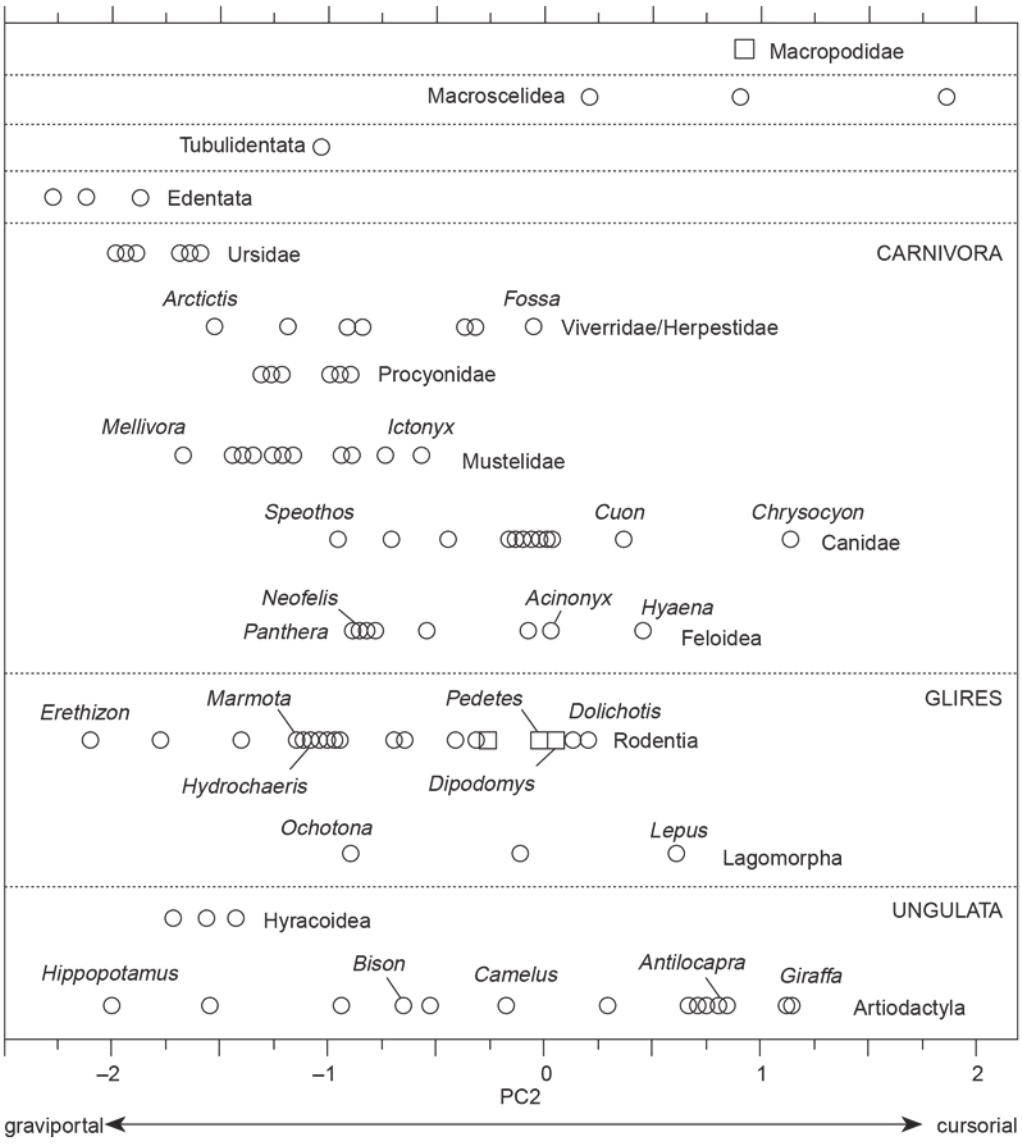

Figure 2: Distribution of quadrupedal (circles) and bipedal (squares) mammal genera along a "graviportal-cursorial" gradient following hind limb measurements. Some small crawling classified as "ambulatory" by Osborn (e.g. canids or lagomorphs) are considered here as "graviportal" or “cursorial”. After Carrano (1999), p. 33.

Consequently, classic discrete locomotor categories remain largely used nowadays in their most “intuitive” way to decipher broad differences between clades along a graviportality-cursoriality gradient, but without really questioning their definition (e.g. Alexander & Pond, 1992; Stein & Casinos, 1997; Becker, 2003; Polly, 2007; Becker et al., 2009; Scherler et al., 2013; Hogervorst & Vereecke, 2014; Houssaye et al., 2016; Stilson, Hopkins & Davis, 2016; Houssaye, Fernandez & Billet, 2016; MacLaren & Nauwelaerts, 2016). More surprisingly, some authors transferred these concepts developed on quadrupeds to the field of anthropology, leading them to consider humans as possessing a graviportal hind limb (Bechtol, 1992): a relevant classification given the general architecture of the human body, but quite unusual and counterintuitive in the classic framework of Gregory and Osborn. All of these

observations demonstrate the difficulty of giving graviportality a precise definition that could be used broadly on any taxon.

Convergence towards high body mass: the "Cope-Depéret's rule"

In addition to discussions about the concept of graviportality, the tendency among many amniote lineages to exhibit an increase in body size through time has been largely documented and studied. This multiple evolutionary convergence towards high body size is often referred to as the "Cope's rule", despite the fact that no clearly formulated rule was present in the work of Cope (1887) (Stanley, 1973; Polly, 1998). Actually, Depéret (1907) was the first, a few decades later, to clearly formalize this distinct trend using both his own observations and the works of Cope – leading some authors to rather talk of "Cope-Depéret" or "Depéret's rule" (Bokma et al., 2016). From there, many experimental works showed that, despite some exceptions (Gotanda et al., 2015), this tendency can indeed be observed among many groups of amniotes (Laurin, 2004), particularly in mammals (e.g. Stanley, 1973; Alroy, 1998; Finarelli, 2007; Raia et al., 2012; Baker et al., 2015; Bokma et al., 2016). Despite many robust examples of this evolutionary pattern, no consensus currently exists concerning the evolutionary mechanisms sustaining it. Some authors have considered this trend as the result of individual variations actively driving the evolution of a whole lineage towards a high body size (Kingsolver & Pfennig, 2004), whereas others have suggested that this trend was more passively constrained (McShea, 1994), notably through ecological specialization (Raia et al., 2012). At a smaller scale, it is likely that an increase of body size is linked to differences in developmental rates (i.e. developmental heterochrony) although these processes have not been extensively investigated, especially in mammals (McKinney, 1986; McKinney & McNamara, 1991; Hone & Benton, 2005; McNamara, 2012).

Different tetrapod lineages display a convergent trend towards high body mass. The most famous examples can be found among Dinosauria, with giant sauropods being considered as the heaviest terrestrial animals that ever existed, as well as among mammal lineages, such as in Proboscidea, some Artiodactyla and Canidae, and in Perissodactyla (Stanley, 1973; Alroy, 1998; Finarelli, 2007; Raia et al., 2012).

Perissodactyla

The order Perissodactyla appears as one of the numerous mammal groups containing some taxa that were considered as graviportal (Osborn, 1929; Guérin, 1989; Prothero & Schoch, 1989; Alexander & Pond, 1992). This clade was created by Owen (1848) grouping together hoofed mammals possessing an odd number of digits. This observation was completed later by Marsh (1884) who observed that the symmetry axis of the Perissodactyla autopodium coincides with the central digit (III), a condition now viewed as plesiomorphic among Mammalia (Antoine, 2002). Marsh proposed to use the term

"Mesaxonia" to define this order, which is now considered as a synonym of Perissodactyla. The first undisputed representatives of this order appeared around 56 Ma around the Paleocene-Eocene transition in the northern hemisphere (Gingerich, 2006).

Although the phylogenetic relations within the order have been highly debated for a century and still remain non-consensual (Prothero & Schoch, 1989; Antoine, 2002; Holbrook & Lapergola, 2011), particularly for early taxa (Bronnert, 2018; Bai, Wang & Meng, 2018), five superfamilies are generally recognized as belonging to Perissodactyla: three with living representatives (Rhinocerotoidea, Tapiroidea, Equoidea) and two extinct groups (Brontotherioidea, Chalicotherioidea) (Figure 3). Reaching a maximal diversity from the Eocene to the Miocene, perissodactyls have gradually declined since then and were frequently replaced by artiodactyls in many ecological niches (Prothero & Schoch, 1989; Antoine, 2002). They are represented nowadays by less than twenty species (4 or 5 tapirs, 6 or 7 equids and 5 rhinoceroses) (Dinerstein, 2011; MacLaren & Nauwelaerts, 2016; Bronnert, 2018).

Rhinocerotoidea

Among these superfamilies, Rhinocerotoidea is by far the one displaying the highest diversity of body size and shape throughout its evolutionary history. Even if only five species of modern rhinos have survived until today (Dinerstein, 2011), the superfamily was flourishing all along the Cenozoic. A rich and well-preserved fossil record led palaeontologists to describe more than a hundred species distributed in Eurasia, North America and Africa, showing a large diversity of ecological niches, body size and locomotor conditions (Prothero & Schoch, 1989; Cerdeño, 1998; Prothero, 2005; Biasatti, Wang & Deng, 2018). In addition to many cases of convergence or parallelism towards high body size, several transitions from a tetradactyl plesiomorphic (i.e. possessing a functional fifth metacarpal – (Antoine, 2002) manus as in tapirs to a tridactyl one similar to modern rhinos can be observed in several lineages (Guérin, 1989; Prothero & Schoch, 1989).

Numerous taxonomic mistakes and reattributions for more than a century, associated with frequent discoveries of new taxa, make it hard to provide an exhaustive inventory of all species and even genera of Rhinocerotoidea. Moreover, like for Perissodactyla, no consensual phylogeny exists to date for the entire group. Three main families are traditionally included within Rhinocerotoidea: Amynodontidae, Hyracodontidae and Rhinocerotidae (Prothero, Manning & Hanson, 1986; Prothero & Schoch, 1989), but recent works argue for the inclusion of the family Hyrachyidae within the superfamily and the split of the family Hyracodontidae, considered as paraphyletic (Wang et al., 2016; Bai et al., 2017; Tissier et al., 2018) (Figure 4).

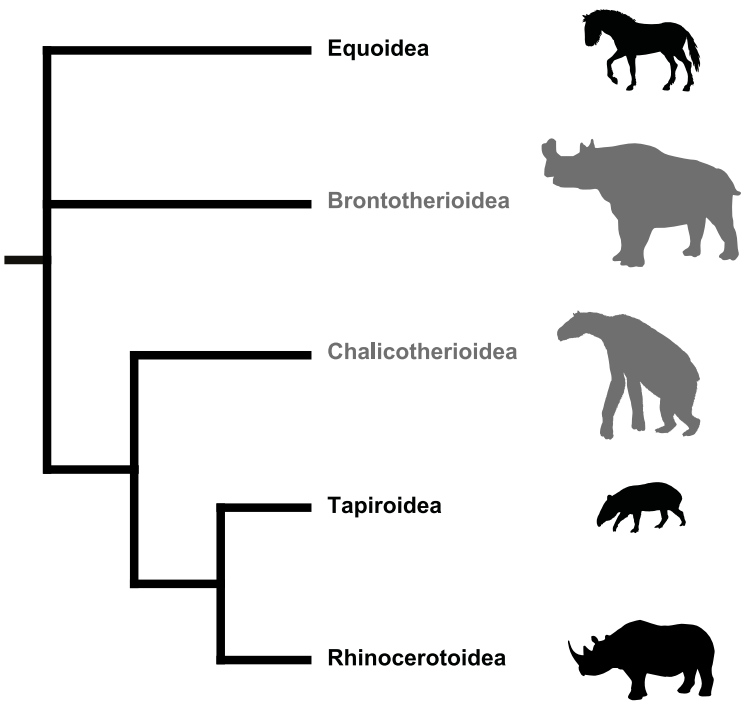

Figure 3: Simplified and non-consensual phylogeny of the order Perissodactyla. Black: groups with extant relatives: grey: extinct groups. Tapiroidea and Rhinocerotoidea, constituting the suborder Ceratomorpha, are considered as sister-taxa in most recent contributions. Relations between Equoidea, Brontotherioidea and the three other superfamilies remain non-consensual. Synthetic phylogeny reconstructed after Prothero & Schoch (1989); Froehlich (1999); Bronnert (2018); Bai, Wang & Meng (2018).

Hyrachyidae

The most ancient representative of the superfamily is the genus *Hyrachyus*. Frequently used as an outgroup relatively to Rhinocerotoidea in anatomical and phylogenetic works, its inclusion in the superfamily has been strongly debated for decades (Cope, 1873; Wood, 1934; Radinsky, 1966, 1967a; Prothero, Manning & Hanson, 1986; Prothero & Schoch, 1989; Cerdeño, 1995; Holbrook, 1999, 2001; Wang et al., 2016; Bai et al., 2017). Recent osteological investigation and comparison with related taxa tend to confirm that the family Hyrachyidae (composed of the single genus *Hyrachyus*) should be considered as belonging to Rhinocerotoidea (Bai et al., 2017; Wang et al., 2018). Known from the Early to the Middle Eocene in North America and Eurasia, *Hyrachyus* species did not exceed 100 kg and less than one meter in height at the shoulder (Damuth & MacFadden, 1990; Stilson, Hopkins & Davis, 2016) (Figure 4). These lightly-build animals where hornless browsers with generalized teeth (Carlson & Park, 2017). Despite a plesiomorphic tetradactyl manus, their “cursorial” appendicular skeleton suggests that characters associated with a running lifestyle where present early among Rhinocerotoidea (Bai et al., 2017) (Figure 5).

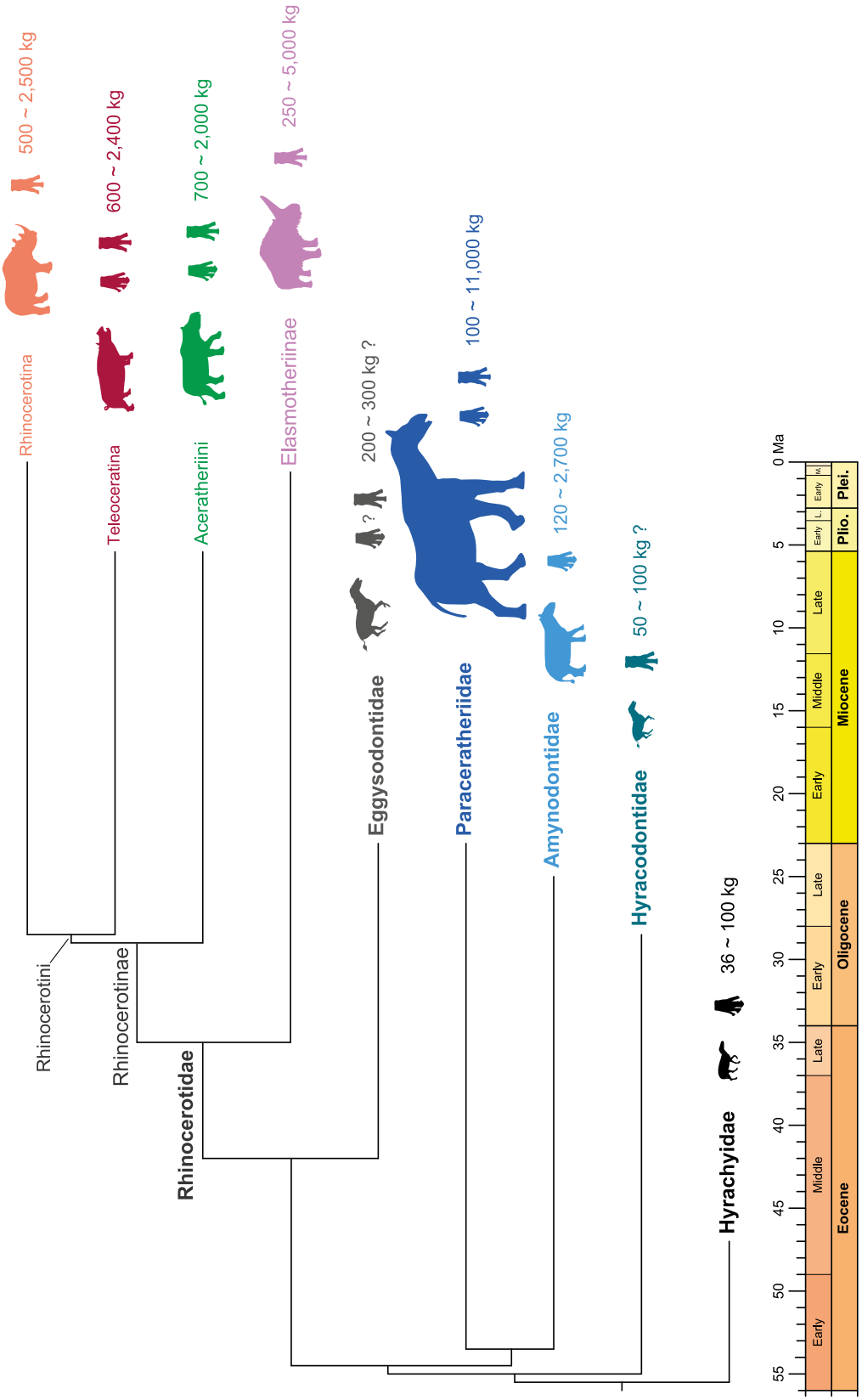

Figure 4: Synthetic phylogenetic relations within the superfamily Rhinocerotoidea with approximate ranges of body mass and number of forelimb digits for each group (question marks indicate strong uncertainties). Silhouettes are at the same scale. Cladistic framework after Antoine et al. (2010) and Becker, Antoine & Maridet (2013). Body mass ranges after Damuth & MacFadden (1990); Becker (2003); Valli (2005); Zhegallo et al. (2005); Qiu & Wang (2007); Becker et al. (2009); Saarinen et al. (2016); Stilson, Hopkins & Davis (2016); Averianov et al. (2017); Jame et al. (2019).

Amynodontidae

Amynodontidae were a group of hornless rhinocerotoids living in North America and Eurasia from the early Eocene to the end of the Oligocene (Wall, 1998; Averianov et al., 2017). If their position within the phylogeny of Rhinocerotoidea remains debated, their monophyly is, nonetheless, largely accepted (Wall, 1998; Tissier et al., 2018). About twelve genera are currently described, most of them being monospecific (Wall, 1998; Averianov et al., 2017; Tissier et al., 2018). These relatively heavy tetradactyl animals weighted from 120 kg to more than 2 tons for some species (Averianov et al., 2017) and possessed distinctive enlarged upper and lower canines possibly associated with sexual dimorphism, a unique trait among Rhinocerotoidea (Wall, 1998). On some species, large nasal openings have been interpreted as potentially linked to the presence of a proboscis as in tapirs (Tissier et al., 2018). Although many species are only known from cranial and dental remains, postcranial characters of Amynodontidae indicate a body construction close to that of tapirs and qualified as "mediportal" (Wall, 1998) or "semi-graviportal" (Colbert, 1938). Largest species like *Metamynodon* have been considered as graviportal (Osborn, 1929) (Figure 5). Sometimes considered as semi-aquatic in the literature, mainly because of their discovery in sandstones formed in ancient river channels, morphofunctional investigations proved that only some taxa like *Paramynodon* or *Metamynodon* actually showed characters potentially related to an amphibious lifestyle similar to that of modern hippos (e.g. high orbits on the skull, low thoracic spine, strongly developed olecranon process) (Wall & Heinbaugh, 1999). Except for these cases, most of the other genera known in North America and Eurasia are considered as fully terrestrial browsers (Wall, 1998).

"Hyracodontidae"

The family Hyracodontidae has long been considered monophyletic, based on cranio-dental characters and the "cursorial" aspect of its representatives due to their elongated limbs. In this group were brought together ones of the smallest and biggest species of the superfamily, some of them being moreover among the largest terrestrial mammals that ever existed (Prothero, 1998a). However, recent advances in the study of this clade strongly support its paraphyly, underlining the need to split the group in at least three distinct families: Hyracodontidae *sensu stricto*, Eggysodontidae and Paraceratheriidae (Wang et al., 2016, 2018; Tissier et al., 2018) (Figure 4). The first family, **Hyracodontidae** *sensu stricto*, is known from the middle Eocene to the end of the early Oligocene in North America and Eurasia. Hyracodontids (*sensu stricto*) were small "cursorial" and hornless animals possessing a derived tridactyl manus (Prothero, 1998a). Less than ten genera (most of them being monospecific) are currently included in Hyracodontidae *sensu stricto* (Wang et al., 2016, 2018). Some of them, like the genus *Triplopus*, were even smaller with a more derived "cursorial" condition than *Hyrachyus* (Bai et al., 2017) (Figure 5).

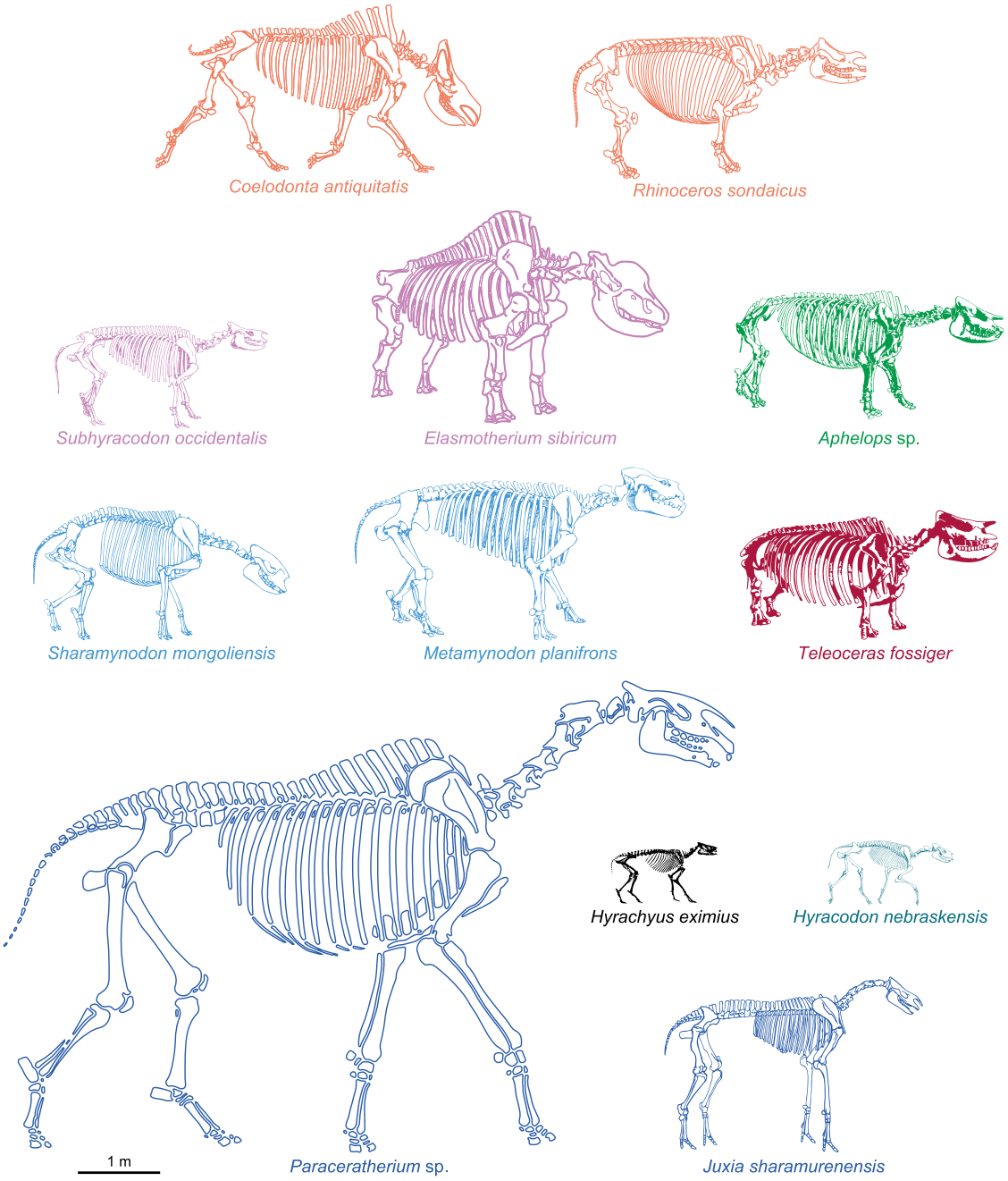

Figure 5: Some skeletal reconstructions illustrating the diversity of body shape among Rhinocerotoidea. All skeletons are at the same scale. Colour code follows that of Figure 4. Skeletons modified after Osborn (1898); Beddard (1902); Osborn & Wood (1936); Scott & Jepsen (1941); Paul (1997); Qiu & Wang (2007). Skeleton of *R. sondaicus* modified from Archeo-zoo.org under Creative Commons license.

Members of the family **Eggysodontidae** (mostly defined on cranial and dental characters) are very similar to Hyracodontidae and are also one of the poorest known representatives of Rhinocerotoidea, with only four genera described to date, uncertain phylogenetic relationships and a very limited fossil record (no Eggysodontidae are included in the present study as postcranial remains are very scarce for

this group) (Prothero & Schoch, 1989; Qiu & Wang, 1999; Bai & Wang, 2012; Wang et al., 2013, 2018). Eggysodontidae are known from the late Eocene to the end of the Oligocene and considered as less "cursorial" than Hyracodontidae (Prothero & Schoch, 1989).

Finally, members of the family **Paraceratheriidae** were thought to derive from small early hyracodontids (Prothero, 1998a) until recent fossil discoveries and new phylogenetic investigations on craniodental and postcranial characters showed that this group is monophyletic and not nested within Hyracodontidae *sensu stricto* (Wang et al., 2016, 2018) (Figure 4). If early diverging Paraceratheriidae from the early Eocene were small animals similar to Hyracodontidae *sensu stricto* (like the genera *Pappaceras* or *Forstercooperia*), later diverging paraceratheriids showed a strong increase in body size until the group's extinction at the end of the Oligocene (Qiu & Wang, 2007; Prothero, 2013). Among them, *Paraceratherium* is supposed to have measured 5 or 6 m at the shoulder for a body weight exceeding 10 tons, making it one of the largest land mammals that ever existed, only exceeded by some proboscideans (Fortelius & Kappelman, 1993; Larramendi, 2016) (Figure 5). Deep taxonomic uncertainties have affected this family for more than a century (Prothero, 2013) but to date, about ten paraceratheriid genera are generally recognized in North America and Asia (Qiu & Wang, 2007). These giant hornless browsers are remarkable for being extremely tall and retaining a "cursorial" general construction with long slender limbs and no reduction of the autopodium relative length (Prothero, 1998a, 2013). Their discovery at the beginning of the 20th century thus challenged the initial concept of graviportality as framed by Gregory and Osborn (Granger & Gregory, 1936; Prothero, 2013).

Rhinocerotidae

This family appeared during the late Eocene (Prothero & Schoch, 1989) and is the only one with extant representatives. It is by far the most diverse and best-known family among all Rhinocerotoidea, documented by a huge fossil record in North America, Eurasia and Africa (some species being known from thousands of individuals – (Prothero, 2005). For two centuries, palaeontologists have described more than 40 genera and 140 species showing an impressive diversity of size, weight, shape and ecology (Cerdeño, 1998). This results in complex and still debated systematics from subfamilies to subtribes (Antoine, 2002). To date, despite the existence of many phylogenetic reconstructions involving dozens of species, no consensual phylogeny of the whole family is available (Cerdeño, 1995; Antoine, 2002; Antoine, Duranthon & Welcomme, 2003; Piras et al., 2010; Antoine et al., 2010; Deng et al., 2011; Becker, Antoine & Maridet, 2013; Lu, 2013; Tissier, Antoine & Becker, 2020) (Figure 4).

Different cases of morphological convergence or parallelism can be observed within this family. Many lineages show an obvious increase of body size and body mass across the Cenozoic, with many late diverging species reaching a weight of several tons (e.g., *Elasmotherium* in Elasmotheriinae, *Aphelops*

in Aceratheriini, *Brachypotherium* in Teleoceratina, *Ceratotherium* or *Rhinoceros* in Rhinocerotina) (Guérin, 1989; Prothero & Schoch, 1989; Damuth & MacFadden, 1990; Dinerstein, 2011; Stilson, Hopkins & Davis, 2016). The development of nasal and/or frontal horns, often associated with a relatively heavy head, occurred both among the subfamilies Elasmotheriinae and Rhinocerotinae, despite some members of the latter group remaining hornless (e.g., most members of the tribe Aceratherinii) (Prothero & Schoch, 1989; Prothero, 1998b; Antoine, 2002). The transition from a tetra- to a tridactyl manus also occurred at least two times independently within Rhinocerotinae (among early genera like *Pleuroceros* and later among the subtribe Teleoceratina in genera like *Teleoceras*) and maybe a third time before the radiation of Elasmotheriinae (all being tridactyl – Antoine, 2002) (Figure 4). Another repeated specialization is the shortening of the limbs leading to a strong brachypody (see below), which reached a maximum among Teleoceratina but also in some Aceratherinii like *Chilotherium* (Guérin, 1989; Cerdeño, 1998). Brachypody also occurred in dwarf species, with cases reported among North American Aceratherinii and Teleoceratina (Prothero & Manning, 1987; Prothero, 2005). Concerning feeding habits, the transition from browsing to grazing, associated with more hypsodont teeth, occurred in several lineages, notably among Teleoceratina and Rhinocerotina, the extant genus *Ceratotherium* being the only grazing modern species (Dinerstein, 2011). This grazer specialization reached a maximum among Elasmotheriinae with the genus *Elasmotherium*, displaying hypselodonty as observed in horses, and probably associated with the consumption of abrasive grasses in open steppes (Guérin, 1989; Antoine, 2002).

After the Miocene, the ecologically successful and well-spread family Rhinocerotidae began to decline in diversity and geographic range throughout the Pliocene and Pleistocene, likely due to deep climatic changes and their replacement in many ecological niches by artiodactyls (Cerdeño, 1998; Antoine, 2002). Nowadays, only five species of modern rhinoceros survive on Earth: the White Rhinoceros (*Ceratotherium simum* (Burchell, 1817)) and the Black Rhinoceros (*Diceros bicornis* (Linnaeus, 1758)) both live in sub-Saharan Africa, whereas the Indian Rhinoceros (*Rhinoceros unicornis* Linnaeus, 1758), the Javan Rhinoceros (*R. sondaicus* Desmarest, 1822) and the Sumatran Rhinoceros (*Dicerorhinus sumatrensis* (Fischer, 1814)) survive in India and Nepal, Java, and Sumatra, respectively (Dinerstein, 2011). Recently, it has been hypothesized that the two subspecies of white rhinoceros should be spited in two distinct species, distinguishing the Northern white rhinoceros (*C. cottoni*) from the Southern white rhinoceros (*C. simum*) (Groves, Fernando & Robovský, 2010). However, this taxonomic reattribution is not consensual (Welker et al., 2015; Harley et al., 2016) and will not be considered in the present study.

Moreover, the phylogenetic relationships between the modern species remain highly debated and non-consensual, whether they are based on morphology, mitochondrial or nuclear DNA or RNA, proteomic data or even the combination of different data sets through meta-analyses. Four different

patterns are frequently hypothesized in the literature (Figure 6): 1) *D. sumatrensis* being the sister-taxon of both African and Asiatic clades (Fernando et al., 2006; Piras et al., 2010; Yuan et al., 2014; Harley et al., 2016); 2) *D. sumatrensis* being the sister-taxon of the African clade (Morales & Melnick, 1994; Antoine, 2002; Antoine, Duranthon & Welcomme, 2003; Antoine et al., 2010; Steiner & Ryder, 2011; Becker, Antoine & Maridet, 2013; Lu, 2013; Gaudry, 2017; Cappellini et al., 2019); 3) *D. sumatrensis* being the sister-taxon of the Asiatic clade (Prothero, Manning & Hanson, 1986; Cerdeño, 1995; Tougard et al., 2001; Orlando et al., 2003; Price & Bininda-Emonds, 2009; Deng et al., 2011; Yuan et al., 2014; Gaudry, 2017; Welker et al., 2017; Zein et al., 2019); 4) a hard polytomy at the base of the crown-group containing the five modern species (Willerslev et al., 2009; Gaudry, 2017). The deep differences in phylogenetic reconstructions could indicate a short divergence time (over about 1 Ma) between the three modern branches (Willerslev et al., 2009). Given these observations and in the absence of consensus, I will consider a polytomy between the three main groups of modern rhinos (Figure 6D). More details concerning the five modern species will be given in Chapter 3.

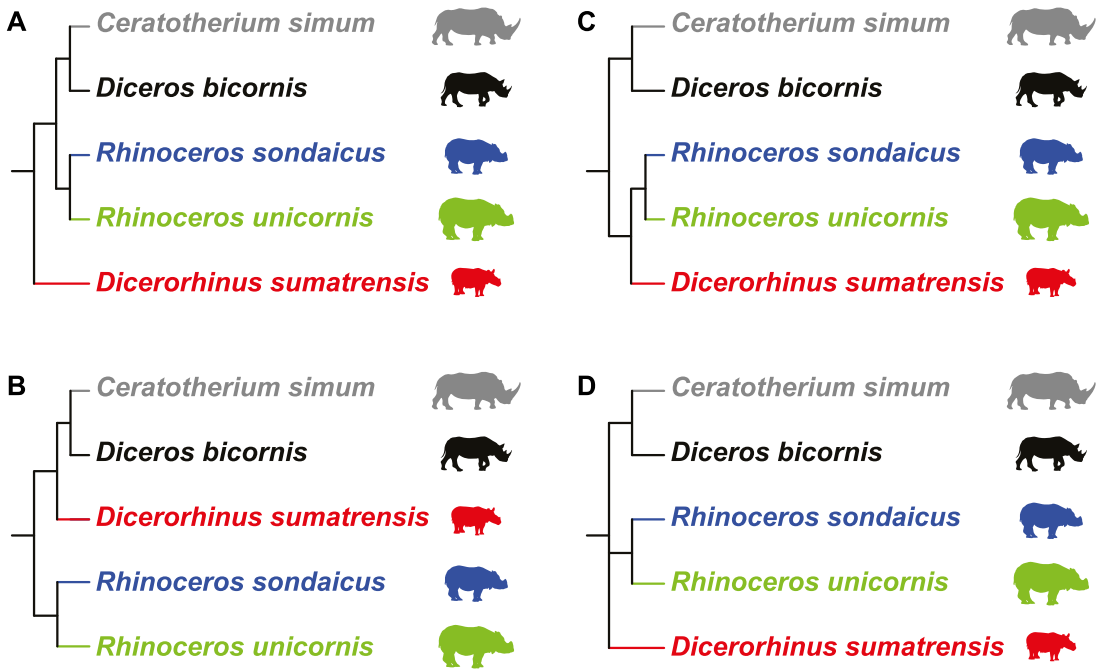

Figure 6: Four potential phylogenetic relationships between the five modern rhino species. A: *D. sumatrensis* sister-taxa of all rhinos, B: *D. sumatrensis* sister-taxa of African rhinos; C: *D. sumatrensis* sister-taxa of Asiatic rhinos; D: hard polytomy.

Graviportality and gracility among Rhinocerotoidea

Given the biological diversity and the repeated size and mass increases encountered within the superfamily Rhinocerotoidea, its members have been classically sorted using the locomotor categories introduced by Gregory (1912) and Osborn (1929) (see above). However, many works tended to use only ratios between limb segments, with little consideration of other morphofunctional criteria like gait or body mass (e.g. Granger & Gregory, 1936; Colbert, 1938; Arambourg, 1959; Guérin, 1980; Eisenmann

& Guérin, 1984). This simplification of the framework of Gregory and Osborn is likely related to the fact that many Rhinocerotoidea representatives show remarkable variations in the relative proportions of their limb segments. This is particularly visible in Paraceratheriidae (see above) but also among the subtribe Teleoceratina displaying extremely short limbs (Prothero, 2005; Becker et al., 2009).

The focus on limb segment proportions led authors to consider the degree of **gracility** (or, at the opposite, **robusticity**) to categorize rhino species, sometimes using a single "gracility index" computed on third metapodials. This index is classically computed by dividing the metapodial transversal width by the total length (e.g. Colbert, 1938; Arambourg, 1959; Cerdeño & Alcalá, 1989; Cerdeño, 1998; Becker, 2003; Becker et al., 2009; Scherler et al., 2013). Like for "graviportality", "gracility" and "rubosticity" appear to be intuitive terms but can refer to many different confusing concepts. Lahr & Wright (1996) defined "robust" as *"something 'strongly formed or constructed'"*, suggesting that "gracile" might be the opposite – something lightly formed or constructed. When talking about the general proportions of an animal, these terms may relate to its overall size and/or mass relatively to other species or clades (e.g. a horse will be considered as robust compared to an antelope, but as gracile compared to an elephant). They may also relate more specifically to anatomical parts, as some limb bones can be considered more robust than others when showing a larger shaft for a given length, conferring again to this term a relative value only. That is why some authors preferred the term "**brachypody**" to talk about the condition of some rhinos, which are both short-legged and showing limb bones with a relatively larger shaft. However, even if it has been used for more than a century (Osborn, 1902), this term is not systematically employed in rhino studies (e.g. Osborn, 1929; Guérin, 1989; Cerdeño, 1993, 1998; Becker, 2003; Ménouret & Guérin, 2009; Becker et al., 2009; Antoine et al., 2018). Furthermore, its contrary ("**dolichopody**", referring to long-legged and slender animals) has almost never been used in rhino studies (Osborn, 1902).

Finally, graviportality has sometimes been confused with brachypody in rhinos, as the reduction of the distal limb elements is one of the criteria associated with the classic framework of Gregory and Osborn, but is not considered as exclusive to define the locomotor category of a quadruped. Consequently, some rhino species might have been exaggeratedly qualified as "graviportal" based on limb element proportions only (e.g. Maynard Smith & Savage, 1956; Prothero & Sereno, 1982; Eisenmann & Guérin, 1984; Becker, 2003; Becker et al., 2009).

Objectives

The superfamily Rhinocerotoidea features prominently among the different clades of quadrupedal amniotes affected by repeated increases in size through their evolutionary history. It therefore appears as a relevant group to study relations between body mass and limb bone shape, and how a same body

mass can be associated with different body shapes. The great diversity in body size and body shape within this superfamily led to confusing uses of concepts like graviportality and brachypody, these concepts themselves having some limits. Moreover, investigations regarding the limbs of rhinos until today mainly focused on the ratios between the different segments. Morphological changes of the limb bones were mostly investigated for systematic and palaeoenvironmental purposes but rarely to address the morphofunctional links between the body size, body mass and degree of brachypody with shape variation.

The main objective of the present study is therefore to **explore the shape variation of the limb long bones among Rhinocerotoidea relatively to body mass and body proportions along their evolutionary history** in order to better understand **how the skeleton modifies to meet the functional requirements of a coordinated locomotion and the support of a heavy weight**. This study will focus on the elements composing the stylopodium and zeugopodium, since their shape is considered as highly influenced by variations of body proportions (Biewener, 1983; Anderson, Hall-Martin & Russell, 1985; Damuth & MacFadden, 1990; Bertram & Biewener, 1992; Campione & Evans, 2012). Girdle elements often appear poorly correlated with shape variation of the other limb elements and variations of body mass in mammalian quadrupeds. Conversely, the shape of autopodium elements is known to be related to ecological factors in addition to body mass (Christiansen, 2002; Martín-Serra et al., 2015; Sears, Capellini & Diogo, 2015; Hanot et al., 2017). For these reasons and given the time constraints to realize this study, they will not be considered in this study. Considerations about the material and the general methodology used in this study are given in Chapter 2.

Understanding the variation in modern representatives of a group is often a very insightful step before studying fossil specimens. Shape variation of the appendicular skeleton of modern rhinos and its relations with body mass have been poorly explored in anatomical works until now. The five modern species of rhinoceros display a broad range of size and mass. The exploration of their shape diversity taking into account their phylogenetic relationships should shed light on the relations between limb morphology and body mass. Moreover, exploring the shape patterns among extant species, while accounting for their intraspecific variation, will allow a preliminary approach to the correspondence between bone shape and phylogeny. This morphofunctional study in modern rhinos is presented in Chapter 3.

Considering the shape variation of each bone individually should bring elements to explore the construction of the limbs relatively to body mass in a global way. As limb bones form a coherent system in themselves and are linked with muscles, tendons and ligaments, their respective shapes are likely to covary under functional constraints like weight support. Fore and hind limbs being constructed with serially homologous elements (Young & Hallgrímsson, 2005), bones are also shaped by shared

developmental processes within and between limbs (Hallgrímsson, Willmore & Hall, 2002; Bininda-Emonds et al., 2007). Consequently, the shape of the various segments of the appendicular skeleton, and particularly the long bones (Schmidt & Fischer, 2009; Martín-Serra et al., 2015; Hanot et al., 2017; Botton-Divet et al., 2018), tend to highly covary with each other among quadruped mammals, a phenomenon called morphological integration (Klingenberg, 2008, 2014; Schmidt & Fischer, 2009). The support of a heavy mass is likely to influence the degree of integration of limb bones, as their shape is submitted to a common stress due to load bearing (Hildebrand, 1974; Biewener, 1983, 1989b). However, the influence of functional constraints, like variation in body mass, on the integration of limb bones has rarely been tested, and almost never on heavy taxa like rhinos. The Chapter 4 will therefore explore how the shape of the long bones covary among modern rhinos, and how could body mass influence these patterns of morphological integration.

The exploration of morphological variation and covariation of limb bones in modern rhinos will allow a better understanding of the relations between bone shape and body mass. However, modern rhinos only represent a small and relatively homogeneous sample compared to the past diversity and repeated increases in body size among Rhinocerotoidea. Consequently, the extension of this exploration to the whole superfamily will give access to a higher diversity of body proportions, allowing to shed light on broader patterns of shape variation of long bones. This approach will allow to understand how long bones are influenced by body size, mass, the degree of brachypody and the evolutionary history. The morphological richness of this group will allow to highlight similarities and differences in the patterns of shape variation for each limb bone, but also between the bones, between the limbs and between the different clades. Chapters 5 and 6 address these questions on forelimb and hind limb bones, respectively.

Finally, this global view of the shape variation among Rhinocerotoidea should bring the necessary elements to precisely highlight if body mass plays a role in shaping long bones and, if so, how it does in multiple ways under the constraint of evolutionary legacy. This large exploration should help to shed light on the common patterns of shape variation related to body mass across the superfamily. At a broader scale, similarities and differences between bones, between limbs and between clades within Rhinocerotoidea will help to discuss the relevance of the concept of graviportality in this group, its relation with the degree of brachypody and the contribution of shape analysis to its definition. These elements are discussed in Chapter 7.

Chapter 2

Material and general methodology

Material

This investigation focuses on the six bones composing the stylopodium and the zeugopodium of both fore and hind limb: humerus, radius, ulna, femur, tibia, fibula. All anatomic terms and morphological descriptions used along this study will be given in Chapter 3 concerning the shape variation of modern rhinos. Specimens of modern and fossil rhinos were gathered in 21 institutions across the world (12 that I visited myself, 3 visited by A. Houssaye and 6 that directly provided me 3D models). A total of almost 500 bones of modern rhinos and around 1,675 bones of fossil rhinos were selected during field missions. Non-suitable specimens (immature, deformed or broken specimens) were discarded afterward from analyses. Details regarding the specimens used in each analysis are given in their respective chapters.

General methodology

The analysis of shape variation has been performed using 3D geometric morphometrics, a widely used approach allowing quantification of morphological differences between objects using landmark coordinates (Adams, Rohlf & Slice, 2004; Zelditch et al., 2012).

3D models

Bones were mostly digitized with a structured-light three-dimensional scanner (Artec Eva) and reconstructed with Artec Studio Professional software (v12.1.1.12 – Artec 3D, 2018). Complementarily, some bones were digitized with a photogrammetric approach, following Mallison & Wings (2014) and Fau, Cornette & Houssaye (2016). Sets of photos were taken all around the bones and aligned to reconstruct a 3D model with Agisoft Photoscan software (v1.4.2 – Agisoft, 2018). Previous studies indicated no significant difference between 3D models obtained with these two methods (Petti et al., 2008; Remondino et al., 2010; Fau, Cornette & Houssaye, 2016). Some bones were digitized using medical computed tomography scanners at the Royal Veterinary College, London (Equine Hospital) and at the University of California, San Francisco (Department of Radiology & Biomedical Imaging) and provided by Pr. J. Hutchinson. Bone surfaces were extracted as meshes using Avizo software (v9.5.0 – Thermo Fisher Scientific, 2018). Each mesh was decimated to reach 250,000 vertices and 500,000 faces using MeshLab software (v2016.12 - Cignoni et al., 2008). I mainly selected left bones during acquisition; when this was impossible, right bones were selected and then mirrored before analysis.

Landmark digitization

Following the procedure described by Gunz, Mitteroecker & Bookstein (2005), Gunz & Mitteroecker (2013) and Botton-Divet et al. (2016), I defined the bones' shape using anatomical landmarks and curve and surface sliding semi-landmarks. Each curve is bordered by anatomical landmarks as recommended

by Gunz & Mitteroecker (2013). All landmarks and curves were placed using the IDAV Landmark software (v3.0 – Wiley et al., 2005). Number and position of landmarks slightly varied depending on the objectives of each chapter. Specific details on landmarks are therefore given in Chapters 3, 4, 5 and 6.

Following the procedure detailed by Botton-Divet et al. (2016), I created a template to place surface semi-landmarks for each bone: a specimen was chosen on which all anatomical landmarks, curve and surface sliding semi-landmarks were placed. As for landmarks, the choice of this specimen is different depending on the performed analyses. Details are provided in the respective chapters. The template was then used for the projection of surface sliding semi-landmarks on the surface of the other specimens. Projection was followed by a relaxation step to ensure that projected points matched the actual surface of the meshes. Curve and surface sliding semi-landmarks were then slid to minimize the bending energy of a Thin Plate Spline between each specimen and the template at first, and then two times between the result of the preceding step and the Procrustes consensus of the complete dataset. Therefore, all landmarks can be treated at the end as geometrically homologous (Gunz, Mitteroecker & Bookstein, 2005) and analysed with classic procedure such as Generalized Procrustes Analysis (see below). Projection, relaxation and sliding processes were conducted using the Morpho package in the R environment (R Core Team, 2014). Details of the process are provided in the documentation of the package (Schlager, 2018).

Generalized Procrustes Analysis

After the sliding of all semi-landmarks, I performed Generalized Procrustes Analyses (GPA) (Gower, 1975; Rohlf & Slice, 1990) to remove the effects of size and of the relative position of the points and to isolate only the shape information. As datasets contained more variables than observations, a Principal Component Analysis (PCA) was used to reduce dimensionality as recommended by Gunz & Mitteroecker (2013) and visualize the specimen distribution in the morphospace. At the end of this step, superimposed landmark coordinates were then used in subsequent analyses detailed in their respective chapters.

Repeatability tests

For each bone, I tested the repeatability of the anatomical landmark digitization taking measurements ten times on three specimens of the same species, *Ceratotherium simum*, chosen to display the closest morphology and size. I superimposed these measurements using a GPA and visualized the results using a Principal Component Analysis (PCA). Results showed a variation within specimens clearly smaller than the variation between specimens (Figure 7) and allowed me to consider the anatomical landmarks as precise enough to describe shape variation. Similar tests were performed with reduced landmark datasets used in Chapters 4, 5 and 6 and showed similar results.

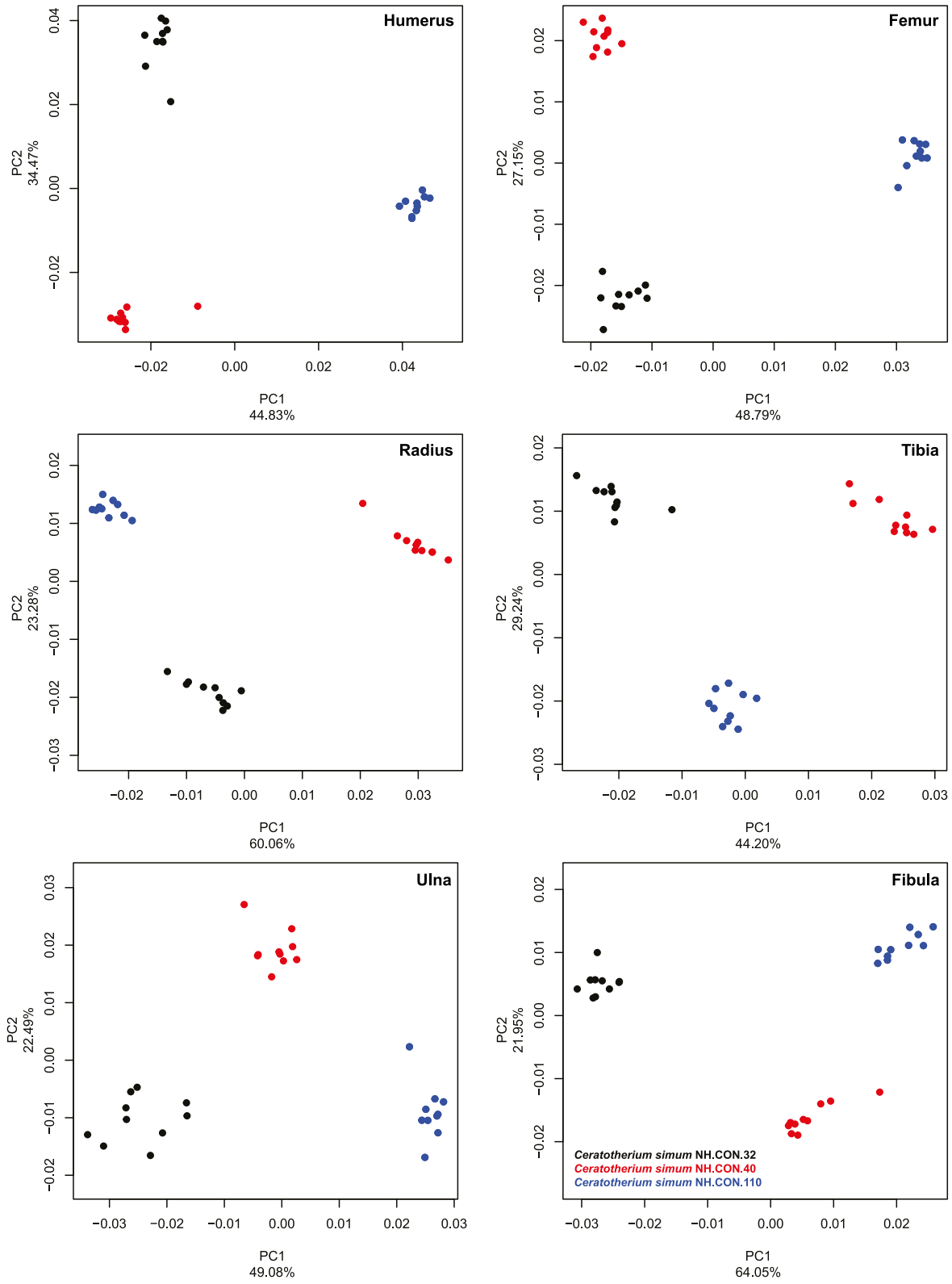

Figure 7: PCA plots of the results of repeatability tests. Each landmark configuration was digitized ten times on three specimens of Ceratotherium simum chosen to display the fewer morphological difference as possible. Each colour corresponds to a specimen. For each bone, the inter-specimen variation is lower than the intra-specimen error due to differences between landmark digitization. I concluded to the relevance of the anatomical landmark configuration to describe shape variation within the sample.

Institutional codes used in this study

AMNH: American Museum of Natural History, New York; **AR**: Association Rhinopolis, Gannat; **BICPC**: Powell Cotton Museum, Birchington-on-Sea; **BSPG**: Bayerische Staatssammlung für Paläontologie und Geologie, Munich; **CCEC**: Centre de Conservation et d'Étude des Collections, Musée des Confluences, Lyon; **FSL**: Collections de Paléontologie – Laboratoire de Géologie de Lyon, Université Claude Bernard, Lyon ; **IVPP**: Institute of Vertebrate Paleontology and Paleoanthropology, Beijing; **MHNT**: Muséum d'Histoire Naturelle de Toulouse, Toulouse ; **MNHN**: Muséum National d'Histoire Naturelle, Paris ; **NHMUK**: Natural History Museum, London; **NHMW**: Naturhistorisches Museum Wien, Vienna; **NMB**: Naturhistorisches Museum Basel, Basel; **NMP**: National Museum of the Philippines, Manila; **NMS**: National Museums Scotland, Edinburgh; **NMP**: National Museum of the Philippines, Manila; **RBINS**: Royal Belgian Institute of Natural Sciences, Brussels; **RMCA**: Royal Museum for Central Africa, Tervuren; **UCMP**: University of California Museum of Paleontology, Berkeley; **UMZC**: University Museum of Zoology Cambridge, Cambridge; **YPM**: Yale Peabody Museum, New Haven; **ZSM**: Zoologische Staatssammlung München, Munich.

Chapter 3

Interspecific variation in the limb long bones among modern rhinoceroses – extent and drivers

Introduction

Among living terrestrial mammals, modern rhinos are generally considered as one of the three heaviest taxa, together with elephants and hippos. All three are commonly considered as graviportal (Alexander & Pond, 1992). However, given the difficulty to find a consensual definition of graviportality (see Chapter 1), categorization of these three taxa may vary depending on authors. Elephants obviously fulfil all the morphological and biomechanical criteria defining graviportality (Coombs, 1978; Langman et al., 1995). However, the peculiar morphology of hippos (barrel-like body and shortened limbs) linked to semi-aquatic habits has been considered alternately as mediportal (Coombs, 1978; Ross, 1984) or graviportal (Alexander & Pond, 1992; Carrano, 1999; MacFadden, 2005; Stilson, Hopkins & Davis, 2016). Rhino's graviportal condition is surely the least consensual: Gregory (1912) and Osborn (1929) considered rhinos as mediportal whereas later works assigned them a graviportal condition (Prothero and Sereno, 1982; Eisenmann and Guérin, 1984). Becker (2003) and Becker et al. (2009) dug into this question and developed a "gracility index" based on the work of Guérin (1980) to categorize modern and fossil rhinos, but only based on third metacarpal and metatarsal proportions. The use of this index refined the classification of modern rhinos distinguishing mediportal and graviportal species instead of a single class attribution for the whole family (Table 1).

Regardless of the locomotor type to which rhinos belong, the family Rhinocerotidae includes five species that all display adaptations to support their high body mass (Alexander & Pond, 1992) (see Chapter 1): the White Rhinoceros (*Ceratotherium simum*), the Black Rhinoceros (*Diceros bicornis*), the Indian Rhinoceros (*Rhinoceros unicornis*), the Javan Rhinoceros (*Rhinoceros sondaicus*) and the Sumatran Rhinoceros (*Dicerorhinus sumatrensis*) (Dinerstein, 2011). These species exhibit an important variation in body mass and size (Table 1), ranging from less than a ton for *Dicerorhinus sumatrensis* to more than three tons for the biggest known specimens of *Ceratotherium simum*. They are all good walkers and runners, able to gallop and reach an elevated speed (27 km/h for *Ceratotherium simum*, Alexander & Pond, 1992; 45 km/h for *Diceros bicornis*, Blanco, Gambini & Fariña, 2003). However, important ecological differences also exist (Groves, 1967a,b, 1972; Groves & Kurt, 1972; Laurie, Lang & Groves, 1983; Hillman-Smith & Groves, 1994; Dinerstein, 2011; Groves & Leslie, 2011): the three Asiatic rhinos are excellent swimmers and very familiar with an aquatic environment whereas the two African ones are easily stopped by a relatively deep river (Guérin, 1980). While *Ceratotherium simum* is a pure grazer,

This work has been published under the reference: Mallet C, Cornette R, Billet G, Houssaye A. 2019. Interspecific variation in the limb long bones among modern rhinoceroses—extent and drivers. PeerJ 7:e7647 https://doi.org/10.7717/peerj.7647

Rhinoceros unicornis can both graze and browse small shrubs, leafy material and fruits, the three other species being mainly leaf browsers. Before the drastic decrease of their natural habitats under human pressure, rhinos occupied a wide geographic range across Africa and Asia (Dinerstein, 2011; Rookmaaker & Antoine, 2012).

Despite the importance of rhino species for understanding evolution towards large body mass and the fact that they are some of the heaviest surviving land mammals, only a few studies really explore the variation of their limb bone morphology in relation to their body proportions (Guérin, 1980; Eisenmann & Guérin, 1984). After the pioneering works of Cuvier (1812) and de Blainville & Nicard (1839) describing the postcranial anatomy of modern rhinos, almost no work tried to broadly analyse and compare the morphology of their limb bones. Guérin (1980) published a substantial comparative anatomy work on the whole skeleton of the five extant species. This study emphasized anatomical descriptions with a direct application on the determination of fossil forms. Despite considerations on inter- and intraspecific osteological variation in modern rhinos, this work did not fully explore the patterns of shape variation in this group. Furthermore, most of the previous studies used a classic morphometric approach with linear measurements on bones, an approach which cannot precisely take into consideration the whole shape of the bone in three dimensions (3D). To date, no morphofunctional analyses have been carried out on limb long bones of modern rhinos taking into consideration their whole shape.

In this chapter, I hypothesize that modern rhinoceroses exhibit a large amount of interspecific variation of the shape of each bone that would be essentially associated with a strong effect of body mass on bone morphology. I predict that this effect will be more pronounced on the stylopodium (humerus and femur) than on the zeugopodium (radius, ulna, tibia and fibula) bones. This would be in accordance with previous works on changes of limb shape between graviportal and cursorial taxa (Biewener, 1989b; Campione & Evans, 2012). In addition, I expect a potential effect of the phylogenetic heritage and different species' ecologies on bone shape. To test these hypotheses, I propose to explore the variation in the shape of the limb long bones among the five modern rhino species using a 3D geometric morphometrics approach. I describe interspecific patterns of morphological variation for the six bones composing the stylopodium and the zeugopodium, taking into account the intraspecific variation.

Species name	Total body length (cm)	Shoulder height (cm)	Mean body mass (kg)	Ecology	Locomotor type		
					(Gregory, 1912; Osborn, 1929; Coombs, 1978)	(Eisenmann & Guérin, 1984)	(Becker, 2003)
*Ceratotherium simum**	340 – 420	150 – 180	2,300	Open savanna	M	G	G
*Dicerorhinus sumatrensis***	236 – 318	100 – 150	775	Dense forests and swampy lakes	M	G	M
*Diceros bicornis**	300 – 380	140 – 170	1,050	Open savanna and clear forest	M	G	M
*Rhinoceros sondaicus***	305 – 344	150 – 170	1,350	Dense forests and swampy areas	M	G	G
*Rhinoceros unicornis***	335 – 346	175 – 200	2,000	Floodplains and swamps	M	G	M

Table 1: Main characteristics of the five studied species. Length, height and body mass data compiled and calculated after Dinerstein (2011). Shoulder height is given at the withers. Ecological data compiled after Becker (2003). G, graviportal; M, mediportal. * African species. ** Asiatic species.

Material and Methods

Sample

I selected 62 dry skeletons in different European museums belonging to the five extant rhino species: *C. simum*, *Dicerorhinus sumatrensis*, *Diceros bicornis*, *R. sondaicus* and *R. unicornis* (Table 2). I followed the taxonomic attribution given by each institution for most of the specimens, except for three individuals determined or reattributed by myself on osteological criteria and later confirmed by the morphometric analysis (see Table 2). I studied altogether 53 humeri, 49 radii, 46 ulnae, 56 femora, 52 tibiae and 50 fibulae, with 37 skeletons being complete. I included only mature specimens with fully fused epiphyses (adults) or specimens where the line of the epiphyseal plates was still visible on some bones (subadults). Bones showing breakages or unnatural deformations were not considered in the analysis. It has been proved that feet bones are subject to important osteopathologic deformations in rhinos (Regnault et al., 2013). However, in accordance with the observations of Guérin (1980), I did not notice any major difference between the long bones of captive and wild animals, neither through visual and osteological observations nor in the morphometric analyses; I therefore did not take into account this parameter. Sexual dimorphism occurs among rhinos but has been mostly investigated regarding the external morphology of the animals (Dinerstein, 1991; Berger, 1994; Zschokke & Baur, 2002; Dinerstein, 2011). The few studies that have explored the osteological variations between sexes indicated only slight absolute metric divergences depending on species (Guérin, 1980; Groves, 1982). This suggests that intraspecific variation due to sex may be marginal when compared to interspecific variation, and probably more related to the size of the bone than to the shape. Furthermore, since almost half of the sample lacked sex information and that I had twice as many males than females, I could not carefully address sex in this study (see Results).

Anatomical terminology

All anatomical terms used to describe bones come from classic references: the *Nomina Anatomica Veterinaria* (World Association of Veterinary Anatomists & International Committee on Veterinary Gross Anatomical Nomenclature, 2005) and anglicized terms of Barone (2010a) for general osteology and bone orientation, Guérin (1980) for specific rhino anatomy, complemented by the contributions of Colyn (1980), Antoine (2002) and Heissig (2012). Despite these previous works, one anatomical feature remained unnamed, leading me to use my own designation: I called “palmar process” the process facing the coronoid process on the palmar border of the radius proximal epiphysis. Muscle insertions were described after the general anatomy of horses (Barone, 2010b), complemented by the work of Beddard & Treves (1889) and some complementary information from Guérin (1980) on rhino myology, Bressou (1961) on that of tapirs and Fisher, Scott & Naples (2007) and Fisher, Scott & Adrian (2010) on that of hippos.

Taxon	Institution	Specimen number	H	R	U	Fe	T	Fi	Sex	Age	Condition	3D acquisition
*Ceratotherium simum**	NHMUK	ZD 2018.143	X	X	X	X	X	X	U	A	U	SS
Ceratotherium simum	NHMW	3086	X	X	X	X	X	X	U	A	W	P
Ceratotherium simum	RBINS	19904	X	X	X	X	X	X	M	S	W	SS
Ceratotherium simum	RBINS	35208	X	X	X	X		X	U	A	U	SS
Ceratotherium simum	RMCA	1985.32-M-0001	X	X	X	X	X	X	U	A	W	SS
Ceratotherium simum	RMCA	RG35146	X	X	X	X	X	X	M	A	W	SS
Ceratotherium simum	UCMP	125000				X			U	A	U	CT
Ceratotherium simum	ZSM	1912/4199				X			U	A	W	SS
Ceratotherium simum	BICPC	NH.CON.20	X	X	X	X	X	X	M	S	W	SS
Ceratotherium simum	BICPC	NH.CON.32	X	X	X	X	X	X	F	S	W	SS
Ceratotherium simum	BICPC	NH.CON.37	X	X		X	X	X	F	A	W	SS
Ceratotherium simum	BICPC	NH.CON.40	X	X	X	X	X	X	F	S	W	SS
Ceratotherium simum	BICPC	NH.CON.110	X	X	X	X	X	X	M	A	W	SS
Ceratotherium simum	BICPC	NH.CON.112	X	X	X	X	X	X	M	A	W	SS
Ceratotherium simum	NMS	NMS.Z.2010.44	X			X			F	A	U	CT
Ceratotherium simum	MNHN	ZM-MO-2005-297	X			X	X	X	M	A	C	SS
Dicerorhinus sumatrensis	MNHN	ZM-AC-1903-300	X	X	X	X	X	X	M	A	W	SS
Dicerorhinus sumatrensis	MNHN	ZM-AC-A7967	X	X	X				F	A	W	SS
Dicerorhinus sumatrensis	NHMUK	ZD 1879.6.14.2	X	X	X	X	X	X	M	A	W	SS
Dicerorhinus sumatrensis	NHMUK	ZD 1894.9.24.1	X	X	X	X	X	X	U	A	W	SS
Dicerorhinus sumatrensis	NHMUK	ZD 1931.5.28.1	X	X	X	X	X	X	M	S	W	SS
Dicerorhinus sumatrensis	NHMUK	ZE 1948.12.20.1	X	X	X	X	X	X	U	A	U	SS
Dicerorhinus sumatrensis	NHMUK	ZE 1949.1.11.1	X	X	X	X	X	X	U	A	W	SS
Dicerorhinus sumatrensis	NHMUK	ZD 2004.23	X			X	X	X	U	A	W	SS
Dicerorhinus sumatrensis	NHMW	1500				X	X	X	M	A	U	P
Dicerorhinus sumatrensis	NHMW	3082	X	X	X	X	X	X	U	A	U	P
Dicerorhinus sumatrensis	NHMW	29568		X	X	X		X	U	S	U	P
Dicerorhinus sumatrensis	RBINS	1204	X	X	X	X	X	X	M	A	W	SS
Dicerorhinus sumatrensis	UMZC	H.6392	X						U	A	U	CT
Dicerorhinus sumatrensis	ZSM	1908/571	X	X		X	X	X	M	A	U	SS
Diceros bicornis	CCEC	50002040	X			X	X	X	U	A	W	SS
Diceros bicornis	CCEC	50002044		X		X			U	S	U	SS
Diceros bicornis	CCEC	50002045				X			U	S	W	SS
Diceros bicornis	CCEC	50002046	X	X	X		X	X	U	S	U	SS
Diceros bicornis	CCEC	50002047		X	X		X	X	U	A	U	SS
Diceros bicornis	MNHN	ZM-AC-1936-644	X	X	X	X	X	X	F	S	U	SS
Diceros bicornis	MNHN	ZM-AC-1944-278	X			X	X	X	M	A	C	SS
Diceros bicornis	MNHN	ZM-AC-1974-124				X	X	X	F	A	C	SS
Diceros bicornis	RBINS	9714	X	X	X	X	X	X	F	A	W	SS
Diceros bicornis	RMCA	RG2133	X	X	X	X	X	X	M	S	W	SS
Diceros bicornis	UCMP	9856					X		U	A	U	CT
Diceros bicornis	ZSM	1961/186	X	X	X	X	X	X	M	S	U	SS
Diceros bicornis	ZSM	1961/187	X	X	X	X	X	X	M	S	U	SS
Diceros bicornis	ZSM	1962/166	X	X	X	X	X		F	S	U	SS
Rhinoceros sondaicus	CCEC	50002041	X	X	X	X	X	X	U	A	W	SS
Rhinoceros sondaicus	CCEC	50002043	X	X	X	X			U	A	W	SS
Rhinoceros sondaicus	MNHN	ZM-AC-A7970	X	X	X	X	X	X	U	A	U	SS
Rhinoceros sondaicus	MNHN	ZM-AC-A7971	X	X	X	X	X	X	U	A	W	SS
Rhinoceros sondaicus	NHMUK	ZD 1861.3.11.1	X	X	X	X	X	X	U	S	W	SS
Rhinoceros sondaicus	NHMUK	ZD 1871.12.29.7	X	X	X	X	X	X	M	A	W	SS
Rhinoceros sondaicus	NHMUK	ZD 1921.5.15.1	X	X	X	X	X	X	F	S	W	SS
Rhinoceros sondaicus	RBINS	1205F	X	X	X	X	X	X	U	S	W	SS
*Rhinoceros unicornis***	MNHN	ZM-AC-1885-734	X	X	X	X	X		U	A	W	SS
Rhinoceros unicornis	MNHN	ZM-AC-1932-49	X				X	X	U	S	U	SS
Rhinoceros unicornis	MNHN	ZM-AC-1960-59	X	X	X	X	X	X	M	A	C	SS
Rhinoceros unicornis	MNHN	ZM-AC-1967-101	X	X	X	X	X		F	A	C	SS
Rhinoceros unicornis	NHMUK	ZD 1884.1.22.1.2	X	X	X	X	X	X	F	A	W	SS
Rhinoceros unicornis	NHMUK	ZE 1950.10.18.5	X	X	X	X	X	X	M	A	W	SS
Rhinoceros unicornis	NHMUK	ZE 1961.5.10.1	X	X	X	X	X	X	M	A	W	SS
*Rhinoceros unicornis**	NHMUK	ZD 1972.822	X	X	X	X	X	X	U	A	U	SS
Rhinoceros unicornis	RBINS	1208	X	X	X	X	X	X	F	A	C	SS
Rhinoceros unicornis	RBINS	33382	X	X	X	X	X	X	U	A	U	SS

Table 2: List of the studied specimens with skeletal composition, sex, age class, condition and 3D acquisition details. Bones—H, humerus; R, radius; U, ulna; Fe, femur; T, tibia; Fi, fibula. Sex: F, female; M, male; U, unknown. Age—A, adult; Sa, sub-adult. Condition—W, wild; C, captive; U, unknown. 3D acquisition—SS, surface scanner; P, photogrammetry; CT, CT-scan. Institutional codes as in Chapter 2. * Specimens NHMUK ZD 2018.143 and NHMUK ZD 1972.822 were determined by ourselves during the visit of the collections on the basis of morphological observations and measurements on the post-cranial elements. These determinations were later confirmed by the shape analysis. ** The specimen MNHN-ZM-AC-1885-734 was previously determined as *Rhinoceros sondaicus* based on a supposed Javan origin. The observations made on both long bones and tarsal elements led me to consider this individual as an Indian rhino (*Rhinoceros unicornis*). This attribution was later confirmed by the shape analysis.

Geometric Morphometrics

I placed 35 anatomical landmarks on the humerus, 23 on the radius, 21 on the ulna, 27 on the femur, 24 on the tibia and 12 on the fibula. Details of landmark numbers and locations used for each bone are given in Appendix 1 of this chapter. The specimen chosen as the template for projection, relax and sliding steps was *Ceratotherium simum* RMCA 1985.32-M-0001. Projection, relax, sliding and GPA were performed as described in Chapter 2.

As the dataset contained more variables than observations, I used a Principal Component Analysis (PCA) to reduce dimensionality as recommended by Gunz & Mitteroecker (2013) and visualize the specimen distribution in the morphospace. I computed theoretical consensus shape of the sample and used it to calculate a TPS deformation of the template mesh. I then used this newly created consensus mesh to compute theoretical shapes associated with the maximum and minimum of both sides of each PCA, as well as mean shapes of each bone for each species. GPA, PCA and shape computations were done using the "Morpho" and "geomorph" packages (Adams & Otárola-Castillo, 2013; Adams, Collyer & Kaliontzopoulou, 2018; Schlager, 2018) in the R environment (R Core Team, 2014). Neighbour Joining method was used to construct trees based on relative Euclidian distances between individuals based on all principal component scores obtained with the PCA, allowing a global visualisation of the relationships between all the specimens. Trees were computed with the "ape" package (Paradis et al., 2018).

Allometry effect

In order to explore the relation between body mass and bone shape, I tested the effect of allometry, defined as "the size-related changes of morphological traits" (Klingenberg, 2016). Pearson's correlation tests were performed to look for correlation between the principal components and the centroid size ($\log_{10}$) for each bone. I also used the function *procD.allometry* of the "geomorph" package to perform a Procrustes ANOVA (a linear regression model using Procrustes distances between species instead of covariance matrices – see Goodall, 1991) to quantify the shape variation related to the centroid size, and to visualize theoretical shapes associated with minimal and maximal sizes of the sample (Adams & Otárola-Castillo, 2013; Adams, Collyer & Kaliontzopoulou, 2018). This test was performed taking into account group affiliation (e.g. species) to highlight respective roles of centroid size and

species determination on the shape variation. In the absence of individual body mass for the majority of the sample, I also performed a Procrustes ANOVA with the cube root of the mean mass attributed to each species (Table 1), each species being associated with the mean mass of its species. Like for the centroid size, theoretical shapes associated with minimal and maximal mean mass were computed using the predicted Procrustes residuals (details on the procedure are given in the "geomorph" documentation). Plots of the multivariate regressions of shape scores (i.e. regression of shape on size; see Drake & Klingenberg, 2008) against log-transformed centroid size were also computed.

Results

Shape analysis

I describe here the results of PCA for each bone and focus on the theoretical shape variations along the two main axes. For each bone, I chose to represent relevant views and anatomical features. Complete visualizations of the different theoretical shapes for the two first axes are available in Appendix 2 of this chapter. Analysis of shape relations among the sample is completed by the Neighbour Joining trees provided in Appendix 3 of this chapter.

Humerus

The first two axes of the PCA computed on the humerus represent 60.6% of the total variance (Figure 8A). The first axis represents more than half of the global variance (53%) and the five species appear clearly sorted along it, opposing *Ds. sumatrensis* on the positive side to *C. simum* on the negative one, i.e. the lightest and heaviest species, respectively. *Dc. bicornis* is grouped with *C. simum* on the negative part of the axis, whereas *R. sondaicus* is on the positive part. *R. unicornis* occupies the centre of the axis, between *Dc. bicornis* and *R. sondaicus*. Points distribution in the morphospace and Neighbour Joining trees indicate a clear separation between African and Asiatic rhinos (see Appendix 3A). The theoretical shape at the PC1 minimum (Figure 8B, D, F, H) shows a massive morphology, with mediolaterally and craniocaudally broad epiphyses and shaft; a wide humeral head, with very little overhanging of the diaphysis in the caudal direction; a lesser tubercle more strongly developed than the greater tubercle, with an intermediate tubercle separating a widely open bicipital groove into unequal parts, the lateral one being the largest; a lesser tubercle convexity medially extended whereas the greater tubercle one is quite reduced in this direction; a broad and diamond-shaped *m. infraspinatus* imprint on the lateral side; a broad deltoid tuberosity not extending beyond the lateral border of the bone; a shaft with its maximal width situated between the head neck and the deltoid tuberosity; a distinct but very smooth and flat *m. teres major* tuberosity; a distal epiphysis very large because of the development of the lateral epicondyle; a smooth epicondylar crest; a medial epicondyle mediolaterally wide and craniocaudally compressed; shallow and proximodistally compressed olecranon fossa and trochlea, a wide trochlea displaying a main axis tilted in the dorsoventral direction; and a capitulum with a relatively small surface area. At the opposite, the theoretical shape at the PC1 maximum (Figure 8C, E, G, I) shows a slender and thin aspect; a more rounded humeral head overhanging caudally the diaphysis; a greater tubercle more strongly developed than the lesser one and extending medially, conferring a more closed aspect to the bicipital groove, where the intermediate tubercle is almost absent; a slightly marked lesser tubercle convexity whereas the greater tubercle one is massive; a rounded and reduced *m. infraspinatus* insertion; a deltoid tuberosity strongly protruding laterally; a straight and thin shaft; no visible *m. teres major* tuberosity; a narrow distal epiphysis, with a small development of

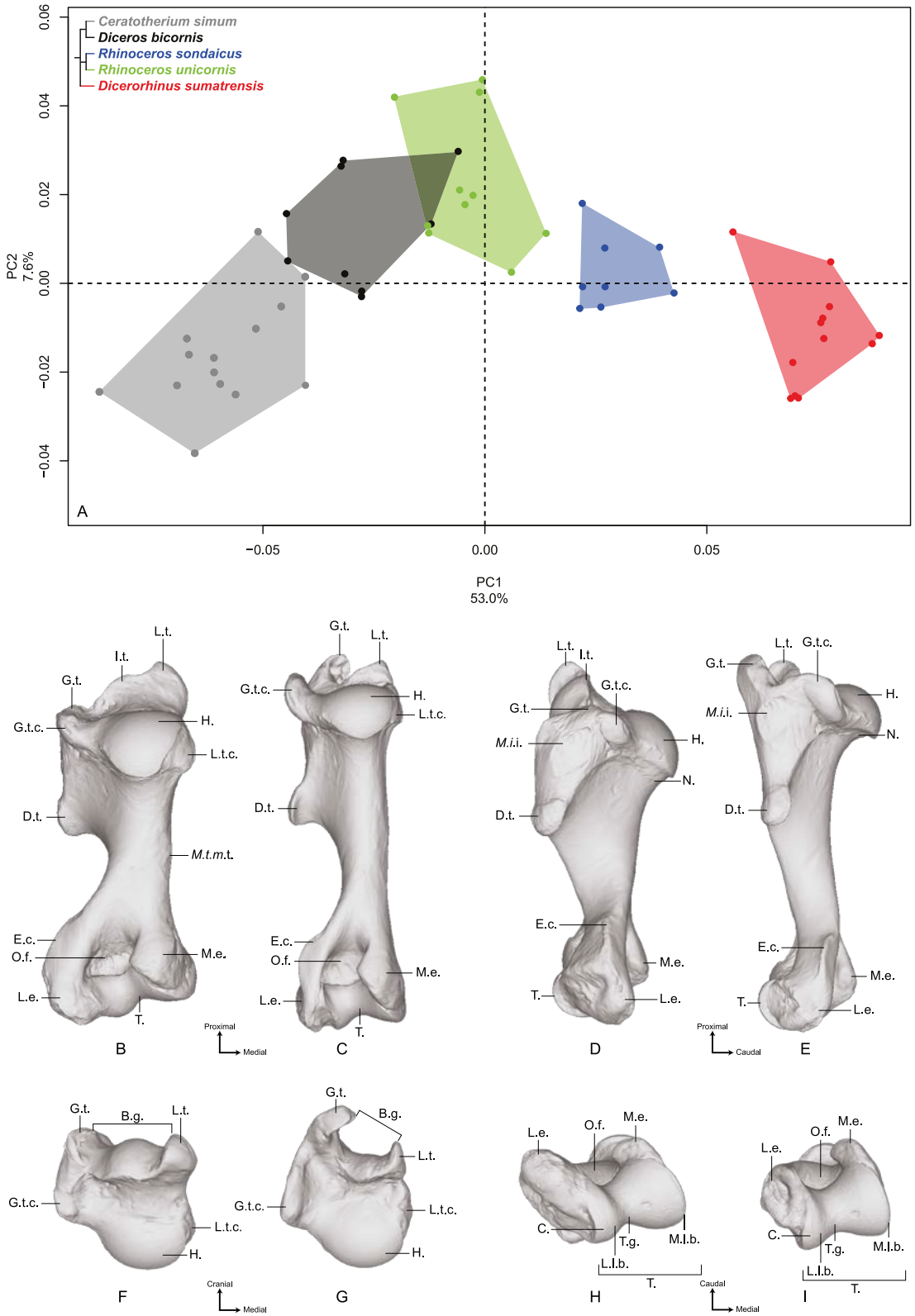

Figure 8: Results of the PCA performed on morphometric data of the humerus. A: Distribution of the specimens along the two first axes of the PCA; B–I: theoretical shapes associated with the minimum and maximum values of PC1: caudal (B, C), lateral (D, E), proximal (F, G) and distal (H, I) views for PC1 minimum (B, D, F, H) and PC1 maximum (C, E, G, I). B.g., bicipital groove; C., capitulum; D.t., deltoid tuberosity; E.c., epicondylar crest; G.t., greater tubercle; G.t.c., greater tubercle convexity; H., head; I.t., intermediate tubercle; L.e., lateral epicondyle; L.l.b., lateral lip border; L.t., lesser tubercle; L.t.c., lesser tubercle convexity; M.e., medial epicondyle; M.i.i., M. infraspinatus insertion; M.l.b., medial lip border; M.t.m.t., M. teres major tuberosity; N., neck; O.f., olecranon fossa; T., trochlea; T.g., trochlear groove.

the lateral epicondyle; a sharp epicondylar crest; a medial epicondyle craniocaudally developed and overhanging the olecranon fossa; a deep and wide olecranon fossa; a far less compressed trochlea, with an axis less dorsoventrally tilted; and a very reduced capitulum.

Along the second axis (7.6%), *C. simum* and *Ds. sumatrensis* are grouped together on the negative part of the axis, with the three other species on the positive part, whereas they are opposed along the first axis. This second axis expresses the separation between the lightest and the heaviest rhino species on the one hand and the three other species on the other hand. The theoretical shape at the PC2 minimum displays a humeral head stretched in the caudal direction; a lesser tubercle more developed than the greater one, delimiting an open bicipital groove; a distal epiphysis proximodistally extended, with an epicondylar crest starting almost on the middle of the shaft; a rounded and wide olecranon fossa. At the opposite, the theoretical shape at the PC2 maximum shows a rounded humeral head; a strong development of both tubercles and a more closed bicipital groove; a distal epiphysis mediolaterally stretched, with the epicondylar crest starting at the distal third of the shaft; an olecranon fossa proximodistally compressed and more rectangular; and a well-developed lateral epicondyle.

Radius

The first two axes of the PCA performed on the radius express 52.3% of the total variance (Figure 9A). The first axis (36.4%) opposes *Ds. sumatrensis* and *Dc. bicornis* to *R. unicornis* and *C. simum*. *R. sondaicus* overlaps both *R. unicornis* and *Dc. bicornis* clusters. The specimens of *Ds. sumatrensis* are split in two discrete clusters along the first axis, but no clear explanation linked to age, sex or geographic origin was associated with this distribution. Point dispersion along this axis indicates an important intraspecific variation for *Ds. sumatrensis*, and to a lesser extent for *Dc. bicornis* and *R. sondaicus*. Unlike for the humerus, phylogenetically related species are not grouped together on PCA and Neighbour Joining trees (see Appendix 3B). The theoretical shape at the PC1 minimum (Figure 9B, D, F, H) shows a massive morphology with large shaft and epiphyses; an asymmetrical proximal articular surface (constituting the ulnar notch), with a medial portion appearing nearly twice as large as the lateral one; a protruding lateral insertion relief (i.e. insertion area of the *m. extensor digitorum*) whereas the radial tuberosity is little prominent; a lateral synovial articulation surface for the ulna mediolaterally reduced; a rectangular and thin medial synovial articulation surface for the ulna; a triangular proximal articular surface for the ulna as wide mediolaterally as proximodistally; a thick shaft with an interosseous space opening close to the proximal epiphysis: consequently, the interosseous crest runs along the diaphysis to the distal articular surface for the ulna; a broad distal epiphysis in the mediolateral direction, with a strong medial tubercle developed on the dorsal face; a distal articular surface compressed in the dorsoventral direction; an articular surface for the scaphoid little extended proximally; a trapezoidal and wide articular surface for the semilunar (i.e. lunate bone or lunatum); a well-developed radial sty-

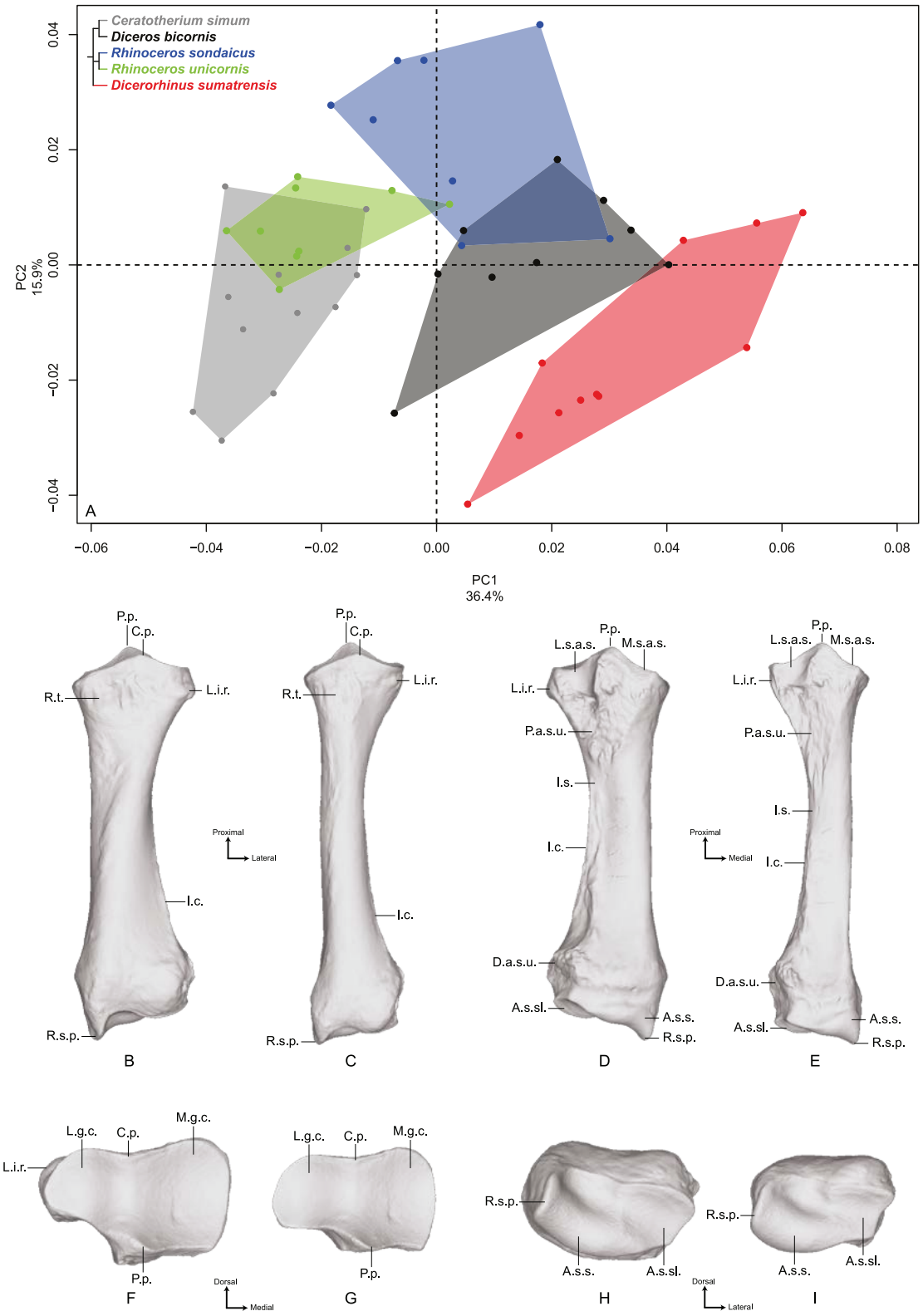

Figure 9: Results of the PCA performed on morphometric data of the radius. A: Distribution of the specimens along the two first axes of the PCA; B–I: theoretical shapes associated with the minimum and maximum values of PC1: dorsal (B, C), palmar (D, E), proximal (F, G) and distal (H, I) views for PC1 minimum (B, D, F, H) and PC1 maximum (C, E, G, I). A.s.s., articular surface for the scaphoid; A.s.sl., articular surface for the semilunar; C.p., coronoid process; D.a.s.u., distal articular surface for the ulna; I.c., interosseous crest; I.s., interosseous space; L.g.c., lateral glenoid cavity; L.i.r., lateral insertion relief; L.s.a.s., lateral synovial articular surface; M.g.c., medial glenoid cavity; M.s.a.s., medial synovial articular surface; P.a.s.u., proximal articular surface for the ulna; P.p., palmar process; R.s.p., radial styloid process; R.t., radial tuberosity.

loid process. The theoretical shape at the PC1 maximum (Figure 9C, E, G, I) displays a more slender morphology; a proximal articular surface less asymmetrical despite the development of the medial part; an almost absent lateral insertion relief; a completely flat radial tuberosity; a lateral synovial articulation for the ulna mediolaterally stretched; a rectangular and thin medial synovial articulation for the ulna; a triangular proximal articular surface for the ulna, mediolaterally short and proximodistally stretched; a thin and slender shaft, with an interosseous space opening at the proximal third of the total length; a poorly visible interosseous crest; a distal epiphysis far less dorsoventrally compressed and a lateral tubercle on the dorsal side poorly developed; a distal articular surface dorsoventrally wide with the surface responding to the scaphoid extending proximally; a trapezoidal and reduced articular surface for the semilunar; a less developed radial styloid process with a rounded border.

The second axis (15.9%) discriminates mainly *R. sondaicus* from the four other species. *R. unicornis* displays little extension along this axis; neither does *Dc. bicornis*, only driven on the negative side by a single individual. *R. unicornis* extension along the second axis is very limited, contrary to that of *C. simum* and *Ds. sumatrensis* clusters. As on the first axis, *Ds. sumatrensis* is split in two clusters, one in the negative part and the other around null values. The theoretical shape at the PC2 minimum displays a slender morphology, with a strongly asymmetrical proximal articular surface; a palmar process opposed to the coronoid process proximally reduced; a distal epiphysis dorsoventrally broad, with a developed lateral prominence; a little developed radial styloid process; an articular surface for the scaphoid proximally extended. The theoretical shape at PC2 maximum displays a more massive shape; a deeper and more symmetrical proximal articular surface with a well-developed palmar process; a dorsoventrally compressed distal epiphysis with a more developed styloid process.

Ulna

The first two axes of the PCA performed on the ulna express 41.5% of the total variance (Figure 10A). The first axis (22.1%) separates *Ds. sumatrensis* and *Dc. bicornis* on the positive part and *R. sondaicus*, *R. unicornis* and *C. simum* on the negative part. However, the clusters of *C. simum* and *R. unicornis* overlap along this axis. The general pattern on both PCA and Neighbour Joining trees is close to the one observed for the radius (see Appendix 3C). The theoretical shape at the PC1 minimum (Figure 10B, D, F, H) displays a thick morphology with large epiphyses; a massive olecranon tuberosity with a medial tubercle – where inserts the medial head of the *m. triceps brachii* – oriented dorsally; an anconeal process poorly developed dorsally and mediolaterally wide, as is the articular surface constituting the trochlear notch (receiving the humeral trochlea); a medially stretched medial part of the articular surface for the humerus; a short interosseous crest ending at the shaft half, with the interosseous space; a broad shaft with a triangular section; a straight palmar border whereas the shaft is medially curved; a massive distal epiphysis with a wide insertion surface for the radius; an articular surface for the tri-

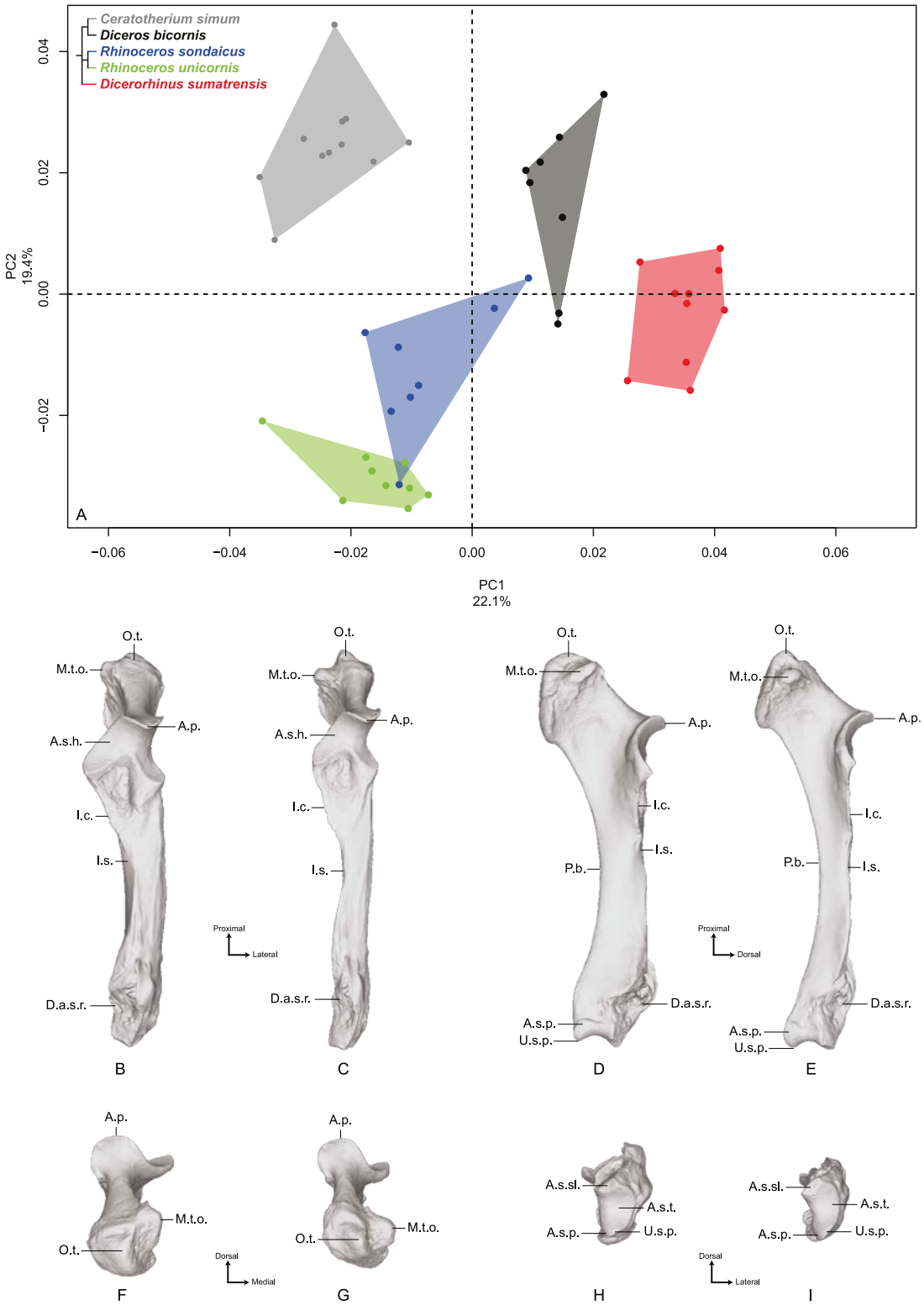

Figure 10: Results of the PCA performed on morphometric data of the ulna. A: Distribution of the specimens along the two first axes of the PCA; B–I: theoretical shapes associated with the minimum and maximum values of PC1: dorsal (B, C), medial (D, E), proximal (F, G) and distal (H, I) views for PC1 minimum (B, D, F, H) and PC1 maximum (C, E, G, I). A.p., anconeal process; A.s.h., articular surface for the humerus; A.s.p., articular surface for the pisiform; A.s.sl., articular surface for the semilunar; A.s.t., articular surface for the triquetrum; D.a.s.r., distal articular surface for the radius; I.c., interosseous crest; I.s., interosseous space; M.t.o., medial tuberosity of the olecranon; O.t., olecranon tuberosity; P.b., palmar border; U.s.p., ulnar styloid process.

quetrum (i.e. triquetral or pyramidal bone) mediolaterally wide and little concave, while the one responding to the pisiform is crescent-shaped and little extended proximally. The theoretical shape for the PC1 maximum (Figure 10C, E, G, I) displays a more gracile morphology; a slender olecranon tuberosity with a medial tubercle where inserts the medial head of the *m. triceps brachii* oriented in the palmar direction; an anconeal process dorsally developed and mediolaterally narrow, as is the articular surface of the trochlear notch; a slightly medially stretched medial part of the articular surface; a sharp interosseous crest; a thin and straight shaft; a distal epiphysis mediolaterally compressed and little concave; an articular surface for the triquetrum mediolaterally narrow; a triangular and proximally well-developed articular surface for the pisiform.

The second axis (19.4%) separates quite clearly the three Asian species from the African ones. The theoretical shape at the PC2 minimum displays a slender and straight morphology with a high square-shaped olecranon process, mediolaterally flattened, more stretched in the palmar direction; a wide and squared anconeal process; a straight and regular shaft; a distal epiphysis mediolaterally compressed with a concave articular surface for the triquetrum and a distally developed styloid process; a proximally extended articular facet for the pisiform. The theoretical shape at the PC2 maximum displays a more massive and medially concave shape with an olecranon process mediolaterally inflated and rounded in the palmar direction; an anconeal process little developed dorsally and laterally tilted; an articular surface constituting the trochlear notch proximodistally compressed and extending medially; a mediolaterally wide articular surface for the triquetrum; a little developed styloid process; an articular surface for the pisiform poorly extended proximally and square-shaped.

Femur

The first two axes of the PCA performed on the femur express 45.0% of the global variance (Figure 11A). The first principal component (36.1%) clearly isolates *Ds. sumatrensis* on the positive part from the other species. The clusters of *Dc. bicornis*, *R. sondaicus* and *R. unicornis* overlap on the negative part of the axis. *Dc. bicornis* and *R. unicornis* specimens overlap a significant part of the cluster of *C. simum* too. The general pattern observed on the Neighbour Joining tree is closer to the humerus one, with African and Asiatic species grouped together, respectively (see Appendix 3D). The theoretical shape at the PC1 minimum (Figure 11B, D, F, H) shows a massive morphology with large epiphyses and a curved medial border, conferring a concave aspect to the diaphysis axis; a large femoral head, off-centred relatively to the shaft main axis, supported by a very large neck; a small and shallow *fovea capitis* oriented mediocaudally; a greater trochanter convexity expanding strongly laterodistally; the absence of trochanteric notch between the convexity and the top of the trochanter (Figure 11F); a proximodistally reduced trochanteric fossa; a sharp lesser trochanter running along the medial edge, which is craniocaudally flattened below the humeral head; a third trochanter extending strongly

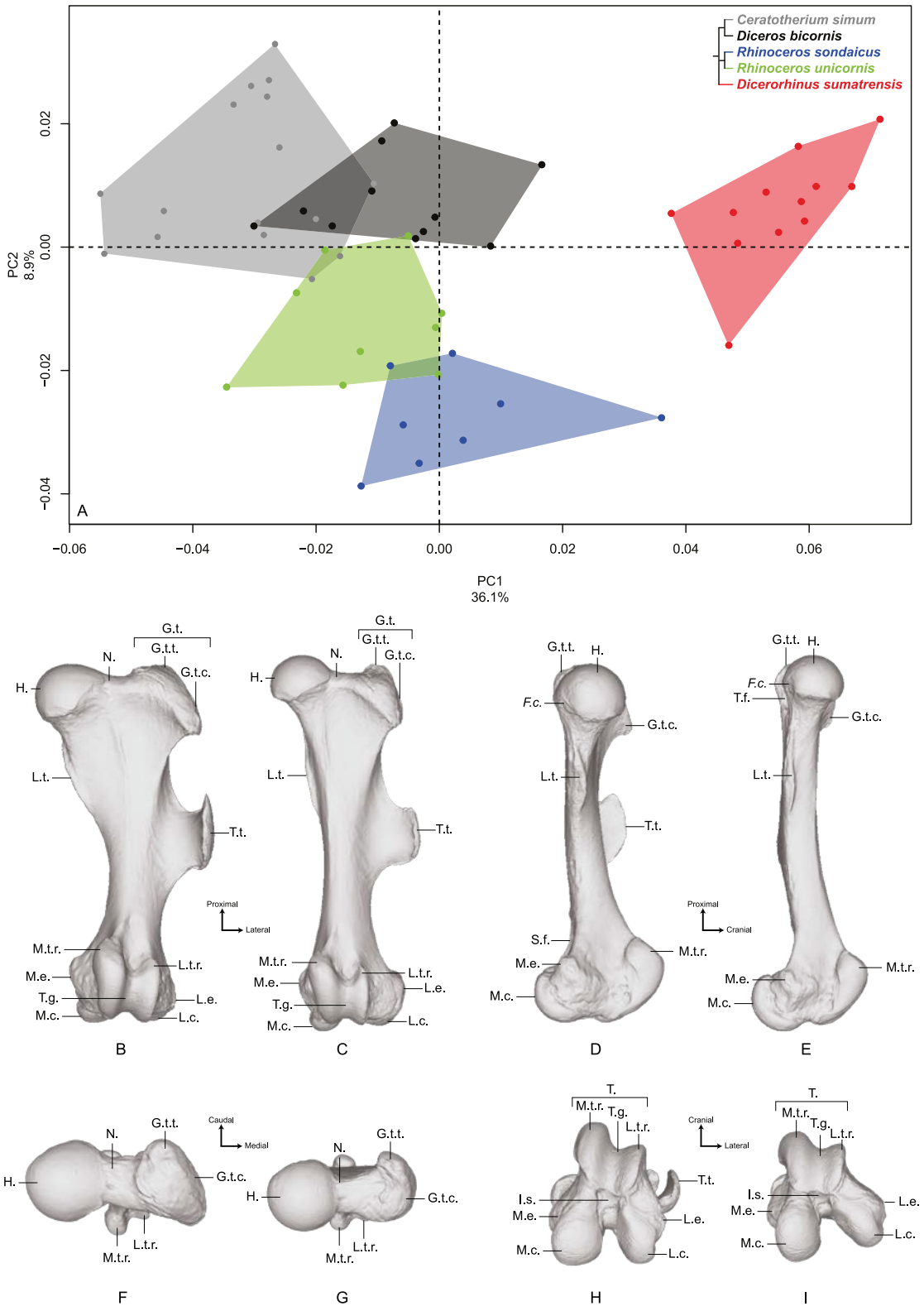

Figure 11: Results of the PCA performed on morphometric data of the femur. A: Distribution of the specimens along the two first axes of the PCA; B–I: theoretical shapes associated with the minimum and maximum values of PC1: cranial (B, C), medial (D, E), proximal (F, G) and distal (H, I) views for PC1 minimum (B, D, F, H) and PC1 maximum (C, E, G, I). F.c., Fovea capitis; G.t., greater trochanter; G.t.c., greater trochanter convexity; G.t.t., greater trochanter top; H., head; I.s., intercondylar space; L.c., lateral condyle; L.e., lateral epicondyle; L.t.r., lateral trochlear ridge; L.t., lesser trochanter; M.c., medial condyle; M.e., medial epicondyle; M.t.r., medial trochlear ridge; N., neck; S.f., supracondylar fossa; T., trochlea; T.f., trochanteric fossa; T.g., trochlear groove; T.t., third trochanter.

laterally, cranially and proximally towards the greater trochanter convexity, and much curved towards the medial direction; a quite irregular shaft section along the bone – flattened below the proximal epiphysis and more trapezoidal towards the distal epiphysis; a broad distal epiphysis with developed medial and lateral epicondyles; a shallow supracondylar fossa; a wide trochlea, with a main rotation axis aligned with the shaft axis; a large and cranially expanded medial ridge of the trochlea separated from the lateral one by a deep trochlear groove; a medial condyle surface area larger than the lateral condyle one, both being separated by a narrow intercondylar space. At the opposite, the theoretical shape at the PC1 maximum (Figure 11C, E, G, I) is more slender with a straight and regular shaft; a rounded femoral head aligned with the shaft main axis and supported by a thinner neck; a more pronounced and rounded *fovea capitis* oriented almost completely caudally; a greater trochanter convexity little developed laterodistally; a more pronounced trochanter top despite the absence of trochanteric notch; a thin lesser trochanter situated on the caudal border of the medial side; a rounded third trochanter more developed laterally than cranially; a quite regular and trapezoidal shaft section; a distal epiphysis mediolaterally broader and oriented medially; an almost absent supracondylar fossa; a less developed medial trochlear ridge separated from the lateral one by a shallow trochlear groove; a lateral condyle more oblique and divergent relatively to the medial one, increasing the intercondylar space; symmetrical medial and lateral condylar surfaces.

The second axis (8.9%) clearly opposes *Ds. sumatrensis, C. simum* and *Dc. bicornis* on the positive part to the two *Rhinoceros* species on the negative part, the cluster of *Ds. sumatrensis* being driven towards negative values by a single individual. The theoretical shape at the PC2 minimum is mainly characterized by a flattened femoral head with a strong neck; a rounded and large *fovea capitis* oriented mediocaudally; a greater trochanter convexity laterodistally expanded; a long and thin lesser trochanter; an extremely developed third trochanter in lateral, cranial and proximal directions; a straight and regular shaft; a broad distal epiphysis with important development of both epicondyles; a trochlea rotation axis aligned with the main axis of the shaft. The theoretical shape at the PC2 maximum displays a more rounded head, with a more stretched neck; no *fovea capitis* at all but a little groove on the head border; a greater trochanter convexity little expanded laterodistally; a short and more medially developed lesser trochanter; a rounded third trochanter little developed in cranial and proximal directions; a straight shaft; a distal epiphysis less mediolaterally broad; a narrower intercondylar space; a more inflated medial condyle.

Tibia

The first two axes of the PCA performed on the tibia express 50.0% of the global variance (Figure 12A). The first axis (29.1%) separates roughly *Dc. bicornis* and *Ds. sumatrensis* on the positive part and *C. simum, R. sondaicus* and *R. unicornis* on the negative part. *Dc. bicornis* shows an important intraspecific

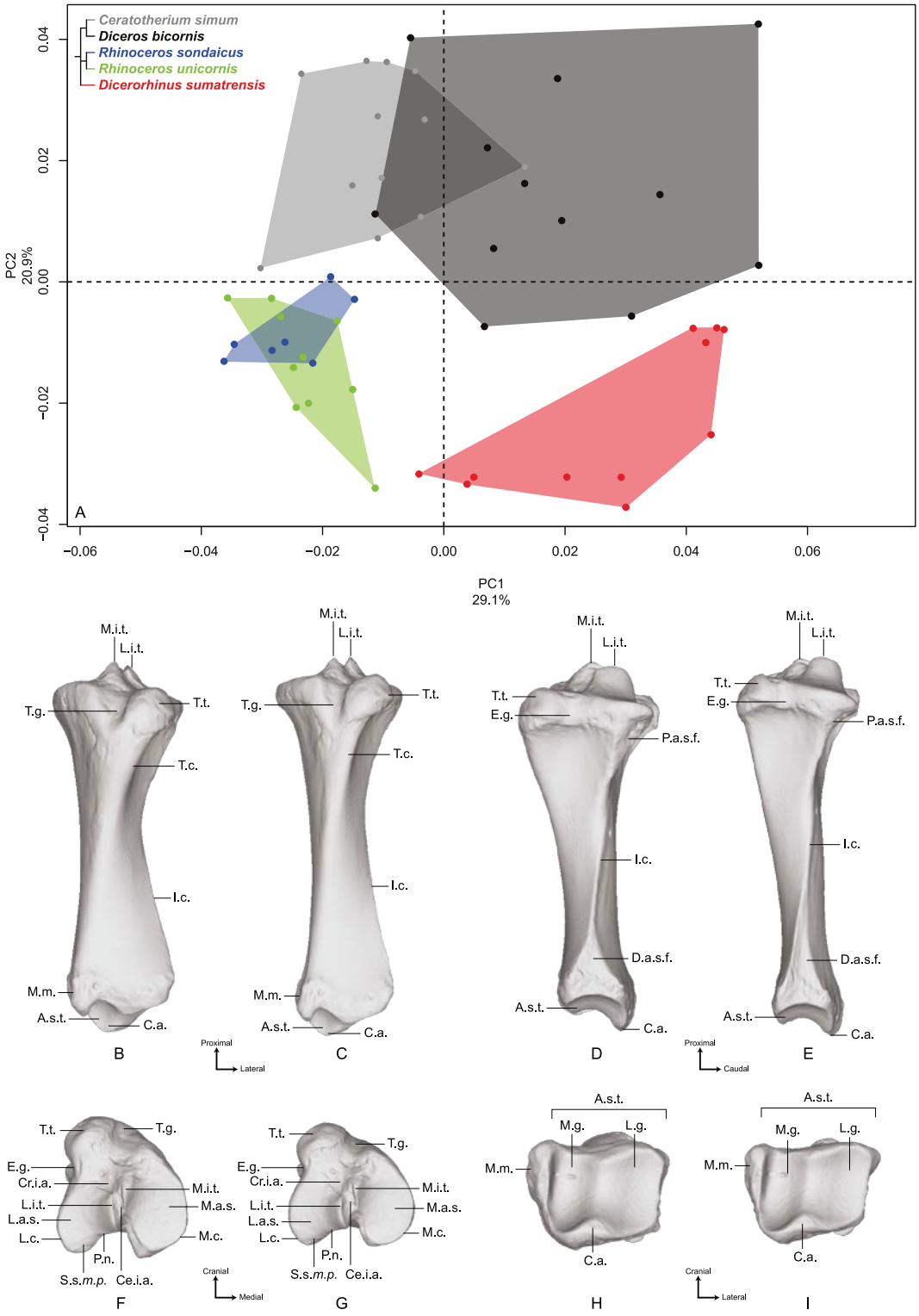

Figure 12: Results of the PCA performed on morphometric data of the tibia. A: Distribution of the specimens along the two first axes of the PCA; B–I: theoretical shapes associated with the minimum and maximum values of PC1: cranial (B, C), lateral (D, E), proximal (F, G) and distal (H, I) views for PC1 minimum (B, D, F, H) and PC1 maximum (C, E, G, I). A.s.t., articular surface for the talus; C.a., caudal apophysis; Ce.i.a., central intercondylar area; Cr.i.a., cranial intercondylar area; D.a.s.f., distal articular surface for the fibula; E.g., extensor groove; I.c., interosseous crest; L.a.s., lateral articular surface; L.c., lateral condyle; L.g., lateral groove; L.i.t., lateral intercondylar tubercle; M.a.s., medial articular surface; M.c., medial condyle; M.g., medial groove; M.i.t., medial intercondylar tubercle; M.m., medial malleolus; P.a.s.f., proximal articular surface for the fibula; P.n., popliteal notch; S.s.m.p., sliding surface for the m. popliteus; T.c., tibial crest; T.g., tuberosity groove; T.t., tibial tuberosity.

variation along both axes. Neighbour Joining tree structure is less clear than for previous bones: both *Rhinoceros* species isolate from most of the other specimens, *C. simum* appears also separated from *Dc. bicornis* and *Ds. sumatrensis*. However, one *C. simum* and three *Ds. sumatrensis* specimens are closer from the *Rhinoceros* group than from their own respective species (see Appendix 3E). The theoretical shape at the PC1 minimum (Figure 12B, D, F, H) shows a massive morphology with broad shaft and epiphyses, both in craniocaudal and mediolateral directions; medial and lateral intercondylar tubercles having the same height and a reduced central intercondylar area; a broad cranial intercondylar area; a medial articular surface larger than the lateral one, with the sliding surface for the *m. popliteus* tendon extending caudally; a U-shaped popliteal notch; a rounded tibial tuberosity, laterally deflected and medially bordered by a shallow groove; a shallow extensor groove; a regularly triangular proximal articular surface for the fibula extending distally; a thick tibial crest disappearing at the middle of the shaft, where the bone section is the smallest; a distal epiphysis mediolaterally broad and rectangular in section; a distal articular surface for the fibula reduced in height and triangular-shaped, surmounted by a smooth interosseous crest running towards the middle of the shaft; a distal articular surface for the talus roughly rectangular, with a lateral groove larger and shallower than the medial one, separated by a prominent intermediate process without synovial fossa; an articular surface with a rotation axis aligned with the bone main axis; a prominent medial malleolus. The theoretical shape at the PC1 maximum (Figure 12C, E, G, I) displays a relatively gracile morphology with a thin shaft; a lateral intercondylar tubercle more proximally extended than the medial one and a relatively large central intercondylar area; a lateral condylar surface extending cranially, reducing the cranial intercondylar area; medial and lateral articular roughly equal surface areas; a V-shaped popliteal notch; a tibial tuberosity slightly more laterally deflected; a deeper tuberosity groove; a nail-shaped proximal articular surface for the fibula; a sharper tibial crest disappearing just before the first half of the shaft; a distal epiphysis more compressed craniocaudally; a distal articular surface for the fibula displaying a large triangle synostosis area occupying a third of the shaft and prolonged by a sharp interosseous crest. There is no major difference in the distal articular shape between PC1 maximum and minimum, except that the caudal apophysis is less prominent in the distal direction.

The second axis (20.9%) clearly separates the two African species (*C. simum* and *Dc. bicornis*) on the positive part from the three Asian species (*Ds. sumatrensis, R. sondaicus* and *R. unicornis*) on the negative part. The theoretical shape at the PC2 minimum displays a slightly more slender morphology; a proximal plateau higher cranially than caudally and forming a closer angle with the diaphysis axis; a high intercondylar eminence; a lateral articular surface more caudally extended than the medial one; a tibial tuberosity well separated from the condyles by deep tuberosity and extensor grooves; a straight shaft ending with divergent borders forming a large and rectangular distal epiphysis; a distal articular

surface for the fibula forming a regular triangle surmounted by a sharp interosseous crest; a medially extended medial malleolus, resulting in a rectangular articular surface with the talus, where the medial groove is narrow and deep, occupying a third of the area, whereas the lateral groove is shallow and broad. The theoretical shape at the PC2 maximum displays a more massive morphology, with a cranio-ocaudal inflation of the epiphyses; a proximal plateau almost perpendicular to the diaphysis axis; a lower intercondylar eminence; a lateral condyle surface almost twice less large than the medial one, which is more developed caudally; a massive tibial tuberosity strongly deviated laterally, delimited by very shallow tuberosity and extensor grooves and resulting in a very large cranial intercondylar area; a straight shaft ending with almost parallel medial and lateral borders and a square-shaped distal epiphysis; a medial malleolus less medially deflated; a squared distal articular surface for the talus with medial and lateral grooves showing similar surface area and depth.

Fibula

The first two axes of the PCA performed on the fibula express 55.9% of the global variance (Figure 13). Contrary to the five previous analyses, the first axis (40.7%) here seems particularly driven by a strong intraspecific variation. The clusters of *C. simum* and *Ds. sumatrensis* are stretched along the PC1 and overlap with almost every other specimen. The cluster of *Dc. bicornis* is quite stretched along the axis too and only the two *Rhinoceros* species display less intraspecific variation. This pattern does not seem linked to sex, age class or condition (wild or captive): despite the presence of slightly more females and subadults on the negative part of the component, I did not consider this observation as robust enough to state on this question. This cluster distribution along the PC1 seems linked to the presence of irregular crests along the shaft, associated with an important variation of the outline of the crests running along the diaphysis, and a slight rotation of the fibular head (see Appendix 2 of this chapter). Consequently, I chose to display and analyse the specimen distribution along the second and third components instead. Theoretical shapes associated with the PC1 are available in the Appendix 2 of this chapter.

PC2 and PC3 express 22.9% of the global variance (Figure 14A). The second component (15.2%) opposes *C. simum* on the negative side to *Ds. sumatrensis* on the positive side, whereas *Dc. bicornis*, *R. sondaicus* and *R. unicornis* have a more central disposition. Like for the tibia, the Neighbour Joining tree structure appears less clearly sorted by species than for other bones. If *Rhinoceros* species group together and African ones as well, *Ds. sumatrensis* sample is split in two subgroups mixed with *R. unicornis* and African rhinos respectively (see Appendix 3F). The theoretical shape at the PC2 minimum (Figure 14B, D, F, H, J) displays a broad morphology with large epiphyses and a straight shaft; a rounded head with a proximal articular surface for the tibia craniomedially oriented; a head width similar to the shaft one; a robust shaft with two strong craniolateral and caudolateral lines running down the distal

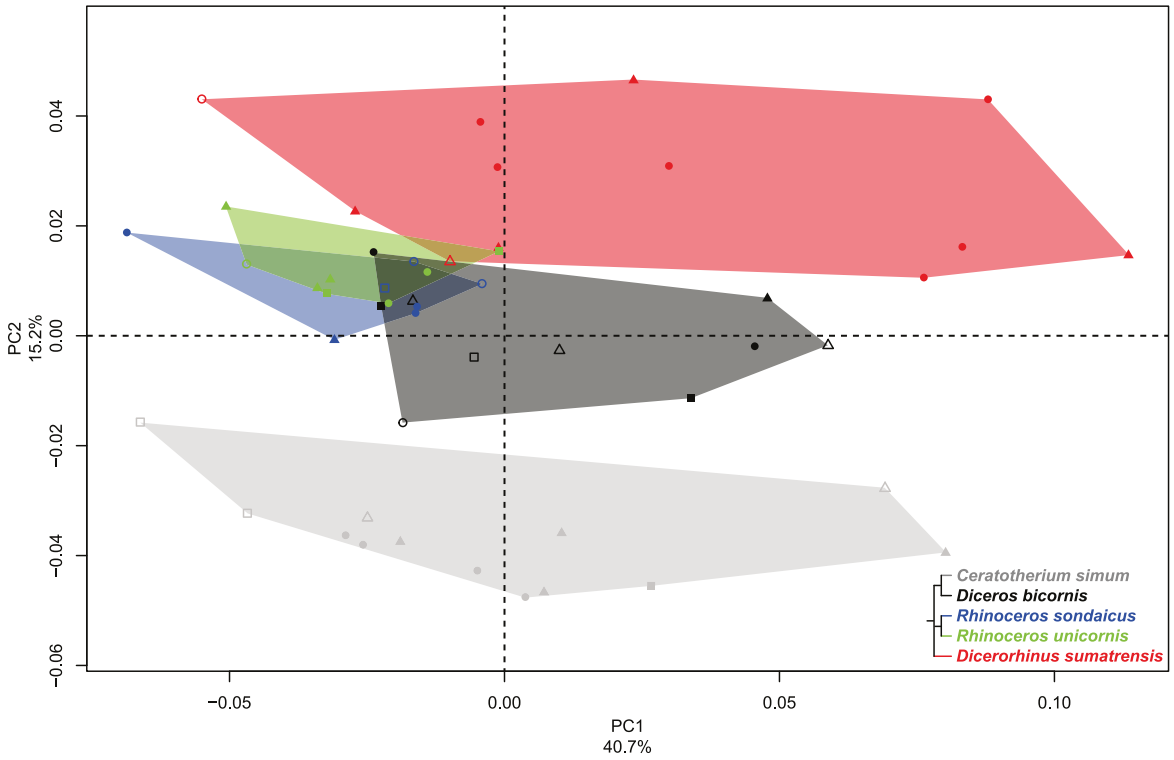

Figure 13: Results of the PCA performed on morphometric data of the fibula. Distribution of the specimens along the two first axes of the PCA, taking into account the age class and the sex of each specimen. Square, female; triangle, male; circle, unknown; empty symbol, subadult; filled symbol, adult.

epiphysis and enlarging craniocaudally towards the distal epiphysis; a sharp and irregular interosseous crest; a distal epiphysis mediolaterally compressed with little development of the two distal tubercles at the end of the lateral crests; a shallow lateral groove; a triangular distal articular surface for the tibia, occupying only the last distal quarter of the bone length; a short and ovoid articular surface for the talus with a sharp distal ridge. The theoretical shape at the PC2 maximum (Figure 14C, E, G, I, K) displays a slender morphology with a strongly curved shaft; a mediolaterally flat head extending craniocaudally and overhanging strongly the diaphysis; a thin shaft with two sharp lateral crests running along it: these crests end with two developed tubercles surrounding a deep lateral groove; a distal articular surface for the tibia extending from the distal third of the shape and forming a stretched triangle; a wider and kidney-shaped articular surface for the talus, forming two distal tips responding to the two lateral tubercles: between them on the distal face, a large groove is visible, ending at the centre of the face.

The third component (7.7%) mainly opposes *Dc. bicornis* on the positive part to *R. sondaicus* on the negative part. However, this opposition is mainly driven by a small number of individuals (two for *Dc. bicornis* and four for *R. sondaicus*). The specimens of *R. sondaicus* are divided into two clusters, with three individuals overlapping notably with *Ds. sumatrensis*. The theoretical shape at the PC3 minimum shows a massive morphology, with broad shaft and epiphyses; a craniocaudally broad head, over-

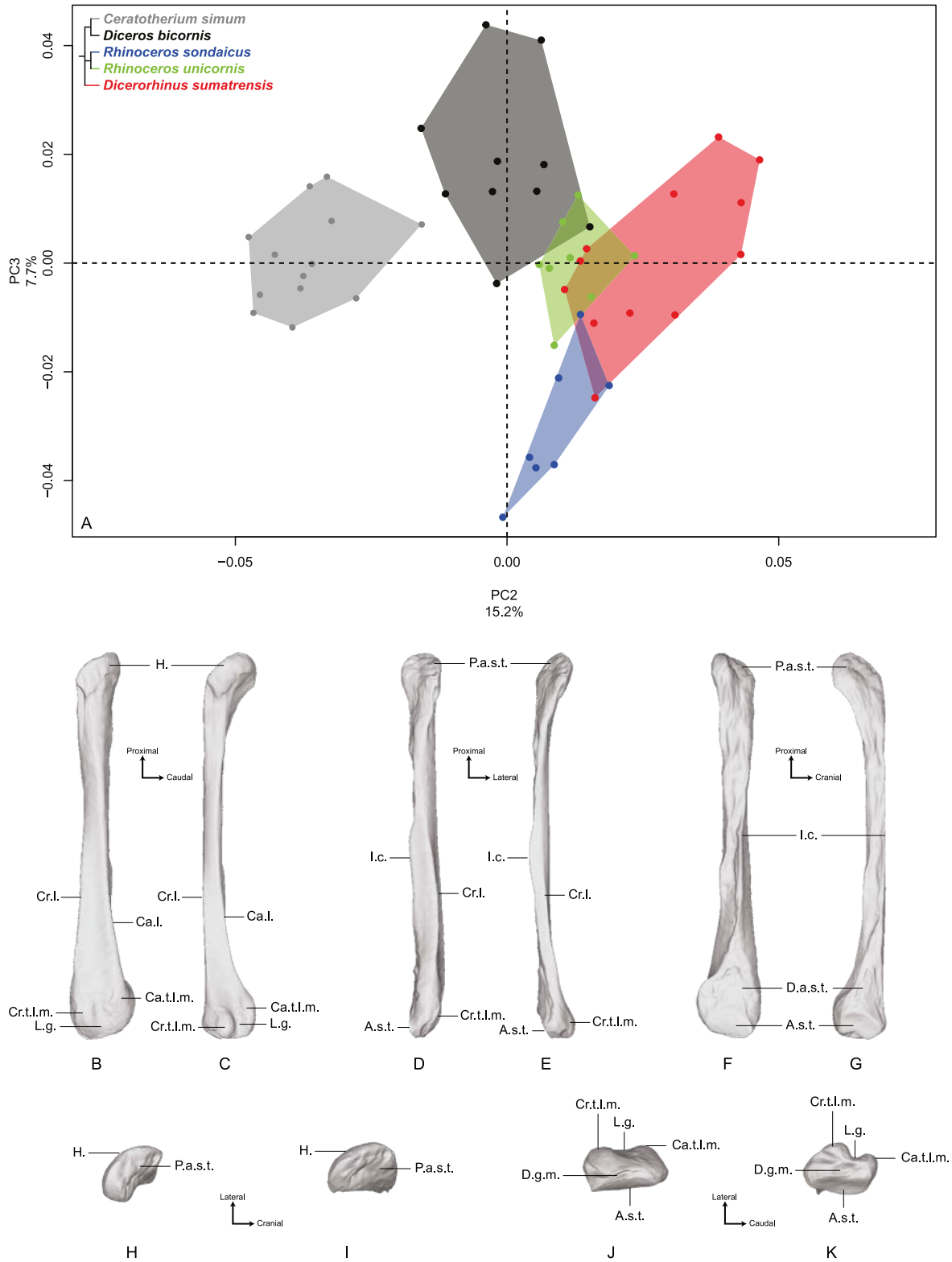

Figure 14: Results of the PCA performed on morphometric data of the fibula (second and third axes). A: Distribution of the specimens along the second and third axes of the PCA; B–K: theoretical shapes associated with the minimum and maximum values of PC2: lateral (B, C), cranial (D, E), medial (F, G), proximal (H, I) and distal (J, K) views for PC2 minimum (B, D, F, H, J) and PC2 maximum (C, E, G, I, K). A.s.t., articular surface for the talus; Ca.l., caudo-lateral line; Ca.t.l.m., caudal tubercle of the lateral malleolus; Cr.l., cranio-lateral line; Cr.t.l.m., cranial tubercle of the lateral malleolus; D.a.s.t., distal articular surface for the tibia; D.g.m., distal groove of the malleolus; H., head; I.c., interosseous crest; L.g., lateral groove; P.a.s.t., proximal articular surface for the tibia.

hanging the shaft laterally; a proximal articular surface for the tibia oriented almost completely medially; a straight shaft displaying a constant width along the bone; craniolateral and caudolateral crests running almost parallel towards the distal end of the bone, forming two developed tubercles surrounding a deep groove; an interosseous space covered by irregular reliefs and bordered by a sharp interosseous crest; a distal articular surface for the tibia forming a triangle cranially deported; a kidney-shaped distal articular surface for the talus, with a distal border separated from the lateral tubercles by a groove stopping at the middle of the distal face. The theoretical shape at the PC3 maximum shows an extremely thin morphology with a flattened and poorly developed head; a proximal articular surface oriented almost completely in the cranial direction; a torsion of almost 90 degrees between the orientation of the proximal and distal articular surfaces for the tibia; a very thin and flat shaft; craniolateral and caudolateral crests running along the diaphysis ending on the distal epiphysis with few developed tubercles; a distal articular surface for the tibia forming a slender triangle; a relatively small distal articular surface for the talus, with a less pronounced kidney-shape; a groove on the distal face mediolaterally compressed.

Interspecific morphological variation

In addition to global interspecific patterns of shape, I shortly describe the main morphological features characterizing each species. Mean shapes of each bone for the five species are available in Appendix 4 of this chapter.

Limb long bones of *C. simum* present a general massive and robust aspect. The humerus is thick and shows a strong development of the lesser tubercle and the lateral epicondyle, as well as a proximal broadening in the craniocaudal direction. The radius and ulna are robust and display an important medial development of the articular parts constituting the trochlear notch. The ulna bears a strong olecranon tubercle. The distal articular surface for the carpals constituted by the two bones is mediolaterally wide and compressed in the craniocaudal direction. The hind limb bones are robust as well, this robustness being mainly expressed in the mediolateral direction for the femur. This bone displays a rounded and thick head, strong greater and third trochanters, and a distal trochlea laterally oriented. The tibia and fibula are robust as well, with a wide tibial plateau supporting the knee articulation and a squared distal articulation for the talus.

For *Dc. bicornis*, the general aspect of the humerus is close to the one observed on *C. simum*, particularly for the epiphyses (e.g. the shape of the bicipital groove, the development of the lesser tubercle and of the lateral epicondyle), though its degree of robustness is less intense. The radius is relatively slender but the proximal articular surface displays a cranial border with a marked groove under the coronoid process, also observed on *C. simum*. The ulna is slender as well with a thin olecranon process

and limited medial development. Both distal epiphyses form a mediolaterally wide articular surface for the carpals, poorly craniocaudally compressed. As for hind limb bones, the femur is only slightly robust, with poorly developed trochanters and a slender diaphysis. Tibia and fibula are less thick too, with a squared articular surface for the talus as well. *Dc. bicornis* displays noticeable morphological similarities with *C. simum*.

The bone general morphology is very similar between both *R. sondaicus* and *R. unicornis*, being often more robust in *R. sondaicus.* For these two species, the humerus displays an important development of both lesser and greater tubercles, resulting in an asymmetrical bicipital groove. The greater tubercle is even sometimes higher than the lesser one in *R. sondaicus*, which is not the case in *R. unicornis*. The distal epiphysis is wide but with a medial epicondyle less developed than in *C. simum* and *Dc. bicornis*, and a rectangular olecranon fossa. The radius exhibits mediolaterally large epiphyses and a quite robust diaphysis, with a proximal articular surface similar in both *Rhinoceros* species, with a straight cranial border unlike in African rhinos. The distal epiphysis is rectangular and craniocaudally compressed. *R. unicornis* distinguishes from *R. sondaicus* in having a more robust radius, with a more asymmetrical proximal epiphysis, a deeper radial tuberosity and a larger distal articular surface. The ulna is also very similar, the one of *R. unicornis* being slightly more robust. The general aspect remains extremely close, with a developed olecranon, a medial development of the articular surface constituting the trochlear notch and a quite wide distal articular surface. On the hind limb, the femur appears different, the *R. unicornis* one showing important development of the greater and third trochanters, sometimes fused by a bony bridge as previously stated by Guérin (1980). The femur of *R. sondaicus* appears slightly less robust, and the greater and third trochanters are less developed and never fused. On the tibia, the proximal plateau is as wide as for the African taxa but the tibial tuberosity is more detached from the condyles by deep tuberosity and extensor grooves. The diaphysis is relatively thick and the distal articular surface is clearly rectangular. The fibula is very similar as well in the two species, with a distal epiphysis curved in the caudal direction and a kidney-shaped articular surface for the talus.

Ds. sumatrensis clearly differs from the other species. Despite clear rhinocerotid features, limb long bones display unique morphological traits, with a more pronounced slenderness. On the humerus, the development of the greater tubercle results in a more closed and asymmetrical bicipital groove. The distal epiphysis is mediolaterally narrow with a straight trochlea axis. The thin radius possesses a proximal articular surface almost symmetrical despite a medial glenoid cavity slightly more developed. The ulna is thin as well, and forms with the radius a rectangular articular surface for the carpals. The femur shows a high and rounded head and a poorly developed third trochanter. The distal trochlea axis is more medially oriented. On the tibia, the plateau is far less wide than in other species and the distal articular surface for the talus is rectangular. The thin fibula displays a large head caudally bordered by

a thin crest and the diaphysis is strongly curved medially towards the tibia. The kidney-shape of the distal articular surface for the talus resembles the *Rhinoceros* ones.

Correlation with the centroid size

Table 3 provides the results of the Pearson's correlation tests between the centroid size and the two first principal components for each bone (and the third component for the fibula). There is a significant correlation in each case between the first component and the centroid size, with higher correlation coefficient values for the radius and ulna, and smaller values for the humerus and fibula. The second principal component is also significantly correlated with the centroid size for the humerus, femur and fibula, with smaller correlation coefficient values than for PC1, except for the humerus.

Bone	Component	r	t	dF	P
Humerus	PC1	-0.38	-2.93	51	**0.01**
	PC2	0.43	3.44	51	**<0.01**
Radius	PC1	-0.64	-5.77	47	**<0.01**
	PC2	0.22	1.58	47	0.12
Ulna	PC1	-0.79	-8.44	44	**<0.01**
	PC2	0.02	0.11	44	0.91
Femur	PC1	-0.56	-5.01	54	**<0.01**
	PC2	0.30	-2.34	54	**0.02**
Tibia	PC1	-0.58	-5.05	51	**<0.01**
	PC2	0.08	0.58	51	0.57
Fibula	PC1	-0.36	-2.69	48	**<0.01**
	PC2	-0.34	-2.47	48	**0.02**
	PC3	0.16	1.12	48	0.27

Table 3 : Results of the Pearson's correlation tests between the log-transformed centroid size and the two first principal components for each bone. r, Pearson's correlation coefficient value; t, student distribution value; dF, degrees of freedom; P, p-value. Significant results are indicated in bold.

Allometry

Table 4 and Table 5 provide the main anatomical differences observed between theoretical shapes associated with minimal and maximal centroid size for the forelimb and hind limb bones, respectively. Theoretical shapes associated with minimal and maximal log centroid size are provided in Appendix 5 of this chapter. In the case of the fibula, I found a pattern very close to the one observed along the second axis of the PCA. Replacing the log centroid size by the cube root of the mean mass of each species results in almost identical theoretical shapes for each bone (Figure 15 and Appendix 6 of this

B	Anatomical feature	Centroid size minimum	Centroid size maximum
H	General aspect	Gracile	Robust
	Head	Rounded, overhanging the shaft	Rounded, overhanging poorly the shaft
	Lesser tubercle	Developed	Poorly developed
	Intermediate tubercle	Almost absent	Poorly developed
	Greater tubercle	Developed	Strongly developed
	Bicipital groove	Asymmetrical and closed	Almost symmetrical and widely open
	M. infraspinatus insertion	Diamond-shaped and strongly developed	Ovoid and less developed
	Deltoid tuberosity	Poorly laterally deviated and caudally sharp	Laterally deviated and caudally smooth
	Distal epiphysis	Medio-laterally compressed	Medio-laterally extended
	Supracondylar crest	Smooth	Very smooth
	Lateral epicondyle	Poorly extended laterally	Strongly extended laterally
	Medial epicondyle	Overhanging the olecranon fossa	Not overhanging the olecranon fossa
	Olecranon fossa	Triangular and deep	Rectangular and deep
	Trochlea	Sharp lips and deep groove	Smooth lips and shallow groove
	Capitulum	Extremely reduced	Extremely reduced
R	General aspect	Gracile	Robust
	Proximal articular surface	Open and little concave; medial glenoid cavity slightly larger than the lateral one	Concave; medial glenoid cavity twice as large as the lateral one
	Radial tuberosity	Poorly developed	Poorly developed
	Lateral insertion relief	Poorly developed	Knob-shaped
	Lateral synovial articulation surface	Trapezoid and laterally extended	Trapezoid and laterally reduced
	Medial synovial articulation surface	Thin and rectangular	Thin and rectangular
	Proximal articular surface for the ulna	Triangular, wide and proximo-distally short	Triangular, slender and proximo-distally long
	Interosseous crest	Smooth	Sharp
	Interosseous space position	Mid-shaft	First proximal third of the shaft
	Distal articular surface for the ulna	Long and slender triangle	Short and wide triangle
	Articular surface for the carpal bones	Broad in dorso-palmar direction	Compressed in dorso-palmar direction
	Articular surface for the scaphoid	Proximally extended	Poorly extended proximally
	Articular surface for the semilunar	Trapezoid and narrow	Trapezoid and wide
	Radial styloid process	Short	Long
U	General aspect	Gracile	Robust
	Olecranon	Medio-laterally compressed	Medio-laterally large
	Olecranon tuberosity	Oriented medially with a medial tubercle pointing in the medio-palmar direction	Oriented laterally with a medial tubercle pointing in the medio-dorsal direction
	Anconeus process	Developed in dorsal direction	Little developed dorsally
	Articular surface for the humerus	Medio-laterally reduced, lateral lip developed in proximal direction	Medio-laterally broad with an important development of the medial part
	Interosseous crest	Irregular and sharp	Smooth
	Distal epiphysis	Thin with a small lateral extension	Large and extending largely in lateral and dorsal directions
	Articular surface for the triquetrum	Narrow and concave	Wide and slightly concave
	Articular surface for the pisiform	Extended in proximal direction	Little developed in proximal direction

Table 4: Main anatomical differences observed between theoretical shapes associated with minimal and maximal centroid size for each bone of the forelimb. B, bone; H, humerus; R, radius; U, ulna.

B	Anatomical feature	Centroid size minimum	Centroid size maximum
Fe	General aspect	Gracile	Robust
	Head	Rounded, well separated from the shaft by a narrow neck	Massive and flattened, surmounting a large neck
	Fovea capitis	Formed by a simple shallow notch on the border head in medio-caudal direction	Small and shallow, oriented more medially
	Greater trochanter	Small and developed in the cranial direction	Large and developed in the latero-distal direction
	Lesser trochanter	Thin and bordering the caudal border of the shaft medial side	Thick, occupying the whole width of the medial side
	Lines on the cranial side	Medial line running straight along the side	Medial line strongly concave along the side
	Third trochanter	Rounded and poorly developed	Strong and developed towards the greater trochanter
	Trochlea	Oriented medially with a shallow groove and developed medial lip	Oriented cranially with a deep groove and an extremely developed medial lip
	Condyles	Almost of the same size	Medial condyle more developed than the lateral one
	Intercondylar space	Wide	Narrow
T	General aspect	Gracile	Robust
	Proximal condyles	Nearly equal surface areas; lateral condyle more developed caudally with a sliding surface for the *m. popliteus*	Medial condyle surface twice as wide as the lateral one and more developed caudally
	Intercondylar tubercles	Nearly of equal height	Medial tubercle higher than the lateral one
	Central intercondylar area	Wide	Narrow
	Tibial tuberosity	Laterally deviated	Massive and oriented in lateral direction
	Tuberosity groove	Deep	Shallow
	Extensor sulcus	Shallow	Shallow
	Proximal articular surface for the fibula	Nail-shaped	Triangular
	Interosseous crest	Sharp	Smooth
	Distal articular surface for the fibula	Narrow and triangular	Wide and triangular
	Articular surface for the talus	Rectangular, slightly tilted laterally	Squared, slightly oriented medially
	Medial groove for the talus	Deep and narrow	Deep and narrow
	Lateral groove for the talus	Shallow and wide	Shallow and wide
Fi	General aspect	Gracile	Robust
	Head	Flat and large, oriented cranio-medially	Small and oriented cranially
	Proximal articular surface for the tibia	Nail-shaped	Triangular
	Shaft	Thin and slightly concave, with two sharp crests running along the lateral side	Broad and straight, with two smooth crests running along the lateral side
	Distal articular surface for the tibia	Triangular, narrow and long	Triangular, wide and short
	Lateral malleolus	Two well-developed tubercles caudally oriented and separated by a deep groove	Two flat tubercles laterally oriented, with the cranial one being more developed, and separated by a shallow groove
	Articular surface for the talus	Kidney-shaped, broad in proximo-distal direction	Triangular, proximo-distally compressed

Table 5: Main anatomical differences observed between theoretical shapes associated with minimal and maximal centroid size for each bone of the hind limb. B, bone; Fe, femur; Fi, fibula; T, tibia.

chapter), only distinguishable by minor shape differences: towards body mass maximum, the radius and ulna appear slightly more robust than for centroid size maximum (Figure 15D, F); the greater and third trochanters of the femur are slightly less developed towards each other (Figure 15H). Theoretical

shapes associated with minimum and maximum of log centroid size are slightly more massive than the ones obtained with the cube root of the body mass for the humerus, the tibia and the fibula. All theoretical shapes associated with minimal and maximal cube root of the mean mass are provided in Appendix 6 of this chapter.

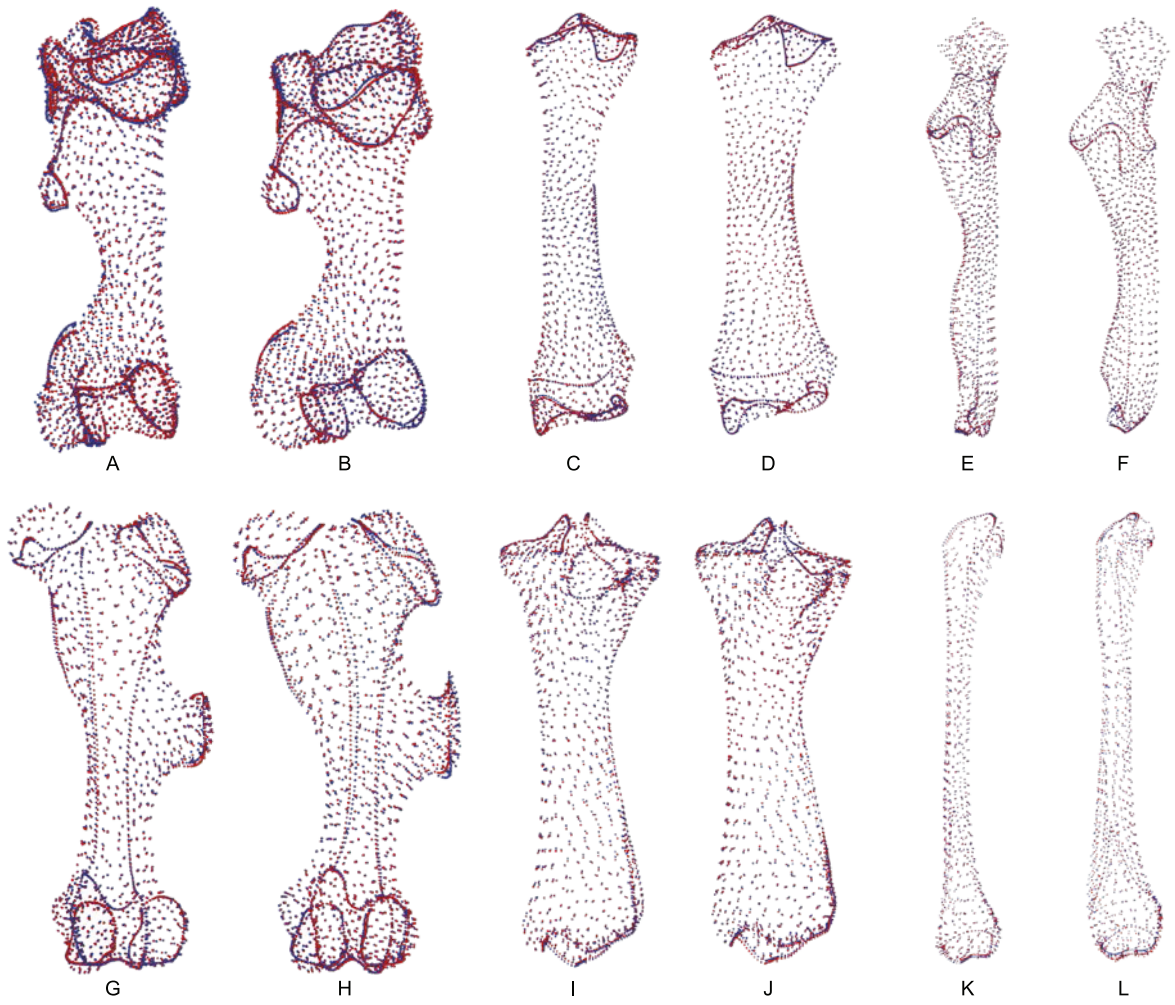

Figure 15: Landmark conformations associated with minimal and maximal centroid size and mean mass for each bone. A, B: Humerus (caudal view); C, D: radius (dorsal view); E, F: ulna (dorsal view); G, H: femur (cranial view); I, J: tibia (cranial view); K, L: fibula (lateral view). Red dots, landmark conformation associated with the mean mass. Blue dots, landmark conformation associated with the centroid size. A, C, E, G, I, K: Landmark conformation associated with the minimum of both parameters; B, D, F, H, J, L: landmark conformation associated with the maximum of both parameters.

Table 6 and Table 7 provide the results of the two Procrustes ANOVAs performed on shape data, where the log centroid size and the cube root of the mean body mass were, respectively, the independent variable. Log centroid size is significantly correlated with shape for the six bones, with a determination coefficient varying between 0.10 for the fibula and 0.18 for the ulna. In every case, the determination coefficient is more than twice as high for species affiliation as for log centroid size, indicating a more important influence of group affiliation than of allometry. This is especially the case for the humerus, with a determination coefficient of 0.53 for species affiliation and of only 0.13 for log centroid size.

Cube root of mean body mass is also significantly correlated with shape for the six bones, with slightly higher determination coefficient values than those obtained with the log centroid size. The humerus, the radius and the femur display the highest coefficients, between 0.33 and 0.26. These higher values may be due to the use of a same mean body mass for each rhino species instead of individual mass. Moreover, group affiliation could not be used in this case because of the mean body mass redundancy.

		R^2	F	Z	P (>F)
Humerus	Cs.	0.13	17.38	5.13	**0.001**
	Sp.	0.53	17.72	8.50	**0.001**
Radius	Cs.	0.18	15.72	5.74	**0.001**
	Sp.	0.32	7.07	8.83	**0.001**
Ulna	Cs.	0.16	12.94	6.19	**0.001**
	Sp.	0.36	7.31	9.27	**0.001**
Femur	Cs.	0.14	14.41	6.07	**0.001**
	Sp.	0.37	9.56	10.08	**0.001**
Tibia	Cs.	0.13	11.62	5.13	**0.001**
	Sp.	0.36	8.06	9.03	**0.001**
Fibula	Cs.	0.10	6.61	3.77	**0.001**
	Sp.	0.26	4.47	5.61	**0.001**

Table 6: Results of the Procrustes ANOVA performed on shape data and log-transformed centroid size (Cs.) taking into account species (Sp.) affiliation. R^2, determination coefficient value; F, Fisher distribution value; Z, normal distribution value; P, p-value. Significant results are indicated in bold.

	R^2	**F**	**Z**	**P (>F)**
Humerus	0.33	25.664	5.73	**0.001**
Radius	0.29	18.77	6.06	**0.001**
Ulna	0.21	11.22	5.57	**0.001**
Femur	0.26	18.61	6.39	**0.001**
Tibia	0.18	11.16	5.50	**0.001**
Fibula	0.11	5.91	3.40	**0.001**

Table 7: Results of the Procrustes ANOVA performed on shape data and cube root of the mean body mass. R^2, determination coefficient value; F, Fisher distribution value; Z, normal distribution value; P, p-value. Significant results are indicated in bold.

Multivariate regressions of shape scores against log-transformed centroid size (Figure 16) show that *Ds. sumatrensis* has the smallest centroid size and is well separated from the other rhino species in most cases, except for the tibia and fibula. *R. unicornis* possesses the highest centroid size in most of the cases, except for the radius and ulna, where it shares similar centroid size values and shape scores as *C. simum* (Table 8). Different tendencies can be observed: for the humerus, Asiatic rhinos have lower shape scores than African ones for a given size. Radius and ulna data display a point pattern similar to

each other, with the isolation of *Ds. sumatrensis* towards low values, a second cluster formed by *Dc. bicornis* and *R. sondaicus* at average values, and a third cluster with *C. simum* and *R. unicornis* showing the highest values. This separation in three groups can be observed at a lesser extent for the femur, where *Dc. bicornis* and *R. sondaicus* share almost the same centroid size and shape score variations, whereas *C. simum* and *R. unicornis* are separated by their respective centroid size despite similar shape scores. Finally, tibia and fibula display rather similar patterns with an important intraspecific shape variation, notably for *Ds. sumatrensis* and *Dc. bicornis*. There is a more important continuity between the different clusters for the tibia and the fibula than for other bones, where clusters are more separated from each other.

	C. simum	***D. sumatrensis***	***D. bicornis***	***R. sondaicus***	***R. unicornis***
Humerus	723 ± 34	626 ± 24	660 ± 49	749 ± 39	812 ± 26
Radius	501 ± 19	403 ± 14	485 ± 19	463 ± 28	520 ± 21
Ulna	512 ± 18	408 ± 14	492 ± 18	478 ± 28	530 ± 22
Femur	724 ± 37	613 ± 18	657 ± 28	686 ± 22	822 ± 34
Tibia	471 ± 17	398 ± 15	442 ± 25	451 ± 39	535 ± 28
Fibula	279 ± 14	233 ± 7	269 ± 14	254 ± 8	327 ± 16

Table 8: Mean centroid size and standard deviation by bone for each species.

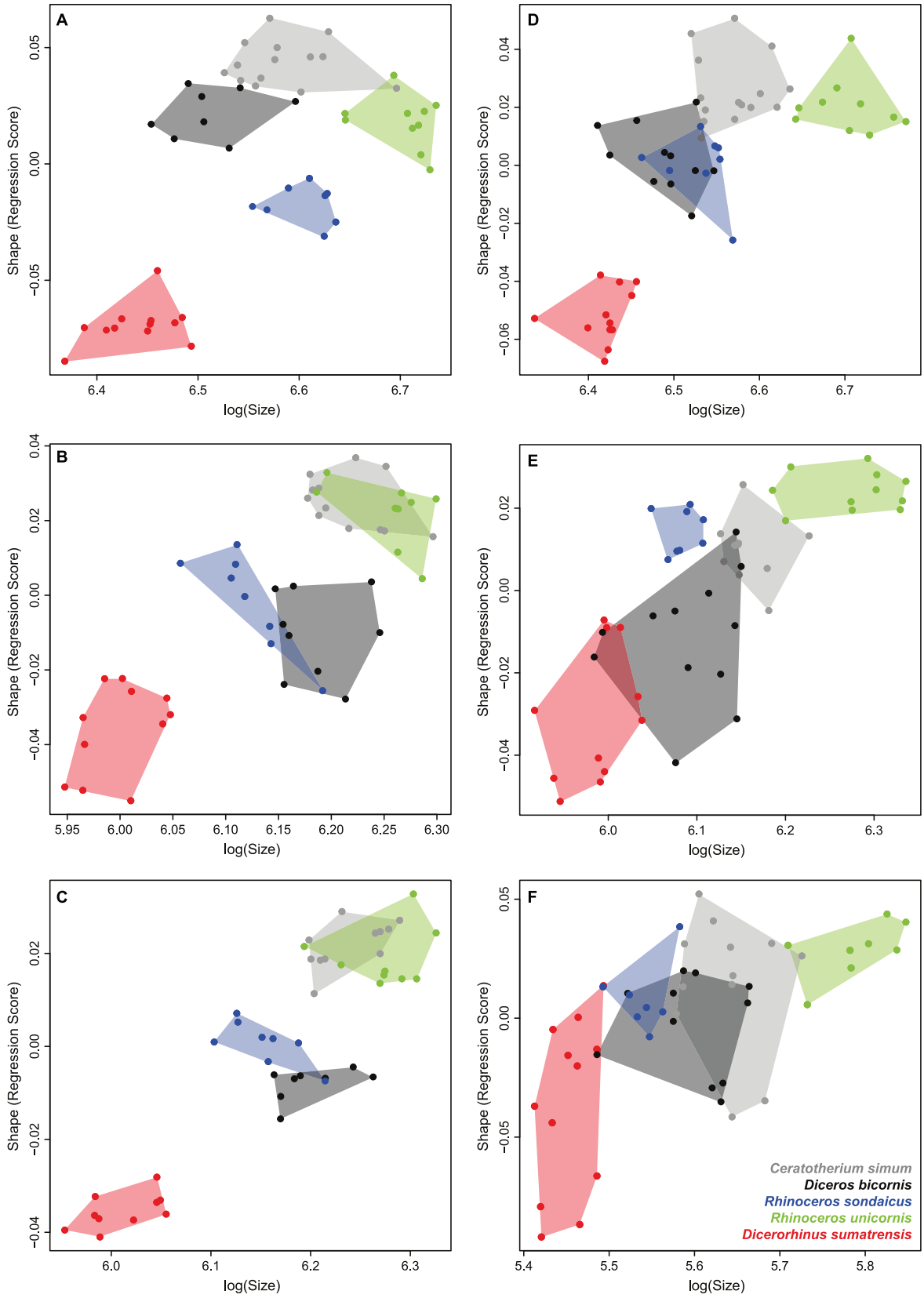

Figure 16: Multivariate regression plots performed on shape data and log-transformed centroid size. A: Humerus; B: Radius; C: Ulna; D: Femur; E: Tibia; F: Fibula.

Discussion

Identification of morphotypes and phylogenetic influence

Morphological variation isolates each rhino species from the others, more or less clearly depending on the bone considered. The shape analysis of the six bones allows for clear isolation of three general bone morphotypes: the African morphotype grouping *C. simum* and *Dc. bicornis*, the *Rhinoceros* morphotype grouping the two *Rhinoceros* species, and the *Ds. sumatrensis* morphotype. The congruence of these morphotypes with the phylogeny indicates that the phylogenetic signal on long bone shape is strong, although it fluctuates among bones. In addition, body mass also appears as an important factor, depending on the considered bones. The phylogeny is clearly the main effect driving the shapes of the humerus and femur. Conversely, the morphological variation observed on the radius and ulna is essentially associated with body mass. The tibia seems to be equally affected by both, which is also the case for the fibula that shows, in addition, an important intraspecific variation.

Despite the fact that I could not test the phylogenetic signal because of the small number of studied species (Adams, 2014), my observations tend to indicate an effect of phylogenetic relations. It is accepted that the two African rhino *C. simum* and *Dc. bicornis* are closely related (Tougard et al., 2001). They may belong to the same subfamily – called Dicerotinae (Guérin, 1982; Gaudry, 2017) or Rhinocerotinae (Antoine, 2002; Becker, Antoine & Maridet, 2013), depending on the authors. The two species composing the genus *Rhinoceros* are also closely related (Tougard et al., 2001), the bones of *R. unicornis* and *R. sondaicus* having sometimes been confused with each other (Groves & Leslie, 2011). Conversely, the phylogenetic position of *Ds. sumatrensis* remains debated (Willerslev et al., 2009; Gaudry, 2017), this species being considered alternately as sister taxon of the two African species (Antoine, Duranthon & Welcomme, 2003; Cappellini et al., 2019), of the two *Rhinoceros* species (Tougard et al., 2001; Welker et al., 2017) or of all four other rhino species (Fernando et al., 2006; Piras et al., 2010) (see Chapter 1). Analyses reveal equally contrasting relationship patterns, with *Ds. sumatrensis* more closely resembling African species for some bones (radius, ulna and tibia) and other Asiatic ones for the others (humerus, femur and fibula).

Some anatomical features seem strongly influenced by phylogenetic relationships, among which some have previously been used as characters for cladistics analyses (Prothero, Manning & Hanson, 1986; Cerdeño, 1995; Antoine, 2002). On the humerus, the bicipital groove allows the sliding of a large *m. biceps brachii*, a forearm flexor playing an important locomotor role in coordinating the scapula and arm movements (Watson & Wilson, 2007; Barone, 2010b). This groove appears more closed by the greater tubercle for Asiatic rhinos, potentially indicating a different length and shape for the transverse humeral ligament. Although most analyses (Prothero, Manning & Hanson, 1986; Antoine, 2002) have

coded a few characters related to the tubercles of the humerus, the complexity of the shape of this bone proximal epiphysis remains generally underestimated in phylogenetic reconstructions. Moreover, the case of the greater tubercle development observed on the humerus of Asiatic species, and mainly for *Ds. sumatrensis*, is of particular interest (see Appendix 4 of this chapter). As mentioned by Hermanson & MacFadden (1992), the greater tubercle "increases mechanical advantages" for the *mm. pectoralis ascendens*, *supraspinatus* and *infraspinatus*. *Ds. sumatrensis* displays the slenderest humerus of all modern rhinos, with morphological traits qualitatively close to tapirs' (MacLaren & Nauwelaerts, 2016). The proximal epiphysis of *Ds. sumatrensis* resembles the tapirs' one, regarded by some authors as a plesiomorphic condition among Perissodactyla (Prothero, Manning & Hanson, 1986; Hermanson & MacFadden, 1992; Antoine, 2002). This particular shape may thus represent an evolutionary heritage and it is unclear whether and how functional constraints may have also affected this shape. The greater tubercle being also an insertion area for the *m. supraspinatus*, extension movements thus seem achieved differently between African and Asiatic rhinos. Watson & Wilson (2007) showed that the *m. supraspinatus* in horses acts more as a shoulder stabilizer than as a true extensor of the shoulder. Given the qualitative similarity of shape of this joint between African rhinos and equids, it is likely that this muscle plays a similar role among these groups. The robustness of the lesser trochanter is consistent with a development of the medial part of the *m. supraspinatus*, to increase the shoulder stabilisation. The lever arm is medially deflected for *C. simum* and *Dc. bicornis*, and distributed both medially and laterally for *Rhinoceros* species and *Ds. sumatrensis*. The role of the shoulder joint remains crucial in weight bearing and locomotion, and its shape may be influenced by several factors. The development of a massive greater tubercle is encountered among hippos (Fisher, Scott & Naples, 2007) and may be interpreted as a direct link with semi-aquatic habits and displacements into muddy swamps or riverbanks. However, this particular morphology is also encountered among domestic bovids for example (Barone, 2010a), which are not semi-aquatic. Conversely, extinct Amynodontidae, presumed to have been semi-aquatic Oligocene rhinos (Averianov et al., 2017), did not display this greater tubercle development (Scott & Jepsen, 1941). The development of the greater tubercle can rather be interpreted as an indicator of a powerful shoulder extension, as well as a feature increasing the resistance to displacement on unstable substrates. However, only a comprehensive study of this convergent trait among diverse artiodactyls and perissodactyls taxa could help to understand the functional role of this anatomical region, and its potential link with the ecological habits. On the distal epiphysis, characters related to the shape of the olecranon fossa have been used in phylogenies (Heissig, 1972; Antoine, 2002). Results confirm that the shape and depth of this fossa do not seem directly linked to the general bone robustness as observed in these studies. Moreover, this fossa is proximodistally larger for the genus *Rhinoceros* than for *Ceratotherium* and *Diceros*.

On the femur, the *fovea capitis* is extremely reduced in *C. simum* and absent in *Dc. bicornis*, whereas it is well developed in Asiatic rhinos, especially in *R. sondaicus*, confirming previous observations (Guérin, 1980; Antoine, 2002). This *fovea* provides an attachment for the accessory ligament and the femoral head ligament (Hermanson & Macfadden, 1996), acting as a hip stabilizer. The absence or reduction of *fovea capitis* in African species may be both associated with their phylogenetic proximity. This *fovea* is indeed present in many fossil rhinos (Antoine, 2002), regardless of the ecological preferences of these species. The shapes of the greater and of the third trochanters also seem driven more by the phylogeny than by functional constraints, supporting their use in phylogenies (Cerdeño, 1995; Antoine, 2002). On the distal epiphysis, the medial trochlear ridge is more developed and inflated in all rhinos than in horses; this feature has been previously interpreted as associated with "locking" the knee joint during long standing periods in equids (Hermanson & Macfadden, 1996) and considered as functionally equivalent in rhinos (Shockey, 2001). Other authors saw in the development of this medial trochlear ridge an adaptation to a more important degree of cursoriality, linked to openness of habitat (Janis et al., 2012). But tapirs, yet able to gallop (Sanborn & Watkins, 1950), do not display such an enlargement of the medial ridge of the trochlea (Holbrook, 2001; C.M. pers. obs.). This trait may thus be phylogenetically inherited between horses and rhinos only, or results of a convergence towards a knee-locking apparatus (which has yet to be fully demonstrated for rhinos).

On the tibia, the massive development of the tibial tuberosity seems more pronounced among African species than in Asiatic ones. The angle between the tibial plateau and the shaft axis is interpreted as a functional character linked to the limb posture (Lessertisseur & Saban, 1967); a plateau caudally lowered may reflect an angled limb associated with a cursorial habit, whereas a horizontal plateau tends to indicate more columnar limbs. Here, despite a slight change in the plateau orientation between light and heavy rhino species, this trait seems more likely related to phylogeny, African species having a more horizontal plateau than African ones. Similarly, on the distal epiphysis, the rectangular shape of the articular surface for the talus is encountered mainly in the three Asiatic species and not in African specimens.

Role of ecology

Phylogenetically related rhinos share ecologies with important similarities, making it difficult to accurately assess the environmental effect on bone shape. Furthermore, as historical ranges and habitats of rhinos have been drastically reduced and modified under human pressure (Hillman-Smith & Groves, 1994; Dinerstein, 2011; Groves & Leslie, 2011; Rookmaaker & Antoine, 2012), ecological inferences must be assessed with caution regarding the current rhino habitats. The related *C. simum* and *Dc. bicornis* both live in African savannas and display a common general bone morphotype (see above). *Dc. bicornis* is a ubiquitous species, often visiting both open savannas and clear forests and browsing

various vegetal species, whereas *C. simum* is an open grassland grazer (Dinerstein, 2011). The same assessment can be done for the two *Rhinoceros* species, closely phylogenetically related and sharing an important part of their historical geographic range. Despite their strong affinity with water, their ecological preferences are quite different, *R. unicornis* feeding frequently in semi-open floodplains whereas *R. sondaicus* prefers denser forests. *R. sondaicus* and *Ds. sumatrensis* share a similar lifestyle in dense and closed forest habitats but only their humerus, femur and fibula tend to display slight shape similarities. If long bone shape is affected by environmental factors, these constraints are difficult to distinguish from the ones linked to phylogeny. This tends to confirm previous observations indicating that rhino long bones can hardly be used as accurate environmental markers (Guérin, 1980; Eisenmann & Guérin, 1984).

Shape variation, evolutionary allometry and functional implications

Increase in body size and mass between the lightest and heaviest rhinos is associated with a global broadening of the limb long bones, with a clear enlargement of both the diaphysis and epiphyses, confirming previous general observations on different mammalian clades (Bertram & Biewener, 1990, 1992). However, this broadening is not uniform for all the bones. It is directed both mediolaterally and craniocaudally for the humerus (especially for the proximal part), and mainly mediolaterally for the radius and the femur. Conversely, for the ulna, tibia and fibula, I rather observe a craniocaudal enlargement, particularly visible on the proximal part of the tibia.

Forelimb bones

The difference between high and low size among extant rhinos is expressed on the humerus by a general enlargement in both craniocaudal and mediolateral directions, particularly for the proximal first half. This may be related to the constraints exerted both by weight bearing and braking role of the forelimb during locomotion (Dutto et al., 2006). The important development of the lesser tubercle at the expense of the greater tubercle in non-*Dicerorhinus* species allows both a greater stability of the shoulder articulation, preventing hyperextension, and a larger insertion area for the medial head of the *m. supraspinatus*, also considered as a shoulder stabilizer (Fisher, Scott & Naples, 2007; Watson & Wilson, 2007). This muscle being one of the main extensors of the forelimb (Barone, 2010b), the developed lesser tubercle acts as a strong medial lever arm for extension movements. This configuration has been previously interpreted as a mechanical advantage for muscles inserting on the shoulder joint, while the lateral reinforcement of the greater tubercle was supposed to help resisting the adduction of the arm (Hermanson & MacFadden, 1992). The development of the lesser trochanter may also help supporting the scapula (more elongated among African rhinos, J. MacLaren, 2019, personal communication) and be associated with a lengthening of the *m. subscapularis* tendons. In addition, the lesser tubercle also displays an important development in *Dc. bicornis*, more pronounced than in *R. unicornis*

and *R. sondaicus*, though these species are heavier and taller. This indicates a possible effect of phylogenetic proximity or similar habitats between the African species (see above). The development of the intermediate tubercle for some rhinos may be related to the presence of a forelimb passive stay apparatus, as demonstrated in horses (Hermanson & MacFadden, 1992; Mihlbachler et al., 2014). Although less developed than in equids, the intermediate tubercle is present in all rhinos at different degrees (well visible in African taxa, less developed in *Rhinoceros* species and poorly developed in *Dicerorhinus*). This may indicate different degrees of development of passive stay mechanism possibly linked to phylogeny and ecology (Shockey, 2001). On the distal epiphysis of the humerus, the mediolateral enlargement observed towards high body mass ensures both a greater stability of the elbow articulation and larger insertion areas for the different flexor and extensor muscles for the digits (Barone, 2010a). The distal trochlea of the humerus is also subjected to a proximodistal compression and a mediolateral extension, increasing the articular surface area to dissipate compressive forces, important for maintaining posture at high body masses (Jenkins, 1973).

Forelimb paired zeugopodial bones seem to express complementary shape variations linked to body mass. Whereas the radius broadens mainly mediolaterally with increasing body mass, the ulna expands in the craniocaudal direction; they respond conjointly to the increase in body mass and bone size to form a structure reinforced in all directions, as it has been observed on the humerus. All rhinos have an ulnar proximal epiphysis situated caudal to the radius, while its shaft expands laterally, possibly allowing a mediolateral weight display. Moreover, almost all the weight is borne by the proximal articular surface of the radius (Bertram & Biewener, 1992), which expands medially and becomes asymmetrical for heavier rhinos. The concave radial tuberosity shows a deep *m. biceps brachii* insertion delivering a strong forearm flexion (Antoine, 2002) and the developed insertion lateral relief offers a greater surface for extensor muscles of the digits (Guérin, 1980). As this relief is more developed in African species than in Asiatic ones, this may suggest an effect of phylogeny or locomotion in different habitats or both. On the ulna, the developed olecranon process constitutes a powerful lever arm for forearm extensors such as the *m. triceps brachii* and the *m. anconeus*, also acting upon the bone for gravitational support. The medial development of the olecranon process is related to larger insertions for the *mm. flexor carpi radialis, flexor digitorum profundus* and *flexor digitorum superficialis*, all essential to resist hyperextension of the wrist. The cranially reduced anconeal process allows a greater extension of the forearm than in other taxa (e.g. bovids or equids) (Hildebrand, 1974) but prevents a complete verticality of the member as observed in elephants for example (Osborn, 1929). The distal epiphysis shows a reduction of both radial and ulnar styloid processes towards high body mass, adding a mediolateral degree of freedom to the wrist articulation. However, the proximally reduced articular surface for the scaphoid limits the craniocaudal wrist flexion (Yalden, 1971). These morphological traits

allow the foot to bear the weight on different substrates while limiting the risk of wrist hyperflexion (Domning, 2002).

Hind limb bones

In the hind limb, the femur expands mainly in the mediolateral direction for rhinos with high body mass and bone size, tending to indicate a stronger resistance to constraints both linked to body propulsion and weight bearing (Lessertisseur & Saban, 1967), exerted in the mediolateral direction (Hildebrand, 1974). The mediolateral reinforcement of the femur is mainly located under the head and the neck, responding to a concomitant enlargement of the medial condyle and epicondyle on the distal epiphysis, both indicating an increase of the body load near the sagittal plane. The more distal location of the lesser trochanter improves the lever arm of the *mm. psoas major* and *iliacus*, developing slower but stronger hip flexions (Hildebrand, 1974; Polly, 2007). The same phenomenon is observed with the third trochanter, situated half way along shaft – contrary to in cursorial Perissodactyla like equids, where the third trochanter is more proximally situated (Hermanson & Macfadden, 1996; Holbrook, 2001; Barone, 2010a). However, it has been shown that the relative position of the third trochanter barely varies among extinct rhinoceroses considered as "cursorial" or "semi-cursorial" (Prothero, 2005). This position along the shaft may thus be influenced by both mechanical and phylogenetic constraints. The extreme development of the third trochanter associated with a distolateral development of the greater trochanter also creates a large lever arm for the *fascia glutea*, the *mm. gluteus superficialis* and *gluteus medius* allowing strong hip flexion and abduction. This association appears the greatest for *R. unicornis*, where the greater and third trochanters can be fused by a bony bridge. Conversely, the greater trochanter is less proximally developed than in related groups like horses and tapirs (Radinsky, 1965; Hermanson & Macfadden, 1996; Holbrook, 2001); as this trochanter is the insertion area for the *m. gluteus medius*, the main extensor of the hip, the extension in rhinos seems less powerful than in cursorial perissodactyls. On the distal epiphysis, the lateral torsion of the rotation axis of the trochlea in heavy rhinos also indicates a more laterally deviated position of the knee. This conformation may improve weight bearing, shifting the body mass laterally to the body, as previously observed on a study of pressure patterns of the feet in *C. simum* (Panagiotopoulou, Pataky & Hutchinson, 2019). No real difference in the bone curvature related to body proportion was noticed, confirming previous observations on the independence of femur curvature with regard to body mass increase in quadrupedal mammals (Bertram & Biewener, 1992).

On the hindlimb zeugopodial elements, when the proximal epiphysis of the tibia broadens craniocaudally, the proximal fibular epiphysis is reduced in this direction, despite an increased general robustness. The proximal epiphysis of the fibula is also oriented far more cranially than in lighter specimens. The enlargement of the tibial plateau thus seems to involve a relative reduction in size of the

fibular head. The distal epiphyses of both bones covary too, with a broadening mainly expressed in the craniocaudal direction. The medial condyle of the tibial plateau enlarges strongly, resulting into an asymmetrical proximal epiphysis. Moreover, the broadening of the tibial tuberosity correlates with a stronger and larger patellar ligament, reinforcing the knee articulation and therefore the lever arm created by the patella (Hildebrand, 1974). On the distal epiphysis, the two malleoli are more mediolaterally inflated but less distally expanded, allowing the tarsal articulation to move more freely in heavier rhinos (Lessertisseur & Saban, 1967). This trait is associated with a slightly shallower distal articular surface, conferring more important degrees of freedom to the ankle articulation for high body mass (Polly, 2007). This observation is coherent with similar analyses conducted on rhino ankle bones (Etienne et al., 2020) showing notably that the talus bone is flattened and has a shallower groove towards high body mass among rhinos.

In addition to the reduction of the proximal epiphysis, the fibula displays a straighter diaphysis for large rhinos as opposed to the greatly curved one for lighter rhinos (see Appendices 5 and 6 of this chapter). This is consistent with previous observations: although the fibula was not considered in their study, Bertram & Biewener (1992) noted a decrease of tibia curvature while body mass increases among terrestrial mammals. In my rhino sample, the tibia shows a very slight straightening of the diaphysis. However, this straightening, perhaps linked to load carrying capacity, appears to be more pronounced on the fibula.

Differences between body mass and body size

As the exact body mass was only known for five specimens of the sample, I was not able to precisely express the shape variation regarding the animal's individual weight. However, theoretical bone shape obtained with mean body mass are very similar to the ones obtained with centroid size (see above). Comparing the values of the centroid size and mean body mass highlights some interspecific differences: if *Ds. sumatrensis*, the smallest rhino, has the lowest values for both centroid size and body mass, *R. unicornis* (the species with the highest values of shoulder height) displays the highest values of centroid size in most cases, which is coherent with its higher height at shoulder compared to other modern rhinos (Guérin, 1980; Dinerstein, 2011), despite a mean body mass (2,000 kg) lower than that of *C. simum* (2,300 kg). Furthermore, the centroid size of an isolated bone may neither reflect the actual global size of an animal, nor be strictly correlated with its body mass. This is particularly visible for taxa displaying brachypodial adaptation (i.e. shortening of limb length relatively to the height at the shoulder), as it is the case for modern hippos or some fossil rhinos like *Brachypotherium* or *Teleoceras* (Cerdeño, 1998). However, results indicate that it does not seem to be the case with the long bones of modern rhinos. As bone size and body mass are intimately entangled (Berner, 2011), the centroid size of isolated bones may still constitute a useful body mass approximation when precise

body mass remains unknown and if considered cautiously – this approximation depending on the number and placement of the landmarks on the bone. This is coherent with previous results obtained on cranial shape data indicating a marked correlation between body mass and centroid size (both of the skull and mandible) for many mammalian lineages, especially modern rhinos (Cassini, Vizcaíno & Bargo, 2012). Another study focusing on tapirs tend to highlight a good correlation between centroid size and body mass estimation when using the forelimb elements (MacLaren et al., 2018).

Limb bone shape and graviportality

One of the criteria defining graviportality is straight and columnar limbs (Gregory, 1912; Osborn, 1929; Biewener, 1989b) (see Chapter 1). Rhino limb long bones do not display a true columnar organisation (Osborn, 1900, 1929). Morphological changes between light and heavy rhino species do not imply a clear change in the orientation of the articular facets: the elbow joint remains unable to completely open like the elephant's one and the knee remains markedly angled. Only the humeral proximal epiphysis displays a tenuous orientation change between light and heavy rhinos, allowing a more slightly vertical orientation of this bone for *C. simum* and *R. unicornis*.

Limb straightness can results from the reorientation of the trochlear notch of the ulna in the dorsal direction, allowing an efficient support of the humerus (Gregory, 1912), as in proboscideans (Christiansen, 1999). My sample tends to indicate instead that the radius is the main support of the body weight in the forelimb among modern rhinos. The shape of the radius becomes gradually more robust from light to heavy rhinos, with a strong medial reinforcement of the proximal epiphysis. The particular role of the radius was previously highlighted among a large sample of mammal clades (Bertram & Biewener, 1992), its vertical position being parallel to ground reaction forces. This supportive role of the radius is widespread among ungulates and remains of importance even in larger fossil rhinos like Elasmotheriinae (Antoine, 2002) and Paraceratheriidae (Qiu & Wang, 2007; Prothero, 2013). Unlike in elephants, increase in body mass among rhinos is correlated with a more important supportive role of the radius. At the opposite, the ulna's role has not been extensively explored in morphofunctional studies. This work underlines the complementary role of the ulna relative to the radius, providing more lateral and caudal weight bearing by an enlargement in the dorsopalmar direction. In this regard, the zeugopodial conformation in rhinos is close to the one encountered in hippos (Fisher, Scott & Naples, 2007).

Forelimb elements bear more weight than hind limb ones (Lessertisseur & Saban, 1967; Hildebrand, 1974; Polly, 2007) and play an additional braking role during locomotion, particularly proximal elements (Dutto et al., 2006). Forelimb bones such as the humerus thus need to be reinforced in all directions in order to support these higher masses in heavier animals. Hind limb bone shape is affected

differently than in forelimb by increases in body mass and size. The hind limb bears relatively less weight than the forelimb in quadrupeds and plays an additional propulsive role during locomotion (Lessertisseur & Saban, 1967; Hildebrand, 1974; Barone, 2010a). The femur displays important reinforcement and development of strong lever arms in large rhino species, possibly to support increasing stress due to locomotion and body mass, but the variations in shape of the tibia and the fibula seem driven as much by the body mass as by the phylogenetic influence. The shape of the fibula is particularly variable within several rhino species, questioning its functional role but also the factors driving this strong intraspecific variation. It has been shown that the human fibula plays, in addition to its ankle stabilizer role, a small but important weight bearing role, receiving one sixth of the load applied to the knee (Lambert, 1971; Takebe et al., 1984). In horses, the diaphysis of the fibula is absent and the malleolus is fused with the tibia, ensuring mainly ankle stabilization (Barone, 2010a). The rhino fibula ensures a talus stabilization role (Polly, 2007) in addition to a potential weight bearing due to the presence of the shaft. In addition, this bone often bears crests along the diaphysis with no apparent correlation with weight bearing (see above). These crest developments may be due to individual variations in bone development, without clear functional implications, but this first analysis does not allow me to address this question.

Bertram & Biewener (1990, 1992) and Polly (2007) previously called “allometry increase” the tendency for body size and mass to rise among terrestrial mammals. Although reduced, this allometry clearly affects this sample (Tables 6 and 7). In addition, robustness increase is associated with a slight relative length reduction of the bone for larger rhinos such as *Ceratotherium* (Guérin, 1980), a general trend observed among heavy mammals (Christiansen, 1999). Another trait associated with body mass augmentation among extant rhino species is the expansion of the medial epiphyses of multiple bones (e.g., medial epicondyle and trochlear lip on the humerus, medial glenoid cavity on the radius, medial condyle and trochlear lip on the femur, medial condyle on the tibia). These medial reinforcements result in more asymmetrical bones, potentially increasing parasagittal weight bearing (Barone, 2010a). This conformation is coherent with foot posture during walk: rhino forefeet are placed under the body, close to the sagittal plane of the animal (Paul & Christiansen, 2000). Hind feet are more spaced and oriented laterally, especially for heavy rhinos (Pfistermüller, Walzer & Licka, 2011; Panagiotopoulou, Pataky & Hutchinson, 2019), which seems to agree with my observations regarding the rotation axis of the femoral trochlea, oriented more laterally as well. However, the distal articular surface of the tibia displays a broader lateral groove and appears as a counterexample (Figure 12). This lateral broadening of the ankle joint, also observed on the talus (Etienne et al., 2020), may be correlated with the hind limb posture of rhinos. As the pelvic bone is large and the feet are placed under the body and oriented more laterally than forefeet, the legs are not parallel to the sagittal plane (Paul & Christiansen,

2000; C.M. pers. obs.). The vertical forces exerted by the body mass may therefore cross the axis of the tibia. This appears in accordance with the fact that the forces may be medially higher on the proximal plateau but laterally higher at the ankle joint; this point would need to be tested more precisely *in vivo*. As studies of pressure patterns indicate that foot pressure is more intense laterally (Pfistermüller, Walzer & Licka, 2011; Panagiotopoulou, Pataky & Hutchinson, 2019), it will be crucial to explore relations that exist between stylopodium, zeugopodium and autopodium organisation in the complete limb, as well as the gait and posture of the rhinos.

Conclusion

This study conducted on the limb long bones among modern rhinos highlights the occurrence of three distinct morphotypes. These reflect phylogenetic relationships, and the bone shape is differently affected by body size and mass. All bones display a common increase of robustness towards high body mass. The shape of the stylopodium bones, though affected by body mass variation, remains highly constrained by phylogeny, whereas zeugopodial bones, especially the radius and ulna, are more strongly affected by body mass, which highlights their important role in weight bearing. The shape of the tibia is influenced by both body mass and phylogeny. The unique pattern of the fibula reveals that, beyond significant intraspecific variation, this bone may play a role in weight bearing. All these results obtained on isolated bones stimulated the exploration of how the shapes of the six bones covary, and how body mass may impact these degrees of covariation.

Appendices

Appendix 1: Designation and location of anatomical landmarks placed on each bone

Bone	Anatomical LM	Curve sliding semi-LM	Surface sliding semi-LM	Total
Humerus	35	639	1437	2111
Radius	23	393	920	1336
Ulna	21	343	822	1142
Femur	27	612	1031	1670
Tibia	24	384	854	1262
Fibula	12	269	454	735

Table S1A: Total number of anatomical landmarks (LM), curve sliding and surface sliding semi-landmarks for each bone.

LM	Designation
1	Most distal point of the lateral border of the bicipital groove
2	Most proximal point of the lateral border of the bicipital groove
3	Most proximal point of the intermediate tubercle
4	Most proximal point of the medial border of the bicipital groove
5	Most distal point of the medial border of the bicipital groove
6	Most distal point of the intermediate tubercle
7	Most medial point of the top of the lesser tubercle
8	Most cranial point of the lesser tubercle convexity
9	Most medio-caudal point of the lesser tubercle convexity
10	Most medial point of the humeral head surface
11	Most caudo-distal point of the humeral head surface
12	Contact point between the tricipital line and the caudal border of the articular head surface
13	Most lateral point of the humeral head surface
14	Most caudal point of the greater tubercle convexity
15	Most proximal point of the greater tubercle convexity
16	Most cranial point of the greater tubercle convexity crest
17	Most proximal point of the m. infraspinatus lateral insertion
18	Most distal point of the m. infraspinatus lateral insertion
19	Most proximal point of the deltoid tuberosity
20	Most distal point of the deltoid tuberosity
21	Most proximal point of the epicondylar crest tuberosity
22	Most distal point of the epicondylar crest tuberosity
23	Most lateral point of the lateral epicondyle
24	Most distal point of the lateral epicondyle
25	Most proximo-lateral point of the capitulum
26	Most cranio-proximal point of contact between the trochlea and the capitulum
27	Most cranial point of the trochlea groove
28	Most cranio-medial point of the dorsal side of the trochlea
29	Most distal contact point between the trochlea border and the medial development of the trochlea lip
30	Most cranio-medial point of the ventral side of the trochlea
31	Most cranio-lateral point of the ventral side of the trochlea
32	Most caudo-distal point of contact between the capitulum and the trochlea
33	Most medial point of the medial epicondyle
34	Most caudal point of the medial epicondyle
35	Most lateral point of the medial epicondyle

Table S1B: Designation of anatomical landmarks on the humerus.

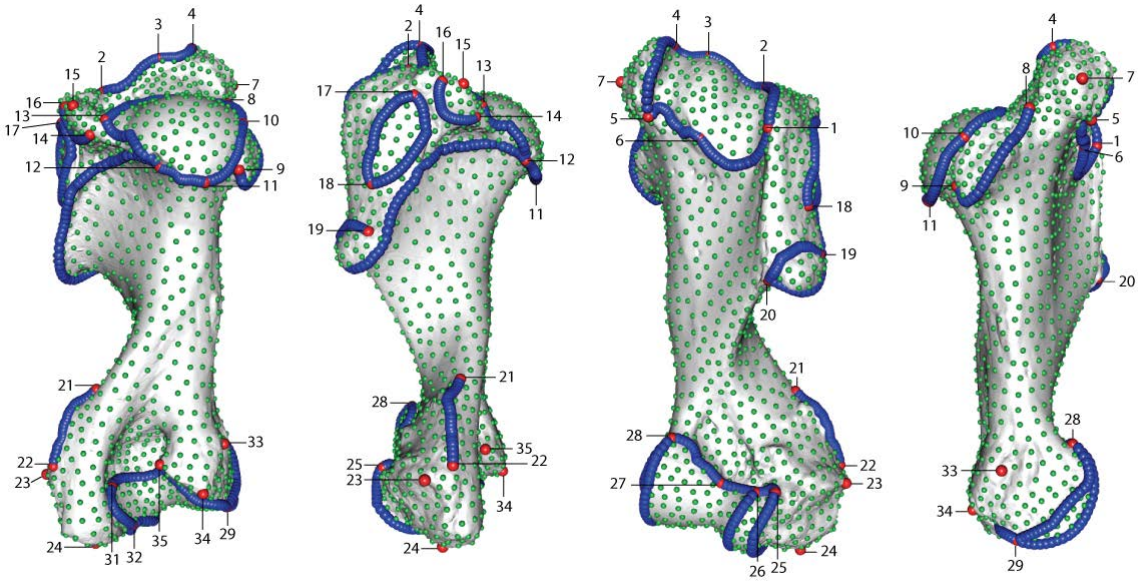

Figure S1C: Location of anatomical landmarks (red spheres), curve sliding (blue spheres) and surface sliding (green spheres) semi-landmarks placed on the humerus. From left to right: caudal, lateral, cranial and medial views. Numbers refer to anatomical landmarks designation detailed in Table S1B. Landmark n°30 situated in the olecranon fossa cannot be seen.

LM	Designation
1	Most caudo-lateral point of the lateral glenoid cavity
2	Most cranio-lateral point of the lateral glenoid cavity
3	Tip of the coronoid process
4	Most cranial point of the medial glenoid cavity
5	Most caudo-medial point of the medial glenoid cavity
6	Tip of the palmar process of the glenoid cavity ridge
7	Most cranial point of the lateral insertion relief
8	Most lateral point of the lateral insertion relief
9	Most caudo-distal point of the proximo-lateral articular facet for the ulna
10	Most caudo-distal point of the proximo-medial articular facet for the ulna
11	Most proximal point of the interosseous crest (= most distal point of the interosseous space)
12	Most distal point of the interosseous crest (crossing the distal epiphysis line)
13	Most cranio-lateral point of the disto-lateral articulation surface for ulna
14	Most proximo-lateral point of the disto-lateral articulation surface for ulna
15	Most caudo-lateral point of the disto-lateral articulation surface for ulna
16	Most medial point of the transversal crest
17	Tip of the radial styloid process
18	Maximum of curvature of the cranial ridge of the articular facet for the scaphoid
19	Most cranio-lateral point of the articular facet for the scaphoid
20	Most lateral point of the articular facet for the semilunar
21	Most caudo-lateral point of the articular facet for the semilunar
22	Most caudo-lateral point of the articular facet for the scaphoid
23	Most cranio-proximal point of the medial facet of distal radius

Table S1D: Designation of anatomical landmarks on the radius.

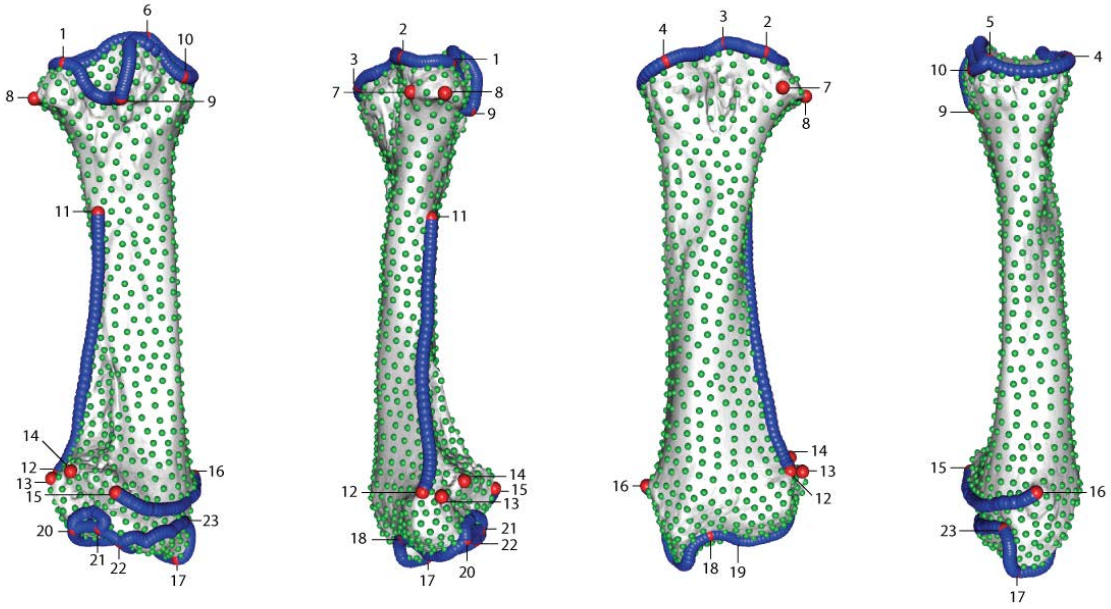

Figure S1E: Location of anatomical landmarks (red spheres), curve sliding (blue spheres) and surface sliding (green spheres) semi-landmarks placed on the radius. From left to right: caudal, lateral, cranial and medial views. Numbers refer to anatomical landmarks designation detailed in Table S1D.

LM	Designation
1	Most proximo-cranial point of the olecranon tuberosity cranial border
2	Most lateral point of the olecranon tuberosity
3	Most caudo-distal point of the olecranon tuberosity
4	Most medial point of the olecranon tuberosity
5	Most proximal point of the olecranon tuberosity
6	Cranial tip of the anconeal process
7	Most distal point of the lateral part of the trochlear notch articular surface
8	Maximum concavity point of the distal border of the trochlear notch articular surface
9	Most distal point of the medial part of the trochlear notch articular surface
10	Most distal point of the proximo-medial articular facet for the radius
11	Most distal point of the proximo-lateral articular facet for the radius
12	Most distal point of the proximal synostosis surface for the radius (= most proximal point of the interosseous space)
13	Most medio-caudal point of the distal radio-ulnar synostosis surface
14	Most disto-medial point of the articular surface with the semilunar bone
15	Most cranio-lateral point of the articular surface with the semilunar bone
16	Most disto-lateral point of the articular surface with the semilunar bone
17	Most cranio-lateral point of the distal radio-ulnar synostosis surface
18	Most lateral point of the distal epiphysis
19	Caudo-distal tip of ulnar styloid process
20	Most proximal contact point between the articular surfaces for the pisiform and the triquetrum
21	Most distal contact point between the caudal border of the ulna and the articular surface with the pisiform

Table S1F: Designation of anatomical landmarks on the ulna.

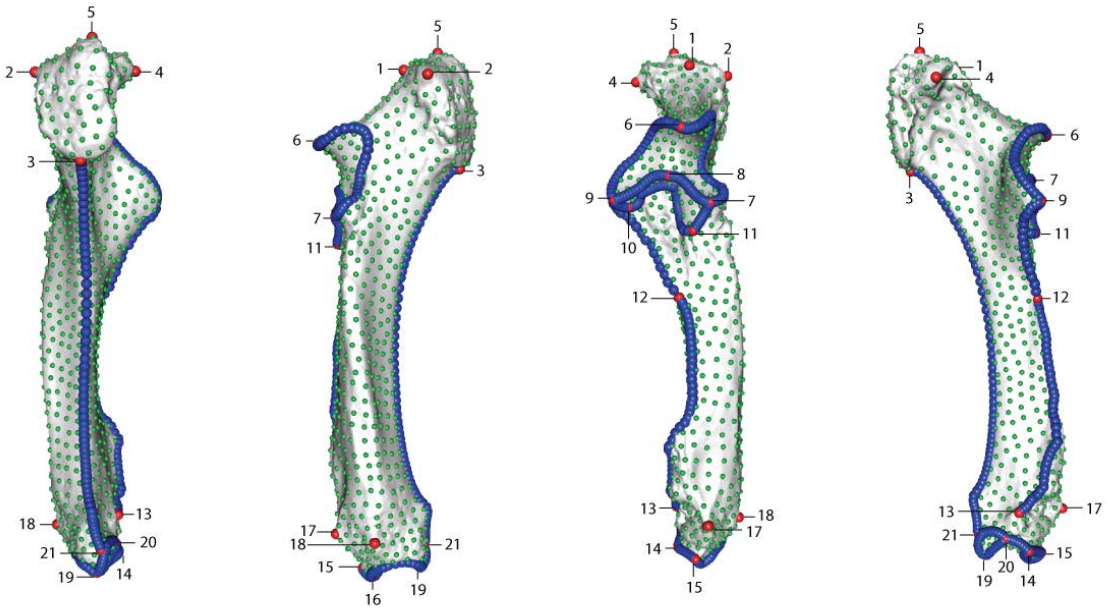

Figure S1G: Location of anatomical landmarks (red spheres), curve sliding (blue spheres) and surface sliding (green spheres) semi-landmarks placed on the ulna. From left to right: caudal, lateral, cranial and medial views. Numbers refer to anatomical landmarks designation detailed in Table S1F.

LM	Designation
1	Most proximo-cranial point of the greater trochanter
2	Most proximo-caudal point of the greater trochanter
3	Most medial point of the greater trochanter convexity
4	Most distal point of the intertrochanteric crest
5	Most disto-caudal point of the greater trochanter
6	Most cranio-lateral point of the convexity of the greater trochanter
7	Most proximal contact point between the intertrochanteric line and the medial line of the cranial face
8	Most lateral point of the border of the head
9	Most proximal point of the lesser trochanter
10	Most distal point of the lesser trochanter
11	Most proximal point of the gluteal tuberosity on the third trochanter
12	Most distal point of the gluteal tuberosity on the third trochanter
13	Most medial point of the medial epicondyle
14	Contact point between the intercondylar line and the medial condyle
15	Contact point between the intercondylar line and the lateral condyle
16	Most lateral point of the lateral epicondyle
17	Most proximal point of the lateral lip of the trochlea
18	Most proximal point of the trochlear groove
19	Most proximal point of the medial lip of the trochlea
20	Most distal point of the medial lip of the trochlea
21	Distal maximum of curvature of the trochlear groove
22	Most distal point of the lateral lip of the trochlea
23	Most medial point of the fossa extensoria
24	Most lateral point of the fossa extensoria
25	Most cranial point of the fossa extensoria
26	Most proximo-medial point of the lateral condyle articular surface
27	Most proximo-lateral point of the medial condyle articular surface

Table S1H: Designation of anatomical landmarks on the femur.

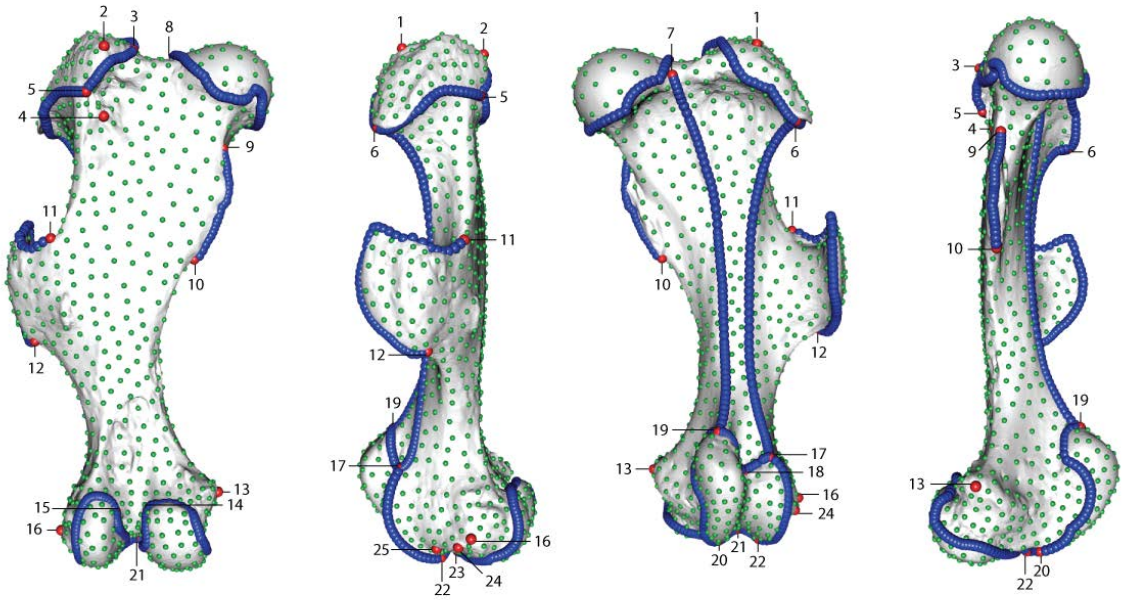

Figure S1I: Location of anatomical landmarks (red spheres), curve sliding (blue spheres) and surface sliding (green spheres) semi-landmarks placed on the femur. From left to right: caudal, lateral, cranial and medial views. Numbers refer to anatomical landmarks designation detailed in Table S1H. Landmarks n°26 and 27 situated in the intercondylar space cannot be seen.

LM	Designation
1	Most proximal point of the lateral tubercle of the intercondylar eminence
2	Most proximo-cranial point of the lateral tubercle of the intercondylar eminence
3	Most cranial point of the articular surface of the lateral condyle
4	Most caudal point of the articular surface of the lateral condyle
5	Most caudal point of the lateral tubercle of the intercondylar eminence
6	Most caudo-proximal point of the medial tubercle of the intercondylar eminence
7	Most proximal point of the medial tubercle of the intercondylar eminence
8	Most cranial point of the articular surface of the medial condyle
9	Most caudal point of the articular surface of the medial condyle
10	Most proximal point of the proximal tibio-fibular synostosis surface
11	Most distal point of the proximal tibio-fibular synostosis surface
12	Most proximal point of the lateral part of the tibial tuberosity
13	Most distal point of the lateral part of the tibial tuberosity
14	Most distal point of the tibial tuberosity groove
15	Most proximal point of the medial part of the tibial tuberosity
16	Most caudal point of the medial condyle
17	Most proximal point of the distal tibio-fibular synostosis surface
18	Most caudo-lateral point of the distal articular surface
19	Most cranio-lateral point of the distal articular surface
20	Most cranio-distal point of the intermediate ridge of the distal articular surface
21	Most distal point of the contact between the medial malleolus and the distal articular surface
22	Most distal point of the medial part of the distal articular surface
23	Most caudo-distal point of the intermediate ridge of the distal articular surface
24	Most medial point of the medial malleolus

Table S1J: Designation of anatomical landmarks on the tibia.

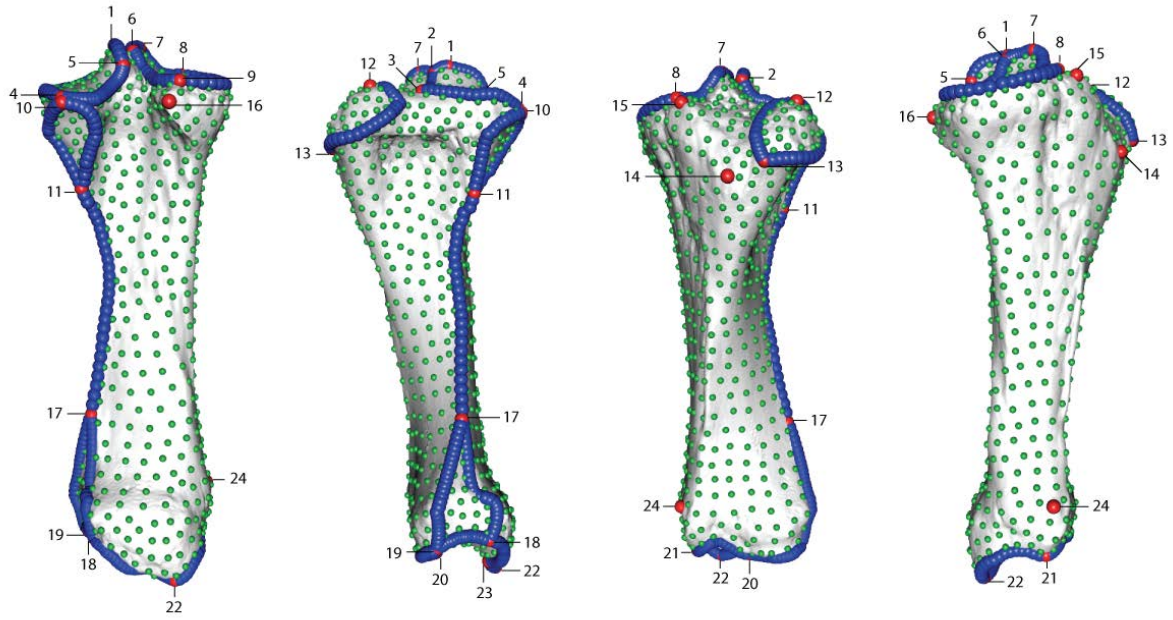

Figure S1K: Location of anatomical landmarks (red spheres), curve sliding (blue spheres) and surface sliding (green spheres) semi-landmarks placed on the tibia. From left to right: caudal, lateral, cranial and medial views. Numbers refer to anatomical landmarks designation detailed in Table S1J.

LM	Designation
1	Most proximal point of the proximal tibio-fibular synostosis surface
2	Most caudo-medial point of the proximal tibio-fibular synostosis surface
3	Most cranio-lateral point of the proximal tibio-fibular synostosis surface
4	Most proximal point of the distal tibio-fibular synostosis surface
5	Most caudal point of the distal articular facet
6	Most distal point of the caudal part of the distal articular facet
7	Most distal point of the cranial part of the distal articular facet
8	Most cranial point of the distal articular facet
9	Distal tip of the caudal ridge of the lateral malleolar sulcus
10	Distal tip of the cranial ridge of the lateral malleolar sulcus
11	Most lateral point of the cranial ridge of the lateral malleolar sulcus
12	Most disto-medial point of the proximal epiphysis = end of the latero-caudal crest

Table S1L: Designation of anatomical landmarks on the fibula.

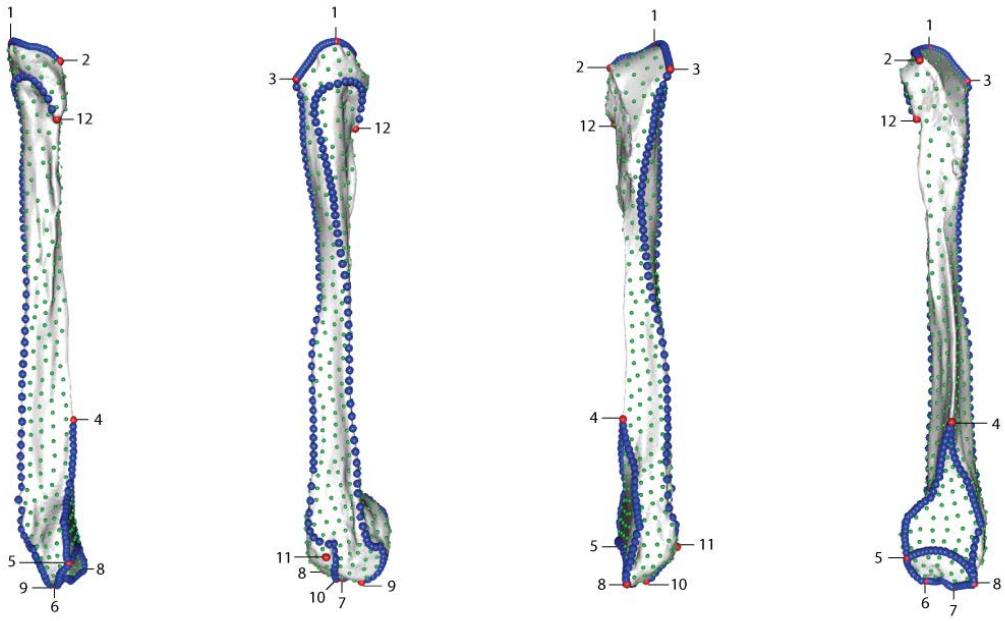

Figure S1M: Location of anatomical landmarks (red spheres), curve sliding (blue spheres) and surface sliding (green spheres) semi-landmarks placed on the fibula. From left to right: caudal, lateral, cranial and medial views. Numbers refer to anatomical landmarks designation detailed in Table S1L.

Appendix 2: Complete visualizations of theoretical shapes associated with the minimal and maximal values for the two first principal components for each bone

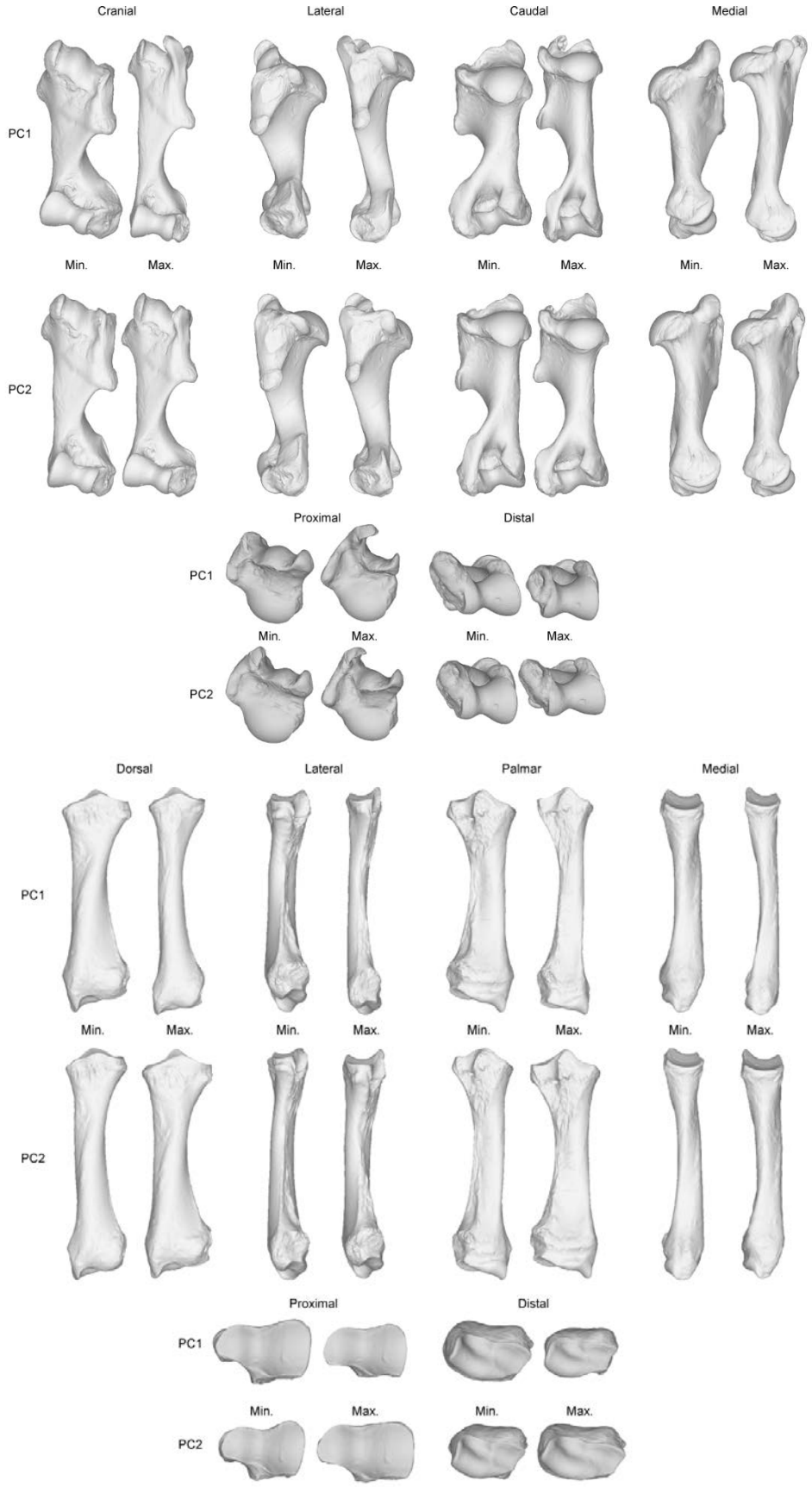

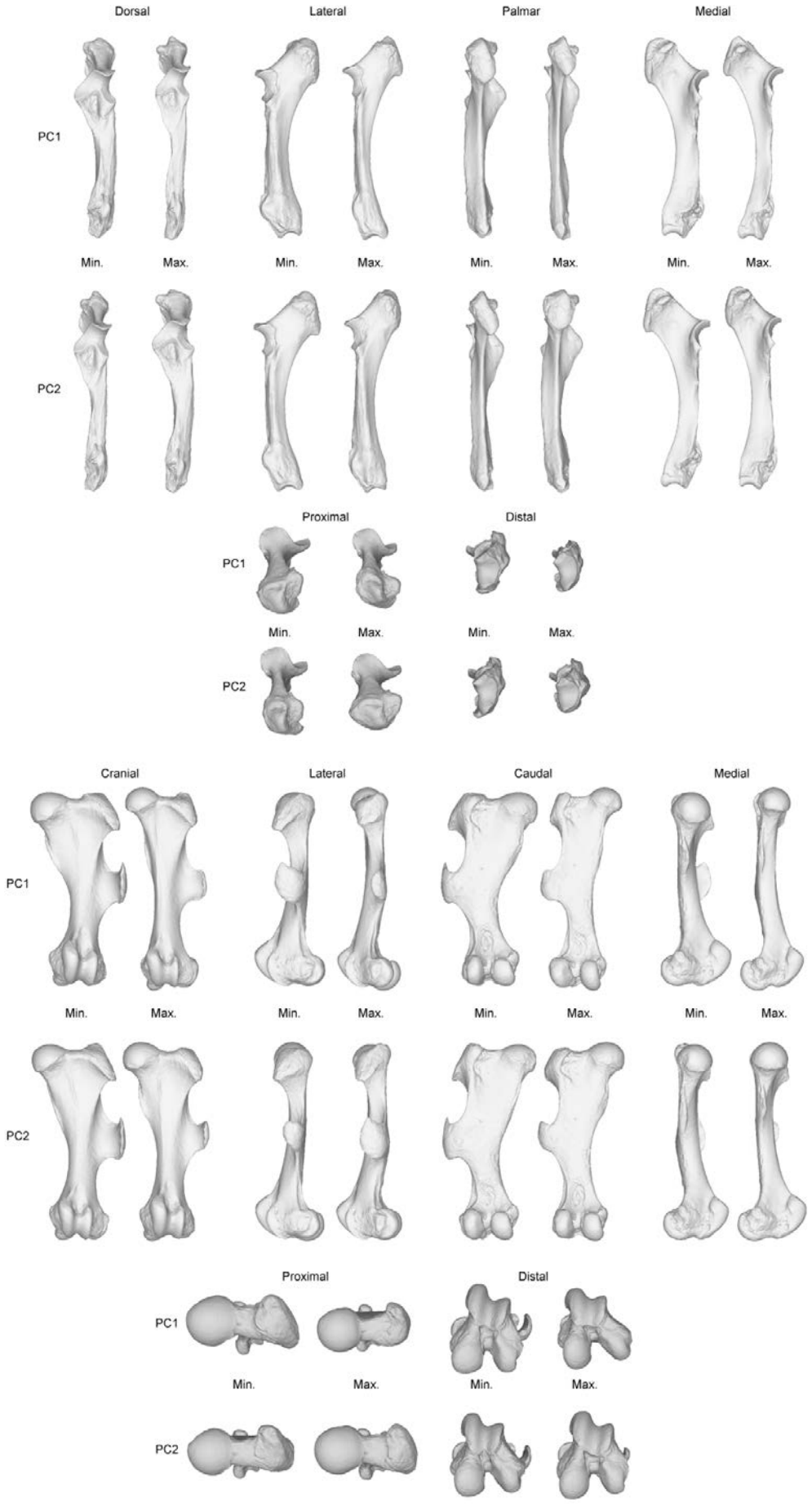
Dorsal
Lateral
Palmar
Medial
PC1
PC2
Min.
Max.
Proximal
Distal
Cranial
Caudal

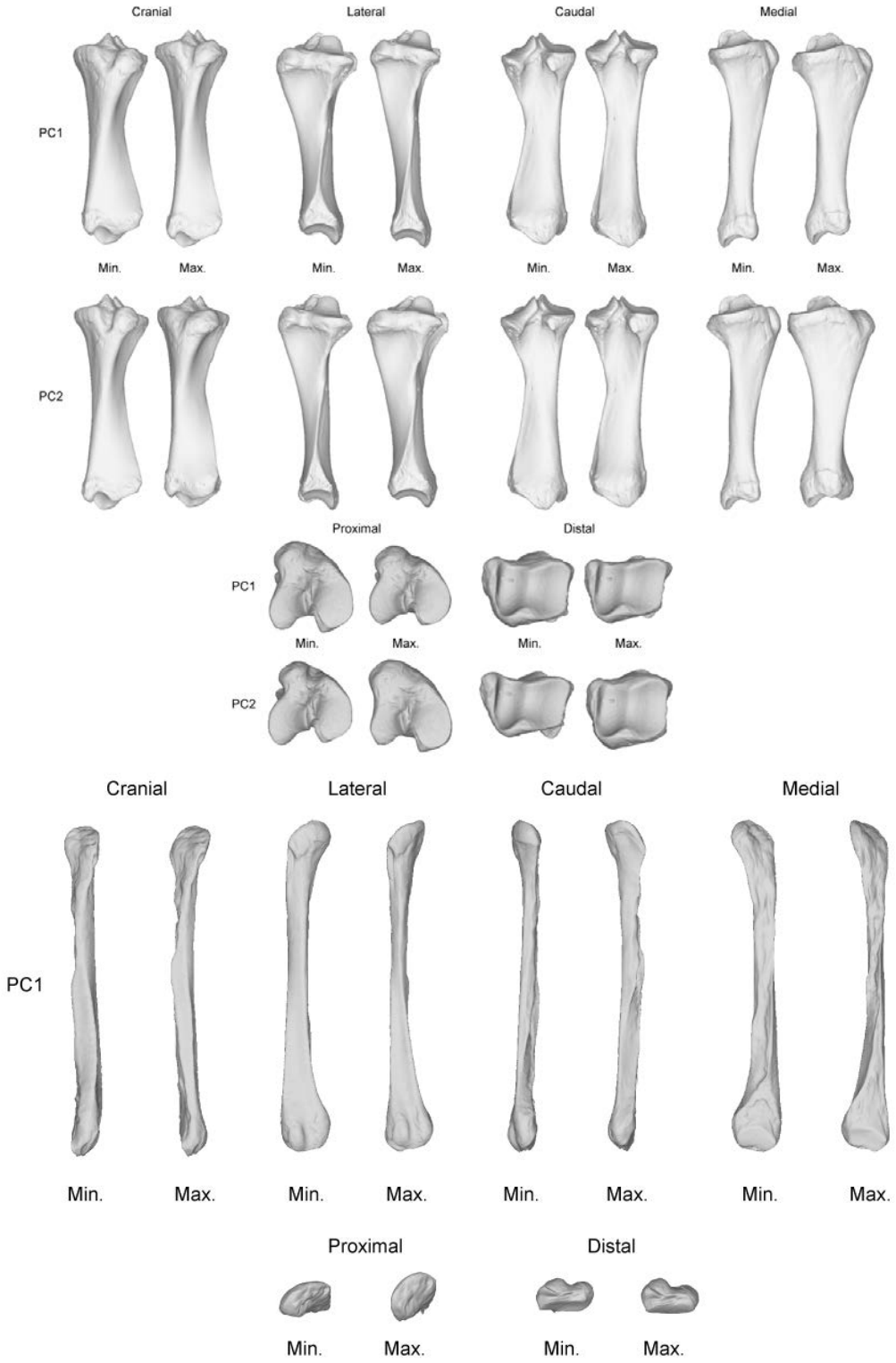
Cranial
Lateral
Caudal
Medial
PC1
Min.
Max.
PC2
Proximal
Distal

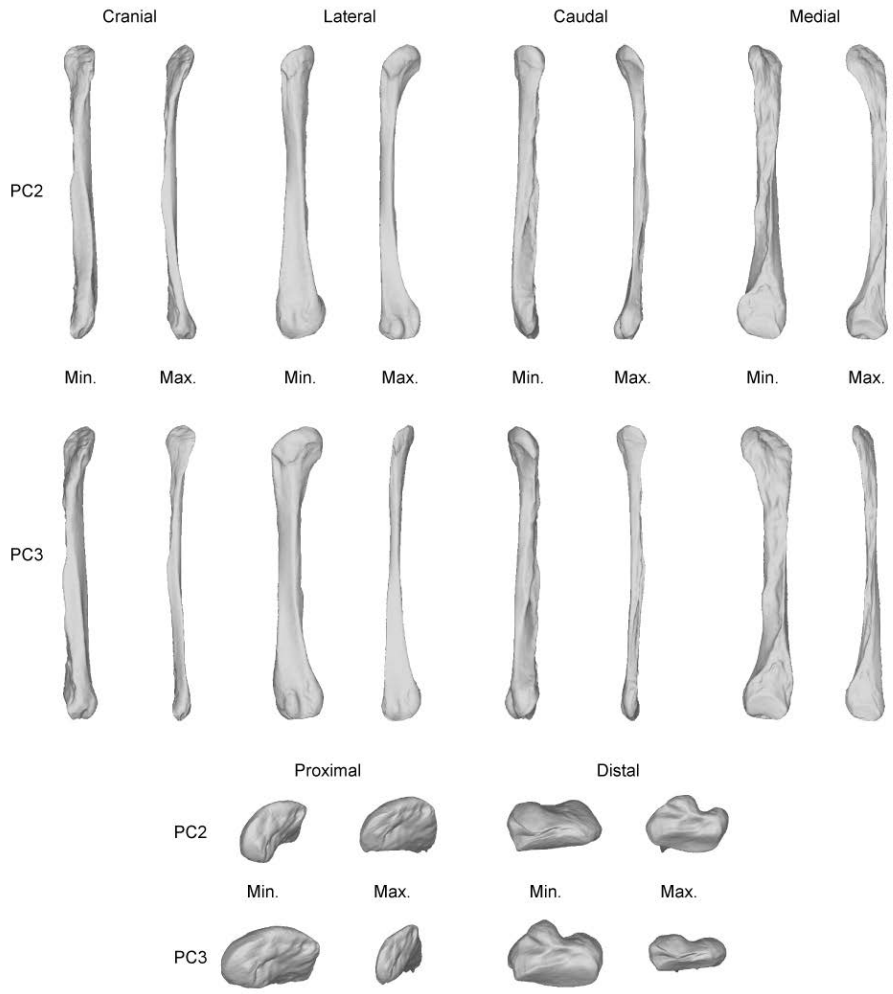
Cranial
Lateral
Caudal
Medial
PC2
Min.
Max.
Min.
Max.
Min.
Max.
Min.
Max.
PC3
Proximal
Distal
PC2
Min.
Max.
Min.
Max.
PC3

Appendix 3: Neighbour Joining trees computed on all PC scores obtained from the PCAs performed on shape data

Specimen codes are given following the Table 2.

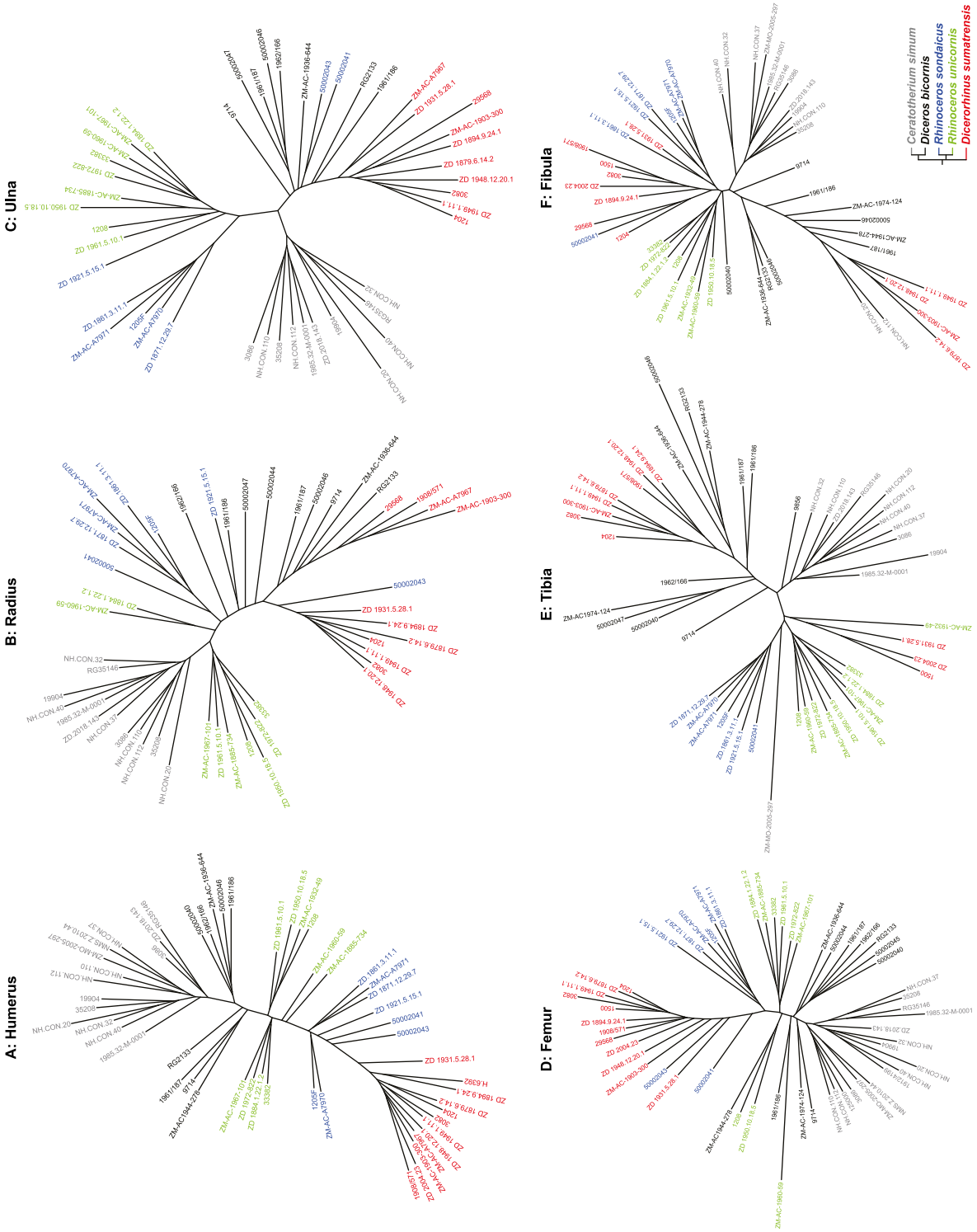

Appendix 4: Complete visualizations of mean shapes of each bone for the five considered species

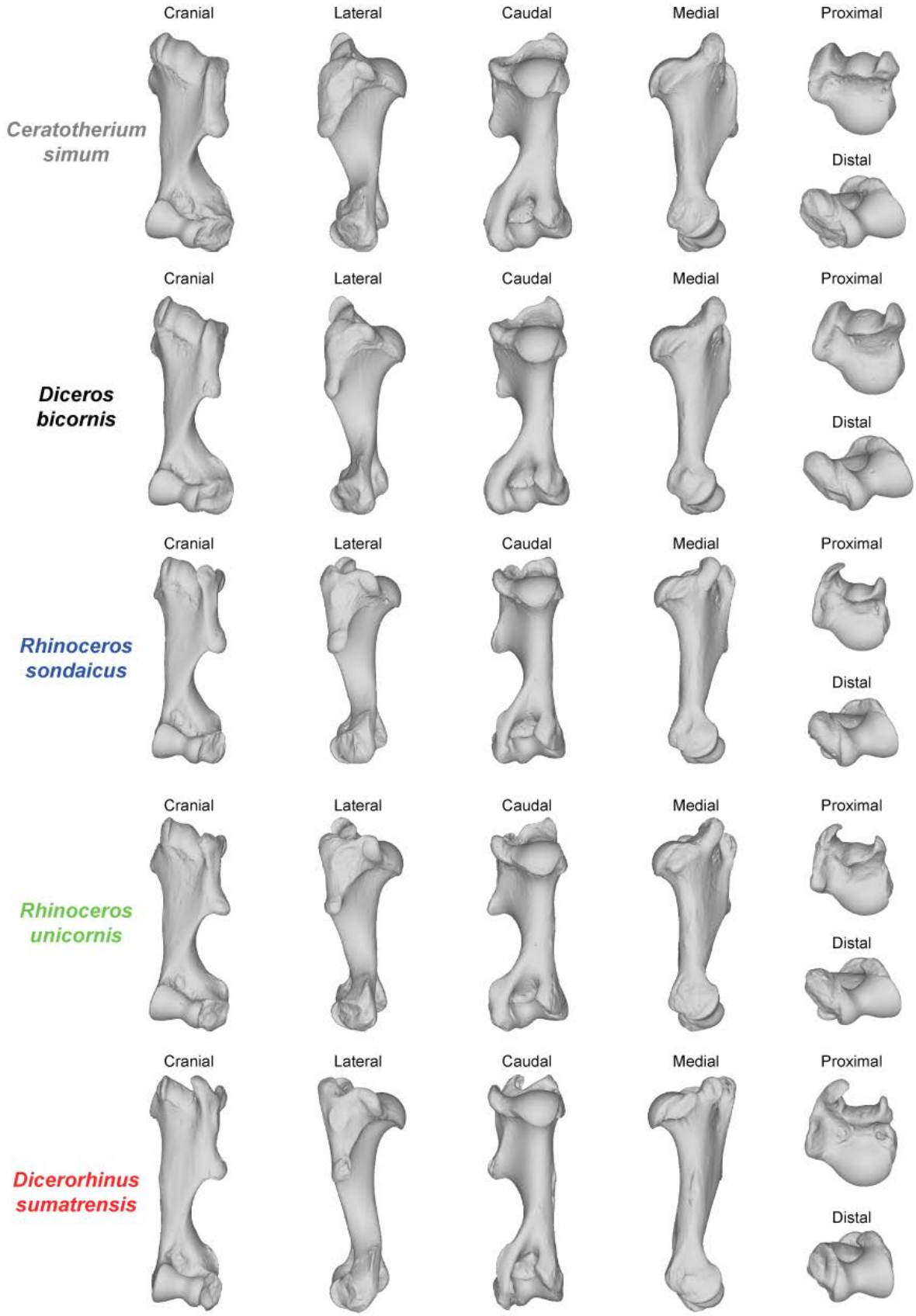

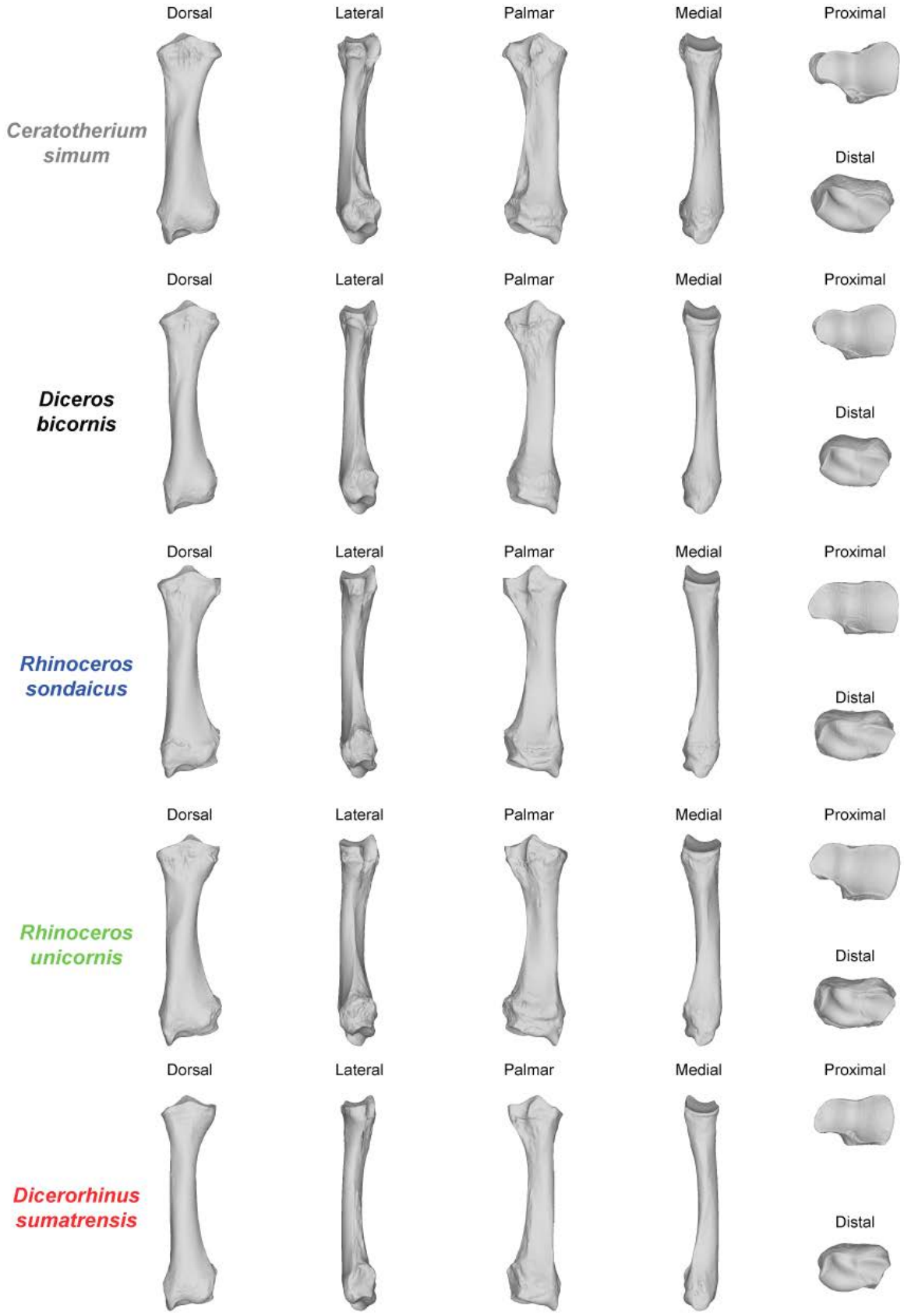
Dorsal
Lateral
Palmar
Medial
Proximal
Distal
Ceratotherium simum
Diceros bicornis
Rhinoceros sondaicus
Rhinoceros unicornis
Dicerorhinus sumatrensis

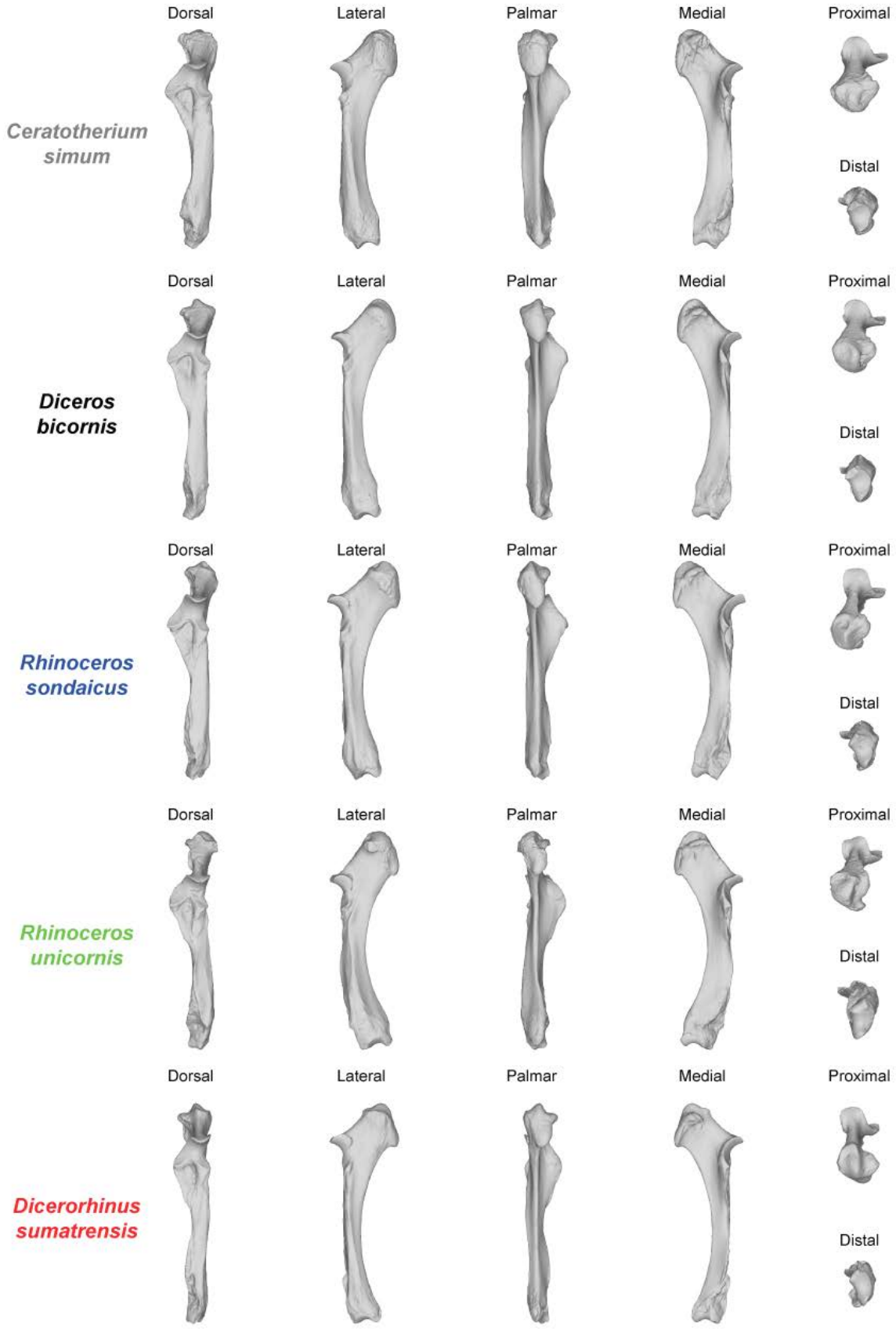
Dorsal
Lateral
Palmar
Medial
Proximal
Distal
Ceratotherium simum
Diceros bicornis
Rhinoceros sondaicus
Rhinoceros unicornis
Dicerorhinus sumatrensis

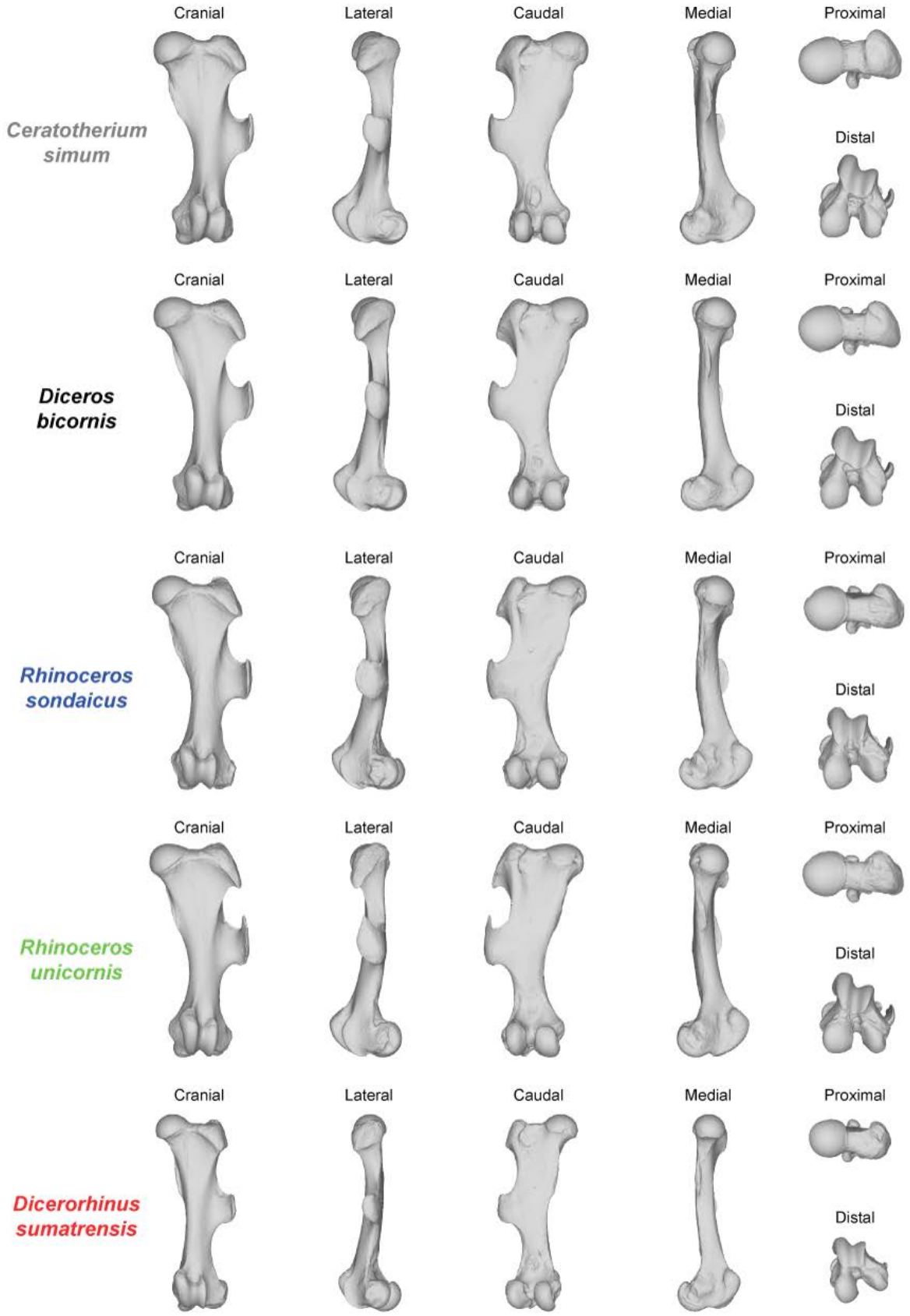
Cranial
Lateral
Caudal
Medial
Proximal
Distal
Ceratotherium simum
Diceros bicornis
Rhinoceros sondaicus
Rhinoceros unicornis
Dicerorhinus sumatrensis

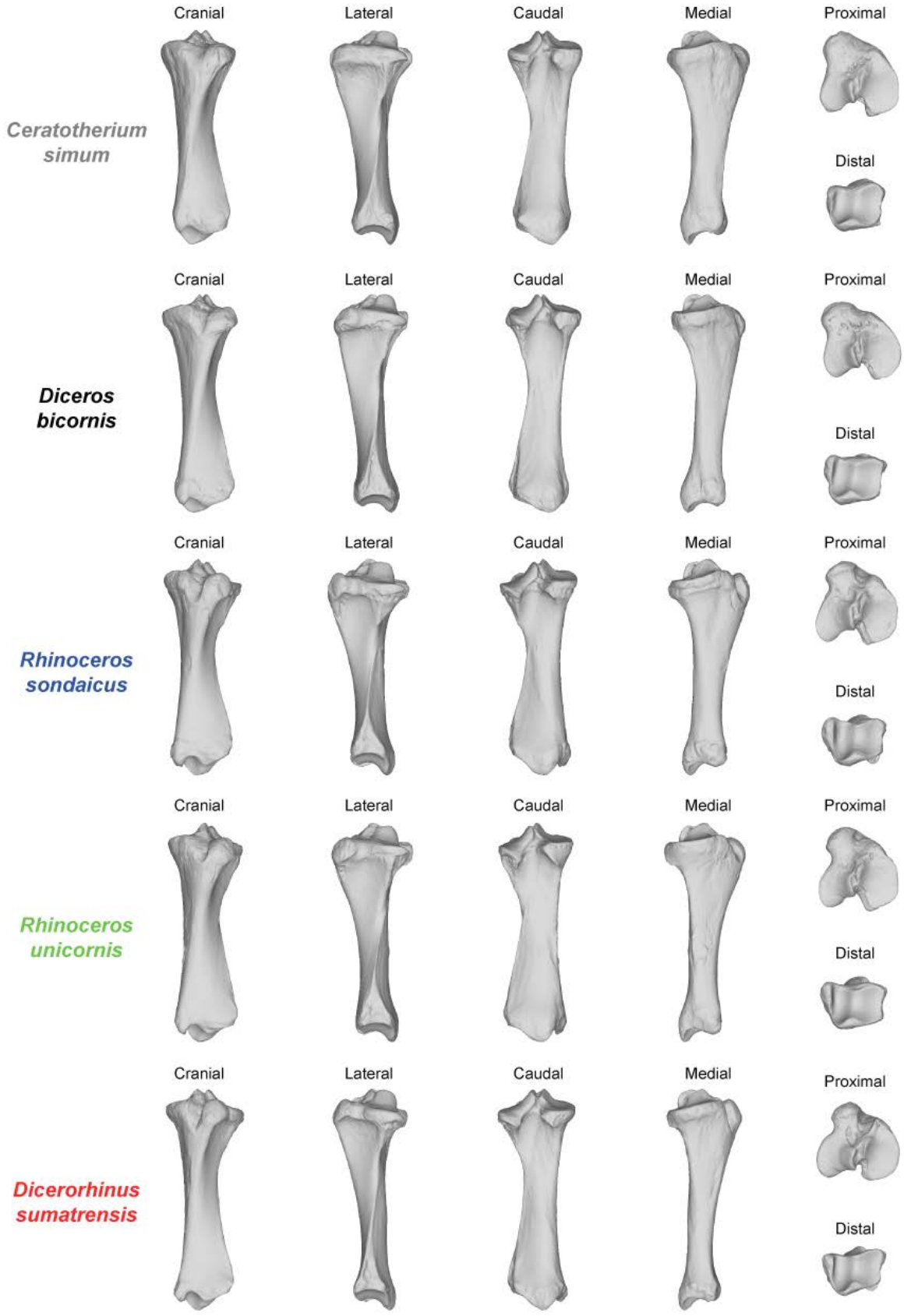
Cranial
Lateral
Caudal
Medial
Proximal
Distal
Ceratotherium simum
Diceros bicornis
Rhinoceros sondaicus
Rhinoceros unicornis
Dicerorhinus sumatrensis

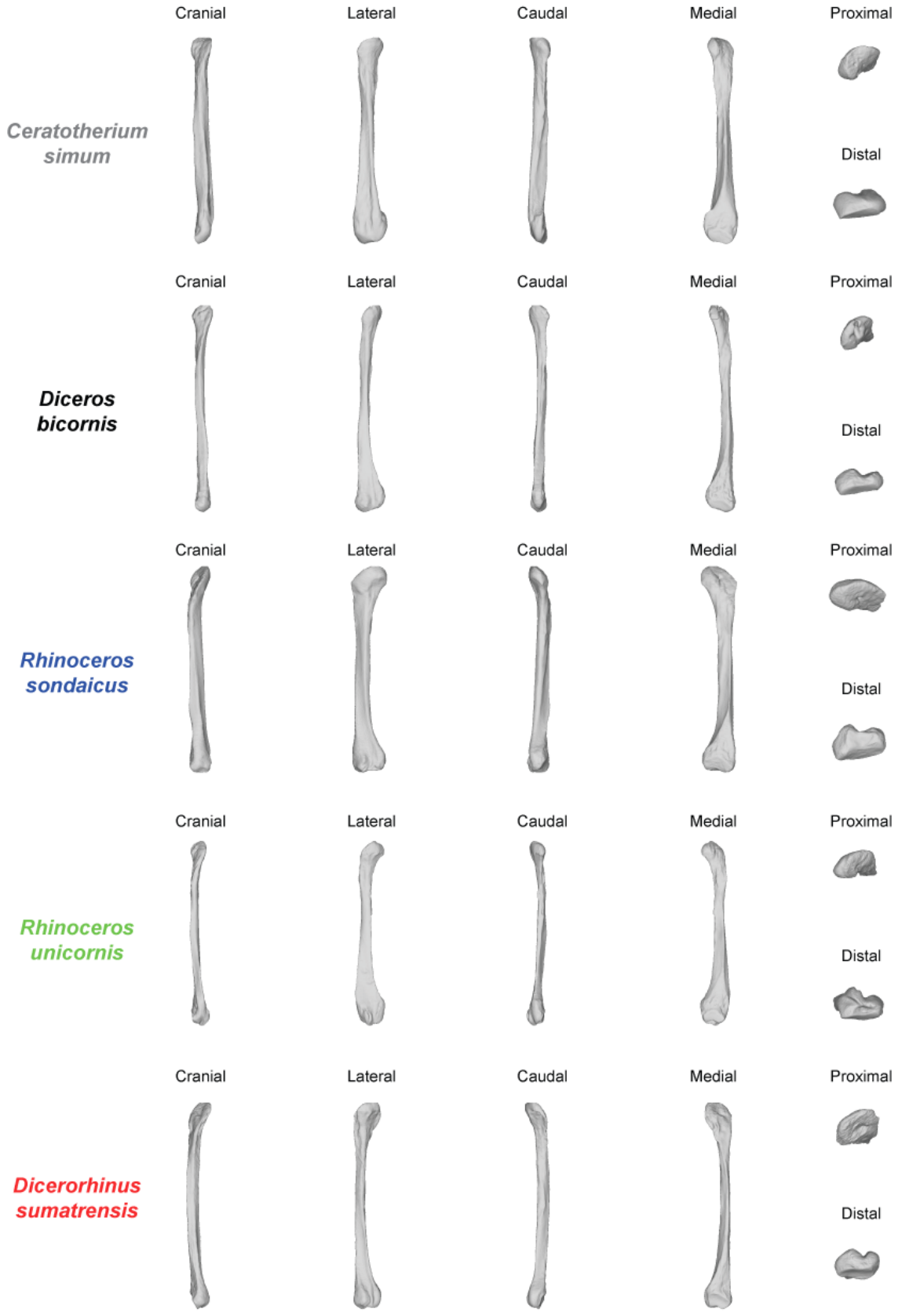
Cranial
Lateral
Caudal
Medial
Proximal
Distal
Ceratotherium simum
Diceros bicornis
Rhinoceros sondaicus
Rhinoceros unicornis
Dicerorhinus sumatrensis

Appendix 5: Complete visualizations of theoretical shapes associated with minimal and maximal centroid sizes for the six bones

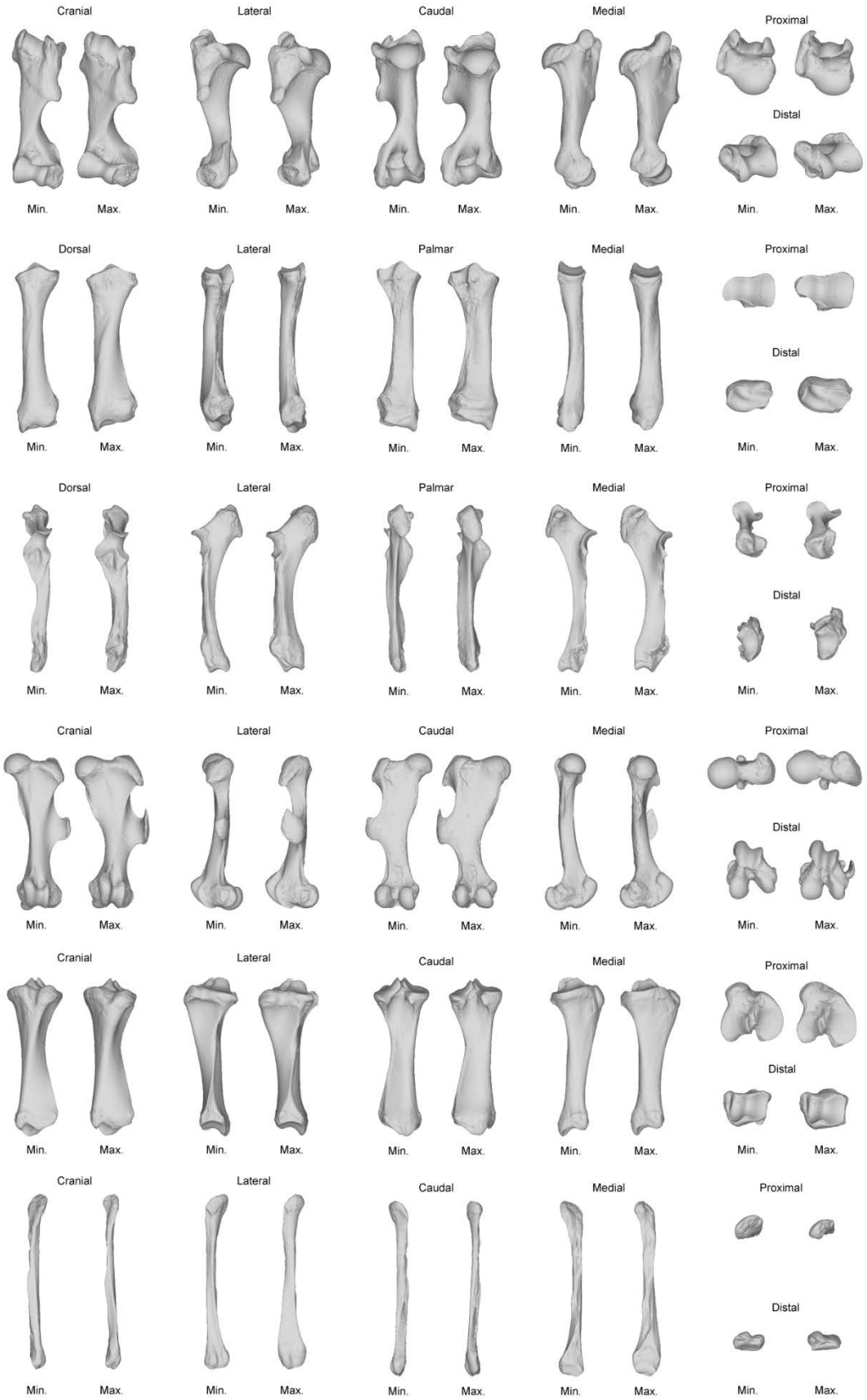

Appendix 6: Complete visualizations of theoretical shapes associated with minimal and maximal mean mass for the six bones

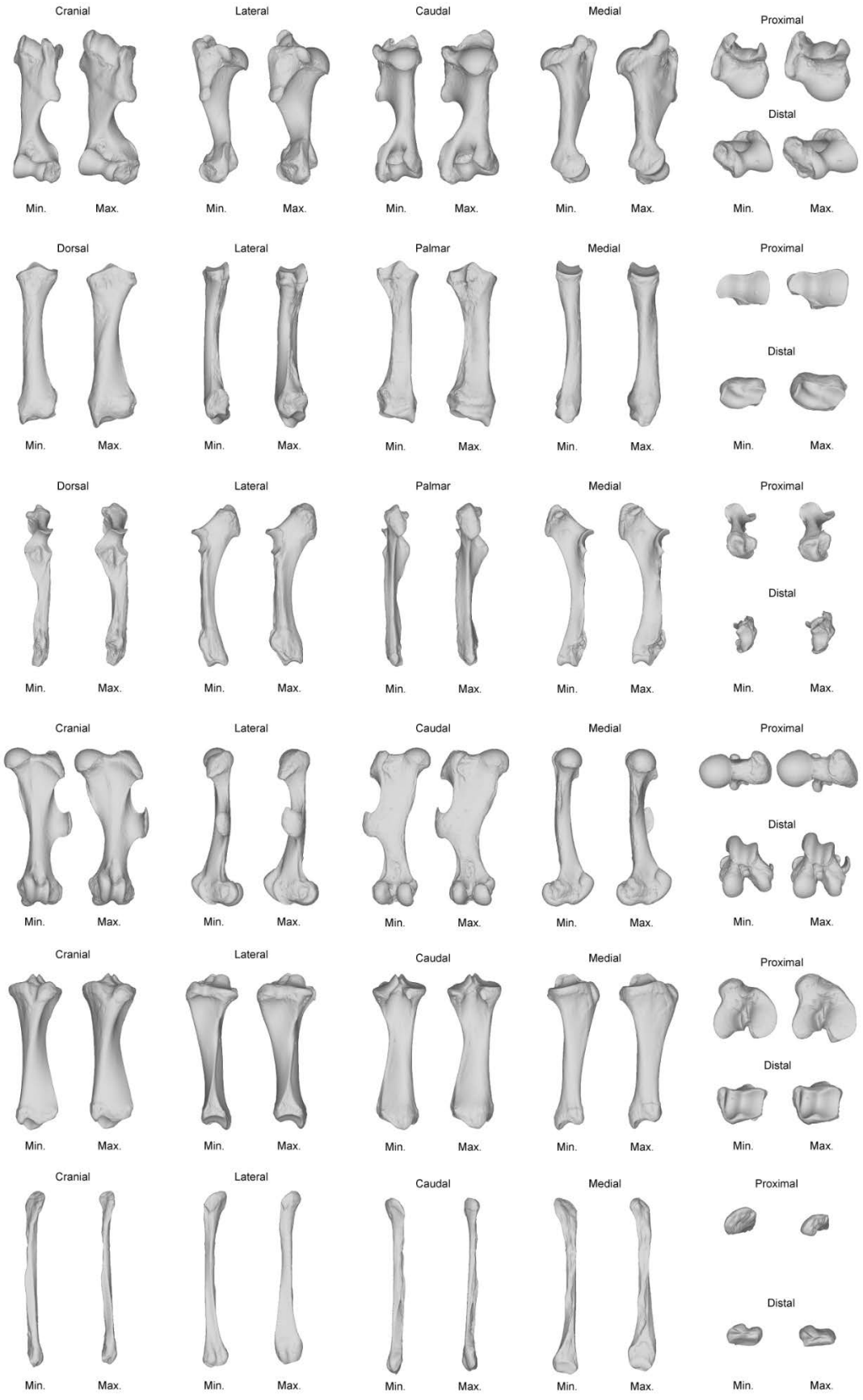

Chapter 4

A first glimpse at the influence of body mass in the morphological integration of the limb bones: an investigation in modern rhinoceroses

Introduction

The morphology of the different anatomical parts constituting organisms are known to be influenced by interactions between these parts due to shared developmental origin, phylogenetic legacy, functional constraints or structural requirements (Olson & Miller, 1958; Van Valen, 1965; Cheverud, 1982; Gould, 2002; Hallgrímsson, Willmore & Hall, 2002; Cubo, 2004; Goswami & Polly, 2010; Goswami et al., 2014). The tendency of morphological traits to covary under the influence of these factors is known as morphological integration (Olson & Miller, 1958; Van Valen, 1965). These factors can indeed increase morphological integration of the whole body or parts of it, but they can also act locally to produce stronger covariation within parts than with other units (e.g. modules – Hallgrímsson et al. 2002; Young & Hallgrímsson 2005; Klingenberg 2008; Goswami et al. 2014). Morphological integration is therefore classically explored through the study of covariation between sets of linear measurements or shape data (Van Valen, 1965; Klingenberg, 2008; Goswami & Polly, 2010; Bookstein, 2015).

Among tetrapods, the appendicular skeleton is a particularly integrated structure due to the common developmental origin of its parts (serial homology – Young & Hallgrímsson 2005; Bininda-Emonds et al. 2007; Sears et al. 2015) and shared functional constraints linked to locomotion and ecology (Hallgrímsson, Willmore & Hall, 2002; Young & Hallgrímsson, 2005; Goswami et al., 2014; Martín-Serra et al., 2015; Botton-Divet et al., 2018). In this framework, it has been hypothesized that the functional specialization of the appendicular skeleton is associated with a decrease of the integration level between limbs and serially homologous elements, and an increase of the within-limb integration (Hallgrímsson, Willmore & Hall, 2002; Young & Hallgrímsson, 2005). This has been particularly observed for some extreme locomotor adaptations like flight in bats or bipedal locomotion in hominoids, which led to a strong specialization of a specific part of the appendicular skeleton and consequently to a decrease of the general integration (Young & Hallgrímsson, 2005; Young, Wagner & Hallgrímsson, 2010; Bell, Andres & Goswami, 2011). Moreover, among quadrupedal mammals, the loss of the clavicle allows a greater mobility of the scapula, playing an active role in locomotion (Gasc, 2001; Schmidt & Fischer, 2009). This led to a shift in the functional relations between limb parts, where the serially homologous elements are not functionally analogous anymore (Gasc, 2001; Schmidt & Fischer, 2009) (Figure 17). At the interspecific level (e.g. evolutionary integration – Klingenberg 2014), it has been shown that many terrestrial taxa (equids, carnivorans, marsupials) present a strong general integration among all their limb long bones (Bennett & Goswami, 2011; Kelly & Sears, 2011; Fabre et al., 2014b; Martín-Serra

This work has been published under the reference*:* Mallet, C, Billet, G, Houssaye, A, Cornette, R. 2020. A first glimpse at the influence of body mass in the morphological integration of the limb long bones: an investigation in modern rhinoceroses. Journal of Anatomy; 237:4: 704– 726. https://doi.org/10.1111/joa.13232

et al., 2015; Hanot et al., 2017, 2018; Botton-Divet et al., 2018; Hanot et al., 2019; Martín-Serra & Benson, 2019), with a covariation mainly linked to the locomotion and shared phylogenetic history. But few studies explored the patterns of morphological integration of the appendicular skeleton among mammals at the intraspecific level (e.g. static or developmental integration – Klingenberg 2014) and tempted to compare them with the patterns observed at the interspecific level (Young, Wagner & Hallgrímsson, 2010; Hanot et al., 2017, 2018, 2019).

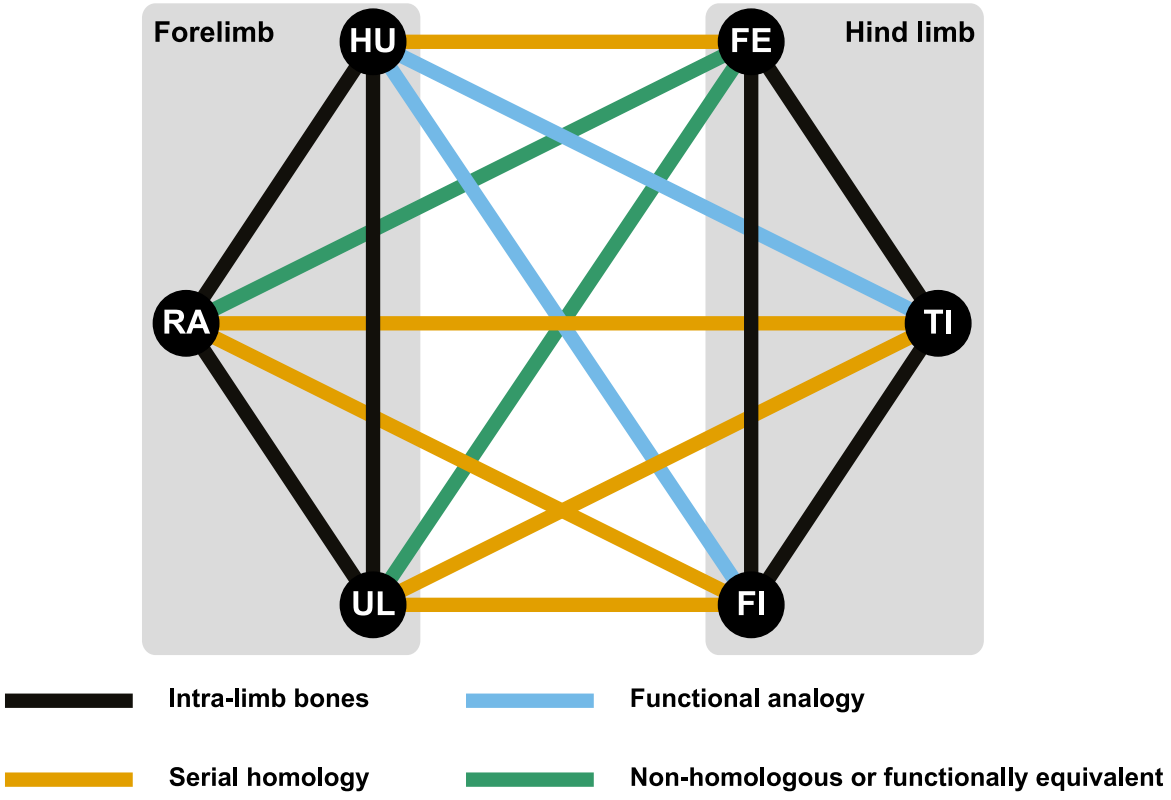

Figure 17 : Graphic model showing the hypotheses of morphological integration tested in this study on the appendicular skeleton of the five modern rhino species. HU: humerus; RA: radius; UL: ulna; FE: femur; TI: tibia; FI: fibula.

The support of a heavy mass is likely an important factor influencing the shape and integration of the appendicular skeleton. As described in Chapter 1, many mammalian lineages displayed an increase of their body mass along their evolutionary history (Depéret, 1907; Raia et al., 2012; Baker et al., 2015; Bokma et al., 2016). Biomechanical studies indicate that the shape of the limb bones should be driven by stress linked to mass support during the stance and the displacement of the animal (Hildebrand, 1974; Biewener, 1983, 1989a,b). However, few studies have explored the precise role exerted by body mass on the shape variation of the limb bones (Biewener, 1983; Bertram & Biewener, 1992; Fabre et al., 2013; Mallet et al., 2019). Likewise, the influence of body mass on integration patterns among limb bones is poorly known. Previous studies on relatively light taxa indicated a limited effect of body mass on integration patterns, overcome by other factors such as locomotor ecology (Martín-Serra et al.,

2015; Botton-Divet et al., 2018; Martín-Serra & Benson, 2019). At the opposite, other works proposed that body mass may still have an impact on the shape covariation of the limb long bones (Hanot et al., 2017; Randau & Goswami, 2018), possibly more pronounced for heavier species (Schmidt & Fischer, 2009). Drawing on this and on the results presented in Chapter 3, I chose to explore the integration patterns among modern rhinoceroses, constituting the second heaviest terrestrial group after elephants among modern mammals (Alexander & Pond, 1992). Whereas body size and mass poorly vary among the three species of elephants, the five modern species of rhinos surviving nowadays display a wide range of body mass (BM): *Dicerorhinus sumatrensis* (Fischer, 1814) – mean BM: 775 kg; *Diceros bicornis* (Linnaeus, 1758) – mean BM: 1,050 kg; *Rhinoceros sondaicus* Desmarest, 1822 – mean BM: 1,350 kg; *Rhinoceros unicornis* Linnaeus, 1758 – mean BM: 2,000 kg; and *Ceratotherium simum* (Burchell, 1817) – mean BM: 2,300 kg (Dinerstein, 2011) (see Table 1 in Chapter 3). This range of body mass can be highly variable within each species due to sexual dimorphism or between wild and captive specimens: 600 – 950 kg for *Ds. sumatrensis*; 800 – 1,300 kg for *Dc. bicornis*; 1,200 – 1,500 kg for *R. sondaicus*; 1,270 – 2,800 kg for *R. unicornis*; 1,350 – 3,500 kg for C. *simum* (Zschokke & Baur, 2002; Dinerstein, 2011). While a few studies have explored the shape variation of their long bones in relation to the ecology, phylogeny and functional constraints, such as body mass (Guérin, 1980; Eisenmann & Guérin, 1984; Mallet et al., 2019), no work has focused on the integration of their appendicular skeleton and its relationship to these factors. The aim of this chapter is thus to explore shape covariation patterns among limb long bones within and between species in order to highlight potential influence of body mass.

In the chapter, I propose to investigate the integration patterns of the shape of the limb long bones among the five species of modern rhinos, to quantify the integration level within and between limbs and to explore whether body mass could influence covariation patterns. In order to describe precisely the shape covariations by taking into consideration the whole shape of the bones in three dimensions, my analyses were done using 3D geometric morphometrics. They were performed at both interspecific and intraspecific levels, taking phylogenetic relationships into account where necessary (see Chapter 1 for details on phylogenetic uncertainties about modern rhinos). In accordance with previous works and the findings of Chapter 3, I hypothesize that the shape of limb long bones among rhinos should be: 1) strongly integrated as in other quadrupedal mammals at both interspecific and intraspecific levels (Hanot et al., 2017); 2) relatively homogenous between fore- and hind limbs as in other quadrupedal mammals (Martín-Serra et al., 2015; Hanot et al., 2017); 3) more strongly integrated than in lighter mammal species (Schmidt & Fischer, 2009); 4) showing similar patterns of shape covariation at both interspecific and intraspecific levels (Klingenberg, 2014). This will allow to emphasize how body mass could influence the structure of the limb long bones among rhinos.

Material and Methods

Studied sample

The dataset was composed of 50 complete skeletons housed in different European and American museums and belonging to the five extant rhino species: *Ceratotherium simum* (15 specimens), *Dicerorhinus sumatrensis* (9 specimens), *Diceros bicornis* (10 specimens), *Rhinoceros sondaicus* (7 specimens) and *Rhinoceros unicornis* (9 specimens) (Table 9). Some specimens are the same as considered in Chapter 3. The sample involved males, females and specimens without sex information, as well as captive and wild specimens. All anatomical terms are the same as used in Chapter 3.

3D geometric morphometrics

I used the same number and position for anatomical landmarks and curve sliding semi-landmarks than in the protocol described in Chapter 3 but the number of surface sliding semi-landmarks was reduced for all the bones – except the fibula – to improve the computation duration (see Appendix 1 of this chapter). The specimen *C. simum* RMCA 1985.32-M-0001 was chosen to be the initial specimen on which all anatomical landmarks, curve and surface sliding semi-landmarks were placed as in Chapter 3.

Study of morphological integration

I explored fifteen covariation patterns among all the possible pairs of bones (Gasc, 2001; Schmidt & Fischer, 2009): within-limbs adjacent bones (humerus-radius, humerus-ulna, radius-ulna, femur-tibia, femur-fibula and tibia-fibula), serially homologous bones (humerus-femur, radius-tibia, radius-fibula, ulna-tibia and ulna-fibula) and functionally analogous bones (humerus-tibia, humerus-fibula) (Figure 17). If the serial homology for the stylopodial bones seems obvious, no clear consensus exists for the serial homology within the zeugopodium elements. Many studies consider the radius and the tibia, and the ulna and the fibula, as serially homologous respectively (Bininda-Emonds et al., 2007; Schmidt & Fischer, 2009; Martín-Serra et al., 2015; Hanot et al., 2017; Botton-Divet et al., 2018), unfortunately without strong developmental or genetic evidences. Recent studies tend to indicate that the apparently obvious homology between fore and hind limb segments might be much more spurious than previously thought (Diogo & Molnar, 2014; Sears, Capellini & Diogo, 2015). In this context, I therefore tested the four possible bone combinations in the zeugopodium. As the appendicular skeleton is known to be highly integrated among quadrupedal mammals (Schmidt & Fischer, 2009; Martín-Serra et al., 2015; Hanot et al., 2017; Botton-Divet et al., 2018), I also tested the combinations involving non-homologous or analogous bones (radius-femur and ulna-femur) (Figure 17). Covariation patterns were investigated using Two-Blocks Partial Least Squares (2BPLS) analyses. The 2BPLS method extracts the

Taxon	Institution	Specimen number	Sex	Age	Condition	3D acquisition
Ceratotherium simum	AMNH	M-51854	F	A	W	SS
Ceratotherium simum	AMNH	M-51855	M	A	W	SS
Ceratotherium simum	AMNH	M-51857	F	A	W	SS
Ceratotherium simum	AMNH	M-51858	M	A	W	SS
Ceratotherium simum	AMNH	M-81815	U	A	U	SS
Ceratotherium simum	BICPC	NH.CON.20	M	S	W	SS
Ceratotherium simum	BICPC	NH.CON.32	F	S	W	SS
Ceratotherium simum	BICPC	NH.CON.40	F	S	W	SS
Ceratotherium simum	BICPC	NH.CON.110	M	A	W	SS
Ceratotherium simum	BICPC	NH.CON.112	M	A	W	SS
Ceratotherium simum	NHMUK	ZD 2018.143	U	A	U	SS
Ceratotherium simum	NHMW	3086	U	A	W	P
Ceratotherium simum	RBINS	19904	M	S	W	SS
Ceratotherium simum	RMCA	1985.32-M-0001	U	A	W	SS
Ceratotherium simum	RMCA	RG35146	M	A	W	SS
Dicerorhinus sumatrensis	MNHN	ZM-AC-1903-300	M	A	W	SS
Dicerorhinus sumatrensis	NHMUK	ZD 1879.6.14.2	M	A	W	SS
Dicerorhinus sumatrensis	NHMUK	ZD 1894.9.24.1	U	A	W	SS
Dicerorhinus sumatrensis	NHMUK	ZD 1931.5.28.1	M	S	W	SS
Dicerorhinus sumatrensis	NHMUK	ZE 1948.12.20.1	U	A	U	SS
Dicerorhinus sumatrensis	NHMUK	ZE 1949.1.11.1	U	A	W	SS
Dicerorhinus sumatrensis	NHMW	3082	U	A	U	P
Dicerorhinus sumatrensis	RBINS	1204	M	A	W	SS
Dicerorhinus sumatrensis	ZSM	1908/571	M	A	U	SS
Diceros bicornis	AMNH	M-81805	U	A	U	SS
Diceros bicornis	AMNH	M-27757	M	S	W	SS
Diceros bicornis	AMNH	M-113776	U	A	W	SS
Diceros bicornis	AMNH	M-113777	U	A	W	SS
Diceros bicornis	AMNH	M-113778	U	A	W	SS
Diceros bicornis	MNHN	ZM-AC-1936-644	F	S	U	SS
Diceros bicornis	RBINS	9714	F	A	W	SS
Diceros bicornis	RMCA	RG2133	M	S	W	SS
Diceros bicornis	ZSM	1961/186	M	S	U	SS
Diceros bicornis	ZSM	1961/187	M	S	U	SS
Rhinoceros sondaicus	CCEC	50002041	U	A	W	SS
Rhinoceros sondaicus	MNHN	ZM-AC-A7970	U	A	U	SS
Rhinoceros sondaicus	MNHN	ZM-AC-A7971	U	A	W	SS
Rhinoceros sondaicus	NHMUK	ZD 1861.3.11.1	U	S	W	SS
Rhinoceros sondaicus	NHMUK	ZD 1871.12.29.7	M	A	W	SS
Rhinoceros sondaicus	NHMUK	ZD 1921.5.15.1	F	S	W	SS
Rhinoceros sondaicus	RBINS	1205F	U	S	W	SS
Rhinoceros unicornis	AMNH	M-35759	M	A	C	SS
Rhinoceros unicornis	AMNH	M-54456	F	A	W	SS
Rhinoceros unicornis	MNHN	ZM-AC-1960-59	M	A	C	SS
Rhinoceros unicornis	NHMUK	ZD 1884.1.22.1.2	F	A	W	SS
Rhinoceros unicornis	NHMUK	ZE 1950.10.18.5	M	A	W	SS
Rhinoceros unicornis	NHMUK	ZE 1961.5.10.1	M	A	W	SS
Rhinoceros unicornis	NHMUK	ZD 1972.822	U	A	U	SS
Rhinoceros unicornis	RBINS	1208	F	A	C	SS
Rhinoceros unicornis	RBINS	33382	U	A	U	SS

Table 9: List of the studied specimens with sex, age class, condition and 3D acquisition details. Sex: F, female; M, male. Age: A, adult; S, sub-adult. Condition: C, captive; U, unknown; W, wild. 3D acquisition: P, photogrammetry; SS, surface scanner. Institutional abbreviations as given in Chapter 2.

principal axes of covariation from a covariance matrix computed on two shape datasets (Rohlf & Corti, 2000; Hanot et al., 2018; Botton-Divet et al., 2018), allowing to visualise the specimen repartition relatively to these axes and the shape changes associated.

Each PLS axis is characterized notably by its explained percentage of the overall covariation, its PLS correlation coefficient (rPLS) and its p-value, computed as a singular warp analysis as detailed in Bookstein et al. (2003). The p-value was considered as significant when the observed rPLS was higher than the ones obtained from randomly permuted blocks (1000 permutations). When the p-value was below 0.05, the PLS was considered as significant, i.e. the two considered blocks as significantly integrated. I used the function "pls2b" in the "Morpho" package to compute the 2BPLS (Schlager, 2017). To visualise these shape changes along the PLS axes, I used the function "plsCoVar" in the "Morpho" package to compute theoretical shapes at two standard deviations on each side of each axis (see Schlager, 2017). These theoretical conformations were then used to calculate a TPS deformation of the template mesh and therefore visualise the shape changes along the PLS axes. I then used the function "meshDist" in the "Morpho" package to create colour maps indicating the location and the intensity of the covariation between two meshes by mapping the distance between the minimum and maximum theoretical shapes along he first PLS axis (i.e. areas in red are the ones showing the most of shape changes within a bone pair whereas the areas in blue are the ones showing the less of shape change).

This procedure was performed at an interspecific level including all the 50 specimens into a single GPA. I also explored the intraspecific level of covariation by performing the sliding and GPA procedures on subsamples containing each different species. I then obtained five specific datasets on which were performed 2BPLS analyses.

Effect of the allometry

It has been previously demonstrated that centroid size may be a good approximation of the body mass of the specimen (Ercoli & Prevosti, 2011; Cassini, Vizcaíno & Bargo, 2012), notably among modern rhinos (see Chapter 3). To assess the effect of body mass on integration patterns – i.e. the effect of evolutionary allometry – I computed a multivariate regression of the shape against the centroid size using the function "procD.lm" in the "geomorph" package (v3.1.2—Adams & Otárola-Castillo, 2013). Then the residuals were used to compute allometry-free shapes, which were analysed with 2BPLS as described previously. Each species may have its own allometric slope, making it difficult to remove the general allometry effect (Klingenberg, 2016). However, considering the results obtained on Chapter 3 indicating close allometric slopes for the different species and the reduced sample size inherent to studying this endangered group, I chose to provide allometry-free shapes considering a single allometric component among all species (evolutionary allometry).

Statistical corrections for multiple comparisons

As explained above, I performed multiple pairwise comparisons when computing the different PLS. Each analysis tested a different pair of bones and contained part of the data present in some other analyses (e.g., landmarks of the humerus are tested for covariation with those of the radius, but also in all other pairs involving the humerus). For each tested pair, the hypothesis was that of a significant covariation between the shapes of the two bones. Given these settings and the exploratory approach of the study, there is no common agreement in the literature regarding whether or not statistical corrections for multiple comparisons should be used in the present case in order to lower the risk of finding false positives (i.e. finding a significant result due to chance) (Cabin & Mitchell, 2000; Streiner & Norman, 2011). In this context, I chose to present and discuss both uncorrected and corrected analyses for multiple comparisons, especially for the analyses at the intraspecific level where the correction had a higher impact (see Results). I applied a Benjamini-Hochberg correction to my data (Benjamini & Hochberg, 1995) as described by Randau & Goswami (2018) in a similar context of covariation tests on 3D geometric morphometric data. The test was run in R using the function “p.adjust” in the “stats” package. This correction was applied to all tests at the interspecific and intraspecific levels.

Results

Covariation at the interspecific level

All the first PLS axes are highly significant (p-values < 0.01 after correction – see Figures 18 and 19). These first axes gather between 53% (tibia-fibula) and 90% (humerus-femur) of the total covariation. Similarly, the rPLS values are high and vary between 0.72 (tibia-fibula) and 0.94 (humerus-ulna), indicating a strong general integration of the limb bones (Figure 20A). Intra-limb bones covary slightly more strongly in the forelimb than in the hind limb (Figure 20A). Surprisingly, the humerus and the ulna covary slightly more together (rPLS = 0.94) than the radius-ulna pair (rPLS = 0.93). In the hind limb, despite a high degree of covariation between the femur and the tibia (rPLS = 0.89), these two bones are poorly integrated with the fibula. When looking at serially homologous bones, the integration appears stronger between the humerus and the femur (rPLS = 0.93) and the ulna and the tibia (rPLS = 0.92) than between the radius and the tibia (rPLS = 0.88) and the ulna and the fibula (rPLS = 0.82). The radius-fibula covariation is the weakest (rPLS = 0.76) of all serially homologous bones. Regarding the functionally analogous bones, the covariation between the humerus and the hind limb zeugopodial bones is strong and more marked with the tibia (rPLS = 0.92) than with the fibula (rPLS = 0.84). Finally, the non-homologous or functionally analogous bones reveal also a stronger covariation between the ulna and the femur (rPLS = 0.90) than between the radius and the femur (rPLS = 0.84). In summary, all categories of pairwise comparisons (intra-limb, serial homology, functional analogy, non-homologous or analogous bones) showed high but unequal degrees of covariation. The fibula particularly stands out as having relatively weak degrees of covariations with other bones, being the only one not showing at least one very high covariation with another bone.

All plots of the first PLS axes are structured by an opposition between *Ds. sumatrensis* in the negative side and *C. simum* in the positive side (Figures 18 and 19), except for the tibia-fibula pair. *Diceros bicornis*, *R. sondaicus* and *R. unicornis* generally plot between these two extremes. All PLS plots involving the humerus display a clear isolation of these three taxa around null values and poorly dispersed clusters (Figure 18A-E). The clusters along the first PLS axis appear structured by a distinction between Asiatic and African taxa (less marked for the humerus-radius [Figure 18A] and the humerus-ulna [Figure 18E] couples) which can reflect an effect of the phylogeny (if considering African and Asiatic groups as sister taxa). This separation between African and Asiatic taxa follows the distribution of body mass within those groups, the lightest species showing the most negative values and the heaviest ones the most positive ones within both geographic groups. For all the bone pairs not involving the humerus, specimens within each species are more widely distributed in the morphospace and are organized differently along the first PLS axis. The radius-ulna first axis clearly expresses a sorting of the species from the lightest (*Ds. sumatrensis*) on the negative side to the heaviest (*C. simum*) on the positive side

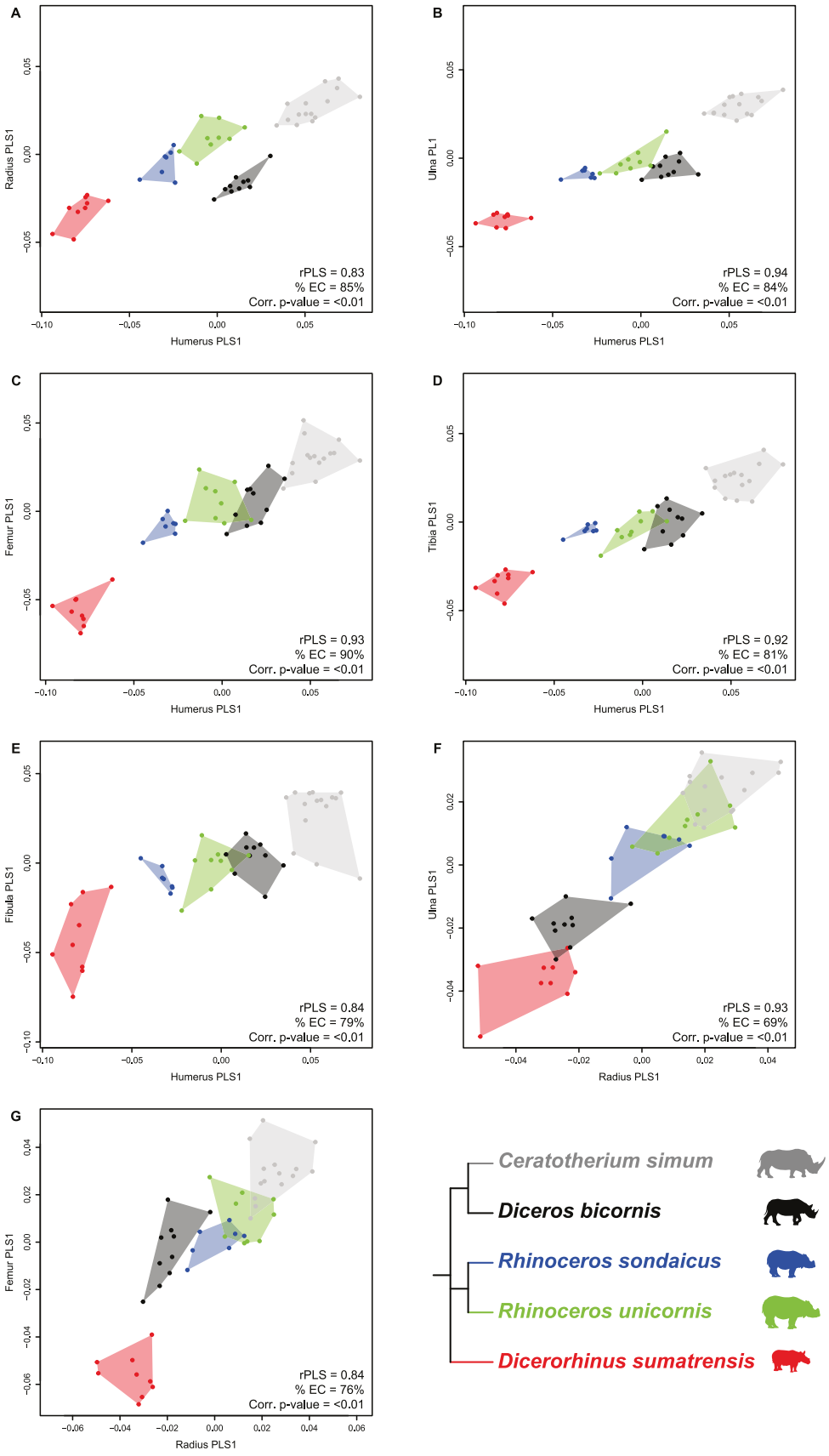

Figure 18: Plots of the first PLS axes computed on raw shapes. A: humerus-radius; B: humerus-ulna; C: humerus-femur; D: humerus-tibia; E: humerus-fibula; F: radius-ulna; G: radius-femur. rPLS: value of the PLS coefficient; % EC: percentage of explained covariation; Corr. p-value: corrected p-value using a Benjamini-Hochberg correction.

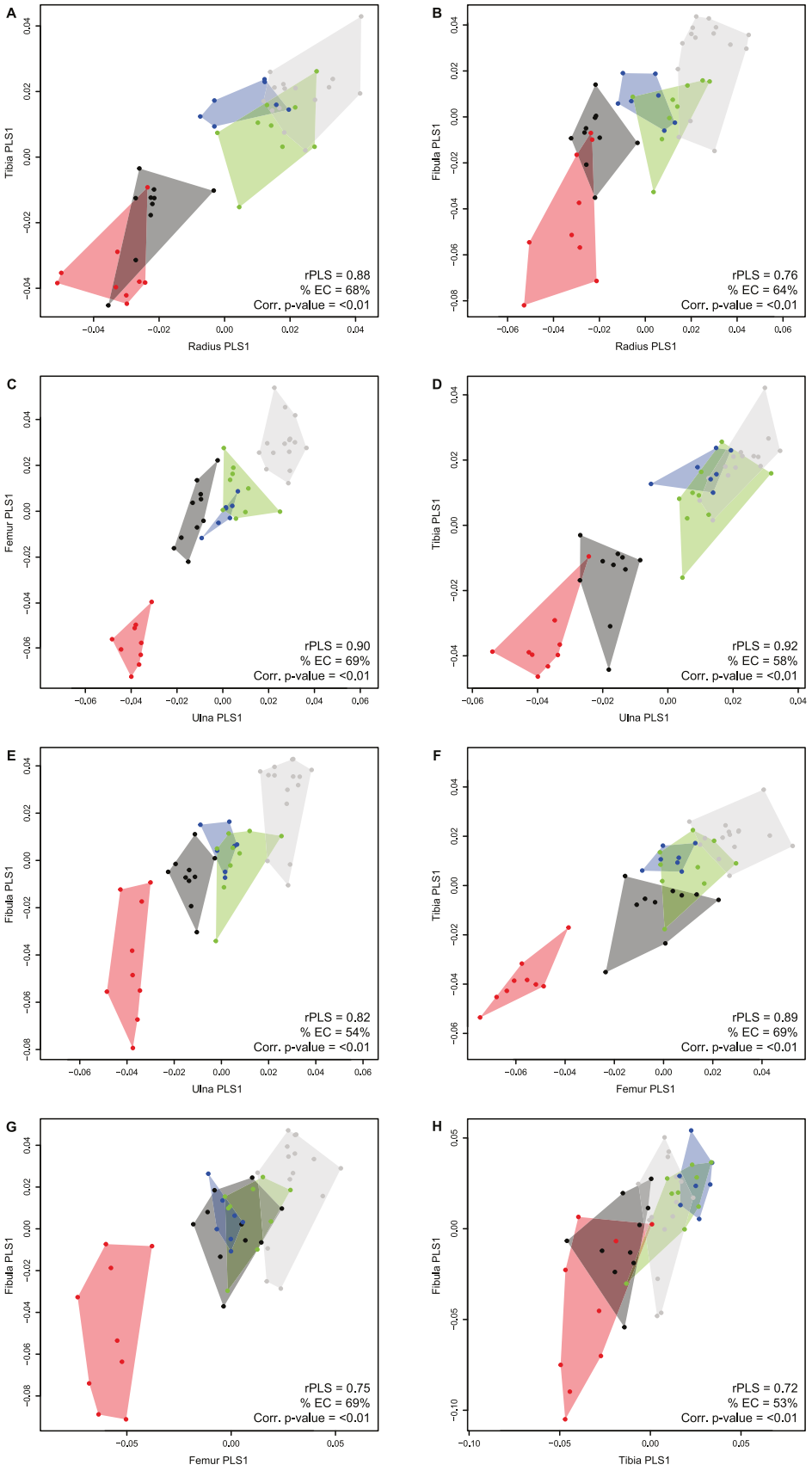

Figure 19: Plots of the first PLS axes computed on raw shapes. A: radius-tibia; B: radius-fibula; C: ulna-femur; D: ulna-tibia; E: ulna-fibula; F: femur-tibia; G: femur-fibula; H: tibia-fibula. rPLS: value of the PLS coefficient; % EC: percentage of explained covariation; Corr. p-value: corrected p-value using a Benjamini-Hochberg correction. Colour code as in Figure 18.

(Figure 18F) independently of the phylogenetic affinities between species. Although less clear, this structure also occurs for the radius-femur, radius-fibula, ulna-femur, ulna-fibula and femur-tibia pairs (Figure 18G and Figure 19B, C, E, F). *Dicerorhinus sumatrensis* is strongly isolated on the negative side on all pairs involving the femur (Figure 18C, G and Figure 19C, F, G). A third pattern isolating *Ds. sumatrensis* and *Dc. bicornis* on the negative part from the three other species on the positive part can be observed for the radius-tibia and ulna-tibia pairs (Figure 19A, D). The only first PLS axis showing a clearly different pattern is that of the tibia-fibula pair, where *R. sondaicus* is the most extreme species on the positive part and *C. simum* and *R. unicornis* clusters overlap (Figure 19H).

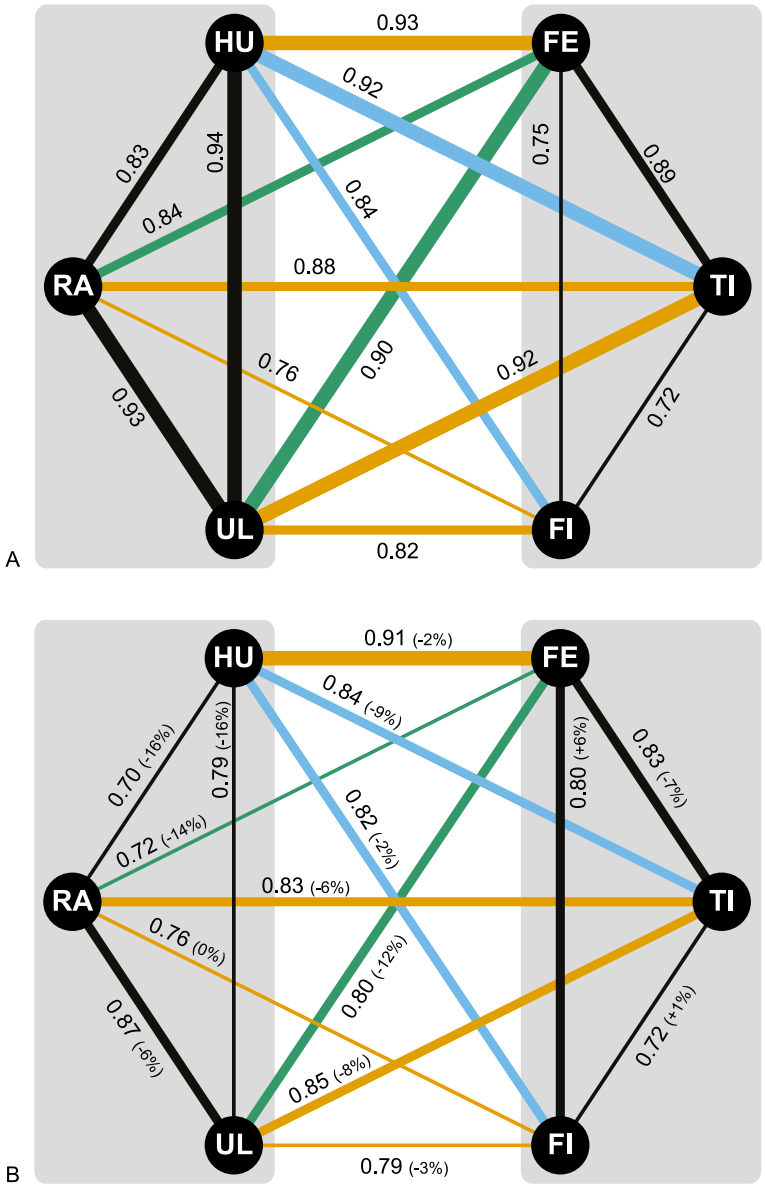

Figure 20 : Graphic model of the rPLS values of the first PLS axes computed on the appendicular skeleton of the five modern rhino species. The line thickness is proportional to the rPLS value. The colour code expresses the type of relation between bones as described in the Figure 17. A: rPLS values obtained on raw shapes. B: rPLS values obtained on allometry-free shapes. In brackets are indicated the percentages of difference between rPLS obtained on raw shapes and allometry-free shapes. Hu: humerus; Ra: radius; Ul: ulna; Fe: femur; Ti: tibia; Fi: fibula.

The second PLS axes are significant in most of the cases, except for the humerus-radius and humerus-femur pairs (p-values > 0.05 – see Appendix 2 of this chapter). These second axes explain between 4% (humerus-femur) and 31% (ulna-tibia) of the global covariation. Most of the PLS plots indicate a separation between the genus *Rhinoceros* and the three other rhino species, with an important overlapping of the clusters in many cases (see Appendix 2 of this chapter). This distinction is however absent for most of the plots involving the fibula, where the genus *Rhinoceros* may overlap the *D.* or *D.* clusters. No clear intraspecific pattern linked to age or sex has been found along these second PLS axes.

Colour maps computed using the theoretical shapes (available in Appendix 3 of this chapter) indicate that covariation associated to the first PLS axes are very similar for each bone regardless of the considered pair. Eight pairs representing the four types of relation existing between bones are presented in Figures 21 and 22. All other pairs are available in Appendix 4 of this chapter. The shape changes are mainly related to an increase of the bone robustness from negative to positive values of the axes, associated to a development of most of the muscular insertions (tubercles and trochanters) and of articular surfaces. For the humerus, most of the shape covariation with the other bones is located on muscular insertion areas, such as the lesser tubercle, the deltoid tuberosity, the lesser tubercle convexity and the epicondylar crest, where insert respectively the *m. supraspinatus*, the *m. deltoideus*, the *m. subscapularis* and the *m. extensor carpi radialis* (Figure 21A, D). The intensity of the covariation of the deltoid tuberosity is higher with the radius than with all other bones. For the radius, the strongest shape covariation with the other bones is located on the lateral insertion relief where inserts the *m. extensor digitorum communis*, on the medial part of the distal epiphysis and, to a lesser extent, on the radial tuberosity where inserts the *m. biceps brachii* (Figure 21B and 22A). On the medial part of the distal epiphysis, the shape covariation is less intense in the humerus-radius and radius-fibula couples than in the other bone pairs. For the ulna, the shape covariation with the other bones is mainly located on the medial and lateral tuberosities of the olecranon (where insert respectively the medial and lateral heads of the *m. triceps brachii*) and along the lateral and palmar edges of the shaft, where insert most of the digit extensors (Figure 21C, 22A and 22D). The shape covariation is slightly more pronounced on the olecranon tuberosity in the radius-ulna pair than in the other pairs. The femur is the bone showing the most similar patterns of shape covariation regardless of the bone pair. The strongest shape covariation with all other bones is located on the third tubercle and corresponds to the insertion of the *m. gluteus superficialis*. Other strong shape covariations between the femur and the other bones are located on the greater trochanter convexity where inserts the *m. gluteus accessorius*, and from the *fovea capitis* to the lesser tubercle where insert both the *mm. psoas major* and *iliacus* as well as the joint capsule of the hip (Figure 21A, 22B and 22D). Unlike the femur, the patterns of shape covariation for the tibia are highly variable depending of the considered bone pair. For the radius-tibia and the

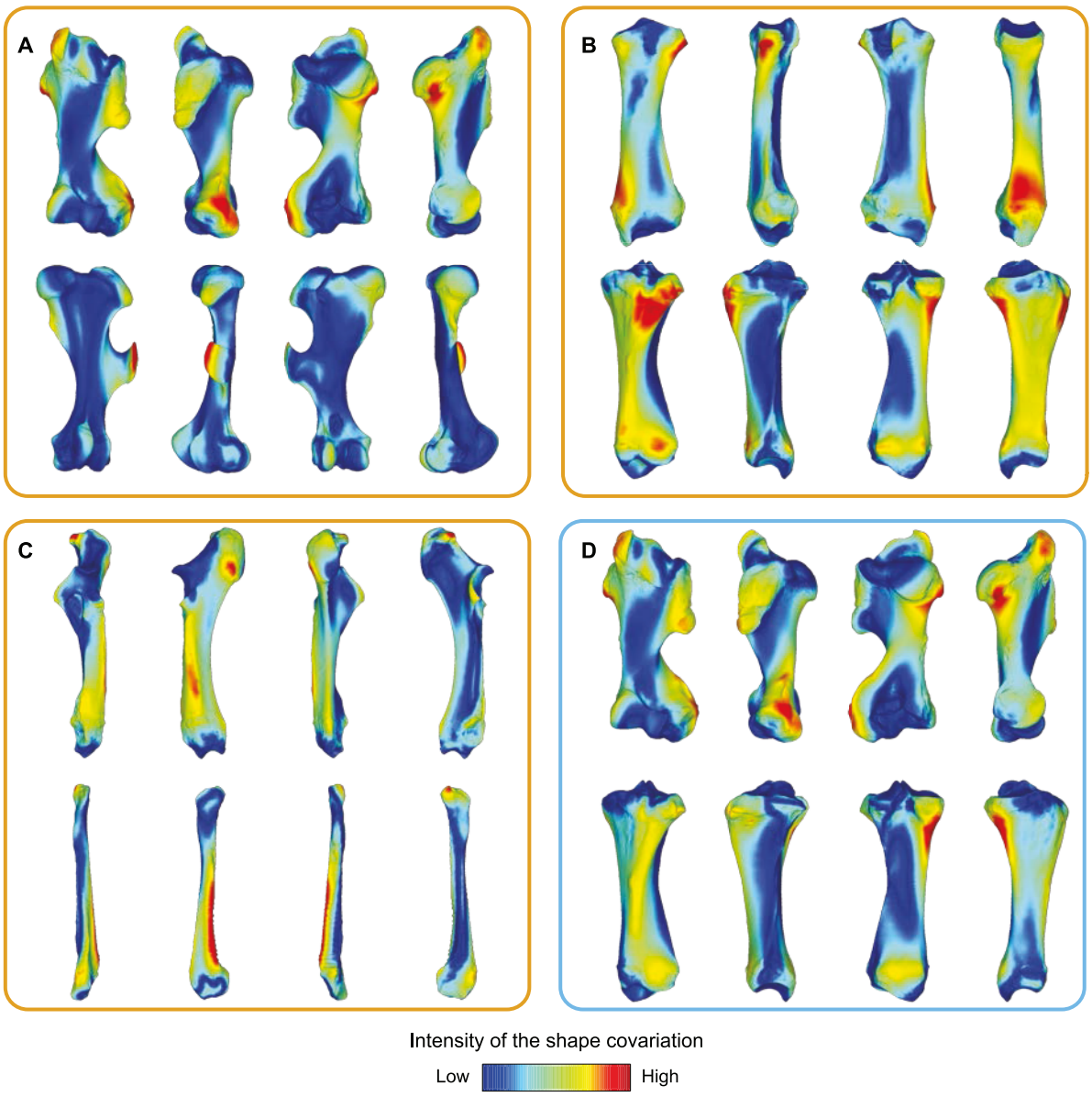

Figure 21: Colour maps of the location and intensity of the shape deformation associated to the first PLS axes for 4 pairs of bones among the five modern species of rhinoceros. For each bone, the shape associated to the positive part of the first PLS axis was coloured depending on its distance to the shape associated to the negative part (blue indicates a low deformation intensity and red indicates a high deformation intensity). The colour code of the squares expresses the type of relation between bones as described in the Figure 1 (orange: serial homology; blue: functional analogy). A: humerus-femur; B: radius-tibia; C: ulna-fibula; D: humerus-tibia (orientation from left to right in each case: cranial, lateral, caudal and medial).

ulna-tibia pairs, the strongest shape covariation is mainly located on the tibial tuberosity (where insert notably the medial, intermediate and lateral patellar ligaments, the patellar fascia and the *fascia lata*), the tibial crest, the area located distally to the medial condyle of the tibia where inserts the *m. popliteus*, and on the cranial and caudal sides of the distal part of the shaft (Figure 21B). The shape covariation is located in the same areas but with less intensity for the femur-tibia and tibia-fibula pairs (Figure 22B, C). The intensity of the shape covariation is minimal for the humerus-tibia pair, except for the insertion of the *m. popliteus* (Figure 21D). Finally, for the fibula, the shape covariation with the other bones is mainly located on the cranial part of the head of the fibula, on the distal part of the cranial

crest and on the caudal crest along the shaft, where insert notably the digit extensors (Figure 21C and 22C).

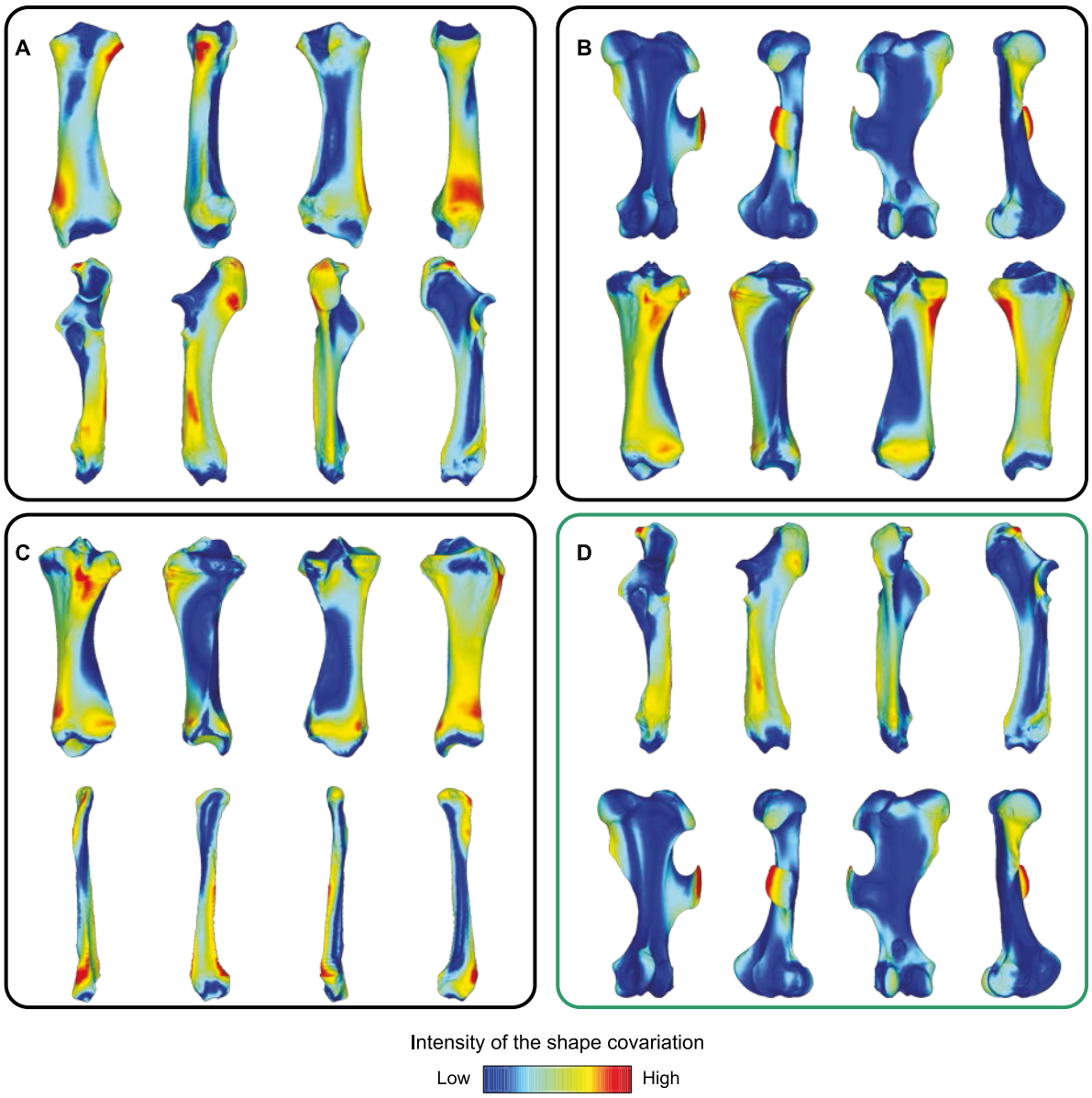

Figure 22: Colour maps of the location and intensity of the shape deformation associated to the first PLS axes for 4 pairs of bones among the five modern species of rhinoceros. For each bone, the shape associated to the positive part of the first PLS axis was coloured depending on its distance to the shape associated to the negative part (blue indicates a low deformation intensity and red indicate a high deformation intensity). The colour code of the squares expresses the type of relation between bones as described in the Figure 1 (black: intra-limb relation; green: non-homologous or analogous bones). A: radius-ulna; B: femur-tibia; C: tibia-fibula; D: ulna-femur (orientation from left to right in each case: cranial, lateral, caudal and medial).

Allometry-free covariation

All the first PLS axes computed on allometry-free shapes are highly significant (p-values after correction < 0.01 – see Figures 23 and 24). The first PLS axes explain between 44% (ulna-fibula) and 87% (humerus-femur) of the total covariation. The rPLS values remain high and range between 0.70 (humerus-

radius) and 0.91 (humerus-femur). The rPLS values are unequally impacted by the correction for allometry depending on the considered bone pair. A drop of 12 – 16% of the rPLS values can be observed between raw and allometry-free shapes for some couples: two intra-limbs pairs (humerus-radius, humerus-ulna) and two non-homologous or functionally analogous bones (radius-femur and ulna-femur) (Figure 20B). The drop of the rPLS values is less marked for other pairs and almost inexistent in the humerus-femur, humerus-fibula and ulna-fibula couples. Moreover, the rPLS value is strictly the same for the radius-fibula pair. I also noticed a slight rise of the rPLS value for the femur-fibula and tibia-fibula pairs by 6% and 1% respectively.

However, the distribution of the different species and specimens along the first PLS axes is different from the previous analyses (Figures 18 and 19) when computed on allometry-free shapes (Figures 23 and 24). All plots involving the humerus are structured in the same way with a strong separation between the three Asiatic species on the negative side and the two African species on the positive side (Figure 23A-E). A relatively similar structure is observed for the ulna-femur plot (Figure 24C) but the patterning of the distribution for all other bone pairs distributions is far less clear. Plots for the radius-ulna and the radius-tibia pairs display a similar pattern with *Dc. bicornis* and *Ds. sumatrensis* grouped together on the negative side, and the three other species on the positive side (Figure 23F and Figure 24A) despite some overlaps. Other plots display various patterns not distinguishing the species based on either size, geography or phylogenetic relationships. An opposition between *R. unicornis* and *C. simum* is also visible at the positive and negative parts of the first axis respectively with *Ds. sumatrensis* and *Dc. bicornis* overlapping around null values for the ulna-fibula pair (Figure 24E), or a slight distinction between the *Rhinoceros* genus and the other species for the ulna-tibia pair, whereas *Dc. bicornis* and *R. sondaicus* are strictly opposed along the first PLS axis (Figure 24D). A separation between *R. sondaicus* and the other species is also clearly visible for the tibia-fibula pair (Figure 24H). As for the raw data, the allometry-free shape changes along the first PLS axes mainly concern the robustness of the bones and shape covariation is very similar for all the bones regardless of the considered pair. All allometry-free theoretical shapes are available in Appendix 5 of this chapter.

Intraspecific covariation

Without Benjamini-Hochberg correction

At the intraspecific level, rPLS values are relatively high but few first PLS axes are statistically significant, even before correction (Table 10). Analyses reveal that the first PLS axis is significant for five bone pairs within *C. simum* (humerus-radius, humerus-ulna, humerus-femur, radius-femur and ulna-femur) and *R. sondaicus* (humerus-radius, radius-tibia, radius-fibula, humerus-tibia and ulna-femur), three for *R. unicornis* (humerus-ulna, tibia-fibula and ulna-tibia), two for *Ds. sumatrensis* (humerus-femur and humerus-tibia) and only one for *Dc. bicornis* (ulna-tibia). The rPLS values are extremely high (from 0.89

		C. simum (n=15)			*D. sumatrensis* (n=9)			*D. bicornis* (n=10)			*R. sondaicus* (n=7)			*R. unicornis* (n=9)		
	Paired bones	**rPLS**	**p**	**p cor.**	**rPLS**	**p**	**p cor.**	**rPLS**	**p**	**p cor.**	**rPLS**	**p**	**p cor.**	**rPLS**	**p**	**p cor.**
Intra-limb bones	Hum-Rad	**0.92**	**0.01**	**0.04**	0.85	0.40	0.59	0.89	0.19	0.55	**0.98**	**0.01**	0.10	0.90	0.37	0.59
	Hum-Uln	**0.91**	**0.04**	0.11	0.96	0.24	0.49	0.91	0.38	0.59	0.98	0.17	0.23	**0.93**	**0.04**	0.25
	Rad-Uln	0.88	0.07	0.16	0.91	0.28	0.49	0.96	0.11	0.55	0.97	0.09	0.15	0.95	0.48	0.59
	Fem-Tib	0.85	0.25	0.36	0.88	0.27	0.49	0.92	0.14	0.55	0.97	0.09	0.15	0.79	0.54	0.59
	Fem-Fib	0.78	0.87	0.87	0.87	0.95	0.95	0.87	0.29	0.55	0.95	0.26	0.30	0.84	0.55	0.59
	Tib-Fib	0.72	0.12	0.26	0.68	0.30	0.49	0.80	0.73	0.92	0.98	0.08	0.15	**0.95**	**0.01**	0.11
Serial homology	Hum-Fem	**0.93**	**0.01**	**0.02**	**0.95**	**0.02**	0.15	0.91	0.59	0.80	0.97	0.30	0.30	0.93	0.21	0.59
	Rad-Tib	0.90	0.27	0.36	0.70	0.77	0.95	0.94	0.23	0.55	**0.98**	**0.03**	0.10	0.93	0.51	0.59
	Rad-Fib	0.73	0.26	0.36	0.66	0.85	0.95	0.76	0.81	0.55	**0.95**	**0.05**	0.15	0.87	0.64	0.64
	Uln-Tib	0.84	0.36	0.41	0.92	0.29	0.49	**0.94**	**0.05**	0.55	0.97	0.09	0.15	**0.91**	**0.05**	0.25
	Uln-Fib	0.76	0.34	0.41	0.93	0.90	0.95	0.89	0.99	0.99	0.97	0.27	0.30	0.90	0.14	0.54
Functional equivalence	Hum-Tib	0.90	0.17	0.33	**0.93**	**0.01**	0.15	0.86	0.21	0.55	**0.99**	**0.01**	0.10	0.96	0.26	0.59
	Hum-Fib	0.77	0.65	0.69	0.80	0.63	0.85	0.90	0.81	0.93	0.95	0.11	0.16	0.91	0.48	0.59
Non-homologous or functionally equivalent	Rad-Fem	**0.89**	**0.01**	**0.05**	0.89	0.07	0.33	0.89	0.40	0.59	0.96	0.29	0.30	0.80	0.36	0.59
	Uln-Fem	**0.94**	**0.01**	**0.04**	0.93	0.19	0.49	0.89	0.86	0.93	**0.98**	**0.02**	0.10	0.97	0.37	0.59

Table 10: Values of the rPLS for the first PLS axes for each of the five species, with respective p-values before (p) and after (p cor.) the Benjamini–Hochberg correction. Statistically significant values are presented in bold (p or p cor. < .05). Fem, femur; Fib, fibula; Hum, humerus; Rad, radius; Tib, tibia; Uln, ulna.

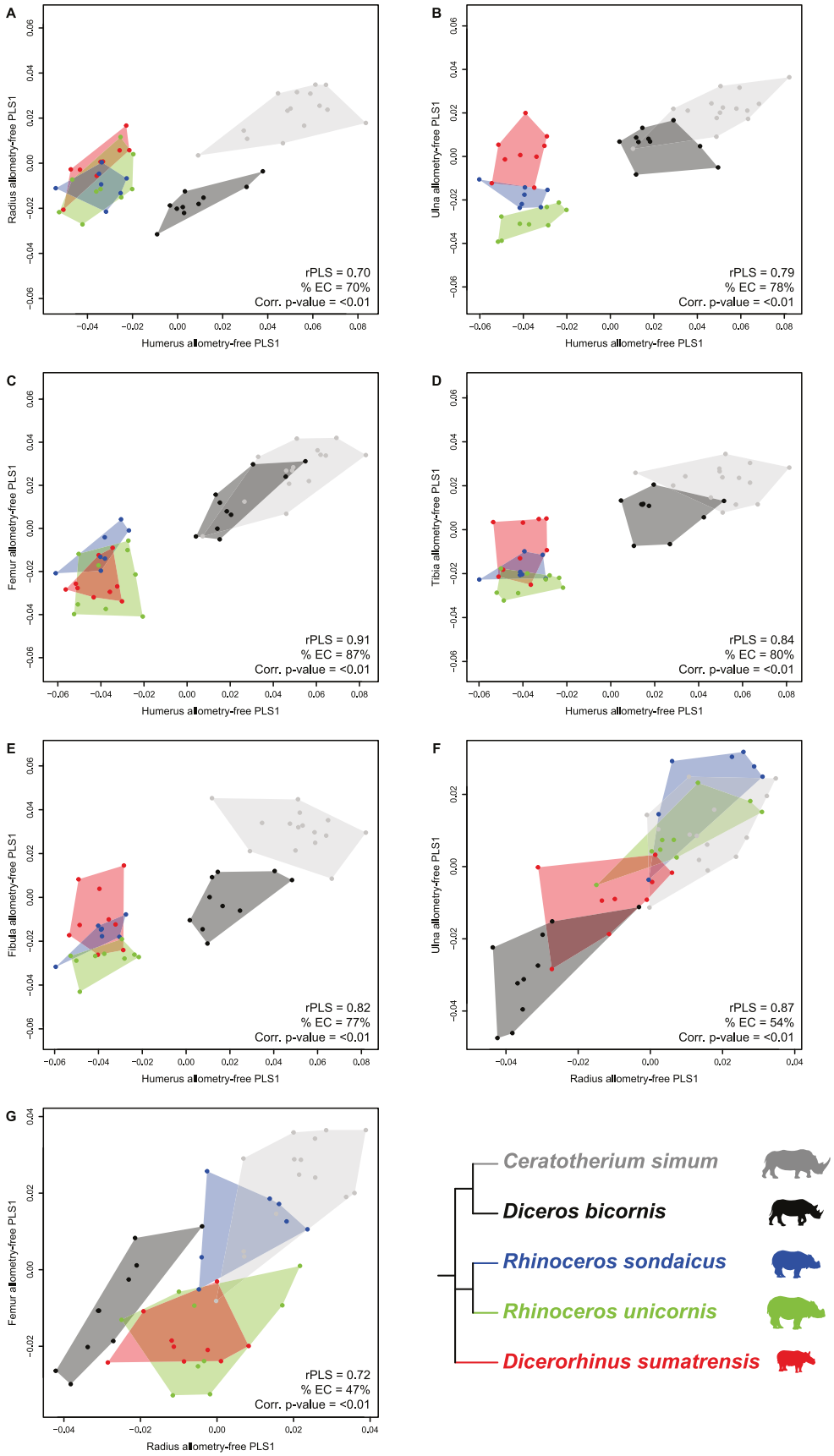

Figure 23: Plots of the first PLS axes computed on allometry-free shapes. A: humerus-radius; B: humerus-ulna; C: humerus-femur; D: humerus-tibia; E: humerus-fibula; F: radius-ulna; G: radius-femur. rPLS: value of the PLS coefficient; % EC: percentage of explained covariation; Corr. p-value: corrected p-value using a Benjamini-Hochberg correction.

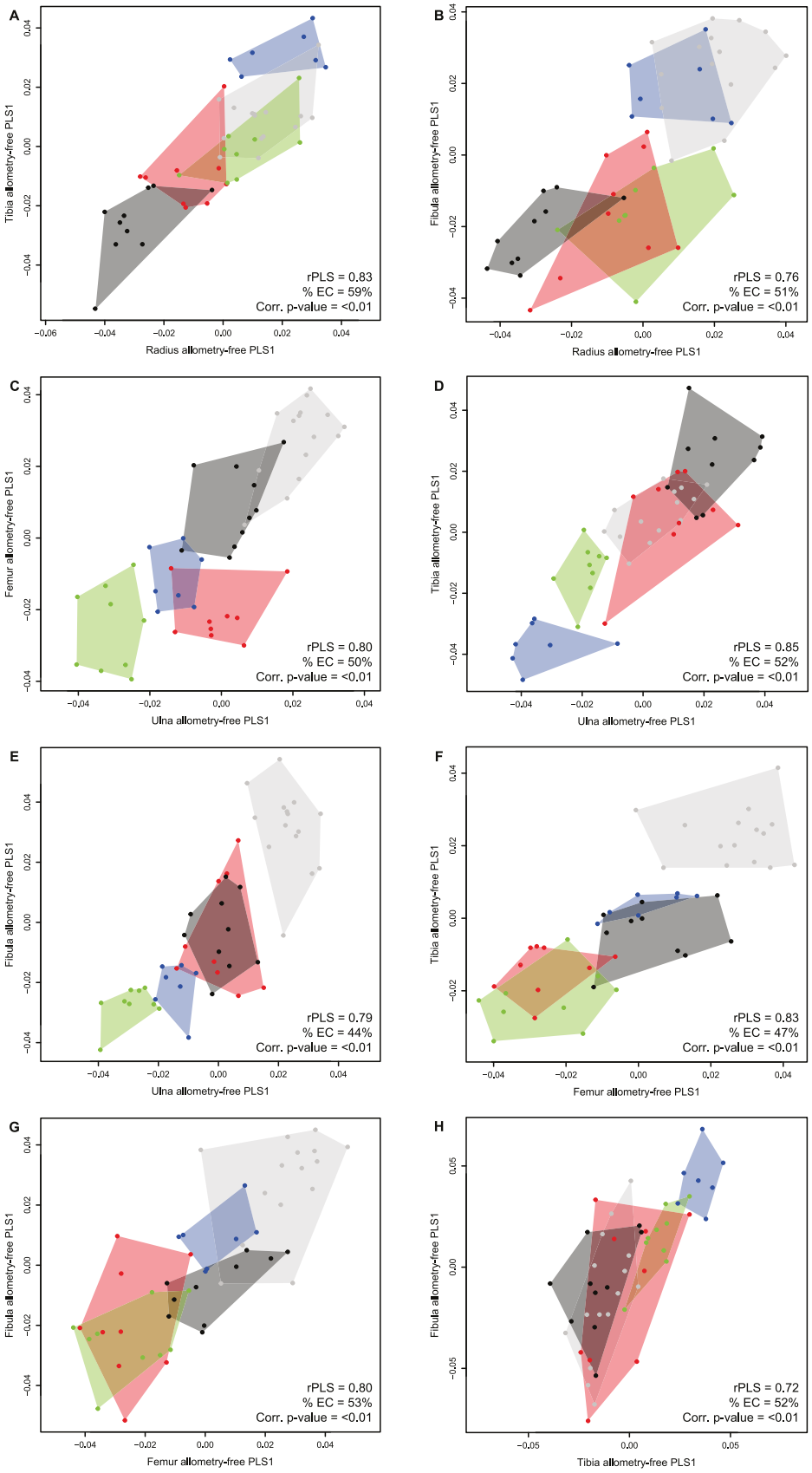

Figure 24: Plots of the first PLS axes computed on allometry-free shapes. A: radius-tibia; B: radius-fibula; C: ulna-femur; D: ulna-tibia; E: ulna-fibula; F: femur-tibia; G: femur-fibula; h: tibia-fibula. rPLS: value of the PLS coefficient; % EC: percentage of explained covariation; Corr. p-value: corrected p-value using a Benjamini-Hochberg correction. Colour code as in Figure 23.

to 0.99) for *R. sondaicus* relatively to the other species (0.72 - 0.94 for *C. simum*, 0.66 - 0.96 for *Ds. sumatrensis*, 0.76 - 0.96 for *Dc. bicornis* and 0.79 - 0.97 for *R. unicornis*). Although the covariation of some pairs may be common to some taxa (e. g. humerus-radius and ulna-femur for *C. simum* and *R. sondaicus*, humerus-tibia for *Ds. sumatrensis* and *R. sondaicus*), each species displays an overall different pattern of covariation. The observed lacks of significance may be due to the small number of specimens per species. However, *C. simum* and *R. sondaicus* show the highest percentage of significant results and are respectively represented by 15 and 7 specimens, these two subsamples being not particularly more diverse than the other species (adults and subadults, males and females, wild and captive specimens – see Appendix 6 of this chapter). This indicates that the observed tendency is not only related to the sample size but may also carry some biological signal. Moreover, some bone pairs show a p-value between 0.05 and 0.1 associated with a high rPLS value. This is notably the case for the tibia-fibula pair in the two *Rhinoceros* species (Table 10). This tends to indicate that the shape covariation between the fibula and the tibia may be higher for this clade than for other rhino species. In addition, the rPLS values of other pairs involving the fibula are often higher in both species of *Rhinoceros* than in other species in the sample, although their covariation is rarely significant.

For all these pairs, shape covariation involves anatomical areas which are similar within each species but often different between species (see Appendix 7 of this chapter). However, some anatomical areas appear to show high shape covariation both at the interspecific and intraspecific levels. This is notably the case of the greater tubercle convexity and the deltoid tuberosity of the humerus and the olecranon tuberosity of the ulna. These areas correspond to the insertion of powerful muscles for flexion and extension of the forearm (respectively the *m. infraspinatus*, the *m. deltoideus* and the *m. triceps brachii*).

After Benjamini-Hochberg correction

After the Benjamini-Hochberg correction of the p-values, rPLS values remain statistically significant for only four bone pairs, all belonging to *C. simum*, which is the species with the highest number of specimens (Table 10). In this species, the covariation is extremely strong for the humerus-radius (rPLS = 0.92), the humerus-femur (rPLS = 0.93) and the ulna-femur (rPLS = 0.94) pairs, and slightly weaker for the radius-femur pair (rPLS = 0.89). When looking at the first PLS axes for these four bone pairs, it appears clearly that the subadults are separated from the adults, sometimes without overlap, as for the ulna-femur pair (Figure 25). Contrary to the age class, the size of the individuals (expressed by the sum of the centroid sizes of the two bones in each case) does not seem to follow a precise pattern along the first PLS axes for these four bone pairs (Figure 25). A slight distinction between males and

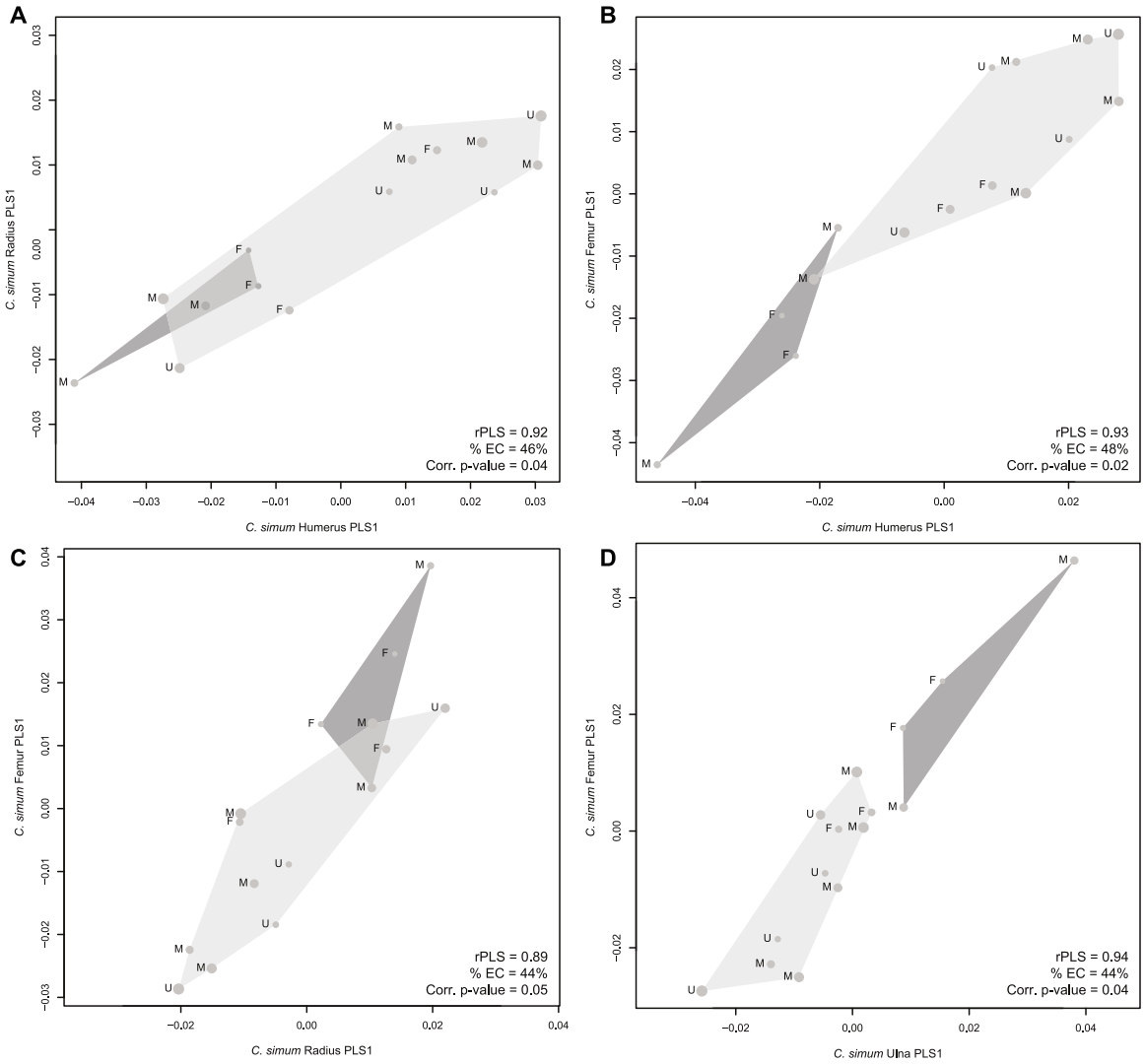

Figure 25: Plots of the first PLS axes computed on the 15 *Ceratotherium simum* specimens. Adults are highlighted in light grey and subadults in dark grey. The size of the dots is proportional to the combined value of the centroid size of the bones for each block and each specimen. A: humerus-radius; B: humerus-femur; C: radius-femur; D: ulna-femur. Sex: F: female; M: male; U: unknown; rPLS: value of the PLS coefficient; % EC: percentage of explained covariation; Corr. p-value: corrected p-value using a Benjamini-Hochberg correction.

females observed along the first PLS axes may partly account for the sexual dimorphism that exists in this species (Groves, 1972; Guérin, 1980). However, data are not sufficient to state on a potential difference of integration level due to sexual dimorphism in *C. simum*.

Although not statistically significant before and after correction, similar distinctions between adults and subadults have been observed on the first PLS axes for *Dc. bicornis* for some bone pairs (mainly humerus-radius, humerus-ulna, humerus-femur, humerus-tibia and radius-femur). Details on age class are too often missing for the three Asiatic species to state on this aspect. Shape variation associated to the first PLS axes in the significant covariations after correction in *C. simum* show a different tendency than at the interspecific level. The increase in robustness mainly concerns the shaft of the bone, both epiphyses tending to be already very large in subadults. This is particularly the case for the

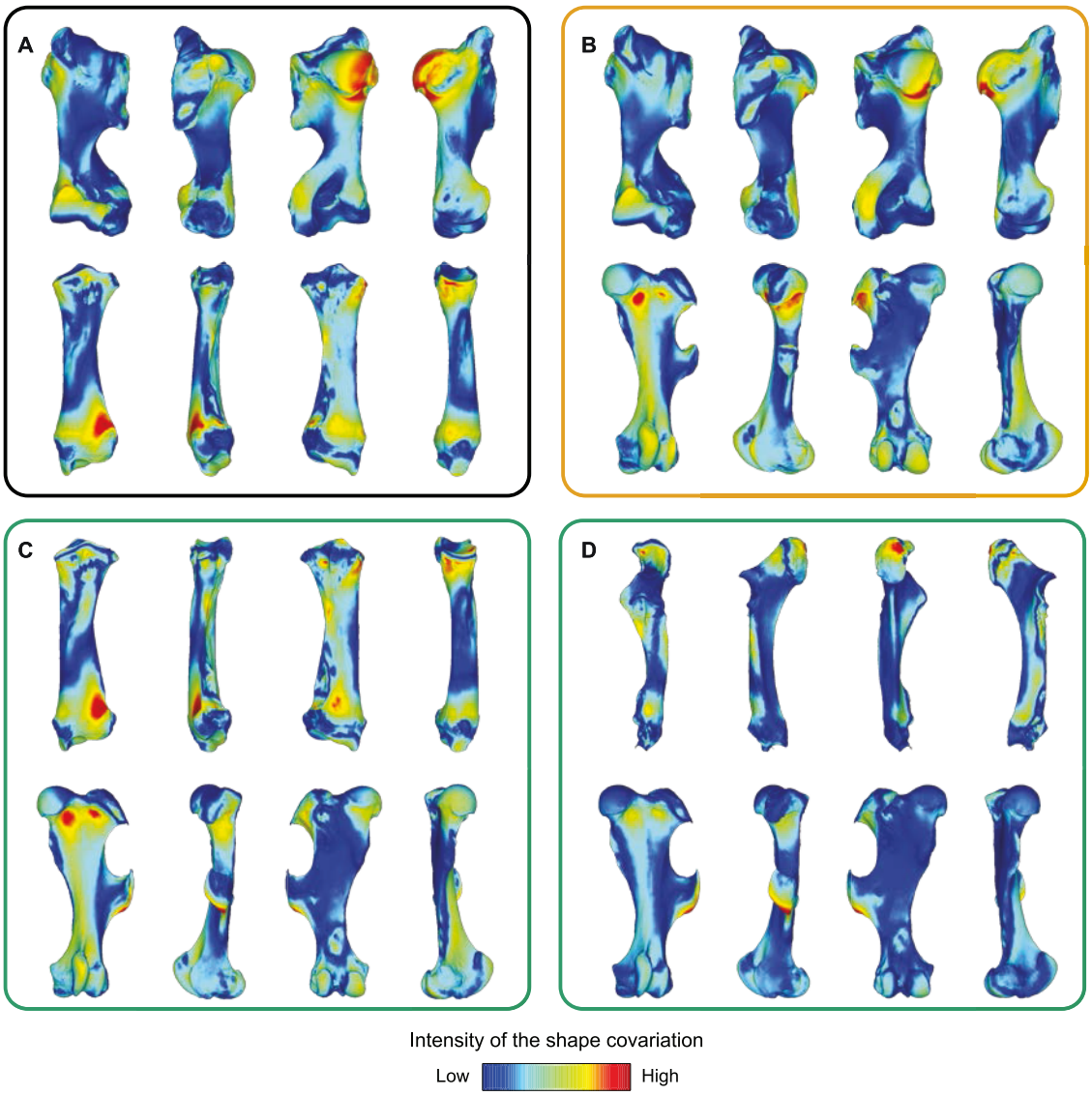

Figure 26: Colour maps of the location and intensity of the shape deformation associated to the first PLS axes for four bones of *Ceratotherium simum*. For each bone, the shape associated to the positive part of the first PLS axis was coloured depending on its distance to the shape associated to the negative part (blue indicates a low deformation intensity and red indicates a high deformation intensity). The colour code of the squares expresses the type of relation between bones as described in the Figure 1 (black: intra-limb relation; orange: serial homology; green: non-homologous or analogous bones). a: humerus-radius; b: humerus-femur; c: radius-femur; d: ulna-femur (orientation from left to right in each case: cranial, lateral, caudal and medial).

humerus and the femur (Figure 26). Colour maps confirm that the shape covariation along the first PLS axes for *C. simum* concerns different areas than at the interspecific level, with a different intensity depending on the bone pairs (Figure 26). It appears that the cranial side of the femur covaries strongly with the humerus and the radius, but visibly less with the ulna (Figure 26B, C and D). However, some anatomical areas are similarly affected by shape covariation both at the intra- and interspecific levels. This is notably the case for the lesser tubercle tuberosity on the humerus (insertion of the *m. subscapularis*) (Figure 26A and B) and the greater trochanter convexity on the femur (insertion of the *m. gluteus accessorius*) (Figure 26B and C).

Discussion

Patterns of evolutionary integration

My results indicate that the limb long bones of modern rhino species are strongly integrated at the interspecific level, confirming the first *a priori* hypothesis. This tendency has been previously observed on limb bones among other terrestrial mammal groups, notably in equids (Hanot et al., 2017, 2018, 2019), but also in more phylogenetically distant and older clades such as carnivorans (Fabre et al., 2014b; Martín-Serra et al., 2015; Botton-Divet et al., 2018) and marsupials (Martín-Serra & Benson, 2019). The high shape covariation between functionally analogous bones (humerus-tibia) as well as between non-analogous bones (ulna-femur) tends to indicate that this strong general integration may be related to a highly coordinated locomotion, as observed in equids at the interspecific level (Hanot et al., 2017), which is coherent with the rhino ability to gallop (Alexander & Pond, 1992) and to reach high running speed (Blanco, Gambini & Fariña, 2003).

However, contrary to the second hypothesis, this integration is unequally distributed among the tested pairs of bones. The within-limb integration is slightly stronger in the forelimb than in the hind limb, whereas in other taxa, the morphological integration is generally higher in the hind limb (Martín-Serra et al., 2015; Hanot et al., 2017; Botton-Divet et al., 2018). The covariation is maximal for the humerus-ulna and the radius-ulna couples. Although the femur and the tibia display a strong covariation with one another, the fibula appears as the bone showing the lowest integration level. This is consistent with the observations described in Chapter 3 on morphological variation of rhino long bones, highlighting that the shape of the fibula is highly variable at the intraspecific level (Mallet et al., 2019). Therefore, the apparent lower integration of the hind limb may be mainly due to the independent shape variation of the fibula. The fibula appears nevertheless to be more strongly integrated with the humerus (functionally analogous) and the ulna (serially homologous) than with other hind limb bones. This confirms that the shape of the fibula remains covariant with other bones beyond stochastic variation, potentially driving the slightly lower integration of the hind limb than of the forelimb.

Body mass and evolutionary integration

Within limbs

Among modern rhinos, most of the shape covariation is mainly driven by an increase in general robustness and in the size of the articular surfaces and muscular insertion areas. This is coherent with previous observations on other quadrupedal mammals (Martín-Serra et al., 2015; Hanot et al., 2018; Botton-Divet et al., 2018). The correction for allometry affects both the rhino species distribution along the PLS axes and the rPLS values in a stronger way than for equids (Hanot et al., 2018), carnivorans (Martín-Serra et al., 2015) or musteloids (Botton-Divet et al., 2018) at the interspecific level, confirming

the third hypothesis specifying that body mass has a stronger influence on the degree of integration among heavy quadrupedal than in lighter mammal species. Allometry is also clearly more pronounced on the forelimb than on the hind limb, as shown by the drastic reduction of the integration intensity when using the allometry-free shapes. This tends to indicate that beyond the strong general integration of the rhino limb bones, the overall higher integration within the forelimb might be caused by a stronger allometry in these bones – and thus more strongly affected by body mass (Ercoli & Prevosti, 2011; Cassini, Vizcaíno & Bargo, 2012; Mallet et al., 2019) – than the hind limb. Heavy quadrupeds bear a larger part of the body weight on their forelimbs than on their hind limbs (Hildebrand, 1974) and rhinos follow this body plan (Regnault et al., 2013) due to their heavy head and horns and their massive trunk muscles and bones. Previous observations (Schmidt & Fischer, 2009; Hanot et al., 2018) led to the conclusion that body mass can contribute to covariation between bones, which data seem to confirm for rhinos. The higher integration of the forelimb may thus be interpreted as a specialization linked to weight bearing (Martín-Serra et al., 2015; Randau & Goswami, 2018).

Furthermore, the covariation of the different elements composing the forelimb is probably related to a complementary effect of phylogenetic relationships, developmental constraints and body mass. The shape covariation between the humerus and the zeugopodium elements in the forelimb is clearly driven by a distinction between Asiatic and African species, associated with a sorting linked to the mean body mass within these two groups. The covariation is particularly strong between the humerus and the ulna, and although it seems to be largely patterned by phylogenetic history, this is congruent with previous studies indicating a high integration level between the bones involved in flexion/extension movements and body stability (Fabre et al., 2014b). Conversely, the interspecific covariation of the radius-ulna pair seems intimately linked to the mean body mass of rhino species, with no distinct link to the phylogenetic pattern. This indicates a likely major impact of mass on the zeugopodium integration coupled with a common developmental origin (Young & Hallgrímsson, 2005; Sears et al., 2007). These results are also in good agreement with the more important impact of body mass observed on the shape of the radius and ulna than on that of the humerus (see Chapter 3) (Mallet et al., 2019) and the role of the zeugopodium in the support of the body weight due to the alignment of this segment with pressure forces (Bertram & Biewener, 1992).

Albeit less obvious, an effect of body mass on the hind limb interspecific integration could also exist, especially between the femur and the tibia when looking at the species distribution along the first PLS axis (raw shapes) and the rPLS values for allometry-free shapes. In a similar way than for the forelimb, these two bones are involved in leg flexion/extension, particularly for propulsion (Hildebrand, 1974; Lawler, 2008; Biewener & Patek, 2018). Conversely, the degree of integration increases between the femur and the fibula (and to a lesser extent between the tibia and the fibula) when the allometric

effect is removed, which is a unique phenomenon among all tested limb bone pairs. One interpretation can be that the allometry effect consists in antagonistic changes between the femur and the fibula, and that the fibula shape covariation at the interspecific level is poorly related to body mass. This is coherent with all low rPLS drops for allometry-free shapes in all other pairs involving the fibula. This difference can also be influenced by a different covariation between the femur and the fibula depending on the rhino species (see below). The independence of the shape variation of the fibula relatively to the tibia also indicates that, contrary to the forelimb zeugopodium, neither common developmental origin nor functional requirements seem to highly constrain the covariation between the two hind limb zeugopodium bones.

Following the hypotheses of Hallgrímsson et al. (2002) and Young & Hallgrímsson (2005) stating that a functionally specialized part covaries less with surrounding elements, the fibula could be interpreted as a highly specialized bone in some rhino species. However, as previously observed for the ulna of musteloids (Botton-Divet et al., 2018), the lower integration of the fibula may be linked to a decrease of the functional constraints exerted on this bone. The fibula supports the insertion of digit flexors and extensors (Barone, 2010a) and is involved in the ankle stability and weight bearing among rhinos. However the fibula shape has been proven to be poorly correlated with body mass (see Chapter 3) (Mallet et al., 2019). Therefore, it is likely that the fibula shape varies more independently and is less functionally constrained by body mass than other limb bones in some rhino species (see below). This may be interpreted as a case of parcellation (Young & Hallgrímsson, 2005) due to a functional dissociation between the bones of a single limb.

All the pairs involving the humerus seem thus more strongly impacted by phylogeny than by functional constraints and, to a lesser extent, by body mass. Most of the other bone pairs rather suggest a dominant effect of body mass, especially the ones involving the radius and the ulna. Although less clear, similar results are obtained for the hind limb bones.

Between limbs

At the interspecific level, serially homologous bones are strongly integrated but their covariation is differently associated with body mass, i.e. more for the zeugopodium elements than for the stylopodium ones. Together with the slightly lower integration values of the zeugopodium elements relatively to the stylopodium, these observations are also coherent with previous studies indicating a decrease of the integration from proximal to distal parts of the limbs linked to a higher degree of specialization of distal elements (Young & Hallgrímsson, 2005). In addition, these results are not congruent with the strict serial homology classically considered for the zeugopodium (radius-tibia and ulna-fibula) by showing a stronger covariation between the ulna and the tibia than between the radius and the tibia.

Similar results were observed on carnivorans and interpreted as a potential functional convergence between these bones (Martín-Serra et al., 2015). These results could also revive doubts on the *a priori* hypothesis of homology between zeugopodium bones, which has long been debated (Owen, 1848; Wyman, 1867; Lessertisseur & Saban, 1967) and, to my knowledge, still remains unresolved although largely taken for granted (i.e. Bininda-Emonds et al. 2007; Bennett & Goswami 2011; Martín-Serra et al. 2015; Botton-Divet et al. 2018). Only a comprehensive study of the genetic processes leading to the development of forelimb and hind limb zeugopodium could clarify this aspect (Klingenberg, 2014).

The strong integration between the humerus and the tibia (and the fibula to a lesser extent) tends to confirm the functional analogy between the forelimb stylopodium and the hind limb zeugopodium (Gasc, 2001; Schmidt & Fischer, 2009). However, the shape covariation is weaker in the humerus-tibia pair than in other bone pairs involving the tibia (e.g. radius-tibia and ulna-tibia), which tends to indicate that, in the present case, the functional requirements linked to locomotion and body support during resting time may less affect the shape covariation than the developmental constraints, contrary to what has been observed in lighter taxa (Fabre et al., 2014b; Hanot et al., 2017; Botton-Divet et al., 2018). Moreover, the high covariation between the ulna and the femur also tackles the classic functional approach, highlighting a strong integration between non-homologous or analogous bones, an observation also recently revealed among marsupials (Martín-Serra & Benson, 2019). Recent work using a network approach on a phylogenetic matrix of characters among modern and fossil rhinos showed that unexpected covariations can exist between cranial, dental and postcranial phenotypic traits in the group (Lord et al., 2019). In particular, the authors observed a frequent co-occurrence of discrete traits between the radius-ulna and the femur among all rhinos, which seems coherent with my results indicating a strong covariation between the forelimb zeugopodium and the hind limb stylopodium. Since the postcranial body plan appears to be implemented early during the Rhinocerotoidea evolutionary history (Lord et al., 2019) and may be less variable than in phylogenetically-close taxa like equids (McHorse, Biewener & Pierce, 2019), this may imply strong inherited developmental constraints within this group canalizing the shape covariation (Hallgrímsson, Willmore & Hall, 2002) even between non-homologous bones. Furthermore, the high integration of non-homologous or analogous bones appears as strongly congruent with the variation in body mass, lending further support to the link between heavy weight and high general integration level (Schmidt & Fischer, 2009; Hanot et al., 2017).

Covariation at the intraspecific level: developmental integration

This exploration of integration patterns at the intraspecific level is limited by the low sample size for all species and the non-significance (at $p>0.05$) of most of the PLS axes obtained for the different pairs of bones, particularly after the Benjamini-Hochberg correction. Beyond this strict non-significance (which is currently criticized in favour of a more continuous approach of the p-value – see Ho et al.

2019; Wasserstein et al. 2019), no clear similar pattern of integration seems to emerge between light and heavy rhino species, or between African and Asiatic species. Some species share the same significant or almost significant bone pairs. The covariation between the tibia and the fibula among *Rhinoceros* notably seems relatively strong as compared to in other species, confirming the results obtained on individual shape variation in Chapter 3. This aspect may indicate that the hind limb zeugopodium – and particularly the fibula – is less variable among the two species of this genus, with a lesser parcellation among this group.

The integration patterns found in *C. simum,* the species with the most specimens, reveal both similarities and divergences with the patterns observed at the interspecific level (i.e. evolutionary integration, see Cheverud 1996; Klingenberg 2014). All the significant PLS axes in this species concern forelimb bones and indicate a very strong integration between the humerus, the radius and the ulna, as well as a high shape covariation between the humerus and the femur (serial homology). The strong integration of the forelimb may be partly related to the heavier and longer head of *C. simum* compared to other species (Guérin, 1980) and highlights different patterns of distribution of body weight among modern rhinos (Antoine, pers. comm. 2020). The shape covariation among *C. simum* specimens reveals a strong effect of age with a clear separation between adults and subadults in all cases. Even if this effect is not visible at the interspecific level, the separation between the two age classes is the main driver of the integration within this species, whereas body mass (approximately expressed through the value of the centroid size) and sex do not seem to play a visible role on the covariation patterns. This tendency is associated with a shape covariation on anatomical areas often different to the ones showing a strong covariation at the interspecific level. Only the greater tubercle convexity and the deltoid tuberosity on the humerus, the olecranon tuberosity on the ulna and the greater trochanter convexity on the femur show a high degree of shape covariance both at both interspecific and intraspecific levels.

Within *C. simum*, developmental integration is more related to proportions between the different bone parts (e.g. shaft and epiphyses) than to the development of powerful muscular insertions ensuring the stability and the locomotion of the body. In the end, the global integration of the rhino limb long bones results in the superposition and association of the different levels of integration (here, developmental and evolutionary). These integration levels are conjointly influenced by shared phylogenetic history, similar developmental origin and constraints due to both locomotion and body mass support (Cheverud, 1996; Hallgrímsson et al., 2009; Klingenberg, 2014). Investigated here among *C. simum*, the static and developmental integration levels remain to be explored with a larger sample for the other rhino species – which remains challenging for these endangered species. Finally, the addition of some of the numerous fossil taxa belonging to the superfamily Rhinocerotoidea and displaying

convergent increases of body mass will help testing the influence of body mass on integration patterns suggested in the present study (Klingenberg, 2014).

Conclusion

This exploration of the integration patterns of the limb long bones among modern rhinos reveals that the appendicular skeleton of these species is strongly integrated, as in other terrestrial quadrupedal mammals. At the interspecific level, the forelimb appears as more covariant than the hind limb, with a more apparent relation to body mass, which appears stronger than for more lightly built terrestrial mammals. This can be interpreted as a higher degree of specialization of the forelimb in body weight support. Proximal elements appear primarily affected by common developmental constraints whereas the distal parts of the limbs seem rather shaped by functional requirements, which would confirm hypotheses addressed on different mammal groups. The appendicular skeleton of rhinos appears to be a compromise between the functional requirements of a highly coordinated locomotion, the necessity to sustain a high body mass and important inherited developmental processes constraining shape covariation – located mostly on insertion areas for powerful flexor and extensor muscles. In addition, the exploration of the shape covariation at the intraspecific level reveals a prominent effect of the age class in shaping the covariation patterns among *C. simum*. These results are a first step to explore further the functional construction of the appendicular skeleton of modern rhinos and to extend this approach to other heavy modern taxa (such as elephants or hippos). Moreover, the numerous fossil taxa composing the superfamily Rhinocerotoidea and showing a broad range of body mass would be a valuable group to extend these results and highlight convergent patterns of shape covariation directly linked to a heavy weight.

Appendices

Appendix 1: Designation and location of anatomical landmarks placed on each bone

Anatomical landmarks and curve sliding semi-landmarks are identical to those used in Chapter 3. Only the number or surface sliding semi-landmarks have been reduced to improve computation time (see Material and Methods). The landmark configuration is unchanged for the fibula (see Appendix 1 of Chapter 3).

Bone	Anatomical LM	Curve sliding semi-LM	Surface sliding semi-LM	Total
Humerus	35	639	559	1233
Radius	23	393	493	909
Ulna	21	343	540	904
Femur	27	612	518	1157
Tibia	24	384	540	948
Fibula	12	269	454	735

Table S1A: Total number of anatomical landmarks (LM), curve sliding and surface sliding semi-landmarks for each bone.

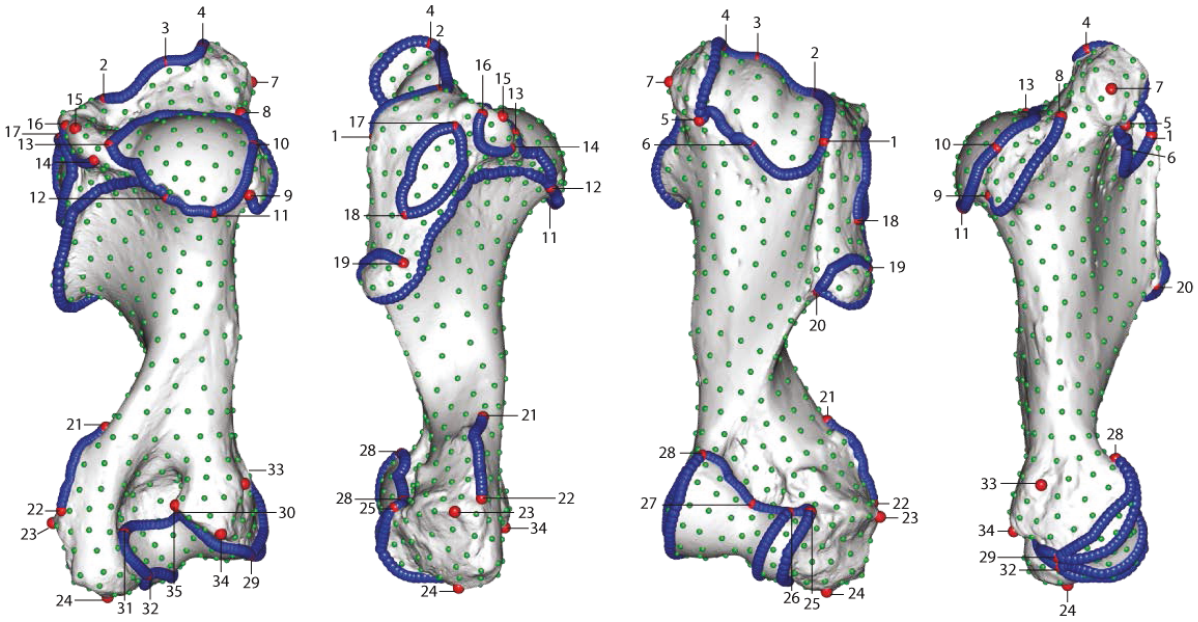

Figure S1B: Location of anatomical landmarks (red spheres), curve sliding (blue spheres) and surface sliding (green spheres) semi-landmarks placed on the humerus. From left to right: caudal, lateral, cranial and medial views. Numbers refer to anatomical landmarks designation detailed in Appendix 1 of Chapter 3.

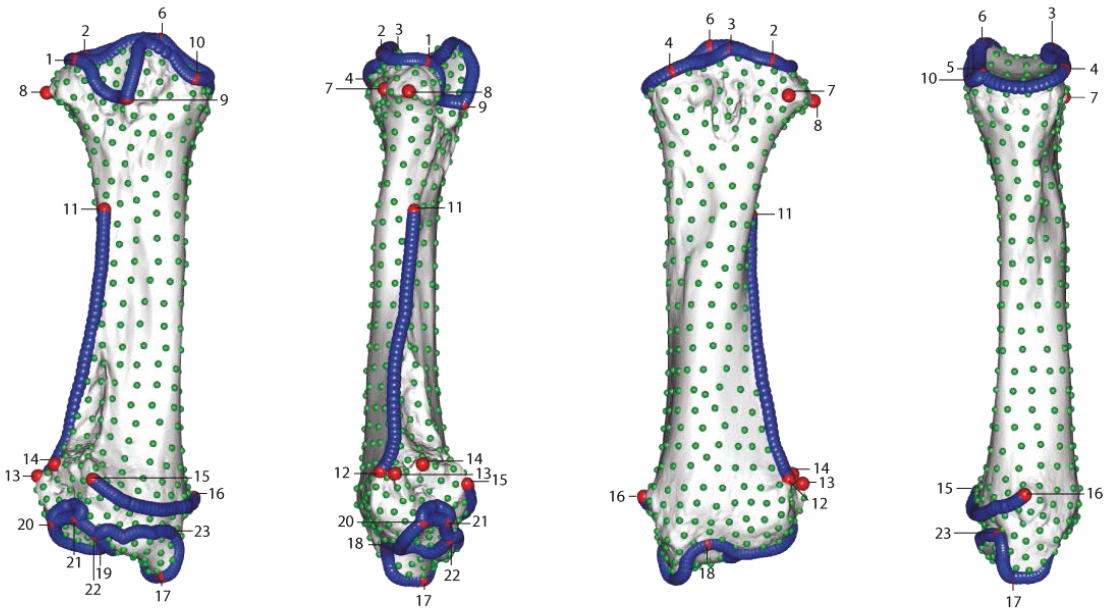

Figure S1C: Location of anatomical landmarks (red spheres), curve sliding (blue spheres) and surface sliding (green spheres) semi-landmarks placed on the radius. From left to right: caudal, lateral, cranial and medial views. Numbers refer to anatomical landmarks designation detailed in Appendix 1 of Chapter 3.

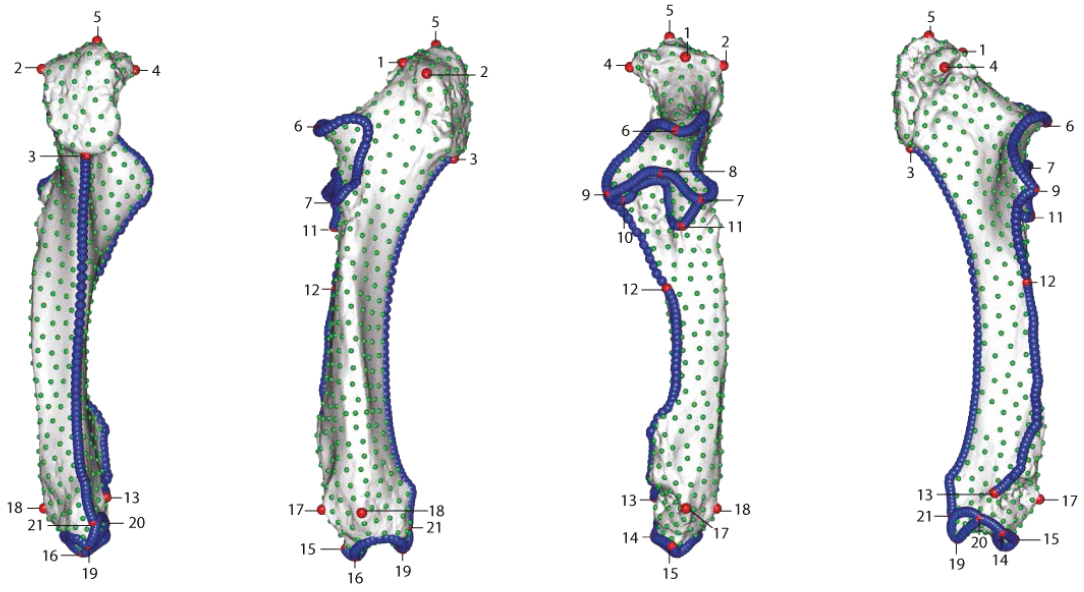

Figure S1D: Location of anatomical landmarks (red spheres), curve sliding (blue spheres) and surface sliding (green spheres) semi-landmarks placed on the ulna. From left to right: caudal, lateral, cranial and medial views. Numbers refer to anatomical landmarks designation detailed in Appendix 1 of Chapter 3.

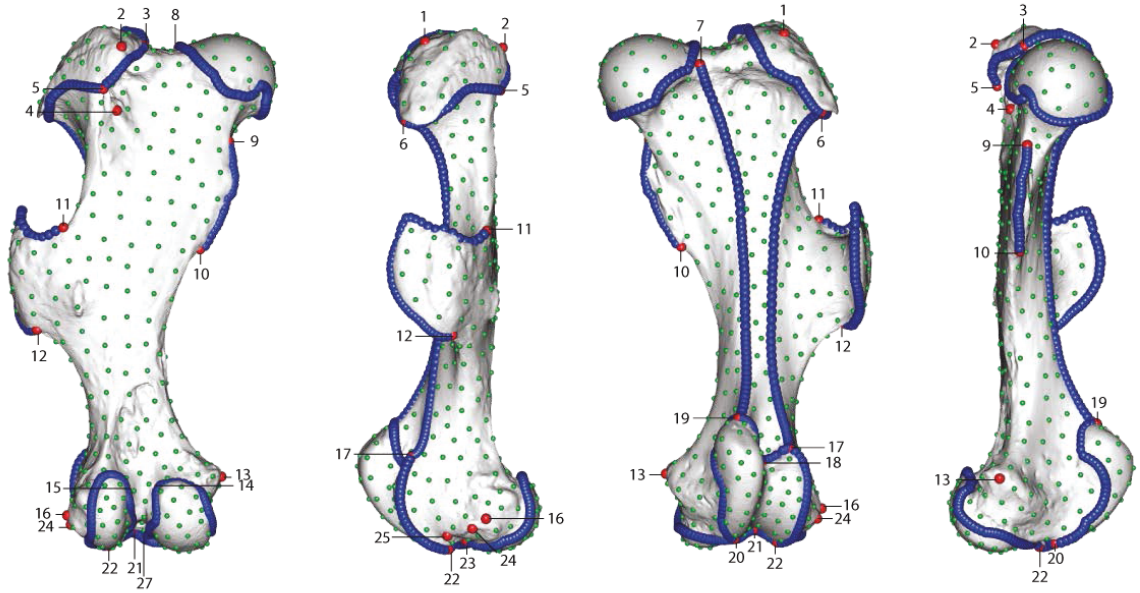

Figure S1E: Location of anatomical landmarks (red spheres), curve sliding (blue spheres) and surface sliding (green spheres) semi-landmarks placed on the femur. From left to right: caudal, lateral, cranial and medial views. Numbers refer to anatomical landmarks designation detailed in Appendix 1 of Chapter 3. Landmarks n°26 situated in the intercondylar space cannot be seen.

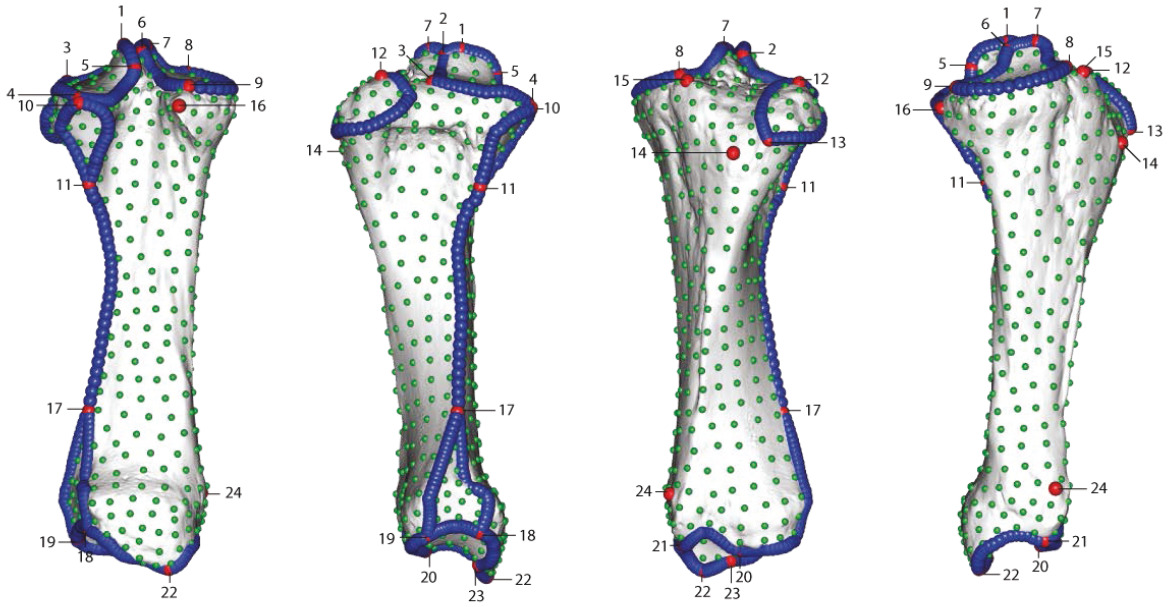

Figure S1F: Location of anatomical landmarks (red spheres), curve sliding (blue spheres) and surface sliding (green spheres) semi-landmarks placed on the tibia. From left to right: caudal, lateral, cranial and medial views. Numbers refer to anatomical landmarks designation detailed in Appendix 1 of Chapter 3.

Appendix 2: Plots of the second PLS axes computed on raw shapes

A: humerus-radius; B: humerus-ulna; C: humerus-femur; D: humerus-tibia; E: humerus-fibula; F: radius-ulna; G: radius-femur; H: radius-tibia; I: radius-fibula; J: ulna-femur; K: ulna-tibia; L: ulna-fibula; M: femur-tibia; N: femur-fibula; O: tibia-fibula. rPLS: value of the PLS coefficient; % EC: percentage of explained covariation; Corr. p-value: corrected p-value using a Benjamini-Hochberg correction.

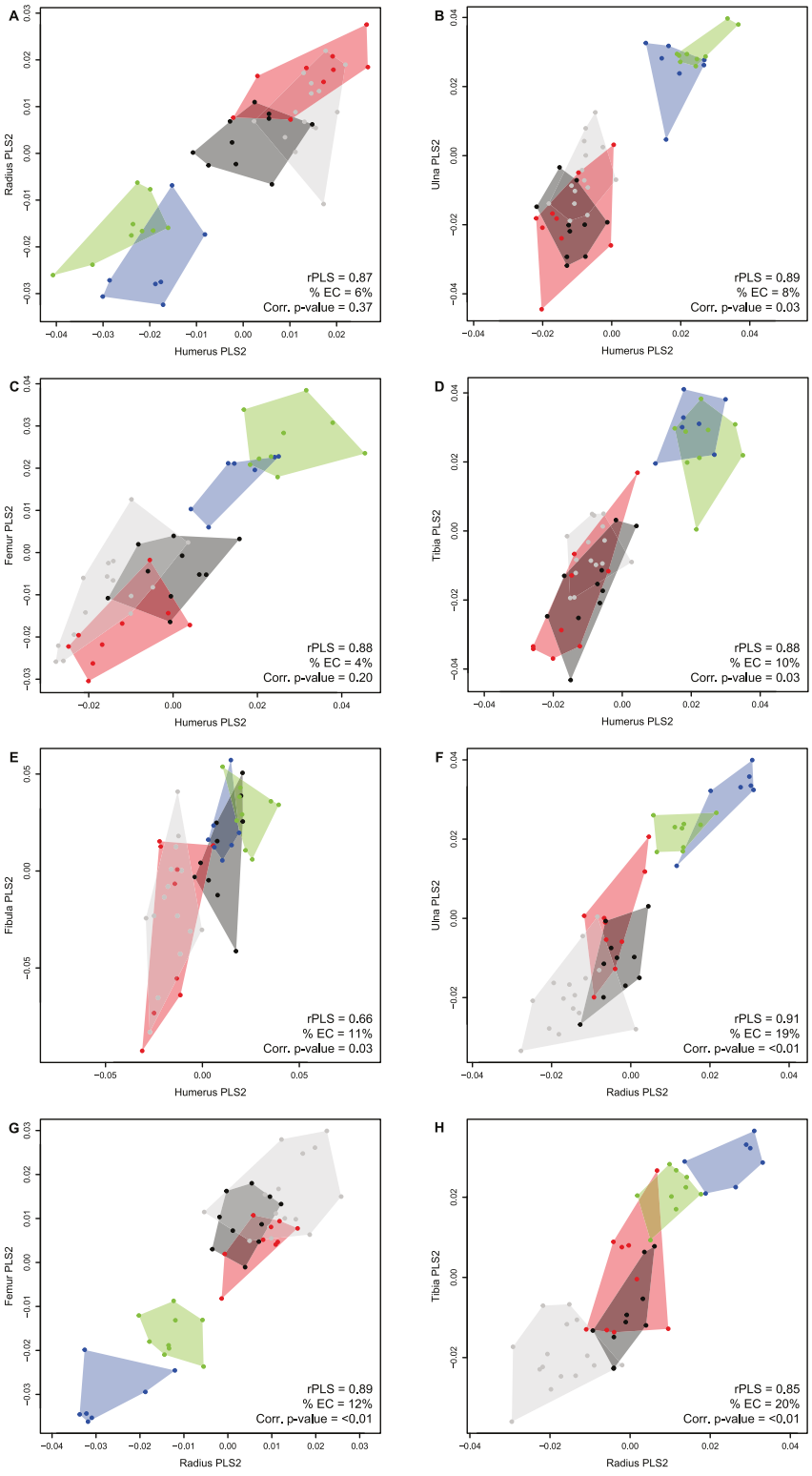

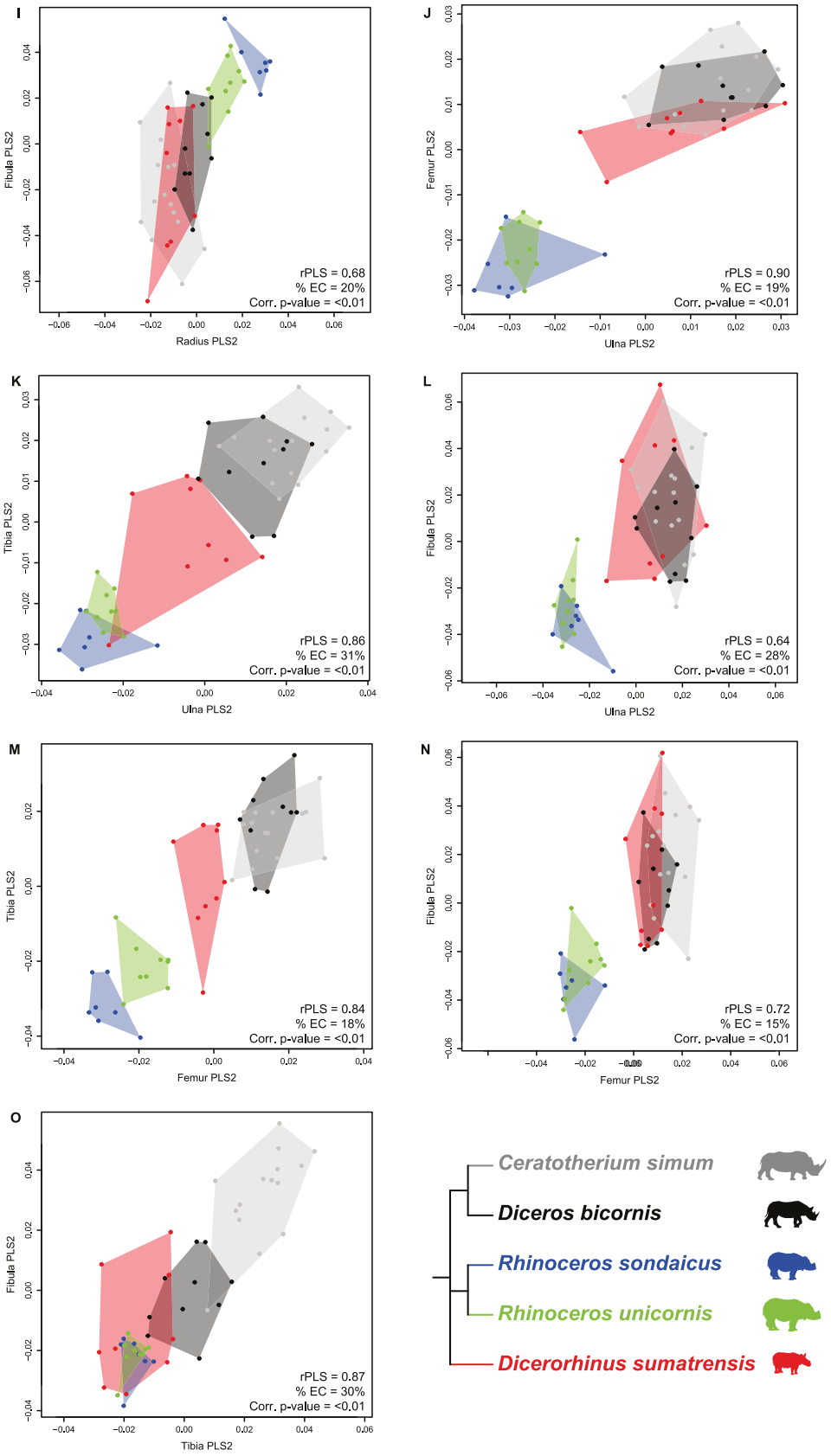
I
Fibula PLS2
Radius PLS2
rPLS = 0.68
% EC = 20%
Corr. p-value = <0.01
J
Femur PLS2
Ulna PLS2
rPLS = 0.90
% EC = 19%
Corr. p-value = <0.01
K
Tibia PLS2
Ulna PLS2
rPLS = 0.86
% EC = 31%
Corr. p-value = <0.01
L
Fibula PLS2
Ulna PLS2
rPLS = 0.64
% EC = 28%
Corr. p-value = <0.01
M
Tibia PLS2
Femur PLS2
rPLS = 0.84
% EC = 18%
Corr. p-value = <0.01
N
Fibula PLS2
Femur PLS2
rPLS = 0.72
% EC = 15%
Corr. p-value = <0.01
O
Fibula PLS2
Tibia PLS2
rPLS = 0.87
% EC = 30%
Corr. p-value = <0.01
Ceratotherium simum
Diceros bicornis
Rhinoceros sondaicus
Rhinoceros unicornis
Dicerorhinus sumatrensis

Appendix 3: Shape deformations associated with the first PLS axes for the fifteen bone pairs

Blue: negative side of the axis. Orange: positive side of the axis. The colour code of the squares expresses the type of relation between bones as described in the Figure 1 (black: intra-limb relation; orange: serial homology; blue: functional analogy; green: non-homologous or analogous bones). A: humerus-radius; B: humerus-ulna; C: radius-ulna; D: femur-tibia; E: femur-fibula; F: tibia-fibula; G: humerus-femur; H: radius-tibia; I: radius-fibula; J: ulna-tibia; K: ulna-fibula; L: humerus-tibia; M: humerus-fibula; N: radius-femur; O: ulna-femur.

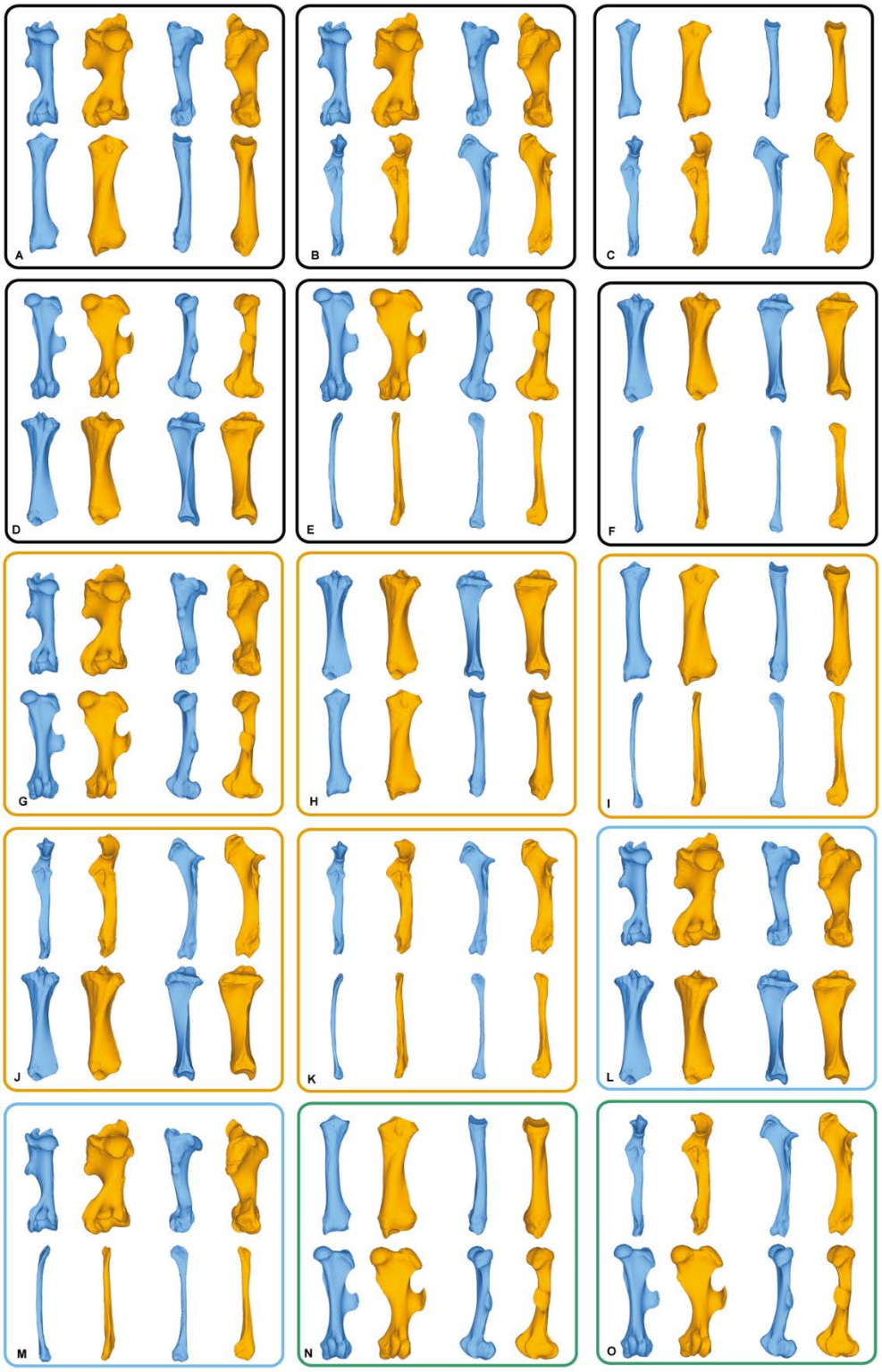

Appendix 4: Colour maps of the location and intensity of the shape deformation associated to the first PLS axes for 4 pairs of bones among the five species of rhinoceros

For each bone, the shape associated to the positive part of the first PLS axis was coloured depending on its distance to the shape associated to the negative part (blue indicates a low deformation intensity and red indicate a high deformation intensity). The colour code of the squares expresses the type of relation between bones as described in the Figure 1 (black: intra-limb relation; orange: serial homology; blue: functional analogy; green: non-homologous or analogous bones). A: humerus-radius; B: humerus-ulna; C: femur-fibula; D: radius-fibula; E: ulna-tibia; F: humerus-fibula; G: radius-femur (orientation from left to right in each case: cranial, lateral, caudal and medial).

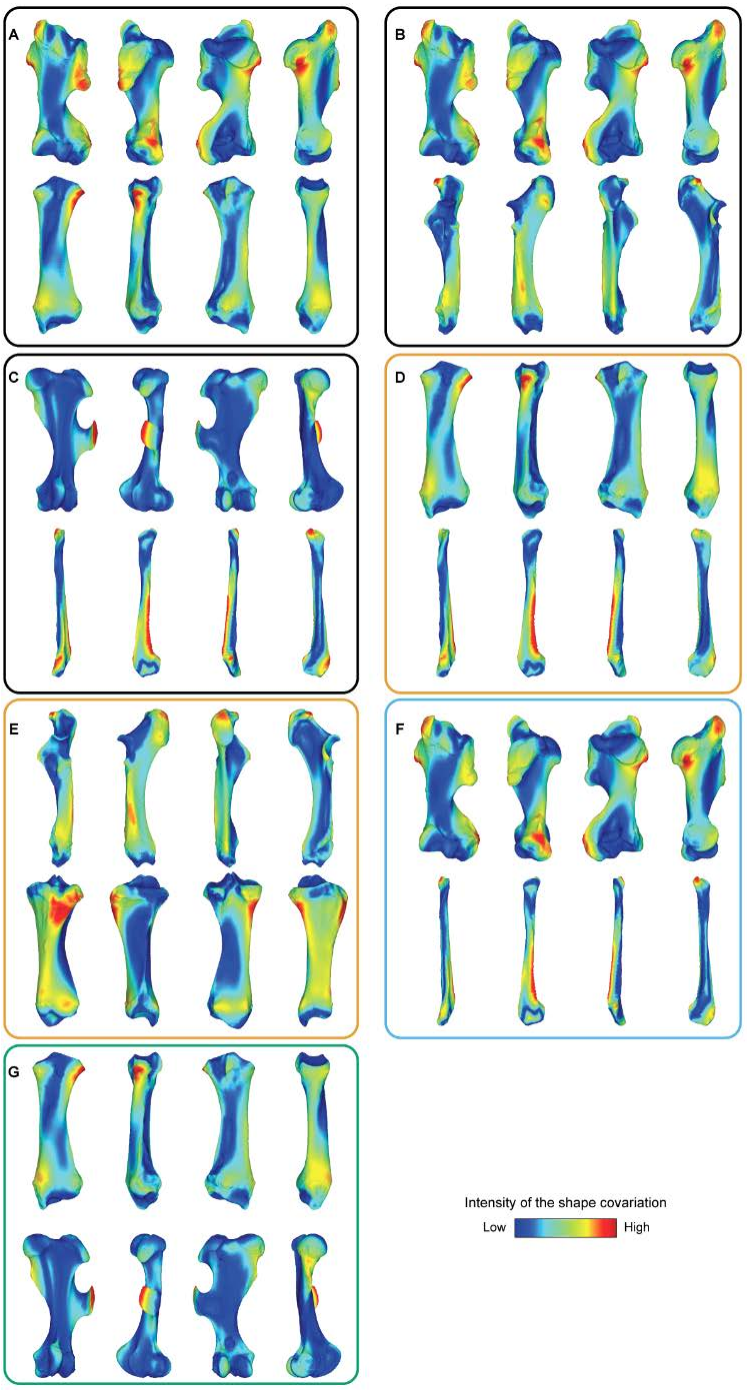

Appendix 5: Allometry-free shape deformations associated with the first PLS axes for the fifteen bone pairs

Blue: negative side of the axis. Orange: positive side of the axis. The colour code of the squares expresses the type of relation between bones as described in the Figure 1 (black: intra-limb relation; orange: serial homology; blue: functional analogy; green: non-homologous or analogous bones). A: humerus-radius; B: humerus-ulna; C: radius-ulna; D: femur-tibia; E: femur-fibula; F: tibia-fibula; G: humerus-femur; H: radius-tibia; I: radius-fibula; J: ulna-tibia; K: ulna-fibula; L: humerus-tibia; M: humerus-fibula; N: radius-femur; O: ulna-femur.

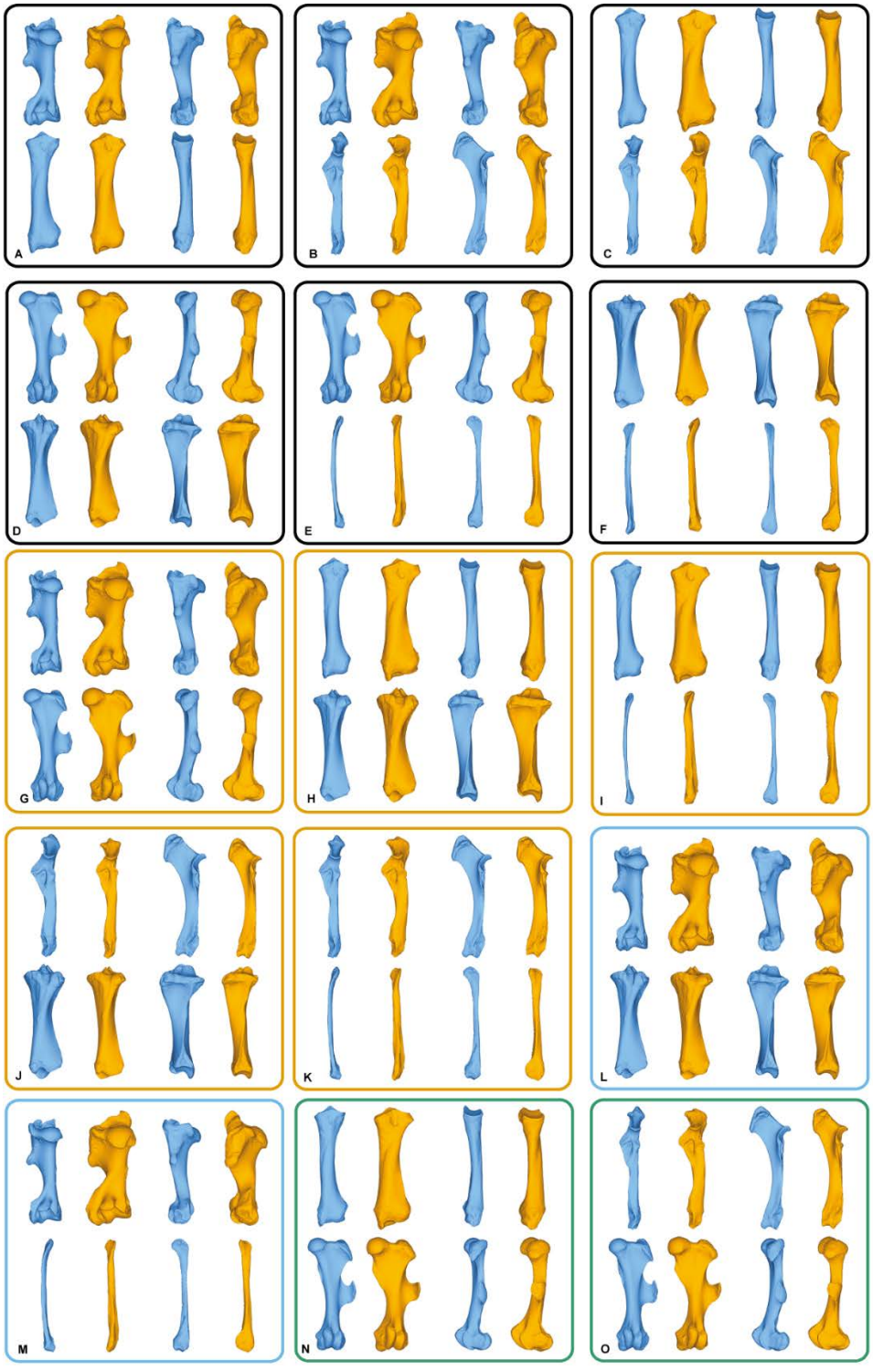

Appendix 6: Plots of the first PLS axes computed at the intraspecific level for all the pairs displaying a significant p-value before the Benjamini-Hochberg correction

Abbreviations: A: adult; SA: subadult; M: male; F: female; U: sex unknown.

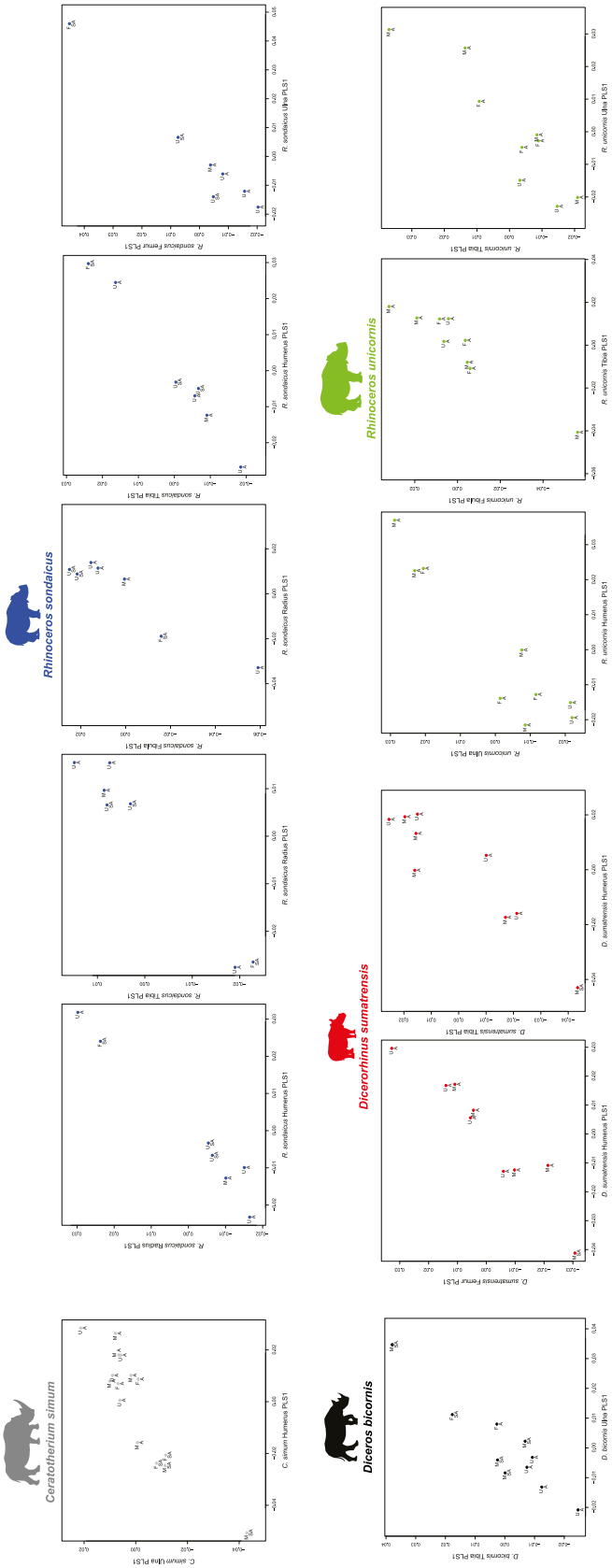

Appendix 7: Colour maps of the location and intensity of the shape deformation associated to the first PLS axes for all the pairs displaying a significant p-value before the Benjamini-Hochberg correction

For each bone, the shape associated to the positive part of the first PLS axis was coloured depending on its distance to the shape associated to the negative part (blue indicates a low deformation intensity and red indicate a high deformation intensity). The colour code of the squares expresses the type of relation between bones as described in the Figure 1 (black: intra-limb relation; orange: serial homology; blue: functional analogy; green: non-homologous or analogous bones).

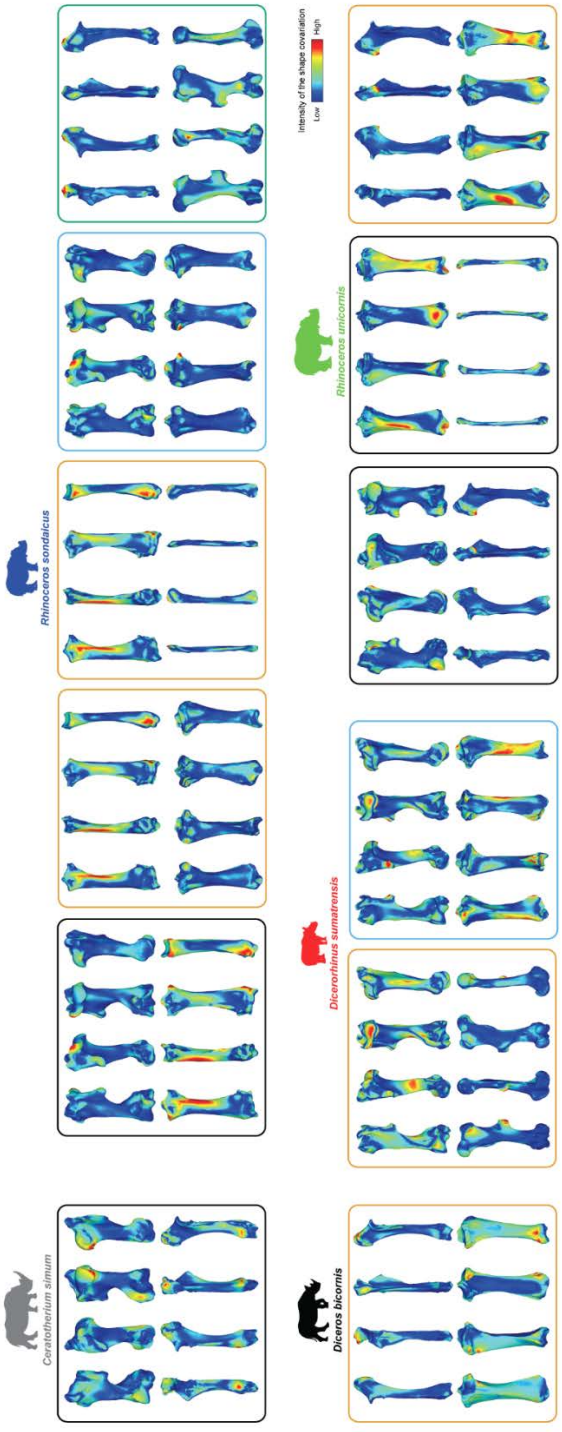

Chapter 5

Long bone shape variation in the fore-limb of Rhinocerotoidea – Relation with size, body mass and body proportions

Introduction

The two previous chapters explored the shape variation and covariation of the limb bones in the five modern species of rhinos and their relation with body mass and phylogeny. These investigations clearly highlight a link between mass and shape, with noticeable differences between fore and hind limbs, as well as between stylopodium and zeugopodium elements. However, these five species only represent a very small and homogenous sample of the past diversity of the superfamily. Moreover, it is likely that the occurrences of high body mass in modern rhinos are not independent as these species are closely related (the highest body mass in extant rhinos only represent two independent events in *C. simum* and *R. unicornis*). That is why I extended this investigation to other members of the superfamily, in order to take into account several independent occurrences of high body mass and a large diversity of body construction.

The Rhinocerotoidea was a flourishing superfamily during the Cenozoic. A rich and well-preserved fossil record led to the description of more than a hundred species distributed in Eurasia, North America and Africa, showing a huge diversity of ecological niches and locomotor conditions (Prothero & Schoch, 1989; Cerdeño, 1998; Prothero, 2005; Biasatti, Wang & Deng, 2018). Rhinocerotoidea ranged from less than 100 kg in *Hyrachyus*, the most ancient representative of the superfamily (Antoine, 2002; Bai et al., 2017), to more than 10 tons in giant Paraceratheriidae (Fortelius & Kappelman, 1993; Prothero, 1998a; Qiu & Wang, 2007; Prothero, 2013) (Table 11). Between these two extremes, numerous lineages showed convergent increases in body mass, with many species exceeding 1 ton or more (Cerdeño, 1998). In addition to this variation in body mass, the evolutionary history of rhinocerotoids exhibit fluctuations in their general body plan (from cursorial to graviportal), their degree of brachypody (or gracility, i.e. reduction of their relative limb length), their ecological affinities (from open environments to presumed semi-aquatic lifestyles), their number of forelimb digits (tetradactyl or tridactyl manus), the presence of horns and the size of their head, all of which may also have covaried with the shape of long bones (Guérin, 1989; Prothero & Schoch, 1989; Prothero, 1998a; Cerdeño, 1998; Antoine, 2002; Becker, 2003; Prothero, 2005; Becker et al., 2009; Prothero, 2013; Bai et al., 2017).

Consequently, members of the superfamily represent a rich diversity of body mass, size and proportions and constitute a great example for exploring how the evolution of long bone shape in the group could be associated with these parameters. A few studies previously investigated the shape variation of the limb bones in either modern or fossil rhinocerotoids, but rarely in regards to mass, size or degree of brachypody / gracility (Guérin, 1980; Prothero & Sereno, 1982; Becker, 2003; Mallet et al., 2019; Etienne et al., 2020; Mallet et al., 2020). To date, no comprehensive morphofunctional analysis has

explored covariation patterns between the shape of the long bones and each of these parameters at the scale of the entire superfamily.

In this chapter, I investigated the shape variation of the forelimb bones among the superfamily Rhinocerotoidea in relation with bone size, body mass and degree of gracility. I performed phylogenetically-informed shape analyses of the three forelimb bones (humerus, radius, ulna) in a 3D geometric morphometric context. I chose to focus on forelimb bones because they play a crucial role in supporting the body weight and in braking during locomotion in quadrupeds (Hildebrand, 1974; Dutto et al., 2006; Henderson, 2006). Moreover, the results obtained in Chapters 3 and 4 on modern rhinos indicate a greater association of both mass and size with the shape of the forelimb bones over that of the hind limb ones (Mallet et al., 2019, 2020). In accordance with literature, I hypothesize: (a) a strong association of bone size, body mass, and degree of gracility with bone shape; (b) different expression of this association on the stylopodium and zeugopodium respectively (Alexander et al., 1979; Prothero & Sereno, 1982; Biewener, 1989b; Bertram & Biewener, 1992; Mallet et al., 2019, 2020); (c) a marked influence of the evolutionary legacy on shape variation, with differences depending on the considered bone.

Taxon	Abbreviation	Mean body mass (kg)	Gracility Index (McIII)	Number of forelimb digits
Acerorhinus zernowi	Ar. z.	700	0.27	4
Alicornops simorrense	Al. s.	875	0.27	4
Amphicaenopus platycephalus	Ac. p.	NA	0.24	NA
Amynodon advenus	Ad. a.	589	0.20	4
Aphelops malacorhinus	Ap. ma.	889	0.23	4
Aphelops megalodus	Ap. me.	NA	0.30	4
Aphelops mutilus	Ap. mu.	1840	0.32	4
Brachypotherium brachypus	Br. b.	2327	0.30	3
Brachypotherium fatehjangense	Br. f.	1999	NA	3
Brachypotherium snowi	Br. s.	NA	0.37	3
Cadurcodon ardynensis	Ca. a.	837	0.17	4
Ceratotherium cf. primaevum	Ce. p.	NA	0.34	3
Ceratotherium mauritanicum	Ce. m.	NA	0.33	3
Ceratotherium neumayri	Ce. n.	1844	0.33	3
Ceratotherium simum	Ce. s.	2300	0.33	3
Chilotherium persiae	Ch. p.	700	0.31	4
Coelodonta antiquitatis	Co. a.	2402	0.30	3
Coelodonta nihowanensis	Co. n.	NA	0.24	3
Diaceratherium aginense	Dia. ag.	1987	0.30	4
Diaceratherium asphaltense	Dia. as.	NA	0.33	4
Diaceratherium aurelianense	Dia. au.	1551	0.36	4
Diaceratherium lamilloquense	Dia. la.	1410	0.29	4
Diaceratherium lemanense	Dia. le.	1590	0.28	4
Diceratherium annectens	Dm. an.	NA	0.21	3
Diceratherium armatum	Dm. ar.	NA	0.21	3
Diceratherium tridactylum	Dm. t.	517	0.25	3
Dicerorhinus aff. sansaniensis	Ds. sa.	1232	NA	3
Dicerorhinus sumatrensis	Ds. su.	775	0.28	3
Diceros bicornis	Dc. b.	1050	0.27	3
Dihoplus megarhinus	Dh. m.	NA	0.27	3
Dihoplus pikermiensis	Dh. p.	1100	0.33	3
Dihoplus schleiermacheri	Dh. s.	2123	0.25	3
Elasmotherium sibiricum	E. s.	4500	0.25	3
Hispanotherium beonense	Hi. b.	NA	0.25	3
Hoploaceratherium tetradactylum	Ho. t.	1197	0.26	4
Hyrachyus eximius	Hy. e.	66.6	0.16	4
Hyrachyus modestus	Hy. m.	NA	0.16	4
Hyracodon leidyanus	Hn. l.	NA	NA	3
Hyracodon nebraskensis	Hn. n.	NA	0.16	3
Juxia sharamurenense	J. s.	888	0.15	4
Lartetotherium sansaniense	L. s.	1204	0.24	3
Menoceras arikarense	Mc. a.	313	0.19	3
Metamynodon planifrons	Md. p.	1340	0.30	4
Paraceratherium bugtiense	Pa. b.	9900	0.26	3
Paraceratherium grangeri	Pa. g.	10950	0.25	3
Paramynodon birmanicus	Pd. b.	NA	0.22	4
Peraceras hessei	Pe. h.	NA	NA	4
Peraceras profectum	Pe. p.	NA	0.33	4
Peraceras superciliosum	Pe. s.	NA	0.32	4
Plesiaceratherium fahlbuschi	Pl. f.	NA	NA	4
Plesiaceratherium mirallesi	Pl. m.	1268	0.24	4
Plesiaceratherium platyodon	Pl. p.	NA	NA	4
Prosantorhinus douvillei	Ps. d.	NA	0.41	3
Protaceratherium minutum	Pt. m.	530	0.20	4
Rhinoceros philippinensis	R. p.	NA	0.27	3

Rhinoceros sondaicus	R. s.	1350	0.32	3
Rhinoceros unicornis	R. u.	2000	0.26	3
Stephanorhinus jeanvireti	St. j.	NA	0.25	3
Stephanorhinus etruscus	St. e.	NA	0.23	3
Stephanorhinus hemitoechus	St. he.	1561	0.28	3
Stephanorhinus hundsheimensis	St. hu.	1348	0.25	3
Subhyracodon mitis	Su. m.	NA	0.22	3
Subhyracodon occidentalis	Su. o.	NA	0.23	3
Teleoceras fossiger	Te. f.	1016	0.44	3
Teleoceras proterum	Te. p.	635	0.44	3
Trigonias osborni	Tg. o.	506	0.21	4
Trigonias wellsi	Tg. w.	NA	0.22	4
Triplopus cubitalis	Tp. c.	NA	0.11	3
Urtinotherium intermedium	U. i.	NA	0.21	3

Table 11 : List of the abbreviations, mean body masses and gracility indexes used in this study, with number of forelimb digits for each species. NA indicates unavailable data. Sources used to compile mean body mass and gracility index are given in Appendix 3.

Material and Methods

Studied sample

I selected 283 modern and fossil specimens housed in fifteen institutions and representing a total of 94 humeri, 105 radii and 84 ulnae (see Appendix 1 of this chapter for the complete list of studied specimens). The dataset included 69 taxa (5 modern and 64 fossil species) belonging to almost all families of the superfamily Rhinocerotoidea (no representative of the family Eggysodontidae were included) (Figure 27). Taxa were selected to include as much body shape and mass diversity as possible and to cover the largest temporal range but this selection also depended much on the available material. Taxonomic attributions were verified or updated using recent literature, directly with specimen numbers when available, or using taxonomic lists and institution databases for each locality. I retained the most recent binomial names considered as correct following the International Commission on Zoological Nomenclature rules (see Appendix 1 of this chapter).

I only considered adult individuals with fully fused epiphyses. I chose complete bones displaying no or negligible taphonomic effects (e.g. shallow surface cracks not altering the global shape), rejecting specimens massively crushed or restored with plaster. I also considered uncomplete bones in partial shape analyses (see below), as long as they were not crushed or distorted. Almost no information regarding sex was available for fossil specimens: even if sexual dimorphism is known for some species and may slightly affect the shape of long bones (Guérin, 1980; Dinerstein, 1991; Mead, 2000; Zschokke & Baur, 2002; Mihlbachler, 2007; Chen et al., 2010), I assumed that this intraspecific variation was largely exceeded by interspecific shape changes (according to Mallet et al., 2019). For each species, I selected between up to three specimens for each bone. All anatomical terms are as described in Chapter 3.

3D models

Scanning process was achieved as described in Chapter 2. As a few specimens displayed small lacking parts on the shaft, I used Geomagic Studio (v2014.3.0.1781—3D Systems Corporation, 2014) to fill holes. I used the “curvature filling” tool to ensure that the added polygons matched the curvature of the surrounding mesh.

3D geometric morphometrics

The geometric location of landmarks and semi-landmarks is derived from those used in Chapter 3 to cover the shape diversity of the sample (see Appendix 2 of this chapter for details on landmark numbers and locations). Two specimens (*Dicerorhinus sumatrensis* NHMUK ZE 1948.12.20.1 for the humerus and the ulna, and *Ceratotherium simum* RMCA 1985.32-M-0001 for the radius) were chosen to be the initial specimens on which all anatomical landmarks, curve and surface sliding semi-landmarks

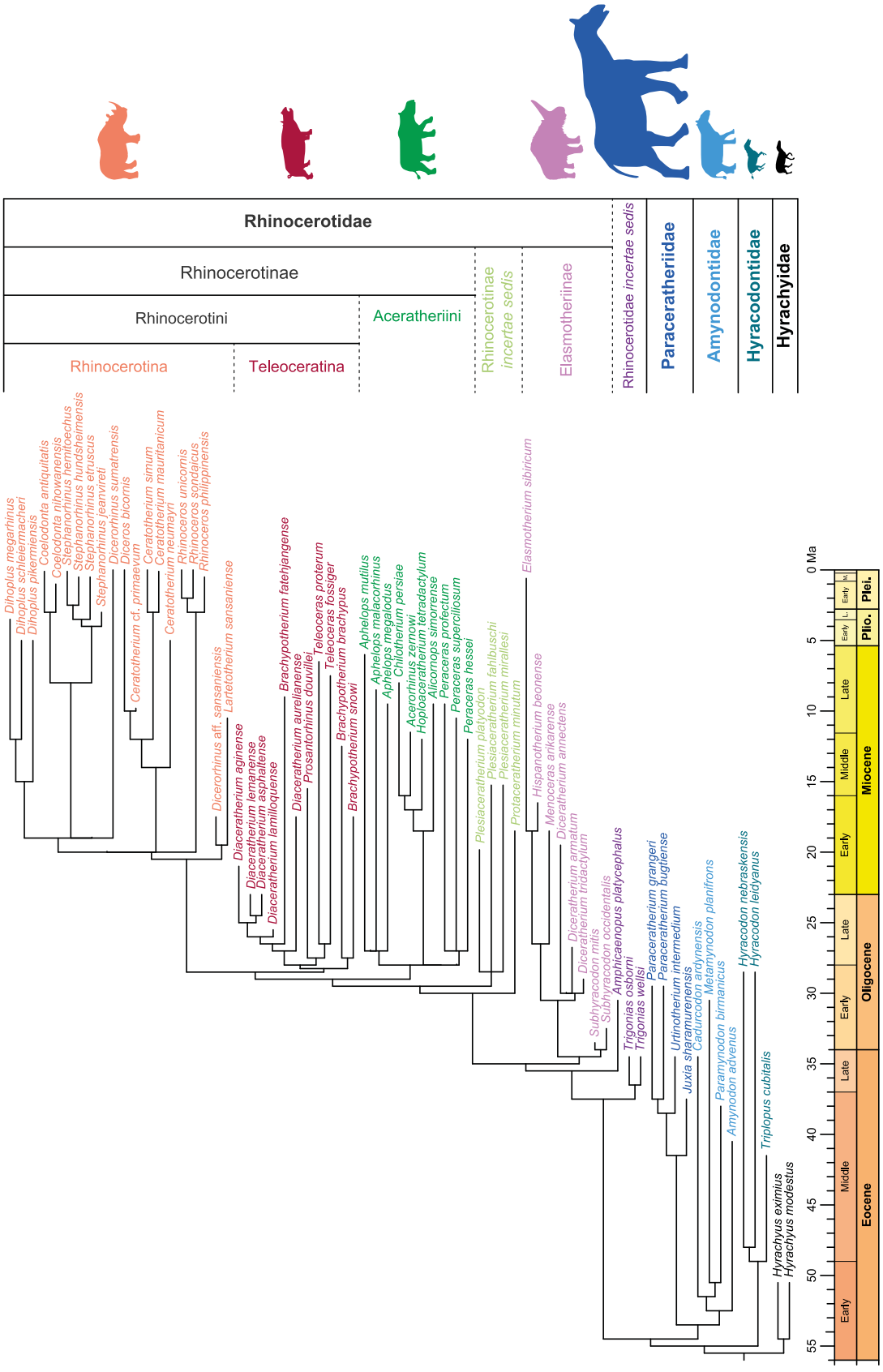

Figure 27: Composite cladogram of the studied species. Families, subfamilies, tribes and subtribes are defined by a colour code following the cladistic framework of Antoine *et al.* (2003) and Becker *et al.* (2013). All silhouettes representing a member of each group are at scale (provided by www.phylopic.org under Creative Commons license).

were placed. I selected these two individuals for their average shape and size ensuring that all points will be correctly projected on other bones despite the great shape and size ranges of the sample.

As I chose to work at the species level, I then computed and analysed species mean shapes (Botton-Divet et al., 2017; Serio, Raia & Meloro, 2020). After the sliding step, I computed a first Generalized Procrustes Analysis (GPA) with all specimens to remove the effect of size, location and orientation of the different landmark conformations (Gower, 1975; Rohlf & Slice, 1990). Then I computed the Procrustes consensus (or mean shape) of each species. A second GPA was then computed on species means. This process was repeated for each bone separately. As my dataset contained more variables than observations, I computed a Principal Component Analysis (PCA) to reduce dimensionality (Gunz & Mitteroecker, 2013) and visualize the distribution of the species in the morphospace. I also computed theoretical shapes associated with both minimum and maximum of the first two components of PCAs using a Thin-Plate Spline (TPS) deformation of a template mesh. Phylogenetic relationships between taxa (see below) were then plotted in the morphospace and compared to Neighbour Joining (NJ) trees computed on PC scores. Projection, relaxation, sliding processes, GPAs, PCAs and theoretical shape computation were conducted using the "Morpho" package (v2.8) in the R environment (v3.5.3—R Core Team, 2014). Details of the process are provided in the documentation of the package (Schlager, 2017). Phylogeny was plotted on the morphospace using the function "plotGMPhyloMorphoSpace" of the "geomorph" package (v3.2.1—Adams & Otárola-Castillo, 2013). NJ trees were computed with the "ape" package (v5.3—Paradis et al., 2018a).

Partial analyses

Fossil long bones of rhinoceros can show redundant breakage patterns due to various taphonomic agents throughout the diagenesis process (e.g. high sedimentary pressure on fragile anatomical areas, scavenger action on parts containing marrow – see Guérin, 1980). This is notably the case of the proximal part of the humerus or the olecranon process of the ulna, frequently damaged and preventing me to use some specimens in whole bone shape analyses. In order to include a higher number of relevant taxa in my sample despite these alterations, I performed partial analyses on bones presenting important lacking parts. I included complete bones as well in these partial analyses. Following Bardua et al. (2019), I used curve semi-landmarks to define artificial lines acting as a limit for the sliding of surface semi-landmarks and virtually remove damaged or lacking parts from analyses. These limit lines involved at least one anatomical landmark to ensure that they were geometrically homologous on all specimens. They were placed as well on complete bones, which were all included in partial analyses. Limit lines were finally removed after the sliding process to consider only true biological shape information in my analyses. Three partial datasets were used: distal half of the humerus, ulna without

olecranon tubercle and proximal half of the ulna (see Appendix 2 of this chapter for details on landmarks in partial templates).

Phylogenetic framework

To date, no comprehensive and consensual phylogeny of the whole superfamily Rhinocerotoidea exists. To assess the effect of phylogenetic relationships on shape variation, I constructed a composite cladogram using trees previously computed on cranio-dental and postcranial characters or molecular data. Branch relations, lengths and occurrence dates were reconstructed after the works of Cerdeño (1995), Antoine (2002), Antoine et al. (2003, 2010), Prothero (2005), Boada-Saña (2008), Piras et al. (2010), Becker et al. (2013), Lu (2013), Wang et al. (2016), Averianov et al. (2017), Tissier et al. (2018). I used the cladistic framework of Antoine et al. (2003) and Becker et al. (2013) to define families, subfamilies, tribes and subtribes (Figure 27). As described in Chapter 3, the relationships between the five modern taxa remain controversial, especially regarding the position of the Sumatran rhinoceros (*Dicerorhinus sumatrensis*) and its extinct relatives (e.g. Tougard et al., 2001; Orlando et al., 2003; Fernando et al., 2006; Price & Bininda-Emonds, 2009; Steiner & Ryder, 2011; Yuan et al., 2014; Welker et al., 2017; Cappellini et al., 2019). It is likely that these uncertainties may be due to a hard polytomy at the base of the crown-group containing the five modern species (Willerslev et al., 2009; Gaudry, 2017). I therefore chose to consider a hard polytomy in my analyses and to address phylogenetic uncertainties using an NNI procedure (see below).

To address the effect of phylogenetic relationships on shape data for each bone, I evaluated their phylogenetic signal by computing a multivariate K statistic (K_{mult}) on PC scores. This index allows the comparison between the rate of observed morphological change and that expected under a Brownian motion on a given phylogeny (Blomberg et al., 2003; Adams, 2014). As the K_{mult} computation requires fully bifurcating trees, I removed polytomies using the function “multi2di” in the “ape” package (Paradis et al., 2018). This function resolves polytomies by randomly creating a new branch with a null length from one branch of the polytomous node (Swenson, 2014; Paradis et al., 2018). K_{mult} was then computed using the function “K.mult” in the “phylocurve” package (Goolsby, 2015).

Body mass, centroid size and gracility index

I explored the association of three variables related to body proportions and size (body mass, centroid size of the bone and gracility index) with the shape of each long bone of the forelimb within Rhinocerotoidea. Mean body mass (BM) of each species was retrieved from the literature, compiling up to three estimations per species to compute mean BMs (see Table 11 and Appendix 3 of this chapter). However, BM estimations are highly heterogenous and can vary by a factor of three for a single species depending on the considered method and morphological proxy (dental, cranial or postcranial

measurements), the specimen developmental stage, and the geological formation. Moreover, regression equations for BM estimation were rarely developed for Perissodactyla or rhinoceroses only, resulting in potentially biased results for fossil Rhinocerotoidea (Prothero & Sereno, 1982). I managed to collect BM estimation for only 40 over the 69 taxa constituting my sample. Consequently, I chose to also consider the centroid size (CS) of each bone, which is classically used to address allometric variation, i.e. the shape variation linked to size (Zelditch et al., 2012; Mitteroecker et al., 2013; Klingenberg, 2016; Hallgrímsson et al., 2019). Centroid size, defined as the square root of the sum of the square of the distance of each point to the centroid of the landmark set (Zelditch et al., 2012), is known to be a good proxy of the mass of the animal (Ercoli & Prevosti, 2011; Cassini, Vizcaíno & Bargo, 2012), especially for limb bones of rhinoceros (Mallet et al., 2019; Etienne et al., 2020). Given the large range of body shapes within Rhinocerotoidea (Figure 27) and the fact that the same mass can be associated with both a slender or a robust body condition, I used the mean gracility index (GI-MC3) as an estimator of the degree of brachypody (see Table 11 and Appendix 3 of this chapter). This index is computed dividing the transverse width of the third metacarpal by its maximal length and has been much used for rhinocerotoids (Colbert, 1938; Arambourg, 1959; Guérin, 1980; Cerdeño, 1998; Becker, 2003; Becker et al., 2009; Scherler et al., 2013). The higher the GI-MC3 value, the shorter the limb length: species with a high GI-MC3 value are considered as more brachypodial (or less gracile) than species with low values. I computed this index by measuring third metacarpals when available in collections or compiling up to three GI-MC3 values in the literature to compute mean GI-MC3. These metacarpals were mostly associated with long bones for modern species, and mostly associated with a similar locality for fossil species (Appendix 3 of this chapter). I addressed the effect of phylogeny on log-transformed CS, log-transformed cubic root of the mean BM, and log-transformed mean GI-MC3 using the univariate K statistic (Blomberg et al., 2003). I tested for correlation between these three variables respectively using a linear regression on Phylogenetic Independent Contrasts (Felsenstein, 1985). I used the function “contMap” of the “phytools” package (Revell, 2012) to plot these three variables along the phylogeny.

Variation patterns, and thus covariation, can be expressed and analysed at different levels: across species (evolutionary variation), within a species at a single developmental stage (static variation), within a species across developmental stages (ontogenetic variation) (Klingenberg, 2014). Here I explored the evolutionary covariation of bone shape with each of the three variables (BM, CS, GI-MC3) considering a multivariate approach using Phylogenetic Generalized Least Squares (PGLS), a regression model taking into account the phylogenetic framework and computed here on Procrustes coordinates to quantify the shape variation related to CS, BM and GI-MC3 (Martins & Hansen, 1997; Rohlf, 2001; Klingenberg & Marugán-Lobón, 2013; Adams & Collyer, 2018). This was done using the function “procD.pgls”

of the "geomorph" package (v3.2.1—(Adams & Otárola-Castillo, 2013), suited for 3D geometric morphometric data. As the phylogeny of Rhinocerotoidea remains debated for both extant and extinct taxa (see above), I assessed the effect of potential uncertainty in taxa position in the phylogeny on PGLS by using a Nearest Neighbour Interchange (NNI) procedure. NNI algorithm generates new trees by swapping two adjacent branches of a specified tree (Felsenstein, 2004). I generated new trees using the "nni" function of the package "phangorn" (Schliep, 2011) and computed PGLS with these rearranged trees to estimate the ranges of R^2 and p values.

All statistic tests have been considered as significant for p-values ≤ 0.01. However, given that recent statistical works call for a continuous approach of the p-value (Wasserstein, Schirm & Lazar, 2019; Ho et al., 2019), I chose to mention results having a p-value up to 0.05 as well.

Results

Correlation between BM and GI-MC3

The evolutionary variation of mean BM and mean GI-MC3 both show a significant phylogenetic signal (K_{BM} = 1.75, p < 0.001; $K_{GI\text{-}MC3}$ = 1.70, p < 0.001) and are significantly correlated with one another when phylogeny is taken into account (r = 0.44, p < 0.001). The mapping of mean BM and GI-MC3 along the phylogeny (Figure 28) clearly indicates that, despite this significant correlation, there is not a strict correspondence between high BM and high GI-MC3 values. This is particularly visible for Paraceratheriidae, large Elasmotheriinae and Teleoceratina.

Humerus – complete bone

The species distributions in the NJ tree (Figure 29A) and in the phylomorphospace (Figure 30A) computed on the complete humeri are mostly congruent with phylogeny, which is not surprising since the phylogenetic signal carried by its shape variation is strong (K_{mult} = 1.16, p < 0.01). Along the NJ tree, small-sized and early-diverging Hyrachyidae and Hyracodontidae are followed by a cluster mixing Rhinocerotidae and Rhinocerotinae *incertae sedis* (*i. s.*) with *Paramynodon*, *Urtinotherium*, *Menoceras*, some Aceratheriini and even *Dicerorhinus sumatrensis*. Other Aceratheriini are grouped close to Teleoceratina and *Dihoplus megarhinus*, while almost all Rhinocerotina form a well-separated group (Figure 29A). The phylomorphospace of the first two axes of the PCA, representing 63.7% of the global variance, is structured in a similar way (Figure 30A). PC1 carries 54% of the variance. Along PC1, Hyrachyidae and Hyracodontidae plot towards negative values while *Paramynodon* is close to a central cluster grouping *Urtinotherium, Menoceras*, Aceratheriini, Teleoceratina, as well as Rhinocerotidae and Rhinocerotinae *i. s.* Within this cluster, *Aphelops* shares a shape proximity with all Teleoceratina, whereas other Aceratheriini are closer to more ancient taxa (*Amphicaenopus*, *Trigonias*, *Protaceratherium*, *Plesiaceratherium*, and *Menoceras*). All members of the subtribe Rhinocerotina group together towards positive values, with *Stephanorhinus, Dicerorhinus, Dihoplus* and *Rhinoceros* overlapping the *Aphelops*-Teleoceratina cluster. The highest PC1 values are associated with the modern African clade (*Ceratotherium-Diceros*) and their extinct relatives, and the *Coelodonta* clade. PC2 represents 9.7% of the global variance. It is mainly driven by an opposition between Hyrachyidae, Hyracodontidae and Rhinocerotina towards negative values and Amynodontidae, Paraceratheriidae and all other Rhinocerotidae towards positive values. *Urtinotherium* is strongly isolated from all other species towards maximal positive values.

The shape variation along PC1 is mainly related to the bone slenderness (Figure 29A and Appendix 4A). Towards the minimal values, the humerus is thin and straight, with a greater trochanter developed cranio-medially; an asymmetrical bicipital groove; a rounded humeral head oriented proximo-caudally;

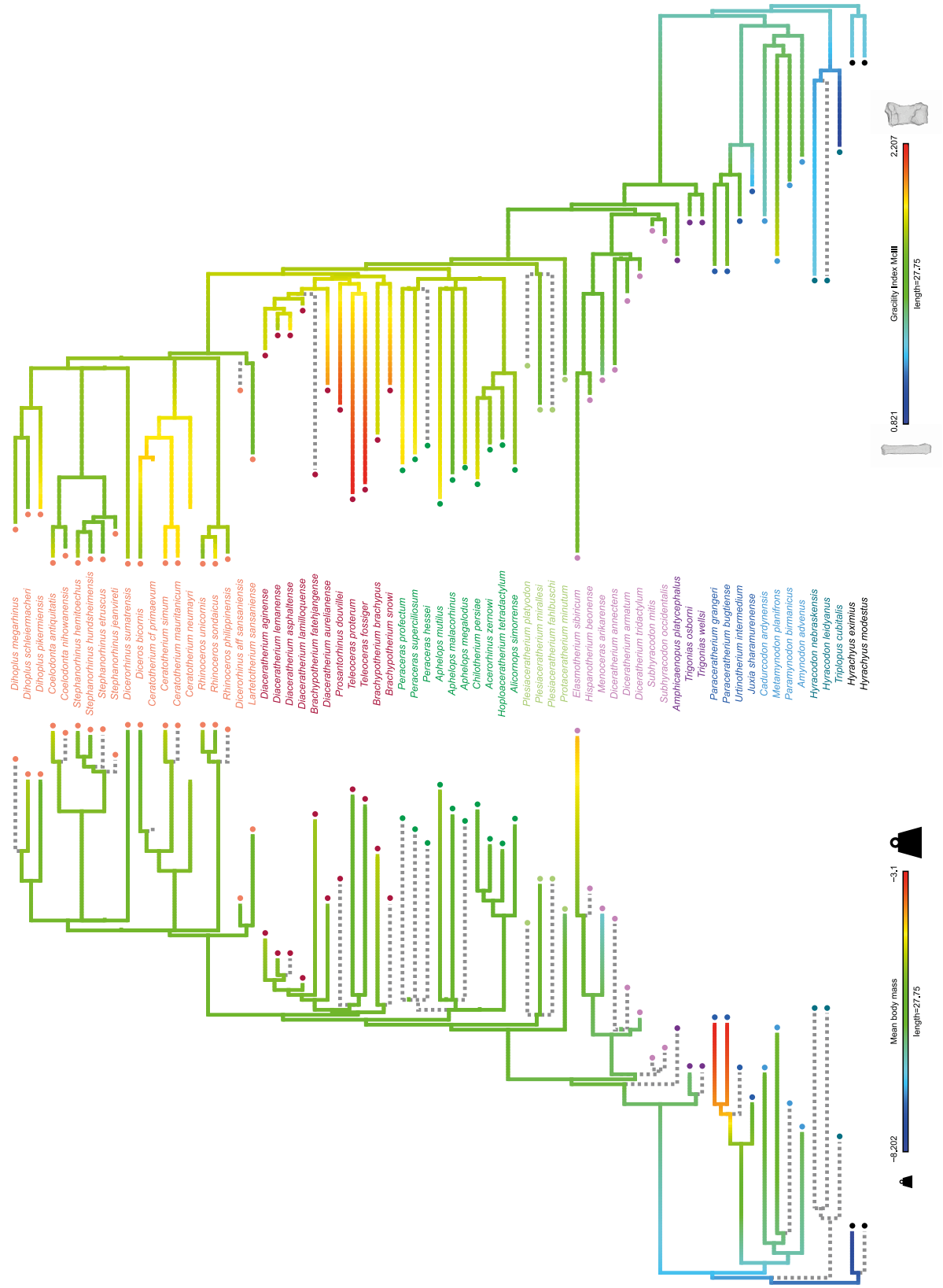

Figure 28: Evolution of BM and GI-MC3 along the phylogeny for the studied species. Left: mean BM; Right: mean GI-MC3. Computations were made on log-transformed cubic root of mean BM (BM) and log-transformed GI-MC3. Values at nodes and along branches were reconstructed based on a Brownian motion model of evolution (Revell, 2012). Colour code for taxa follows Figure 27. Dashed lines indicate missing data. Evolution of the third metacarpal shape depending on the GI-MC3 value is illustrated by specimens *Hyrachyus modestus* AMNH FM 17436 (minimum) and *Teleoceras fossiger* AMNH FM 2636 (maximum).

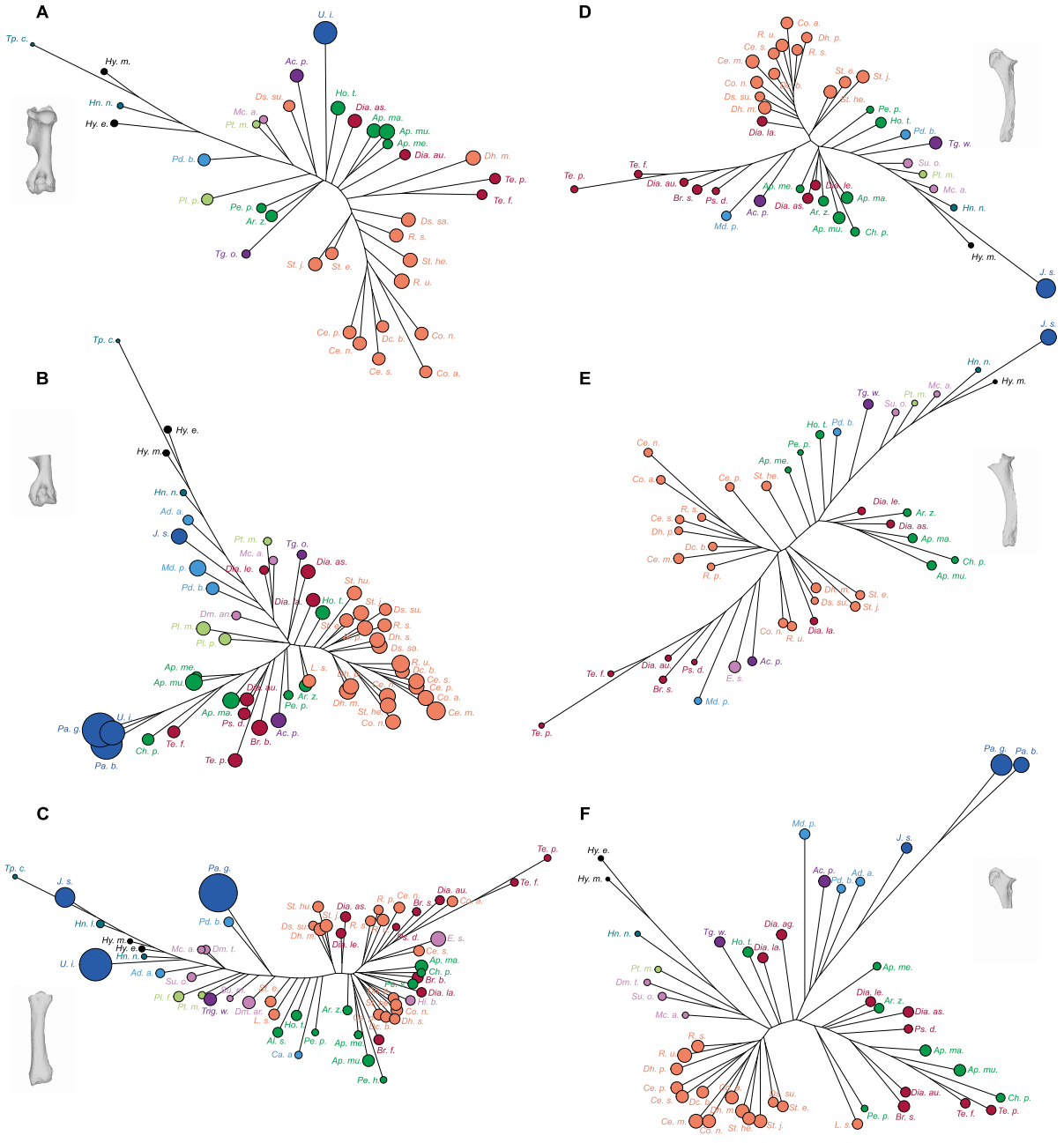

Figure 29: Neighbour Joining trees computed on all PC scores obtained from the PCAs performed on shape data. Colour code follows Figure 27 and abbreviations follow Table 11. Point size is proportional to the mean log centroid size of each species. A: complete humerus; B: distal partial humerus; C: radius; D: complete ulna; E: ulna without olecranon tuberosity; F: proximal partial ulna.

a poorly developed deltoid tuberosity; a poorly developed supracondylar crest; a narrow olecranon fossa; a symmetrical trochlea with a developed capitulum. The shape associated with maximal values is highly robust and thick, with a strong development of the lesser tubercle over the greater one; a large symmetrical bicipital groove with an intermediate tubercle; a deltoid tuberosity highly developed laterally; a strong development of the lateral epicondyle and the epicondylar crest; a large and rectangular olecranon fossa; an asymmetrical trochlea with a reduced capitulum. Along PC2, the shape

variation mainly concerns epiphyseal elements. Towards positive maximum, the humerus displays a greater tubercle developed cranially; a rounded head oriented proximally; a strong deltoid tuberosity situated at the middle of the shaft; a larger shaft diameter; a strong proximo-lateral development of the epicondylar crest; a trochlea flattened proximo-distally. The shape associated with minimal values exhibits a deltoid tuberosity situated above the midshaft; a poorly developed epicondylar crest with a lateral epicondyle directed latero-distally; and an asymmetrical trochlea medially developed.

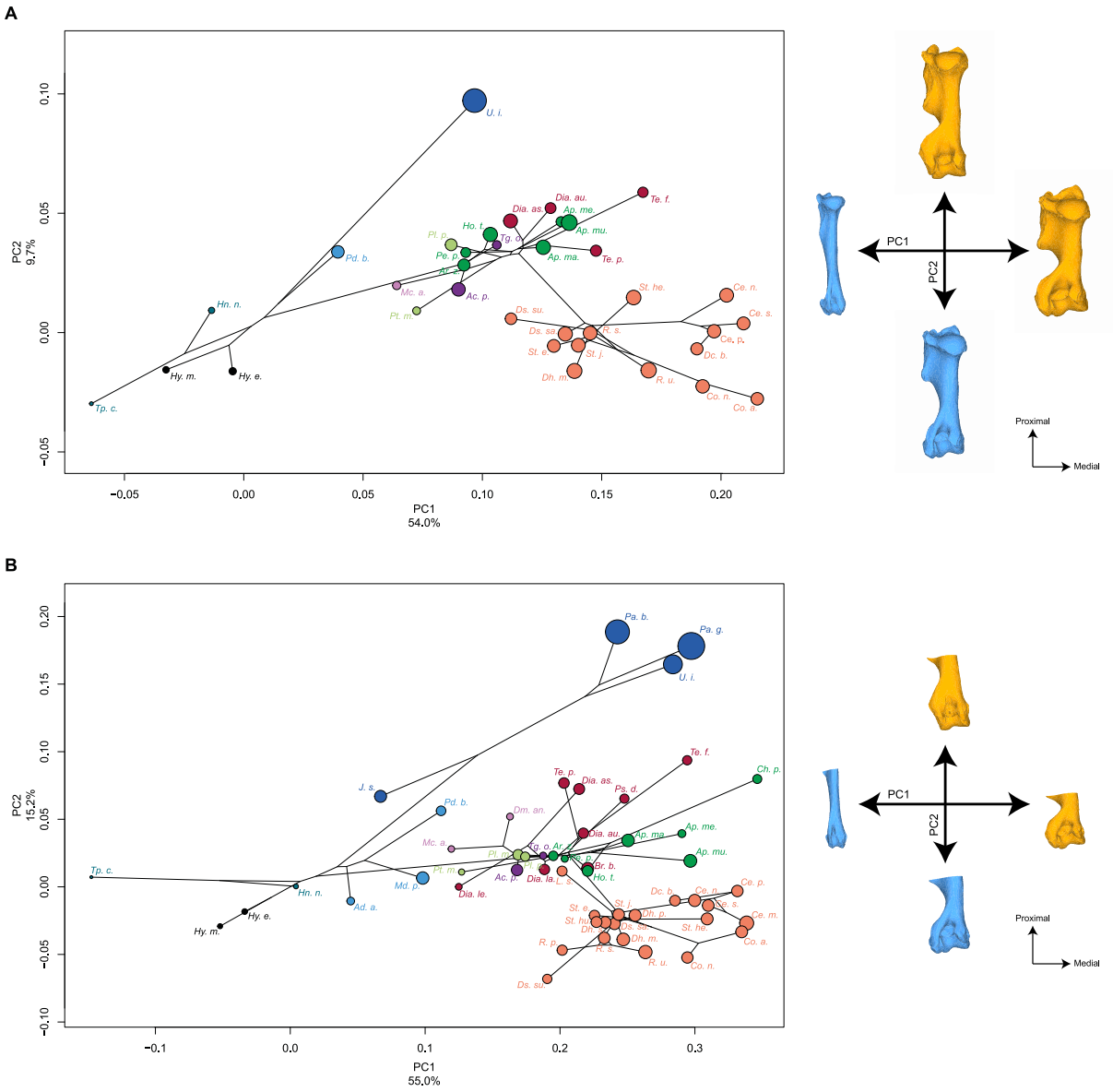

Figure 30: Results of the PCA performed on morphometric data of complete humerus (A) and distal partial humerus (B) and shape variation associated with the first two axes of the PCA (caudal view). Blue: negative side of the axis. Orange: positive side of the axis. Phylogenetic relationships are plotted in the morphospace. Colour code follows Figure 27 and abbreviations follow Table 11. Point size is proportional to the centroid size of each species.

The evolutionary variation of the centroid size of complete humeri bears a significant phylogenetic signal (K_{CS} = 1.28, $p < 0.001$) and is highly correlated with BM (r = 0.62) and marginally correlated with

GI-MC3 (r = 0.37, p = 0.03) (Table 12). PGLS results indicate that CS, BM and GI-MC3 are all significantly correlated with humerus shape (Table 13). NNI procedure indicates that the correlation with BM is more strongly affected by phylogenetic uncertainties than that with CS (Table 13). This may be related to a smaller and less diverse sample for BM values. Regression of shape against CS shows a very good fit to the regression line, most of the species following a marked common trend with little divergences far away from the line (Figure 31A). Most of the Rhinocerotina and Teleoceratina are situated below the regression line while the other species are situated above. *Urtinotherium* appears as slightly shifted from the general trend. In the absence of many taxa such as Hyracodontidae, Amynodontidae and Paraceratheriidae, regression of shape against BM shows a good fit to the regression line. The trend is strongly driven by *Hyrachyus*, which potentially constitutes a bias. However, a clear separation exists between Aceratheriini, all situated below the regression line, and Rhinocerotina and Teleoceratina, mainly situated above the line (Figure 31B). Results for GI-MC3 indicate a very good fit to the regression line as well. Rhinocerotina group almost all together above the line while Teleoceratina are situated below the line. All other species are mixed close to the common trend. Hyrachyidae and Hyracodontidae are isolated towards minimal values (Figure 31C). If shape variation related to these three variables mainly concerns an increase of robustness towards maximal values (Figure 31 and Appendix 5A, B, C), that related to BM (that lacks heavy Paraceratheriidae) is slightly different from those related to CS and GI-MC3, with a stronger medio-lateral development of both epiphyses relatively to the shaft (Figure 31B). Most of the shape variation occurs on the medial face of the bone and on strong muscular insertions like the deltoid tuberosity and the epicondylar crest for the three variables. In addition, BM variation affects the bicipital groove while variation of GI-MC3 implies shape changes located distally and caudally to the humeral head, from the deltoid tuberosity and tricipital line to the lesser tubercle convexity (Figure 31C).

Bone	Variables	r	t	dF	p
Humerus (complete)	**CS ~ BM**	**0.62**	**3.15**	**16**	**<0.01**
	CS ~ GI-MC3	0.37	2.16	30	0.03
Humerus (distal partial)	**CS ~ BM**	**0.73**	**5.77**	**30**	**<0.01**
	CS ~ GI-MC3	**0.50**	**3.91**	**47**	**<0.01**
Radius	**CS ~ BM**	**0.80**	**7.35**	**31**	**<0.01**
	CS ~ GI-MC3	0.06	0.41	51	0.68
Ulna (complete)	CS ~ BM	0.42	2.06	19	0.05
	CS ~ GI-MC3	-0.12	-0.73	35	0.47
Ulna (without ol. tub.)	**CS ~ BM**	**0.50**	**2.63**	**21**	**0.01**
	CS ~ GI-MC3	-0.13	-0.82	39	0.41
Ulna (proximal partial)	**CS ~ BM**	**0.85**	**8.40**	**26**	**<0.01**
	CS ~ GI-MC3	0.28	1.92	43	0.06

Table 12: Results of the Pearson's correlation tests between centroid size (CS), and mean body mass (BM) and mean gracility index (GI-MC3) respectively for each bone (computed on Phylogenetic Independent Contrasts). r: Pearson's correlation coefficient value; t: student distribution value; dF: degrees of freedom; p: p-value. Significant results (for p < 0.01) are indicated in bold.

Bone	Variable	N	R^2			p-value		
			Min.	Max.	Mean	Min.	Max.	Mean
Humerus (complete)	**CS**	**66**	**0.09**	**0.12**	**0.11**	**0.001**	**0.006**	**0.002**
	BM	**34**	**0.19**	**0.40**	**0.22**	**0.001**	**0.002**	**0.001**
	GI-MC3	**62**	**0.10**	**0.17**	**0.12**	**0.001**	**0.002**	**0.001**
Humerus (distal partial)	**CS**	**102**	**0.20**	**0.28**	**0.22**	**0.001**	**0.001**	**0.001**
	BM	**62**	**0.17**	**0.25**	**0.18**	**0.001**	**0.003**	**0.001**
	GI-MC3	**96**	**0.14**	**0.24**	**0.21**	**0.001**	**0.001**	**0.001**
Radius	CS	114	0.02	0.03	0.02	0.083	0.306	0.226
	BM	64	0.03	0.16	0.09	0.004	0.341	0.040
	GI-MC3	**104**	**0.17**	**0.22**	**0.20**	**0.001**	**0.002**	**0.001**
Ulna (complete)	CS	72	0.02	0.04	0.03	0.203	0.615	0.382
	BM	40	0.05	0.08	0.07	0.128	0.329	0.214
	GI-MC3	**72**	**0.20**	**0.26**	**0.23**	**0.001**	**0.001**	**0.001**
Ulna (without ol. tub.)	CS	80	0.02	0.03	0.02	0.268	0.741	0.661
	BM	44	0.08	0.11	0.10	0.034	0.100	0.062
	GI-MC3	**80**	**0.18**	**0.22**	**0.20**	**0.001**	**0.001**	**0.001**
Ulna (proximal partial)	**CS**	**88**	**0.06**	**0.13**	**0.08**	**0.001**	**0.008**	**0.002**
	BM	**54**	**0.13**	**0.24**	**0.16**	**0.001**	**0.005**	**0.002**
	GI-MC3	**88**	**0.06**	**0.09**	**0.08**	**0.001**	**0.007**	**0.002**

Table 13: Range of R^2 and p-values for PGLS computed with NNI permuted trees on shape data and log-transformed centroid size (CS), log-transformed cubic root of mean body mass (BM) and log-transformed mean gracility index (GI-MC3). N: number of trees obtained after NNI procedure; R^2: determination coefficient value. Significant results (for $p < 0.01$) are indicated in bold.

Humerus – distal part

The phylogenetic signal carried by the shape variation of the distal humeri is strong ($K_{mult} = 1.22$, $p < 0.01$). The species distributions in the NJ tree (Figure 29B) and in the phylomorphospace are highly similar to those observed for the complete humeri (Figure 30B). On the NJ tree, all Amynodontidae are grouped together with *Juxia* (small Paraceratheriidae) while giant Paraceratheriidae group together close to some Aceratheriini (*Aphelops*, *Chilotherium*). Other Aceratheriini are mixed with Teleoceratina and more basal taxa, while Rhinocerotina form a homogeneous cluster all together. A similar organisation is observable in the phylomorphospace, where the first two axes represent 70.2% of the global variance. PC1 carries 55% of the global variance and PC2 carries 15.2%. The species distribution along both axes is largely similar to that observed for the complete humerus (Figure 30B). Small and large Amynodontidae group together with the light Paraceratheriidae *Juxia*, while heavier Paraceratheriidae form an isolated cluster along PC2. Within Rhinocerotina, species seem distributed from the smallest to the largest along PC1 despite some exceptions (e.g. *Dihoplus megarhinus*, *Rhinoceros unicornis*). *Chilotherium* shows the highest positive value on PC1.

The shape variation along PC1 is highly similar to that observed on complete bones (Figure 30B and Appendix 4B). Towards positive maximal values, PC1 is mainly associated with an increase of thickness, with a strong development of the epicondylar crest; a broad olecranon fossa; an asymmetrical trochlea

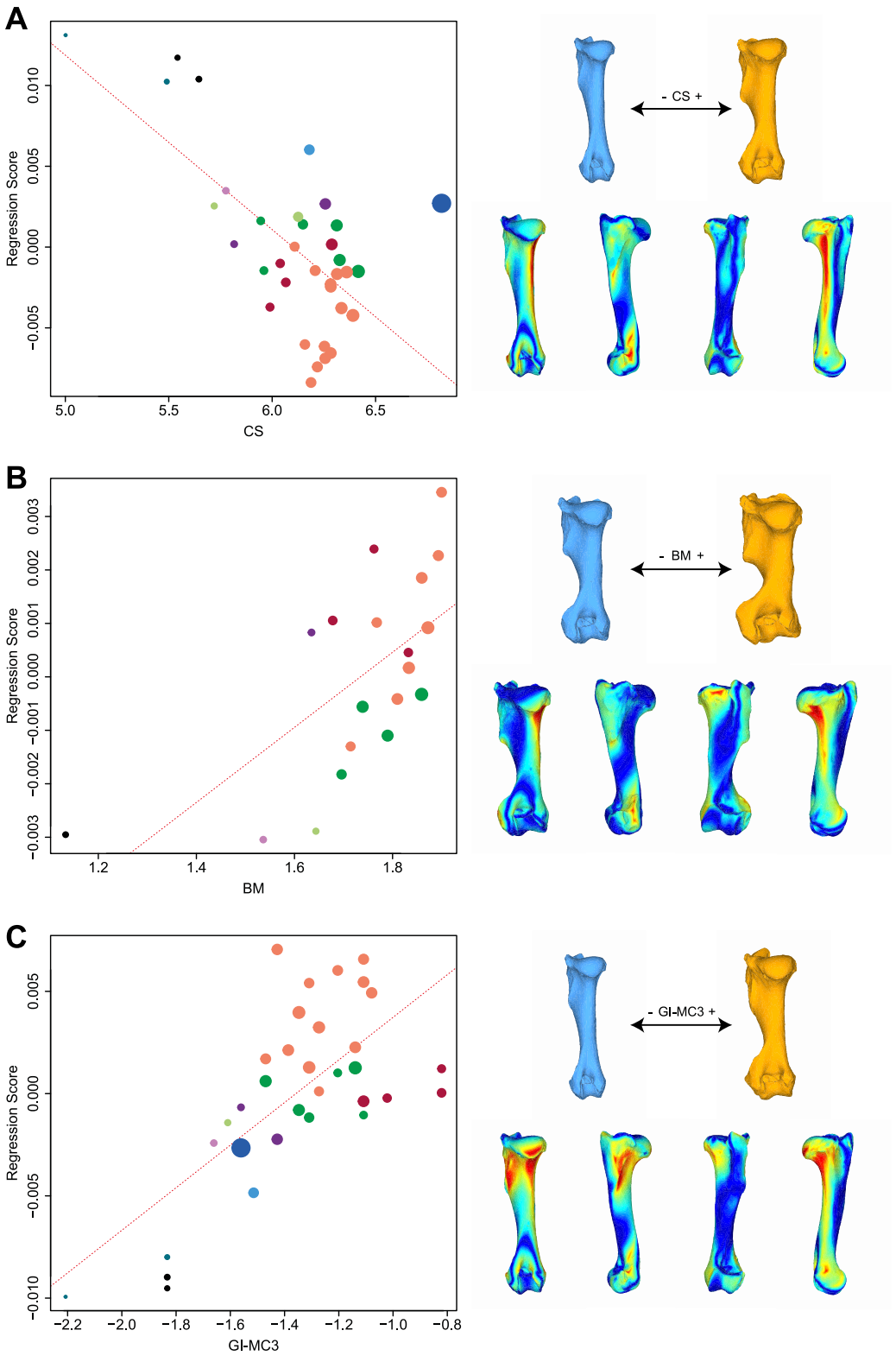

Figure 31: Significant PGLS regression plots for complete humerus performed on shape data and log-transformed centroid size (CS) (A), log-transformed cubic root of mean body mass (BM) (B), log-transformed mean gracility index (GI-MC3) (C). Points colour code follows Figure 27. Point size is proportional to mean log CS of each species. On the right, shapes associated with minimum and maximum fitted values (top row) and colour maps of the location and intensity of the shape deformation (bottom row). Blue: minimum value of the regression. Orange: maximum value of the regression. For each bone, the shape associated with the minimum was coloured depending on its distance to the shape associated with the maximum (blue indicates a low deformation intensity and red indicates a high deformation intensity). Orientation from left to right in each case: caudal, lateral, cranial and medial.

with a reduced capitulum. Along PC2, the shape variation is also almost identical to that observed on complete bones.

The evolutionary variation of the centroid size of partial humeri carries a significant phylogenetic signal (K_{CS} = 1.39, p < 0.001). The correlation between CS and BM is higher than for the complete humeri (r = 0.73) and correlation between CS and GI-MC3 is significant (r = 0.50) (Table 12). Like for complete bones, PGLS results indicate a significant correlation between humerus shape and CS, BM and GI-MC3, respectively. NNI procedure indicates that phylogenetic uncertainties do not highly affect the relation between shape and the three variables (Table 13). The regression plot of shape against CS indicates an excellent fit to the regression line with a tendency similar to that observed on complete bones, but with Hyrachyidae, Hyracodontidae, Amynodontidae and Paraceratheriidae slightly shifted towards less robust shapes for a given CS than Rhinocerotidae (Figure 32A). The presence of Amynodontidae and Paraceratheriidae in the regression of shape against BM highlights a strongly similar tendency and a very strong fit to the regression line (Figure 32B). The regression plot of shape against GI-MC3 is almost identical to that obtained on complete bones with a good fit to the regression line as well (Figure 32C). Similarly, the shape variation is very similar to that of complete bones for the three variables, mainly affecting the general robustness and muscular insertions such as the epicondylar crest that is broadened (Figure 32 and Appendix 5D, E, F). Only the shape variation associated with BM slightly differs with an epicondylar crest less developed than for complete bones towards maximum values.

Radius

Like for the humerus, the phylogenetic signal carried by shape data of the radii is strong (K_{mult} = 1.15, p < 0.01). However, the species distributions in the NJ tree (Figure 29C) and in the phylomorphospace (Figure 33) are less reminiscent of the phylogeny and seem likely related to the degree of brachypody. Along the NJ tree, Hyrachyidae group with Hyracodontidae, Paraceratheriidae and small Elasmotheriinae. Aceratheriini, Teleoceratina and Rhinocerotina are mixed together with larger Elasmotheriinae, most of the species being sorted by their gracility rather than mass or size. This pattern is highly similar to that seen on the PCA, with the first two axes representing 75% of the global variance (Figure 33). PC1 gathers 70.7% of the global variance. Along this axis, *Triplopus* constitutes the positive maximum. Contrary to the morphospace obtained for the humerus, two of the biggest species of the sample, *Juxia* and *Urtinotherium,* plot together with the smallest and lightest species. *Paraceratherium* groups with small Elasmotheriinae and Rhinocerotidae *i. s.*, as well as *Amynodon* and *Paramynodon*. Towards negative values, Aceratheriini, Teleoceratina and Rhinocerotina are grouped together with larger Elasmotheriinae (*Hispanotherium* and *Elasmotherium*). Within this cluster, *Stephanorhinus, Dicerorhinus* and some *Dihoplus* plot with *Aphelops, Peraceras* and *Hoploaceratherium*, whereas larger

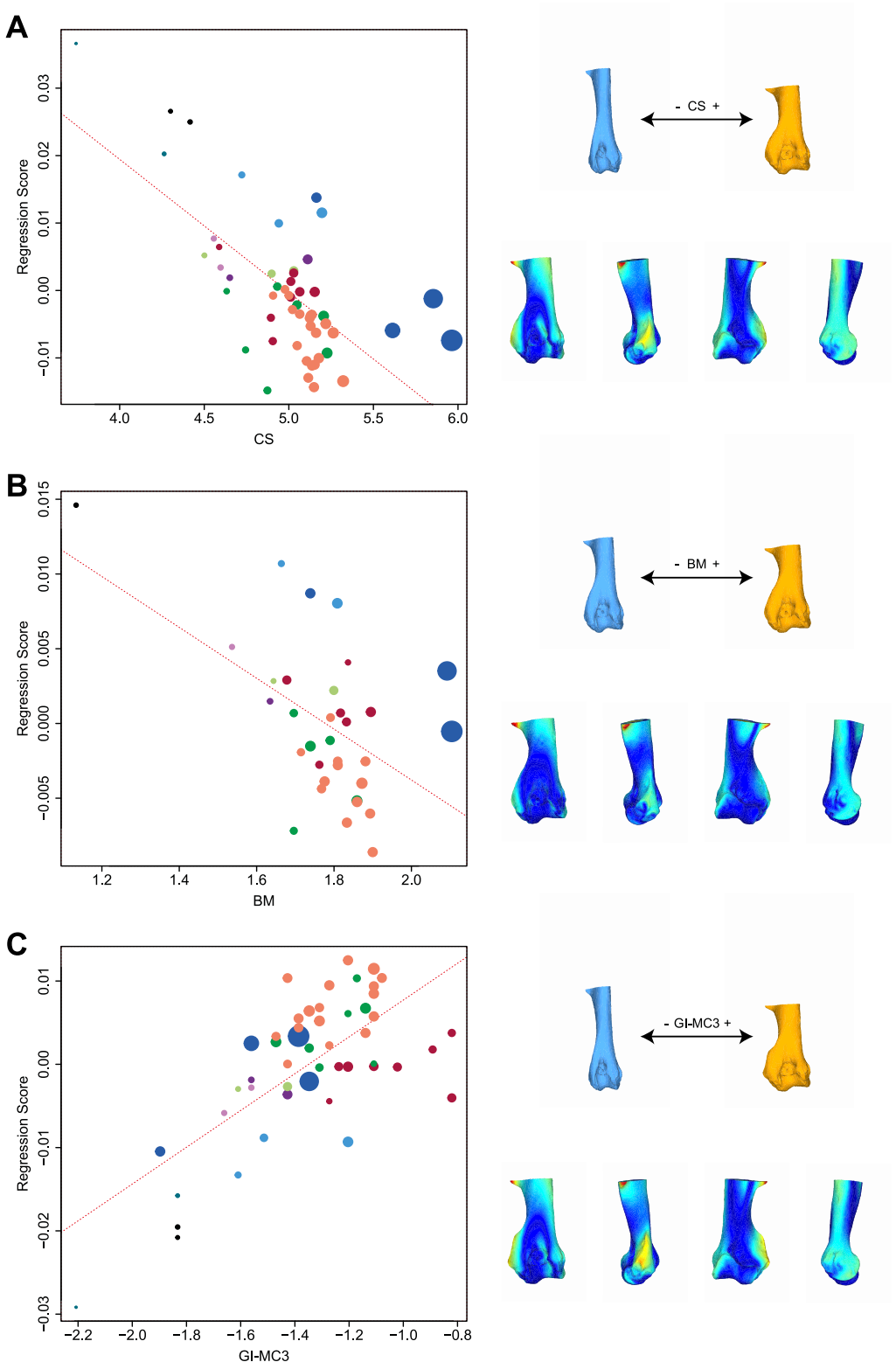

Figure 32: Significant PGLS regression plots for distal partial humerus performed on shape data and log-transformed centroid size (CS) (A), log-transformed cubic root of mean body mass (BM) (B), log-transformed mean gracility index (GI-MC3) (C). Points colour code follows Figure 27. Point size is proportional to mean log CS of each species. On the right, shapes associated with minimum and maximum fitted values (top row) and colour maps of the location and intensity of the shape deformation (bottom row). Blue: minimum value of the regression. Orange: maximum value of the regression. For each bone, the shape associated with the maximum was coloured depending on its distance to the shape associated with the minimum (blue indicates a low deformation intensity and red indicates a high deformation intensity). Orientation from left to right in each case: caudal, lateral, cranial and medial.

Rhinocerotina (*Ceratotherium, Rhinoceros, Diceros, Coelodonta*) are closer to *Brachypotherium* and *Diaceratherium*. Only *Teleoceras* and *Coelodonta antiquitatis* plot outside the main cluster towards the maximal negative values. PC2 represents only 4.3% of the variance and no obvious organisation of the specimens is visible along this axis.

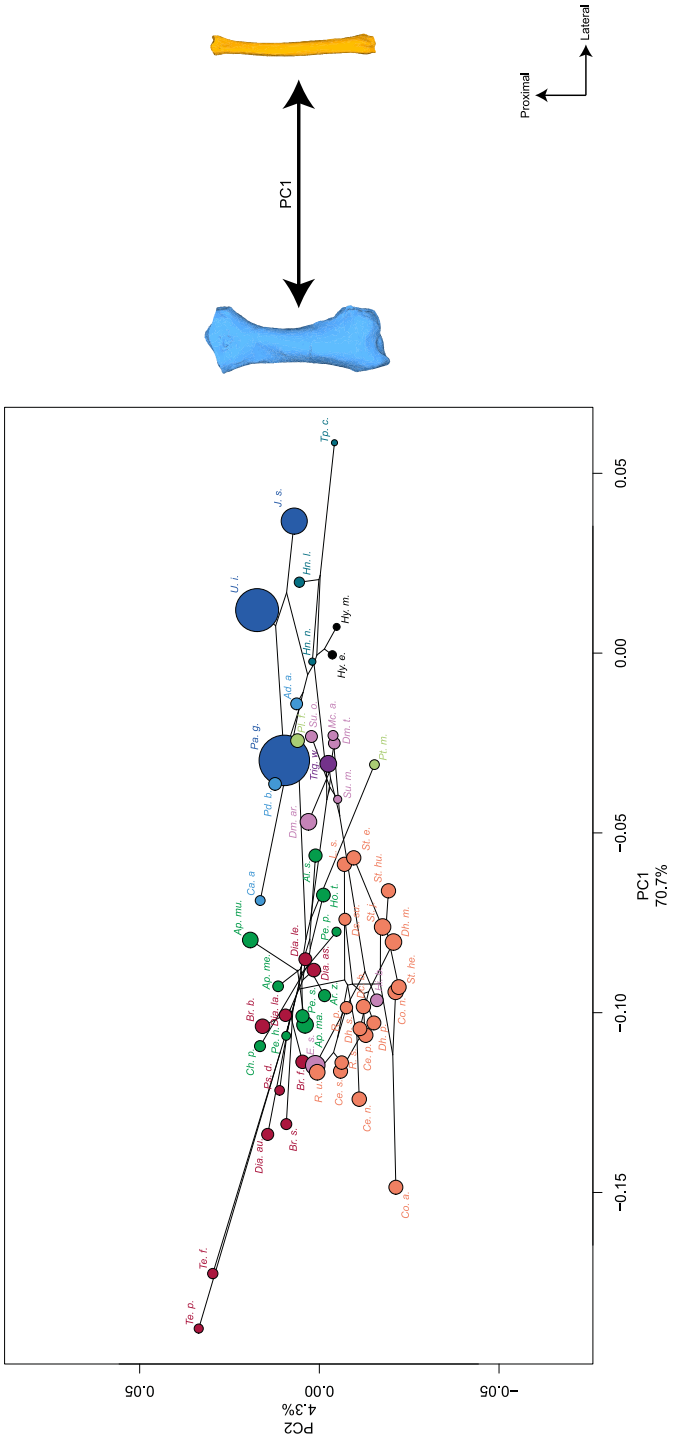

Figure 33: Results of the PCA performed on morphometric data of the radius and shape variation associated with the first axis of the PCA (cranial view). Blue: negative side of the axis. Orange: positive side of the axis. Phylogenetic relationships are plotted in the morphospace. Colour code follows Figure 27 and abbreviations follow Table 11. Point size is proportional to the mean log centroid size of each species.

Like for the humerus, the shape variation of the radius along PC1 is mainly related to the bone slenderness (Figure 33 and Appendix 4C). The shape associated with maximal values is thin and slender, with slight cranio-caudal and medio-lateral bends; a rectangular glenoid cavity with a lateral expansion for the capitulum; a shaft as large medio-laterally as the two epiphyses; a rectangular and shallow distal articular surface; a poorly developed radial styloid process. Conversely, the shape associated with the minimal values is massive with a large asymmetrical glenoid cavity; almost no lateral development of the cavity for the capitulum; both epiphyses medio-laterally larger than the diaphysis; a radial styloid process developed distally; a rectangular and deep distal articular surface.

Like for humerus, the evolutionary variation of the centroid size of the radius carries a significant phylogenetic signal (K_{CS} = 0.82, p < 0.001). The correlation between CS and BM is significant and high (r = 0.80) whereas CS and GI-MC3 are not correlated (Table 12). However, PGLS results indicate a strong and significant correlation between the radius shape and GI-MC3 only (Table 13). PGLS computed on NNI trees indicate that correlation with BM is affected by phylogenetic uncertainties and may be significant or not depending on the tree configuration. Conversely, correlation with CS appears as always non-significant and GI-MC3 as always significant for whatever the tree configuration (Table 13). The regression plot of shape against GI-MC3 indicates an excellent fit to the regression line, with a strong common trend shared by all members of the superfamily. Although most Rhinocerotina are situated above the regression line, they are mixed together with Aceratheriini, Teleoceratina and large Elasmotheriinae. Giant Paraceratheriidae plot together with small Elasmotheriinae and almost all Amynodontidae, while *Juxia* is close to *Hyrachyus* and *Hyracodon*. *Triplopus* plots towards minimal values (Figure 34A). GI-MC3 variation is correlated to a medio-lateral development of the bone appearing stronger on the lateral side of both epiphyses than on the medial one (Figure 34A and Appendix 5G) and to an overall increase in robustness. The correlation between radius shape and BM is marginally non-significant (p = 0.04) (Table 13), although the dispersion of species indicates a rather good fit to the regression line. Paraceratheriidae and *Teleoceras* deviate strongly from the common regression trend, while Rhinocerotina and Elasmotheriinae strongly follow it (see Appendix 6A for regression plot). If the shape variation associated with maximal values of BM is mainly related to a medio-lateral development of both epiphyses like for GI-MC3, the deformation shows a higher intensity for BM on the lateral part of the proximal epiphysis, where inserts the *m. biceps brachii*, and a lower intensity on the distal epiphysis. These changes are also associated to a slight increase of robustness towards high BM values (see Appendix 6A for shape variation).

Ulna – complete bone

The shape variation of the complete ulnae carries a strong phylogenetic signal (K_{mult} = 0.93, p < 0.01). The NJ tree (Figure 29D) shows a grouping of Hyrachyidae, Hyracodontidae, small Elasmotheriinae and

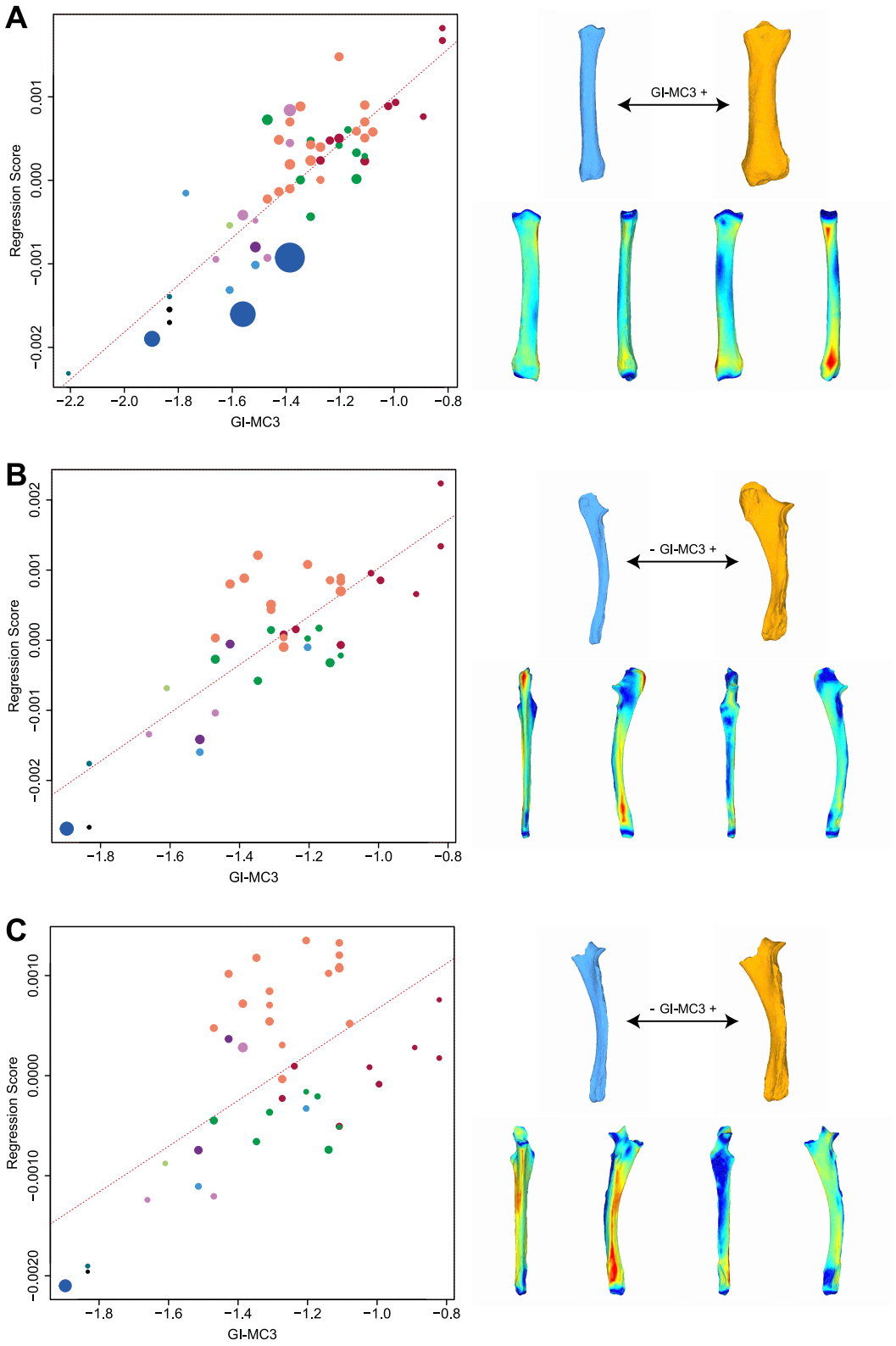

Figure 34: Significant PGLS regression plots for radius (A), complete ulna (B) and ulna without olecranon tuberosity (C) performed on shape data and log-transformed mean gracility index (GI-MC3). Points colour code follows Figure 27. Point size is proportional to mean log CS of each species. On the right, shapes associated with minimum and maximum fitted values (top row) and colour maps of the location and intensity of the shape deformation (bottom row). Blue: minimum value of the regression. Orange: maximum value of the regression. For each bone, the shape associated with the minimum was coloured depending on its distance to the shape associated with the maximum (blue indicates a low deformation intensity and red indicates a high deformation intensity). Orientation from left to right in each case: caudal, lateral, cranial and medial.

Juxia (which slightly isolates from this cluster). Aceratheriini group together with some *Diaceratherium* but also the Amynodontidae, while all other Teleoceratina are grouped together and slightly isolate from other species. *Metamynodon* is placed between Aceratheriini and Teleoceratina, while all Rhinocerotina group together (also with *Dia. lamilloquense*). A similar structure is observed on the phylomorphospace, with the first two axes representing 70.2% of the global variance (Figure 35A). The first axis carries 54.7% of the variance. *Juxia* plots towards minimal values. Small Elasmotheriinae group together with *Trigonias*, *Protaceratherium* and *Paramynodon* towards minimal values. However, *Amphicaenopus* and *Metamynodon* group with a cluster containing Aceratheriini and Rhinocerotini, as well as some *Diaceratherium*. Within Rhinocerotina, larger taxa such as *Ce. simum*, *R. unicornis*, *Co. antiquitatis* or *Dh. pikermiensis* group towards slightly higher values. *Prosantorhinus*, *Brachypotherium, Dia. aurelianense* and *Teleoceras* constitute the highest positive values. The second axis accounts for 15.5% of the global variance. *Hyrachyus* and Rhinocerotina group together in the negative part of the axis with almost no overlapping of the other species. Rhinocerotidae *i. s.* plot around null values together with *Hyracodon*, Amynodontidae, small Elasmotheriinae, *Hoploaceratherium* and *Dia. lamilloquense*. All other Teleoceratina group with Aceratheriini and *Juxia* towards the highest positive values.

Like for the humerus and the radius, the shape variation of the ulna along PC1 is mainly related to the bone slenderness (Figure 35A and Appendix 4D). The shape associated with minimal values is highly thin and slender with an olecranon tuberosity developed proximally; a symmetrical and medio-laterally flattened articular surface for the humerus; a shaft bended in cranio-caudal direction and highly compressed medio-laterally; a narrow and shallow distal articular surface; an articular surface for the pisiform developed proximally. Conversely, the shape associated with maximal values is robust and massive with a strong olecranon tuberosity developed proximo-caudally; a large and asymmetrical articular surface for the humerus; a massive and straight shaft with a triangular section; a distal epiphysis developed medio-laterally; a distal articular surface wide and deep; a reduced articular surface for the pisiform. Along PC2, the shape associated with minimal values display an olecranon tuberosity developed proximo-distally; an anconeus process developed cranially; a shaft bended cranio-caudally; a narrow distal articular surface. The shape associated with maximal values displays an olecranon tuberosity developed mainly caudally; an anconeus process poorly developed cranially; a shaft with a curved caudal border and a straight cranial border; a wide and medially tilted distal articular surface.

The evolutionary variation of the centroid size of the complete ulnae carries a significant phylogenetic signal (K_{CS} = 0.84, p = 0.002). Neither BM nor GI-MC3 are significantly correlated with CS (Table 12). Like for the radius, PGLS results highlight only a strong and significant correlation between the ulna shape and GI-MC3 (Table 13). PGLS computed on NNI trees confirm that neither BM nor CS are

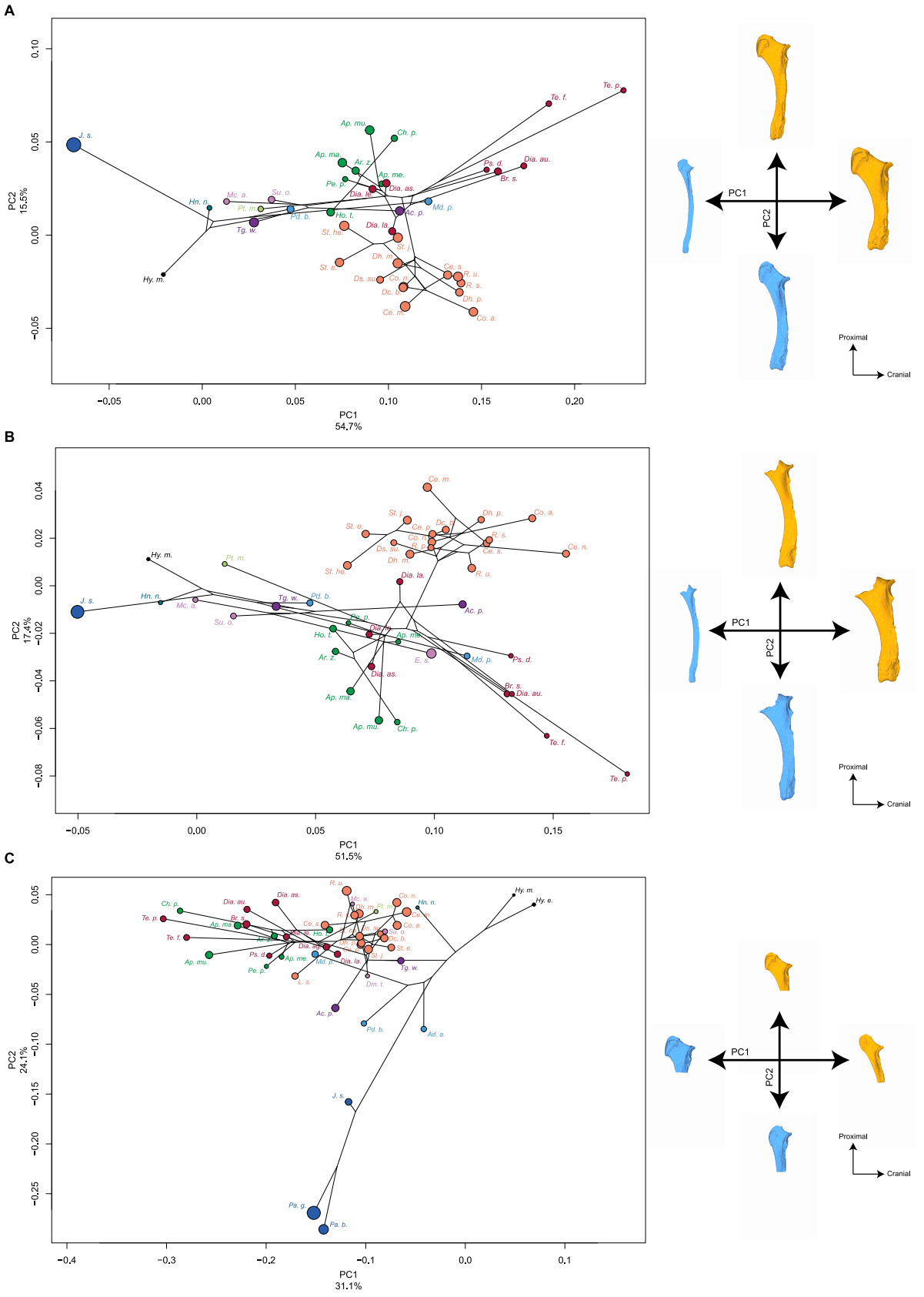

Figure 35: Results of the PCA performed on morphometric data of complete ulna (A), ulna without olecranon tuberosity (B) and distal partial ulna (C) and shape variation associated with the first two axes of the PCA (caudal view). Blue: negative side of the axis. Orange: positive side of the axis. Phylogenetic relationships are plotted in the morphospace. Colour code follows Figure 27 and abbreviations follow Table 11. Point size is proportional to the mean log centroid size of each species.

significantly correlated with shape whatever the phylogenetic configuration (Table 13). Like for the radius, the regression plot of shape against GI-MC3 shows a very good fit to the regression line and highlights a strong common trend with few outliers. However, groups are more clearly separated than for the radius, with almost all Rhinocerotina plotting above the regression line, while other species plot below the line. Teleoceratina and Aceratheriini form well-separated groups with few overlapping with other species. Small Elasmotheriinae plot with Amynodontidae while *Hyrachyus* and *Juxia* plot towards minimal values (Figure 34B). A higher GI-MC3 is associated with a more robust and straighter ulna, showing a cranio-caudal and medio-lateral broadening and a strong development of the olecranon tubercle, as well as a development of the lateral insertion area for digit extensors along the shaft (Figure 34B and Appendix 5H).

Ulna – without the olecranon tuberosity

Shape data of the ulna without the olecranon tuberosity carry a strong phylogenetic signal (K_{mult} = 0.81, $p < 0.01$). The NJ tree (Figure 29E) and phylomorphospace (Figure 35B) are very similar to those obtained for the complete ulnae. One of the main differences with the complete ulna is the position of the heavy *Elasmotherium*: the NJ tree highlights that this genus shares shape similarity with poorly related taxa like *Amphicaenopus* and *Metamynodon*. On the phylomorphospace, the two first axes of the PCA account for 68.9% of the global variance. PC1 represent 51.5% while PC2 accounts for 17.4%. Again, *Elasmotherium* plots far away from smaller Elasmotheriinae like *Subhyracodon* and *Menoceras* along PC1, and closer to *Amphicaenopus*, *Metamynodon and Aphelops* (Figure 35B). The shape variation associated with both axes is largely equivalent to that observed for the complete ulna (Figure 35B and Appendix 4E). PC1 is mainly driven by a change of slenderness and proportion of both epiphyses relatively to the shaft, with a highly massive and robust bone towards positive maximum. PC2 is mainly driven by changes of both orientation of the olecranon development and straightness of the shaft. Towards minimal values, the olecranon is oriented almost completely caudally and the cranial border of the shaft is fully straight.

Like for the complete ulna, the evolutionary variation of the CS of the ulna without olecranon carries a significant phylogenetic signal (K_{CS} = 0.78, p = 0.003). Conversely, CS is significantly and strongly correlated with BM (r = 0.50) but not with GI-MC3 (Table 12). Results of the PGLS indicate only a significant correlation between shape and GI-MC3, which is not affected by phylogenetic uncertainties. Conversely, the correlation between shape and CS remains non-significant regardless of phylogenetic uncertainties (Table 13). If the regression plot displays a trend relatively similar to that observed on complete ulnae, the fit to the regression line is poorer. Rhinocerotina and Teleoceratina are much more distant from the common regression slope, contrary to what it is observed for the radius and complete ulna. *Elasmotherium* and *Amphicaenopus* plot close to Rhinocerotina, which form a well-isolated

cluster above the regression line (Figure 34C). Shape variation related to GI-MC3 is highly similar to that observed along PC1, with a much more pronounced variation along the lateral side of the shaft (Figure 34C and Appendix 5I). As observed on the radius, PGLS computed on BM display marginally non-significant results and NNI trees lead to significant or non-significant correlations between shape and BM depending on the considered phylogeny (Table 13). The regression plot shows a rather good fit to the regression line, despite some clear outliers. Most Rhinocerotina plot below the regression line, together with some Teleoceratina, while Aceratheriini form a central cluster. *Elasmotherium* plots towards maximal values while *Menoceras* plots towards negative values. This poorly significant regression can be related to the isolation of *Juxia* away from the common trend (see Appendix 6B for regression plot). The shape variation related to BM mainly concerns the caudal border of the ulna, particularly the area placed distally to the olecranon (see Appendix 6B).

Ulna – proximal part

Shape data of the proximal parts of the ulnae carry a strong phylogenetic signal (K_{mult} = 0.72, $p < 0.01$). The NJ tree (Figure 29F) and the phylomorphospace (Figure 35C) show marked differences with previous analyses on the complete bones or on the ulna without the olecranon tubercle. The NJ tree is more congruent with phylogenetic groupings than is the phylomorphospace (Figure 29F and 9C). Rhinocerotina form a homogeneous cluster (except for *Lartetotherium*) close to a group containing small Elasmotheriinae, *Protaceratherium*, *Hyracodon* and *Hyrachyus*. Aceratheriini and Teleoceratina are mixed together. Paraceratheriidae and Amynodontidae plot with *Amphicaenopus* among the Aceratheriini-Teleoceratina group. On the phylomorphospace, the two first axes of the PCA carry 55.2% of the global variance (Figure 35C). PC1 represent 31.1% of the global variance. Along this axis, *Hyrachyus* is isolated towards positive values. *Hyracodon* and Amynodontidae plot in a cluster grouping Rhinocerotina, Elasmotheriinae and Rhinocerotidae *i. s.* Aceratheriini and Teleoceratina isolate towards negative values. Paraceratheriidae are placed between the Rhinocerotina cluster and the Aceratheriini-Teleoceratina one, together with other taxa like *Lartetotherium, Metamynodon* and *Amphicaenopus*. The second axis, representing 24.1% of the variance, is mainly driven by the isolation of Paraceratheriidae from all other species, especially the two big forms of the genus *Paraceratherium*, towards minimal values. Almost all other species form a single and mixed cluster from null to positive values without any clear organisation.

Like for the complete ulna, the shape variation of the proximal part of the ulna along PC1 mainly relates to the slenderness of the bone (Figure 35C and Appendix 4F). The shape associated with maximal values is thin and slender with a high olecranon tuberosity, developed in proximal direction and medio-laterally flattened; an anconeus process developed cranially; a symmetrical articular surface for the humerus flattened medio-laterally; a long synostosis surface for the radius. Conversely, the shape

associated with minimal values is thick and massive, with a strong olecranon tubercle developed proximo-caudally and enlarged medio-laterally; an anconeus process poorly developed; a wide and asymmetrical articular surface for the humerus; a short synostosis surface for the radius. Along PC2, the variation is mainly driven by the proportion, shape and orientation of the olecranon. Towards minimal values, the proximal part of the ulna displays a massive and short olecranon, medio-laterally compressed and poorly caudally developed; a large and trapezoid articular surface for the humerus; a poorly developed anconeus process; a long synostosis surface for the radius developed medially. The shape associated with maximal values displays a thinner and squared olecranon developed proximo-caudally; a more triangular articular surface for the humerus; a short synostosis surface for the radius.

The evolutionary variation of the centroid size of the proximal part of the ulna carries a significant phylogenetic signal (K_{CS} = 1.91, $p < 0.001$). Like for the ulna without the olecranon tuberosity, the centroid size is significantly and very strongly correlated with BM (r = 0.85) but not with GI-MC3 (Table 12). PGLS indicate a significant and high correlation between shape and each of the three variables, similarly to what is observed on the complete and partial humerus (Table 13). However, both regression plots of shape against CS and BM must be considered with caution, as the dispersion of specimens poorly fits the regression line. For CS, Aceratheriini and Teleoceratina form a cluster situated below the regression line, together with *Protaceratherium* and small Elasmotheriinae, while Rhinocerotina plot near the line. Paraceratheriidae, Amynodontidae and Rhinocerotidae *i. s.* plot above the line, while *Hyrachyus* plots towards minimal CS values (Figure 36A). Similarly, for BM, Hyrachyidae and Paraceratheriidae plot far away from the common regression slope, whereas among Rhinocerotidae, some Aceratheriini and Teleoceratina are grouped together below the line (Figure 36B). Conversely, the regression plot for the GI-MC3 is very close to those obtained on the humerus and radius, with an excellent fit to the regression line. All species are very close to the common regression line, with a marked overlap between the different groups (Figure 36C). Shape variation related to both CS, BM and GI-MC3 is highly similar and mainly concerns a medio-lateral broadening towards high values, as well as a caudal development of the caudal border of the ulna (Figure 36 and Appendix 5J, K, L). This broadening is more marked for shape variation correlated with GI-MC3.

Evolution of CS values along the phylogeny

The evolution of CS values along the phylogeny for the distal part of the humerus, complete radius and proximal part of the ulna (these three samples being the largest) is relatively congruent between the different taxa (Figure 37). Hyrachyidae-Hyracodontidae and giant Paraceratheriidae possess, respectively, the lowest and highest values for each bone. However, the CS of the radius shows a greater variation along the phylogeny than that of the humerus and ulna. Many taxa among Elasmotheriinae,

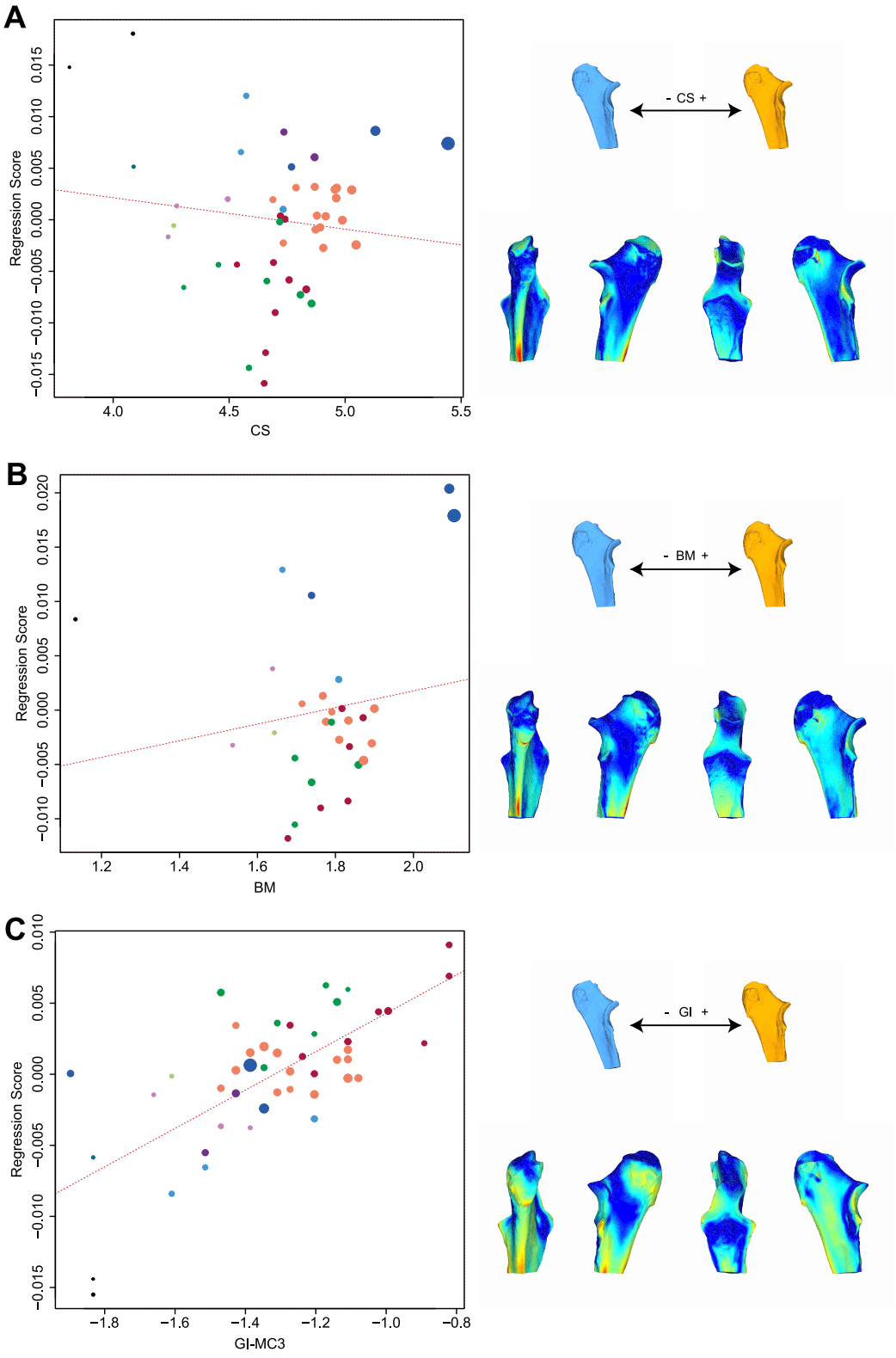

Figure 36: Significant PGLS regression plots for proximal partial ulna performed on shape data and log-transformed centroid size (CS) (A), log-transformed cubic root of mean body mass (BM) (B), log-transformed mean gracility index (GI-MC3) (C). Points colour code follows Figure 27. Point size is proportional to mean log CS of each species. On the right, shapes associated with minimum and maximum fitted values (top row) and colour maps of the location and intensity of the shape deformation (bottom row). Blue: minimum value of the regression. Orange: maximum value of the regression. For each bone, the shape associated with the minimum was coloured depending on its distance to the shape associated with the maximum (blue indicates a low deformation intensity and red indicates a high deformation intensity). Orientation from left to right in each case: caudal, lateral, cranial and medial.

Aceratheriini and Teleoceratina display low values relatively to those observed on the humerus and ulna, these two bones displaying similar patterns of CS variation.

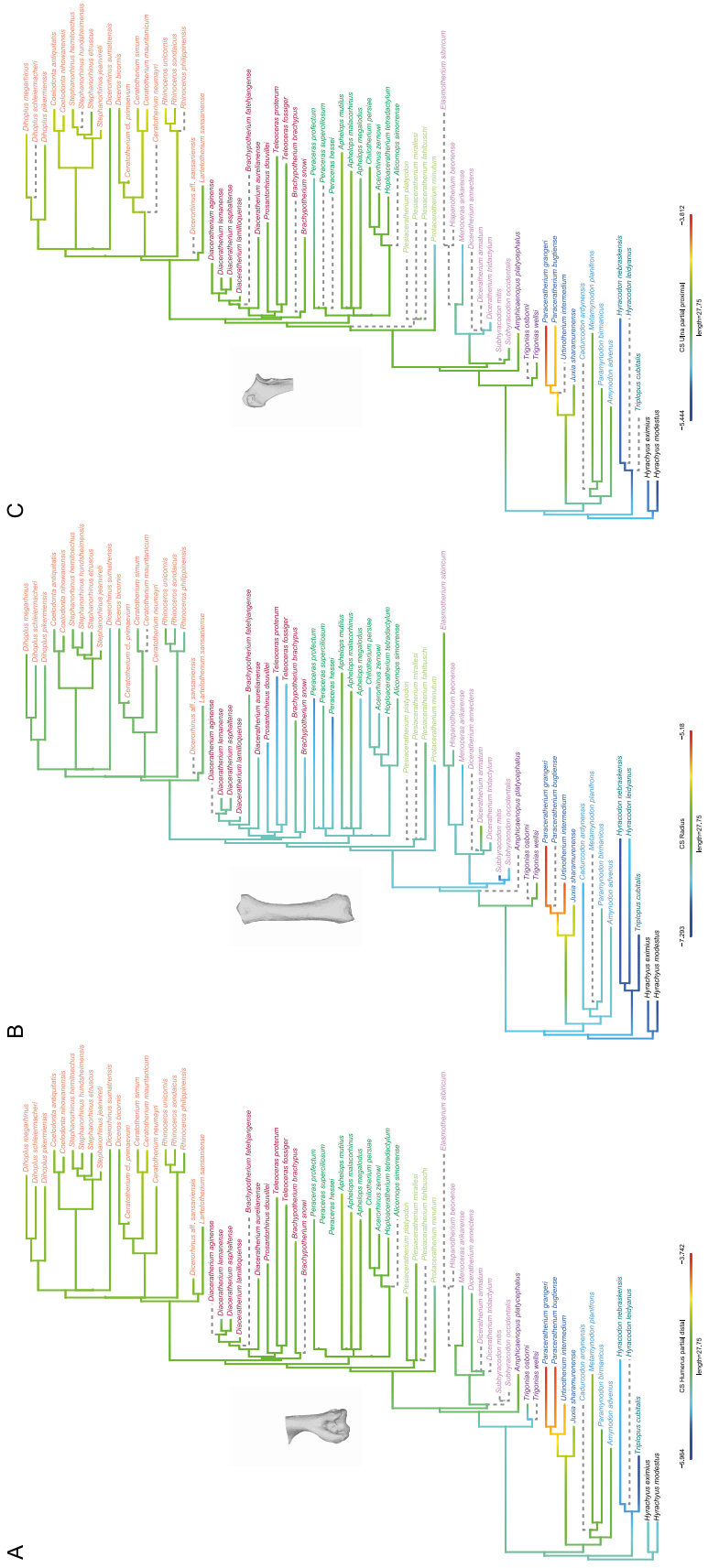

Figure 37: Evolution of centroid size (CS) along the phylogeny for the studied species. A: distal partial humerus, B: radius, C: proximal partial ulna. Computations were made on log-transformed CS. Values at nodes and along branches were reconstructed based on a Brownian motion model of evolution (Revell, 2012). Colour code for taxa follows Figure 27.

Discussion

Relations between bone shape and mass, size and gracility

Results highlight the strong relations existing between the shape variation of the forelimb bones and the changes in bone size, body mass and degree of gracility within Rhinocerotoidea, confirming the first hypothesis. However, these relations appear complex and variable depending on the bone, the anatomical area and the considerer parameter, resulting in congruent and non-congruent changes along the limb.

Congruent shape variation associated with all variables

Centroid size appears almost always significantly correlated with body mass, despite missing data, heterogeneous weight estimations and marginally non-significant results for the complete ulna. This suggests that the CS of the long bones is relevant to approximate the weight of a species (Ercoli & Prevosti, 2011; Cassini, Vizcaíno & Bargo, 2012; Botton-Divet et al., 2017), at least on rhinos despite their diversity of body size and shape. However, beyond this general strong correlation, the variation of CS along the phylogeny for the radius differs from that observed for the humerus and ulna. Some groups may also strongly differ from the general trend shown by the whole superfamily because of specific morphological changes (i.e. Teleoceratina) (see below). Conversely, while BM correlates with GI-MC3, the latter is poorly related to CS except for the distal part of the humerus (and marginally for the complete humerus and proximal part of the ulna). This highlights that, beyond the significant correlation between bone size and body mass, these parameters do not vary conjointly with the degree of brachypody among the superfamily.

The complete humerus, distal humerus and proximal ulna share strong similarities in having their shape variation always correlated with CS, BM and GI-MC3. An increase of these variables is always associated with an increase of the bone robustness, confirming previous observations on modern (Mallet et al., 2019, 2020) and fossil rhinos (Prothero & Sereno, 1982; Etienne et al., 2020). Other areas mainly impacted by shape modification across the superfamily are epiphyses, which mainly extend in the medio-lateral direction in heavy species. These global changes tend to indicate the existence of a common trend within the entire superfamily Rhinocerotoidea for these bones, where shape varies relatively congruously with size, mass and gracility despite the morphological diversity of these species.

The shape changes linked to size, mass or gracility are particularly congruent on the humerus, affecting mainly the medial side of the bone, from the lesser tubercle tuberosity where inserts the *m. subscapularis* to the midshaft where insert the *m. teres major* and the *m. latissimus dorsi*, these muscles acting as adductors and extensors of the arm. On the lateral side, most shape changes are located on the deltoid tuberosity, where inserts the *m. deltoideus*, being more laterally developed and more distally

situated on the shaft for high values of body mass, centroid size and gracility index (with a maximum for GI-MC3 – see below). This distal displacement of the *mm. deltoideus* and of the *teres major* is coherent with an increase in strength of the lever arm for arm flexion and extension required to move heavier body and limbs (Hildebrand, 1974; Polly, 2007). Such a distal displacement observed simultaneously among taxa opposed in gracility and body mass (like Teleoceratina and Paraceratheriidae) can appear paradoxical. A longer and stronger lever arm in large Paraceratheriidae is likely related to longer and heavier limbs requiring more strength to be moved. Similarly, this condition in highly brachypodial taxa may result from a difference in mass repartition: a lower centre of gravity associated with a relatively high body mass and small limbs require powerful muscles with strong insertions to move efficiently (Hildebrand, 1974; Coughlin & Fish, 2009; Biewener & Patek, 2018). Similar observations can be done for the distal epiphysis, where most of the changes are located on the medial and lateral epicondyles and the epicondylar crest when mass, size and brachypody increase. These changes are likely associated with the development of powerful muscles for the extension movements of carpals and digits (Fisher, Scott & Naples, 2007; Barone, 2010a) and can relate to changes in mass repartition and position of the centre of gravity as well.

Contrary to what is observed for the humerus and the proximal ulna, the shape variation of the radius and ulna (complete and without the olecranon) are only significantly correlated with the gracility index, and marginally with body mass. Both the radius and ulna show a reduction of the cranio-caudal curvature and a straightening of the shaft with increasing body mass and brachypody. These changes are coherent with modifications observed on the humerus, highlighting the necessity to resist both higher pressure forces and stronger bending in brachypodial species (Bertram & Biewener, 1992; Milne, 2016; Henderson et al., 2017). On the ulna, the congruent changes observed along the caudal edge of the bone towards high body mass and degree of brachypody are likely linked to a modification of the orientation of the olecranon tuberosity (see below).

Non-congruent shape variation associated with variables

Beyond congruent shape variations between bones or body proportions (size, mass and gracility), some anatomical areas appear to vary more in association with one particular variable. On the humerus, this is likely the case of the bicipital groove, which is reoriented cranially and becomes more symmetrical with the apparition of an intermediate tubercle for high body mass only. This conformation is likely to play a role as a "passive stay-apparatus", a feature convergently present in horses as well, reducing the muscular energy needed to stand for long periods (Hermanson & MacFadden, 1992). A relatively developed intermediate tubercle is observed in many groups showing high body mass (Paraceratheriidae, Aceratheriini, Rhinocerotina, Teleoceratina and, to a lesser extent, Amynodontidae), indicating the presence of a partially or fully functional passive stay-apparatus in these

heavy species. Although this feature in horses is associated with a cursorial condition, equids spending long periods of time in a standing pose, its development among Rhinocerotoidea appears mainly related to their body mass.

A pronounced development of the radial tuberosity, where inserts the *m. biceps brachii*, is observable on the radius. This development is only associated with body mass increase. This may be related to the strong flexion forces exerted by this muscle on the radius, likely related to the strength needed to move heavier limbs in large taxa (or a relatively short limb in species with a low centre of gravity). Moreover, the *m. biceps brachii* is also a relevant muscle involved in the passive-stay apparatus of the shoulder joint (Hermanson & MacFadden, 1992). The development of the radial tuberosity in association with body mass only is therefore coherent with changes observed on the humeral bicipital groove for the same variable.

On the ulna, the lateral border of the shaft shows a marked variation associated only with a high degree of brachypody. This area corresponds to the insertion of the carpal extensors (Barone, 2010b) and its development is coherent with that observed on the epicondylar crest of the humerus (see above). Like for other extensors previously described, the marked development of these insertions along the ulna in brachypodial species may relate to the lowering of the centre of gravity and the higher power needed to move efficiently a short-limb body.

Congruent variations between bones

Congruent shape variations are also observed between bones, which partially infirm the second hypothesis. The tricipital line running from the deltoid process to the humeral head on the humerus is particularly affected by changes in the degree of brachypody. This area corresponds to the insertion of the lateral head of the *m. triceps brachii*. On the proximal ulna, an increase of size and mass, but above all of brachypody, involves morphological changes of the olecranon tuberosity, where inserts the terminal heads of the *m. triceps brachii* as well, one of the most powerful extensors of the forelimb ensuring stance of the body and opposing to gravity (Watson & Wilson, 2007; Barone, 2010b). Furthermore, the development of its insertion is associated with a reorientation of the whole olecranon towards high body mass and degree of brachypody. These changes indicate a wider angle for elbow opening and a modification of the angulation of the olecranon process relatively to the shaft, known to strongly change with body mass among quadrupeds (Jenkins, 1973; Fujiwara, 2009; Fujiwara & Hutchinson, 2012; Milne, 2016; Henderson et al., 2017).

Similarly, the distal trochlea of the humerus undergoes strong changes linked simultaneously to increases in mass, size and brachypody, becoming asymmetrical, wider and flattened, with a drastic reduction of the capitulum and a huge development of the medial lip. This conformation responds to

changes observed on the radius and ulna when mass and brachypody increase. The proximal articular surfaces of the radius and ulna, forming the trochlear notch, lose their asymmetry and concavity in brachypodial taxa. Such coherent changes of the elbow region confer more degrees of freedom in the medio-lateral direction, contrary to the structure encountered in light and cursorial rhinos only allowing cranio-caudally constrained movements. This likely allows the elbow joint to support stronger constraints in multiple directions due to heavy weight (Polly, 2007). Such changes are coherent with similar modifications observed on the ankle joint of Rhinocerotoidea (Etienne et al., 2020), but also with observations made on modern rhinos presented in Chapter 3 (Mallet et al., 2019), indicating a development of the medial parts of limb bones over lateral ones for heavier species. All these morphological modifications in the elbow region, directly linked to a higher mass in heavy taxa, may relate to a lowering of the centre of gravity of the animal in brachypodial species, involving more muscle power and longer lever arms when associated with shorter limb segments for a given mass (Hildebrand, 1974).

Differences between the stylopodium and zeugopodium

Beyond these coherent changes located on precise anatomical areas, the patterns of shape variations appear very different between the stylopodial and the zeugopodial elements. While the variations of the humeral shape follow a trend common to the whole superfamily and are simultaneously related to size, mass and gracility, those of the radius and the ulna are only related to the degree of brachypody (with a marginal effect of body mass). This relation between shape and brachypody is strikingly high for the radius. All these results likely indicate a deep functional breakdown between the stylopodium and the zeugopodium. This is coherent with an increase of the variation of limb elements along a proximo-distal gradient, as hypothesized by previous authors (Hallgrímsson, Willmore & Hall, 2002; Young & Hallgrímsson, 2005). Thanks to its oblique orientation in the limb, the humerus ensures weight support by allowing the dissipation of stresses, while also being the support of muscles linked both to the pectoral girdle and the carpals. It therefore ensures the flexion and extension of the whole forelimb (Polly, 2007). At the opposite, the radius and the shaft of the ulna, oriented vertically, are strongly aligned with pressure constraints due to gravity. The proximal articular surface of the radius supports the entirety of the humerus and, consequently, a significant part of the body weight – the forelimb itself supporting a larger proportion of the total weight than the hind limb (Henderson, 2006; Regnault et al., 2013; Stilson, Hopkins & Davis, 2016; Panagiotopoulou, Pataky & Hutchinson, 2019). Results highlight however that the zeugopodial shape is only related to variations of brachypody, underlining the importance of the repartition of mass in the body and the position of the centre of gravity, rather than to the absolute body mass itself. The influence of the body mass value itself is more visible at lower taxonomic levels (i.e. within families or subfamilies), as it has been observed among modern rhinos in Chapters 3 and 4 (Mallet et al., 2019, 2020).

Modularity of the elbow joint

Beyond the congruences previously described between the humerus and the ulna, the exploration of the shape of both complete and partial bones, driven at first by taphonomic constraints, led to unexpected functional observations. Whereas the complete and distal humerus show similar results, strong differences occur between the whole ulna and its proximal part (in their relations between shape, size, mass and gracility, while the shaft and the distal part seem to follow the same pattern as the radius. The proximal part of the ulna displays similar patterns of variation as the humerus ones (complete and distal), its shape being not only linked to gracility as in the complete ulna, but also to mass and size. This is particularly visible in Paraceratheriidae, whose complete ulna is close to the plesiomorphic condition but whose proximal part of the ulna shows a derived morphology coherent with the humerus one. Additional analyses on the isolated proximal part of the radius do not show this morphological shift and led to results highly similar to those obtained on complete radius (pers. obs.). The elbow is known as a simple yet crucial hinge joint among quadrupeds, involved both in locomotion and stability of the body (Jenkins, 1973; Fujiwara, 2009; Fujiwara & Hutchinson, 2012). The humerus and ulna share complementary articular surfaces and are connected by numerous muscles (*m. anconeus* and flexor and extensor muscles of the carpals and digits) and a strong joint cap (Barone, 2010a). Consequently, the humerus and ulna are strongly integrated among quadrupeds, i.e. show a noticeable shape covariation (Fabre et al., 2014b; Martín-Serra et al., 2015; Hanot et al., 2017; Botton-Divet et al., 2018), notably among modern rhinos as observed in Chapter 4 (Mallet et al., 2020). My results indicate that this covariation is likely to concern mainly the distal part of the humerus and the proximal part of the ulna, leading to consider the elbow as a probable modular structure among Rhinocerotoidea, i.e. an anatomical unit covarying more in itself than with other units (Klingenberg, 2008). Beyond purely functional requirements, this potential modularity can also be related to an evolutionary covariation of size, mass and gracility among Rhinocerotoidea. Similar observations have been highlighted in small carnivorans (Fabre et al., 2014b) and this assertion yet remains to be tested on modern and fossil rhinos through modularity tests (Goswami & Polly, 2010).

Bone shape and phylogenetic relationships

In addition to functional requirements, the evolutionary legacy between species has a strong but unequally distributed influence on the shape variation of the forelimb. Shape, size, mass and the degree of brachypody all carry a strong phylogenetic signal underlining that their variation is constrained by historical factors (Cubo, 2004). This influence is particularly visible on the humerus: most of the considered groups display a marked shape homogeneity despite variation in body proportions. This is not the case for the radius and the ulna, where the different groups are split depending more on their mass or degree of brachypody rather than their phylogenetic affinities. This is coherent with previous

results on modern rhinos indicating that the shape of the stylopodium is more related to the phylogeny than that of the zeugopodium (Mallet et al., 2019, 2020). This pattern seems to occur at the level of the whole superfamily, in accordance with the hypothesis of an increase of variation of the limb elements along a proximo-distal gradient (Hallgrímsson, Willmore & Hall, 2002; Young & Hallgrímsson, 2005).

However, one particular group does not seem to follow this general trend. While being closely related to stem clades like Hyracodontidae, giant Paraceratheriidae exhibit a humeral shape close to that of more derived groups like Aceratheriini. Marked shape changes relatively to the shape displayed by Hyracodontidae or Hyrachyidae are observable on the humerus. Conversely, the shapes of the radius and ulna (except for the proximal part of the latter) appear to retain a plesiomorphic condition close to that of small Hyrachyidae and Hyracodontidae, these bones displaying little morphological changes except their striking relative size. These observations underline the particularity of this group among Rhinocerotoidea, whose unique body shape has puzzled biologists since their discovery (Granger & Gregory, 1936; Prothero, 2013). These considerations appear contradictory with my previous findings indicating that the radius shape is strongly related to the degree of brachypody and poorly to phylogeny (and conversely for the humerus). It is possible that Paraceratheriidae underwent particular developmental processes constraining the zeugopodium shape, while the stylopodium was subject to marked morphological changes to ensure its role in body support and propulsion, constituting a unique pattern within the superfamily. Ecological factors may also have a role in shaping the forelimb of Paraceratheriidae but this question remains to be address in a dedicated study.

Two other groups show marked differences with the common trend of shape variation among Rhinocerotoidea: the subtribes Teleoceratina and Rhinocerotina. Species belonging to Teleoceratina like *Teleoceras* show a high degree of brachypody and their forelimb bones often display an extreme shape relatively to the whole superfamily, particularly on the zeugopodium. Their extreme brachypody had sometimes been associated with a semi-aquatic ecology, although this hypothesis is now considered unlikely (MacFadden, 1998; Mead, 2000; Mihlbachler, 2003; Prothero, 2005; Clementz, Holroyd, & Koch, 2008; Wang & Secord, 2020). Despite the unique limb morphology of Teleoceratina, my results highlight many shape resemblances with fully terrestrial Aceratheriini (*Aphelops*, *Peraceras*) and Rhinocerotina (*Coelodonta*) and do not support the hypothesis of a semi-aquatic ecology either. A morphofunctional analysis focused on this subtribe could help to understand the factors driving this particular limb construction.

Finally, Rhinocerotina display a high shape homogeneity, particularly on the humerus and the ulna, despite a broad range of body mass and body proportions. The range of shape variation within this

subtribe appears thus highly constrained by the evolutionary history. The diverse ecological preferences encountered in Rhinocerotina do not seem to strongly impact the shape variation (Guérin, 1980; Cerdeño, 1998). However, this relative homogeneity relatively to the whole superfamily likely encompasses different trends of shape variation between genera that remain to be explored in detail.

Conclusion

The relations between shape variation of the forelimb bones, body proportions and phylogeny among Rhinocerotoidea vary but general trends are clearly observed despite this complexity. A trend common to the whole superfamily is the increase of bone robustness towards a higher body mass and higher degree of brachypody. The reinforcement of the insertions for the extensor muscles enables the animals to counteract the gravitational constraints when body mass increases. However, strong differences in shape variation exist between the stylopodium and the zeugopodium. The shape of the humerus modifies following size, mass and brachypody in a similar way within the whole superfamily, while being also strongly constrained by the evolutionary history. Conversely, the shape of the zeugopodium appears only driven by the degree of brachypody, namely the distribution of mass within the body (centre of gravity), rather than by the absolute mass itself. Surprisingly, the shape variation of bones in the elbow caudal region show striking similarities, suggesting a likely modular organisation of the humerus and ulna. Beyond these general trends, groups like Paraceratheriidae, Teleoceratina and Rhinocerotina display divergent patterns that remain to be fully understood. Consequently, this exploration of the forelimb shape among Rhinocerotoidea encourages the application of the same morphofunctional approach on the hind limb to highlight how shape patterns converge or diverge between limbs under a similar weight constraint.

Appendices

Appendix 1: Complete list of all the studied specimens

Institutional abbreviations as given in Chapter 2. Age: E: Early; L: Late; M: Middle; Side: L: left; R: Right.

Humerus

Genus	Species	Institution	Number	Locality	Country	Epoch	Side	Condition	Confirmation of specific attribution
Acerorhinus	*zernowi*	AMNH	F:AM 129840	Gur Tung Khara Usu	China	M. Miocene	R	Complete	Cerdeño, 1996a
Amphicaenopus	*platycephalus*	AMNH	FM 548	"Protoceras beds", Brule Form.	South Dakota, USA	E. Oligocene	R	Partial distal	Prothero, 2005
Amphicaenopus	*platycephalus*	YPM	VPPU 011016	Brule Form.	South Dakota, USA	E. Oligocene	R	Complete	YPM database
Amynodon	*advenus*	AMNH	FM 1961	White River Form.	Utah, USA	M. Eocene	L	Partial distal	Wall, 1982
Aphelops	*malacorhinus*	AMNH	F:AM 114357	Wray Area, Loc. B, Ogallala Form.	Colorado, USA	L. Miocene	R	Partial distal	Prothero, 2005
Aphelops	*malacorhinus*	AMNH	F:AM 114831B	Box T Ranch, West Draw, Ogallala Form.	Texas, USA	L. Miocene	L	Complete	Prothero, 2005
Aphelops	*megalodus*	AMNH	F:AM 108898C	Trinity River Pit 1, Burkeville Fauna	Texas, USA	M. Miocene	R	Complete	Prothero, 2005
Aphelops	*megalodus*	AMNH	F:AM 114612E	Thistle Quarry, Sheep Creek Form.	Nebraska, USA	E. Miocene	L	Complete	Prothero, 2005
Aphelops	*mutilus*	AMNH	F:AM 104037	Rhino Hill Quarry Area, Ogallala Form.	Kansas, USA	L. Miocene	R	Complete	Prothero, 2005
Brachypotherium	*brachypus*	MNHN	F.BA 2735	Baigneaux	France	E. Miocene	R	Partial distal	Cerdeño, 1993
Ceratotherium	*cf. primaevum*	MNHN	F.1951-9-214	Bou Hanifia	Algeria	L. Miocene	L	Complete	Arambourg, 1959; Geraads, 2010
Ceratotherium	*mauritanicum*	MNHN	F.1949-1-2	Ichkeul	Tunisia	E. Pliocene	R	Partial distal	Indirect confirmation in Geraads, 2010
Ceratotherium	*neumayri*	AMNH	FM 20675	Samos Island	Greece	L. Miocene	R	Complete	Indirect confirmation in Geraads, 1988; Giaourtsakis, 2009
Ceratotherium	*neumayri*	MNHN	F.PIK 1319	Pikermi	Greece	L. Miocene	R	Partial distal	Indirect confirmation in Pandolfi, 2016; Antoine & Sen, 2016
Ceratotherium	*neumayri*	MNHN	F.PIK 974	Pikermi	Greece	L. Miocene	L	Partial distal	Indirect confirmation in Pandolfi, 2016; Antoine & Sen, 2016
Ceratotherium	*simum*	NHMUK	ZD 2018.143	Unknown	Unknown	Modern	L	Complete	Mallet et al., 2019
Ceratotherium	*simum*	RBINS	35208	Unknown	Unknown	Modern	L	Complete	RBINS database
Ceratotherium	*simum*	RMCA	1985.32-M-0001	Unknown	Sudan	Modern	L	Complete	RMCA database

Chilotherium	*persiae*	MNHN	F.MAR 3904	Maragha	Iran	L. Miocene	R	Partial distal	Indirect confirmation in Pandolfi, 2016
Coelodonta	*antiquitatis*	MHNT	PAL.2010.23.1	Tyumen Oblast	Russia	Pleistocene	R	Complete	MHNT database
Coelodonta	*antiquitatis*	RBINS	I.G.8151-8435-H33	Hofstade	Belgium	Pleistocene	L	Partial distal	Indirect confirmation in Guérin, 2010
Coelodonta	*antiquitatis*	RBINS	Vert-00000-00217	Unknown	Unknown	Pleistocene	L	Partial distal	RBINS database
Coelodonta	*nihowanensis*	MNHN	F.NIH 154	Nihewan	China	L. Pliocene	L	Complete	MNHN database
Diaceratherium	*asphaltense*	NMB	SAU-1662	Saulcet	France	E. Miocene	L	Complete	Jame et al., 2019
Diaceratherium	*aurelianense*	MNHN	F.AR 2160	Artenay	France	E. Miocene	L	Partial distal	Cerdeño, 1993
Diaceratherium	*aurelianense*	NHMUK	PAL PV M 7752	Chilleurs	France	E. Miocene	R	Partial distal	In situ determination by P.-O. Antoine
Diaceratherium	*aurelianense*	NMB	S.O.5574	Ronville	France	E. Miocene	R	Complete	Indirect confirmation in Jame et al., 2019
Diaceratherium	*lamilloquense*	MHNT	PAL.2014.0.2574	Castelmaurou	France	L. Oligocene	R	Partial distal	Indirect confirmation in Ménouret & Guérin, 2009
Diaceratherium	*lemanense*	MNHN	F.SG 9505	Saint-Gérand-le-Puy	France	E. Miocene	R	Partial distal	Bucher, Ginsburg & Cheneval, 1985
Diceratherium	*annectens*	AMNH	FM 7324	John Day beds	Oregon, USA	L. Oligocene – E. Miocene	R	Partial distal	Prothero, 2005
Diceratherium	*annectens*	YPM	VP 012493	John Day beds	Oregon, USA	L. Oligocene – E. Miocene	L	Partial distal	Indirect confirmation in Prothero, 2005
Dicerorhinus	*aff. sansaniensis*	NHMUK	PAL PV M 36909	Al Dabtiyah	Saudi Arabia	E. Miocene	R	Complete	Gentry, 1987
Dicerorhinus	*sumatrensis*	NHMUK	ZD 1879.6.14.2	Unknown	Malaysia	Modern	R	Complete	NHMUK database
Dicerorhinus	*sumatrensis*	NHMUK	ZE 1948.12.20.1	Unknown	Unknown	Modern	L	Complete	NHMUK database
Dicerorhinus	*sumatrensis*	NHMUK	ZE 1949.1.11.1	Tring	Indonesia	Modern	L	Complete	NHMUK database
Diceros	*bicornis*	MNHN	ZM-AC-1936-644	Unknown	Unknown	Modern	L	Complete	MNHN database
Diceros	*bicornis*	CCEC	50002040	Natal	South Africa	Modern	L	Complete	CCEC database
Diceros	*bicornis*	RBINS	9714	Unknown	Democratic Republic of the Congo	Modern	L	Complete	RBINS database
Dihoplus	*megarhinus*	FSL	40029	Montpellier	France	L. Pliocene	R	Partial distal	Indirect confirmation in Guérin, 1980
Dihoplus	*megarhinus*	FSL	40033	Montpellier	France	L. Pliocene	L	Complete	Indirect confirmation in Guérin, 1980

Dihoplus	*megarhinus*	FSL	40425	Montpellier	France	L. Pliocene	L	Partial distal	Indirect confirmation in Guérin, 1980
Dihoplus	*pikermiensis*	NHMUK	PAL PV M 11282A	Pikermi	Greece	E. Pliocene	L	Partial distal	Indirect confirmation in Geraads, 1988
Dihoplus	*pikermiensis*	MNHN	F.PIK 976	Pikermi	Greece	L. Miocene	R	Partial distal	Indirect confirmation in Antoine & Saraç, 2005; Pandolfi, Gasparik & Piras, 2015
Dihoplus	*schleiermacheri*	RBINS	Cast-Vert-RM-2680	Eppelsheim	Germany	M. Miocene	R	Partial distal	Indirect confirmation in Geraads, 1988; Giaourtsakis & Heissig, 2004
Hoploaceratherium	*tetradactylum*	NHMUK	PAL PV M 27456	Sansan	France	M. Miocene	L	Partial distal	In situ determination by P.-O. Antoine
Hoploaceratherium	*tetradactylum*	MNHN	F.SA 15624	Sansan	France	M. Miocene	L	Partial distal	Heissig, 2012
Hoploaceratherium	*tetradactylum*	MNHN	F.SA 6305	Sansan	France	M. Miocene	R	Complete	Heissig, 2012
Hyrachyus	*eximius*	AMNH	FM 12225	Summers Dry Creek, Bridger Form.	Wyoming, USA	M. Eocene	L	Complete	Bai et al., 2017
Hyrachyus	*eximius*	AMNH	FM 5065a	Bridger Basin, Bridger Form.	Wyoming, USA	M. Eocene	L	Partial distal	Bai et al., 2017
Hyrachyus	*modestus*	AMNH	FM 17436	Upper Huerfano	Colorado, USA	E. Eocene	R	Complete	Robinson, 1966
Hyrachyus	*modestus*	AMNH	FM 93045	Twin Buttes, Bridger Form.	Wyoming, USA	M. Eocene	R	Partial distal	Indirect confirmation in Radinsky, 1967
Hyracodon	*nebraskensis*	AMNH	FM 1176	Cheyenne River, Brule Form.	South Dakota, USA	E. Oligocene	R	Partial distal	Wall & Hickerson, 1995
Hyracodon	*nebraskensis*	AMNH	FM 9789	Cedar Draw, Brule Form.	South Dakota, USA	E. Oligocene	R	Complete	Wall & Hickerson, 1995
Hyracodon	*nebraskensis*	AMNH	FM 9789	Cedar Draw, Brule Form.	South Dakota, USA	E. Oligocene	L	Partial distal	Wall & Hickerson, 1995
Juxia	*sharamurenense*	IVPP	V 2891	Ula Usu, Shara Murun Form.	China	M. Eocene	L	Partial distal	Qiu & Wang, 2007
Lartetotherium	*sansaniense*	MNHN	F.SA 15622	Sansan	France	M. Miocene	L	Partial distal	Heissig, 2012
Lartetotherium	*sansaniense*	MNHN	F.SA 15623	Sansan	France	M. Miocene	L	Partial distal	Heissig, 2012
Menoceras	*arikarense*	AMNH	FM 14214	Agate Springs Quarry, Anderson Ranch Form.	Nebraska, USA	E. Miocene	L	Complete	Indirect confirmation in Prothero, 2005
Menoceras	*arikarense*	AMNH	FM 144590	Agate Springs Quarry, Anderson Ranch Form.	Nebraska, USA	E. Miocene	R	Complete	Indirect confirmation in Prothero, 2005

Menoceras	*arikarense*	AMNH	FM 22486	Agate Springs Quarry, Anderson Ranch Form.	Nebraska, USA	E. Miocene	L	Complete	Indirect confirmation in Prothero, 2005
Metamynodon	*planifrons*	AMNH	FM 1088	Metamynodon Beds, Cottonwood Creek	South Dakota, USA	E. Oligocene	L	Partial distal	Scott & Jepsen, 1941
Metamynodon	*planifrons*	YPM	VPPU 011017	Metamynodon Beds, Cottonwood Creek	South Dakota, USA	E. Oligocene	L	Partial distal	Indirect confirmation in Scott & Jepsen, 1941
Paraceratherium	*bugtiense*	NHMUK	PAL PV M 12251	Bugti Beds, Churlando	Pakistan	Oligocene	L	Partial distal	Indirect confirmation in Qiu & Wang, 2007
Paraceratherium	*grangeri*	AMNH	FM 26166	Urtyn Obo	China	E. Oligocene	L	Partial distal	Qiu & Wang, 2007; Bai et al., 2018
Paramynodon	*birmanicus*	AMNH	FM 20013	Top Pondaung Clays, Bahin	Burma	M. Eocene	R	Partial distal	Colbert, 1938
Peraceras	*profectum*	AMNH	F:AM 114401	Pojoaque Bluffs, Tesuque Form.	New Mexico, USA	M. Miocene	L	Partial distal	Prothero, 2005
Peraceras	*profectum*	AMNH	F:AM 114947	District #2, Tesuque Form.	New Mexico, USA	M. Miocene	L	Complete	Prothero, 2005
Peraceras	*profectum*	AMNH	F:AM 114970	Pojoaque Bluffs, Tesuque Form.	New Mexico, USA	M. Miocene	R	Partial distal	Prothero, 2005
Plesiaceratherium	*mirallesi*	MHNT	PAL.2015.0.965	Montréal-du-Gers	France	E. Miocene	L	Partial distal	In situ determination by P.-O. Antoine
Plesiaceratherium	*platyodon*	FSL	320240	La Romieu	France	E. Miocene	L	Complete	Ginsburg & Bulot, 1984; Antunes & Ginsburg, 2010
Prosantorhinus	*douvillei*	MHNT	PAL.2015.0.1466.1	Montréal-du-Gers	France	E. Miocene	R	Partial distal	Indirect confirmation in Antoine et al., 2018
Prosantorhinus	*douvillei*	MNHN	F.BA 2695	Baigneaux	France	E. Miocene	R	Partial distal	Cerdeño, 1996b
Protaceratherium	*minutum*	FSL	213781	Budenheim	Germany	L. Oligocene	R	Complete	Antunes & Ginsburg, 1983
Rhinoceros	*philippinensis*	NMP	2014-II-J1-289	Kalinga	Philippines	M. Pleistocene	R	Partial distal	Ingicco et al., 2018
Rhinoceros	*sondaicus*	CCEC	50002041	Cochinchina	Vietnam	Modern	R	Complete	CCEC database
Rhinoceros	*sondaicus*	MNHN	ZM-AC-A7970	Unknown	Unknown	Modern	L	Complete	MNHN database
Rhinoceros	*sondaicus*	MNHN	ZM-AC-A7971	Java	Indonesia	Modern	L	Complete	MNHN database
Rhinoceros	*unicornis*	NHMUK	ZD 1884.1.22.1.2	Assam	India	Modern	R	Complete	NHMUK database
Rhinoceros	*unicornis*	NHMUK	ZE 1950.10.18.5	Unknown	Nepal	Modern	L	Complete	NHMUK database
Rhinoceros	*unicornis*	MNHN	ZM-AC-1960-59	Vincennes Zoo	France	Modern	L	Complete	MNHN database
Stephanorhinus	*jeanvireti*	CCEC	V272	Vialette	France	L. Pliocene	R	Complete	Guérin, 1972; Pandolfi, Codrea, & Popescu, 2019

Stephanorhinus	*jeanvireti*	CCEC	V273	Vialette	France	L. Pliocene	L	Partial distal	Guérin, 1972; Pandolfi, Codrea, & Popescu, 2019
Stephanorhinus	*etruscus*	MNHN	F.1923-8	Senèze	France	L. Pliocene	R	Complete	Indirect confirmation in Guérin, 1980; Pandolfi et al., 2017b
Stephanorhinus	*etruscus*	CCEC	20164113	Saint-Vallier	France	E. Pleistocene	L	Complete	Indirect confirmation in Guérin et al., 2004; Pandolfi et al., 2017b
Stephanorhinus	*etruscus*	FSL	210954	Senèze	France	L. Pliocene	R	Complete	Indirect confirmation in Guérin, 1980; Pandolfi et al., 2017b
Stephanorhinus	*hemitoechus*	NHMUK	PAL PV OR 23111	Ilford	UK	M. Pleistocene	L	Complete	Indirect confirmation in Fortelius, Mazza & Sala, 1993; Scott, 2007
Stephanorhinus	*hundsheimensis*	NHMUK	PAL PV M 17843	Forest Bed, Trimingham	UK	M. Pleistocene	R	Partial distal	Fortelius, Mazza & Sala, 1993
Teleoceras	*fossiger*	AMNH	FM 2643	Long Island Rhino Quarry, Ogallala Form.	Kansas, USA	L. Miocene	L	Complete	Indirect confirmation in Prothero, 2005
Teleoceras	*fossiger*	AMNH	FM 2665	Long Island Rhino Quarry, Ogallala Form.	Kansas, USA	L. Miocene	R	Partial distal	Indirect confirmation in Prothero, 2005
Teleoceras	*fossiger*	YPM	VP 038689	Long Island Rhino Quarry, Ogallala Form.	Kansas, USA	L. Miocene	R	Complete	Indirect confirmation in Prothero, 2005
Teleoceras	*proterum*	AMNH	F:AM 104197	Mixson's Bone Bed, Alucha Form.	Florida, USA	L. Miocene	R	Complete	Indirect confirmation in Prothero, 2005
Trigonias	*osborni*	UCMP	32011	Figgins Quarry	Colorado, USA	L. Eocene	L	Complete	Prothero & Schoch, 1989
Triplopus	*cubitalis*	AMNH	FM 5095	S. Bitter Creek, Washakie Basin	Wyoming, USA	M. Eocene	R	Complete	Bai et al., 2017
Urtinotherium	*intermedium*	AMNH	FM 26191	Nom Khong Obo	China	L. Eocene	L	Complete	Indirect confirmation in Qiu & Wang, 2007

Radius

Genus	Species	Institution	Number	Locality	Country	Age	Side	Condition	Confirmation of specific attribution
Acerorhinus	*zernowi*	BSPG	1968 VI 303	Konya-Hatunsaray-Kayadibi	Turkey	L. Miocene	L	Complete	Heissig, 1975
Acerorhinus	*zernowi*	AMNH	FM 129837	Gur Tung Khara Usu	China	M. Miocene	R	Complete	Cerdeño, 1996a
Acerorhinus	*zernowi*	AMNH	FM 26215	Gur Tung Khara Usu	China	M. Miocene	L	Complete	Cerdeño, 1996a
Alicornops	*simorrense*	MNHN	F.SA 6307	Sansan	France	M. Miocene	R	Complete	Heissig, 2012
Amynodon	*advenus*	AMNH	FM 1961	White River Form.	Utah, USA	M. Eocene	L	Complete	Wall, 1982
Aphelops	*malacorhinus*	AMNH	F:AM 114834	Box T Ranch, West Draw, Ogallala Form.	Texas, USA	L. Miocene	R	Complete	Prothero, 2005
Aphelops	*megalodus*	AMNH	F:AM 108899B	Trinity River Pit 1, Burkeville Fauna	Texas, USA	M. Miocene	R	Complete	Prothero, 2005
Aphelops	*megalodus*	AMNH	F:AM 114610E	Buck Quarry, Sheep Creek Form.	Nebraska, USA	E. Miocene	L	Complete	Prothero, 2005
Aphelops	*mutilus*	AMNH	F:AM 104037	Rhino Hill Quarry Area, Ogallala Form.	Kansas, USA	L. Miocene	R	Complete	Indirect confirmation in Prothero, 2005
Brachypotherium	*brachypus*	MHNT	PAL.2015.0.1379	Montréal-du-Gers	France	E. Miocene	L	Complete	MHNT database
Brachypotherium	*brachypus*	MNHN	F.BA 2713	Baigneaux	France	E. Miocene	R	Complete	Cerdeño, 1993
Brachypotherium	*brachypus*	MNHN	F.FP 2684	Thenay	France	M. Miocene	R	Complete	Cerdeño, 1993
Brachypotherium	*brachypus*	MNHN	F.SML 331	Malartic	France	M. Miocene	L	Complete	Cerdeño, 1993
Brachypotherium	*fatehjangense*	MHNT	PAL. 2014.0.2409	Dera Bugti	Pakistan	E. Miocene	R	Complete	MHNT database
Brachypotherium	*snowi*	NHMUK	PAL PV M 29274	Jebel Zelten	Libya	E. Miocene	R	Complete	Hamilton, 1973; Geraads, 2010
Cadurcodon	*ardynensis*	AMNH	FM 20442	Ardyn Obo	Mongolia	M. Eocene	L	Complete	Lucas, Emry, & Bayshashov, 1996
Ceratotherium	*cf. primaevum*	MNHN	F.1951-9-170	Bou Hanifia	Algeria	L. Miocene	R	Complete	Arambourg, 1959; Geraads, 2010
Ceratotherium	*cf. primaevum*	MNHN	F.1951-9-213	Bou Hanifia	Algeria	L. Miocene	L	Complete	Arambourg, 1959; Geraads, 2010
Ceratotherium	*neumayri*	MNHN	F.PIK 1026	Pikermi	Greece	L. Miocene	L	Complete	Indirect confirmation in Pandolfi, 2016; Antoine & Sen, 2016
Ceratotherium	*simum*	NHMUK	ZD 2018.143	Unknown	Unknown	Modern	L	Complete	Mallet et al., 2019

Ceratotherium	*simum*	RBINS	35208	Unknown	Unknown	Modern	R	Complete	RBINS database
Ceratotherium	*simum*	RMCA	1985.32-M-0001	Unknown	Sudan	Modern	L	Complete	RMCA database
Chilotherium	*persiae*	MNHN	F.MAR 3906	Maragha	Iran	L. Miocene	R	Complete	Indirect confirmation in Pandolfi, 2016
Chilotherium	*persiae*	MNHN	F.MAR 3912	Maragha	Iran	L. Miocene	R	Complete	Indirect confirmation in Pandolfi, 2016
Coelodonta	*antiquitatis*	RBINS	I.G.8151-8435-R23	Hofstade	Belgium	Pleistocene	L	Complete	Indirect confirmation in Guérin, 2010
Coelodonta	*antiquitatis*	CCEC	QL183	Rue de l'Antiquaire, Lyon	France	Pleistocene	L	Complete	CCEC database
Coelodonta	*antiquitatis*	RBINS	Vert-00000-000506	Unknown	Unknown	Pleistocene	R	Complete	RBINS database
Coelodonta	*nihowanensis*	MNHN	F.NIH 046	Nihewan	China	L. Pliocene	R	Complete	MNHN database
Coelodonta	*nihowanensis*	MNHN	F.NIH 049	Nihewan	China	L. Pliocene	L	Complete	MNHN database
Diaceratherium	*asphaltense*	NMB	SAU-1662	Saulcet	France	E. Miocene	L	Complete	Jame et al., 2019
Diaceratherium	*aurelianense*	MNHN	F.AR 2160	Artenay	France	E. Miocene	L	Complete	Cerdeño, 1993
Diaceratherium	*lamilloquense*	MHNT	PAL.2014.0.2573	Castelmaurou	France	L. Oligocene	R	Complete	Ménouret & Guérin, 2009
Diaceratherium	*lemanense*	AR	B2-1473	Gannat	France	E. Miocene	L	Complete	Boada-Saña, 2008
Diaceratherium	*lemanense*	MNHN	F.SG 9533	Saint-Gérand-le-Puy	France	E. Miocene	R	Complete	Bucher, Ginsburg & Cheneval, 1985
Diceratherium	*armatum*	AMNH	F:AM 42954	Turtle Butte Form.	South Dakota, USA	L. Oligocene	R	Complete	Prothero, 2005
Diceratherium	*tridactylum*	AMNH	FM 525	Big Badlands, Brule Form.	South Dakota, USA	E. Oligocene	R	Complete	Prothero, 2005
Diceratherium	*tridactylum*	AMNH	FM 8092	Chalky Buttes, Killdeer Form	North Dakota, USA	E. Oligocene	L	Complete	Prothero, 2005
Dicerorhinus	*sumatrensis*	NHMUK	ZD 1879.6.14.2	Unknown	Malaysia	Modern	R	Complete	NHMUK database
Dicerorhinus	*sumatrensis*	NHMUK	ZE 1948.12.20.1	Unknown	Unknown	Modern	L	Complete	NHMUK database
Dicerorhinus	*sumatrensis*	NHMUK	ZE 1949.1.11.1	Tring	Indonesia	Modern	L	Complete	NHMUK database
Diceros	*bicornis*	MNHN	ZM-AC-1936-644	Unknown	Unknown	Modern	L	Complete	MNHN database
Diceros	*bicornis*	CCEC	50002047	Unknown	Unknown	Modern	R	Complete	CCEC database
Diceros	*bicornis*	RBINS	9714	Unknown	Democratic Repub-lic of the Congo	Modern	L	Complete	RBINS database
Dihoplus	*megarhinus*	FSL	40061	Montpellier	France	L. Pliocene	L	Complete	Guérin, 1980

Dihoplus	*megarhinus*	FSL	41325	Perpignan	France	L. Pliocene	L	Complete	Indirect confirmation in Guérin, 1980
Dihoplus	*pikermiensis*	MNHN	F.PIK 1022	Pikermi	Greece	L. Miocene	R	Complete	Indirect confirmation in Antoine & Saraç, 2005; Pandolfi, Gasparik & Piras, 2015
Dihoplus	*pikermiensis*	MNHN	F.PIK 1025	Pikermi	Greece	L. Miocene	L	Complete	Indirect confirmation in Antoine & Saraç, 2005; Pandolfi, Gasparik & Piras, 2015
Dihoplus	*schleiermacheri*	MNHN	FMCF 60	Saint-Bauzille	France	L. Miocene	R	Complete	Métais & Sen, 2018
Elasmotherium	*sibiricum*	NHMUK	PAL PV M 5229a	Siberia	Russia	Pleistocene	R	Complete	NHMUK database
Elasmotherium	*sibiricum*	NHMUK	PAL PV M 5229b	Siberia	Russia	Pleistocene	L	Complete	NHMUK database
Hispanotherium	*beonense*	FSL	320440	Pellecahus, La Romieu	France	E. Miocene	R	Complete	Antoine, Bulot, & Ginsburg, 2000a
Hispanotherium	*beonense*	MHNT	PAL.2015.0.808.2	Montréal-du-Gers	France	E. Miocene	R	Complete	MHNT database
Hoploaceratherium	*tetradactylum*	NHMUK	PAL PV OR 27459	Sansan	France	M. Miocene	L	Complete	Heissig, 2012
Hoploaceratherium	*tetradactylum*	MNHN	F.SA 5329	Sansan	France	M. Miocene	L	Complete	Heissig, 2012
Hoploaceratherium	*tetradactylum*	MNHN	F.SA 5328	Sansan	France	M. Miocene	R	Complete	Heissig, 2012
Hyrachyus	*eximius*	AMNH	FM 12673	Henry's Fork, Bridger Form.	Wyoming, USA	M. Eocene	L	Complete	Indirect confirmation in Radinsky, 1967
Hyrachyus	*eximius*	AMNH	FM 1638	Cottonwood Creek, Bridger Form.	Wyoming, USA	M. Eocene	R	Complete	Indirect confirmation in Radinsky, 1967
Hyrachyus	*eximius*	AMNH	FM 93050	Henry's Fork, Bridger Form.	Wyoming, USA	M. Eocene	R	Complete	Bai et al., 2017
Hyrachyus	*modestus*	AMNH	FM 12667	Millersville, Bridger Form.	Wyoming, USA	M. Eocene	L	Complete	AMNH database
Hyrachyus	*modestus*	AMNH	FM 13089	Cottonwood Creek, Bridger Form.	Wyoming, USA	M. Eocene	L	Complete	Indirect confirmation in Radinsky, 1967
Hyrachyus	*modestus*	AMNH	FM 17436	Upper Huerfano	Colorado, USA	E. Eocene	L	Complete	Robinson, 1966
Hyracodon	*leidyanus*	YPM	VPPU 010802	Corral Draw	South Dakota, USA	Oligocene	L	Complete	Sinclair, 1922
Hyracodon	*nebraskensis*	AMNH	FM 9789	Cedar Draw, Brule Form.	South Dakota, USA	E. Oligocene	L	Complete	Wall & Hickerson, 1995
Juxia	*sharamurenense*	AMNH	FM 20264	Ula Usu, Shara Murun Form.	China	Oligocene	R	Complete	Bai et al., 2018

Lartetotherium	*sansaniense*	MNHN	F.SA 6308	Sansan	France	M. Miocene	R	Complete	Heissig, 2012
Menoceras	*arikarense*	AMNH	FM 144609	Agate Springs Quarry, Anderson Ranch Form.	Nebraska, USA	E. Miocene	L	Complete	Indirect confirmation in Prothero, 2005
Menoceras	*arikarense*	AMNH	FM 22486	Agate Springs Quarry, Anderson Ranch Form.	Nebraska, USA	E. Miocene	L	Complete	Indirect confirmation in Prothero, 2005
Menoceras	*arikarense*	YPM	VPPU 012213	Agate Springs Quarry, Anderson Ranch Form.	Nebraska, USA	E. Miocene	L	Complete	Indirect confirmation in Prothero, 2005
Paraceratherium	*grangeri*	AMNH	FM 26166	Urtyn Obo	China	E. Oligocene	R	Complete	Qiu & Wang, 2007; Bai et al., 2018
Paramynodon	*birmanicus*	AMNH	FM 20013	Top Pondaung Clays, Bahin	Burma	M. Eocene	R	Complete	Colbert, 1938
Paramynodon	*birmanicus*	AMNH	FM 20032	Pondaung Clays, Kyaw-daw	Burma	M. Eocene	R	Complete	Colbert, 1938
Peraceras	*hessei*	AMNH	F:AM 108321	McMurry Pit 2, U. Fleming Form.	Texas, USA	M. Miocene	L	Complete	Prothero & Manning, 1987
Peraceras	*profectum*	AMNH	F:AM 114970	Pojoaque Bluffs, Tesuque Form	New Mexico, USA	M. Miocene	R	Complete	Prothero, 2005
Peraceras	*superciliosum*	AMNH	F:AM 114914	Elliot Quarry, Valentine Form.	Nebraska, USA	M. Miocene	R	Complete	Prothero, 2005
Plesiaceratherium	*fahlbuschi*	BSPG	1959 II 183	Sandelzhausen	Germany	E. – M. Mio-cene	R	Complete	Heissig, 2006
Prosantorhinus	*douvillei*	MNHN	F.BA 2717	Baigneaux	France	E. Miocene	R	Complete	Cerdeño, 1996b
Prosantorhinus	*douvillei*	MNHN	F.BA 2718	Baigneaux	France	E. Miocene	L	Complete	Cerdeño, 1996b
Prosantorhinus	*douvillei*	MHNT	PAL.2015.0.3382	Montréal-du-Gers	France	E. Miocene	L	Complete	Indirect confirmation in Antoine et al., 2018
Protaceratherium	*minutum*	FSL	213781	Budenheim	Germany	L. Oligocene	R	Complete	Antunes & Ginsburg, 1983
Rhinoceros	*philippinensis*	NMP	2014-II-J1-297	Kalinga	Philippines	M. Pleisto-cene	L	Complete	Ingicco et al., 2018
Rhinoceros	*sondaicus*	CCEC	50002041	Cochinchina	Vietnam	Modern	R	Complete	CCEC database
Rhinoceros	*sondaicus*	MNHN	ZM-AC-A7970	Unknown	Unknown	Modern	R	Complete	MNHN database
Rhinoceros	*sondaicus*	MNHN	ZM-AC-A7971	Java	Indonesia	Modern	R	Complete	MNHN database
Rhinoceros	*unicornis*	NHMUK	ZD 1884.1.22.1.2	Assam	India	Modern	R	Complete	NHMUK database
Rhinoceros	*unicornis*	NHMUK	ZE 1950.10.18.5	Unknown	Nepal	Modern	L	Complete	NHMUK database
Rhinoceros	*unicornis*	MNHN	ZM-AC-1960-59	Vincennes Zoo	France	Modern	L	Complete	MNHN database

Stephanorhinus	*jeanvireti*	CCEC	V275	Vialette	France	L. Pliocene	R	Complete	Guérin, 1972; Pandolfi, Codrea, & Popescu, 2019
Stephanorhinus	*jeanvireti*	CCEC	V276	Vialette	France	L. Pliocene	L	Complete	Guérin, 1972; Pandolfi, Codrea, & Popescu, 2019
Stephanorhinus	*etruscus*	MNHN	F.1922-5	Senèze	France	L. Pliocene	R	Complete	Indirect confirmation in Guérin, 1980; Pandolfi et al., 2017b
Stephanorhinus	*etruscus*	FSL	210936	Senèze	France	L. Pliocene	R	Complete	Indirect confirmation in Guérin, 1980; Pandolfi et al., 2017b
Stephanorhinus	*etruscus*	FSL	210959	Senèze	France	L. Pliocene	L	Complete	Indirect confirmation in Guérin, 1980; Pandolfi et al., 2017b
Stephanorhinus	*hemitoechus*	NHMUK	PAL PV M 5135	Grays	UK	Pleistocene	R	Complete	Fortelius, Mazza & Sala, 1993
Stephanorhinus	*hemitoechus*	NHMUK	PAL PV OR 45254	Ilford	UK	M. Pleistocene	R	Complete	Fortelius, Mazza & Sala, 1993
Stephanorhinus	*hemitoechus*	CCEC	Pp256	Perpignan	France	Pleistocene	R	Complete	CCEC database
Stephanorhinus	*hundsheimensis*	MNHN	F.SPR 129	Saint-Prest	France	M. Pleistocene	L	Complete	Guérin, Dewolf, & Lautridou, 2003; Pandolfi et al., 2018
Subhyracodon	*mitis*	AMNH	FM 6325	Cedar Creek, White River Form.	Colorado, USA	L. Eocene	R	Complete	Prothero, 2005
Subhyracodon	*occidentalis*	AMNH	FM 1132	Cheyenne River, White River Form.	South Dakota, USA	E. Oligocene	R	Complete	Prothero, 2005
Subhyracodon	*occidentalis*	AMNH	FM 1159	White River Beds	South Dakota, USA	E. Oligocene	R	Complete	Indirect confirmation in Prothero, 2005
Teleoceras	*fossiger*	AMNH	FM 2652	Long Island Rhino Quarry, Ogallala Form.	Kansas, USA	L. Miocene	L	Complete	Indirect confirmation in Prothero, 2005
Teleoceras	*fossiger*	AMNH	FM 2670	Long Island Rhino Quarry, Ogallala Form.	Kansas, USA	L. Miocene	R	Complete	Indirect confirmation in Prothero, 2005
Teleoceras	*fossiger*	YPM	VP 038473	Long Island Rhino Quarry, Ogallala Form.	Kansas, USA	L. Miocene	R	Complete	Indirect confirmation in Prothero, 2005
Teleoceras	*proterum*	AMNH	F:AM 104199	Mixson's Bone Bed, Alucha Form.	Florida, USA	L. Miocene	R	Complete	Indirect confirmation in Prothero, 2005
Trigonias	*wellsi*	AMNH	FM 13226E	Corral Draw, Chadron Form.	South Dakota, USA	L. Eocene	L	Complete	Prothero, 2005

Triplopus	*cubitalis*	AMNH	FM 5095	S. Bitter Creek, Washakie Basin	Wyoming, USA	M. Eocene	R	Complete	Bai et al., 2017
Urtinotherium	*intermedium*	AMNH	FM 26026	Urtyn Obo	China	L. Eocene	R	Complete	Qiu & Wang, 2007; Bai et al., 2018

Ulna

Genus	Species	Institution	Number	Locality	Country	Age	Side	Condition	Confirmation of specific attribution
Acerorhinus	*zernowi*	BSPG	1968 VI 307	Konya-Hatunsaray-Kayadibi-Sarisikinleri	Turkey	L. Miocene	R	Partial proximal	Heissig, 1975
Acerorhinus	*zernowi*	AMNH	FM 26215	Gur Tung Khara Usu	China	M. Miocene	L	Complete	Cerdeño, 1996a
Amphicaenopus	*platycephalus*	AMNH	FM 548	"Protoceras beds", Brule Form.	South Dakota, USA	E. Oligocene	R	Complete	Prothero, 2005
Amynodon	sp.	YPM	VPPU 011219	White River	Utah, USA	M. Eocene	R	Partial proximal	YPM database – very likely *A. advenus*
Aphelops	*malacorhinus*	AMNH	F:AM 104207	Mixson's Bone Bed, Alucha Form.	Florida, USA	L. Miocene	R	Complete	Indirect confirmation in Prothero, 2005
Aphelops	*malacorhinus*	AMNH	F:AM 114832	Box T Ranch, West Draw, Ogallala Form.	Texas, USA	L. Miocene	R	Complete	Prothero, 2005
Aphelops	*malacorhinus*	AMNH	FM 8439	Sappa Creek, Loup Fork Form.	Kansas, USA	L. Miocene	L	Complete	Indirect confirmation in Prothero, 2005
Aphelops	*megalodus*	AMNH	F:AM 114611C	Ashbrook Quarry, Sheep Creek Form.	Nebraska, USA	E. Miocene	L	Complete	Prothero, 2005
Aphelops	*mutilus*	AMNH	F:AM 104037	Rhino Hill Quarry Area, Ogallala Form.	Kansas, USA	L. Miocene	R	Complete	Indirect confirmation in Prothero, 2005
Brachypotherium	*snowi*	MNHN	F.Z-1961	Jebel Zelten	Libya	E. Miocene	L	Complete	Indirect confirmation in Geraads, 2010
Ceratotherium	*cf. primaevum*	MNHN	F.1951-9-189	Bou Hanifia	Algeria	L. Miocene	R	Partial proximal	Arambourg, 1959; Geraads, 2010
Ceratotherium	*cf. primaevum*	MNHN	F.1951-9-213	Bou Hanifia	Algeria	L. Miocene	L	No olecranon tuberosity	Arambourg, 1959; Geraads, 2010
Ceratotherium	*mauritanicum*	MNHN	F.1948-1-151	Aïn Hanech	Algeria	E. Pliocene	L	Complete	Indirect confirmation in Geraads, 2010
Ceratotherium	*neumayri*	MNHN	F.PIK 1040	Pikermi	Greece	L. Miocene	R	No olecranon tuberosity	Indirect confirmation in Pandolfi, 2016; Antoine & Sen, 2016
Ceratotherium	*simum*	NHMUK	ZD 2018.143	Unknown	Unknown	Modern	L	Complete	Mallet et al., 2019
Ceratotherium	*simum*	RBINS	35208	Unknown	Unknown	Modern	R	Complete	RBINS database
Ceratotherium	*simum*	RMCA	1985.32-M-0001	Unknown	Sudan	Modern	L	Complete	RMCA database
Chilotherium	*persiae*	MNHN	F.MAR 3907	Maragha	Iran	L. Miocene	L	Complete	Indirect confirmation in Pandolfi, 2016

Coelodonta	*antiquitatis*	RBINS	I.G.8151-8435-U15	Hofstade	Belgium	Pleistocene	R	No olecranon tuberosity	Indirect confirmation in Guérin, 2010
Coelodonta	*antiquitatis*	RBINS	I.G.8151-8435-U23	Hofstade	Belgium	Pleistocene	R	No olecranon tuberosity	Indirect confirmation in Guérin, 2010
Coelodonta	*antiquitatis*	NHMUK	PAL PV M 12575	Lloyd's Ban, Leadenhall Street, London	UK	Pleistocene	R	Complete	Indirect confirmation in Stuart, 1991
Coelodonta	*antiquitatis*	NHMUK	PAL PV M 5136	Crayford	UK	Pleistocene	R	Partial proximal	Indirect confirmation in Kennard, 1944
Coelodonta	*nihowanensis*	MNHN	F.NIH 048	Nihewan	China	L. Pliocene	L	Complete	MNHN database
Diaceratherium	*aginense*	MHNT	PAL.2013.0.43	Cintegabelle	France	E. Miocene	R	Partial proximal	Indirect confirmation in Ménouret & Guérin, 2009
Diaceratherium	*asphaltense*	NMB	SAU-1662	Saulcet	France	E. Miocene	L	Complete	Jame et al., 2019
Diaceratherium	*aurelianense*	MHNT	PAL.2012.0.61	Marsolan	France	E. Miocene	R	Complete	Formerly *B. brachypus* - Reattribution following Antoine, Bulot & Ginsburg, 2000b; Jame et al., 2019
Diaceratherium	*aurelianense*	MNHN	F.AR 2160	Artenay	France	E. Miocene	R	Complete	Cerdeño, 1993
Diaceratherium	*aurelianense*	NMB	S.O.5573	Ronville	France	E. Miocene	L	Complete	Indirect confirmation in Jame et al., 2019
Diaceratherium	*lamilloquense*	MHNT	PAL.2014.0.2565	Castelmaurou	France	L. Oligocene	R	Complete	Indirect confirmation in Ménouret & Guérin, 2009
Diaceratherium	*lemanense*	AR	B2-1472	Gannat	France	E. Miocene	L	Complete	Boada-Saña, 2008
Diaceratherium	*lemanense*	MNHN	F.SG 9534	Saint-Gérand-le-Puy	France	E. Miocene	R	Complete	Bucher, Ginsburg & Cheneval, 1985
Diceratherium	*tridactylum*	AMNH	FM 525	Big Badlands, Brule Form.	South Dakota, USA	E. Oligocene	R	Partial proximal	Prothero, 2005
Dicerorhinus	*sumatrensis*	NHMUK	ZD 1879.6.14.2	Unknown	Malaysia	Modern	R	Complete	NHMUK database
Dicerorhinus	*sumatrensis*	NHMUK	ZE 1948.12.20.1	Unknown	Unknown	Modern	L	Complete	NHMUK database
Dicerorhinus	*sumatrensis*	NHMUK	ZE 1949.1.11.1	Tring	Indonesia	Modern	L	Complete	NHMUK database
Diceros	*bicornis*	MNHN	ZM-AC-1936-644	Unknown	Unknown	Modern	L	Complete	MNHN database
Diceros	*bicornis*	CCEC	50002047	Unknown	Unknown	Modern	R	Complete	CCEC database

Diceros	*bicornis*	RBINS	9714	Unknown	Democratic Republic of the Congo	Modern	L	Complete	RBINS database
Dihoplus	*megarhinus*	FSL	41321	Perpignan	France	L. Pliocene	L	Complete	Indirect confirmation in Guérin, 1980
Dihoplus	*megarhinus*	CCEC	Pp308	Perpignan	France	L. Pliocene	R	Complete	Indirect confirmation in Guérin, 1980
Dihoplus	*pikermiensis*	MNHN	F.PIK 920	Pikermi	Greece	L. Miocene	R	Complete	Indirect confirmation in Antoine & Saraç, 2005; Pandolfi, Gasparik & Piras, 2015
Elasmotherium	*sibiricum*	NHMUK	PAL PV M 5230a	Siberia	Russia	Pleistocene	R	No olecranon tuberosity	NHMUK database
Hoploaceratherium	*tetradactylum*	MNHN	F.SA 10170-28	Sansan	France	M. Miocene	R	Complete	Heissig, 2012
Hoploaceratherium	*tetradactylum*	MNHN	F.SA 15628	Sansan	France	M. Miocene	L	Complete	Heissig, 2012
Hyrachyus	*eximius*	AMNH	FM 12673	Henry's Fork, Bridger Form.	Wyoming, USA	M. Eocene	L	Partial proximal	Indirect confirmation in Radinsky, 1967
Hyrachyus	*modestus*	AMNH	FM 12667	Millersville, Bridger Form.	Wyoming, USA	M. Eocene	L	Complete	Indirect confirmation in Radinsky, 1967
Hyrachyus	*modestus*	AMNH	FM 13089	Cottonwood Creek, Bridger Form.	Wyoming, USA	M. Eocene	R	Complete	Bai et al., 2017
Hyrachyus	*modestus*	AMNH	FM 17436	Upper Huerfano	Colorado, USA	E. Eocene	R	Complete	Robinson, 1966
Hyracodon	*nebraskensis*	AMNH	FM 1176	Cheyenne River, Brule Form.	South Dakota, USA	E. Oligocene	L	Complete	Wall & Hickerson, 1995
Juxia	*sharamurenense*	AMNH	FM 20264	Ula Usu, Shara Murun Form.	China	M. Eocene	R	Complete	Bai et al., 2018
Lartetotherium	*sansaniense*	MNHN	F.SA 15629	Sansan	France	M. Miocene	L	Partial proximal	Heissig, 2012
Menoceras	*arikarense*	AMNH	FM 144599	Agate Springs Quarry, Anderson Ranch Form.	Nebraska, USA	E. Miocene	L	Complete	Indirect confirmation in Prothero, 2005
Menoceras	*arikarense*	AMNH	FM 144603	Agate Springs Quarry, Anderson Ranch Form.	Nebraska, USA	E. Miocene	L	Complete	Indirect confirmation in Prothero, 2005
Menoceras	*arikarense*	AMNH	FM 22487	Agate Springs Quarry, Anderson Ranch Form.	Nebraska, USA	E. Miocene	R	Complete	Indirect confirmation in Prothero, 2005

Metamynodon	*planifrons*	AMNH	FM 1089	Metamynodon Beds, Cottonwood Creek	South Dakota, USA	E. Oligo-cene	R	Complete	AMNH database
Paraceratherium	*bugtiense*	AMNH	FM 21977	Dera Bugti	Pakistan	E. Miocene	R	Partial proximal	Indirect confirmation in Qiu & Wang, 2007; Bai et al., 2018
Paraceratherium	*grangeri*	AMNH	FM 26169	Nom Khong Obo	China	E. Oligo-cene	R	Partial proximal	Qiu & Wang, 2007
Paramynodon	*birmanicus*	AMNH	FM 20013	Top Pondaung Clays, Bahin	Burma	M. Eocene	R	Complete	Colbert, 1938
Peraceras	*profectum*	AMNH	F:AM 114931	Pojoaque Bluffs, Tesuque Form.	New Mexico, USA	M. Mio-cene	R	Complete	Prothero, 2005
Peraceras	*profectum*	AMNH	F:AM 114970	Pojoaque Bluffs, Tesuque Form.	New Mexico, USA	M. Mio-cene	R	Partial proximal	Prothero, 2005
Prosantorhinus	*douvillei*	MNHN	F.BA 2722	Baigneaux	France	E. Miocene	L	Complete	Cerdeño, 1996b
Prosantorhinus	*douvillei*	MNHN	F.BA 2723	Baigneaux	France	E. Miocene	L	Complete	Cerdeño, 1996b
Prosantorhinus	*douvillei*	MNHN	F.BA 2725	Baigneaux	France	E. Miocene	L	Complete	Cerdeño, 1996b
Protaceratherium	*minutum*	FSL	213781	Budenheim	Germany	L. Oligo-cene	R	Complete	Antunes & Ginsburg, 1983
Rhinoceros	*philippinensis*	NMP	2014-II-J1-284	Kalinga	Philippines	M. Pleisto-cene	R	No olecranon tuberosity	Ingicco et al., 2018
Rhinoceros	*sondaicus*	CCEC	50002041	Cochinchina	Vietnam	Modern	R	Complete	CCEC database
Rhinoceros	*sondaicus*	MNHN	ZM-AC-A7970	Unknown	Unknown	Modern	R	Complete	MNHN database
Rhinoceros	*sondaicus*	MNHN	ZM-AC-A7971	Java	Indonesia	Modern	R	Complete	MNHN database
Rhinoceros	*unicornis*	NHMUK	ZD 1884.1.22.1.2	Assam	India	Modern	R	Complete	NHMUK database
Rhinoceros	*unicornis*	NHMUK	ZE 1950.10.18.5	Unknown	Nepal	Modern	L	Complete	NHMUK database
Rhinoceros	*unicornis*	MNHN	ZM-AC-1960-59	Vincennes Zoo	France	Modern	L	Complete	MNHN database
Stephanorhinus	*jeanvireti*	CCEC	V274	Vialette	France	L. Pliocene	R	Complete	Guérin, 1972; Pan-dolfi, Codrea, & Popescu, 2019
Stephanorhinus	*etruscus*	CCEC	20164166	Saint-Vallier	France	E. Pleisto-cene	R	Complete	Indirect confirmation in Guérin et al., 2004; Pandolfi et al., 2017b
Stephanorhinus	*hemitoechus*	NHMUK	PAL PV OR 45249	Ilford	UK	M. Pleisto-cene	R	No olecranon tuberosity	Fortelius, Mazza & Sala, 1993

Stephanorhinus	*hemitoechus*	CCEC	Pp256	Perpignan	France	Pleistocene	R	Complete	CCEC database
Subhyracodon	*occidentalis*	AMNH	FM 1132	Cheyenne River, White River Form.	South Dakota, USA	E. Oligo-cene	R	Complete	Prothero, 2005
Subhyracodon	*occidentalis*	AMNH	FM 1140	Cheyenne River, White River Form.	South Dakota, USA	E. Oligo-cene	L	Complete	Prothero, 2005
Subhyracodon	*occidentalis*	AMNH	FM 563	Oreodon beds, White River Form.	South Dakota, USA	E. Oligo-cene	L	Complete	Indirect confirmation in Prothero, 2005
Teleoceras	*fossiger*	AMNH	FM 2656	Long Island Rhino Quarry, Ogallala Form.	Kansas, USA	L. Miocene	L	Complete	Indirect confirmation in Prothero, 2005
Teleoceras	*fossiger*	YPM	VP 038658	Long Island Rhino Quarry, Ogallala Form.	Kansas, USA	L. Miocene	L	Complete	Indirect confirmation in Prothero, 2005
Teleoceras	*fossiger*	YPM	VP 038660	Long Island Rhino Quarry, Ogallala Form.	Kansas, USA	L. Miocene	L	Complete	Indirect confirmation in Prothero, 2005
Teleoceras	*proterum*	AMNH	F:AM 104200	Mixson's Bone Bed, Alucha Form.	Florida, USA	L. Miocene	R	Complete	Prothero, 2005
Trigonias	*wellsi*	AMNH	FM 13226E	Corral Draw, Chadron Form.	South Dakota, USA	L. Eocene	R	Complete	Prothero, 2005
Trigonias	*wellsi*	AMNH	FM 13226E	Corral Draw, Chadron Form.	South Dakota, USA	L. Eocene	R	Partial proximal	Prothero, 2005

Appendix 2: Designation and location of the anatomical landmarks placed on each bone

Bone	Anatomical LM	Curve sliding semi-LM	Surface sliding semi-LM	Total
Humerus (complete)	25	457	598	1080
Humerus (partial distal part)	12	206	280	498
Radius	14	309	510	833
Ulna (complete)	18	265	393	676
Ulna (without olecranon tubercle)	15	299	314	592
Ulna (partial proximal part)	10	181	236	427

Table S2A: Total number of anatomical landmarks (LM), curve sliding and surface sliding semi-landmarks for each bone.

LM	Designation
1	Most distal point of the lateral border of the bicipital groove
2	Most proximal point of the lateral border of the bicipital groove
3	Most proximal point of the medial border of the bicipital groove
4	Most distal point of the medial border of the bicipital groove
5	Most cranial point of the lesser tubercle convexity
6	Most medio-caudal point of the lesser tubercle convexity
7	Most medial point of the humeral head surface
8	Most caudo-distal point of the humeral head surface
9	Most lateral point of the humeral head surface
10	Most proximal point of the greater tubercle convexity
11	Most proximal point of the m. infraspinatus lateral insertion
12	Most distal point of the m. infraspinatus lateral insertion
13	Most distal point of the deltoid tuberosity
14	Most lateral point of the lateral epicondyle
15	Most cranio-lateral point of the capitulum
16	Most cranio-proximal point of contact between the trochlea and the capitulum
17	Most cranial point of the trochlea groove
18	Most cranio-medial point of the dorsal side of the trochlea
19	Most cranio-medial point of the ventral side of the trochlea
20	Most cranio-lateral point of the ventral side of the trochlea
21	Most caudo-distal point of contact between the capitulum and the trochlea
22	Most medial point of the medial epicondyle
23	Most medial point of the medial condyle
24	Most proximal point of the greater tubercle
25	Most proximal point of the epicondylar crest
Curve	**Designation**
C1	Bicipital groove: from LM1 to LM4
C2	Lesser tubercle convexity crest: from LM5 to LM6
C3	Humeral head: from LM7 to LM9
C4	M. infraspinatus cranio-distal insertion: from LM10 to LM11
C5	Tricipital line: from LM13 to LM8
C6	Trochlea: from LM15 to LM21
C7	Crest between capitulum and trochlea: from LM16 to LM21
C8	Epicondylar crest: from LM25 to LM14

Table S2B: Designation of anatomical landmarks on the humerus.

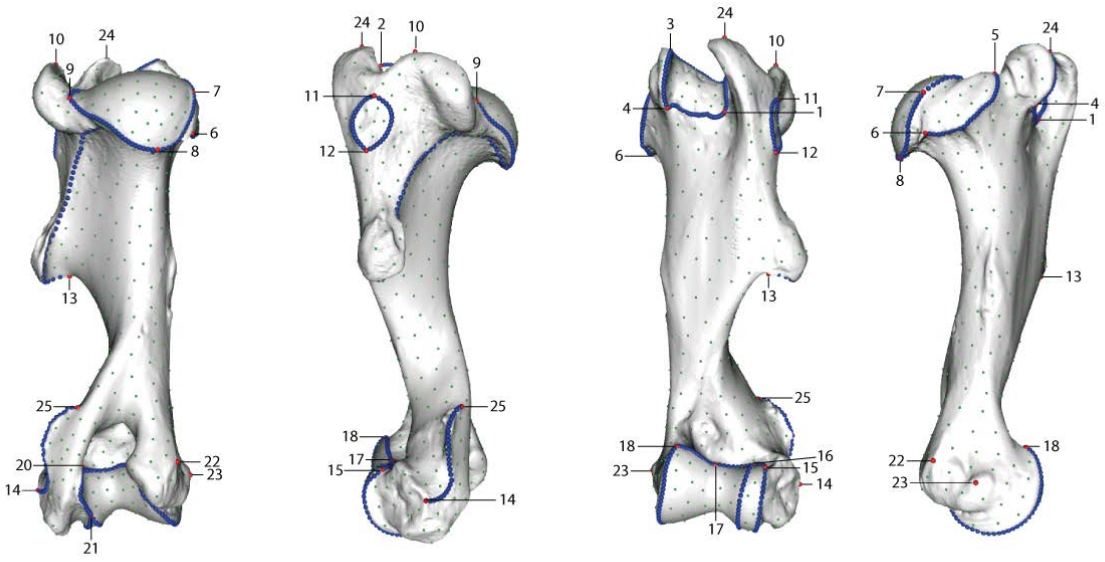

Figure S2C: Location of anatomical landmarks (red spheres), curve sliding (blue spheres) and surface sliding (green spheres) semi-landmarks placed on the humerus (complete analysis). From left to right: caudal, lateral, cranial and medial views. Numbers refer to anatomical landmarks designation detailed in Table S2B. Landmark n°19 situated in the olecranon fossa is not visible.

LM	Designation
1	Most distal point of the deltoid tuberosity
2	Most lateral point of the lateral epicondyle
3	Most cranio-lateral point of the capitulum
4	Most cranio-proximal point of contact between the trochlea and the capitulum
5	Most cranial point of the trochlea groove
6	Most cranio-medial point of the dorsal side of the trochlea
7	Most cranio-medial point of the ventral side of the trochlea
8	Most cranio-lateral point of the ventral side of the trochlea
9	Most caudo-distal point of contact between the capitulum and the trochlea
10	Most medial point of the medial epicondyle
11	Most medial point of the medial condyle
12	Most proximal point of the epicondylar crest
Curve	**Designation**
C1	Limit line: from LM1 to LM1 (perpendicular to the shaft axis)
C2	Trochlea: from LM3 to LM9
C3	Crest between capitulum and trochlea: from LM4 to LM9
C4	Epicondylar crest: from LM12 to LM2

Table S2D: Designation of anatomical landmarks on the humerus (partial analysis).

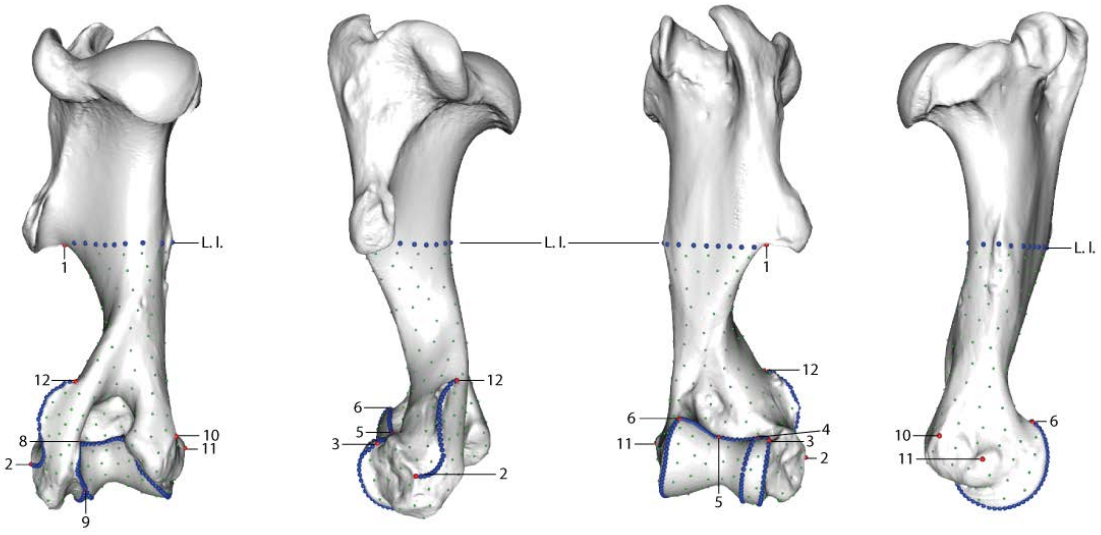

Figure S2E: Location of anatomical landmarks (red spheres), curve sliding (blue spheres) and surface sliding (green spheres) semi-landmarks placed on the humerus (partial distal part). From left to right: caudal, lateral, cranial and medial views. Numbers refer to anatomical landmarks designation detailed in Table S2D. Landmark n°7 situated in the olecranon fossa is not visible. L.l.: limit line (removed after sliding process).

LM	Designation
1	Most caudo-lateral point of the lateral glenoid cavity
2	Most cranio-lateral point of the lateral glenoid cavity
3	Tip of the coronoid process
4	Most cranial point of the medial glenoid cavity
5	Most caudo-medial point of the medial glenoid cavity
6	Tip of the caudal process of the glenoid cavity ridge
7	Most lateral point of the lateral tuberosity
8	Most medial point of the transversal crest
9	Tip of the radial styloid process
10	Most cranio-lateral point of the articular facet for the scaphoid
11	Most lateral point of the articular facet for the semilunar
12	Most caudo-lateral point of the articular facet for the semilunar
13	Most caudo-lateral point of the articular facet for the scaphoid
14	Most cranio-proximal point of the dorsal extension of the articular facet for the scaphoid
Curve	**Designation**
C1	Proximal glenoid cavity: from LM1 to LM6
C2	Lateral synovial articulation for the ulna: from LM1 to LM6
C3	Articular facet for the scaphoid: from LM9 to LM14
C4	Articular facet for the semilunar: from LM10 to LM13
C5	Disto-lateral articulation surface for ulna: from LM11 to LM12

Table S2F: Designation of anatomical landmarks on the radius.

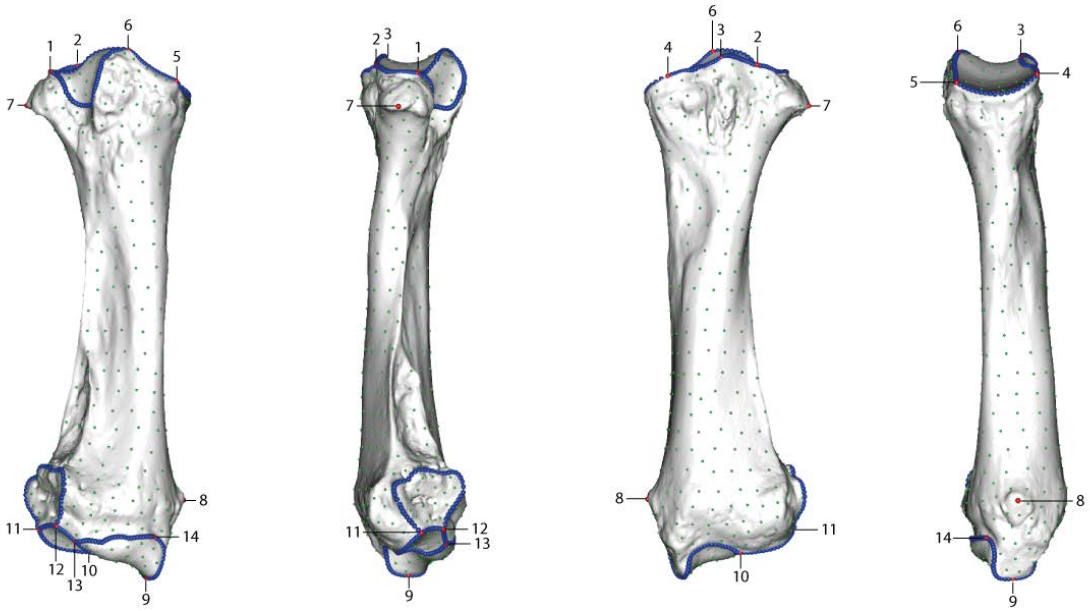

Figure S2G: Location of anatomical landmarks (red spheres), curve sliding (blue spheres) and surface sliding (green spheres) semi-landmarks placed on the radius. From left to right: caudal, lateral, cranial and medial views. Numbers refer to anatomical landmarks designation detailed in Table S2F.

LM	Designation
1	Most proximal point of the olecranon tuberosity
2	Most lateral point of the olecranon tuberosity
3	Most caudo-distal point of the olecranon tuberosity
4	Most medial point of the olecranon tuberosity
5	Cranial tip of the anconeus process
6	Most latero-distal point of the lateral part of the trochlear notch articular surface
7	Maximum concavity point of the distal border of the trochlear notch articular surface
8	Most medio-distal point of the medial part of the trochlear notch articular surface
9	Most distal point of the proximo-lateral articular facet for the radius
10	Most distal point of the proximal synostosis surface for the radius (= most proximal point of the interosseus space)
11	Most medio-caudal point of the distal radio-ulnar synostosis surface
12	Most cranio-lateral point of the distal radio-ulnar synostosis surface
13	Most disto-medial point of the distal articular surface with the radius
14	Most disto-lateral point of the articular surface with the radius
15	Caudo-distal tip of ulnar styloid process
16	Most proximal contact point between the articular surfaces for the pisiform and the triquetrum
17	Most lateral point of the distal epiphysis
18	Most distal contact point between the caudal border of the ulna and the articular surface with the pisiform
Curve	**Designation**
C1	Articular surface of the trochlear notch: from LM5 to LM8
C2	Proximal articular facet for the radius: from LM8 to LM6
C3	Medial border of the proximal radio-ulnar synostosis surface: from LM8 to LM10
C4	Articular facet with the triquetrum: from LM13 to LM16
C5	Articular facet with the radius: from LM13 to LM14
C6	Articular facet with the pisiform: from LM15 to LM16
C7	Caudal border of the ulna: from LM3 to LM18

Table S2H: Designation of anatomical landmarks on the ulna (complete analysis).

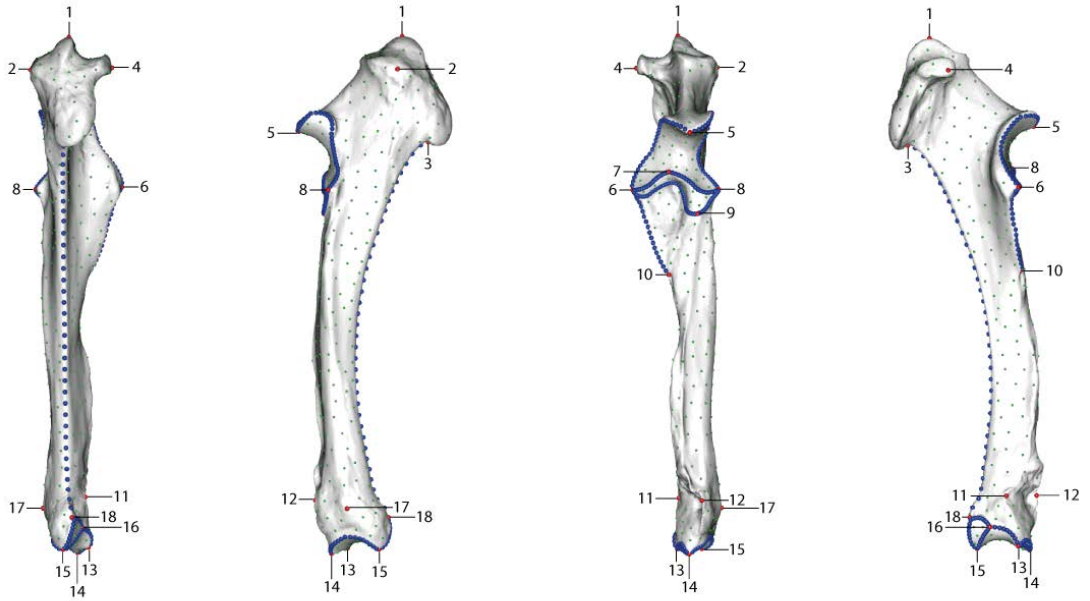

Figure S2I: Location of anatomical landmarks (red spheres), curve sliding (blue spheres) and surface sliding (green spheres) semi-landmarks placed on the ulna (complete analysis). From left to right: caudal, lateral, cranial and medial views. Numbers refer to anatomical landmarks designation detailed in Table S2H.

LM	Designation
1	Most caudo-distal point of the olecranon tuberosity
2	Cranial tip of the anconeus process
3	Most latero-distal point of the lateral part of the trochlear notch articular surface
4	Maximum concavity point of the distal border of the trochlear notch articular surface
5	Most medio-distal point of the medial part of the trochlear notch articular surface
6	Most distal point of the proximo-lateral articular facet for the radius
7	Most distal point of the proximal synostosis surface for the radius (= most proximal point of the interosseus space)
8	Most medio-caudal point of the distal radio-ulnar synostosis surface
9	Most cranio-lateral point of the distal radio-ulnar synostosis surface
10	Most disto-medial point of the distal articular surface with the radius
11	Most disto-lateral point of the articular surface with the radius
12	Caudo-distal tip of ulnar styloid process
13	Most proximal contact point between the articular surfaces for the pisiform and the triquetrum
14	Most lateral point of the distal epiphysis
15	Most distal contact point between the caudal border of the ulna and the articular surface with the pisiform
Curve	**Designation**
C1	Articular surface of the trochlear notch: from LM2 to LM5
C2	Proximal articular facet for the radius: from LM5 to LM3
C3	Medial border of the proximal radio-ulnar synostosis surface: from LM5 to LM7
C4	Articular facet with the triquetrum: from LM10 to LM13
C5	Articular facet with the radius: from LM10 to LM11
C6	Articular facet with the pisiform: from LM12 to LM13
C8	Medial proximal limit: from LM1 to LM3 (straight line between the two landmarks)
C9	Lateral proximal limit: from LM1 to LM5 (straight line between the two landmarks)

Table S2J: Designation of anatomical landmarks on the ulna (without olecranon tubercle).

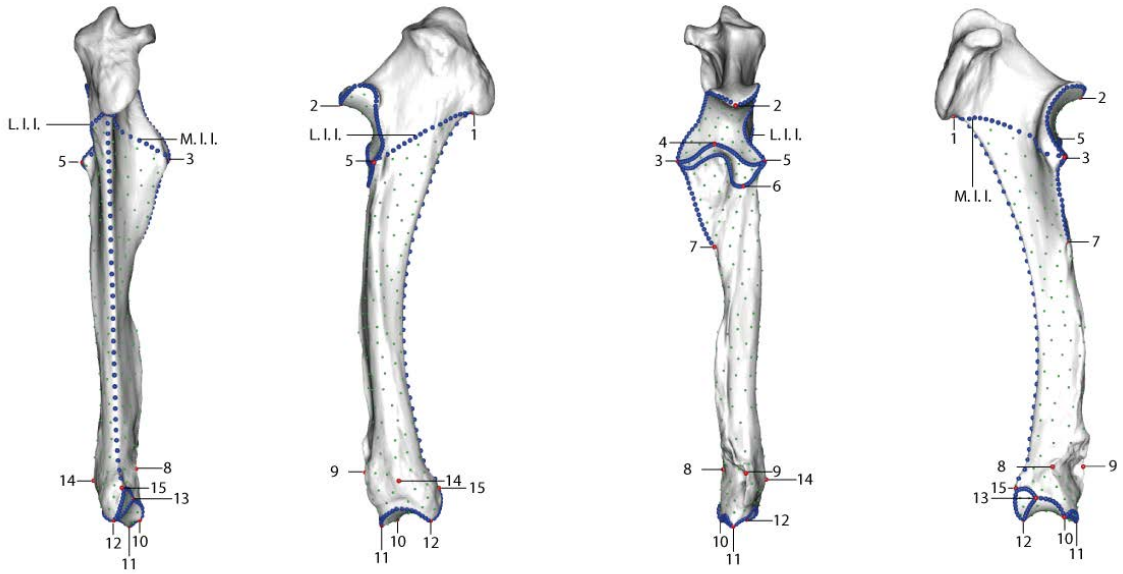

Figure S2K: Location of anatomical landmarks (red spheres), curve sliding (blue spheres) and surface sliding (green spheres) semi-landmarks placed on the ulna (without olecranon tubercle). From left to right: caudal, lateral, cranial and medial views. Numbers refer to anatomical landmarks designation detailed in Table S2J. L.l.l.: lateral limit line; M.l.l.: medial limit line (both removed after sliding process).

LM	Designation
1	Most proximal point of the olecranon tuberosity
2	Most lateral point of the olecranon tuberosity
3	Most caudo-distal point of the olecranon tuberosity
4	Most medial point of the olecranon tuberosity
5	Cranial tip of the anconeus process
6	Most latero-distal point of the lateral part of the trochlear notch articular surface
7	Maximum concavity point of the distal border of the trochlear notch articular surface
8	Most medio-distal point of the medial part of the trochlear notch articular surface
9	Most distal point of the proximo-lateral articular facet for the radius
10	Most distal point of the proximal synostosis surface for the radius (= most proximal point of the interosseus space)
Curve	**Designation**
C1	Articular surface of the trochlear notch: from LM5 to LM8
C2	Proximal articular facet for the radius: from LM8 to LM6
C3	Medial border of the proximal radio-ulnar synostosis surface: from LM8 to LM10
C4	Limit line: from LM10 to LM10 (perpendicular to the shaft axis)

Table S2L: Designation of anatomical landmarks on the ulna (proximal partial analysis).

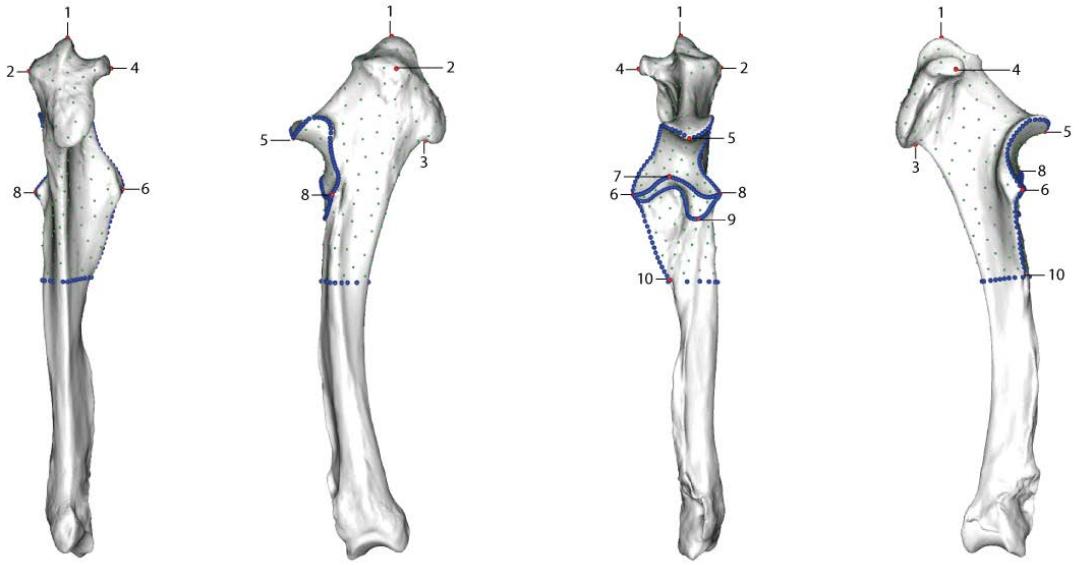

Figure S2M: Location of anatomical landmarks (red spheres), curve sliding (blue spheres) and surface sliding (green spheres) semi-landmarks placed on the ulna (proximal partial analysis). From left to right: caudal, lateral, cranial and medial views. Numbers refer to anatomical landmarks designation detailed in Table S2L.

Appendix 3: Complete list of gracility index and mean body mass compiled from literature

Taxa	Meas.	TD	Length	GI-MC3	Mean	Sources
Acerorhinus zernowi	#1	44.00	168.50	0.26	0.27	Measurement given on AMNH FM 129918 by Cerdeño, 1996a
	#2	44.60	166.00	0.27		Measurement given on AMNH FM 129855 by Cerdeño, 1996a
	#3	41.50	152.10	0.27		Measurement given on AMNH FM 129899 by Cerdeño, 1996a
Alicornops simorrense	#1	41.50	165.50	0.25	0.27	Measurement given on MNHN F. SA 5863 by Heissig, 2012
	#2	41.50	168.50	0.25		Measurement given on MNHN F. SA 5869 by Heissig, 2012
	#3	35.25	117.75	0.30		Mean measurements given by Guérin, 1980
Amphicaenopus platycephalus	#1	44.42	174.43	0.25	0.24	Direct measurement on AMNH FM 548
	#2	26.00	116.00	0.22		Measurement on picture of AMNH FM 12453 in Prothero, 2005
Amynodon advenus	#1	30.80	156.00	0.20	0.20	Measurement given on YPM VPPU 41372-552 by Wilson & Schiebout, 1981
	#2	1.03	5.35	0.19		Measurement on picture of mounted specimen at the AMNH (in pixels)
	#3	33.00	163.00	0.20		Measurement given on AMNH FM 1933 in Colbert, 1938
Aphelops malacorhinus	#1	39.40	169.20	0.23	0.23	Direct measurement on YPM VP 38249
	#2	38.50	164.50	0.23		Measurement on picture of AMNH F:AM 104164 in Prothero, 2005
	#3	40.60	178.00	0.23		Mean measurements given by Mihlbachler, 2005
Aphelops megalodus	#1	38.25	131.51	0.29	0.30	Direct measurement on AMNH F:AM 108926A
	#2	41.00	140.00	0.29		Mean measurements given by Prothero, 2005
	#3	36.50	120.50	0.30		Mean measurements given by Prothero & Manning, 1987
Aphelops mutilus	#1	54.14	184.20	0.29	0.32	Direct measurement on AMNH F:AM 104038
	#2	48.00	153.00	0.31		Mean measurements given by Prothero, 2005
	#3	46.00	136.00	0.34		Measurement given by Mead, 2000
Brachypotherium brachypus	#1	56.56	185.63	0.30	0.30	Measurement on picture on FSL 320481
	#2	55.58	189.19	0.29		Measurement on picture on FSL 320232
	#3	55.20	184.40	0.30		Measurement given by Cerdeño, 1993
Brachypotherium fatehjan-gense	#1	NA	NA	NA	NA	No data
Brachypotherium snowi	#1	57.07	161.85	0.35	0.37	Measurement on picture on NHMUK PAL VP M 29275
	#2	60.50	159.50	0.38		Measurement given by Guerin, 2000
Cadurcodon ardynensis	#1	1.08	6.33	0.17	0.17	Measurement on picture in Gromova, 1954
Ceratotherium cf. primaevum	#1	61.00	179.00	0.34	0.34	Measurement given by Arambourg, 1959
Ceratotherium mauritanicum	#1	72.00	215.00	0.33	0.33	Measurement given by Arambourg, 1970
Ceratotherium neumayri	#1	57.63	174.43	0.33	0.33	Direct measurement on YPM VP 20687

	#2	62.50	188.40	0.33		Mean measurements given by Guérin, 1980
	#3	63.55	187.17	0.34		Mean measurements given by Guérin, 2011
Ceratotherium simum	#1	53.26	147.23	0.36	0.33	Direct measurement on NHMUK ZD 1964.3.9.1
	#2	57.15	184.06	0.31		Direct measurement on AMNH M-51854
	#3	59.49	188.69	0.32		Direct measurement on AMNH M-51855
Chilotherium persiae	#1	41.00	134.00	0.31	0.31	Measurement given by Geraads, 1994
	#2	43.00	141.00	0.30		Measurement given by Geraads, 1994
Coelodonta antiquitatis	#1	56.93	189.10	0.30	0.30	Measurement on picture on FSL 396158
	#2	55.79	181.40	0.31		Measurement on picture on NHMUK PAL PV M 13672
	#3	56.87	190.54	0.30		Measurement on picture of NHMUK PAL PV OR 28567
Coelodonta nihowanensis	#1	48.81	200.00	0.24	0.24	Measurement on picture in Tong *et al.*, 2014
Diaceratherium aginense	#1	52.06	157.97	0.33	0.30	Direct measurement on AR B2 1503
	#2	38.90	145.57	0.27		Direct measurement on AR B2 2141
	#3	36.65	125.64	0.29		Measurement on picture in Ménouret & Guérin, 2009
Diaceratherium asphaltense	#1	51.63	155.35	0.33	0.33	Measurement on picture in Boada-Saña, 2008
	#2	NA	NA	0.33		Gracility index given by Becker, 2009
Diaceratherium aurelianense	#1	43.20	124.40	0.35	0.36	Measurement given by Cerdeño, 1993
	#2	47.60	133.40	0.36		Measurement given by Cerdeño, 1993
	#3	53.70	143.20	0.38		Measurement given by Cerdeño, 1993
Diaceratherium lamilloquense	#1	46.14	158.54	0.29	0.29	Direct measurement on MHNT PAL.2014.0.2564
	#2	45.33	162.93	0.28		Measurement on picture in Boada-Saña, 2008
	#3	47.69	163.44	0.29		Measurement on picture AR B2 3246 in Boada-Saña, 2008
Diaceratherium lemanense	#1	43.53	152.57	0.29	0.28	Direct measurement on AR B2 1482
	#2	40.63	149.20	0.27		Measurement on picture in Ménouret & Guérin, 2009
	#3	52.48	177.54	0.30		Measurement on picture in Ménouret & Guérin, 2009
Diceratherium annectens	#1	33.94	160.96	0.21	0.21	Direct measurement on YPM VP 12492
	#2	45.00	225.00	0.20		Measurement on picture of AMNH FM 112188 in Prothero, 2005
	#3	37.00	168.00	0.22		Mean measurements given by Prothero, 2005
Diceratherium armatum	#1	41.95	213.26	0.20	0.21	Direct measurement on AMNH F:AM 112178
	#2	45.00	203.00	0.22		Mean measurements given by Prothero, 2005
Diceratherium tridactylum	#1	1.51	5.98	0.25	0.25	Measurement on picture of AMNH FM 538 (in pixels)
Dicerorhinus aff. sansaniensis	#1	NA	NA	NA	NA	No data
Dicerorhinus sumatrensis	#1	44.03	159.52	0.28	0.28	Direct measurement on NHMUK ZD 1879.6.14.2
	#2	49.95	166.37	0.30		Direct measurement on NHMUK ZD 1894.9.24.1

	#3	44.99	166.49	0.27		Direct measurement on NHMUK ZD 1931.5.28.1
Diceros bicornis	#1	51.23	191.39	0.27	0.27	Direct measurement on AMNH M-27757
	#2	43.74	178.41	0.25		Direct measurement on AMNH M-81805
	#3	51.34	177.08	0.29		Direct measurement on AMNH M-113776
Dihoplus megarhinus	#1	60.77	225.00	0.27	0.27	Mean measurements given by Guérin, 1980
Dihoplus pikermiensis	#1	54.13	174.04	0.31	0.33	Measurement on picture in Giaourtsakis, 2009
	#2	60.02	176.55	0.34		Measurement on picture in Giaourtsakis, 2009
Dihoplus schleiermacheri	#1	50.41	203.00	0.25	0.25	Measurement on picture on NHMUK PAL PV OR 1282
	#2	55.10	193.50	0.28		Mean measurements given by Guérin, 1980
	#3	35.39	155.45	0.23		Measurement on picture on MNHN FMCF 60 in Métais & Sen, 2018
Elasmotherium sibiricum	#1	70.76	285.21	0.25	0.25	Measurement on picture on NHMUK PAL PV M 12429
	#2	0.66	2.58	0.26		Measurement on picture in Kosintsev et al., 2018 (in pixels)
	#3	0.89	3.49	0.26		Measurement on picture in Belyaeva, 1977 (in pixels)
Hispanotherium beonense	#1	43.54	178.31	0.24	0.25	Direct measurement on MHNT PAL.2015.0.838
	#2	45.65	175.73	0.26		Measurement on picture in Antoine 2002
	#3	40.64	169.21	0.24		Measurement on picture in Antoine 2002
Hoploaceratherium tetradactylum	#1	46.96	180.87	0.26	0.26	Measurement on picture on MNHN F. SA 10170 in Heissig, 2012
	#2	42.83	169.57	0.25		Measurement on picture on MNHN F. SA 13495 in Heissig, 2012
	#3	45.70	168.70	0.27		Mean measurements given by Guérin, 1980
Hyrachyus eximius	#1	19.50	106.06	0.18	0.16	Direct measurement on AMNH FM 1607a
	#2	16.33	100.08	0.16		Direct measurement on AMNH FM 12673
	#3	15.42	107.94	0.14		Direct measurement on AMNH FM 93050
Hyrachyus modestus	#1	16.50	92.93	0.18	0.16	Direct measurement on AMNH FM 17436
	#2	11.12	74.66	0.15		Direct measurement on AMNH FM 91775
	#3	11.70	78.50	0.15		Measurement given on AMNH FM 12664 in Bai et al., 2017
Hyracodon leidyanus	#1	NA	NA	NA	NA	No data
Hyracodon nebraskensis	#1	1.54	10.19	0.15	0.16	Measurement on picture on YPM VPPU 11414 in Scott & Jepsen, 1941 (in pixels)
	#2	18.55	113.26	0.16		Measurement on picture on YPM VPPU 12591
Juxia sharamurenense	#1	38.25	229.37	0.17	0.15	Direct measurement on AMNH FM 20289
	#2	38.50	268.99	0.14		Measurement on picture on IVPP V.2891 in Qiu & Wang, 2007
Lartetotherium sansaniense	#1	47.41	171.48	0.28	0.24	Measurement on picture on FSL 214225

	#2	41.00	182.50	0.22		Measurement given on MNHN F. SA 5852 by Heissig, 2012
	#3	42.50	185.00	0.23		Measurement given on MNHN F. SA 13493 by Heissig, 2012
Menoceras arikarense	#1	25.80	135.60	0.19	0.19	Mean measurements given by Mihlbachler, 2007
	#2	26.00	132.00	0.20		Mean measurements given by Prothero, 2005
Metamynodon planifrons	#1	42.47	135.70	0.31	0.30	Direct measurement on YPM VPPU 10886
	#2	46.00	166.00	0.28		Measurement given on AMNH FM 546 in Colbert, 1938
Paraceratherium bugtiense	#1	106.69	406.79	0.26	0.26	Direct measurement on NHMUK PAL PV M 12268
Paraceratherium grangeri	#1	163.00	535.00	0.30	0.25	Measurement given in Qiu & Wang, 2007
	#2	1.32	5.69	0.23		Measurement on picture on AMNH FM 26166 in Granger & Gregory, 1936 (in pixels)
	#3	1.88	8.75	0.21		Measurement on picture on AMNH FM 21618 in Granger & Gregory, 1936 (in pixels)
Paramynodon birmanicus	#1	36.17	160.21	0.23	0.22	Direct measurement on AMNH FM 20013
	#2	33.00	152.00	0.22		Measurement given on AMNH FM 20034 in Colbert, 1938
Peraceras hessei	#1	NA	NA	NA	NA	No data
Peraceras profectum	#1	33.00	101.00	0.33	0.33	Mean measurements given by Prothero, 2005
Peraceras superciliosum	#1	47.57	168.03	0.28	0.32	Direct measurement on AMNH F:AM 114915
	#2	47.50	143.00	0.33		Measurement given by Mead, 2000
	#3	56.40	165.50	0.34		Measurement given by Mead, 2000
Plesiaceratherium fahlbuschi	#1	NA	NA	NA	NA	No data
Plesiaceratherium mirallesi	#1	43.77	186.45	0.23	0.24	Direct measurement on MHNT PAL.2015.0.902
	#2	44.80	186.03	0.24		Direct measurement on MHNT PAL.2015.0.1338.1
	#3	42.75	176.89	0.24		Measurement on picture in Antoine 2002
Plesiaceratherium platyodon	#1	NA	NA	NA	NA	No data
Prosantorhinus douvillei	#1	32.00	81.50	0.39	0.42	Measurement given by Heissig, 2017
	#2	31.50	79.00	0.40		Measurement given by Heissig, 2017
	#3	39.50	82.00	0.48		Measurement given by Heissig, 2017
Protaceratherium minutum	#1	1.71	8.57	0.20	0.20	Measurement on picture in Roman, 1924 (in pixels)
Rhinoceros philippinensis	#1	1.08	3.99	0.27	0.27	Direct measurement on NMP 2014-II-J1-288
Rhinoceros sondaicus	#1	44.53	145.90	0.31	0.32	Direct measurement on NHMUK ZD 1865.8.22.1
	#2	57.29	178.80	0.32		Direct measurement on NHMUK ZD 1871.12.29.7
	#3	59.70	186.66	0.32		Direct measurement on NHMUK ZD 1921.5.15.1
Rhinoceros unicornis	#1	57.28	221.38	0.26	0.26	Direct measurement on NHMUK ZD 1884.1.22.1.2
	#2	48.17	192.67	0.25		Direct measurement on NHMUK ZD 1953.8.13.2
	#3	56.01	199.76	0.28		Direct measurement on NHMUK ZE 1961.5.10.1
Stephanorhinus jeanvireti	#1	57.55	226.91	0.25	0.25	Mean measurements given by Guérin, 1980

Stephanorhinus etruscus	#1	46.89	203.31	0.23	0.23	Measurement on picture on NHMUK PAL PV OM 44571
	#2	48.33	201.55	0.24		Mean measurements given by Guérin, 1980
	#3	47.91	204.32	0.23		Measurement on picture in Pandolfi *et al.*, 2017
Stephanorhinus hemitoechus	#1	55.76	198.48	0.28	0.28	Measurement on picture on NHMUK PAV PV M 36620
	#2	49.73	172.86	0.29		Measurement on picture on NHMUK PAL PV M 82703
	#3	52.17	191.79	0.27		Mean measurements given by Guérin, 1980
Stephanorhinus hundsheimensis	#1	51.06	204.69	0.25	0.25	Mean measurements given by Guérin, 1980
Subhyracodon mitis	#1	3.98	17.83	0.22	0.22	Measurement on picture on YPM VPPU 11418 in Scott & Jepsen, 1941 (in pixels)
	#2	27.00	120.00	0.23		Mean measurements given by Prothero, 2005
Subhyracodon occidentalis	#1	36.82	160.24	0.23	0.23	Direct measurement on AMNH FM 1140
	#2	9.68	41.48	0.23		Measurement on picture in Scott & Jepsen, 1941 (in pixels)
Teleoceras fossiger	#1	46.49	109.47	0.42	0.44	Direct measurement on AMNH FM 2636
	#2	48.44	110.82	0.44		Direct measurement on YPM VP 38942
	#3	56.71	123.26	0.46		Direct measurement on YPM VP 38944
Teleoceras proterum	#1	51.00	105.00	0.49	0.44	Measurement on picture of AMNH FM 104163 in Prothero, 2005
	#2	50.56	108.46	0.47		Mean measurements given by Mihlbachler, 2005
	#3	42.60	112.20	0.38		Mean measurements given by Mihlbachler, 2005
Trigonias osborni	#1	28.00	133.20	0.21	0.21	Direct measurement on AMNH FM 9847 in Scott & Jepsen, 1941
Trigonias wellsi	#1	40.25	185.30	0.22	0.22	Direct measurement on AMNH FM 13226E
Triplopus cubitalis	#1	1.40	12.52	0.11	0.11	Measurement on picture in Cope, 1884 (in pixels)
Urtinotherium intermedium	#1	88.37	430.42	0.21	0.21	Direct measurement on AMNH FM 26389

Table S3A: Measurements used to compute mean gracility index on third metacarpal for each species of the sample. For measurements taken on unscaled pictures, values are given directly in pixels. GI-MC3: gracility index; Meas.: measurement; TD: transverse diameter. Institution codes are detailed in Chapter 2.

Taxa	Estimation	BM	Mean BM	Sources
Acerorhinus zernowi	#1	700	700	Valli, 2005
Alicornops simorrense	#1	875	875	Antoine, In Press
Amphicaenopus platycephalus	#1	NA	NA	No data
Amynodon advenus	#1	589	589	Averianov et al., 2017a
Aphelops malacorhinus	#1	889	889	Damuth & MacFadden, 1990
Aphelops megalodus	#1	NA	NA	No data
Aphelops mutilus	#1	1840	1840	Stilson, Hopkins & Davis, 2016
Brachypotherium brachypus	#1	2327	2327	Becker, 2003
Brachypotherium fatehjangense	#1	1999	1999	Antoine, In Press
Brachypotherium snowi	#1	NA	NA	No data
Cadurcodon ardynensis	#1	837	837	Averianov et al., 2017a
Ceratotherium cf. primaevum	#1	NA	NA	No data
Ceratotherium mauritanicum	#1	NA	NA	No data
Ceratotherium neumayri	#1	1200	1844	Valli, 2005
	#2	2487		Antoine, In Press
Ceratotherium simum	#1	2300	2300	Dinerstein, 2011
Chilotherium persiae	#1	700	700	Valli, 2005
Coelodonta antiquitatis	#1	1905	2403	Saarinen et al., 2016
	#2	2900		Stuart, 1991
Coelodonta nihowanensis	#1	NA	NA	No data
Diaceratherium aginense	#1	1987	1987	Becker, 2003
Diaceratherium asphaltense	#1	NA	NA	No data
Diaceratherium aurelianense	#1	1551	1551	Becker, 2003
Diaceratherium lamilloquense	#1	1410	1410	Becker, 2003
Diaceratherium lemanense	#1	1730	1590	Jame et al., 2019
	#2	1417		Jame et al., 2019
	#3	1624		Jame et al., 2019
Diceratherium annectens	#1	NA	NA	No data
Diceratherium armatum	#1	NA	NA	No data
Diceratherium tridactylum	#1	517	517	Damuth & MacFadden, 1990
Dicerorhinus aff. sansaniensis	#1	NA	NA	No data
Dicerorhinus sumatrensis	#1	775	775	Dinerstein, 2011
Diceros bicornis	#1	1050	1050	Dinerstein, 2011
Dihoplus megarhinus	#1	NA	NA	No data
Dihoplus pikermiensis	#1	1100	1100	Valli, 2005
Dihoplus schleiermacheri	#1	1812	2123	Becker, 2003
	#2	2433		Costeur et al., 2013
Elasmotherium sibiricum	#1	4000	4500	Zhegallo et al., 2005
	#2	4000		Zhegallo et al., 2005
Hispanotherium beonense	#1	NA	NA	No data
Hoploaceratherium tetradactylum	#1	1197	1197	Becker, 2003
Hyrachyus eximius	#1	97	67	Damuth & MacFadden, 1990
	#2	36		Stilson, Hopkins & Davis, 2016
Hyrachyus modestus	#1	NA	NA	No data
Hyracodon leidyanus	#1	NA	NA	No data
Hyracodon nebraskensis	#1	NA	NA	No data
Juxia sharamurenense	#1	888	888	Qiu & Wang, 2007
Lartetotherium sansaniense	#1	1204	1204	Becker, 2003
Menoceras arikarense	#1	251	313	Damuth & MacFadden, 1990
	#2	375		Stilson, Hopkins & Davis, 2016
Metamynodon planifrons	#1	887	1340	Damuth & MacFadden, 1990
	#2	1794		Averianov et al., 2017a
Paraceratherium bugtiense	#1	12400	9900	Gromova, 1959
	#2	7400		Fortelius & Kappelman, 1993
Paraceratherium grangeri	#1	10100	10950	Fortelius & Kappelman, 1993
	#2	11800		Gromova, 1959
Paramynodon birmanicus	#1	NA	NA	No data
Peraceras hessei	#1	NA	NA	No data
Peraceras profectum	#1	NA	NA	No data
Peraceras superciliosum	#1	NA	NA	No data

Plesiaceratherium fahlbuschi	#1	NA	NA	No data
Plesiaceratherium mirallesi	#1	1268	1268	Pers. calculation after Fukuchi & Kawai, 2011
Plesiaceratherium platyodon	#1	NA	NA	No data
Prosantorhinus douvillei	#1	NA	NA	No data
Protaceratherium minutum	#1	530	530	Becker, 2003
Rhinoceros philippinensis	#1	NA	NA	No data
Rhinoceros sondaicus	#1	1350	1350	Dinerstein, 2011
Rhinoceros unicornis	#1	2000	2000	Dinerstein, 2011
Stephanorhinus jeanvireti	#1	NA	NA	No data
Stephanorhinus etruscus	#1	NA	NA	No data
Stephanorhinus hemitoechus	#1	1522	1561	Saarinen et al., 2016
	#2	1600		Stuart, 1991
Stephanorhinus hundsheimensis	#1	1348	1348	Saarinen et al., 2016
Subhyracodon mitis	#1	NA	NA	No data
Subhyracodon occidentalis	#1	NA	NA	No data
Teleoceras fossiger	#1	1016	1016	Damuth & MacFadden, 1990
Teleoceras proterum	#1	635	635	Damuth & MacFadden, 1990
Trigonias osborni	#1	334	506	Damuth & MacFadden, 1990
	#2	677		Stilson, Hopkins & Davis, 2016
Trigonias wellsi	#1	NA	NA	No data
Triplopus cubitalis	#1	NA	NA	No data
Urtinotherium intermedium	#1	NA	NA	No data

Table 3B: Mean body mass (BM) estimations (in kg) computed on previous estimations given in literature for each species of the sample.

Appendix 4: Shape deformations associated with the first two axes of the PCA for each bone

Blue: minimal values. Orange: maximal values. Orientation from left to right: caudal, lateral, cranial, medial, proximal and distal views. A: complete humerus; B: distal partial humerus; C: radius; D: complete ulna; E: ulna without olecranon tuberosity; F: proximal partial ulna.

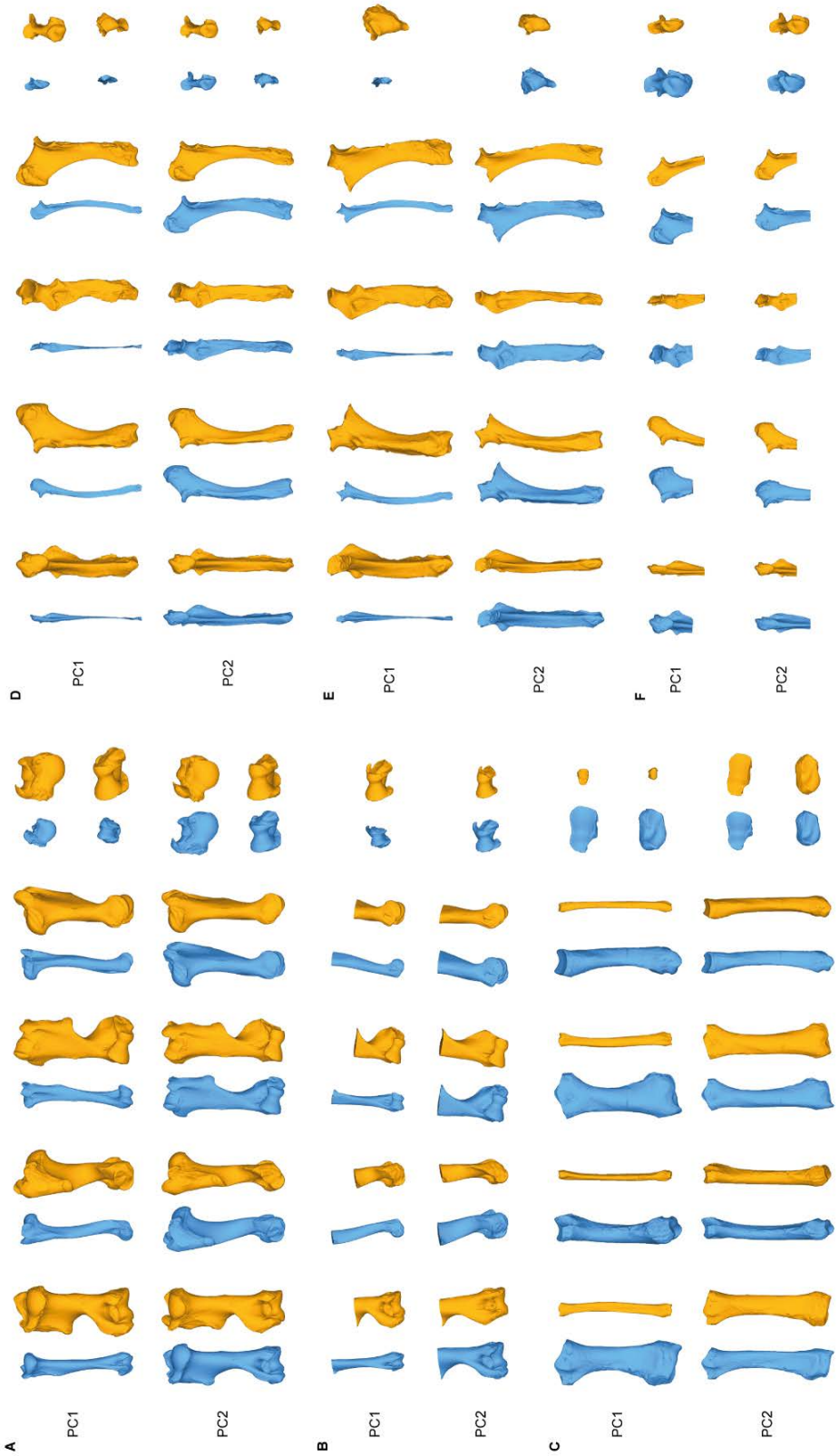

Appendix 5: Shape deformations associated with minimum and maximum values of the centroid size (CS), body mass (BM) and gracility index (GI-MC3) for significant regressions with shape

Blue: minimal values. Orange: maximal values. Orientation from left to right: caudal, lateral, cranial, medial, proximal and distal views. A, B, C: complete humerus; D, E, F: distal partial humerus; G: radius; H: complete ulna; I: ulna without olecranon tuberosity; J, K, L: proximal partial ulna.

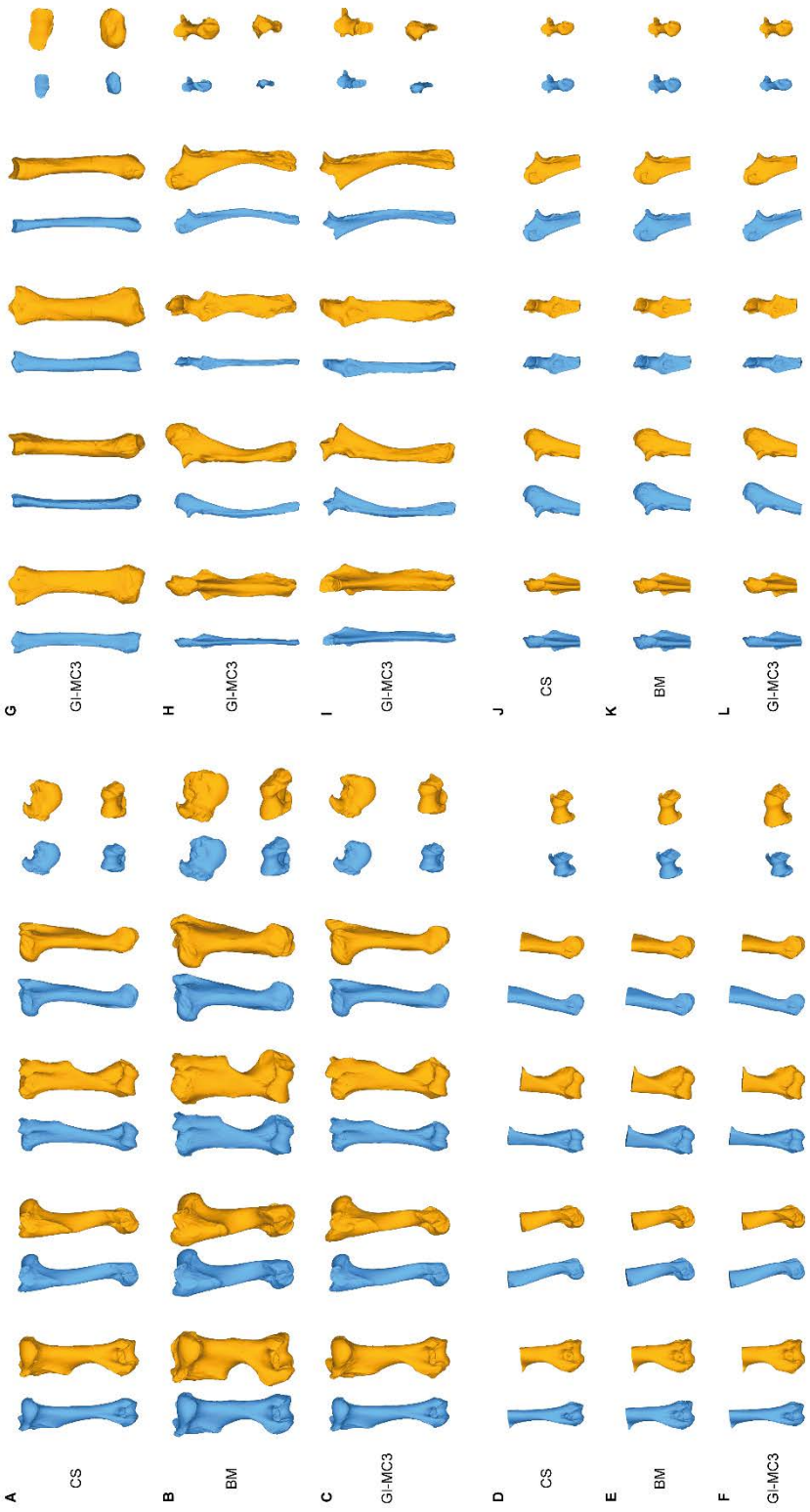

Appendix 6: Significant PGLS regression plots for radius (A) and complete ulna (B) performed on shape data and log-transformed cubic root of mean body mass (BM).

Points colour code follows Figure 27. Point size is proportional to mean log CS of each species. On the right, shapes associated with minimum and maximum fitted values (top row) and colour maps of the location and intensity of the shape deformation (bottom row). Blue: minimal values. Orange: maximal values. For each bone, the shape associated with the minimum was coloured depending on its distance to the shape associated with the maximum (blue indicates a low deformation intensity and red indicates a high deformation intensity). Orientation from left to right in each case: caudal, lateral, cranial and medial views.

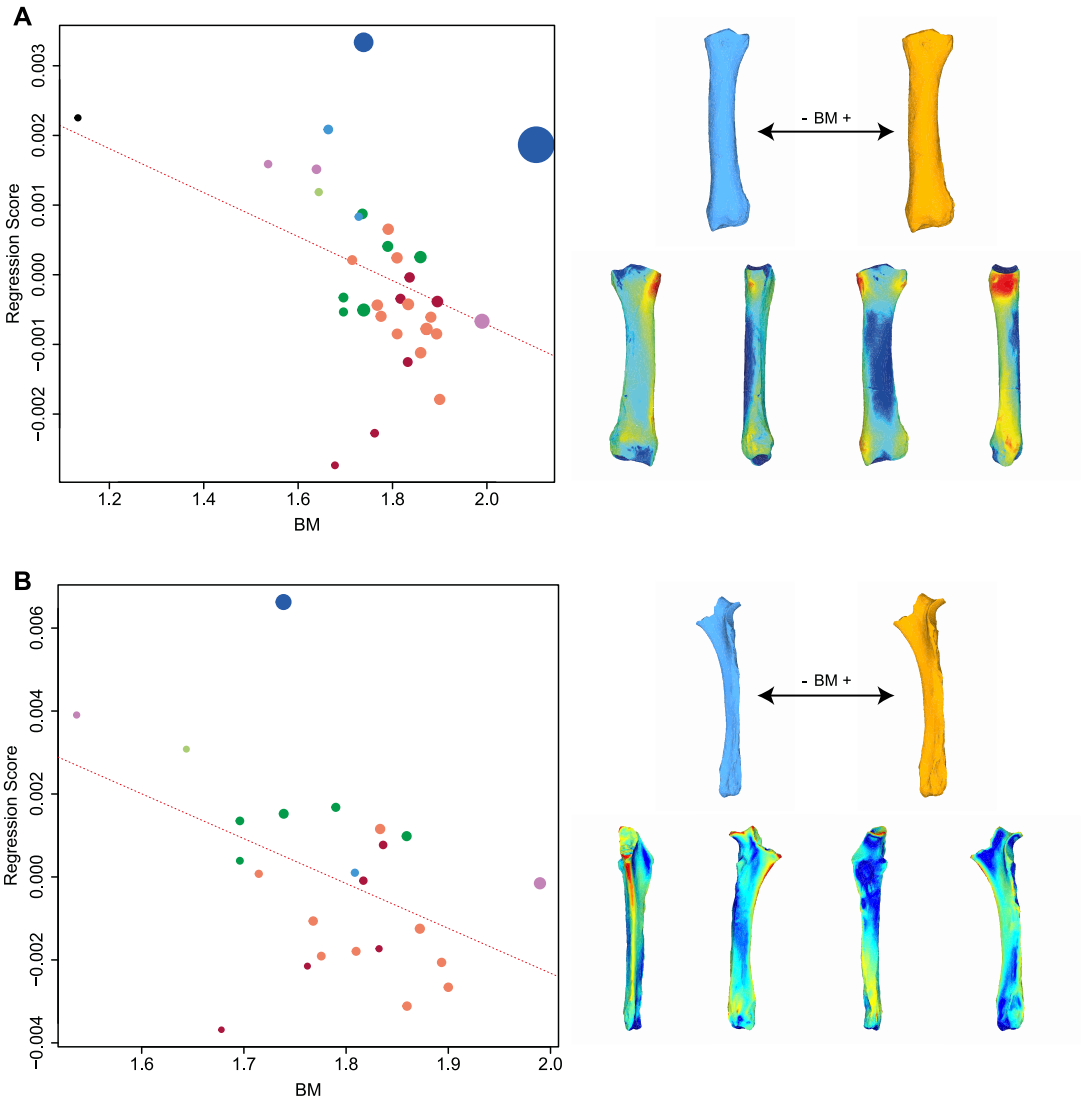

Chapter 6

Long bone shape variation in the hind limb of Rhinocerotoidea – Relation with size, body mass and body proportions

Introduction

The previous chapter explored the shape variation of forelimb elements among the superfamily Rhinocerotoidea. It notably highlighted a common general increase of bone robustness towards high body mass, associated with relatively larger epiphyses. Il also underlines that shape is not equally associated with size, mass and gracility among forelimb bones. If centroid size correlated strongly with body mass, and may be considered as a good proxy of the latter, these two parameters appeared as decoupled from the level of brachypody (i.e. the degree of limb shortening) for some taxa, especially in Paraceratheriidae, Elasmotheriinae and Teleoceratina. Whereas humerus shape seemed to be significantly related to these three factors, the radius and ulna ones were more strongly correlated with the species degree of brachypody, and poorly follow body mass variation. The shape variation patterns observed on the stylopodium followed more the evolutionary history than those observed on the zeugopodium. The study of some partial anatomical areas, first driven by the need to include more specimens despite taphonomic alterations, highlighted that proximal or distal epiphyses may vary differently than the rest of the bone in relation to different parameters like size, mass or gracility. It notably appeared that the elbow joint may represent a morphological module.

These results encouraged me to extend this approach to the hind limb elements. Previous results on modern rhinos (Chapters 3 and 4) indicated congruent shape variation between fore and hind limb stylopodium elements (i.e. similar trends and high integration between the humerus and femur). It appeared that shape variation and covariation were more likely related to phylogeny than body mass. They also highlighted remarkable differences between fore and hind limb zeugopodial elements and a stronger correlation between shape variation and body mass. These differences between fore and hind limb elements may be related to divergent functional roles. Although all four limbs sustain the whole body mass, quadrupedal mammals bear a significantly higher part of their body mass on the forelimbs (Alexander, 1985; Henderson, 2006). This fact is particularly noticeable on rhinos, whose massive head, powerful muscles forming their withers and presence of horns in some species, are likely to increase the proportion of the total body mass carried by the forelimbs (Henderson, 1999; Regnault et al., 2013; Stilson, Hopkins & Davis, 2016; Panagiotopoulou, Pataky & Hutchinson, 2019). Moreover, fore and hind limbs do not act similarly during quadrupedal mammal locomotion, the former functioning as brakes while the latter ensure body propulsion (Lessertisseur & Saban, 1967; Dutto et al., 2006). In addition, even if the length of the fore and hind limbs is relatively similar in most Rhinocerotoidea, some taxa like Paraceratheriidae display a non-horizontal spine associated with a reduction of the length of their hind limb. This particular body plan likely changes which limbs support the largest part of the body mass. This could be related to noticeable features in the shape of some hind limb elements, as it has been previously observed on ankle bones of Perissodactyla (Etienne et al., 2020).

Like for the forelimb, the exploration of the shape variation of the hind limb bones could help understand how the body mass and its repartition is associated with bone shape variation. Some similar modifications are likely to be observed, as an increase of bone robustness towards high body mass. However, relations between shape variation and centroid size, mean body mass and degree of gracility might not be equivalent between the different hind limb bones (femur, tibia and fibula). Moreover, the different roles of fore and hind limbs in the weight support and body propulsion of rhinos should be associated with remarkable differences in their shape variation. Given previous results, I hypothesize: (a) congruences and incongruences between the shape variation and mass, size and gracility; (b) differences between stylopodial and zeugopodial elements in their patterns of shape variation with size, mass and gracility, but also (c) between complete and partial analyses; (d) a link between phylogeny and bone shape, likely different between the three studied bones; (e) differences in trends of shape variation between the fore and the hind limbs possibly related to their distinct functional roles.

Material & Methods

The studied sample was composed of 215 bones of modern and fossil species of Rhinocerotoidea. The sample includes 79 femora, 83 tibiae and 53 fibulae (see Appendix 1 of this chapter for the complete list of studied specimens) representing 53 taxa (5 modern and 48 fossil species) (Figure 38). Due to lack of well-preserved specimens, some species included in the forelimb analysis were absent from the hind limb one (like many Amynodontidae or *Juxia* [Paraceratheriidae]). Reciprocally, others, like *Pleuroceros blanfordi* (Rhinocerotinae *incertae sedis*) and *Teleoceras hicksi* (Teleoceratina), were only present in the hind limb analysis. All anatomical terms are similar to those used in previous chapters and are summarize in Chapter 3.

As the methodology of this chapter is almost strictly identical to that used in Chapter 5, I will only briefly summarize hereafter the main differences with the study conducted on the forelimb bones. As on the forelimb, some parts of the hind limb bones are often damaged or absent in fossil specimens. This is notably the case on the femur, where the femoral head, the third trochanter, the medial lip of the trochlea and the condyles were frequently too damaged to be included in shape analyses. To overcome these taphonomic problems and include as many relevant specimens as possible (i.e. cover the broadest range of body mass and size as possible), I extended the approach on partial bone analyses previously applied on the humerus and the ulna. In addition to complete femur, tibia and fibula, I performed partial analyses on isolated proximal and distal parts of the femur, using the same protocol as described in Chapter 5 (see Appendix 2 of this chapter for details on landmarks in partial templates). Moreover, given the results obtained on the forelimb bones (highlighting differences in shape variation patterns between partial and complete humerus and ulna), the inclusion of partial parts of the femur allowed to test if similar results would be discernible in hind limb bones.

A similar analytical framework was used: Neighbour Joining (NJ) trees and Principal Component Analyses (PCA) were computed on landmarks coordinates after a Generalized Procrustes Analysis (GPA) and shape deformation along the two first axes. Multivariate regressions using Phylogenetic Generalized Least Squares (PGLS) were used to explore the association between bone shape and three variables (called “body proportions” when taken together): species mean body mass (BM), bone centroid size (CS) and species mean gracility index (computed here on the third metatarsal dividing its transverse width by its maximal length (GI-MT3) (see Table 14 and Appendix 3 of this chapter on variable computation). I addressed the effect of potential phylogenetic uncertainties on PGLS by using a Nearest Neighbour Interchange (NNI) procedure as in Chapter 5.

All statistic tests have been considered as significant for p-values ≤ 0.01 but I also took into consideration results associated with a p-value up to 0.05 (Wasserstein, Schirm & Lazar, 2019; Ho et al., 2019).

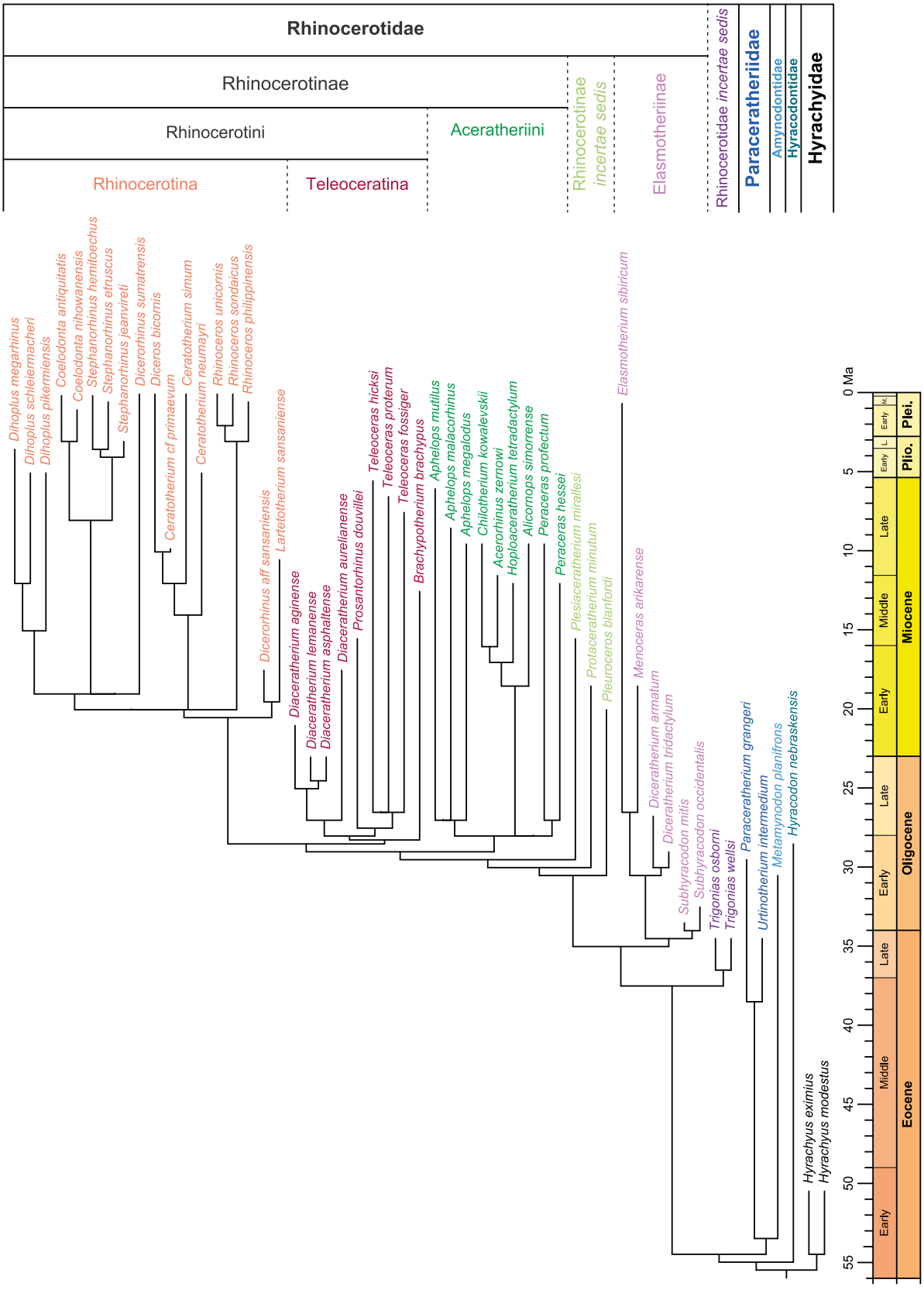

Figure 38: Composite cladogram of the studied species. Families, subfamilies, tribes and subtribes are defined by a colour code following the cladistic framework of Antoine et al. (2003) and Becker et al. (2013). All silhouettes representing a member of each group are at scale (provided by www.phylopic.org under Creative Commons license).

Taxon	Abbreviation	Mean body mass (kg)	Gracility Index (MtIII)
Acerorhinus zernowi	Ar. z.	700	0.26
Alicornops simorrense	Al. s.	875	0.29
Aphelops malacorhinus	Ap. ma.	889	0.25
Aphelops megalodus	Ap. me.	NA	0.26
Aphelops mutilus	Ap. mu.	1840	0.31
Brachypotherium brachypus	Br. b.	2327	0.35
Ceratotherium cf. *primaevum*	Ce. p.	NA	0.32
Ceratotherium neumayri	Ce. n.	1843	0.30
Ceratotherium simum	Ce. s.	2300	0.27
Chilotherium kowalevskii	Ch. k.	700	0.36
Coelodonta antiquitatis	Co. a.	2402	0.29
Coelodonta nihowanensis	Co. n.	NA	0.24
Diaceratherium aginense	Dia. ag.	1987	0.31
Diaceratherium asphaltense	Dia. as.	NA	0.31
Diaceratherium aurelianense	Dia. au.	1551	0.38
Diaceratherium lemanense	Dia. le.	1590	0.30
Diceratherium armatum	Dm. ar.	NA	0.21
Diceratherium tridactylum	Dm. t.	517	0.25
Dicerorhinus aff. *sansaniensis*	Ds. sa.	NA	0.25
Dicerorhinus sumatrensis	Ds. su.	775	0.27
Diceros bicornis	Dc. b.	1050	0.27
Dihoplus megarhinus	Dh. m.	NA	0.27
Dihoplus pikermiensis	Dh. p.	1100	0.28
Dihoplus schleiermacheri	Dh. s.	2122	0.26
Elasmotherium sibiricum	E. s.	4500	0.24
Hoploaceratherium tetradactylum	Ho. t.	1197	0.26
Hyrachyus eximius	Hy. e.	67	0.17
Hyrachyus modestus	Hy. m.	NA	0.16
Hyracodon nebraskensis	Hn. n.	NA	0.16
Lartetotherium sansaniense	L. s.	1204	0.24
Menoceras arikarense	Mc. a.	313	0.17
Metamynodon planifrons	Md. p.	1340	0.34
Paraceratherium grangeri	Pa. g.	10950	0.24
Peraceras hessei	Pe. h.	NA	0.26
Peraceras profectum	Pe. p.	NA	0.26
Plesiaceratherium mirallesi	Pl. m.	1268	0.25
Pleuroceros blanfordi	Pc. b.	1343	NA
Prosantorhinus douvillei	Ps. d.	NA	0.45
Protaceratherium minutum	Pt. m.	530	0.22
Rhinoceros philippinensis	R. p.	NA	0.28
Rhinoceros sondaicus	R. s.	1350	0.35
Rhinoceros unicornis	R. u.	2000	0.27
Stephanorhinus jeanvireti	St. j.	NA	0.23
Stephanorhinus etruscus	St. e.	NA	0.24
Stephanorhinus hemitoechus	St. he.	1561	0.26
Subhyracodon mitis	Su. m.	NA	0.26
Subhyracodon occidentalis	Su. o.	NA	0.24
Teleoceras fossiger	Te. f.	1016	0.44
Teleoceras hicksi	Te. h.	1660	0.46
Teleoceras proterum	Te. p.	635	0.43
Trigonias osborni	Tg. o.	505	0.22
Trigonias wellsi	Tg. w.	NA	NA
Urtinotherium intermedium	U. i.	NA	0.23

Table 14: List of the abbreviations, mean body masses and gracility indexes used in this study. NA indicates unavailable data. Sources used to compile mean body mass and gracility index are given in Appendix 3.

Results

Correlation between BM and GI-MT3

Both mean BM and mean GI-MT3 carry a significant phylogenetic signal (K_{BM} = 1.75, $p < 0.01$; $K_{GI\text{-}MT3}$ = 1.08, $p < 0.01$) but are not significantly correlated to each other when taking into account phylogenetic relationships ($p = 0.06$). The evolution of both parameters along the phylogeny (Figure 39) highlights that the evolution of these parameters within the superfamily is decoupled in some taxa like Paraceratheriidae, Teleoceratina and, at a lesser extent, large Elasmotheriinae

Femur – complete bone

Shape data for the complete femur carry a strong phylogenetic signal (K_{mult} = 0.93, $p < 0.01$). The distribution of the species both in the NJ tree (Figure 40A) and in the phylomorphospace (Figure 41) is strongly reminiscent of the phylogenetic relationships between taxa. Along the NJ tree, Hyrachyidae group with Hyracodontidae, Elasmotheriinae (all of small size in the absence of *Elasmotherium*) and some Rhinocerotinae (*Protaceratherium* and *Pe. profectum*). *Paraceratherium* groups with two species of *Aphelops* while *Metamynodon* is close to some Aceratheriini (*Hoploaceratherium*) as well as some Rhinocerotina (*Lartetotherium*). While Aceratheriini are dispersed along the tree, most of the Rhinocerotina are grouped together. Similarly, Teleoceratina form a homogeneous cluster despite the presence of *P. hessei*. Conversely, *Chilotherium* and *Pleuroceros*, two highly brachypodial taxa, plot within Rhinocerotina, far from other brachypodial species like *Teleoceras*. On the phylomorphospace, the first two axes gather 58.4% of the global variance. PC1, which carries 42.9% of the variance, displays a structure similar to the general organisation of the NJ tree. Small taxa such as *Hyrachyus* and *Hyracodon* plot toward positive values. Towards negative values, small Elasmotheriinae plot near *Metamynodon*, *Trigonias* and small Aceratheriini. The giant Paraceratheriidae *Urtinotherium* plots near small taxa like *Trigonias* or *Protaceratherium*, but also near *Metamynodon*. Towards the most negative values, large Aceratheriini are mixed with Teleoceratina and Rhinocerotina. Along PC2, which carries 15.5% of the variance, Rhinocerotina form a homogeneous cluster plotting towards negative values, together with *Metamynodon*, *Hyrachyus* and *Subhyracodon*. Teleoceratina and Aceratheriini (except *Ap. malacorhinus*) group together with *Urtinotherium*, *Subhyracodon mitis* and *Hyracodon* towards positive values.

The shape variation along PC1 is mainly related to the bone robustness (Figure 41 and Appendix 4A). Positive values are associated with a slender bone showing a rounded hemispherical head with a narrow neck; a proximally developed greater trochanter tuberosity protruding over the head; an oval *fovea capitis*; a third trochanter situated at the first proximal third of the shaft, more developed caudally than laterally; a cranio-caudally straight shaft; a relatively symmetrical distal trochlea with a poorly

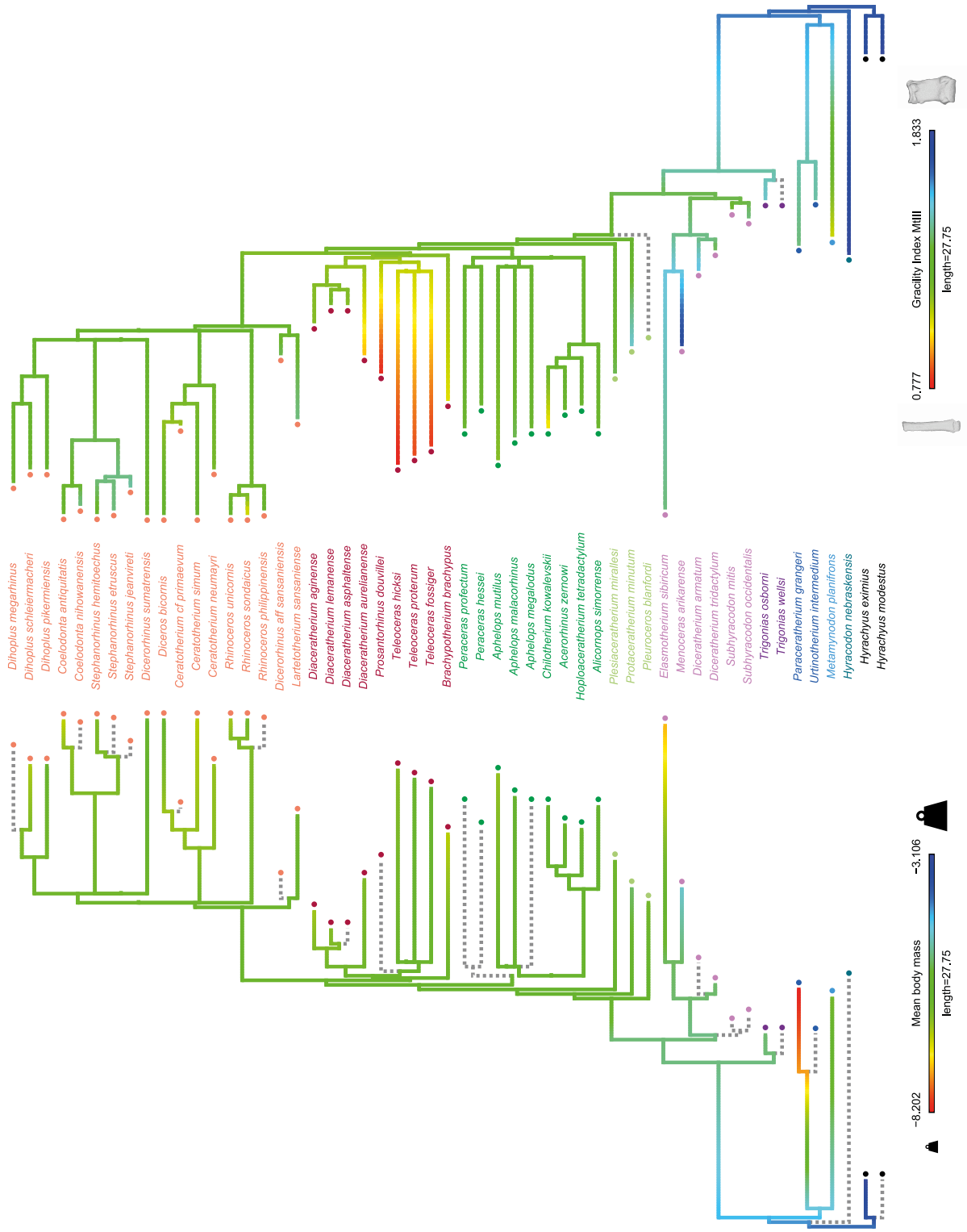

Figure 39: Evolution of BM and GI-MT3 along the phylogeny for the studied species. Left: mean BM; Right: mean GI-MT3. Computations were made on log-transformed cubic root of mean BM (BM) and log-transformed GI-MT3. Values at nodes and along branches were reconstructed based on a Brownian motion model of evolution (Revell, 2012). Colour code for taxa follows Figure 39. Evolution of the third metatarsal shape depending on the GI-MT3 value is illustrated by specimens *Hyrachyus eximius* AMNH FM 12675 (minimum) and *Teleoceras fossiger* YPM VP 039358 (maximum).

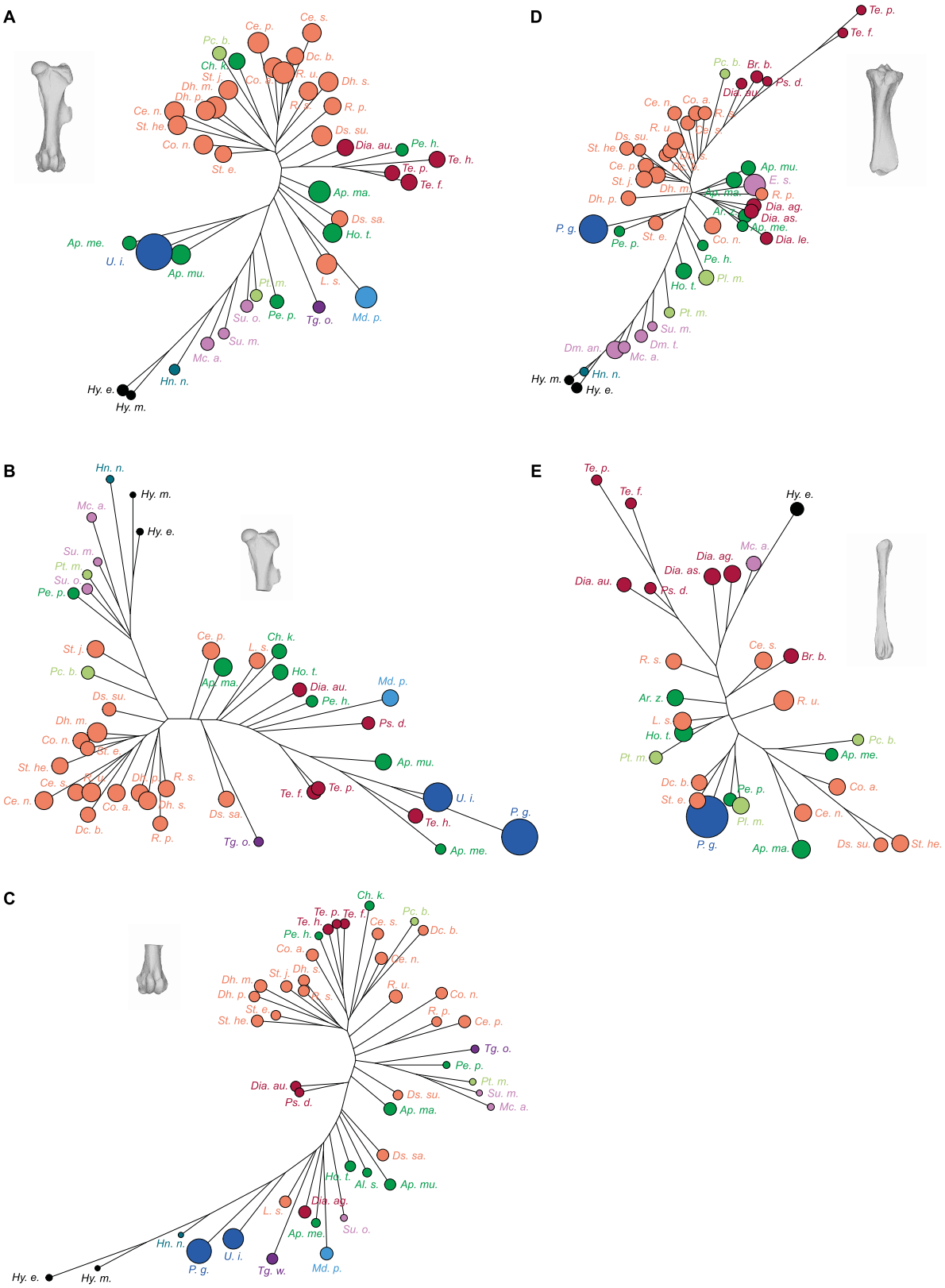

Figure 40: Neighbour Joining trees computed on all PC scores obtained from the PCAs performed on shape data. Colour code follows Figure 38 and abbreviations follow Table 14. Point size is proportional to the mean log centroid size of each species. A: complete femur; B: proximal partial femur; C: distal partial femur; D: tibia; E: fibula.

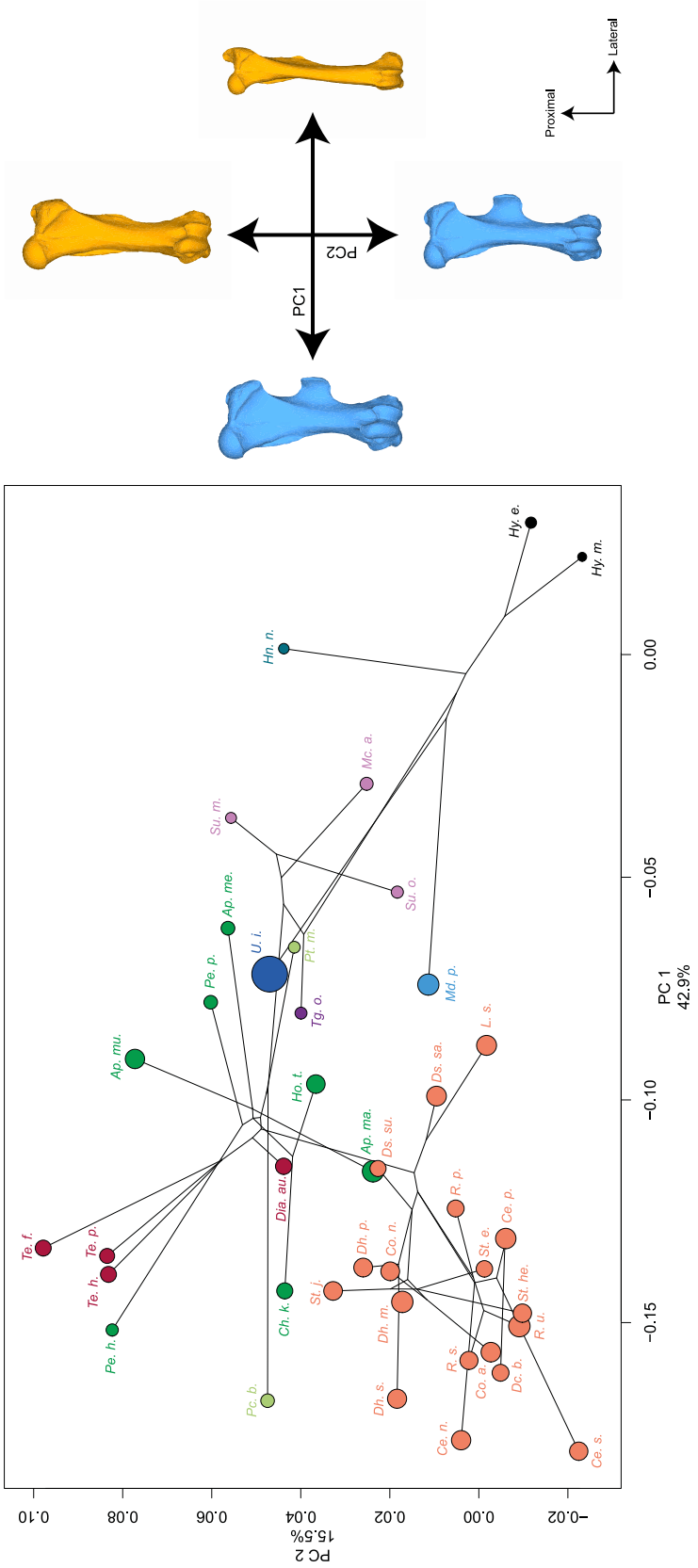

Figure 41: Results of the PCA performed on morphometric data of the complete femur and shape variation associated with the first axis of the PCA (cranial view). Blue: negative side of the axis. Orange: positive side of the axis. Phylogenetic relationships are plotted in the morphospace. Colour code follows Figure 38 and abbreviations follow Table 14. Point size is proportional to the mean log centroid size of each species.

developed medial lip; a long and narrow trochlear groove running caudally to the shaft; a distal epiphysis showing a medial torsion relatively to the shaft; relatively symmetrical medial and lateral condyles. Conversely, negative values are associated with a thick and massive bone, with a general hourglass shape in cranial view; a more flattened and wide head with a large neck; a greater trochanter tuberosity poorly developed proximally and not protruding over the head; a small rounded *fovea capitis*; a strong third trochanter clearly protruding laterally and cranially from the shaft; a shaft slightly curved in the caudal direction; a strongly asymmetrical trochlea with a broad medial lip; a short and wide trochlear groove; a distal epiphysis oriented cranially relatively to the shaft; a medial condyle more developed than the lateral one. Along PC2, the shape variation mostly concerns the development of the trochanters and the relative proportions of the epiphyses. The theoretical shape associated with negative values shows proximal and distal epiphyses of similar medio-lateral width; a lesser trochanter situated just below the head and above the third trochanter on the opposite side; a third trochanter developed in both cranial and lateral directions. Conversely, the shape associated with positive values displays a head and greater trochanter relatively larger; a head oriented more proximally; lesser and third trochanters facing each other on the medial and lateral side of the shaft, respectively; a third trochanter reduced to a bony ridge; a medial lip of the trochlea more developed cranially.

The centroid size of the complete femurs bears a significant phylogenetic signal (K_{CS} = 1.05, $p < 0.01$) and is significantly correlated with BM ($r = 0.68$, $p < 0.01$) but not with GI-MT3 ($p = 0.37$) (Table 15). PGLS results indicate that shape is significantly correlated with CS, BM and GI-MT3. PGLS computed on NNI trees highlight that variations in phylogenetic trees may result in marginally non-significant correlations for CS and GI-MT3 but mean p-values are strongly significant (Table 16). In the regression plot of shape against CS, the distribution of taxa shows a moderately good fit to the regression line. *Hyrachyus*, *Hyracodon* and *Paraceratherium* plots far from the regression line. Small Elasmotheriinae group together with *Protaceratherium* and *Trigonias*. If some Aceratheriini group with these small taxa, most of them are grouped with Rhinocerotina and Teleoceratina. *Metamynodon* also plots with this large group, although further away from the regression line (Figure 42A). Hyrachyidae, Hyracodontidae, Amynodontidae and Paraceratheriidae seem to follow an independent path parallel to the Rhinocerotidae one, but as these groups have few representatives here, this observation must be taken with caution. Changes in CS values mainly affect the general robustness of the bone, as well as the greater trochanter tuberosity and convexity, the femoral head and particularly the *fovea capitis*. Along the shaft, the main changes are located on the lateral part between the greater trochanter convexity and the third trochanter (where inserts the *m. vastus lateralis*), as well as along the distal half of the diaphysis, on cranial and caudal sides. Lateral and medial parts of both condyles are also strongly modified by CS variations (Figure 42A and Appendix 5A). The structure of the regression plot of shape against

Bone	Variables	r	t	dF	p
Femur (complete)	**CS ~ BM**	**0.68**	**4.38**	**22**	**<0.01**
	CS ~ GI	0.15	0.91	36	0.37
Femur (proximal partial)	**CS ~ BM**	**0.91**	**10.25**	**23**	**<0.01**
	CS ~ GI	0.22	1.36	38	0.18
Femur (distal partial)	**CS ~ BM**	**0.86**	**8.29**	**25**	**<0.01**
	CS ~ GI	0.16	0.99	40	0.32
Tibia	**CS ~ BM**	**0.72**	**5.19**	**25**	**<0.01**
	CS ~ GI	-0.23	-1.51	39	0.14
Fibula	**CS ~ BM**	**0.71**	**4.46**	**20**	**<0.01**
	CS ~ GI	-0.28	-1.41	24	0.17

Table 15: Results of the Pearson's correlation tests between centroid size (CS), and mean body mass (BM) and mean gracility index (GI-MT3) respectively for each bone (computed on Phylogenetic Independent Contrasts). r: Pearson's correlation coefficient value; t: student distribution value; dF: degrees of freedom; p: p-value. Significant results (for $p < 0.01$) are indicated in bold.

Bone	Variable	N	R^2			p-value		
			Min.	Max.	Mean	Min.	Max.	Mean
Femur (complete)	**CS**	**76**	**0.06**	**0.10**	**0.07**	**0.001**	**0.022**	**0.003**
	BM	**46**	**0.15**	**0.26**	**0.16**	**0.001**	**0.007**	**0.002**
	GI	**74**	**0.06**	**0.07**	**0.09**	**0.001**	**0.011**	**0.003**
Femur (proximal partial)	**CS**	**80**	**0.05**	**0.11**	**0.07**	**0.001**	**0.015**	**0.004**
	BM	**48**	**0.07**	**0.12**	**0.11**	**0.003**	**0.065**	**0.006**
	GI	**78**	**0.05**	**0.07**	**0.06**	**0.001**	**0.030**	**0.009**
Femur (distal partial)	CS	86	0.06	0.07	0.06	0.017	0.051	0.033
	BM	52	0.09	0.16	0.10	0.017	0.095	0.073
	GI	**82**	**0.06**	**0.08**	**0.07**	**0.002**	**0.025**	**0.011**
Tibia	CS	82	0.04	0.06	0.04	0.040	0.119	0.082
	BM	52	0.09	0.20	0.14	0.003	0.070	0.020
	GI	**80**	**0.22**	**0.31**	**0.27**	**0.001**	**0.001**	**0.001**
Fibula	CS	52	0.05	0.10	0.08	0.018	0.267	0.046
	BM	42	0.04	0.12	0.09	0.035	0.539	0.113
	GI	**50**	**0.17**	**0.22**	**0.20**	**0.001**	**0.003**	**0.001**

Table 16: Range of R^2 and p-values for PGLS computed with NNI permuted trees on shape data and log-transformed centroid size (CS), log-transformed cubic root of mean body mass (BM) and log-transformed mean gracility index (GI-MT3). N: number of trees obtained after NNI procedure; R^2: determination coefficient value. Significant results (for $p < 0.01$) are indicated in bold.

BM is similar to that obtained with CS, with a moderately good fit to the regression line. *Hyrachyus* is clearly isolated from all other species that form a large cluster at high BM values (Figure 42B). *Metamynodon* plots outside this cluster and far away from the regression line. A variation of BM results in the modifications of the same anatomical areas like for CS, although to a stronger extent, particularly for the femoral head and the greater trochanter convexity. An increase of robustness is observed towards high BM values. Shape changes are also located along the lesser trochanter, the medial lip of the trochlea and the medial epicondyle (Figure 42B and Appendix 5B). The regression plot of shape against GI-MT3 indicates a very good fit to the regression line. A clear opposition is observable between Rhinocerotina, being almost all above the regression line, to all other species below the line.

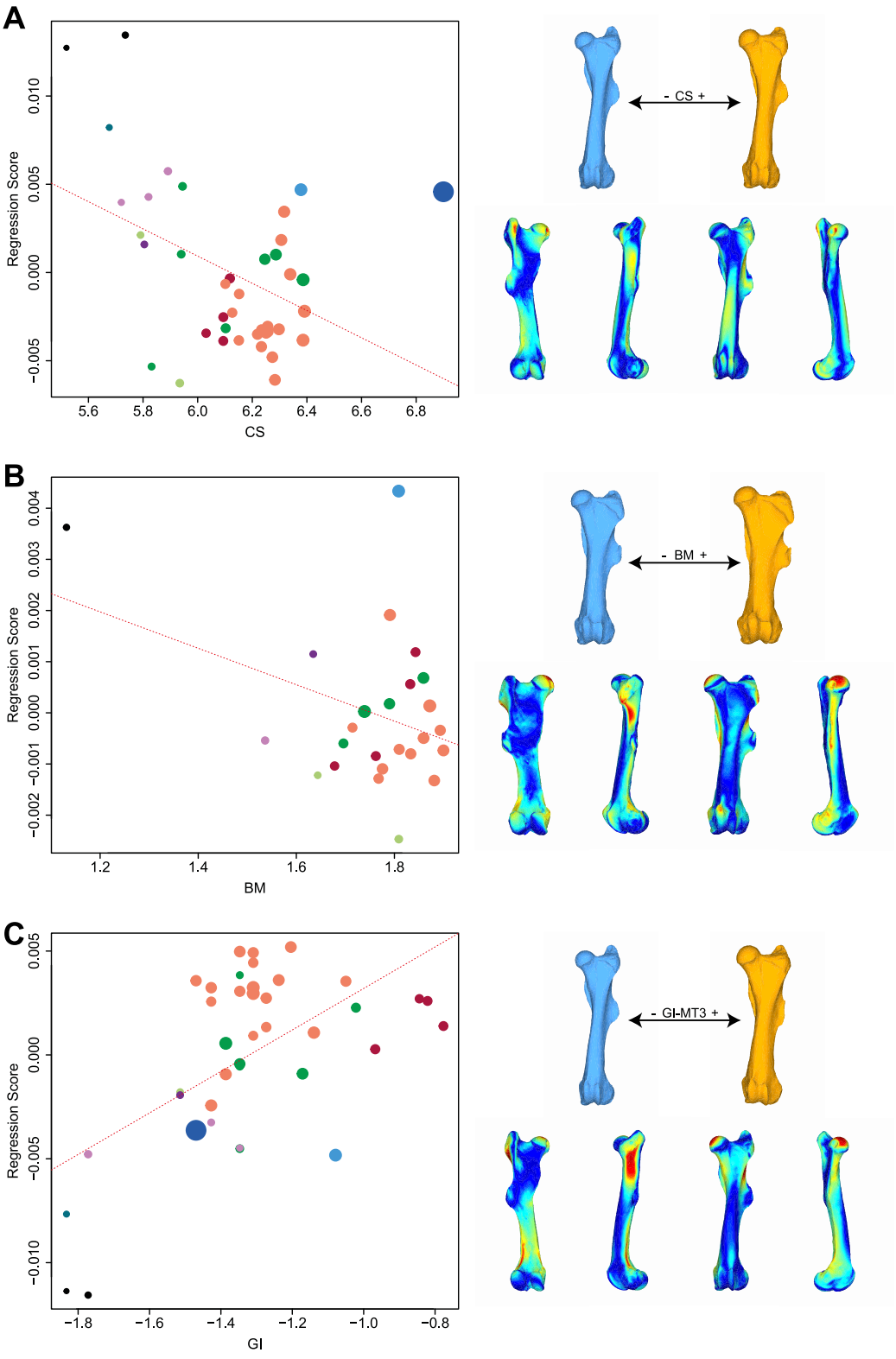

Figure 42: Significant PGLS regression plots for complete femur performed on shape data and log-transformed centroid size (CS) (A), log-transformed cubic root of mean body mass (BM) (B), log-transformed mean gracility index (GI-MT3) (C). Points colour code follows Figure 38. Point size is proportional to mean log CS of each species. On the right, shapes associated with minimum and maximum fitted values (top row) and colour maps of the location and intensity of the shape deformation (bottom row). Blue: minimum value of the regression. Orange: maximum value of the regression. For each bone, the shape associated with the minimum was coloured depending on its distance to the shape associated with the maximum (blue indicates a low deformation intensity and red indicates a high deformation intensity). Orientation from left to right in each case: caudal, lateral, cranial and medial.

Hyrachyidae and Hyracodontidae isolated towards minimal values, together with *Menoceras*, while other small Elasmotheriinae group with *Paraceratherium*, *Trigonias* and some gracile Aceratheriini and Rhinocerotina. Teleoceratina form a homogeneous cluster slightly isolated from other species (Figure 42C). Like for BM and CS, variations of GI-MT3 are associated with changes in the bone robustness, but are also related to modifications located on both medial and lateral supracondylar areas where inserts the *m. gastrocnemius*. However, contrary to what it is observed with BM, the medial lip of the trochlea and the medial epicondyle are poorly modified with variations of GI-MT3 values (Figure 42C and Appendix 5C).

Femur – proximal part

Shape data for the proximal part of the femur carry a significant phylogenetic signal (K_{mult} = 0.62, p < 0.01). The distribution of the species in the NJ tree (Figure 40B) and in the phylomorphospace (Figure 43A) shows marked differences with the results obtained on complete bones. The NJ tree is structured by the separation in three main clusters: 1) Hyrachyidae, Hyracodontidae, small Elasmotheriinae together with one Rhinocerotinae *incertae sedis* (*i. s.*) (*Protaceratherium*) and one Aceratheriini (*Pe. profectum*), 2) almost all Rhinocerotina together with *Pleuroceros*, and 3) Aceratheriini, Teleoceratina and Paraceratheriidae, together with *Metamynodon* and *Trigonias*. A similar structure is observed in the phylomorphospace, where the two first axes carry 62.1% of the total variance. PC1, which gathers 42.2% of the variance, is mainly structured by an opposition between giant Paraceratheriidae on positive values and Rhinocerotina on negative values. PC2 gathers 19.9% of the variance and mainly separates small taxa (*Hyrachyus*, *Hyracodon*, small Elasmotheriinae, *Protaceratherium*, *Pe. profectum*) towards negative values from all other species towards positive values. *Metamynodon* and *Aphelops megalodus* occupy the highest positive values along this axis.

Along PC1, shape variation is mostly related to the general orientation of the proximal part relatively to the rest of the bone and the development and position of the trochanters (Figure 43A and Appendix 5B). Towards negative values, the proximal part of the femur is tilted medially, with a relatively flattened head; a poorly developed greater trochanter tuberosity; a lesser trochanter placed directly below the femoral neck and above the third trochanter along the shaft; a third trochanter strongly extended cranially and laterally. Towards positive values, the proximal part of the femur is more vertical, with a rounded head supported by a thick neck; a greater trochanter tuberosity developed proximally and caudally; a long lesser trochanter situated in front of the third trochanter along the shaft; a third trochanter almost absent and reduced to a bony rugosity. Along PC2, the shape associated with negative values is long and slender, with a rounded head oriented proximo-medially; a high greater trochanter tuberosity; a short lesser trochanter; a long and poorly laterally developed third trochanter.

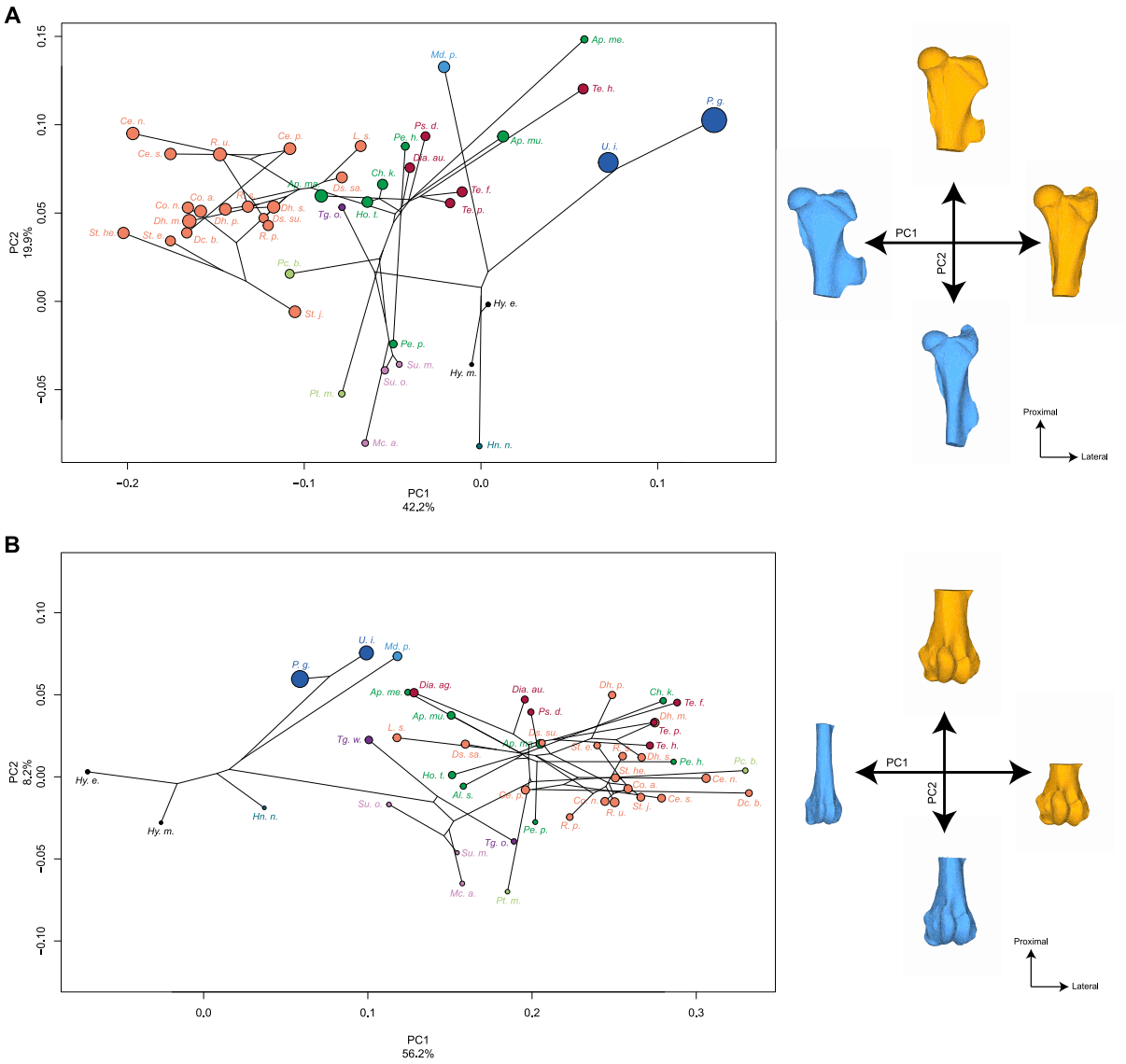

Figure 43: Results of the PCA performed on morphometric data of proximal partial femur (A) and distal partial femur (B) and shape variation associated with the first two axes of the PCA (caudal view). Blue: negative side of the axis. Orange: positive side of the axis. Phylogenetic relationships are plotted in the morphospace. Colour code follows Figure 38 and abbreviations follow Table 14. Point size is proportional to the mean log centroid size of each species.

The shape associated with positive values shows a flattened head oriented proximally; a low greater trochanter tuberosity; a long lesser trochanter; a third trochanter developed laterally and cranially.

Like for complete bones, CS of the proximal femur carries a strong phylogenetic signal (K_{CS} = 1.86, p < 0.01) and is highly correlated with BM (r = 0.91, p < 0.01) but not with GI-MT3 (p = 0.18) (Table 15). Similarly, PGLS regressions indicate a significant correlation between shape and the three variables. NNI procedure highlights that some phylogenetic uncertainties can lead to marginally non-significant results (Table 16). The regression plot of shape against CS displays a poor fit to the regression line, with a high dispersion of specimens. Almost all Rhinocerotina are below the regression line, only associated with Rhinocerotinae *i. s.*, *Trigonias*, *Subhyracodon* and *Aphelops*. Above the regression line, Aceratheriini and Teleoceratina group together with *Metamynodon*, while Hyrachyidae and Hyracodontidae

plots slightly outside this central cluster. Giant Paraceratheriidae plot far away from the regression line. They do not seem to follow the main regression trend (Figure 44A). The high dispersion of species may underline that the different families or subfamilies do not follow the same allometric trend. A similar observation can be done on the regression plot of shape against BM, displaying a relatively poor fit to the regression line. *Hyrachyus* and *Paraceratherium* are isolated from most other taxa and plot far away from the regression line. Again, almost all Rhinocerotina, situated below the line, are separated from other species situated above the line (Figure 44B). Contrary to the results obtained on complete bones, the regression plot of shape against GI-MT3 shows a more scattered dispersion of the species. There is also no clear preferential direction shown by the overall distribution of all specimens, which highlights a relatively poor fit to the regression line. Like for CS and BM, Rhinocerotina clearly isolate above the regression line while almost all other species plot below the line. Although dispersed in the plot, Aceratheriini and Teleoceratina remain relatively grouped, with *Metamynodon* plotting between them (Figure 44C). Like for complete bones, shape variation associated with changes in CS and BM values impacts similar anatomical areas: mainly the greater trochanter tuberosity, the lesser trochanter and the cranial side of the shaft. However, the increase of robustness towards high values is not clear. The intensity of shape variation is slightly higher for BM than CS (Figure 44A, B and Appendix 5D, E). The shape changes associated with variations of GI-MT3 values mainly concern the femoral head, the lesser and third trochanters and the insertion area of the *m. vastus lateralis* (Figure 44C and Appendix 5F).

Femur – distal part

The phylogenetic signal carried by shape data for the distal part of the femur is strong and significant (K_{mult} = 1.06, $p < 0.01$). The distribution of the species in the NJ tree (Figure 40C) and in the phylomorphospace (Figure 43B) differs noticeably from those obtained on the complete bone and proximal part. The NJ tree seems mainly patterned by an opposition between gracile and brachypodial taxa, with a poor influence of phylogenetic relationships: only Rhinocerotina group almost all together, despite the presence of Aceratheriini and Teleoceratina close to them. This sorting along the degree of brachypody is also observed on the phylomorphospace (especially PC1), where the first two axes gather 64.6% of the global variance. Along PC1, which carries 56.2% of the variance, *Hyrachyus* and *Hyracodon* plot together around null values, close to giant Paraceratheriidae and *Metamynodon*. Small Elasmotheriinae, *Trigonias* and *Protaceratherium* are mixed with relatively gracile Aceratheriini, Rhinocerotina and Teleoceratina while the most brachypodial taxa (*Teleoceras*, *Chilotherium*, *Pleuroceros*) plot towards the maximal positive values, together with some *Dihoplus*, *Ceratotherium* and *Diceros*. PC2, which gathers 8.2% of the variance, mainly opposes small Elasmotheriinae and *Protaceratherium*

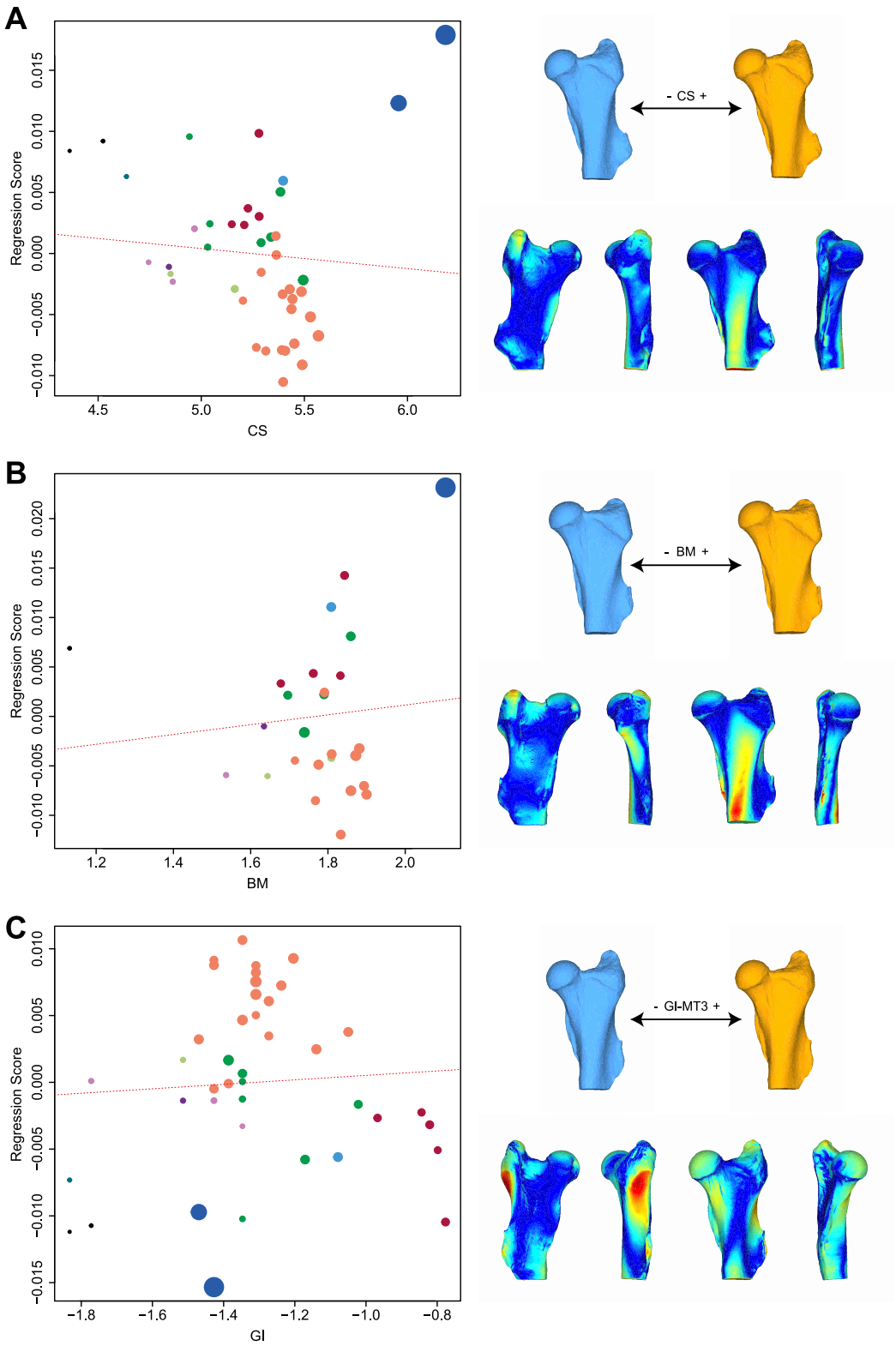

Figure 44: Significant PGLS regression plots for proximal partial femur performed on shape data and log-transformed centroid size (CS) (A), log-transformed cubic root of mean body mass (BM) (B), log-transformed mean gracility index (GI-MT3) (C). Points colour code follows Figure 38. Point size is proportional to mean log CS of each species. On the right, shapes associated with minimum and maximum fitted values (top row) and colour maps of the location and intensity of the shape deformation (bottom row). Blue: minimum value of the regression. Orange: maximum value of the regression. For each bone, the shape associated with the minimum was coloured depending on its distance to the shape associated with the maximum (blue indicates a low deformation intensity and red indicates a high deformation intensity). Orientation from left to right in each case: caudal, lateral, cranial and medial.

towards negative values to giant Paraceratheriidae and *Metamynodon* towards positive values. However, no clear pattern is visible concerning other taxa between these two extremes.

Like for complete bones, the shape variation along PC1 is mainly related to the general robustness of the bone (Figure 43B and Appendix 4C). Theoretical shape associated with negative values displays a long and slender shaft; a narrow symmetrical trochlea developing caudally towards the condyles; symmetrical medial and lateral condyles. Conversely, the shape associated with positive values shows a robust and thick shaft, compressed proximo-distally; an asymmetrical trochlea with a massive medial lip; a medial condyle more developed than the lateral one; a protruding medial epicondyle. Along PC2, the shape associated with negative values has a narrower shaft; a medial lip of the trochlea poorly developed in the cranial direction; a narrow and deep V-profiled trochlear groove; medial and lateral condyles developed in the caudal direction. Conversely, the shape associated with positive values shows a more robust shaft; a medial lip of the trochlea more developed in the cranial direction; a wide and shallow trochlear groove; medial and lateral condyles poorly developed in the caudal direction.

The centroid size of the distal femur carries a significant phylogenetic signal (K_{CS} = 0.91, $p < 0.01$) and is highly correlated with BM ($r = 0.86$, $p < 0.01$) but not with GI-MT3 ($p = 0.32$) (Table 15). However, contrary to what is observed on the complete bone and proximal part, PGLS regressions are only significant between shape and GI-MT3 (and marginally between shape and CS) (Table 16). The regression plot of shape against GI-MT3 is very similar to that observed on the complete femur and indicate a relatively good fit to the regression line. Almost all Rhinocerotina are above the regression line, together with *Trigonias*, *Protaceratherium* and *Menoceras*. Aceratheriini are dispersed on each side of the line, some being mixed with Rhinocerotina. Below the regression line, Teleoceratina are grouped together with Paraceratheriidae and *Metamynodon*, while Hyrachyidae and Hyracodontidae isolates towards minimal values (Figure 45A). Like for complete bones, beyond a slight increase of robustness, the shape variation associated with variations of GI-MT3 values is mainly located on both medial and lateral supracondylar areas where inserts the *m. gastrocnemius* (Figure 45A and Appendix 5G). Although marginally non-significant, the regression plot of shape against CS displays a strong similarity with those obtained on the complete bone and proximal part, with a relatively weak fit to the regression line. An opposition is observable between almost all Rhinocerotina and Teleoceratina below the regression line (together with Rhinocerotinae *i. s*.), and all other species above the line. Like in previous results, Aceratheriini are dispersed among this central cluster, while *Hyrachyus-Hyracodon* and giant Paraceratheriidae plot far away from the line at minimal and maximal CS values respectively. Similarly, the shape variation associated with changes of CS values mainly affects the third trochanter, the cranial side of the shaft and both medial and lateral condyles (see Appendix 6A for regression plot and shape deformation).

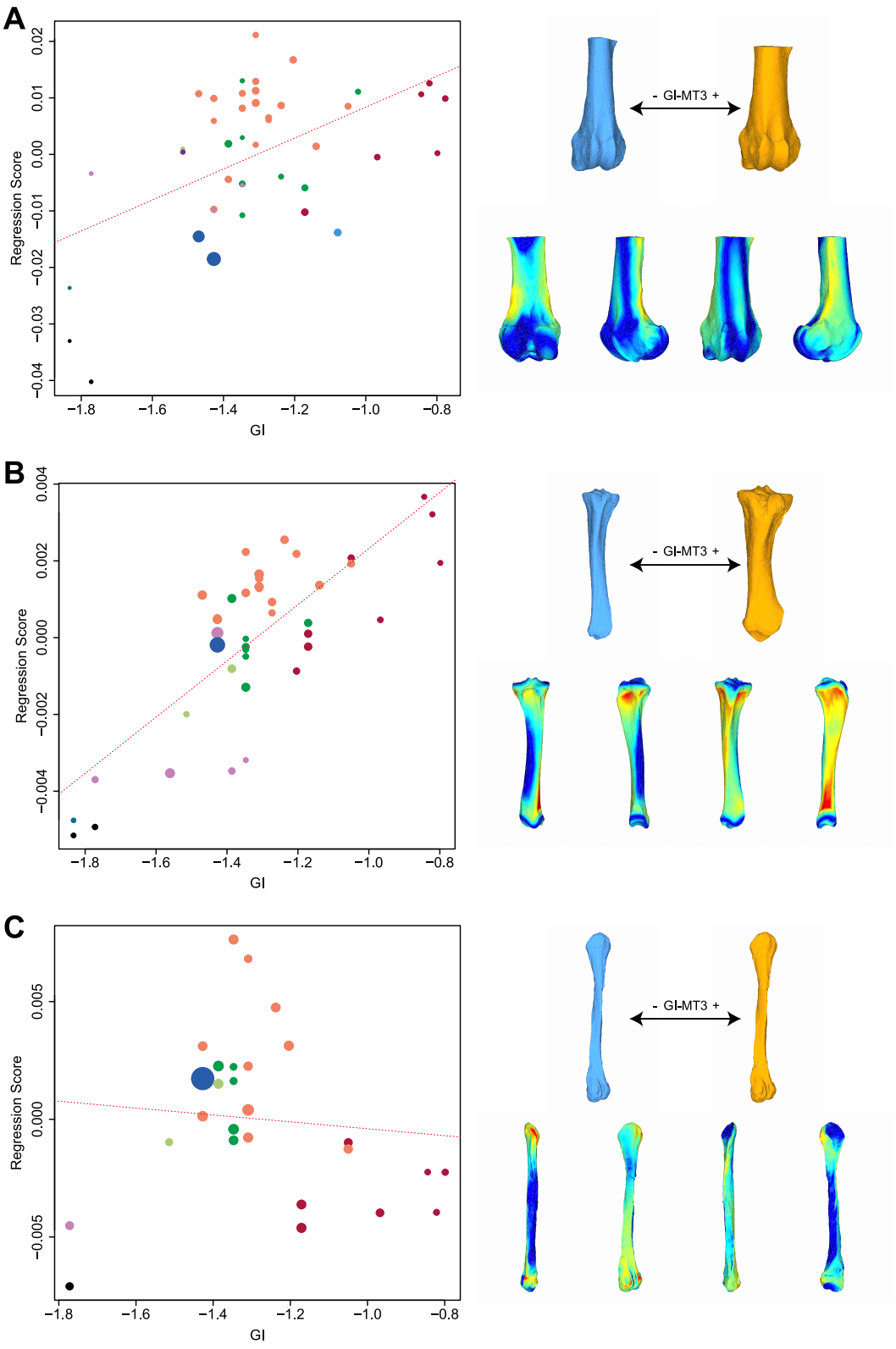

Figure 45: Significant PGLS regression plots for distal partial femur (A), tibia (B) and fibula (C) performed on shape data and log-transformed mean gracility index (GI-MT3). Points colour code follows Figure 38. Point size is proportional to mean log CS of each species. On the right, shapes associated with minimum and maximum fitted values (top row) and colour maps of the location and intensity of the shape deformation (bottom row). Blue: minimum value of the regression. Orange: maximum value of the regression. For each bone, the shape associated with the minimum was coloured depending on its distance to the shape associated with the maximum (blue indicates a low deformation intensity and red indicates a high deformation intensity). Orientation from left to right in each case: caudal, lateral, cranial and medial.

Tibia

Like for the femur, shape data obtained on the tibia carry a significant phylogenetic signal (K_{mult} = 1.27, $p < 0.01$). The NJ tree is strongly structured by the degree of brachypody, opposing mainly Hyrachyidae to the most brachypodial species of Teleoceratina (Figure 40D). Rhinocerotina are grouped almost all together. *Elasmotherium* and *Diaceratherium* plot within the Aceratheriini group, whereas all other Teleoceratina are isolated at an extremity of the tree. *Paraceratherium* is close to *Peraceras* and Rhinocerotina, but also of all other Aceratheriini. The first two axes of the phylomorphospace gather 78.0% of the total variance and display a structure similar to that of the NJ tree (Figure 46A). PC1 carries 65.4% of the variance and opposes Hyrachyidae and Hyracodontidae towards positive values to Teleoceratina towards negative values. Along this axis, small Elasmotheriinae plot next to Hyrachyidae and Hyracodontidae, together with *Protaceratherium*. Larger species like *Elasmotherium* and *Paraceratherium* plot together with most of the Aceratheriini, the genus *Diaceratherium* and some Rhinocerotina. Highly brachypodial taxa like *Teleoceras*, *Brachypotherium*, *Prosantorhinus* and *Pleuroceros* occupy the most negative values. PC2 carries 12.6% of the variance and mainly opposes highly brachypodial Teleoceratina towards negative values to some Rhinocerotina (with gracile genera like *Stephanorhinus*, *Dicerorhinus* and more brachypodial ones like *Ceratotherium* and *Dihoplus*), as well as *Pe. profectum* and *Paraceratherium* towards positive values.

Shape variation along PC1 is mostly related to the general robustness of the bone (Figure 46A and Appendix 4D). Towards positive values, the tibia is thin and slender, with: a triangular tibial plateau tilted in the caudal direction and showing similar surface areas for the medial and lateral articular surfaces; a lateral surface area highly developed in the caudal direction towards the popliteal notch; medial and lateral intercondylar tubercles separated by a large gap; a small and flat tibial tuberosity associated with a narrow and deep tibial groove; a long and narrow shaft with relatively parallel medial and lateral edges; a distal articular surface for the fibula forming an isosceles triangle; a narrow and asymmetrical articular surface for the astragalus, with a lateral groove deeper than the medial one; a caudal apophysis stretched caudally. Conversely, the theoretical shape associated with negative values is highly robust and thick, with: an irregular tibial plateau tilted medially and cranially; a medial articular surface wider than the lateral one; a lateral surface area poorly developed in the caudal direction towards the popliteal notch; medial and lateral intercondylar tubercles separated by a narrow gap; a strong and massive tibial tuberosity oriented laterally and associated with a wide and shallow tibial groove; a massive diaphysis displaying a narrowing at midshaft, conferring to the bone a hourglass aspect in cranial view; a distal articular surface for the fibula forming an equilateral triangle; a wide, shallow and relatively symmetrical articular surface for the astragalus. Along PC2, the shape variation mainly affects both epiphyses. Towards positive values, the tibia has high intercondylar tubercles, with

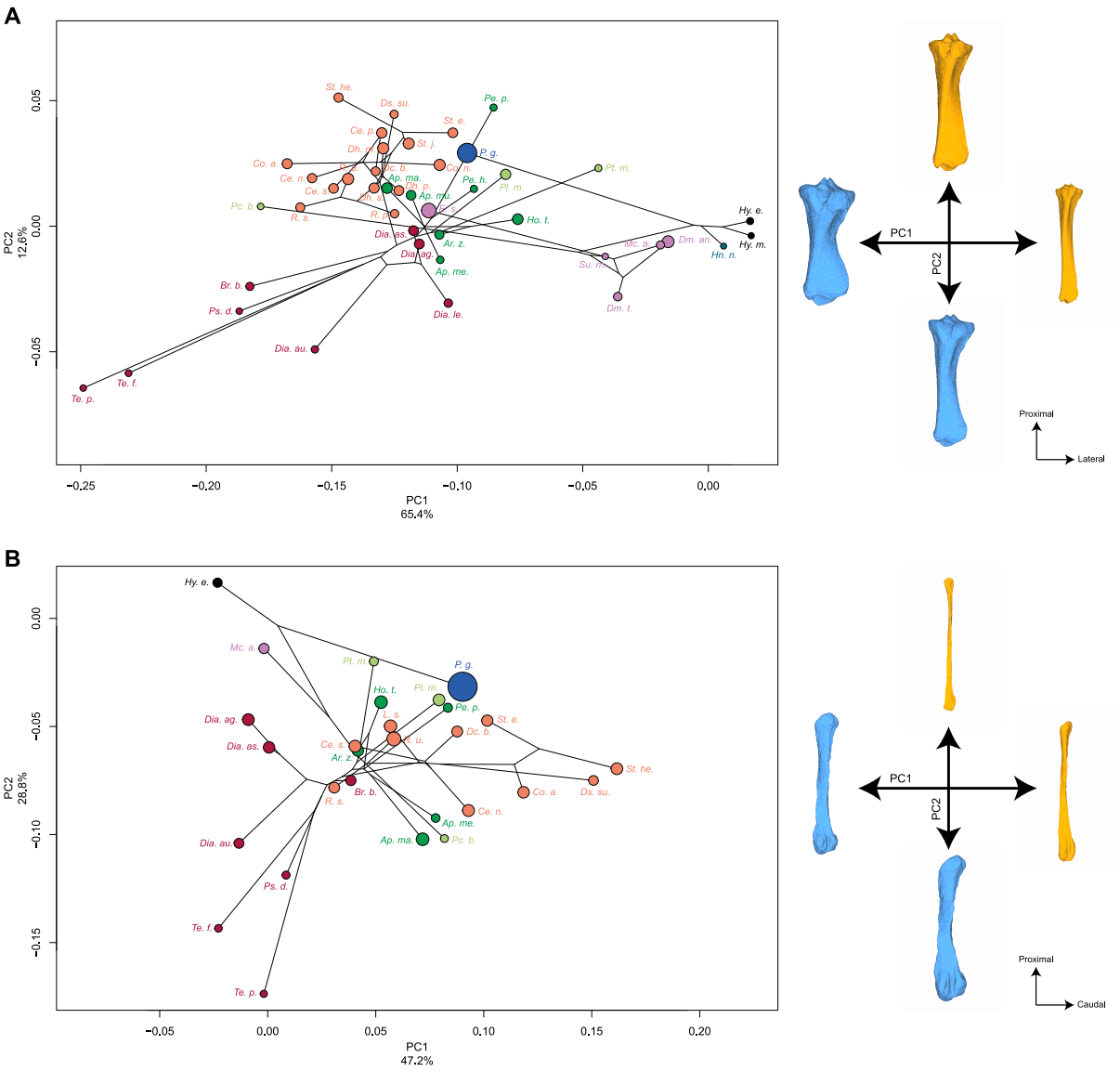

Figure 46: Results of the PCA performed on morphometric data of tibia (A) and fibula (B) and shape variation associated with the first two axes of the PCA (caudal view). Blue: negative side of the axis. Orange: positive side of the axis. Phylogenetic relationships are plotted in the morphospace. Colour code follows Figure 38 and abbreviations follow Table 14. Point size is proportional to the mean log centroid size of each species.

the medial one being placed more cranially than the lateral one; both medial and lateral condyles being developed caudally defining a deep popliteal notch; a high tibial tuberosity; a straight interosseous crest; a long distal articular surface for the fibula forming an isosceles triangle; a symmetrical articular surface for the astragalus; a medial malleolus developed distally. Conversely, towards negative values, the tibia has low intercondylar tubercles, both facing each other; medial and lateral condyles poorly developed caudally resulting in a narrow popliteal notch; a low tibial tuberosity; a rounded and concave interosseous crest; a short kidney-shaped distal articular surface for the fibula; an articular surface for the astragalus with a cranio-caudally tilted general axis; a medial malleolus poorly developed distally.

The centroid size of the tibia carries a significant although weak phylogenetic signal relatively to the results obtained on the femur (K_{CS} = 0.56, p = 0.01). Similarly, CS is highly correlated with BM (r = 0.72, p < 0.01) but not with GI-MT3 (p = 0.14) (Table 15). Like for the distal part of the femur, PGLS regressions are only significant between shape and GI-MT3. PGLS regression between shape and BM also appears as marginally non-significant (Table 16). The regression plot of shape against GI-MT3 shows a very good fit with the regression line. This plot is very similar to that obtained on the femur, with the isolation of almost all Rhinocerotina above the regression line, only associated with *Elasmotherium*, *Paraceratherium* and *Aphelops*. Below the regression line, Hyrachyidae-Hyracodontidae, small Elasmotheriinae, Aceratheriini and Teleoceratina all form homogeneous groups separated from each other (Figure 45B). Towards high values of GI-MT3, shape variation involves an increase of robustness and a medio-lateral broadening of both epiphyses (Figure 45B and Appendix 5H). Most of the shape variation is located directly under the tibial plateau on the medial and lateral sides of the shaft, but also along all the tibial crest. The medial side of the tibial shaft is particularly affected by shape changes, especially distally. The regression plot of shape against BM, although marginally non-significant, shares strong similarities with that obtained on the femur. Specimens show a rather good fit to the regression line with few outliers. Towards high BM values, there is a high dispersion of the species and a strong opposition between large Paraceratheriidae and some Teleoceratina on each side of the common slope. Conversely, Elasmotheriinae follow a trend parallel to the common regression line (see Appendix 6B for regression plot). The shape variation associated with changes of BM values is similar to that observed for changes in GI-MT3 values, with a stronger general robustness, but also strong modifications located under the tibial plateau. These changes are mainly located on the proximal part of the medial side of the tibia, and distally to the tibial tuberosity. The distal part of the shaft is also affected, notably the distal articular surface for the fibula (see Appendix 6B for shape deformation).

Fibula

The results obtained on the fibula differ strongly from those obtained on previous bones. Although significant, the phylogenetic signal carried by shape data is almost equal to 1 (K_{mult} = 0.99, p < 0.01). The distribution of the species on the NJ tree (Figure 40D) and on the phylomorphospace (Figure 46B) strongly differs from those obtained for the femur and the tibia. The NJ tree is mainly structured by an opposition between Teleoceratina, *Hyrachyus* and *Menoceras* on the one hand and Rhinocerotinae *i. s*., Aceratheriini, Paraceratheriidae and Rhinocerotina strongly mixed together on the other hand. The first two axes of the phylomorphospace, gathering 76.0% of the global variance, reflect a similar structure to the NJ tree. PC1, accounting for 47.2% of the variance, opposes *Hyrachyus*, *Menoceras* and almost all Teleoceratina in the negative part to all other species on the positive part. Rhinocerotina, Aceratheriini and Rhinocerotinae *i. s* form a cluster with no obvious organisation. *Paraceratherium*

plots near small taxa like *Protaceratherium* and *Peraceras*, but also near *Pleuroceros* and *Aphelops*. PC2, which gathers 28.8% of the variance, is mainly driven by an opposition between *Hyrachyus* and *Menoceras* towards positive values and *Teleoceras* towards negative values. Along this axis, while Rhinocerotina plot mainly with Teleoceratina, *Paraceratherium* is close to small taxa like *Menoceras*, *Plesiaceratherium* and *Protaceratherium*. Aceratheriini are mixed together with Rhinocerotinae *i. s.*, Rhinocerotina and poorly brachypodial Teleoceratina.

Like for the femur and the tibia, the shape variation along PC1 is related to a change in the general robustness of the bone (Figure 46B and Appendix 4E). The shape associated with positive values is thin and slender with a small rounded proximal articular surface for the tibia oriented cranially; a very thin central shaft with a sharp interosseous crest; a long distal articular surface for the tibia forming an isosceles triangle; a medio-laterally flattened distal epiphysis; both cranial and caudal tubercles of the lateral malleolus being oriented caudally; a symmetrical kidney-shaped articular surface for the astragalus. Conversely, the shape associated with negative values is massive and thick with a large proximal articular surface for the tibia oriented more medially; a strong central shaft with a smooth interosseous crest; a very short distal articular surface for the tibia forming an equilateral triangle; a medio-laterally broadened distal epiphysis; both cranial and caudal tubercles of the lateral malleolus oriented laterally; an asymmetrical kidney-shaped articular surface for the astragalus. Surprisingly, the shape variation along PC2 also involves a huge change in robustness associated with morphological changes of both epiphyses. The shape associated with positive values is extremely thin and flat, with a spoon-like proximal articular surface for the tibia; a straight and flat shaft; a distal epiphysis with a caudal development conferring it a squared shape; a small rectangular articular surface for the astragalus. The shape associated with negative values is extremely thick and massive with a large proximal articular surface for the tibia; a strong shaft with a cranio-caudal curvature; a triangular and thick distal epiphysis; a kidney-shaped articular surface for the astragalus.

Contrary to what is observed in other bones, the centroid size of the fibula does not carry a significant phylogenetic signal ($p = 0.22$). CS is highly correlated with BM ($r = 0.71$, $p < 0.01$) but not with GI-MT3 ($p = 0.17$) (Table 15). Like for the distal femur and the tibia, PGLS regressions are only significant between shape and GI-MT3 (and marginally between shape and CS, like for the distal tibia) (Table 16). However, the regression plot of shape against GI-MT3 indicates a weak fit to the regression line, with many species plotting far away from the common slope (Figure 45C). Rhinocerotina are almost all grouped above the regression line, while Teleoceratina are grouped below the line. Aceratheriini plot near Rhinocerotinae *i. s.* and *Paraceratherium* in the central cluster while *Hyrachyus* and *Menoceras* isolate towards minimal values. The shape variation associated with changes of GI-MT3 values mainly involves morphological modifications of the caudal side of the fibula head, of the lateral part of the

shaft and of the distal epiphysis, particularly the cranial and caudal tubercles of the malleolus and the distal articular surface for the tibia (Figure 45C and Appendix 5I). Like for the distal femur, PGLS regression between shape and CS is marginally non-significant (Table 16). The regression plot indicates a very weak fit to the regression line. *Paraceratherium* appears to strongly drive the regression trend relatively to all other species (see Appendix 6C for regression plot). The shape variation associated with a higher CS involves mainly the same anatomical areas than those described for the shape variation related to GI-MT3 (see Appendix 6C for shape deformation).

Evolution of CS values along the phylogeny

The evolution of CS values along the phylogeny for the distal femur (being that with the least amount of missing data), complete tibia and complete fibula (Figure 47) highlights important disparities between the three bones. The distribution of CS values along the tree for the tibia is particularly distinct from those observed on the femur and the fibula. While the lowest values are represented by Hyrachyidae and the highest by Paraceratheriidae on the femur, many other taxa show very low CS values for the tibia within Rhinocerotidae (small Elasmotheriinae, Rhinocerotinae *i. s.*, Aceratheriini, Teleoceratina). On the fibula, the lowest values are not represented by *Hyrachyus* but by *Teleoceras*, whereas most CS values for other taxa are congruent with the distribution observed for the femur.

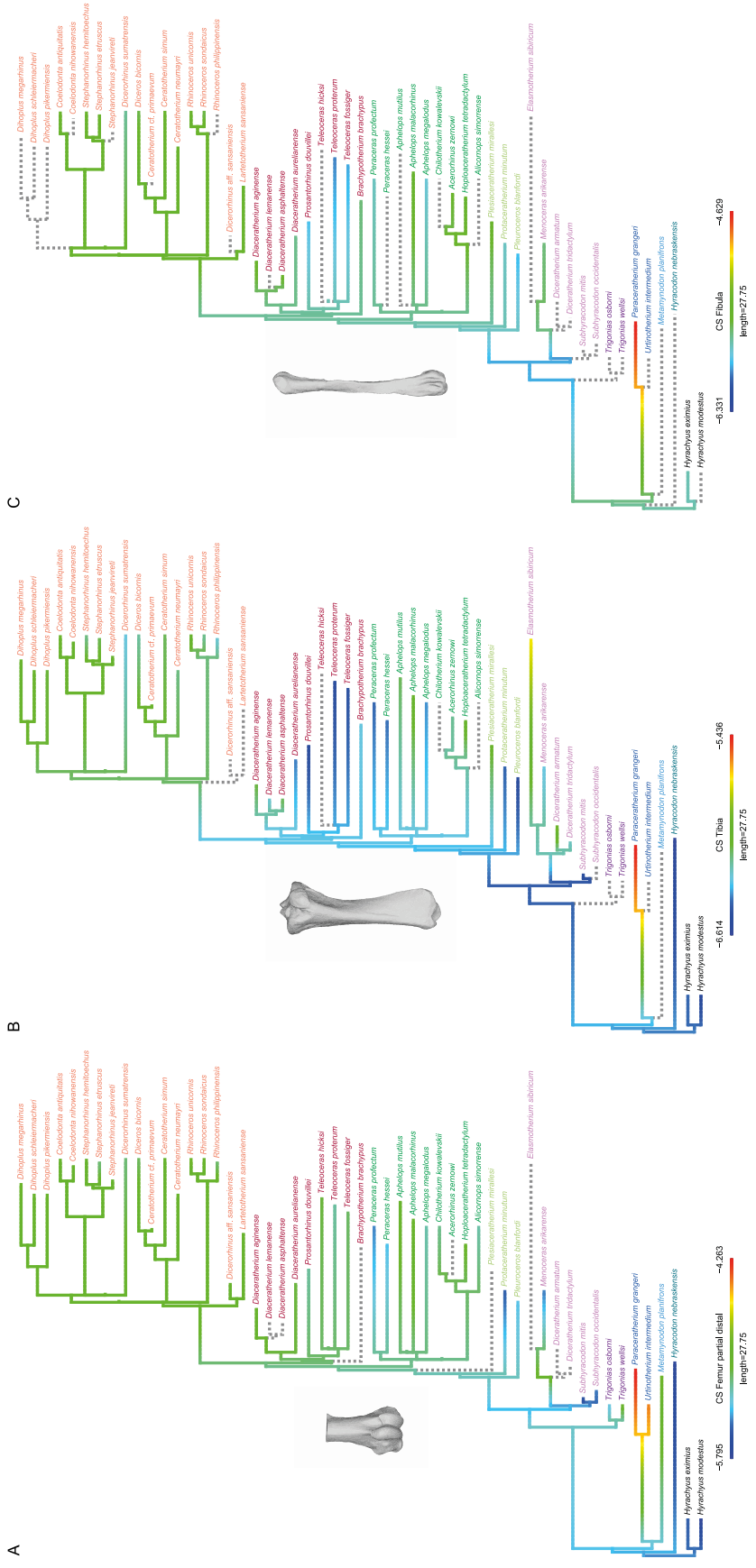

Figure 47: Evolution of centroid size (CS) along the phylogeny for the studied species. A: distal partial femur, B: tibia, C: fibula. Computations were made on log-transformed CS. Values at nodes and along branches were reconstructed based on a Brownian motion model of evolution (Revell, 2012). Colour code for taxa follows Figure 38.

Discussion

Association of mass, size and gracility with bone shape

Congruent shape variation associated with all variables

Although not significantly correlated either with CS or BM, the gracility index GI-MT3 is always significantly correlated with shape variation. Centroid size is always significantly and highly correlated with body mass. However, this significant relation between CS and BM should be taken carefully, as CS values can be very different between taxa depending on the considered bone. This is particularly obvious when comparing *Hyrachyus* and *Teleoceras*, displaying similar values of CS for the tibia and the fibula, whereas the mass of the former taxon was around ten times lower than that of the latter. Moreover, these similar CS values are associated with very different bone shapes. Conversely, this relation between CS and BM seems more relevant on the femur, where size, mass and shape vary in a more congruent way. These differences highlight the limits of considering CS as a proxy of BM, which seems more relevant for stylopodium than zeugopodium bones on the hind limb (see below and Chapter 5).

Femur

On the femur, a higher size, mass, or degree of brachypody is always associated with an increase of the bone general robustness, which is coherent with previous observations on rhinos (Prothero & Sereno, 1982; Mallet et al., 2019; Etienne et al., 2020). Moreover, these variables affect many similar anatomical areas though not always with the same intensity.

The femoral head is particularly affected by an increase of size, mass, or brachypody, with a higher intensity for the two latter variables. The shape and head orientation change when these parameters increase, the head becoming more flattened and oriented proximally. This is likely to indicate a reorientation of the limb (and of its rotation axis), being more vertical and placed closer from the parasagittal axis of the animal when size, weight or brachypody increase. This conformation is classically associated with a “graviportal” body plan (Gregory, 1912; Osborn, 1919) and its presence in giant Paraceratheriidae confirm that their hip joint is oriented more distally with a femur placed close to the parasagittal plane (Prothero, 2013). However, such reorientation is also present among Teleoceratina in lighter and more brachypodial species. This highlights the fact that characters classically associated with graviportality, like the reorientation of a femoral head, can be present in taxa displaying very different body organisations.

Along the femoral shaft, strong shape changes related to muscle insertions are distinguished, with a maximal intensity when body mass and brachypody increase. Such changes are notably observed for the insertion of the *m. vastus lateralis* (between the greater trochanter convexity and the third trochanter) and on both medial and lateral supracondylar tuberosities, where insert the *m. gastrocnemius*

and digit flexors. These powerful muscles are respectively the main extensors of the zeugopodium and autopodium (Barone, 2010b). Such shape changes towards high body mass and high degree of brachypody are coherent with more powerful muscles ensuring the propulsion and support of a higher absolute weight or of a body with a lower centre of gravity. If a given mass is supported by a brachypodial species, the position of their centre of gravity is lowered and their shorter limbs constitute shorter lever arms. Consequently, muscles will need to produce more power to apply higher forces on these shorter lever arms and ensure efficient movements and body support (McGhee & Frank, 1968; Hildebrand, 1974; Fischer & Blickhan, 2006).

On the distal epiphysis, an increase of CS, BM and GI-MT3 is also always associated with more asymmetrical trochlea and condyles. The asymmetry of the distal epiphysis, previously observed on modern rhinos in Chapter 3 (Mallet et al., 2019), but also in equids (Hermanson & Macfadden, 1996) and bovids (Kappelman, 1988), is likely associated with the need to resist higher constraints exerted near the sagittal plane in taller and heavier quadrupeds. Surprisingly, this asymmetry seems however poorly correlated with the thickening of the medial lip of the trochlea, related to body mass increase only (see below).

Tibia and fibula

Contrary to what is observed in the femur, shape variation in the tibia and the fibula is only significantly correlated with the degree of brachypody, although marginal significant results were obtained with body mass and centroid size respectively. On the tibia, an increase of both body mass and brachypody is associated with an increase of the general robustness, as well as broader epiphyses. The tibial plateau is clearly wider for high values of these parameters. The same observation can be done for the distal epiphysis, since the contact surface with the astragalus is wider in both cases, which is coherent with previous results obtained on this bone among Rhinocerotoidea (Etienne et al., 2020). These proximal and distal broadenings likely confer a better stability of the knee and ankle joints by ensuring the dissipation of higher constraints (due to a higher mass or a lower centre of gravity) on a larger surface area. Moreover, most of the shape change common to high mass and brachypody is situated distally to the proximal epiphysis and involves the tibial fossa, the tibia crest and the lateral side of the shaft. These changes appear of higher intensity for body mass than for brachypody. These areas constitute the insertion sites of powerful flexor muscles, respectively the *m. tibialis cranialis*, a foot flexor, and the *mm. biceps femoris*, *popliteus*, *semitendinosus* and *sartorius*, all being flexors of the leg. Reinforcement of insertions for flexors and extensors are congruent with the higher energy needed to move a heavier body or to move a body with a lower centre of gravity and short legs.

Like for the tibia, the fibula shape variation is only significantly correlated with the degree of brachypody (and marginally with the centroid size). However, no clear increase of robustness is related to an increase of brachypody. Morphological changes mainly involve the head and the proximal part of the shaft, where insert flexor and extensor muscles for digits, as well as the distal part of the fibula, which gives way to the tendons of these muscles and is linked to ankle bones by the collateral ligament (Barone, 2010a; Fisher, Scott & Adrian, 2010). Surprisingly, variations of centroid size and degree of brachypody involve similar shape changes, although these two parameters are not significantly correlated. This indicates that convergent shape changes may be present in the fibula of taxa showing a very different body shape.

Non-congruent shape variation associated with variables

Although many shape changes appear similarly related to variation of size, mass and brachypody, other morphological modifications can be more directly related to one specific parameter. This is notably the case of the *fovea capitis* on the femoral head, which appears impacted by changes of the centroid size only. This fovea, where inserts the foveal ligament, may be almost absent in some rhino species like the modern black rhinoceros or the giant *Paraceratherium*. The disappearing of the fovea might be interpreted as the absence of this ligament (Crelin, 1988). However, a previous analysis on the elephant hip indicated that this ligament can be present despite the absence of fovea and attached on the head distal ridge (Crelin, 1988). The functional role of the foveal ligament is poorly known but supposed to limit the abduction of the femur and prevent the dislocation of the hip joint (Crelin, 1988; Barone, 2010b). Consequently, the shape change associated with an increase of centroid size may not be due to the disappearing of this ligament but to the displacement of its insertion on the femoral head, which could be related to higher constraints due to size to prevent the hip dislocation. However, this *fovea* is also absent or poorly marked in non-related and lighter taxa like *Diceros bicornis* (Guérin, 1980; Antoine, 2002), making it hard to relate its shape and presence or absence to high body mass only. My results do not allow to highlight precisely the morphofunctional implications of the shape changes of this fovea, which remains to be explored deeper among quadrupeds in relation with body proportion.

On the femur, all three trochanters are strongly affected by an increase of CS, BM or GI-MT3, but not always similarly. An increase of mass and brachypody is associated with a lateral development of the greater trochanter convexity, where inserts the *m. gluteus minimus*, an extensor of the limb (Barone, 2010b). Conversely, an increase of the centroid size affects mostly the top of the greater trochanter tuberosity, where inserts the *m. gluteus medius*, considered as the main limb extensor (Barone, 2010b). A higher centroid size is associated with a lower tuberosity developed more caudally. The lateral development of the convexity in heavy and brachypodial taxa and the caudal development of the

tuberosity lengthen the lever arms laterally and caudally, allowing slower but more powerful extensions and increasing the efficiency of muscular contractions for extending the limb (Hildebrand, 1974). The variation of body mass and brachypody is particularly related to the variation of the lesser trochanter, where inserts the *m. iliopsoas*, showing a distal displacement for heavier and brachypodial species. To a lesser extent, the third trochanter, where inserts the *m. gluteus maximus*, displays the same distal displacement (with shape changes only associated with variation of gracility). Both trochanters are then facing each other at midshaft in heavy and brachypodial taxa, constituting longer lever arms for muscles, a conformation often observed in heavy taxa (Hildebrand, 1974).

On the distal epiphysis, the asymmetry of the femoral trochlea is associated with a broadening of the medial lip for high body mass only. This medial lip, also called medial trochlear ridge, is considered as indicating the presence of a "passive stay-apparatus" in equids but also in rhinos and in some bovids, allowing the animal to endure long periods of standing during feeding or resting times (Hermanson & Macfadden, 1996). The apparition of this feature, that emerged independently in different lineages, is supposed to be related to habitat (Kappelman, 1988) or to body mass (Hermanson & Macfadden, 1996). Although I did not test the hypothesis of a relation with habitat, results on fossil rhinos tend to highlight an actual link between the development of the medial trochlear ridge and a high body mass., as this feature is present in all heavy taxa (in *Metamynodon*, large Paraceratheriidae and all heavy Rhinocerotidae). This passive "lock" of the knee joint likely allows heavy rhinos to stand during feeding or resting times without spending too much energy to counteract gravity constraint. Furthermore, a similar pattern has been observed on the forelimb bone, with the bicipital groove of the humerus being only affected by changes of the body mass (see Chapter 5). As the bicipital groove is also likely involved in a passive-stay apparatus for the forelimb (Hermanson & MacFadden, 1992), these particularly congruent results underline that the development of joint lock systems is directly related to an increase of body mass among Rhinocerotoidea.

Differences in stylopodium and zeugopodium shape changes with body proportions

In accordance with the second hypothesis, the comparison of patterns of shape change clearly highlights that the stylopodium and the zeugopodium do not follow the same trends of morphological variations. Whereas the shape variation of the femur is conjointly related to size, mass and gracility, those of the tibia and fibula appear related to the degree of brachypody only (and marginally to mass and size respectively). Beyond the general increase of robustness underwent by the bones towards high body mass, these strong differences tend to indicate a functional breakdown between the evolution of the stylopodium and zeugopodium among Rhinocerotoidea, in addition with differences related to phylogenetic relationships (see below). Hallgrímsson, Willmore, and Hall (2002) and Young and Hallgrímsson (2005) hypothesized an increase of variation of the limb elements along the proximo-distal axis,

especially in quadrupeds, relating this phenomenon to postnatal processes like functional specialization under specific environmental constraints. My results tend to confirm these observations among Rhinocerotoidea at the evolutionary level, the femoral shape varying conjointly with body proportions while the shapes of the tibia and fibula display less correlation with body proportions except the degree of brachypody. This decoupling might be related to a divergence in the role of these bones, the femur being more involved in flexion and extension movements of both hip and leg, to ensure propulsion while the tibia mainly ensures weight support and gives attach for flexor and extensors muscles of the foot (together with the fibula). The poor correlation between tibial shape and body mass variations tends to indicate that the shape of this bone is more related to the distribution of the weight in the body (i.e. position of the centre of gravity, muscles and other organs) than to the absolute weight of the species. These results appear as partly contradictory to what has been observed on modern rhinos in Chapters 3 and 4, where zeugopodial shape was more directly linked to body mass than stylopodium's one (Mallet et al., 2019, 2020). However, the five modern species only represent a small sample of the past diversity of Rhinocerotoidea, and the trend displayed by the Rhinocerotina representatives appear as limited to this group only (see below). This underlines that, at the scale of the whole superfamily, the degree of brachypody (and, consequently, the body mass repartition and the position of the centre of gravity) may be a major driver of the morphological changes of the hind limb zeugopodium. Body mass itself may have a more visible impact at a lower taxonomic level, as it have been observed among modern rhinos as described in Chapters 3 and 4 (Mallet et al., 2019, 2020). A similar trend can be observed on forelimb elements of the superfamily (see Chapter 5 and below).

Modularity of the femur

Beyond this strict distinction between the stylopodium and zeugopodium, the multiple investigation of the femur based on complete or partial bone analyses reveals that the shape variation of the whole bone, the proximal and the distal part does not exhibit the same relation with size, mass and gracility, confirming the third hypothesis. The shape of the proximal part appears significantly correlated with size, mass and gracility, like that of the complete bone, but the species dispersion in the NJ trees, phylomorphospaces and regression plots highlights noticeable divergences. It notably appears that small taxa like Hyrachyidae, Hyracodontidae, small Elasmotheriinae and Rhinocerotinae *i. s.* share marked morphological affinities with heavy Paraceratheriidae concerning the whole bone, but barely when looking at their proximal part only. This tends to indicate that the proximal part of the femur undergoes shape modification decoupled from the ones observed on the rest of the bone between these taxa. These modifications notably concern the size and the shape of the trochanters, as well as the head orientation. Conversely, the shape variation of the distal part of the femur is more congruent with the ones of the tibia and fibula than with the whole femur. Like for the zeugopodial elements, it is only

correlated with the degree of brachypody of the species, highlighting that the shape variation of the complete bone is more congruent with its proximal part than its distal part. All these observations lead me to hypothesize that proximal and distal parts of the femur as potential morphological modules, i.e. anatomical units covarying more in themselves than with other units (Klingenberg, 2008). The congruence between the shape variation of the distal femur and the tibia could indicate that the knee joint, with the inclusion of the patella, might display a modular organisation. Similarly, the shape of the proximal femur could covary with the pelvic bone, although this covariation has been proved to be weak or inexistent on other mammal groups like equids or marsupials (Hanot et al., 2017; Martín-Serra & Benson, 2019). All these questions remain to be addressed among modern and fossil rhinos through relevant modularity test (Goswami & Polly, 2010; Klingenberg, 2014).

Bone shape and phylogenetic relationships

The differences of shape variation patterns between the stylopodium and the zeugopodium may be related to functional modifications of the limb parts. In addition, and except for the fibula (see below), shape as well as size, mass and gracility carry a strong phylogenetic signal. The shape variation of the complete femur remains very similar among each clade and poorly converge with morphology observed in other clades. This likely underlines the influence of the evolutionary legacy on the morphological diversity of this bone. This is less clear for its distal part only as well as the tibia, for which some taxa can share shape similarities despite being phylogenetically distant (i.e. *Elasmotherium*, *Aphelops* and *Diaceratherium*). This tends to confirm previous observations among modern rhinos, indicating a stronger effect of evolutionary relationships on the stylopodium than on the zeugopodium (see Chapters 3 and 4 - Mallet et al., 2019; 2020).

The fibula appears as an exception among these bones, as its shape and its centroid size carry almost no phylogenetic signal. Among the superfamily, only the subtribe Teleoceratina display a relative shape homogeneity for the fibula. No clear link between the shape of the fibula and the body mass can be seen either within the superfamily. These observations somewhat echo with previous results on modern rhinos, showing a puzzling intraspecific shape variation of this bone, exceeding the interspecific variation (Mallet et al., 2019). In addition, the proximal and distal synostosis surfaces of the fibula are fused with the tibia in some specimens, this fusion being potentially related to evolutionary legacy, to the high body mass of the concerned species, or the ontogenetic stage of the individual (Antoine, 2002; Polly, 2007). However, the fusion between these two bones can be observed on very different taxa, such as *Ceratotherium*, *Teleoceras* or *Menoceras*, without any obvious trend linked to phylogeny or body mass. This fusion can slightly modify the shape of the fibula, notably the interosseous crest and the size and shape of the distal synostosis surface. Moreover, shape data show important differences between the patterns of variation of the tibia and fibula, suggesting some level of independency

between these two bones, as previously observed on modern rhinos in Chapter 4 (Mallet et al., 2020). The relationships between shape variation, function and phylogeny thus remain unclear for the fibula and needs further investigations.

Beyond these general trends, some groups among the superfamily follow remarkably different tendencies in their shape variation. Giant Paraceratheriidae, despite their extreme size and mass, rarely possess a shape appearing as extreme relatively to other Rhinocerotoidea. In fact, their hind limb bones show surprising proximities with some Aceratheriini, Teleoceratina or Rhinocerotina. This underlines that these extreme proportions are not directly related to extreme shape conformations and, conversely, that taxa with very different body mass can share shape similarities. This proximity could be related to the general body plan of these species: Paraceratheriidae are known to retain a "cursorial" body plan with a high degree of gracility (Granger & Gregory, 1936; Prothero, 2013) and their limb bones seem more constrained by this general body organisation than by constraints due to high body weight support and propulsion.

Conversely, Teleoceratina is another group deviating from the general trend of shape variation common to the whole superfamily. Teleoceratina often constitute extremes of shape variation, particularly the zeugopodial bones of highly brachypodial taxa like *Teleoceras*. This high degree of brachypody is also encountered in phylogenetically distant genera like *Pleuroceros* and *Chilotherium*, leading to marked shape similarities, especially on the zeugopodium. This convergent condition might be related to particular developmental trends among these groups, leading to a shortening of the distal limb. Such a particular condition may be involved in functional roles specific to these groups, as walking on soft and unstable grounds (Boada-Saña, Hervet & Antoine, 2007) or even a semi-aquatic ecology, although this hypothesis seems unlikely given recent work (MacFadden, 1998; Mead, 2000; Mihlbachler, 2003; Prothero, 2005; Clementz, Holroyd & Koch, 2008; Wang & Secord, 2020). Further investigations on brachypodial taxa should help to clarify the origin and functional roles of this particular condition.

Differences between fore and hind limb bones

These results on hind limb bones can be put into perspective with those obtained on forelimb bones (see Chapter 5). It clearly appears that the stylopodial elements of the fore and hind limbs share similar patterns of shape variation. The morphological changes of both the humerus and femur appear simultaneously correlated with size, mass and gracility while also carrying a strong phylogenetic signal. Toward high body mass, both humerus and femur display an increase of the general robustness, associated with a development of both epiphyses, the reinforcement of muscular insertions and their displacement leading to lengthened lever arms. At the opposite, zeugopodial elements are only impacted by the degree of brachypody (at the scale of the whole superfamily), related to the distribution of the

mass within the body rather to the absolute mass itself. Highly brachypodial taxa display an increase of robustness and a development of the epiphyses as well. Some anatomical areas, like the medial and lateral parts of the proximal epiphysis of both the radius and tibia, show a remarkably similar trend of shape variation towards a high degree of brachypody. All these results partially invalidate the fifth hypothesis, as differences in patterns of shape variation are stronger between the stylopodium and zeugopodium than between the fore and hind limbs. Similar observations were partially obtained on modern rhinos in Chapters 3 and 4 (Mallet et al., 2019, 2020) and this general trend may indicate that serial homology between fore and hind limb elements remain strong (Young & Hallgrímsson, 2005) despite slightly different functional requirements (Henderson, 1999; Regnault et al., 2013; Panagiotopoulou, Pataky & Hutchinson, 2019).

However, some differences in functional role may exist between fore and hind limbs. While the body mass and gracility index (GI-MC3 computed on the third metacarpal) were correlated in the fore limb bones (see Chapter 5), this correlation with the same index (GI-MT3) computed on metatarsals is not significant. In other words, the variation in gracility of the hind limb is decoupled from that of body mass, while they are closely associated for the fore limb. This highlights differences of general organisation between fore and hind limbs and supports the idea that forelimb bones among Rhinocerotoidea may be more constrained by the weight repartition than are the hind limb ones, in association with their involvement in other functions like ensuring a powerful propulsion (Alexander, 1985; Dutto et al., 2006; Henderson, 2006; Regnault et al., 2013; Panagiotopoulou, Pataky & Hutchinson, 2019). Moreover, some bones might show a modular organisation, notably the ones constituting the elbow (ulna) and knee (femur) joints (the modular condition of the tibia remaining to be tested as well). However, in the forelimb, the trends in shape variation (as observed in morphospaces, NJ trees and regression plots) were similar between the complete humerus and its distal part, which displayed similarities with the proximal ulna. Conversely, on the hind limb, the shape variation of the complete femur (observed in morphospaces, NJ trees and regression plots as well) is only congruent with its proximal part, while that of the distal part of the femur is more congruent with the tibia one. Consequently, if morphological modules exist in the elbow and the knee joints of Rhinocerotoidea, they may not be organised in a homologous way, the former involving the humerus and the proximal ulna while the latter would involve the distal femur and the tibia. These differences may be related to the distinct joint construction between the fore and hind limb. Beyond their respective bending in opposite directions, the elbow joint constitutes a strongly constrained hinge restricted to craniocaudal movements only, formed by the humerus, the radius and the ulna together. Conversely, the knee joint, involving the femur and the tibia held together by powerful ligaments only, allows slight mediolateral rotations in addition to craniocaudal movements (Hildebrand, 1974). Moreover, the presence of the patella, considered as

functionally homologous to the olecranon process of the ulna but being an independent bone, confers to the knee cap a very different structure than that of the elbow joint, likely related to the observed variations in shape patterns. Only a larger investigation of potential morphological modules and on the construction of these joints could shed light on these questions.

Conclusion

Among Rhinocerotoidea, the shape of hind limb bones appears related to body proportions in a complex way. Beyond a common increase of robustness and reinforcement of muscular insertions towards higher body mass, the shape of stylopodial and zeugopodial bones does not follow the same patterns of variation. In addition to a clear impact of body proportions, shape changes carry a strong phylogenetic signal, to a much larger extent for the femur than for the tibia and fibula. At the scale of the superfamily, the degree of brachypody is the only tested parameter that is almost exclusively correlated to the shape of the zeugopodial bones. More than the overall absolute mass, it is its distribution in the body and the position of the centre of gravity that may drive the shape variation of hind limb bones. Only the fibula exhibits puzzling and unclear relations between shape and variations of body proportions. Moreover, the potential modularity of the femur, coupled with that observed on the forelimb, suggesting the singularity of the bones forming the knee joint, confirming the need to explore further covariations patterns between bone parts. Finally, more differences are observed between stylopodium and zeugopodium than between fore and hind limbs, suggesting to explore further the origin of these differences through a more integrative approach.

Appendices

Appendix 1: Complete list of all the studied specimens

Institutional abbreviations as given in Chapter 2. Age: E: Early; L: Late; M: Middle; Side: L: left; R: Right.

Femur

Genus	Species	Institution	Number	Locality	Country	Epoch	Side	Condition	Confirmation of specific attribution
Alicornops	*simorrense*	NHMUK	PAL PV OR 33531	Villefranche d'Astarac	France	M. Miocene	R	Partial distal	In situ determination by P.-O. Antoine
Aphelops	*malacorhinus*	AMNH	F:AM 104153	Mixson's Bone Bed, Alucha Form.	Florida, USA	L. Miocene	R	Complete	Indirect confirmation in Prothero, 2005
Aphelops	*malacorhinus*	AMNH	F:AM 114361	Wray Area, Loc. B, Ogallala Form.	Colorado, USA	L. Miocene	L	Complete	Prothero, 2005
Aphelops	*megalodus*	AMNH	F:AM 114622	Ranch House Draw, Sheep Creek Form.	Nebraska, USA	E. Miocene	L	Complete	Prothero, 2005
Aphelops	*mutilus*	AMNH	F:AM 114882B	Coffee Ranch, Hemphill Beds	Texas, USA	L. Miocene	R	Complete	Prothero, 2005
Ceratotherium	*cf. primaevum*	MNHN	F.1951-9-232	Bou Hanifia	Algeria	L. Miocene	R	Complete	Arambourg, 1959; Geraads, 2010
Ceratotherium	*neumayri*	MNHN	F.PIK 1323	Pikermi	Greece	L. Miocene	R	Complete	Indirect confirmation in Pandolfi, 2016; Antoine & Sen, 2016
Ceratotherium	*simum*	NHMUK	ZD 2018.143	Unknown	Unknown	Modern	L	Complete	Mallet et al., 2019
Ceratotherium	*simum*	RBINS	35208	Unknown	Unknown	Modern	R	Complete	RBINS database
Ceratotherium	*simum*	RMCA	1985.32-M-0001	Unknown	Sudan	Modern	L	Complete	RMCA database
Chilotherium	*kowalevskii*	BSPG	1968 VI 393	Afyon / Sandikli / Garkin	Turkey	L. Miocene	R	Complete	Heissig, 1975
Coelodonta	*antiquitatis*	MHNT	PAL.2010.23.1	Tyumen Oblast	Russia	Pleistocene	L	Complete	MHNT database
Coelodonta	*antiquitatis*	RBINS	Vert-00000-00217	Unknown	Unknown	Pleistocene	L	Complete	RBINS database
Coelodonta	*nihowanensis*	MNHN	F.NIH 156	Pikermi	Greece	L. Pliocene	R	Complete	MNHN database
Diaceratherium	*aginense*	AR	B2-0008	Gannat	France	E. Miocene	L	Partial distal	Indirect confirmation in Boada-Saña, 2008
Diaceratherium	*aurelianense*	MNHN	F.NEU 14	Neuville-aux-bois	France	E. Miocene	L	Complete	Indirect confirmation in Cerdeño, 1993
Diaceratherium	*aurelianense*	NMB	S.O.5544	Ronville	France	E. Miocene	R	Complete	Indirect confirmation in Jame et al., 2019

Diaceratherium	*aurelianense*	NMB	S.O.5560	Ronville	France	E. Miocene	R	Complete	Indirect confirmation in Jame et al., 2019
Dicerorhinus	*aff. sansaniensis*	NHMUK	PAL PV M 36783	Al Dabtiyah	Saudi Arabia	E. Miocene	L	Complete	Gentry, 1987
Dicerorhinus	*sumatrensis*	NHMUK	ZD 1879.6.14.2	Unknown	Malaysia	Modern	R	Complete	NHMUK database
Dicerorhinus	*sumatrensis*	NHMUK	ZE 1948.12.20.1	Unknown	Unknown	Modern	L	Complete	NHMUK database
Dicerorhinus	*sumatrensis*	NHMUK	ZE 1949.1.11.1	Tring	Indonesia	Modern	L	Complete	NHMUK database
Diceros	*bicornis*	MNHN	ZM-AC-1936-644	Unknown	Unknown	Modern	L	Complete	MNHN database
Diceros	*bicornis*	CCEC	50002040	Natal	South Africa	Modern	R	Complete	CCEC database
Diceros	*bicornis*	RBINS	9714	Unknown	Democratic Republic of the Congo	Modern	L	Complete	RBINS database
Dihoplus	*megarhinus*	FSL	40030	Montpellier	France	L. Pliocene	R	Complete	Indirect confirmation in Guérin, 1980
Dihoplus	*megarhinus*	FSL	40034	Montpellier	France	L. Pliocene	L	Complete	Indirect confirmation in Guérin, 1980
Dihoplus	*megarhinus*	FSL	40422	Montpellier	France	L. Pliocene	L	Complete	Indirect confirmation in Guérin, 1980
Dihoplus	*pikermiensis*	MNHN	F.PIK 955	Pikermi	Greece	L. Miocene	L	Complete	Indirect confirmation in Antoine & Saraç, 2005; Pandolfi, Gasparik & Piras, 2015
Dihoplus	*schleiermacheri*	MNHN	F.LUB 953	Luberon	France	L. Miocene	L	Partial proximal	Pernègre & Tassy, 2014
Dihoplus	*schleiermacheri*	MNHN	FMCF 60	Saint-Bauzille	France	L. Miocene	R	Complete	Métais & Sen, 2018
Hoploaceratherium	*tetradactylum*	MNHN	F.SA 10172-K	Sansan	France	M. Miocene	R	Partial proximal and distal	Heissig, 2012
Hoploaceratherium	*tetradactylum*	MNHN	F.SA 15636	Sansan	France	M. Miocene	R	Partial distal	Heissig, 2012
Hyrachyus	*eximius*	AMNH	FM 11712	Church Buttes, Bridger Form.	Wyoming, USA	M. Eocene	L	Complete	Indirect confirmation in Wood, 1934
Hyrachyus	*eximius*	AMNH	FM 12665	Church Buttes, Bridger Form.	Wyoming, USA	M. Eocene	L	Complete	Bai et al., 2017
Hyrachyus	*eximius*	AMNH	FM 12675	Millersville, Bridger Form.	Wyoming, USA	M. Eocene	L	Complete	Bai et al., 2017

Hyrachyus	*modestus*	AMNH	FM 11662	Millersville, Bridger Form.	Wyoming, USA	M. Eocene	L	Complete	Bai et al., 2017
Hyracodon	*nebraskensis*	AMNH	FM 1168	Hat Creek Basin, Brule Form.	Nebraska, USA	E. Oligocene	L	Complete	Wall & Hickerson, 1995
Hyracodon	*nebraskensis*	AMNH	FM 1480	Hat Creek Basin, Brule Form.	Nebraska, USA	E. Oligocene	R	Partial distal	Wall & Hickerson, 1995
Hyracodon	*nebraskensis*	AMNH	FM 560	Cheyenne River, Brule Form.	South Dakota, USA	E. Oligocene	R	Complete	AMNH database
Lartetotherium	*sansaniense*	MNHN	F.SA 15635	Sansan	France	M. Miocene	R	Complete	Heissig, 2012
Menoceras	*arikarense*	AMNH	FM 22486	Agate Springs Quarry, Anderson Ranch Form.	Nebraska, USA	E. Miocene	R	Complete	Indirect confirmation in Prothero, 2005
Menoceras	*arikarense*	YPM	VPPU 012213	Agate Springs Quarry, Anderson Ranch Form.	Nebraska, USA	E. Miocene	L	Complete (2 bones)	Indirect confirmation in Prothero, 2005
Metamynodon	*planifrons*	YPM	VPPU 010887	Metamynodon Beds, Cottonwood Creek	South Dakota, USA	E. Oligocene	R	Partial proximal	Indirect confirmation in Scott & Jepsen, 1941
Metamynodon	*planifrons*	YPM	VPPU 011017	Metamynodon Beds, Cottonwood Creek	South Dakota, USA	E. Oligocene	R	Complete	Indirect confirmation in Scott & Jepsen, 1941
Paraceratherium	*grangeri*	AMNH	FM 26169	Nom Khong Obo	China	E. Oligocene	R	Partial proximal	Qiu & Wang, 2007
Paraceratheirum	*grangeri*	AMNH	FM 26169	Nom Khong Obo	China	E. Oligocene	L	Partial distal	Qiu & Wang, 2007
Paraceratherium	*grangeri*	AMNH	FM 21619	Övörkhangai province	Mongolia	E. Oligocene	L	Partial distal	Qiu & Wang, 2007
Peraceras	*hessei*	AMNH	F:AM 108327	McMurry Pit 2, U. Fleming Form.	Texas, USA	M. Miocene	R	Complete	Prothero & Manning, 1987
Peraceras	*profectum*	AMNH	F:AM 114970	Pojoaque Bluffs, Tesuque Form.	New Mexico, USA	M. Miocene	R	Complete	Prothero, 2005
Pleuroceros	*blanfordi*	AMNH	FM 29832	Siwalik, Dhok Pathan	India	E. Miocene	R	Complete	Colbert, 1935
Prosantorhinus	*douvillei*	MHNT	PAL.2013.0.1007	Montréal-du-Gers	France	E. Miocene	R	Partial proximal and distal	In situ determination by P.-O. Antoine
Prosantorhinus	*douvillei*	MHNT	PAL.2015.0.1045.1	Montréal-du-Gers	France	E. Miocene	L	Partial distal	In situ determination by P.-O. Antoine
Protaceratherium	*minutum*	FSL	213781	Budenheim	Germany	L. Oligocene	R	Complete	Antunes & Ginsburg, 1983
Rhinoceros	*philippinensis*	NMP	2014-II-J1-287	Kalinga	Philippines	M. Pleistocene	R	Complete	Ingicco et al., 2018

Rhinoceros	*sondaicus*	CCEC	50002041	Cochinchina	Vietnam	Modern	R	Complete	CCEC database
Rhinoceros	*sondaicus*	MNHN	ZM-AC-A7970	Unknown	Unknown	Modern	L	Complete	MNHN database
Rhinoceros	*sondaicus*	MNHN	ZM-AC-A7971	Java	Indonesia	Modern	L	Complete	MNHN database
Rhinoceros	*unicornis*	NHMUK	ZD 1884.1.22.1.2	Assam	India	Modern	R	Complete	NHMUK database
Rhinoceros	*unicornis*	NHMUK	ZE 1950.10.18.5	Unknown	Nepal	Modern	L	Complete	NHMUK database
Rhinoceros	*unicornis*	NHMUK	ZE 1961.5.10.1	Assam	India	Modern	L	Partial distal	NHMUK database
Stephanorhinus	*jeanvireti*	MNHN	F.PET 2003	Perrier-Etouaires	France	E. Pliocene	R	Complete	Indirect confirmation in Guérin, 1980
Stephanorhinus	*jeanvireti*	CCEC	V180	Vialette	France	L. Pliocene	L	Partial distal	Guérin, 1972; Pandolfi, Codrea, & Popescu, 2019
Stephanorhinus	*etruscus*	MNHN	F.1923-8	Senèze	France	L. Pliocene	R	Complete	Indirect confirmation in Guérin, 1980; Pandolfi et al., 2017b
Stephanorhinus	*etruscus*	FSL	210953	Senèze	France	L. Pliocene	R	Complete	Indirect confirmation in Guérin, 1980; Pandolfi et al., 2017b
Stephanorhinus	*etruscus*	FSL	210955	Senèze	France	L. Pliocene	L	Complete	Indirect confirmation in Guérin, 1980; Pandolfi et al., 2017b
Stephanorhinus	*hemitoechus*	NHMUK	PAL PV M 36620a	Selsey	UK	L. Pleistocene	L	Partial proximal	Indirect confirmation in Fortelius, Mazza & Sala, 1993; Scott, 2007
Stephanorhinus	*hemitoechus*	CCEC	Pp256	Perpignan	France	Pleistocene	L	Complete	CCEC database
Subhyracodon	*mitis*	AMNH	FM 6325	Horsetail Creek, Brule Form.	Colorado, USA	L. Eocene	R	Complete	Prothero, 2005
Subhyracodon	*occidentalis*	AMNH	FM 1019	Cheyenne River, White River Form.	South Dakota, USA	E. Oligocene	R	Complete	Indirect confirmation in Prothero, 2005
Subhyracodon	*occidentalis*	AMNH	FM 6325	Cheyenne River, Brule Form.	South Dakota, USA	E. Oligocene	L	Partial proximal	Prothero, 2005

Teleoceras	*fossiger*	AMNH	FM 2665	Long Island Rhino Quarry, Ogallala Form.	Kansas, USA	L. Miocene	R	Complete	Indirect confirmation in Prothero, 2005
Teleoceras	*fossiger*	YPM	VP 039025	Long Island Rhino Quarry, Ogallala Form.	Kansas, USA	L. Miocene	L	Complete	Indirect confirmation in Prothero, 2005
Teleoceras	*fossiger*	YPM	VP 039026	Long Island Rhino Quarry, Ogallala Form.	Kansas, USA	L. Miocene	L	Complete	Indirect confirmation in Prothero, 2005
Teleoceras	*hicksi*	AMNH	F:AM 114588	Wray Locality C, Ogallala Form.	Colorado, USA	L. Miocene	L	Complete	Prothero, 2005
Teleoceras	*proterum*	AMNH	F:AM 104155	Mixson's Bone Bed, Alucha Form.	Florida, USA	L. Miocene	R	Complete	Indirect confirmation in Prothero, 2005
Trigonias	*osborni*	UCMP	32011	Figgins Quarry	Colorado, USA	L. Eocene	L	Complete	Prothero & Schoch, 1989
Trigonias	*wellsi*	AMNH	FM 13226E	Corral Draw, Chadron Form.	South Dakota, USA	L. Eocene	L	Partial distal	Prothero, 2005
Urtinotherium	*intermedium*	AMNH	FM 26393	Camp Margetts, Sui-yuan Province	China	Oligocene	L	Complete	Indirect confirmation in Bai et al., 2018

Tibia

Genus	Species	Institution	Number	Locality	Country	Age	Side	Condition	Confirmation of specific attribution
Acerorhinus	*zernowi*	AMNH	FM 129841	Gur Tung Khara Usu	China	M. Miocene	R	Complete	Cerdeño, 1996a
Acerorhinus	*zernowi*	AMNH	FM 26215	Gur Tung Khara Usu	China	M. Miocene	R	Complete	Cerdeño, 1996a
Aphelops	*malacorhinus*	AMNH	F:AM 104154	Mixson's Bone Bed, Alucha Form.	Florida, USA	L. Miocene	R	Complete	Indirect confirmation in Prothero, 2005
Aphelops	*malacorhinus*	AMNH	F:AM 114833B	Box T Ranch, West Draw, Ogallala Form.	Texas, USA	L. Miocene	L	Complete	Prothero, 2005
Aphelops	*malacorhinus*	AMNH	F:AM 114844	Box T Ranch, West Draw, Ogallala Form.	Texas, USA	L. Miocene	L	Complete	Prothero, 2005
Aphelops	*megalodus*	AMNH	F:AM 108905A	Trinity River Pit 1, Fleming Form.	Texas, USA	M. Miocene	L	Complete	Prothero, 2005
Aphelops	*megalodus*	AMNH	F:AM 114621	Hilltop Quarry, Sheep Creek Form.	Nebraska, USA	E. Miocene	L	Complete	Prothero, 2005
Aphelops	*mutilus*	AMNH	F:AM 114883F	Coffee Ranch, Hemphill Beds	Texas, USA	L. Miocene	R	Complete	Prothero, 2005
Brachypotherium	*brachypus*	MNHN	F.SML 284	Malartic	France	M. Miocene	L	Complete	Cerdeño, 1993
Brachypotherium	*brachypus*	NMB	S.O.4178	Baigneaux	France	E. Miocene	L	Complete	NMB database
Ceratotherium	*cf. primaevum*	MNHN	F.1951-9-139	Bou Hanifia	Algeria	L. Miocene	L	Complete	Arambourg, 1959; Geraads, 2010
Ceratotherium	*cf. primaevum*	MNHN	F.1951-9-182	Bou Hanifia	Algeria	L. Miocene	R	Complete	Arambourg, 1959; Geraads, 2010
Ceratotherium	*cf. primaevum*	MNHN	F.1951-9-227	Bou Hanifia	Algeria	L. Miocene	R	Complete	Arambourg, 1959; Geraads, 2010
Ceratotherium	*neumayri*	NHMUK	PAL PV M 4419	Samos Island	Greece	L. Miocene	R	Complete	Indirect confirmation in Geraads, 1988; Giaourtsakis, 2009
Ceratotherium	*neumayri*	NHMUK	PAL PV M 5423	Samos Island	Greece	L. Miocene	L	Complete	Indirect confirmation in Geraads, 1988; Giaourtsakis, 2009
Ceratotherium	*simum*	NHMUK	ZD 2018.143	Unknown	Unknown	Modern	L	Complete	Mallet et al., 2019
Ceratotherium	*simum*	RMCA	1985.32-M-0001	Unknown	Sudan	Modern	L	Complete	RMCA database
Ceratotherium	*simum*	AMNH	M-51854	Faradje	Democratic Republic of the Congo	Modern	L	Complete	AMNH database

Coelodonta	*antiquitatis*	MHNT	PAL.2010.23.1	Tyumen Oblast	Russia	Pleistocene	L	Complete	MHNT database
Coelodonta	*antiquitatis*	NHMUK	PAL PV M 82733	Cross-at-Hand, Tonbridge	UK	Pleistocene	R	Complete	NHMUK database
Coelodonta	*antiquitatis*	RBINS	Vert-00000-000506	Unknown	Unknown	Pleistocene	L	Complete	RBINS database
Coelodonta	*nihowanensis*	MNHN	F.NIH 152	Nihewan	China	L. Pliocene	R	Complete	MNHN database
Diaceratherium	*aginense*	AR	B2-1396	Gannat	France	E. Miocene	R	Complete	Boada-Saña, 2008
Diaceratherium	*aginense*	AR	B2-1716	Gannat	France	E. Miocene	R	Complete	Boada-Saña, 2008
Diaceratherium	*asphaltense*	NMB	SAU-1662	Saulcet	France	E. Miocene	R	Complete	Indirect confirmation in Jame et al., 2019
Diaceratherium	*aurelianense*	MNHN	F.AR 2160	Artenay	France	E. Miocene	R	Complete	Cerdeño, 1993
Diaceratherium	*aurelianense*	NMB	S.O.5591	Chilleurs	France	E. Miocene	L	Complete	NMB database
Diaceratherium	*lemanense*	AR	B2-1716	Gannat	France	E. Miocene	R	Complete	Boada-Saña, 2008
Diaceratherium	*lemanense*	MNHN	F.SG 9580	Saint-Gérand-le-Puy	France	E. Miocene	L	Complete	Bucher, Ginsburg & Cheneval, 1985
Diceratherium	*armatum*	AMNH	F:AM 132058	77 Hill Quarry, Harrison Form.	Wyoming, USA	L. Oligocene	R	Complete	Indirect confirmation in Prothero, 2005
Diceratherium	*tridactylum*	AMNH	FM 537	Big Badlands, Brule Form.	South Dakota, USA	E. Oligocene	R	Complete	Prothero, 2005
Dicerorhinus	*sumatrensis*	NHMUK	ZD 1879.6.14.2	Unknown	Malaysia	Modern	R	Complete	NHMUK database
Dicerorhinus	*sumatrensis*	NHMUK	ZE 1948.12.20.1	Unknown	Unknown	Modern	L	Complete	NHMUK database
Dicerorhinus	*sumatrensis*	NHMUK	ZE 1949.1.11.1	Tring	Indonesia	Modern	L	Complete	NHMUK database
Diceros	*bicornis*	MNHN	ZM-AC-1936-644	Unknown	Unknown	Modern	L	Complete	MNHN database
Diceros	*bicornis*	CCEC	50002040	Natal	South Africa	Modern	R	Complete	CCEC database
Diceros	*bicornis*	RBINS	9714	Unknown	Democratic Republic of the Congo	Modern	L	Complete	RBINS database
Dihoplus	*megarhinus*	FSL	40031	Montpellier	France	L. Pliocene	L	Complete	Indirect confirmation in Guérin, 1980
Dihoplus	*megarhinus*	FSL	40032	Montpellier	France	L. Pliocene	R	Complete	Indirect confirmation in Guérin, 1980
Dihoplus	*megarhinus*	FSL	40421	Montpellier	France	L. Pliocene	L	Complete	Indirect confirmation in Guérin, 1980
Dihoplus	*pikermiensis*	MNHN	F.PIK 993	Pikermi	Greece	L. Miocene	R	Complete	Indirect confirmation in Antoine & Saraç,

									2005; Pandolfi, Gasparik & Piras, 2015
Dihoplus	*schleiermacheri*	FSL	M.633	Saint-Bauzille	France	L. Miocene	R	Complete	Métais & Sen, 2018
Dihoplus	*schleiermacheri*	MNHN	FMCF 60	Saint-Bauzille	France	L. Miocene	R	Complete	Métais & Sen, 2018
Elasmotherium	*sibiricum*	NHMUK	PAL PV M 5227a	Siberia	Russia	Pleistocene	L	Complete	NHMUK database
Hoploaceratherium	*tetradactylum*	NHMUK	PAL PV M 27458	Sansan	France	M. Miocene	L	Complete	In situ determination by P.-O. Antoine
Hoploaceratherium	*tetradactylum*	MNHN	F.SA 10170-68	Sansan	France	M. Miocene	L	Complete	Heissig, 2012
Hoploaceratherium	*tetradactylum*	MNHN	F.SA 5419	Sansan	France	M. Miocene	L	Complete	Heissig, 2012
Hyrachyus	*eximius*	AMNH	FM 11712	Church Buttes, Bridger Form.	Wyoming, USA	M. Eocene	L	Complete	Indirect confirmation in Wood, 1934
Hyrachyus	*eximius*	AMNH	FM 12364	Henry's Fork, Bridger Form.	Wyoming, USA	M. Eocene	R	Complete	Bai et al., 2017
Hyrachyus	*eximius*	AMNH	FM 93065	Grizzly Butte, Bridger Form.	Wyoming, USA	M. Eocene	L	Complete	AMNH database
Hyrachyus	*modestus*	AMNH	FM 11662	Millersville, Bridger Form.	Wyoming, USA	M. Eocene	L	Complete	Bai et al., 2017
Hyracodon	*nebraskensis*	AMNH	FM 9789	Cedar Draw, Brule Form.	South Dakota, USA	E. Oligocene	R	Complete	Wall & Hickerson, 1995
Hyracodon	*nebraskensis*	AMNH	FM 9789	Cedar Draw, Brule Form.	South Dakota, USA	E. Oligocene	L	Complete	Wall & Hickerson, 1995
Menoceras	*arikarense*	AMNH	F:AM 116317A	Agate Springs Quarry, Anderson Ranch Form.	Nebraska, USA	E. Miocene	L	Complete	Indirect confirmation in Prothero, 2005
Menoceras	*arikarense*	AMNH	F:AM 116319	Agate Springs Quarry, Anderson Ranch Form.	Nebraska, USA	E. Miocene	R	Complete	Indirect confirmation in Prothero, 2005
Menoceras	*arikarense*	NHMUK	PAL PV M 15497	Agate Springs Quarry, Anderson Ranch Form.	Nebraska, USA	E. Miocene	R	Complete	Indirect confirmation in Prothero, 2005
Paraceratherium	*grangeri*	MNHN	F.1924-14	Ordos	China	M. Eocene	L	Complete (2 bones)	Indirect confirmation in Qiu & Wang, 2007
Peraceras	*hessei*	AMNH	F:AM 108274	McMurry Pit 2, U. Fleming Form.	Texas, USA	M. Miocene	R	Complete	Prothero & Manning, 1987
Peraceras	*profectum*	AMNH	F:AM 114970	Pojoaque Bluffs, Tesuque Form	New Mexico, USA	M. Miocene	R	Complete	Prothero, 2005

Plesiaceratherium	*mirallesi*	MHNT	PAL.2015.0.1414	Montréal-du-Gers	France	E. Miocene	R	Complete	In situ determination by P.-O. Antoine
Pleuroceros	*blanfordi*	AMNH	FM 29832	Siwalik, Dhok Pathan	India	E. Miocene	R	Complete	Colbert, 1935
Prosantorhinus	*douvillei*	MHNT	PAL.2015.0.1043.1	Montréal-du-Gers	France	E. Miocene	R	Complete	In situ determination by P.-O. Antoine
Prosantorhinus	*douvillei*	MHNT	PAL.2020.0.1	Montréal-du-Gers	France	E. Miocene	L	Complete	MHNT database
Prosantorhinus	*douvillei*	MHNT	PAL.2020.0.2	Montréal-du-Gers	France	E. Miocene	R	Complete	MHNT database
Protaceratherium	*minutum*	FSL	213781	Budenheim	Germany	L. Oligocene	R	Complete	Antunes & Ginsburg, 1983
Rhinoceros	*philippinensis*	NMP	2014-II-J1-286	Kalinga	Philippines	M. Pleistocene	R	Complete	Ingicco et al., 2018
Rhinoceros	*sondaicus*	CCEC	50002041	Cochinchina	Vietnam	Modern	R	Complete	CCEC database
Rhinoceros	*sondaicus*	MNHN	ZM-AC-A7970	Unknown	Unknown	Modern	L	Complete	MNHN database
Rhinoceros	*sondaicus*	MNHN	ZM-AC-A7971	Java	Indonesia	Modern	R	Complete	MNHN database
Rhinoceros	*unicornis*	NHMUK	ZD 1884.1.22.1.2	Assam	India	Modern	R	Complete	NHMUK database
Rhinoceros	*unicornis*	NHMUK	ZE 1950.10.18.5	Unknown	Nepal	Modern	L	Complete	NHMUK database
Rhinoceros	*unicornis*	MNHN	ZM-AC-1960-59	Vincennes Zoo	France	Modern	L	Complete	MNHN database
Stephanorhinus	*jeanvireti*	CCEC	V236	Vialette	France	L. Pliocene	R	Complete	Guérin, 1972; Pandolfi, Codrea, & Popescu, 2019
Stephanorhinus	*jeanvireti*	CCEC	V237	Vialette	France	L. Pliocene	R	Complete	Guérin, 1972; Pandolfi, Codrea, & Popescu, 2019
Stephanorhinus	*etruscus*	MNHN	F.1923-8	Senèze	France	L. Pliocene	L	Complete	Indirect confirmation in Guérin, 1980; Pandolfi et al., 2017b
Stephanorhinus	*etruscus*	FSL	210959	Senèze	France	L. Pliocene	R	Complete	Indirect confirmation in Guérin, 1980; Pandolfi et al., 2017b
Stephanorhinus	*hemitoechus*	NHMUK	PAL PV M 36620a	Selsey	UK	L. Pleistocene	L	Complete	Indirect confirmation in Fortelius, Mazza & Sala, 1993; Scott, 2007
Stephanorhinus	*hemitoechus*	NHMUK	PAL PV OR 38570	Ilford	UK	M. Pleistocene	R	Complete	Indirect confirmation in Fortelius, Mazza & Sala, 1993

Subhyracodon	*mitis*	AMNH	FM 6325	Cedar Creek, White River Form.	Colorado, USA	L. Eocene	L	Complete	Prothero, 2005
Teleoceras	*fossiger*	AMNH	FM 2649	Long Island Rhino Quarry, Ogallala Form.	Kansas, USA	L. Miocene	R	Complete	Indirect confirmation in Prothero, 2005
Teleoceras	*fossiger*	AMNH	FM 2651	Long Island Rhino Quarry, Ogallala Form.	Kansas, USA	L. Miocene	L	Complete	Indirect confirmation in Prothero, 2005
Teleoceras	*fossiger*	YPM	VP 039042	Long Island Rhino Quarry, Ogallala Form.	Kansas, USA	L. Miocene	L	Complete	Indirect confirmation in Prothero, 2005
Teleoceras	*proterum*	AMNH	F:AM 104156	Mixson's Bone Bed, Alucha Form.	Florida, USA	L. Miocene	R	Complete	Prothero, 2005

Fibula

Genus	Species	Institution	Number	Locality	Country	Age	Side	Condition	Confirmation of specific attribution
Acerorhinus	*zernowi*	AMNH	FM 26215	Gur Tung Khara Usu	China	M. Miocene	L	Complete	Cerdeño, 1996a
Aphelops	*malacorhinus*	AMNH	F:AM 114844	Box T Pit, Ogallala Form.	Texas, USA	L. Miocene	L	Complete	Prothero, 2005
Aphelops	*megalodus*	AMNH	F:AM 108948A	McMurry Pit 2, U. Fleming Form.	Texas, USA	M. Miocene	L	Complete	Prothero & Manning, 1987
Aphelops	*megalodus*	AMNH	F:AM 114642A	Observation Quarry, Olcott Form.	Nebraska, USA	M. Eocene	R	Complete	Prothero, 2005
Brachypotherium	*brachypus*	MNHN	F.BA 2808	Baigneaux	France	E. Miocene	L	Complete	Cerdeño, 1993
Brachypotherium	*brachypus*	MNHN	F.SML 1086	Malartic	France	M. Miocene	R	Complete	Cerdeño, 1993
Brachypotherium	*brachypus*	MNHN	F.SML 1224	Malartic	France	M. Miocene	R	Complete	Indirect confirmation in Cerdeño, 1993
Ceratotherium	*neumayri*	AMNH	FM 22866	Samos Island	Greece	L. Miocene	L	Complete	Indirect confirmation in Geraads, 1988; Giaourtsakis, 2009
Ceratotherium	*neumayri*	MNHN	F.PIK 1325	Pikermi	Greece	L. Miocene	R	Complete	Indirect confirmation in Antoine & Saraç, 2005; Pandolfi, Gasparik & Piras, 2015
Ceratotherium	*simum*	NHMUK	ZD 2018.143	Unknown	Unknown	Modern	L	Complete	Mallet et al., 2019
Ceratotherium	*simum*	RMCA	1985.32-M-0001	Unknown	Sudan	Modern	L	Complete	RMCA database
Ceratotherium	*simum*	AMNH	M-51854	Faradje	Democratic Republic of the Congo	Modern	L	Complete	AMNH database
Coelodonta	*antiquitatis*	MHNT	PAL.2010.23.1	Tyumen Oblast	Russia	Pleistocene	L	Complete	MHNT database
Coelodonta	*antiquitatis*	NHMUK	PAL PV OR 44079	Pikermi	Greece	L. Miocene	R	Complete	NHMUK database
Diaceratherium	*aginense*	AR	B2-1356	Gannat	France	E. Miocene	R	Complete	Boada-Saña, 2008
Diaceratherium	*aginense*	AR	B2-1614	Gannat	France	E. Miocene	L	Complete	Boada-Saña, 2008
Diaceratherium	*asphaltense*	NMB	SAU-1662	Saulcet	France	E. Miocene	R	Complete	Indirect confirmation in Jame et al., 2019
Diaceratherium	*aurelianense*	MNHN	F.AR 2160	Artenay	France	E. Miocene	R	Complete	Cerdeño, 1993
Dicerorhinus	*sumatrensis*	NHMUK	ZD 1879.6.14.2	Unknown	Malaysia	Modern	R	Complete	NHMUK database

Dicerorhinus	*sumatrensis*	NHMUK	ZE 1948.12.20.1	Unknown	Unknown	Modern	L	Complete	NHMUK database
Dicerorhinus	*sumatrensis*	NHMUK	ZE 1949.1.11.1	Tring	Indonesia	Modern	L	Complete	NHMUK database
Diceros	*bicornis*	MNHN	ZM-AC-1936-644	Unknown	Unknown	Modern	L	Complete	MNHN database
Diceros	*bicornis*	CCEC	50002040	Natal	South Africa	Modern	R	Complete	CCEC database
Diceros	*bicornis*	RBINS	9714	Unknown	Democratic Repub-lic of the Congo	Modern	L	Complete	RBINS database
Hoploaceratherium	*tetradactylum*	MNHN	F.SA 10170-69	Sansan	France	M. Miocene	L	Complete	Heissig, 2012
Hoploaceratherium	*tetradactylum*	MNHN	F.SA 5420	Sansan	France	M. Miocene	L	Complete	Heissig, 2012
Hoploaceratherium	*tetradactylum*	MNHN	F.SA 6317	Sansan	France	M. Miocene	L	Complete	Heissig, 2012
Hyrachyus	*eximius*	AMNH	FM 12364	Henry's Fork, Bridger Form.	Wyoming, USA	M. Eocene	R	Complete	Bai et al., 2017
Hyrachyus	*eximius*	AMNH	FM 12675	Millersville, Bridger Form.	Wyoming, USA	M. Eocene	L	Complete	Bai et al., 2017
Lartetotherium	*sansaniense*	MNHN	F.SA 6318	Sansan	France	M. Miocene	L	Complete	Heissig, 2012
Menoceras	*arikarense*	AMNH	F:AM 116317A	Agate Springs Quarry, Anderson Ranch Form.	Nebraska, USA	E. Miocene	L	Complete	Indirect confirmation in Prothero, 2005
Menoceras	*arikarense*	AMNH	FM 22487	Agate Springs Quarry, Anderson Ranch Form.	Nebraska, USA	E. Miocene	L	Complete	Indirect confirmation in Prothero, 2005
Paracerathierum	*grangeri*	AMNH	FM 26387	Camp Margetts, Suiyuan Province	China	Oligocene	L	Complete	Bai et al., 2018
Peraceras	*profectum*	AMNH	F:AM 114970	Pojoaque Bluffs, Tesuque Form.	New Mexico, USA	M. Miocene	R	Complete	Prothero, 2005
Plesiaceratherium	*mirallesi*	MHNT	PAL.2015.0.953.1	Montréal-du-Gers	France	E. Miocene	L	Complete	In situ determination by P.-O. Antoine
Pleuroceros	*blanfordi*	AMNH	FM 29832	Siwalik, Dhok Pathan	India	E. Miocene	R	Complete	Colbert, 1935
Prosantorhinus	*douvillei*	MHNT	PAL.2013.0.1007	Montréal-du-Gers	France	E. Miocene	L	Complete	In situ determination by P.-O. Antoine
Prosantorhinus	*douvillei*	MHNT	PAL.2015.0.1044.1	Montréal-du-Gers	France	E. Miocene	L	Complete	In situ determination by P.-O. Antoine
Prosantorhinus	*douvillei*	MHNT	PAL.2020.0.3	Montréal-du-Gers	France	E. Miocene	L	Complete	MHNT database
Protaceratherium	*minutum*	FSL	213781	Budenheim	Germany	L. Oligocene	R	Complete	Antunes & Ginsburg, 1983
Rhinoceros	*sondaicus*	CCEC	50002041	Cochinchina	Vietnam	Modern	R	Complete	CCEC database

Rhinoceros	*sondaicus*	MNHN	ZM-AC-A7970	Unknown	Unknown	Modern	L	Complete	MNHN database
Rhinoceros	*sondaicus*	MNHN	ZM-AC-A7971	Java	Indonesia	Modern	R	Complete	MNHN database
Rhinoceros	*unicornis*	NHMUK	ZD 1884.1.22.1.2	Assam	India	Modern	R	Complete	NHMUK database
Rhinoceros	*unicornis*	NHMUK	ZE 1950.10.18.5	Unknown	Nepal	Modern	L	Complete	NHMUK database
Rhinoceros	*unicornis*	MNHN	ZM-AC-1960-59	Vincennes Zoo	France	Modern	L	Complete	MNHN database
Stephanorhinus	*etruscus*	MNHN	F.1922-5	Senèze	France	L. Pliocene	R	Complete	Indirect confirmation in Guérin, 1980; Pandolfi et al., 2017b
Stephanorhinus	*etruscus*	NMB	515A13	Unknown	Unknown	L. Pliocene	R	Complete	NMB database
Stephanorhinus	*hemitoechus*	NHMUK	PAL PV M 36620c	Selsey	UK	L. Pleistocene	R	Complete	Indirect confirmation in Fortelius, Mazza & Sala, 1993; Scott, 2007
Teleoceras	*fossiger*	AMNH	FM 2639	Long Island Rhino Quarry, Ogallala Form.	Kansas, USA	L. Miocene	R	Complete	Indirect confirmation in Prothero, 2005
Teleoceras	*fossiger*	AMNH	FM 2645	Long Island Rhino Quarry, Ogallala Form.	Kansas, USA	L. Miocene	L	Complete	Indirect confirmation in Prothero, 2005
Teleoceras	*fossiger*	YPM	VP 039116	Long Island Rhino Quarry, Ogallala Form.	Kansas, USA	L. Miocene	L	Complete	Indirect confirmation in Prothero, 2005
Teleoceras	*proterum*	AMNH	F:AM 104156	Mixson's Bone Bed, Alucha Form.	Florida, USA	L. Miocene	R	Complete	Prothero, 2005

Appendix 2: Designation and location of the anatomical landmarks placed on each bone

Bone	Anatomical LM	Curve sliding semi-LM	Surface sliding semi-LM	Total
Femur (complete)	19	321	488	828
Femur (partial proximal part)	9	139	254	402
Femur (partial distal part)	11	216	234	461
Tibia (complete)	20	307	421	748
Fibula (complete)	9	153	258	420

Table S2A: Total number of anatomical landmarks (LM), curve sliding and surface sliding semi-landmarks for each bone.

LM	Designation
1	Most proximal point of the greater trochanter
2	Most caudal point of the greater trochanter
3	Most caudo-lateral point of the greater trochanter
4	Most lateral point of the border of the head
5	Most medial point of the border of the head
6	Most proximal point of the lesser trochanter
7	Most distal point of the lesser trochanter
8	Most proximal point of the border of the third trochanter (i.e. slope break relatively to the shaft border)
9	Most distal point of the border of the third trochanter (i.e. slope break relatively to the shaft border)
10	Most lateral point of the lateral epicondyle
11	Most proximal point of the lateral lip of the trochlea
12	Most proximal point of the trochlear groove
13	Most proximal point of the medial lip of the trochlea
14	Most medial point of the medial epicondyle
15	Most proximal point of the medial condyle border
16	Most proximal point of the lateral condyle border
17	Most distal point of the medial lip of the trochlea
18	Distal maximum of curvature of the trochlear groove
19	Most distal point of the lateral lip of the trochlea
Curve	**Designation**
C1	Distal border of the femoral head: from LM4 to LM5
C2	Lesser trochanter crest: from LM6 to LM7
C3	Third trochanter crest: from LM8 to LM9
C4	Trochlea ridge: from LM11 to LM13 + LM17 to LM19
C5	Medial condyle: from LM15 to LM15
C6	Lateral condyle: from LM16 to LM16

Table S2B: Designation of anatomical landmarks on the femur (complete analysis).

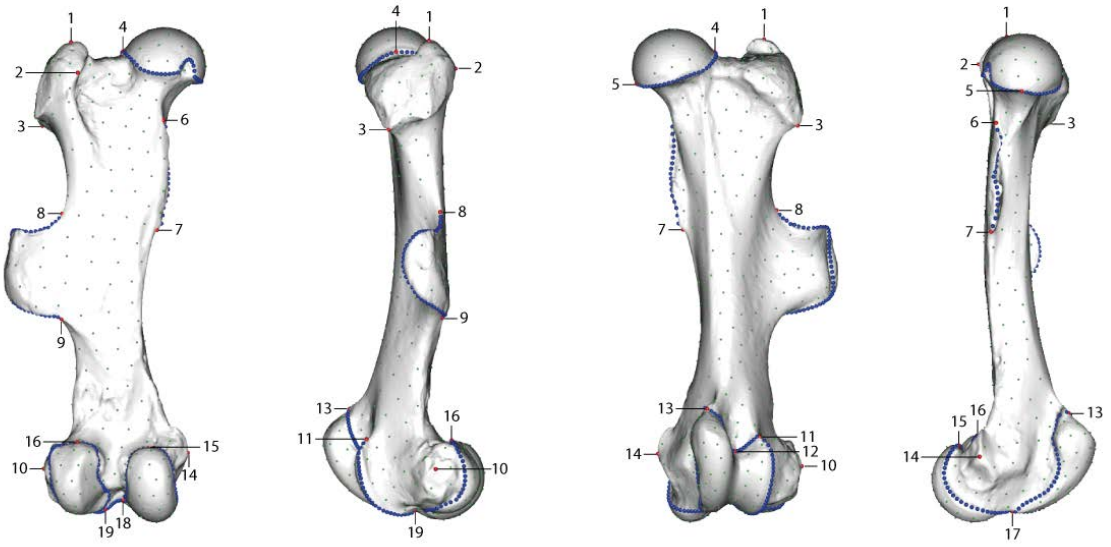

Figure S2C: Location of anatomical landmarks (red spheres), curve sliding (blue spheres) and surface sliding (green spheres) semi-landmarks placed on the femur (complete analysis). From left to right: caudal, lateral, cranial and medial views. Numbers refer to anatomical landmarks designation detailed in Table S2B.

LM	Designation
1	Most proximal point of the greater trochanter
2	Most caudal point of the greater trochanter
3	Most caudo-lateral point of the greater trochanter
4	Most lateral point of the border of the head
5	Most medial point of the border of the head
6	Most proximal point of the lesser trochanter
7	Most distal point of the lesser trochanter
8	Most proximal point of the border of the third trochanter (i.e. slope break relatively to the shaft border)
9	Most distal point of the border of the third trochanter (i.e. slope break relatively to the shaft border)
Curve	**Designation**
C1	Distal border of the femoral head: from LM4 to LM5
C2	Lesser trochanter crest: from LM6 to LM7
C3	Third trochanter crest: from LM8 to LM9
C4	Distal limit: from LM9 to LM9

Table S2D: Designation of anatomical landmarks on the femur (partial proximal analysis).

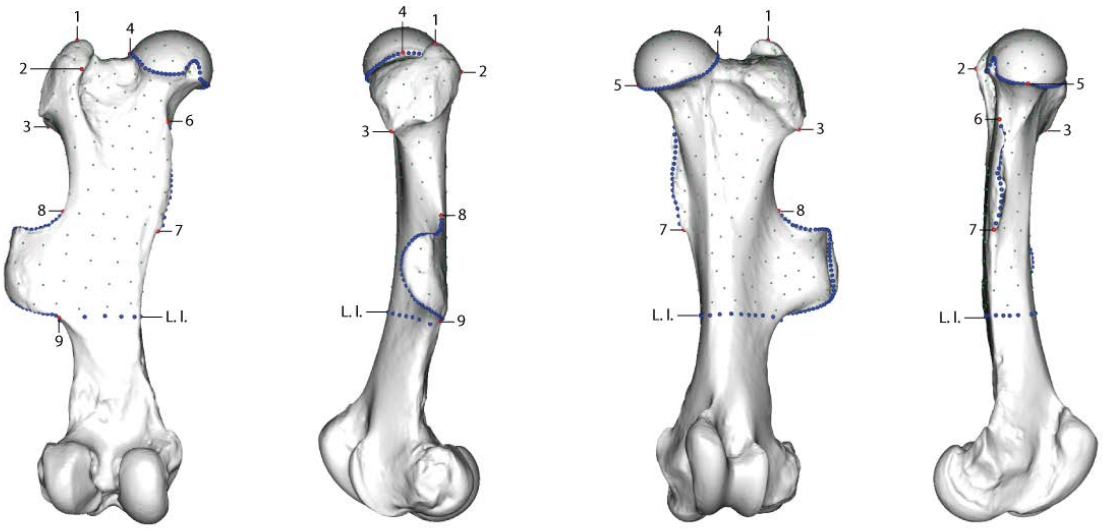

Figure S2E: Location of anatomical landmarks (red spheres), curve sliding (blue spheres) and surface sliding (green spheres) semi-landmarks placed on the femur (partial proximal part). From left to right: caudal, lateral, cranial and medial views. Numbers refer to anatomical landmarks designation detailed in Table S2D. L.l.: limit line (removed after sliding process).

LM	Designation
1	Most distal point of the border of the third trochanter (i.e. slope break relatively to the shaft border)
2	Most lateral point of the lateral epicondyle
3	Most proximal point of the lateral lip of the trochlea
4	Most proximal point of the trochlear groove
5	Most proximal point of the medial lip of the trochlea
6	Most medial point of the medial epicondyle
7	Most proximal point of the medial condyle border
8	Most proximal point of the lateral condyle border
9	Most distal point of the medial lip of the trochlea
10	Distal maximum of curvature of the trochlear groove
11	Most distal point of the lateral lip of the trochlea
Curve	**Designation**
C1	Trochlea ridge: from LM3 to LM5 + LM9 to LM11
C2	Medial condyle: from LM7 to LM7
C3	Lateral condyle: from LM8 to LM8
C4	Proximal limit: from LM1 to LM1

Table S2F: Designation of anatomical landmarks on the femur (partial distal analysis).

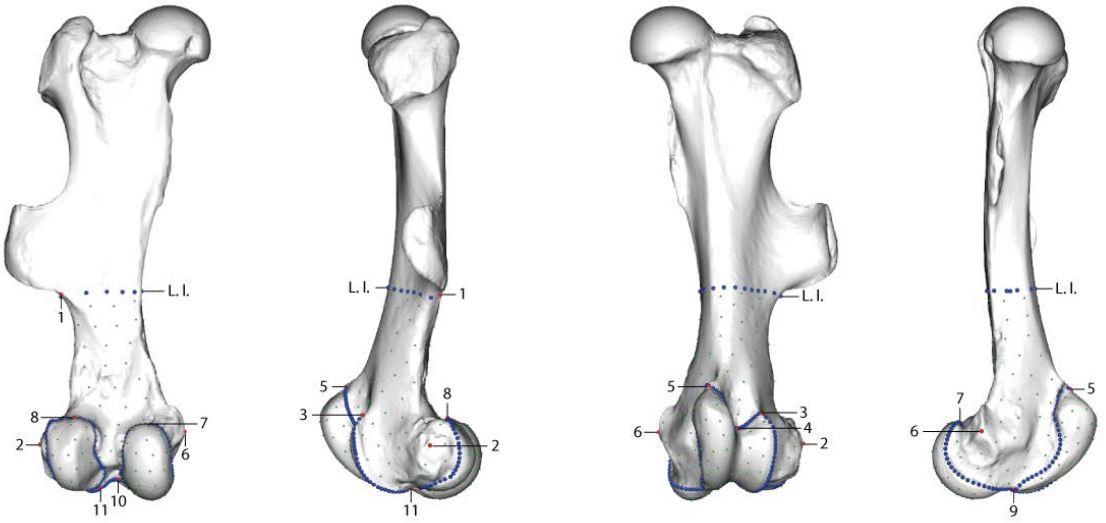

Figure S2G: Location of anatomical landmarks (red spheres), curve sliding (blue spheres) and surface sliding (green spheres) semi-landmarks placed on the femur (partial distal part). From left to right: caudal, lateral, cranial and medial views. Numbers refer to anatomical landmarks designation detailed in Table S2F. L.l.: limit line (removed after sliding process).

LM	Designation
1	Most proximal point of the lateral tubercle of the intercondylar eminence
2	Most cranial point of the articular surface of the lateral condyle
3	Most caudo-distal point of the articular surface of the lateral condyle
4	Most proximal point of the medial tubercle of the intercondylar eminence
5	Most cranial point of the articular surface of the medial condyle
6	Most caudal point of the articular surface of the medial condyle
7	Most proximal point of the proximal tibio-fibular synostosis surface
8	Most distal point of the proximal tibio-fibular synostosis surface
9	Most proximal point of the lateral part of the tibial tuberosity
10	Most lateral point of the lateral part of the tibial tuberosity
11	Most distal point of the tibial tuberosity groove
12	Most caudal point of the medial condyle
13	Most proximal point of the distal tibio-fibular synostosis surface
14	Most caudo-lateral point of the distal articular surface
15	Most cranio-lateral point of the distal articular surface
16	Most cranio-distal point of the intermediate ridge of the distal articular surface
17	Most distal point of the contact between the medial malleolus and the distal articular surface
18	Most distal point of the medial part of the distal articular surface
19	Most caudo-distal point of the intermediate ridge of the distal articular surface
20	Most medial point of the medial malleolus
Curve	**Designation**
C1	Lateral condyle articular surface: from LM1 to LM3
C2	Medial condyle articular surface: from LM4 to LM6
C3	Proximal tibio-fibular synostosis surface: from LM7 to LM8
C4	Interosseus crest: from LM8 to LM13
C5	Distal tibio-fibular synostosis surface: from LM13 to LM15
C6	Distal articular surface: from LM15 to LM14

Table S2H: Designation of anatomical landmarks on the tibia.

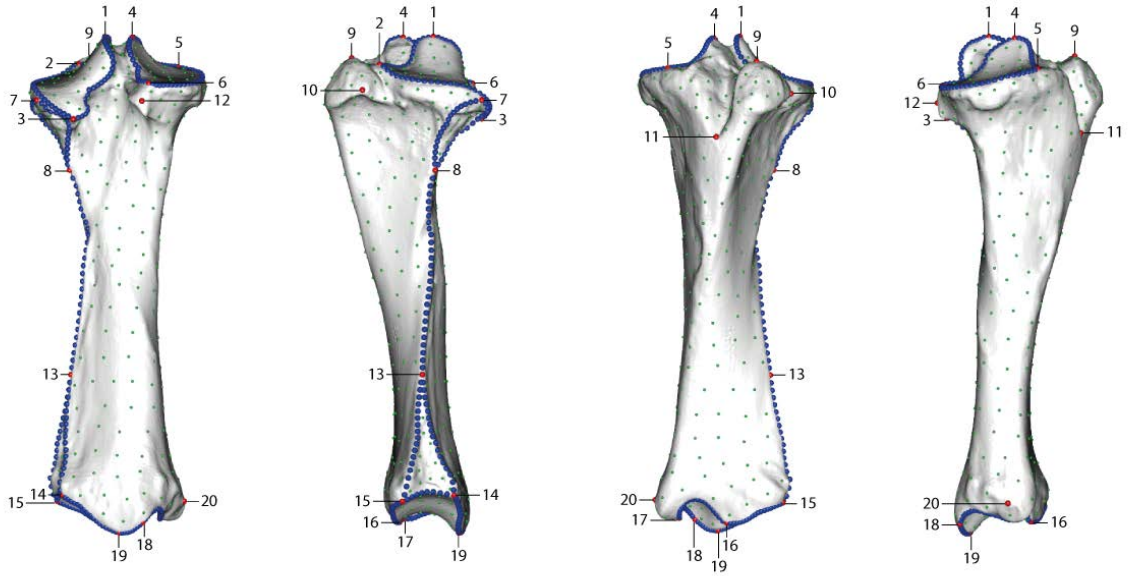

Figure S2I: Location of anatomical landmarks (red spheres), curve sliding (blue spheres) and surface sliding (green spheres) semi-landmarks placed on the tibia. From left to right: caudal, lateral, cranial and medial views. Numbers refer to anatomical landmarks designation detailed in Table S2H.

LM	Designation
1	Most caudo-medial point of the proximal tibio-fibular synostosis surface
2	Most proximal point of the proximal tibio-fibular synostosis surface
3	Most cranio-lateral point of the proximal tibio-fibular synostosis surface
4	Most proximal point of the distal tibio-fibular synostosis surface
5	Most caudal point of the distal articular facet
6	Most distal point of the caudal part of the distal articular facet
7	Most distal point of the cranial part of the distal articular facet
8	Most cranial point of the distal articular facet
9	Most lateral point of the distal epiphysis
Curve	**Designation**
C1	Proximal tibio-fibular synostosis surface: from LM1 to LM3
C2	Interosseous crest: from LM3 to LM4
C3	Distal tibio-fibular synostosis surface: from LM4 to LM5
C4	Distal articular facet: from LM5 to LM8

Table S2J: Designation of anatomical landmarks on the fibula.

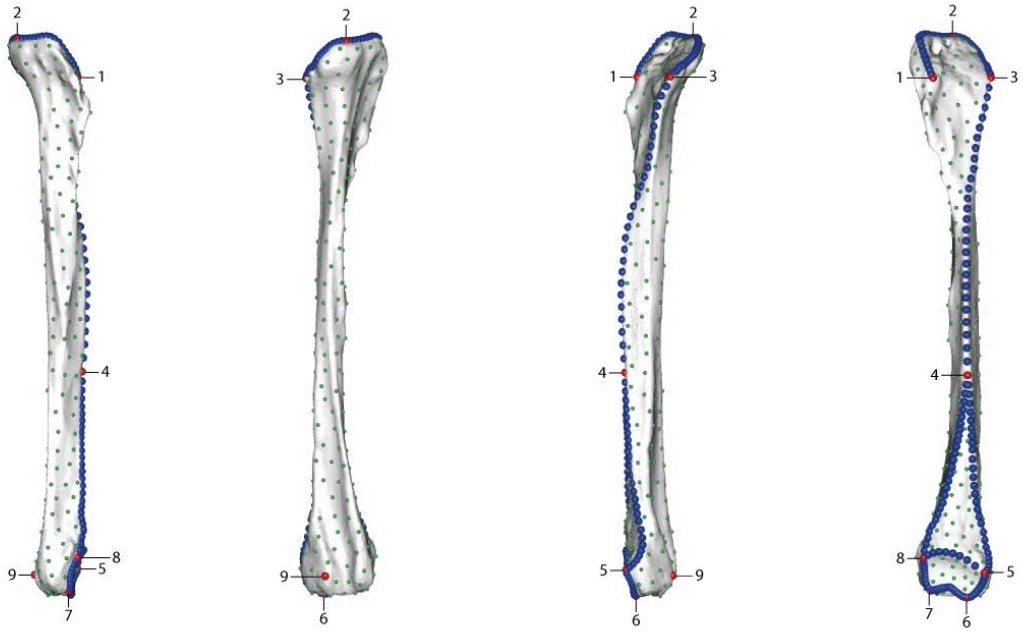

Figure S2K: Location of anatomical landmarks (red spheres), curve sliding (blue spheres) and surface sliding (green spheres) semi-landmarks placed on the fibula. From left to right: caudal, lateral, cranial and medial views. Numbers refer to anatomical landmarks designation detailed in Table S2J.

Appendix 3: Complete list of gracility index and mean body mass compiled from literature

Taxa	Meas.	TD	Length	GI-MT3	Mean	Sources
Acerorhinus zernowi	#1	36.80	141.80	0.26	0.26	Measurement given on AMNH FM 129904 by Cerdeño, 1996a
	#2	38.10	137.20	0.28		Measurement given on AMNH FM 129912 by Cerdeño, 1996a
	#3	33.80	147.50	0.23		Measurement given on AMNH FM 129993 by Cerdeño, 1996a
Alicornops simorrense	#1	37.39	148.10	0.25	0.29	Measurement given by Heissig, 2012
	#2	40.42	121.92	0.33		Measurement given by Guérin, 1980
Aphelops malacorhinus	#1	28.00	110.00	0.25	0.25	Measurement on picture of AMNH F:AM 104164 in Prothero, 2005
	#2	36.4.	143.00	0.25		Mean measurements given by Mihlbachler, 2005
	#3	36.00	145.00	0.25		Mean measurements given by Prothero, 2005
Aphelops megalodus	#2	36.00	139.00	0.26	0.26	Mean measurements given by Prothero, 2005
	#3	26.30	99.10	0.27		Mean measurements given by Prothero & Manning, 1987
Aphelops mutilus	#1	17.00	69.00	0.25	0.32	Measurement on picture of AMNH F:AM 114981 in Prothero, 2005 (in pixels)
	#2	16.00	45.00	0.36		Measurement on picture on AMNH FM 8293 (in pixels)
	#3	42.00	128.00	0.33		Mean measurements given by Prothero, 2005
Brachypotherium brachypus	#1	57.68	165.65	57.68	0.30	Measurement on picture on FSL 320233
	#2	52.20	152.60	52.20		Measurement given by Cerdeño, 1993
	#3	55.00	148.00	55.00		Measurement given by Cerdeño, 1993
Ceratotherium cf. primaevum	#1	52.00	165.00	0.32	0.32	Measurement given by Arambourg, 1959
Ceratotherium neumayri	#1	52.93	176.83	0.30	0.33	Mean measurements given by Guérin, 1980
	#2	53.22	174.56	0.30		Mean measurements given by Guérin, 1980
	#3	51.94	178.60	0.29		Measurement on picture in Antoine & Saraç, 2005
Ceratotherium simum	#1	41.86	162.50	0.26	0.27	Direct measurement on BICPC NH.CON.32
	#2	45.29	155.73	0.29		Direct measurement on BICPC NH.CON.37
	#3	42.52	162.47	0.26		Direct measurement on BICPC NH.CON.40
Chilotherium kowalevskii	#1	0.92	2.55	0.36	0.36	Measurement on picture in Pavlow, 1913 (in pixels)
Coelodonta antiquitatis	#1	49.08	164.02	0.30	0.29	Measurement on picture on FSL 396154
	#2	47.16	166.54	0.28		Mean measurements given by Guérin, 1980
Coelodonta nihowanensis	#1	44.54	185.78	0.24	0.24	Measurement on picture in Tong *et al.*, 2014
Diaceratherium aginense	#1	40.26	137.88	0.29	0.31	Direct measurement on AR B2 1556
	#2	41.70	127.50	0.33		Measurement given by Jame et al., 2019
Diaceratherium asphaltense	#1	39.	128.00	0.31	0.31	Measurement given by Jame et al., 2019

	#2	40.00	131.50	0.30		Measurement given by Jame et al., 2019
	#3	NA	NA	0.31		Gracility index given by Becker, 2009a
Diaceratherium aurelianense	#1	43.80	117.00	0.37	0.38	Measurement given by Cerdeño, 1993
	#2	42.00	118.50	0.35		Measurement given by Cerdeño, 1993
	#3	48.00	117.00	0.41		Measurement given by Cerdeño, 1993
Diaceratherium lemanense	#1	45.38	155.52	0.29	0.30	Direct measurement on AR B2 1435
	#2	41.92	140.45	0.30		Direct measurement on AR B2 1973
	#3	45.84	151.22	0.30		Measurement on picture of NMBE5026811 in Jame et al., 2019
Diceratherium armatum	#1	17.00	93.00	0.18	0.21	Measurement on picture of AMNH F:AM 112178 in Prothero, 2005 (in pixels)
	#2	35.00	151.00	0.23		Mean measurements given by Prothero, 2005
Diceratherium tridactylum	#1	0.63	2.55	0.25	0.25	Measurement on picture of AMNH FM 538 (in pixels)
Dicerorhinus aff. sansaniensis	#1	43.48	173.91	0.25	0.25	Measurement on picture of NHMUK PAL M 36299 in Gentry, 1987
Dicerorhinus sumatrensis	#1	41.41	160.77	0.26	0.27	Direct measurement on NHMW 1500
	#2	40.70	148.77	0.27		Direct measurement on NHMW 3082
	#3	39.99	149.28	0.27		Mean measurements given by Guérin, 1980
Diceros bicornis	#1	45.22	170.69	0.26	0.27	Measurement on picture of NHMW 55210
	#2	42.53	157.09	0.27		Mean measurements given by Guérin, 1980
Dihoplus megarhinus	#1	62.67	212.53	0.29	0.27	Measurement on picture on FSL 40405
	#2	57.39	209.80	0.27		Measurement on picture on FSL 40407
	#3	54.94	215.19	0.26		Measurement on picture on FSL 40052
Dihoplus pikermiensis	#1	49.06	173.60	0.28	0.28	Measurement on picture in Antoine & Saraç, 2005
Dihoplus schleiermacheri	#1	45.00	173.25	0.26	0.26	Mean measurements given by Guérin, 1980
Elasmotherium sibiricum	#1	0.40	1.65	0.24	0.24	Measurement on picture in Kosintsev et al., 2018 (in pixels)
Hoploaceratherium tetradacty-lum	#1	36.45	158.63	0.23	0.26	Measurement on picture on FSL 214235
	#2	45.45	163.21	0.28		Measurement on picture on MNHN F. SA 5912 in Heissig, 2012
	#3	40.00	155.50	0.26		Measurement given on MNHN F. SA 10170 by Heissig, 2012
Hyrachyus eximius	#1	17.35	112.08	0.18	0.17	Direct measurement on AMNH FM 12675
	#2	20.00	107.00	0.16		Measurements given by Cope, 1873
Hyrachyus modestus	#1	17.50	112.20	0.16	0.16	Measurement given on AMNH FM 1612 in Bai et al., 2017
Hyracodon nebraskensis	#1	1.49	9.94	0.15	0.16	Measurement on picture on YPM VPPU 11414 in Scott & Jepsen, 1941 (in pixels)
	#2	20.00	113.00	0.18		Measurements given by Qiu & Wang, 2007
Lartetotherium sansaniense	#1	39.08	153.45	0.25	0.24	Measurement on picture on FSL 214233

	#2	38.73	168.58	0.23		Measurement given on MNHN F. SA 6470 by Heissig, 2012
Menoceras arikarense	#1	22.00	130.00	0.17	0.17	Measurement on picture of AMNH F:AM 99260 in Prothero, 2005
	#2	22.90	128.30	0.18		Mean measurements given by Mihlbachler, 2007
	#3	22.00	126.00	0.17		Mean measurements given by Prothero, 2005
Metamynodon planifrons	#1	44.00	121.00	0.36	0.34	Measurement given on YPM VPPU 10886 by Scott & Jepsen, 1941
	#2	40.00	120.00	0.33		Measurement given on YPM AMNH FM 1100 by Scott & Jepsen, 1941
	#3	1.35	4.13	0.33		Measurement on picture on AMNH FM 546 (in pixels)
Paraceratherium grangeri	#1	104.00	418.00	0.25	0.24	Measurement given in Qiu & Wang, 2007
	#2	1.73	7.60	0.23		Measurements on picture on AMNH FM 21618 in Granger & Gregory, 1936 (in pixels)
	#3	0.97	4.08	0.24		Measurement on picture on AMNH FM 26169 in Granger & Gregory, 1936 (in pixels)
Peraceras hessei	#1	26.80	101.40	0.26	0.26	Mean measurements given by Prothero & Manning, 1987
Peraceras profectum	#1	28.00	108.00	0.26	0.26	Mean measurements given by Prothero, 2005
Plesiaceratherium mirallesi	#1	42.46	170.21	0.25	0.2	Measurement on picture in Antoine 2002
Pleuroceros blanfordi	#1	NA	NA	NA	NA	No data
Prosantorhinus douvillei	#1	32.20	80.10	0.40	0.45	Mean measurements given by Cerdeño, 1996b
	#2	43.06	84.78	0.51		Measurement on picture in Antoine, 2002
Protaceratherium minutum	#1	1.69	7.61	0.22	0.22	Measurement on picture in Roman, 1924 (in pixels)
Rhinoceros philippinensis	#1	42.61	152.63	0.28	0.28	Direct measurement on NMP 2014-II-J1-288
Rhinoceros sondaicus	#1	54.73	157.85	0.35	0.35	Mean measurements given by Guérin, 1980
Rhinoceros unicornis	#1	52.68	192.66	0.27	0.27	Mean measurements given by Guérin, 1980
Stephanorhinus jeanvireti	#1	49.42	205.11	0.24	0.23	Mean measurements given by Guérin, 1980
	#2	45.43	206.91	0.22		Measurement on picture in Pandolfi, Codrea, & Popescu, 2019
Stephanorhinus etruscus	#1	41.65	167.03	0.25	0.24	Measurement on picture on FSL 210940
	#2	40.18	175.92	0.23		Mean measurements given by Guérin, 1980
Stephanorhinus hemitoechus	#1	43.76	167.59	0.26	0.26	Mean measurements given by Guérin, 1980
	#2	47.72	185.80	0.26		Measurement on picture in Pandolfi & Tagliacozzo, 2015
	#3	46.72	179.35	0.26		Mean measurements given by Pandolfi & Tagliacozzo, 2015
Subhyracodon mitis	#1	32.00	121.00	0.26	0.26	Mean measurements given by Prothero, 2005
Subhyracodon occidentalis	#1	4.52	21.02	0.22	0.23	Measurement on picture in Scott & Jepsen, 1941 (in pixels)
	#2	36.00	133.00	0.27		Measurement on picture in Scott & Jepsen, 1941

Teleoceras fossiger	#1	45.38	99.59	0.46	0.44	Direct measurement on YPM VP 39358
	#2	12.50	30.00	0.42		Measurement on picture of AMNH FM 9745 in Prothero, 2005 (in pixels)
Teleoceras hicksi	#1	39.00	84.00	0.46	0.46	Mean measurements given by Prothero, 2005
Teleoceras proterum	#1	36.57	82.29	0.44	0.43	Measurement on picture of AMNH FM 104163 in Prothero, 2005
	#2	40.70	88.80	0.46		Mean measurements given by Mihlbachler, 2005
	#3	35.40	89.40	0.40		Mean measurements given by Mihlbachler, 2005
Trigonias osborni	#1	27.60	125.60	0.22	0.22	Direct measurement on AMNH FM 9847 in Scott & Jepsen, 1941
Trigonias wellsi	#1	NA	NA	NA	NA	No data
Urtinotherium intermedium	#1	79.00	338.00	0.23	0.23	Measurements given in Qiu & Wang, 2007

Table S3A: Measurements used to compute mean gracility index on third metatarsal for each species of the sample. For measurements taken on unscaled pictures, values are given directly in pixels. GI-MT3: gracility index; Meas.: measurement; TD: transverse diameter. Institution codes as in Chapter 2.

Taxa	Estimation	BM	Mean BM	Sources
Acerorhinus zernowi	#1	700	700	Valli, 2005
Alicornops simorrense	#1	875	875	Antoine, In Press
Aphelops malacorhinus	#1	889	889	Damuth & MacFadden, 1990
Aphelops megalodus	#1	NA	NA	No data
Aphelops mutilus	#1	1840	1840	Stilson, Hopkins & Davis, 2016
Brachypotherium brachypus	#1	2327	2327	Becker, 2003
Ceratotherium cf. primaevum	#1	NA	NA	No data
Ceratotherium neumayri	#1	1200	1844	Valli, 2005
	#2	2487		Antoine, In Press
Ceratotherium simum	#1	2300	2300	Dinerstein, 2011
Chilotherium kowalevskii	#1	700	700	Valli, 2005
Coelodonta antiquitatis	#1	1905	2403	Saarinen et al., 2016
	#2	2900		Stuart, 1991
Coelodonta nihowanensis	#1	NA	NA	No data
Diaceratherium aginense	#1	1987	1987	Becker, 2003
Diaceratherium asphaltense	#1	NA	NA	No data
Diaceratherium aurelianense	#1	1551	1551	Becker, 2003
Diaceratherium lemanense	#1	1730	1590	Jame et al., 2019
	#2	1417		Jame et al., 2019
	#3	1624		Jame et al., 2019
Diceratherium armatum	#1	NA	NA	No data
Diceratherium tridactylum	#1	517	517	Damuth & MacFadden, 1990
Dicerorhinus aff. sansaniensis	#1	NA	NA	No data
Dicerorhinus sumatrensis	#1	775	775	Dinerstein, 2011
Diceros bicornis	#1	1050	1050	Dinerstein, 2011
Dihoplus megarhinus	#1	NA	NA	No data
Dihoplus pikermiensis	#1	1100	1100	Valli, 2005
Dihoplus schleiermacheri	#1	1812	2123	Becker, 2003
	#2	2433		Costeur et al., 2013
Elasmotherium sibiricum	#1	4000	4500	Zhegallo et al., 2005
	#2	4000		Zhegallo et al., 2005
Hoploaceratherium tetradactylum	#1	1197	1197	Becker, 2003
Hyrachyus eximius	#1	97	67	Damuth & MacFadden, 1990
	#2	36		Stilson, Hopkins & Davis, 2016
Hyrachyus modestus	#1	NA	NA	No data
Hyracodon nebraskensis	#1	NA	NA	No data
Lartetotherium sansaniense	#1	1204	1204	Becker, 2003
Menoceras arikarense	#1	251	313	Damuth & MacFadden, 1990
	#2	375		Stilson, Hopkins & Davis, 2016
Metamynodon planifrons	#1	887	1340	Damuth & MacFadden, 1990
	#2	1794		Averianov et al., 2017a
Paraceratherium grangeri	#1	10100	10950	Fortelius & Kappelman, 1993
	#2	11800		Gromova, 1959
Peraceras hessei	#1	NA	NA	No data
Peraceras profectum	#1	NA	NA	No data
Plesiaceratherium mirallesi	#1	1268	1268	Pers. calculation after Fukuchi & Kawai, 2011
Pleuroceros blanfordi	#1	1343	1343	Pers. calculation after Antoine et al., 2010
Prosantorhinus douvillei	#1	NA	NA	No data
Protaceratherium minutum	#1	530	530	Becker, 2003
Rhinoceros philippinensis	#1	NA	NA	No data
Rhinoceros sondaicus	#1	1350	1350	Dinerstein, 2011
Rhinoceros unicornis	#1	2000	2000	Dinerstein, 2011
Stephanorhinus jeanvireti	#1	NA	NA	No data
Stephanorhinus etruscus	#1	NA	NA	No data
Stephanorhinus hemitoechus	#1	1522	1561	Saarinen et al., 2016
	#2	1600		Stuart, 1991
Subhyracodon mitis	#1	NA	NA	No data
Subhyracodon occidentalis	#1	NA	NA	No data
Teleoceras fossiger	#1	1016	1016	Damuth & MacFadden, 1990
Teleoceras hicksi	#1	1660	1660	Stilson, Hopkins & Davis, 2016

Teleoceras proterum	#1	635	635	Damuth & MacFadden, 1990
Trigonias osborni	#1	334	506	Damuth & MacFadden, 1990
	#2	677		Stilson, Hopkins & Davis, 2016
Trigonias wellsi	#1	NA	NA	No data
Urtinotherium intermedium	#1	NA	NA	No data

Table 3B: Mean body mass (BM) estimations (in kg) computed on previous estimations given in literature for each species of the sample.

Appendix 4: Shape deformations associated with the first two axes of the PCA for each bone

Blue: minimal values. Orange: maximal values. Orientation from left to right: caudal, lateral, cranial, medial, proximal and distal views. A: complete femur; B: proximal partial femur; C: distal partial femur; D: tibia; E: fibula.

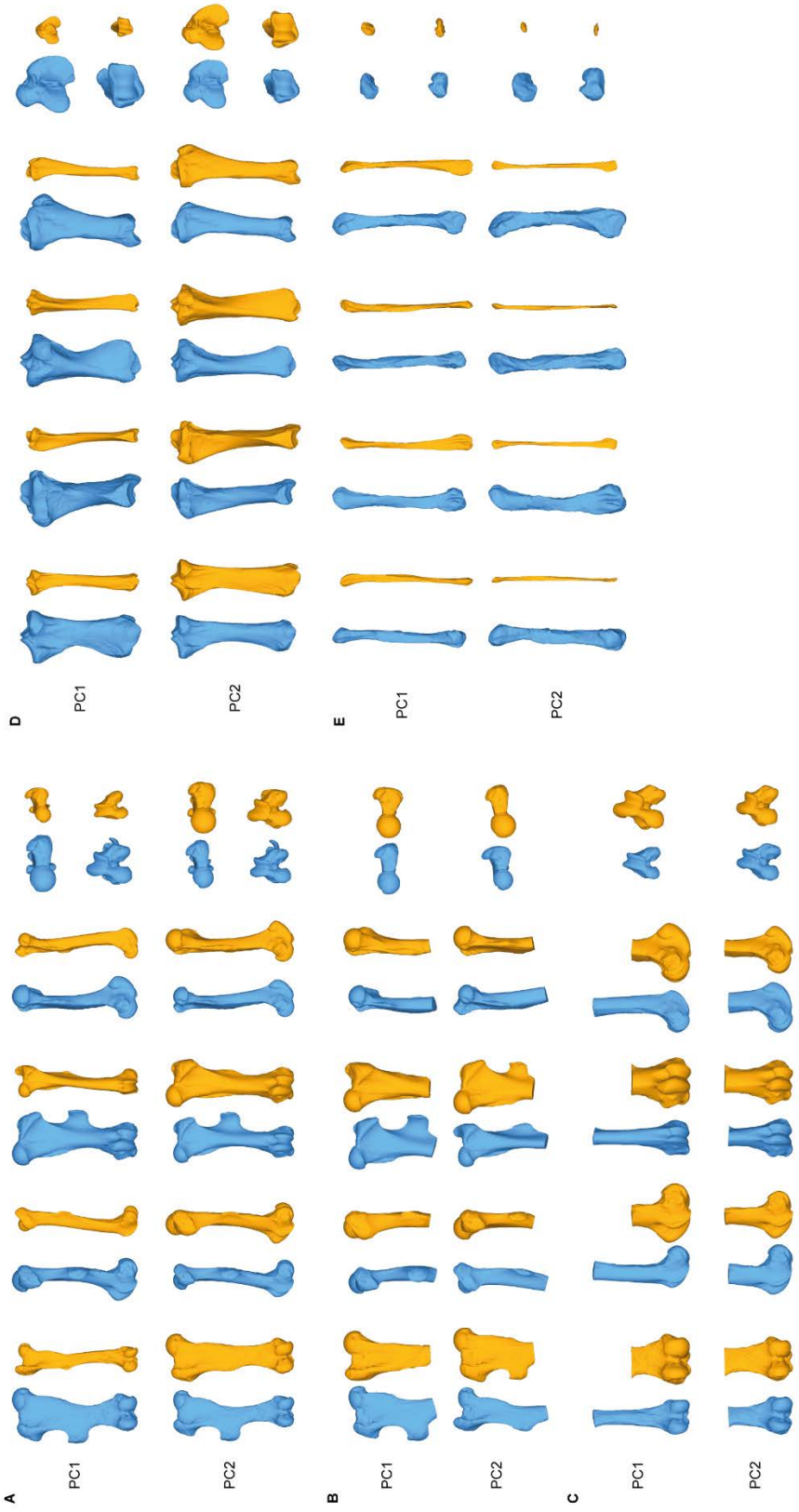

Appendix 5: Shape deformations associated with minimum and maximum values of the centroid size (CS), body mass (BM) and gracility index (GI-MT3) for significant regressions with shape

Blue: minimal values. Orange: maximal values. Orientation from left to right: caudal, lateral, cranial, medial, proximal and distal views. A, B, C: complete femur; D, E, F: proximal partial femur; G: distal partial femur; H: tibia; I: fibula.

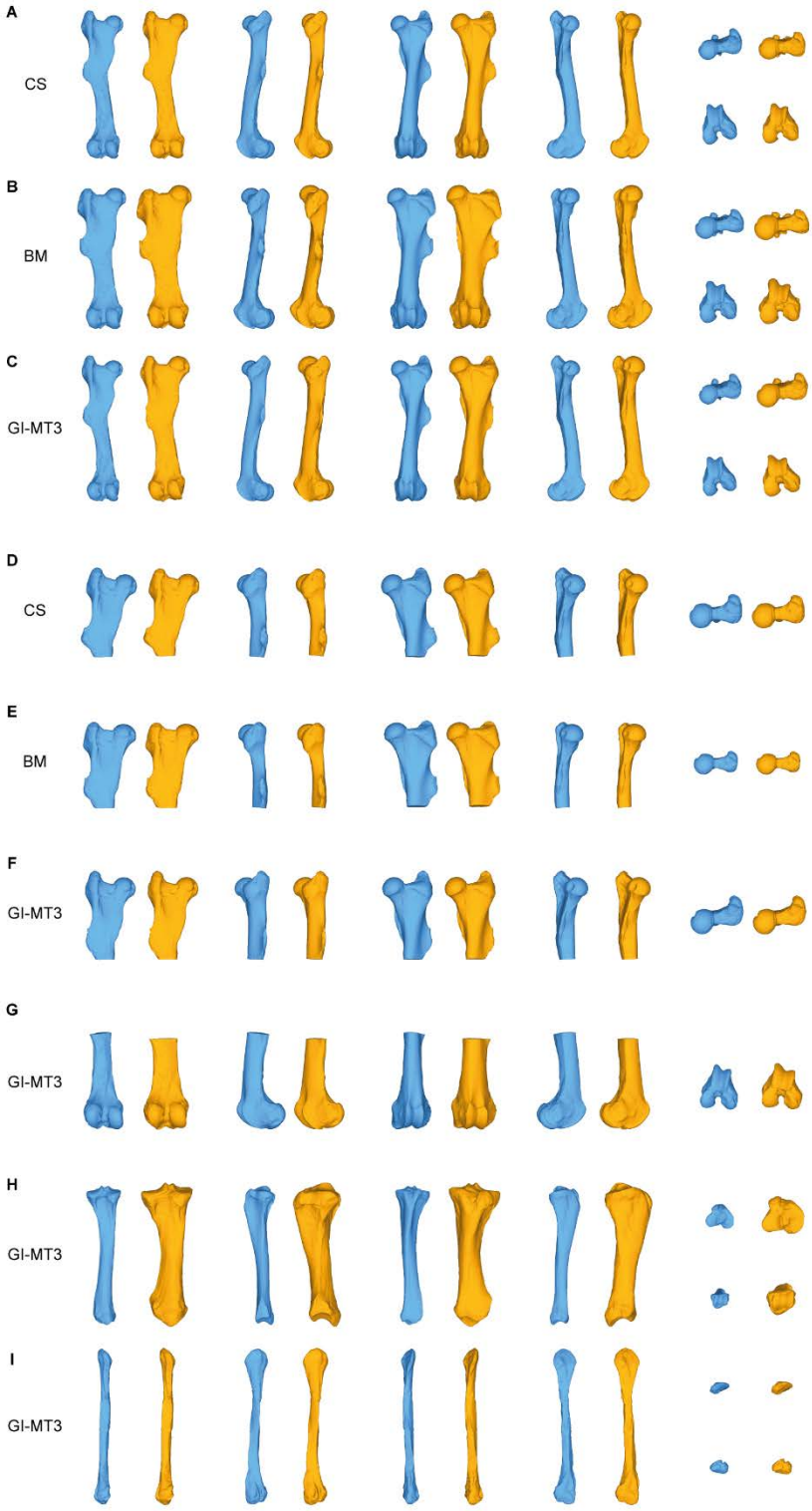

Appendix 6: Significant PGLS regression plots for partial femur (A), tibia (B) and fibula performed on shape data and log-transformed cubic root of mean body mass (BM).

Points colour code follows Figure 38. Point size is proportional to mean log CS of each species. On the right, shapes associated with minimum and maximum fitted values (top row) and colour maps of the location and intensity of the shape deformation (bottom row). Blue: minimal values. Orange: maximal values. For each bone, the shape associated with the minimum was coloured depending on its distance to the shape associated with the maximum (blue indicates a low deformation intensity and red indicates a high deformation intensity). Orientation from left to right in each case: caudal, lateral, cranial and medial views.

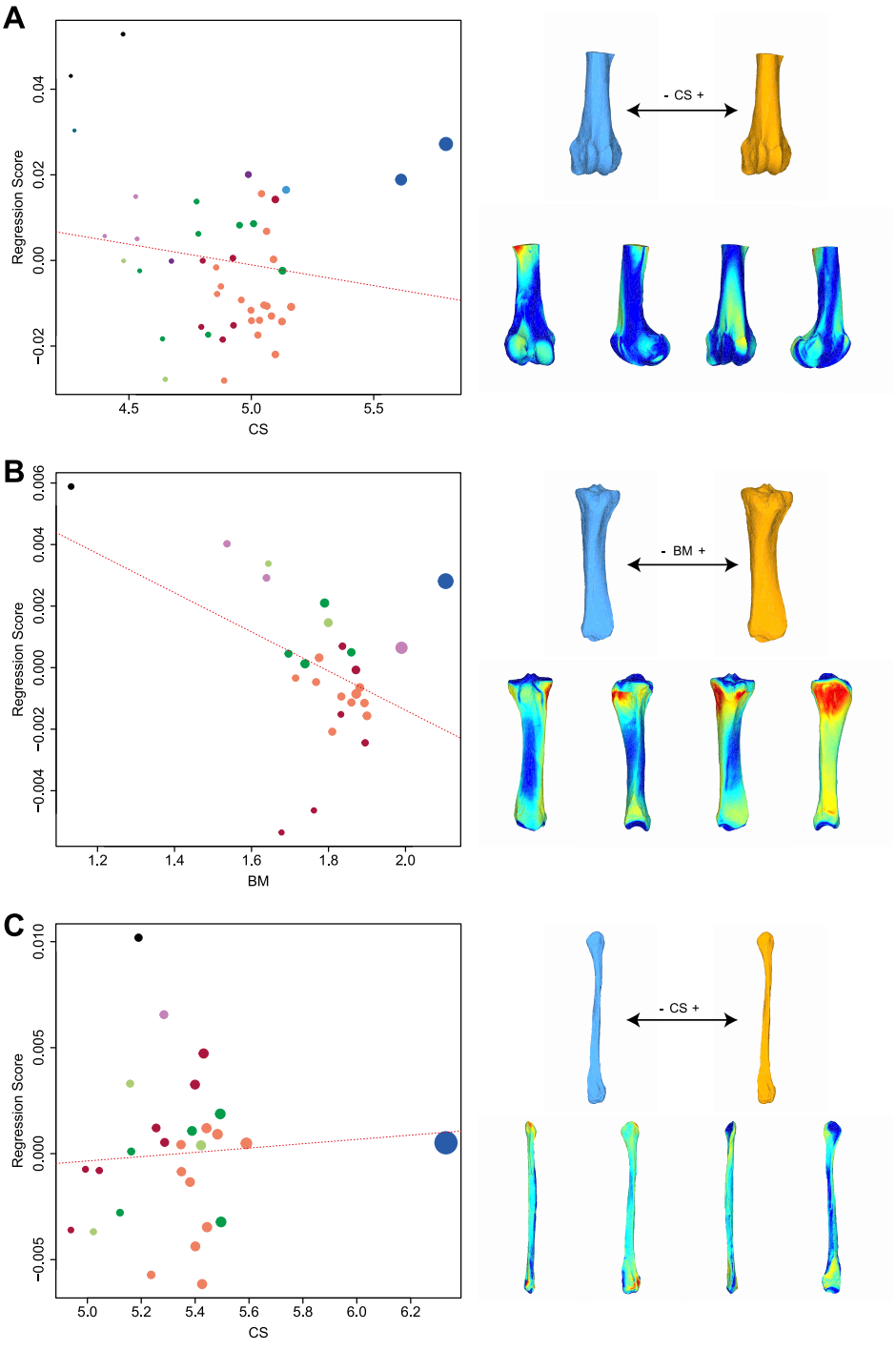

Chapter 7

General discussion and perspectives

General discussion

At the end of this investigation, the study of patterns of variation in the shape of long bones in Rhinocerotoidea delivers a complex, and often dual, signal related to body mass and body proportions in general. On the one hand, it clearly appears that shape varies in part according to body mass among Rhinocerotoidea. On the other hand, the diversity in bone shape in relation to body proportions highlights several ways to support a high body mass within the superfamily. A same body mass can also be associated with different bone shapes and, at a broader scale, with different limb constructions depending on the considered group (e.g. the paraceratheriid *Juxia* and the teleoceratin *Teleoceras* both weight around 900-1,000 kg but have a totally different limb construction). Conversely, shape similarity can be observed in taxa showing a distinct construction (e.g. shape similarity between giant Paraceratheriidae and smaller Amynodontidae). This is due to the complex combination of general and more specific trends of shape change between bones and between taxa, leading a puzzling diversity of body construction within the superfamily (Figure 48).

Common trends of shape variation

Increase of robustness

Results obtained on modern (Chapters 3 and 4) and fossil (Chapters 5 and 6) rhinos coherently highlight that an increase of body mass is associated with an increase of bone robustness on most or all long bones, i.e. proportionally larger shaft and epiphyses. These convergent allometric trends are in perfect accordance with conclusions obtained in other mammalian clades, from the very first observations of Galilei (1638) almost four centuries ago to far more recent works using linear measurements (e.g. Anderson, Hall-Martin & Russell, 1985; Bertram & Biewener, 1990, 1992; Biewener, 1990; Christiansen, 2007) or a geometric morphometric approach on the whole bone shape (e.g. Fabre et al., 2013; Martín-Serra, Figueirido & Palmqvist, 2014; Botton-Divet et al., 2016; Hanot et al., 2018; MacLaren et al., 2018; Serio, Raia & Meloro, 2020). It is well known that, when an object increases in size, surface area increases by a power of 2 while volume (and, consequently, mass) increases by a power of 3. In this context, as demonstrated by Alexander et al. (1979) and Schmidt-Nielsen (1984), when all proportions of an animal are doubled, its mass (and, consequently, the vertical stress exerted on the limb bones) increases by a factor of 8. If bones scale isometrically, their diameter would only increase by a factor of 4, leading to an insufficient surface area to resist pressure constraint. As a consequence, the width of the limb bone in quadrupedal mammals must scale allometrically to avoid crushing with body mass.

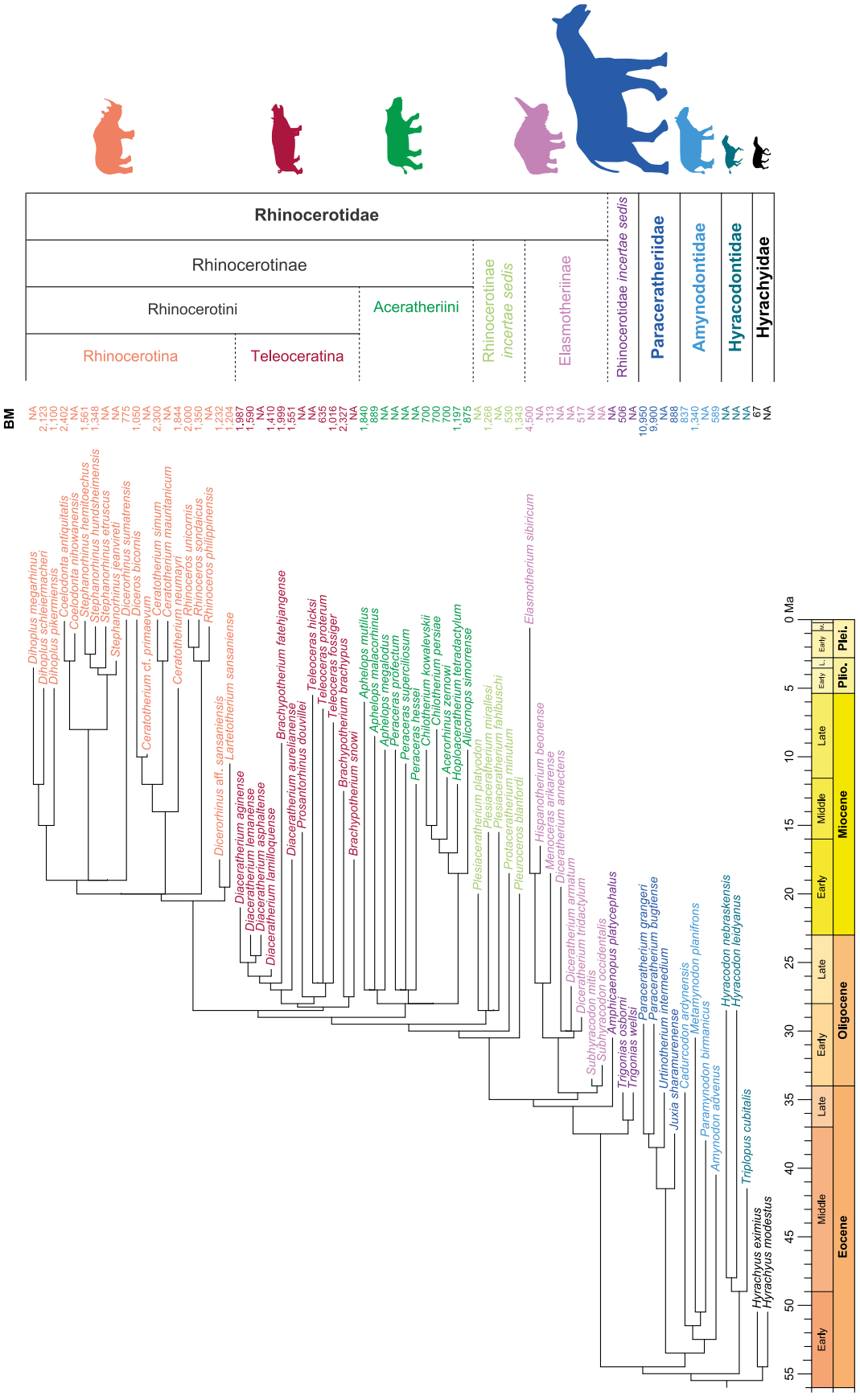

Figure 48: Synthetic phylogeny of all the species considered in the present work with their respective mean body mass. Colour code and phylogenetic framework as in Chapters 1, 5 and 6. Body masses compiled from Chapters 5 and 6 (NA indicates unavailable data). All silhouettes are scaled.

This leads notably to large cross-sectional areas in the limb bones of heavy animals (Schmidt-Nielsen, 1984; Christiansen, 1999). This trend has been observed in many different taxa: for example, rodents, proboscideans, primates, with the only exception of bovids that do not scale following the same trend (Alexander et al., 1979). My work tends to show that Rhinocerotoidea follow this rule, this trend being clearly visible within the superfamily, even at a low taxonomic level as observed in modern rhinos. Moreover, previous studies on bone robustness showed that many modern and fossil rhinos display even larger bones that what would be expected following the allometric trend common to most ungulates, and even larger than those of elephants relatively to their length (Prothero & Sereno, 1982; Christiansen, 1999, 2002). These extremely robust bones in rhinos may be related to the flexed nature of their limbs, in most representatives of the superfamily (see below), coupled with body masses among the highest known in quadrupedal mammals. As limbs must resist extreme stress caused by a weight of several tons, while maintaining a flexed construction, their bones must reach an exceptional robustness to avoid crushing.

Muscle insertions and passive-stay apparatuses

Another consequence of an increase of body mass among Rhinocerotoidea consists in the reinforcement of insertion areas for muscles, particularly for extensors, like the olecranon process of the ulna (where inserts the *m. triceps brachii*) and the great trochanter of the femur (where inserts the *m. gluteus medius*). As in most quadrupedal mammals, rhino's limbs display a "Z" aspect, segments being angled between each other. Consequently, limbs will naturally undergo flexion when submitted to loading. Columnar limbs are one way to resist this tendency, as it leads to a vertical alignment of the loading constraint with the limb axis and drastically less bent limbs (Hildebrand, 1974). Another way to prevent this natural flexion is with powerful extensor muscles counteracting vertical loading (Hildebrand, 1974; Biewener & Patek, 2018), as observed here in modern and fossil rhinos (Chapters 4, 5 and 6). Moreover, in addition to these morphological changes linked to limb extension, some flexor insertions are strongly developed in heavy rhinos (e.g. the radial tuberosity for the *m. biceps brachii* and the deltoid tuberosity for the *m. deltoideus*). Developed flexors allow powerful limb movements involved in locomotion, notably for running. Modern rhinos are able to practice gallop up to 40 km/h in some species (Alexander & Pond, 1992; Blanco, Gambini & Fariña, 2003). Furthermore, given their general construction, it is likely that most heavy fossil species were capable of relatively fast movements, although doubts subsist for the largest genera like *Paraceratherium* (Paul & Christiansen, 2000). In summary, towards high body mass, muscular insertions in rhinos modify to meet the functional requirements of both weight support and a relatively rapid locomotion.

In addition to these reinforcements of muscular insertions toward high body mass, my results also highlight the particular development of humeral and femoral anatomical features in heavy taxa; the

intermediate tubercle of the bicipital groove and the medial lip of the femoral trochlea, respectively (Chapters 3, 5 and 6). This development is likely related to the presence of passive-stay mechanisms at shoulder and knee joints. Well described in horses but absent in tapirs, these features allowing to "lock" the limbs in the standing posture and to reduce the energy dedicated to the body stance are suspected in rhinos as well. However, their presence has never been strictly demonstrated (Hermanson & MacFadden, 1992; Hermanson & Macfadden, 1996). These features, which were regarded as associated to a BM increase, may also be related to locomotor ecology, as they are often encountered in relatively cursorial taxa living in open environments (Kappelman, 1988; Janis et al., 2012). My results indicate a clear development of these humeral and femoral areas towards high body mass, both in modern (Chapter 3) and fossils taxa (Chapters 5 and 6), and therefore suggest the existence of passive-stay apparatuses in some heavy Rhinocerotoidea. The presence of such features in rhinos would be coherent with their general constitution meeting both requirements for weight support and relatively fast locomotion. Moreover, the presence of these apparatuses in horses but not in tapirs (Hermanson & MacFadden, 1992; Hermanson & Macfadden, 1996) further suggests a functional origin linked both to weight and locomotion rather than an evolutionary legacy common to all Perissodactyla. The presence of passive-stay apparatuses in modern rhinos remains to be clearly asserted *in vivo* observations regarding their locomotion and by dissections to compare the knee of rhinos with that of horses, possessing this locking feature.

All these observations indicate that along their evolutionary history, from a lightly build plesiomorphic condition without passive-stay apparatuses, Rhinocerotoidea have underwent common skeletal changes directly related to weight bearing, modifying deeply their appendicular skeleton but without obliterating all its "cursorial" aspects (e.g. flexed limbs, powerful flexor muscles, relatively elongated autopodium).

Differences in shape patterns between and within limbs

Beyond these trends common to the whole superfamily and to the six studied bones, the association of body mass with shape also differs between and within the limbs. In quadrupedal mammals, fore and hind limbs do not support the same proportion of the total mass (e.g. around 60 and 40%, respectively, in elephant; Henderson, 2006) and do not fulfil the same locomotor function (brake and propulsion, respectively; Dutto et al., 2006). Consequently, it is likely that the influence of body mass should be higher on the forelimb than on the hind limb, as braking involves higher pressure forces on the forelimb in heavier animals (Pandy et al., 1988; Granatosky et al., 2018). This effect might be even stronger on taxa with a particularly large head sometimes wearing heavy horns like rhinos. My results highlight a stronger link between body mass and shape variation in the forelimb than in the hind lomb among modern rhinos (and, at a lesser extent, at the superfamily level), particularly when looking at

integration patterns. This suggests a closer link between body mass and shape covariation within the forelimb, due to the need to resist higher constraints due to weight support (Chapter 4).

However, differences in shape variation are far more marked between the stylopodium and zeugopodium than between the fore and hind limbs. Results obtained on modern rhinos highlight that the shape of the stylopodium is strongly related to phylogenetic relationships (Chapter 3), and highly covariant between the fore and hind limb (Chapter 4), likely due to shared developmental trajectories related to their serial homology (Hallgrímsson, Willmore & Hall, 2002). Conversely, the influence of body mass on the shape variation of the stylopodium appears secondary. At the superfamily level, the shape of the stylopodium in most Rhinocerotoidea follow a strong common trend of variation intimately related to phylogeny as well (Chapters 5 and 6). All these observations lead to the conclusion that morphological changes related to functional factors like weight support do not overcome those related to historical factors in the stylopodium of Rhinocerotoidea.

My observations on modern rhinos indicate that the shape of the zeugopodium is much more related to body mass, notably in the forelimb (see above), than to historical factors. Yet, at the scale of the superfamily, it is the degree of brachypody that appears more strongly associated with the zeugopodial shape than with the body mass itself (Chapters 5 and 6). As it is related to the relative length of the limb, the degree of brachypody can be interpreted as a proxy of the vertical position of the centre of gravity for a given species: the more brachypodial the species, the lower its centre of gravity (Henderson, 1999, 2006), as observed for example in hippos (Coughlin & Fish, 2009). The influence of body mass itself seems more visible at a lower taxonomic level, as observed in modern rhinos. The influence of the evolutionary history remains present, each group retaining some distinct morphological features. The relation between shape and evolutionary legacy yet appears secondary, since phylogenetically distant taxa can display convergent body proportions and, consequently, a convergent zeugopodial shape (i.e. *Elasmotherium*, *Amphicaenopus* and *Metamynodon; Pleuroceros*, *Chilotherium* and *Teleoceras*). This link between body mass and zeugopodial shape is more marked on the forelimb than on the hind limb, which seems coherent with previous observations regarding the higher impact of body mass on the former than on the latter (see above) (Figure 49).

All these observations are coherent with previous works highlighting distinct trends of shape variation between the stylopodium and zeugopodium related to body mass (Bertram & Biewener, 1992; Fabre et al., 2013). Moreover, this higher influence of functional factors on the zeugopodium than on the stylopodium is in accordance with the framework developed by Hallgrímsson, Willmore & Hall (2002), hypothesising that, given the proximo-distal development of the limbs (from girdle to autopodium), shape variation is more likely to accumulate in distal elements than in proximal ones under external

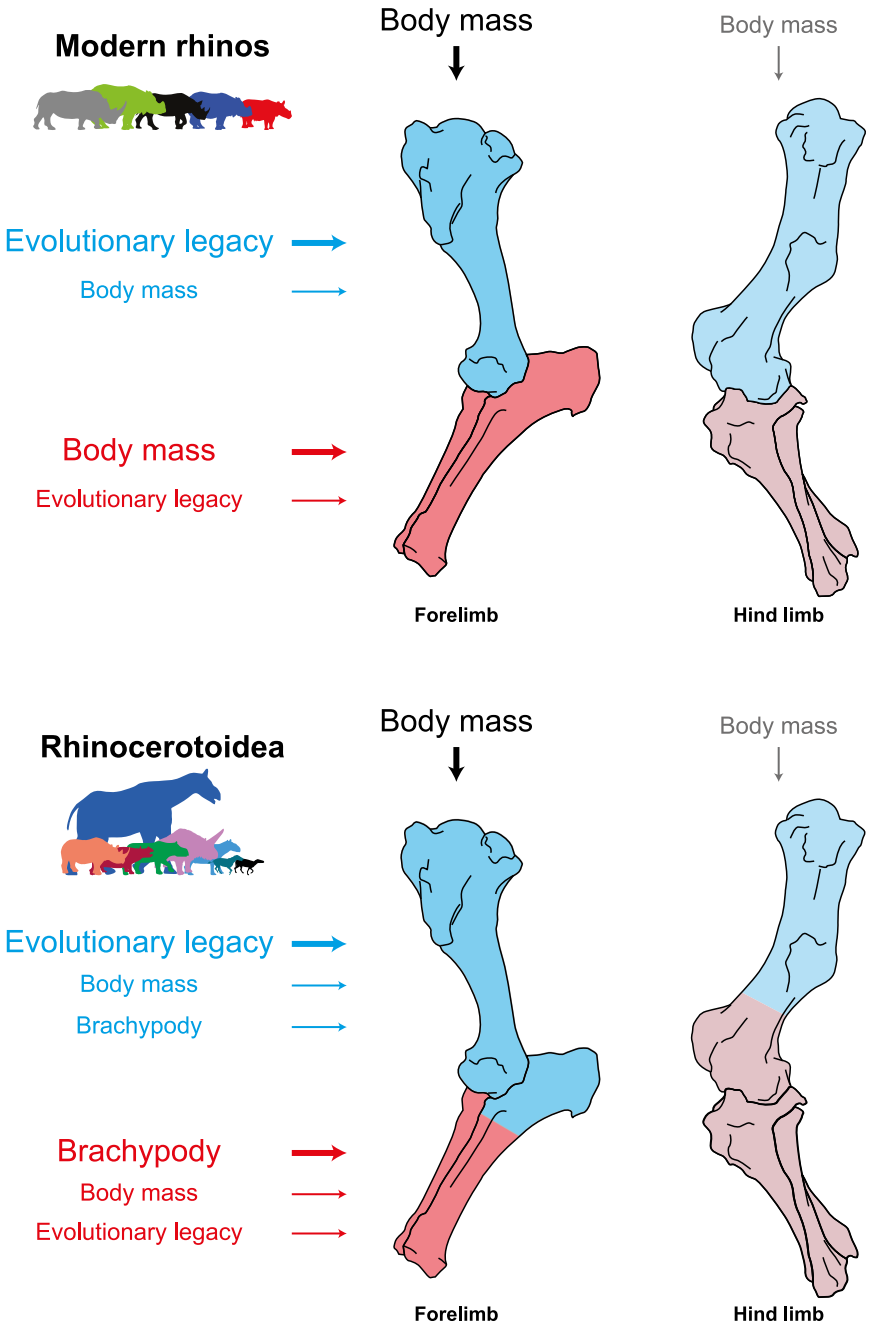

Figure 49: Schematic summary of the relations between bone shape and the different variables tested during this work. Blue indicates a shape variation mainly associated with evolutionary legacy. Red indicates a shape variation mainly associated with body mass and/or brachypody. This relative influence is based on the results obtained through the NJ trees, the PCA and the regression plots of the PGLS described in the previous chapters. The size of the font and arrows for each variable is proportional to its relation with the shape for each bone or part of bone. Faded colours on the hind limb indicate a lower association with body mass in general. Bones modified from Archeozoo.org under Creative Commons license.

constraints (e.g. weight bearing, locomotor substrate) (Young & Hallgrímsson, 2005; Hanot et al., 2017, 2018). Moreover, the degree of brachypody is computed on metapodial measurements: the anatomical and developmental proximity with metapodial elements may be another reason why the shape of the zeugopodium correlates more with brachypody than does the stylopodial shape. Moreover, given the accumulation of variation along a proximo-distal gradient in quadruped limbs (Hallgrímsson,

Willmore & Hall, 2002; Young & Hallgrímsson, 2005), it may be useful to estimate the degree of brachypody not only on a single bone but using the relative proportions of all limb segments.

The particular case of the fibula

Among the six studied bones, the fibula clearly appears as the one showing the most puzzling patterns of shape variation. Its morphology is strongly dominated by intraspecific variation in modern rhinos, with a reduced influence of the evolutionary legacy (except in the genus *Rhinoceros* – Chapter 3) and it is the only bone for which the degree of shape covariation with adjacent bones (femur and tibia) is higher when the effect of size is removed (Chapter 4). Moreover, investigations in fossil rhinos highlight surprising proximity between taxa with strongly different body constructions, such as Hyrachyidae and Teleoceratina (Chapter 6). The fusion of the fibula with the tibia, hardly associated with specific factors (e.g. age, species, body mass) is even more confusing (Chapter 6). These results question the functional role of this bone and the nature of the constraints related to its shape variation. As this bone is reduced or absent in many ungulates (Polly, 2007; Barone, 2010a), the functional role of the fibula and its potential link with weight bearing has been poorly explored, except in humans (where the fibula does support part of the body mass – Lambert, 1971; Takebe et al., 1984). The persistence of this bone in all rhinos, maybe related to evolutionary legacy (tapirs, which are sister-taxa of rhinos, retain a fibula while it almost disappears in equids), likely indicates a potential functional role. Among Rhinocerotoidea, despite a contact between the femur and the fibula in some fossil species (Antoine, 2002), the most of the body mass seems supported by the tibial plateau in the knee joint. Consequently, main functional roles of the fibula in rhinos are likely to allow the insertion of flexors and extensors of the autopodium, as well as to ensure the ankle joint stability with the lateral malleolus (Barone, 2010a). As these functions involve only limited areas of the bone, it is possible that a large part of the fibula is poorly constrained, leading the shape to vary relatively independently from body mass variation or evolutionary legacy. The fibula might be compared to what is observed in some vestigial organs, known to be less constrained by functional factors and to vary independently from adjacent organs (Walker-Larsen & Harder, 2001).

Limitations of the study

Sampling

Although this work includes hundreds of modern and fossil specimens, some limits may be linked to the sampling representativity. Many crucial information was often lacking for modern rhinos in most institutions, like age, sex, locality and, most importantly, body mass (see below). Subspecies are known for four modern rhinos (two for *C. simum*, seven or eight for *Dc. bicornis* and three for *Ds. sumatrensis* and *R. sondaicus* – Groves, 1972; Groves & Kurt, 1972; Laurie, Lang & Groves, 1983; Hillman-Smith &

Groves, 1994; Groves & Leslie, 2011) but subspecific attribution was almost often missing too, except for some *C. simum* specimens. Consequently, the potential shape patterns associated with all these variables could not been addressed. Unfortunately, these limitations seem difficult to overcome given the numerous threats facing most rhino species nowadays. Habitat destruction, intense poaching and diseases led to a drastic reduction of the wild rhino populations and led most species to the brink of extinction (Hillman-Smith & Groves, 1994; Groves, Fernando & Robovský, 2010; Dinerstein, 2011; Groves & Leslie, 2011; Goossens et al., 2013; Mays et al., 2018). In this context, sampling of studies on modern rhinos can hardly be drastically extended, particularly for *Ds. sumatrensis* and *R. sondaicus*, each currently represented by less than one hundred living individuals.

Other sampling biases are noticeable for fossil rhinos. Although some limited taphonomic problems have been overcome using partial templates (Chapters 5 and 6), many specimens in the collections are too damaged or uncomplete to be included in shape analyses (less than half of all the bones scanned during my fieldtrips could be analysed). This prevented me to include some taxa constituting relevant occurrences of high body mass in poorly represented clades (e.g. hind limb bones of *Paramynodon* and *Cadurcodon* for Amynodontidae, or the elasmothere *Iranotherium* totally absent from my analysis). If some taxa are known from hundreds of specimens, others are only known by poorly preserved long bones or even by craniodental remains only, making it impossible to include them in such analyses. This is notably the case of some early Rhinocerotidae (e.g. *Epiaceratherium*, *Molassitherium*, *Ronzotherium*, *Mesaceratherium* – Becker, 2009; Becker, Antoine & Maridet, 2013; Tissier & Becker, 2018; Tissier, Antoine & Becker, 2020) or many representatives of Elasmotheriinae (e.g. *Kenyatherium*, *Bugtirhinus*, *Caementodon* – (Antoine, 2002). Finally, despite the diversity encountered in Rhinocerotoidea, relatively few independent occurrences of high body mass can be detected. Heavy mass (i.e. several hundreds of kilograms) arises at least in two tribes of Amynodontidae (Metamynodontini and Cadurcodontini – Averianov et al., 2017; Tissier et al., 2018) and in one subfamily of Paraceratheriidae (Paraceratheriinae – Wang et al., 2016). Within Rhinocerotidae, occurrences of high body mass are present in both subfamilies (Elasmotheriinae and Rhinocerotinae). Numerous taxa within Rhinocerotinae display a high body mass (among Aceratheriini, Teleoceratina and Rhinocerotina) but these occurrences can hardly be considered as totally independent as most of the members of this group weight at least several hundreds of kilograms (even early representatives – Becker, 2003, 2009; Becker et al., 2009). A similar observation can be done for high brachypody, whose occurrences arise mainly within the subfamily Rhinocerotinae (in taxa like *Pleuroceros*, *Chilotherium* and most Teleoceratina – Figure 48) and can therefore be considered as not totally independent. Consequently, the trends of shape variation observed in Rhinocerotoidea and related to an increase of body mass should be reinforced by the consideration of other independent occurrences of heavy mass outside of the group (see

Perspectives below). Replicated events are needed to avoid spurious correlations between traits (like body mass and bone shape) that are evolving independently (Felsenstein, 1985; Maddison & FitzJohn, 2015; Uyeda, Zenil-Ferguson & Pennell, 2018).

Body mass and centroid size

Body mass, which is a central parameter in my study, is a variable that must be considered carefully. Its value is highly variable in extant species depending on the age, sex, physical condition and environment of the specimen. Body mass is barely available in institutional databases for large animals like extant rhinos, only a few specimens being weighted after death – weight being difficult to measure for large animals and subject to additional variations due to loss of water or body decomposition. Ranges of body mass in modern rhinos are subject to impressive variations along lifetime and between males and females (up to 30-40% in *C. simum* – Zschokke & Baur, 2002). Moreover, demographic studies of fossil assemblages (e.g. *Menoceras*, *Aphelops*, *Teleoceras*) likely indicate broad ranges of weight in some extinct species due to ontogeny and sexual dimorphism (Guérin, 1980; Fortelius & Kappelman, 1993; Mead, 2000; Mihlbachler, 2005; Prothero, 2005; Mihlbachler, 2007; Chen et al., 2010; Prothero, 2013). Many methods of body mass estimation have been developed for decades using craniodental and postcranial measurements (e.g. Talbot & McCulloch, 1965; Anderson, Hall-Martin & Russell, 1985; Legendre, 1989; Scott, 1990; Damuth & MacFadden, 1990; Mendoza, Janis & Palmqvist, 2006; Campione & Evans, 2012; Tsubamoto, 2014; Hopkins, 2018) but very few have included rhinos, which do not seem to follow the same allometric trend as other ungulates (Prothero & Sereno, 1982). In this context, the alternative use of the centroid size of long bones was necessary to overcome lacking or unprecise body mass data – as well as a potential circular reasoning using mass estimation computed on the circumference of bones included in the shape study. Along this study, the centroid size has proven to be a relevant (but sometimes loose) proxy to estimate body mass in both modern and fossil rhinos – at least based on the masses available for the various taxa and based on diverse types of measurements – confirming similar results obtained on their tarsal bones (Etienne et al., 2020) and in other mammals (Ercoli & Prevosti, 2011; Cassini, Vizcaíno & Bargo, 2012). Since centroid size is computed on the distances between each landmark and the centroid of the object, it is almost proportional to the object volume when a high number of landmarks is used, making it vary congruently with body mass as well (see above). However, this approach suffers some limits, notably since all bones are not correlated similarly with body mass. If results obtained on the stylopodium are robust (possibly confirming the relevance of body mass estimation methods using stylopodium circumferences – Anderson, Hall-Martin & Russell, 1985; Campione & Evans, 2012), they are less pertinent on the zeugopodium, especially on the fibula, for which a single centroid size value can be associated with very different body masses and bone shapes in highly distinct taxa (Chapter 6). This link may also be even poorer in highly

brachypodial species having a strongly modified zeugopodium. More investigations on other mammal groups are needed to test further the link between the centroid size of limb bones and body mass in order to use it more broadly in shape studies.

Potential influence of ecology

While body proportions and evolutionary history are associated with bone shape variation, the latter might also be related to other factors. Rhinocerotoidea are known as a group showing a high diversity of ecologies throughout their evolution, with various feeding habits (browsers, grazers, mixed-feeders), and habitats (from open cold steppes, temperate plains and hot savannas to dense tropical forests) encountered in various and non-related groups (Guérin, 1980; Prothero & Schoch, 1989; Prothero, 2005, 2013). However, the role of ecology is not directly addressed in this study, mainly because ecological data for both modern and fossil rhinos can be highly spurious. Ecological affinities of modern rhinos are intimately intricated with phylogenetic relationships, making it hard to untangle their respective link with bone shape. Furthermore, historical ranges and habitats of modern rhinos have been drastically reduced and modified under human pressure (Hillman-Smith & Groves, 1994; Dinerstein, 2011; Groves & Leslie, 2011; Rookmaaker & Antoine, 2012), leading to potential bias when trying to interpret bone shape in regard to current ecologies. Palaecological studies of extinct rhinos are often focused on species known from extensive fossil records (e.g. Prothero & Sereno, 1982; Wilcots, 1992; MacFadden, 1998; Mead & Wall, 1998; Mead, 1999, 2000; Costeur et al., 2012; Boeskorov, 2012; Wang & Secord, 2020) while ecologies of less-documented taxa remain poorly known.

Nevertheless, the limb morphology appears related to ecological factors in other mammals (e.g. Harris & Steudel, 1997; Fabre et al., 2014; Martín-Serra, Figueirido & Palmqvist, 2014; Martín-Serra et al., 2015; Botton-Divet et al., 2016, 2018; MacLaren et al., 2018; Serio, Raia & Meloro, 2020). As regards rhinos, previous studies tended to indicate a poor correlation between limb construction and ecology (Guérin, 1980; Eisenmann & Guérin, 1984). My preliminary observations tend to show that the role of ecology in shaping limb bones, if it exists, is not the main driver of the shape variation in rhinos. For example, the large elasmothere *Elasmotherium*, the short-legged *Teleoceras* and the extant white rhino *C. simum* are generally all considered as highly specialised animals living in open environments (Mihlbachler, 2003; Prothero, 2005; Dinerstein, 2011; Kosintsev et al., 2018). Despite similar ecological affinities, my results highlight that their limb bones do not show a convergence towards a common shape (*Elasmotherium* retains long and slender limbs like other Elasmotheriinae, while *C. simum* does not reach the extreme brachypodial condition displayed by *Teleoceras*). Similarly, based on morphological considerations (e.g. short limbs, barrel-like body), it has been assumed that taxa like *Teleoceras* and *Metamynodon* could have been semi-aquatic like modern hippos, although this hypothesis is not consensual (MacFadden, 1998; Wall & Heinbaugh, 1999; Mead, 2000; Mihlbachler, 2003; Clementz,

Holroyd & Koch, 2008; Wang & Secord, 2020). Although this hypothesis has not been tested here, results indicate no convergent shape between these taxa that could be related to a similar lifestyle.

Potential influence of ontogeny

Developmental constraints likely play a role in shaping limb bones, although this aspect is not directly addressed in this study. Personal observations on modern rhinos indicate a marked shape variation between juvenile and adult specimens, the formers having larger epiphyses relatively to the shaft leading to a general hourglass shape (Figure 50). This has been observed on all six bones, tending to indicate that the diaphysis enlarges more than the epiphyses during growth. This is coherent with the increase of robustness previously described (see above "Common trends of shape variation"), the shaft needing to be broader to support body weight as the specimen grows. Moreover, I have observed a similar tendency in different fossil taxa displaying juvenile specimens (e.g. *Teleoceras*, *Coelodonta*, *Hispanotherium*). These observations tend to indicate a potential allometric trend at the ontogenetic level showing similarities with that observed at the static level in adult specimens (i.e. increase of robustness and large epiphyses towards high body mass) (Chapter 3). These different allometric scales remain to be directly compared and quantified (Klingenberg, 2016).

At the scale of the superfamily, morphological differences in long bones may also be related to differences in developmental trends and rhythms between taxa (i.e. heterochrony – McKinney & McNamara, 1991; Bininda-Emonds et al., 2007; Richardson et al., 2009; McNamara, 2012). The degree of brachypody could particularly be related to a reduced or accelerated growth of some bones in brachypodial and gracile taxa, respectively. Developmental heterochrony has been previously suggested in *Teleoceras major* to explain sexual dimorphism (Mead, 2000). Such different developmental rhythms are likely to exist also between species. Coupled with body support and evolutionary legacy, these factors could be strongly related to the diversity of bone shape among Rhinocerotoidea.

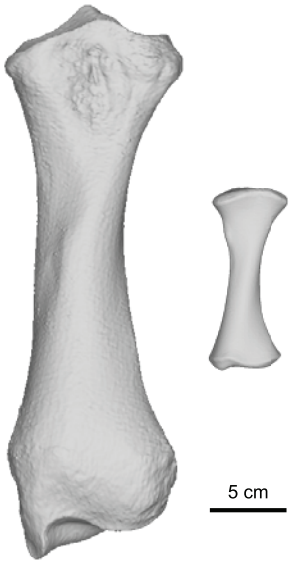

Figure 50: Size and shape comparison of a radius between adult (left) and juvenile without epiphyses (right) specimens of *C. simum* (left: BICPC NH.CON.20, Powell Cotton Museum, Birchington-on-Sea; right: MNHN-ZM-AC-2000-440, MNHN, Paris).

Beyond graviportality

Finally, this works allows to question the concept of graviportality and its application to Rhinocerotoidea. It appears that the shape of the limb bones in Rhinocerotoidea modifies under loading stress while still carrying a strong phylogenetic signal. The general construction of the rhino limbs remains however largely the same across all the superfamily. When considering the morphofunctional framework of Gregory (1912) and Osborn (1929) and the classic criteria associated with graviportality (i.e. long stylopodium and short autopodium, body mass of several hundreds of kilograms, columnar limbs, large and strong bones, large feet, slow pace), no deep architectural breakdown towards this peculiar limb organisation has been observed in rhinos. The high body mass and the increase in bone robustness (and potentially the enlarged feet although this criterion is relative – Panagiotopoulou, Pataky & Hutchinson, 2019) are almost the only graviportal features encountered in the superfamily. The morphology of the elbow and knee joints indicate that almost all taxa retain flexed limbs with no convergence towards a strictly columnar organisation. Only large Paraceratheriidae display straighter limbs although they are not totally columnar (elbow and knee joints likely remaining flexed) (Fortelius & Kappelman, 1993; Paul, 1997; Paul & Christiansen, 2000). The lengthening of the stylopodium relatively to the other limb elements is far from being clear except in highly brachypodial species (but more likely to a shortening of the zeugopodium). The reduction of the autopodium elements (i.e. degree of brachypody) appears associated with various body mass values and not only the highest ones (Chapters 5 and 6). Conversely, the reduction of the autopodium is not always marked in heavy taxa, as observed in *Elasmotherium* and *Paraceratherium* (Chapters 5 and 6). Although not directly studied here, the gait of rhinos seems also relatively conservative: modern rhinos are able to gallop and given

the similar general construction of the limbs in large fossil taxa, it is likely that most of them could reach a relatively fast pace (Paul & Christiansen, 2000).

The detailed study of shape variation in rhinos allows to highlight morphological changes linked to the support and propulsion of heavy weight that are nearly absent from this classical framework. The consideration of the shape of the whole bones highlights morphological changes of paramount importance that are complementary to those underlined by linear measurements (e.g. relative length and angle of the olecranon process or the femoral head). The increase of robustness for all long bones is the most obvious morphological modification related to an increase of body mass in Rhinocerotoidea. Moreover, the shape changes observed in the zeugopodial elements relatively to the degree of brachypody (and, consequently, to the vertical position of the centre of gravity) shed light on the impact of mass on this segment. The classical framework of Gregory and Osborn underlines that the relative length of this central segment is poorly modified between cursorial and graviportal taxa (Gregory, 1912; Osborn, 1929) (see Figure 1 in Chapter 1). My results highlight that the zeugopodial shape however is deeply modified between light and heavy rhinos.

One group among the superfamily is particularly challenging the concept of graviportality: the Paraceratheriidae. It has been observed since their discovery that giant rhinos like *Paraceratherium* challenge the classic definition of graviportality even more than other rhinos (Granger & Gregory, 1936; Fortelius & Kappelman, 1993). Particularly, they do not show the relative reduction of the autopodium length or the fully columnar limbs expected for such big quadrupeds. Moreover, the ratio "humeral length over radial length" is below 1 in *Juxia* and *Urtinotherium* while above 1 for *Hyrachyus* and *Hyracodon*, making Paraceratheriidae close to more gracile taxa such as modern equids (ratio < 1). This ratio is also different from that observed in other rhinos (e.g. above 1 for modern rhinos). Conversely, the ratio "femoral length over tibial length" is higher in *Paraceratherium* (1.4) than in *Hyrachyus* (1.1) and modern horses (1.1). This ratio on the hind limb is close to that observed in modern rhinos (1.5 in *C. simum*, 1.4 in *Dc. bicornis*) (personal computations). These ratios coupled with my results show that Paraceratheriidae appear to follow a different trend of shape variation than the rest of the superfamily. Contrary to in other Rhinocerotoidea, the shape of their stylopodium seems more affected by functional factors (i.e. weight support) while zeugopodial shape is poorly modified and retain a plesiomorphic aspect (although relatively slightly more robust) close to small taxa like Hyrachyidae and Hyracodontidae (Chapters 5 and 6). This conservative shape of the zeugopodium in paraceratheres is more marked on the forelimb than on the hind limb, which would appear in contradiction with the forelimb supporting a higher part of the total weight. It is therefore possible that the hind limb in giant Paraceratheriidae supports more weight due to a slightly sloped backbone (Prothero, 2005), an uncommon feature among Rhinocerotoidea which mostly display a relatively horizontal spine. This remains

hypothetical, as skeletal reconstructions for these animals are not consensual (Paul & Christiansen, 2000; Qiu & Wang, 2007; Prothero, 2013). It is also possible that the forelimb of Paraceratheriidae hardly follows the general trend common to most Rhinocerotoidea, maybe due to strong developmental or evolutionary constraints. All these features highlight both morphological changes linked to mass support (e.g. robustness of the stylopodium, shortening of the tibia) and the persistence of a cursorial construction close to that of small Hyrachyidae and Hyracodontidae. This unusual architecture tackles the classical opposition between "cursorial" and "graviportal" categories, Paraceratheriidae appearing to show features characterizing both categories simultaneously.

As Rhinocerotoidea hardly display the anatomical criteria classically associated with graviportality, two possible assessments arise: either Rhinocerotoidea should not be considered graviportal, or the graviportal framework is too limited to describe the diverse conditions by which species adapt to heavy weight. My study shows unambiguously that morphological changes (increase of robustness, larger epiphyses) linked to a heavy body mass – one of the highest in terrestrial mammals – arise across the evolutionary history of rhinos. The limitations of the historical framework of Gregory (1912) and Osborn (1929) may be related to the archetypal groups used to define graviportality (and cursoriality). Graviportality was mainly defined using elephants as a model, coupled with extinct groups showing a similar limb architecture like Dinocerata (Osborn, 1900). However, it is not sure that all anatomical features potentially linked to a heavy weight encountered in these groups are characteristic of a general trend shared by all quadrupedal taxa showing an increase of body mass. Most Proboscidea retain poorly modified limbs, with no reduction of the digit number, no radio-ulnar and tibio-fibular fusion, and other particular features like the ulna supporting the humerus in the elbow joint (contrary to the condition in most ungulates, where the humerus is supported only by the radius) or the symmetrical femoral trochlea (Fujiwara, 2009; Janis et al., 2012; Larramendi, 2016). Morphofunctional investigations highlight that the limb structure and motion in Proboscidea is atypical compared to in most mammalian quadrupeds, including heavy ones (Ren et al., 2010). Except in their general increase of robustness, Rhinocerotoidea show no clear convergence of shape or limb construction towards that of Proboscidea, even in extremely large taxa like Paraceratheriidae. Most criteria associated with graviportality in elephants are not universally shared in heavy quadrupeds. Therefore, the classic graviportal framework should be considered with caution. It may be more relevant to search what the features repeatedly encountered within diverse taxa showing a high body mass are before defining a general concept such as graviportality. As there are likely multiple ways to sustain a heavy weight, graviportality should only be used after deciphering the repeated features potentially associated to it and the special adaptations limited to a particular group.

Perspectives

Girdles, autopodium and patella

This investigation of the relation between body mass and bone shape in Rhinocerotoidea could be the first step for a morphological exploration of the influence of weight on other limb elements. Girdle bones (scapula and pelvis) and autopodium elements are respectively the most proximal and distal segments of the limbs. Following the developmental hypothesis of Hallgrímsson, Willmore & Hall (2002), suggesting an increase of morphological variation from proximal to distal limb elements, the shape of girdles should show poorer correlation with body mass variation. Investigations on tapirs yet indicate slight modifications of the shape of the scapula in heavy species (MacLaren & Nauwelaerts, 2016). Moreover, very different shapes are observed among Rhinocerotoidea, from oval scapulae in small cursorial Hyrachyidae and Hyracodontidae to squared ones in some Amynodontidae and Teleoceratina (Scott & Jepsen, 1941; Wall & Hickerson, 1995; Prothero, 2005; Bai et al., 2017) suggesting noticeable scapular changes link to body mass in rhinos as well. Shape variation of the pelvic bone is poorly known in perissodactyls. Results obtained on modern horses indicate a poor influence of body mass on its shape variation and a poor covariation with other limb elements (Hanot et al., 2017, 2018). As pelvis is united to the backbone while the scapula is only maintained by muscles in ungulates, it is likely that the latter may be less constrained by adjacent bones than the former.

Conversely, autopodium elements can vary not only in relation to weight but also with locomotion, ecology and environment (Warner et al., 2013). If metapodial proportions have been indirectly considered here through the gracility index, their shape variation and its relation with body mass remain to be addressed in a global morphometric approach. In horses, despite a small effect of body mass on the covariation of the limb elements, the autopodium (especially the metapodials) does not follow the developmental hypothesis of Hallgrímsson, Willmore & Hall (2002), likely due to the cursorial specialisation of this group (Hanot et al., 2017, 2018). Results obtained on the forelimb of tapirs seem to confirm the double influence of body mass and locomotor ecology on the shape of the autopodium elements (MacLaren & Nauwelaerts, 2017). Investigation on the talus and the calcaneum of Rhinocerotoidea highlights a link between body mass and bone shape, although not as strong as expected, suggesting a significant influence of other factors on the morphology (environment, substrate, evolutionary legacy) (Etienne et al., 2020 – see General appendix). Given these results and the influence of the degree of brachypody on the other limb segments (Chapters 5 and 6), it is very likely that the autopodium in Rhinocerotoidea should show a great diversity of shape in relation with mass, substrate and locomotor ecology.

In addition, the consideration of the patella in the hind limb appears as a crucial complementary approach to understand the shape variation of the knee joint. The powerful leg extensors and knee ligaments inserted on the patella confer to this sesamoid bone a functional role analogous to that of the olecranon tuberosity of the ulna (Hildebrand, 1974; Barone, 2010b). Moreover, its involvement in the passive-stay apparatus of the knee (present in horses and likely in rhinos but not in tapirs – see above) suggests that the patella plays a major functional role in the hind limb architecture (Hermanson & Macfadden, 1996). Consequently, the patella may display shape modifications linked to body mass and to highly covary with other hind limb bones, particularly the femur on which the patella slides.

Joints and modularity

The exploration of the morphological integration showed that limb bones strongly covary in modern rhinos (Chapter 4). However, investigation of partial bones has highlighted unexpected differences in shape patterns between complete and partial bones (Chapters 5 and 6). These results should foster future tests on the modular construction of limb elements, not only through a bone by bone approach but also on specific parts of the bone. A module is defined as an anatomical unit covarying more in itself than with other units (Klingenberg, 2008). Given that the epiphyses and diaphysis develop from different ossification centres and that some bones are related to each other through strong joint caps (Barone, 2010b,a), adjacent epiphyses may covary more strongly between them than with their respective shaft (or their opposite epiphysis on the same bone), the joint therefore constituting a morphological module. Broadly explored in cranial elements, morphological modularity is poorly investigated in mammalian limb bones (Young & Hallgrímsson, 2005; Wagner, Pavlicev & Cheverud, 2007; Goswami, Weisbecker & Sánchez-Villagra, 2009; Diogo et al., 2018; Montoya-Sanhueza, Wilson & Chinsamy, 2019). The modularity of the limb bones in rhinos, as well as its relation with body mass, is therefore virtually unknown, despite a potentially crucial role in the construction of the appendicular skeleton.

Inner structure of long bones

As my study focuses on the external shape variation of long bones, it provides no information about the potential internal structural changes linked to body mass. The inner structure of bones is known to be highly influenced by functional factors, like body mass and locomotor ecology (Turner, 1998; Robling, Castillo & Turner, 2006) and evolutionary legacy (Cubo et al., 2005). Consequently, heavy quadrupeds are likely to present a particular inner structure directly linked to the higher loading constraints exerted on bones. Moreover, bone is a living tissue that constantly remodels under mechanical constraints to maintain the functional structure of the body (i.e. accommodation – Lanyon, Magee & Baggott, 1979; Lanyon et al., 1982; Hadjidakis & Androulakis, 2006). In addition to a higher osseous

mass (Christiansen, 1999, 2002), heavy quadrupeds display thicker trabeculae (Doube et al., 2011), a broader cortex and a filling of the medullar cavity by spongious bone (Wall, 1983; Oxnard, 1993; Houssaye et al., 2016; Houssaye, Fernandez & Billet, 2016). All these features are likely to play a role in dissipating more efficiently high loading stress due to a heavy mass (Warner et al., 2013). The inner structure of long bones in modern rhinos is almost unknown, and rare works concerning their microanatomy highlighted particular features, like the filling of the medullary cavity as in semi-aquatic hippos, a marked reinforcement of the cortex at midshaft and thin trabeculae (Wall, 1983) (Figure 51). Bone density of rhinos has also been described as “slightly different” from that of other heavy mammals by Alexander and Pond (1992) but without more explanation (Christiansen, 2002). Consequently, given the range of body mass and the ecological differences between the five modern rhinos (e.g. Asiatic rhinos being more aquatic than African ones), a microanatomical exploration of the long bones could highlight modifications of the inner structure related to weight and ecology. A similar approach on fossil taxa would likely complete the external approach developed here and highlight particular modifications of the inner structure linked to the support of an extreme weight by comparing distinct high taxa searching for similar or dissimilar inner structures (e.g. Paraceratheriidae and Elasmotheriidae) or the microanatomical modifications associated with an extreme brachypody (e.g. Teleoceratina).

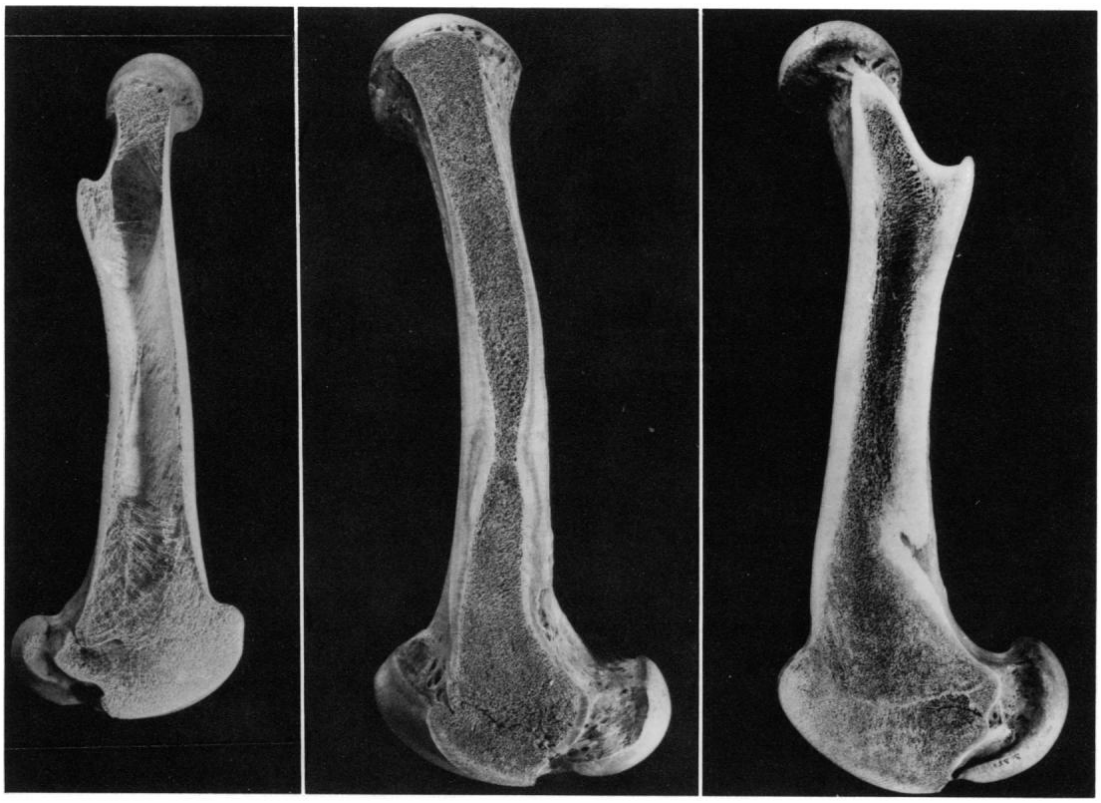

Figure 51: Sectioned femora illustrating the diversity of inner structure in heavy quadrupedal mammals. From left to right: *Bison* (empty medullary cavity), *Ceratotherium* (filled medullary cavity, thin trabeculae and variable cortex thickness) and *Hippopotamus* (filled medullary cavity and very thick cortex). From Wall (1983).

Investigation in other heavy taxa

Finally, the approach of the present study could be enhanced by the inclusion of other taxa showing independent occurrences of high body mass. This could allow to test if convergent or divergent morphological changes arise under a similar increase in weight in a larger sample comprising a greater number of replicated increases in body mass (see above "Limitations of the study"). Convergence towards a high body mass can be observed in other clades within Perissodactyla: Tapiroidea (Lophiodontidae weighting more than 2,000 kg – Robinet et al., 2015), Brontotherioidea (more than 2,000 kg – Damuth & MacFadden, 1990) and Chalicotherioidea (more than 1,500 kg – Guérin, 2012) (see Figure 3 in Chapter 1). These convergent high body masses occur in taxa showing a great diversity of morphologies and proportions. Lophiodontidae display a general body construction similar to tapirs' but with limb bones showing marked similarities with those of quadrupedal chalicotheres (e.g. rounded head and symmetrical trochlea on the femur – Figure 51) (Holbrook, 2009). Similarly, large brontotherids, despite a general aspect close to rhinos', show marked anatomical differences in their appendicular skeleton (e.g. extreme development of the greater tubercle of the humerus, relatively slender femur with a symmetrical trochlea – Figure 51) (Osborn, 1929). Moreover, chalicotheriids are split in two subfamilies showing, in addition to a heavy mass, a facultative bipedalism (Chalicotheriinae) and a full quadrupedalism (Schizotheriinae), respectively (Coombs, 1983). Another example of independent convergence towards a high body mass can be found in some South American native ungulates (belonging to the non-consensual clade Meridiungulata now considered as the sister-taxon of all Perissodactyla) (Buckley, 2015; Welker et al., 2015). Groups like Notoungulata and Litopterna include species weighting more than a ton (*Toxodon*, *Macrauchenia* – MacFadden, 2005; Fariña, Czerwonogora & Giacomo, 2014) (Figure 51). The inclusion of these taxa, coupled with the different approaches previously described (inclusion of all limb segments, modular and microanatomical investigation) should enable to highlight how the shape of the bone modifies in each group to support a high body mass and to search for potential common variation trends despite a strong diversity of body constructions.

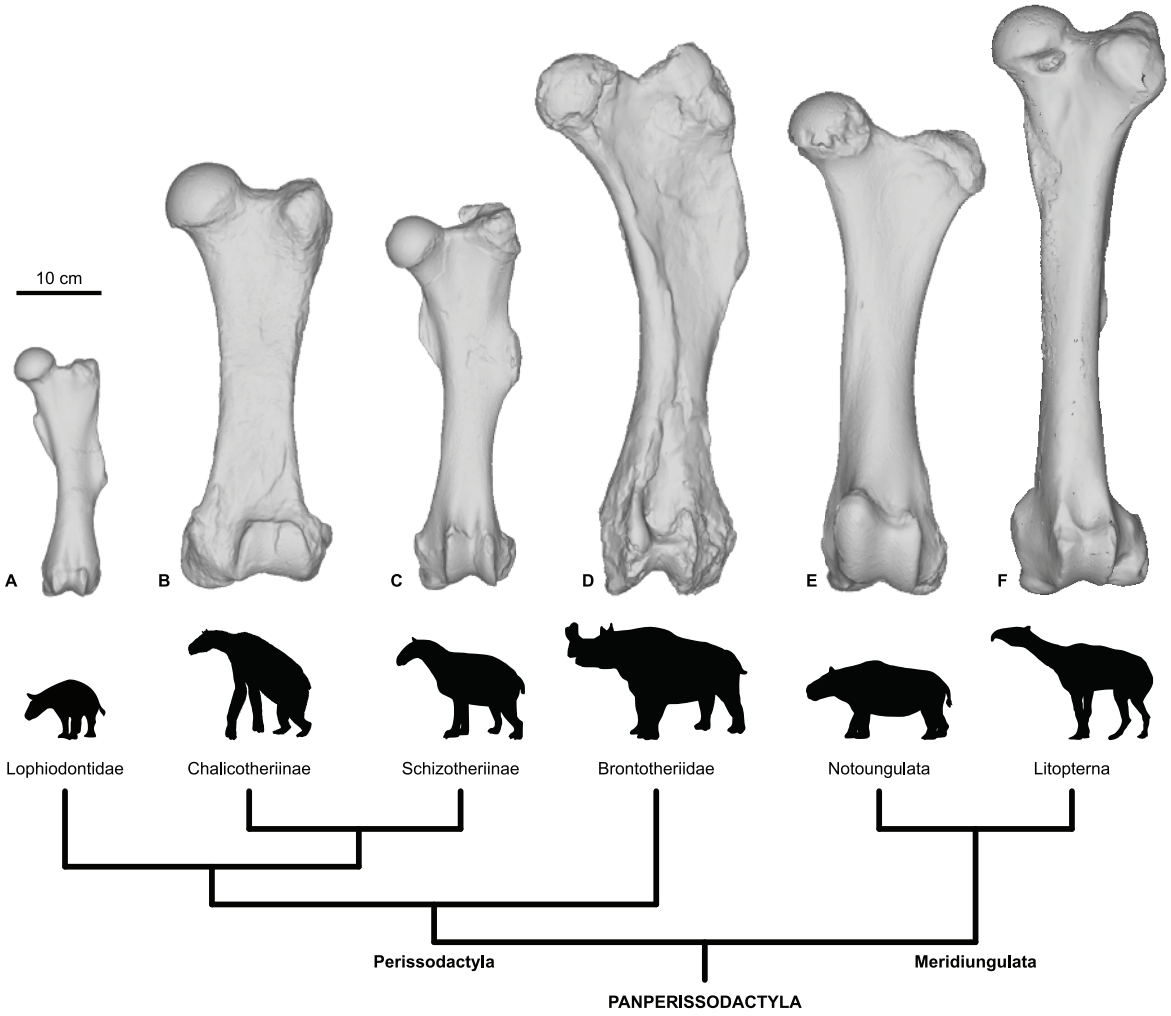

Figure 52: Overview of the femoral shape diversity of heavy taxa within Panperissodactyla. Some morphological changes are noticeable, e.g. variable bone thickness, shape and orientation of the head, development of the third trochanter and position along the shaft, presence or absence of a developed medial ridge of the trochlea. A: *Lophiodon* sp., FSL 2998, FSL, Lyon; B: *Anisodon grande*, MNHN.F.SA9589, MHHN, Paris; C: *Moropus elatus* (mirrored), FM 14379, AMNH, New York; D: *Megacerops* sp. (mirrored), FM 9848, AMNH, New York; E: *Toxodon platiensis* (mirrored), MNHN.F.PAM84, MNHN, Paris; F: *Macrauchenia patachonica* (mirrored), MHNH.F.PAM78, Paris. Phylogenetic relations between groups after Holbrook & Lapergola (2011) and Welker et al. (2015). All silhouettes are scaled.

Bibliography

3D Systems Corporation. 2014. *Geomagic Studio*. 3D Systems Corporation.

Adams DC. 2014. A generalized K statistic for estimating phylogenetic signal from shape and other high-dimensional multivariate data. *Systematic Biology* 63:685–697. DOI: 10.1093/sysbio/syu030.

Adams DC, Collyer ML. 2018. Multivariate Phylogenetic Comparative Methods: Evaluations, Comparisons, and Recommendations. *Systematic Biology* 67:14–31. DOI: 10.1093/sysbio/syx055.

Adams DC, Collyer M, Kaliontzopoulou A. 2018. *Geometric Morphometric Analyses of 2D/3D Landmark Data*.

Adams DC, Otárola-Castillo E. 2013. geomorph: an r package for the collection and analysis of geometric morphometric shape data. *Methods in Ecology and Evolution* 4:393–399. DOI: 10.1111/2041-210X.12035.

Adams DC, Rohlf FJ, Slice DE. 2004. Geometric morphometrics: Ten years of progress following the 'revolution.' *Italian Journal of Zoology* 71:5–16. DOI: 10.1080/11250000409356545.

Agisoft. 2018. *PhotoScan Professional Edition*. Agisoft.

Alexander RM. 1985. Mechanics of posture and gait of some large dinosaurs. *Zoological Journal of the Linnean Society* 83:1–25. DOI: 10.1111/j.1096-3642.1985.tb00871.x.

Alexander RM, Jayes AS, Maloiy GMO, Wathuta EM. 1979. Allometry of the limb bones of mammals from shrews (*Sorex*) to elephant (*Loxodonta*). *Journal of Zoology* 189:305–314. DOI: 10.1111/j.1469-7998.1979.tb03964.x.

Alexander RMcN, Pond CM. 1992. Locomotion and bone strength of the white rhinoceros, *Ceratotherium simum*. *Journal of Zoology* 227:63–69. DOI: 10.1111/j.1469-7998.1992.tb04344.x.

Alroy J. 1998. Cope's Rule and the Dynamics of Body Mass Evolution in North American Fossil Mammals. *Science* 280:731–734. DOI: 10.1126/science.280.5364.731.

Anderson JF, Hall-Martin A, Russell DA. 1985. Long-bone circumference and weight in mammals, birds and dinosaurs. *Journal of Zoology* 207:53–61. DOI: 10.1111/j.1469-7998.1985.tb04915.x.

Antoine P-O. 2002. Phylogénie et évolution des Elasmotheriina (Mammalia, Rhinocerotidae). *Mémoires du Muséum National d'Histoire Naturelle (1993)* 188:5–350.

Antoine P-O. In Press. Rhinocerotids from the Siwalik faunal sequence

Antoine P-O, Becker D, Laurent Y, Duranthon F. 2018. The Early Miocene teleoceratine *Prosantorhinus* aff. *douvillei* (Mammalia, Perissodactyla, Rhinocerotidae) from Béon 2, Southwestern France. *Revue de Paléobiologie* 37:367-377.

Antoine P-O, Bulot C, Ginsburg L. 2000a. Une faune rare de rhinocérotidés (Mammalia, Perissodactyla) dans le Miocène inférieur de Pellecahus (Gers, France). *Geobios* 33:249–255. DOI: 10.1016/S0016-6995(00)80022-4.

Antoine P-O, Bulot C, Ginsburg L. 2000b. Les rhinocérotidés (Mammalia, Perissodactyla) de l'Orléanien des bassins de la Garonne et de la Loire (France) : intérêt biostratigraphique. *Comptes Rendus de l'Académie des Sciences - Series IIA - Earth and Planetary Science* 330:571–576. DOI: 10.1016/S1251-8050(00)00174-9.

Antoine P-O, Downing KF, Crochet J-Y, Duranthon F, Flynn LJ, Marivaux L, Métais G, Rajpar AR, Roohi G. 2010. A revision of *Aceratherium blanfordi* Lydekker, 1884 (Mammalia: Rhinocerotidae) from the Early Miocene of Pakistan: postcranials as a key. *Zoological Journal of the Linnean Society* 160:139–194. DOI: 10.1111/j.1096-3642.2009.00597.x.

Antoine P-O, Duranthon F, Welcomme J-L. 2003. *Alicornops* (Mammalia, Rhinocerotidae) dans le Miocène supérieur des Collines Bugti (Balouchistan, Pakistan): implications phylogénétiques. *Geodiversitas* 25:575–603.

Antoine P-O, Saraç G. 2005. Rhinocerotidae (Mammalia, Perissodactyla) from the late Miocene of Akkaşdagı, Turkey. *Geodiversitas* 27:601–632.

Antoine P-O, Sen S. 2016. Rhinocerotidae and Chalicotheriidae (Perissodactyla, Tapiromorpha). *Geodiversitas* 38:245–259. DOI: 10.5252/g2016n2a6.

Antunes MT, Ginsburg L. 1983. Les rhinocérotidés du Miocène de Lisbonne - systématique, écologie, paleobiogéographie, valeur stratigraphique. *Ciencias da Terra (UNL)*:17–98.

Antunes MT, Ginsburg L. 2010. Les Périssodactyles (Mammalia) du Miocène de Lisbonne. *Ciencias da Terra (UNL)* 14:349-354.

Arambourg C. 1959. Vertébrés continentaux du Miocène supérieur de l'Afrique du Nord. *Publications du Service de la Carte Géologique de l'Algérie (Nouvelle Série), Paléontologie, Mémoire, Serv. de la Carte Géol. de l'Algérie* 4:1–161.

Arambourg C. 1970. Les vertébrés du Pléistocène de l'Afrique du Nord. *Archives du Muséum d'Histoire Naturelle* 7:1–126.

Artec 3D. 2018. *Artec Studio Professional*. Artec 3D.

Averianov A, Danilov I, Jin J, Wang Y. 2017. A new amynodontid from the Eocene of South China and phylogeny of Amynodontidae (Perissodactyla: Rhinocerotoidea). *Journal of Systematic Palaeontology* 15:927–945. DOI: 10.1080/14772019.2016.1256914.

Bai B, Meng J, Wang Y-Q, Wang H-B, Holbrook L. 2017. Osteology of The Middle Eocene Ceratomorph *Hyrachyus modestus* (Mammalia, Perissodactyla). *Bulletin of the American Museum of Natural History* 413:1–70. DOI: 10.1206/0003-0090-413.1.1.

Bai B, Wang Y-Q. 2012. *Proeggysodon* gen. nov., a primitive Eocene eggysodontine (Mammalia, Perissodactyla) from Erden Obo, Siziwangqi, Nei Mongol, China. *Vertebrata PalAsiatica* 50:204–218.

Bai B, Wang Y-Q, Li Q, Wang H-B, Mao F-Y, Gong Y-X, Meng J. 2018. Biostratigraphy and Diversity of Paleogene Perissodactyls from the Erlian Basin of Inner Mongolia, China. *American Museum Novitates* 2018:1–60. DOI: 10.1206/3914.1.

Bai B, Wang Y-Q, Meng J. 2018. The divergence and dispersal of early perissodactyls as evidenced by early Eocene equids from Asia. *Communications Biology* 1:115. DOI: 10.1038/s42003-018-0116-5.

Baker J, Meade A, Pagel M, Venditti C. 2015. Adaptive evolution toward larger size in mammals. *Proceedings of the National Academy of Sciences* 112:5093–5098. DOI: 10.1073/pnas.1419823112.

Bardua C, Felice RN, Watanabe A, Fabre A-C, Goswami A. 2019. A Practical Guide to Sliding and Surface Semilandmarks in Morphometric Analyses. *Integrative Organismal Biology* 1:1-34. DOI: 10.1093/iob/obz016.

Barone R. 2010a. *Anatomie comparée des mammifères domestiques. Tome 1 : Ostéologie*. Paris: Vigot Frères.

Barone R. 2010b. *Anatomie comparée des mammifères domestiques. Tome 2 : Arthrologie et myologie*. Paris: Vigot Frères.

Bechtol CO. 1992. Difficulties in Duplicating the Human Upright, Graviportal, Plantigrade Posture in Sitting, Standing, and Walking by the Use of Animal Models. *Journal of Investigative Surgery* 5:161–166. DOI: 10.3109/08941939209012433.

Becker D. 2003. Paléoécologie et paléoclimats de la molasse du Jura (oligo-miocène). Université de Fribourg.

Becker D. 2009. Earliest record of rhinocerotoids (Mammalia: Perissodactyla) from Switzerland: systematics and biostratigraphy. *Swiss Journal of Geosciences* 102:489-504. DOI: 10.1007/s00015-009-1330-4.

Becker D, Antoine P-O, Maridet O. 2013. A new genus of Rhinocerotidae (Mammalia, Perissodactyla) from the Oligocene of Europe. *Journal of Systematic Palaeontology* 11:947–972. DOI: 10.1080/14772019.2012.699007.

Becker D, Bürgin T, Oberli U, Scherler L. 2009. *Diaceratherium lemanense* (Rhinocerotidae) from Eschenbach (eastern Switzerland): systematics, palaeoecology, palaeobiogeography. *Neues Jahrbuch für Geologie und Paläontologie-Abhandlungen* 254:5–39. DOI: 10.1127/0077-7749/2009/0002.

Beddard FE. 1902. *The Cambridge Natural History: Mammalia*. Library of Alexandria.

Beddard FE, Treves F. 1889. On the Anatomy of *Rhinoceros sumatrensis*. *Proceedings of the Zoological Society of London* 57:7–25. DOI: 10.1111/j.1469-7998.1889.tb06740.x.

Bell E, Andres B, Goswami A. 2011. Integration and dissociation of limb elements in flying vertebrates: a comparison of pterosaurs, birds and bats. *Journal of Evolutionary Biology* 24:2586–2599. DOI: 10.1111/j.1420-9101.2011.02381.x.

Belyaeva EI. 1977. About the hyoideum, sternum and metcarpale V bones of *Elasmotherium sibiricum* Fischer (Rhinocerotidae). *Journal of the Palaeontological Society of India* 20:10–15.

Benjamini Y, Hochberg Y. 1995. Controlling the False Discovery Rate: A Practical and Powerful Approach to Multiple Testing. *Journal of the Royal Statistical Society: Series B (Methodological)* 57:289–300. DOI: 10.1111/j.2517-6161.1995.tb02031.x.

Bennett CV, Goswami A. 2011. Does developmental strategy drive limb integration in marsupials and monotremes? *Mammalian Biology* 76:79–83. DOI: 10.1016/j.mambio.2010.01.004.

Berger J. 1994. Science, Conservation, and Black Rhinos. *Journal of Mammalogy* 75:298–308. DOI: 10.2307/1382548.

Berner D. 2011. Size correction in biology: how reliable are approaches based on (common) principal component analysis? *Oecologia* 166:961–971. DOI: 10.1007/s00442-011-1934-z.

Bertram JEA, Biewener AA. 1990. Differential scaling of the long bones in the terrestrial carnivora and other mammals. *Journal of Morphology* 204:157–169. DOI: 10.1002/jmor.1052040205.

Bertram JEA, Biewener AA. 1992. Allometry and curvature in the long bones of quadrupedal mammals. *Journal of Zoology* 226:455–467. DOI: 10.1111/j.1469-7998.1992.tb07492.x.

Biasatti D, Wang Y, Deng T. 2018. Paleoecology of Cenozoic rhinos from northwest China: a stable isotope perspective. *Vertebrata PalAsiatica* 56:45–68.

Biewener AA. 1983. Allometry of quadrupedal locomotion: the scaling of duty factor, bone curvature and limb orientation to body size. *Journal of Experimental Biology* 105:147–171.

Biewener AA. 1989a. Mammalian Terrestrial Locomotion and Size. *BioScience* 39:776–783. DOI: 10.2307/1311183.

Biewener AA. 1989b. Scaling body support in mammals: limb posture and muscle mechanics. *Science* 245:45–48. DOI: 10.1126/science.2740914.

Biewener AA. 1990. Biomechanics of mammalian terrestrial locomotion. *Science* 250:1097–1103. DOI: 10.1126/science.2251499.

Biewener AA, Patek SN. 2018. *Animal locomotion*. New York: Oxford University Press.

Bininda-Emonds OR, Jeffery JE, Sánchez-Villagra MR, Hanken J, Colbert M, Pieau C, Selwood L, ten Cate C, Raynaud A, Osabutey CK, Richardson MK. 2007. Forelimb-hindlimb developmental timing changes across tetrapod phylogeny. *BMC Evolutionary Biology* 7:1–7. DOI: 10.1186/1471-2148-7-182.

de Blainville H-MD, Nicard P. 1839. *Ostéographie, ou Description iconographique comparée du squelette et du système dentaire des mammifères récents et fossiles pour servir de base à la zoologie et à la géologie. Tome 3*. Paris: J.B. Baillère & Fils.

Blanco RE, Gambini R, Fariña RA. 2003. Mechanical model for theoretical determination of maximum running speed in mammals. *Journal of Theoretical Biology* 222:117–125. DOI: 10.1016/S0022-5193(03)00019-5.

Blomberg SP, Garland T. 2002. Tempo and mode in evolution: phylogenetic inertia, adaptation and comparative methods. *Journal of Evolutionary Biology* 15:899–910. DOI: 10.1046/j.1420-9101.2002.00472.x.

Blomberg SP, Garland T, Ives AR, Crespi B. 2003. Testing for phylogenetic signal in comparative data: behavioral traits are more labile. *Evolution* 57:717–745. DOI: 10.1554/0014-3820(2003)057[0717:TFPSIC]2.0.CO;2.

Boada-Saña A. 2008. Phylogénie du rhinocérotidé *Diaceratherium* Dietrich, 1931 (Mammalia, Perissodactyla). Mémoire de Master.

Boada-Saña A, Hervet S, Antoine P-O. 2007. Nouvelles données sur les rhinocéros fossiles de Gannat (Allier, limite Oligocène-Miocène). *Revue des Sciences Naturelles d'Auvergne* 71:3–25.

Boeskorov GG. 2012. Some specific morphological and ecological features of the fossil woolly rhinoceros (*Coelodonta antiquitatis* Blumenbach 1799). *Biology Bulletin* 39:692–707. DOI: 10.1134/S106235901208002X.

Bokma F, Godinot M, Maridet O, Ladevèze S, Costeur L, Solé F, Gheerbrant E, Peigné S, Jacques F, Laurin M. 2016. Testing for Depéret's Rule (Body Size Increase) in Mammals using Combined Extinct and Extant Data. *Systematic Biology* 65:98–108. DOI: 10.1093/sysbio/syv075.

Bookstein FL. 2015. Integration, Disintegration, and Self-Similarity: Characterizing the Scales of Shape Variation in Landmark Data. *Evolutionary Biology* 42:395–426. DOI: 10.1007/s11692-015-9317-8.

Bookstein FL, Gunz P, Mitterœcker P, Prossinger H, Schæfer K, Seidler H. 2003. Cranial integration in *Homo*: singular warps analysis of the midsagittal plane in ontogeny and evolution. *Journal of Human Evolution* 44:167–187. DOI: 10.1016/S0047-2484(02)00201-4.

Botton-Divet L, Cornette R, Fabre A-C, Herrel A, Houssaye A. 2016. Morphological Analysis of Long Bones in Semi-aquatic Mustelids and their Terrestrial Relatives. *Integrative and Comparative Biology* 56:1298–1309. DOI: 10.1093/icb/icw124.

Botton-Divet L, Cornette R, Houssaye A, Fabre A-C, Herrel A. 2017. Swimming and running: a study of the convergence in long bone morphology among semi-aquatic mustelids (Carnivora: Mustelidae). *Biological Journal of the Linnean Society* 121:38–49. DOI: 10.1093/biolinnean/blw027.

Botton-Divet L, Houssaye A, Herrel A, Fabre A-C, Cornette R. 2018. Swimmers, Diggers, Climbers and More, a Study of Integration Across the Mustelids' Locomotor Apparatus (Carnivora: Mustelidae). *Evolutionary Biology* 45:182–195. DOI: 10.1007/s11692-017-9442-7.

Bressou C. 1961. La myologie du tapir (*Tapirus indicus* L.). *Mammalia* 25:358–400. DOI: 10.1515/mamm.1961.25.3.358.

Bronnert C. 2018. Origine et premières dichotomies des périssodactyles (Mammalia, Laurasiatheria) : Apport des faunes de l'Éocène inférieur du Bassin de Paris. Thèse de doctorat Thesis. Paris: Sorbonne Université.

Bucher H, Ginsburg L, Cheneval J. 1985. Nouvelles données et interprétations sur la formation des gisements de vertébrés aquitaniens de Saint-Gérand-le-Puy (Allier, France). *Geobios* 18:823–832. DOI: 10.1016/S0016-6995(85)80037-1.

Buckley M. 2015. Ancient collagen reveals evolutionary history of the endemic South American 'ungulates.' *Proc. R. Soc. B* 282:20142671. DOI: 10.1098/rspb.2014.2671.

Cabin RJ, Mitchell RJ. 2000. To Bonferroni or Not to Bonferroni: When and How Are the Questions. *Bulletin of the Ecological Society of America* 81:246–248.

Campione NE, Evans DC. 2012. A universal scaling relationship between body mass and proximal limb bone dimensions in quadrupedal terrestrial tetrapods. *BMC Biology* 10:1–21. DOI: 10.1186/1741-7007-10-60.

Cappellini E, Welker F, Pandolfi L, Ramos-Madrigal J, Samodova D, Rüther PL, Fotakis AK, Lyon D, Moreno-Mayar JV, Bukhsianidze M, Jersie-Christensen RR, Mackie M, Ginolhac A, Ferring R, Tappen M, Palkopoulou E, Dickinson MR, Stafford TW, Chan YL, Götherström A, Nathan SKSS, Heintzman PD, Kapp JD, Kirillova I, Moodley Y, Agusti J, Kahlke R-D, Kiladze G, Martínez-Navarro B, Liu S, Velasco MS, Sinding M-HS, Kelstrup CD, Allentoft ME, Orlando L, Penkman K, Shapiro B, Rook L, Dalén L, Gilbert MTP, Olsen JV, Lordkipanidze D, Willerslev E. 2019. Early Pleistocene enamel proteome from Dmanisi resolves *Stephanorhinus* phylogeny. *Nature* 574:103–107. DOI: 10.1038/s41586-019-1555-y.

Carlson B, Park J. 2017. Feeding and Digestion Behaviors of *Hyrachyus eximius*. *ZOOL430*.

Carrano MT. 1999. What, if anything, is a cursor? Categories versus continua for determining locomotor habit in mammals and dinosaurs. *Journal of Zoology* 247:29–42. DOI: 10.1111/j.1469-7998.1999.tb00190.x.

Cassini GH, Vizcaíno SF, Bargo MS. 2012. Body mass estimation in Early Miocene native South American ungulates: a predictive equation based on 3D landmarks. *Journal of Zoology* 287:53–64. DOI: 10.1111/j.1469-7998.2011.00886.x.

Cerdeño E. 1993. Étude sur *Diaceratherium aurelianense* et *Brachypotherium brachypus* (Rhinocerotidae, Mammalia) du Miocène moyen de France. *Bulletin du Muséum National d'Histoire Naturelle, 4ème série* 15:25–77.

Cerdeño E. 1995. Cladistic analysis of the family Rhinocerotidae (Perissodactyla). *American Museum novitates* 3143:1–25.

Cerdeño E. 1996a. Rhinocerotidae from the Middle Miocene of the Tung-gur Formation, Inner Mongolia (China). *American Museum Novitates* 3184:1–43.

Cerdeño E. 1996b. *Prosantorhinus*, the small teleoceratine rhinocerotid from the Miocene of Western Europe. *Geobios* 29:111–124. DOI: 10.1016/S0016-6995(96)80077-5.

Cerdeño E. 1998. Diversity and evolutionary trends of the Family Rhinocerotidae (Perissodactyla). *Palaeogeography, Palaeoclimatology, Palaeoecology* 141:13–34. DOI: 10.1016/S0031-0182(98)00003-0.

Cerdeño E, Alcalá L. 1989. *Aceratherium alfambrense* n. sp., nuevo rinocerótido del Vallesiense superior de Teruel (España). *Revista Española de Paleontología* 4:39–51.

Chen S, Deng T, Hou S, Shi Q, Pang L. 2010. Sexual Dimorphism in Perissodactyl Rhinocerotid *Chilotherium wimani* from the Late Miocene of the Linxia Basin (Gansu, China). *Acta Palaeontologica Polonica* 55:587–597. DOI: 10.4202/app.2009.0001.

Cheverud JM. 1982. Phenotypic, Genetic, and Environmental Morphological Integration in the Cranium. *Evolution* 36:499–516. DOI: 10.1111/j.1558-5646.1982.tb05070.x.

Cheverud JM. 1996. Developmental Integration and the Evolution of Pleiotropy. *Integrative and Comparative Biology* 36:44–50. DOI: 10.1093/icb/36.1.44.

Christiansen P. 1999. Scaling of mammalian long bones: small and large mammals compared. *Journal of Zoology* 247:333–348. DOI: 10.1111/j.1469-7998.1999.tb00996.x.

Christiansen P. 2002. Mass allometry of the appendicular skeleton in terrestrial mammals. *Journal of Morphology* 251:195–209. DOI: 10.1002/jmor.1083.

Christiansen P. 2007. Long-bone geometry in columnar-limbed animals: allometry of the proboscidean appendicular skeleton. *Zoological Journal of the Linnean Society* 149:423–436. DOI: 10.1111/j.1096-3642.2007.00249.x.

Cignoni P, Callieri M, Corsini M, Dellepiane M, Ganovelli F, Ranzuglia G. 2008. *MeshLab: an Open-Source Mesh Processing Tool*. The Eurographics Association. DOI: http://dx.doi.org/10.2312/LocalChapterEvents/ItalChap/ItalianChapConf2008/129-136.

Clementz MT, Holroyd PA, Koch PL. 2008. Identifying Aquatic Habits Of Herbivorous Mammals Through Stable Isotope Analysis. *Palaios* 23:574–585. DOI: 10.2110/palo.2007.p07-054r.

Colbert EH. 1935. Siwalik mammals in the American Museum of natural History. *American philosophical Society*:38–78.

Colbert EH. 1938. Fossil mammals from Burma in the American Museum of Natural History. *Bulletin of the American Museum of Natural History* 74:255–436.

Colyn M. 1980. Ostéologie descriptive de *Ceratotherium simum cottoni* Lydekker, 1908.

Coombs WP. 1978. Theoretical Aspects of Cursorial Adaptations in Dinosaurs. *The Quarterly Review of Biology* 53:393–418. DOI: 10.1086/410790.

Coombs MC. 1983. Large Mammalian Clawed Herbivores: A Comparative Study. *Transactions of the American Philosophical Society* 73:1–96. DOI: 10.2307/3137420.

Cope ED. 1873. On the Osteology of the Extinct Tapiroid *Hyrachyus*. *Proceedings of the American Philosophical Society* 13:212–224.

Cope ED. 1884. The Vertebrata of the Tertiary Formations of the West. In: *Report U. S. Geological Survey of the Territories*. Hayden F.V., 1–1009.

Cope ED. 1887. *The origin of the fittest: Essays on evolution*. New York: Appleton.

Costeur L, Maridet O, Montuire S, Legendre S. 2013. Evidence of northern Turolian savanna-woodland from the Dorn-Dürkheim 1 fauna (Germany). *Palaeobiodiversity and Palaeoenvironments* 93:259–275. DOI: 10.1007/s12549-013-0116-x.

Costeur L, Maridet O, Peigné S, Heizmann EPJ. 2012. Palaeoecology and palaeoenvironment of the Aquitanian locality Ulm-Westtangente (MN2, Lower Freshwater Molasse, Germany). *Swiss Journal of Palaeontology* 131:183–199. DOI: 10.1007/s13358-011-0034-3.

Coughlin BL, Fish FE. 2009. Hippopotamus Underwater Locomotion: Reduced-Gravity Movements for a Massive Mammal. *Journal of Mammalogy* 90:675–679. DOI: 10.1644/08-MAMM-A-279R.1.

Crelin ES. 1988. Ligament of the head of the femur in the orangutan and Indian elephant. *The Yale Journal of Biology and Medicine* 61:383–388.

Cubo J. 2004. Pattern and process in constructional morphology. *Evolution & Development* 6:131–133. DOI: 10.1111/j.1525-142X.2004.04018.x.

Cubo J, Ponton F, Laurin M, De Margerie E, Castanet J. 2005. Phylogenetic Signal in Bone Microstructure of Sauropsids. *Systematic Biology* 54:562–574. DOI: 10.1080/10635150591003461.

Currey JD. 2006. *Bones: Structure and Mechanics*. Princeton University Press.

Cuvier G. 1812. *Recherches sur les ossements fossiles de quadrupèdes. Tome 2*. Paris: Deterville.

Damuth JD, MacFadden BJ. 1990. *Body Size in Mammalian Paleobiology: Estimation and Biological Implications*. Cambridge University Press.

Deng T, Wang X, Fortelius M, Li Q, Wang Y, Tseng ZJ, Takeuchi GT, Saylor JE, Säilä LK, Xie G. 2011. Out of Tibet: Pliocene Woolly Rhino Suggests High-Plateau Origin of Ice Age Megaherbivores. *Science* 333:1285–1288. DOI: 10.1126/science.1206594.

Depéret C. 1907. *Les transformations du monde animal*. Paris: Flammarion.

Dinerstein E. 1991. Sexual Dimorphism in the Greater One-Horned Rhinoceros (*Rhinoceros unicornis*). *Journal of Mammalogy* 72:450–457. DOI: 10.2307/1382127.

Dinerstein E. 2011. Family Rhinocerotidae (Rhinoceroses). In: *Handbook of the Mammals of the World*. Barcelona: Don E. Wilson & Russel A. Mittermeier, 144–181.

Diogo R, Molnar J. 2014. Comparative anatomy, evolution, and homologies of tetrapod hindlimb muscles, comparison with forelimb muscles, and deconstruction of the forelimb-hindlimb serial homology hypothesis. *Anatomical Record (Hoboken, N.J.: 2007)* 297:1047–1075. DOI: 10.1002/ar.22919.

Diogo R, Molnar JL, Rolian C, Esteve-Altava B. 2018. First anatomical network analysis of fore- and hindlimb musculoskeletal modularity in bonobos, common chimpanzees, and humans. *Scientific Reports* 8:6885. DOI: 10.1038/s41598-018-25262-6.

Domning DP. 2002. The terrestrial posture of desmostylians. *Smithsonian Contributions to Paleobiology* 93:99–111.

Doube M, Kłosowski MM, Wiktorowicz-Conroy AM, Hutchinson JR, Shefelbine SJ. 2011. Trabecular bone scales allometrically in mammals and birds. *Proceedings of the Royal Society B: Biological Sciences* 278:3067–3073. DOI: 10.1098/rspb.2011.0069.

Drake AG, Klingenberg CP. 2008. The pace of morphological change: historical transformation of skull shape in St Bernard dogs. *Proceedings of the Royal Society B: Biological Sciences* 275:71–76. DOI: 10.1098/rspb.2007.1169.

Dutto DJ, Hoyt DF, Clayton HM, Cogger EA, Wickler SJ. 2006. Joint work and power for both the forelimb and hindlimb during trotting in the horse. *Journal of Experimental Biology* 209:3990–3999. DOI: 10.1242/jeb.02471.

Eisenmann V, Guérin C. 1984. Morphologie fonctionnelle et environnement chez les périssodactyles. *Geobios* 17:69–74. DOI: 10.1016/S0016-6995(84)80158-8.

Ercoli MD, Prevosti FJ. 2011. Estimación de Masa de las Especies de Sparassodonta (Mammalia, Metatheria) de Edad Santacrucense (Mioceno Temprano) a Partir del Tamaño del Centroide de los Elementos Apendiculares: Inferencias Paleoecológicas. *Ameghiniana* 48:462–479. DOI: 10.5710/AMGH.v48i4(347).

Etienne C, Mallet C, Cornette R, Houssaye A. 2020. Influence of mass on tarsus shape variation: a morphometrical investigation among Rhinocerotidae (Mammalia: Perissodactyla). *Biological Journal of the Linnean Society*. DOI: 10.1093/biolinnean/blaa005.

Fabre A-C, Cornette R, Peigné S, Goswami A. 2013. Influence of body mass on the shape of forelimb in musteloid carnivorans. *Biological Journal of the Linnean Society* 110:91–103. DOI: 10.1111/bij.12103.

Fabre A-C, Cornette R, Perrard A, Boyer DM, Prasad GVR, Hooker JJ, Goswami A. 2014a. A three-dimensional morphometric analysis of the locomotory ecology of *Deccanolestes*, a eutherian mammal from the Late Cretaceous of India. *Journal of Vertebrate Paleontology* 34:146–156. DOI: 10.1080/02724634.2013.789437.

Fabre A-C, Goswami A, Peigné S, Cornette R. 2014b. Morphological integration in the forelimb of musteloid carnivorans. *Journal of Anatomy* 225:19–30. DOI: 10.1111/joa.12194.

Farina RA, Czerwonogora A, Giacomo MD. 2014. Splendid oddness: revisiting the curious trophic relationships of South American Pleistocene mammals and their abundance. *Anais da Academia Brasileira de Ciências* 86:311–331. DOI: 10.1590/0001-3765201420120010.

Fau M, Cornette R, Houssaye A. 2016. Photogrammetry for 3D digitizing bones of mounted skeletons: Potential and limits. *Comptes Rendus Palevol* 15:968–977. DOI: 10.1016/j.crpv.2016.08.003.

Felsenstein J. 1985. Phylogenies and the Comparative Method. *The American Naturalist* 125:1–15. DOI: 10.1086/284325.

Felsenstein J. 2004. *Inferring Phylogenies*. Sunderland, Mass: OUP USA.

Fernando P, Polet G, Foead N, Ng LS, Pastorini J, Melnick DJ. 2006. Genetic diversity, phylogeny and conservation of the Javan rhinoceros (*Rhinoceros sondaicus*). *Conservation Genetics* 7:439–448. DOI: 10.1007/s10592-006-9139-4.

Finarelli JA. 2007. Mechanisms behind Active Trends in Body Size Evolution of the Canidae (Carnivora: Mammalia). *The American Naturalist* 170:876–885. DOI: 10.1086/522846.

Fischer MS, Blickhan R. 2006. The tri-segmented limbs of therian mammals: kinematics, dynamics, and self-stabilization—a review. *Journal of Experimental Zoology Part A: Comparative Experimental Biology* 305A:935–952. DOI: 10.1002/jez.a.333.

Fisher RE, Scott KM, Adrian B. 2010. Hind limb myology of the common hippopotamus, *Hippopotamus amphibius* (Artiodactyla: Hippopotamidae). *Zoological Journal of the Linnean Society* 158:661–682. DOI: 10.1111/j.1096-3642.2009.00558.x.

Fisher RE, Scott KM, Naples VL. 2007. Forelimb myology of the pygmy hippopotamus (*Choeropsis liberiensis*). *The Anatomical Record* 290:673–693. DOI: 10.1002/ar.20531.

Fortelius M, Kappelman J. 1993. The largest land mammal ever imagined. *Zoological Journal of the Linnean Society* 108:85–101. DOI: 10.1111/j.1096-3642.1993.tb02560.x.

Fortelius M, Mazza PPA, Sala B. 1993. *Stephanorhinus* (Mammalia: Rhinocerotidae) of the western European Pleistocene, with a revision of *S. etruscus* (Falconer, 1868). *Palaeontographia Italica* 80:63–155.

Froehlich DJ. 1999. Phylogenetic systematics of basal perissodactyls. *Journal of Vertebrate Paleontology* 19:140–159. DOI: 10.1080/02724634.1999.10011129.

Fujiwara S. 2009. Olecranon orientation as an indicator of elbow joint angle in the stance phase, and estimation of forelimb posture in extinct quadruped animals. *Journal of Morphology* 270:1107–1121. DOI: 10.1002/jmor.10748.

Fujiwara S, Hutchinson JR. 2012. Elbow joint adductor moment arm as an indicator of forelimb posture in extinct quadrupedal tetrapods. *Proceedings of the Royal Society of London B: Biological Sciences* 279:2561–2570. DOI: 10.1098/rspb.2012.0190.

Fukuchi A, Kawai K. 2011. Revision of Fossil Rhinoceroses from the Miocene Mizunami Group, Japan. *Paleontological Research* 15:247–257. DOI: 10.2517/1342-8144-15.4.247.

Galilei G. 1638. *Discours et démonstrations mathématiques concernant deux sciences nouvelles*. Paris: PUF.

Gasc J-P. 2001. Comparative aspects of gait, scaling and mechanics in mammals. *Comparative Biochemistry and Physiology Part A: Molecular & Integrative Physiology* 131:121–133. DOI: 10.1016/S1095-6433(01)00457-3.

Gaudry M. 2017. Molecular phylogenetics of the rhinoceros clade and evolution of UCP1 transcriptional regulatory elements across the mammalian phylogeny. Master of Science Thesis. Winnipeg: University of Manitoba.

Gentry AW. 1987. Rhinoceroses from the Miocene of Saudi Arabia. *Bulletin of the British Museum (Natural History), Geology* 41:409–432.

Geraads D. 1988. Révision des Rhinocerotinae (Mammalia) du Turolien de Pikermi. Comparaison avec les formes voisines. *Annales de Paléontologie* 74:13–41.

Geraads D. 1994. Les gisements de mammifères du Miocène supérieur de Kemiklitepe, Turquie: 4. Rhinocerotidae. *Bulletin du Muséum National d'Histoire Naturelle, 4ème série* 16:81–95.

Geraads D. 2010. Rhinocerotidae. In: *Cenozoic Mammals of Africa*. Londres: Univ of California Press, 659–667.

Giaourtsakis IX. 2009. The Late Miocene Mammal Faunas of the Mytilinii Basin, Samos Island, Greece: New Collection. 9. Rhinocerotidae. *Beiträge zur Paläontologie* 31:157–187.

Giaourtsakis IX, Heissig K. 2004. On the nomenclatural status of *Aceratherium incisivum* (Rhinocerotidae, Mammalia). In: *Proceedings of 5th International Symposium on Eastern Mediterranean Geology*. Thessaloniki, Greece. Aristotle University, Thessaloniki: A. A. Chatzipetros and S. B. Pavlides, 314–317.

Gingerich PD. 2006. Environment and evolution through the Paleocene–Eocene thermal maximum. *Trends in Ecology & Evolution* 21:246–253. DOI: 10.1016/j.tree.2006.03.006.

Ginsburg L, Bulot C. 1984. Les Rhinocerotidae (Perissodactyla, Mammalia) du Miocène de Bézian à La Romieu (Gers). *Bulletin du Muséum National d'Histoire Naturelle* 6:353–3777.

Goodall C. 1991. Procrustes Methods in the Statistical Analysis of Shape. *Journal of the Royal Statistical Society: Series B (Methodological)* 53:285–321. DOI: 10.1111/j.2517-6161.1991.tb01825.x.

Goolsby EW. 2015. Phylogenetic Comparative Methods for Evaluating the Evolutionary History of Function-Valued Traits. *Systematic Biology* 64:568–578. DOI: 10.1093/sysbio/syv012.

Goossens B, Salgado-Lynn M, Rovie-Ryan JJ, Ahmad AH, Payne J, Zainuddin ZZ, Nathan SKSS, Ambu LN. 2013. Genetics and the last stand of the Sumatran rhinoceros *Dicerorhinus sumatrensis*. *Oryx* 47:340–344. DOI: 10.1017/S0030605313000045.

Goswami A, Polly PD. 2010. Methods for Studying Morphological Integration and Modularity. *The Paleontological Society Papers* 16:213–243. DOI: 10.1017/S1089332600001881.

Goswami A, Smaers JB, Soligo C, Polly PD. 2014. The macroevolutionary consequences of phenotypic integration: from development to deep time. *Philosophical Transactions of the Royal Society B: Biological Sciences* 369:20130254. DOI: 10.1098/rstb.2013.0254.

Goswami A, Weisbecker V, Sánchez-Villagra MR. 2009. Developmental modularity and the marsupial–placental dichotomy. *Journal of Experimental Zoology Part B: Molecular and Developmental Evolution* 312B:186–195. DOI: 10.1002/jez.b.21283.

Gotanda KM, Correa C, Turcotte MM, Rolshausen G, Hendry AP. 2015. Linking macrotrends and microrates: Re-evaluating microevolutionary support for Cope's rule. *Evolution* 69:1345–1354. DOI: 10.1111/evo.12653.

Gould SJ. 2002. *The Structure of Evolutionary Theory*. Cambridge, Massachusetts; London, England: Harvard University Press.

Gould SJ, Lewontin RC, Maynard Smith J, Holliday R. 1979. The spandrels of San Marco and the Panglossian paradigm: a critique of the adaptationist programme. *Proceedings of the Royal Society of London. Series B. Biological Sciences* 205:581–598. DOI: 10.1098/rspb.1979.0086.

Goussard F. 2009. Etude morpho-fonctionnelle de la main des dinosaures sauropodomorphes : implications évolutives et apport de l'analyse en éléments finis. These de doctorat. Paris, Muséum national d'histoire naturelle.

Gower JC. 1975. Generalized procrustes analysis. *Psychometrika* 40:33–51. DOI: 10.1007/BF02291478.

Granatosky MC, Fitzsimons A, Zeininger A, Schmitt D. 2018. Mechanisms for the functional differentiation of the propulsive and braking roles of the forelimbs and hindlimbs during quadrupedal walking in primates and felines. *Journal of Experimental Biology* 221. DOI: 10.1242/jeb.162917.

Granger W, Gregory WK (William K. 1936. Further notes on the gigantic extinct rhinoceros, *Baluchitherium*, from the Oligocene of Mongolia. *Bulletin of the American Museum of Natural History* 72:1–73.

Gregory WK. 1912. Notes on the Principles of Quadrupedal Locomotion and on the Mechanism of the Limbs in Hoofed Animals. *Annals of the New York Academy of Sciences* 22:267–294. DOI: 10.1111/j.1749-6632.1912.tb55164.x.

Gromova V. 1954. Bolotnye nosorogi (Amynodontidae) Mongolii [Paludal rhinoceroses (Amynodontidae) of Mongolia]. *Trudy Paleontologicheskogo Instituta AN SSSR* 55:85–189.

Gromova V. 1959. Gigantskie Nosorogi [Giant Rhinoceroses]. *Trudy PIN AN SSSR* 71:1–185.

Groves CP. 1967a. Geographic variation in the black rhinoceros, *Diceros bicornis* (L, 1758). *Zeitschrift fur Saugetierkunde* 32:267–276.

Groves CP. 1967b. On the rhinoceroses of South-East Asia. *Saugetierkundliche Mitteilungen* 15:221–237.

Groves CP. 1972. *Ceratotherium simum*. *Mammalian Species*:1–6. DOI: 10.2307/3503966.

Groves CP. 1982. The skulls of Asian rhinoceroses: Wild and captive. *Zoo Biology* 1:251–261. DOI: 10.1002/zoo.1430010309.

Groves CP, Fernando P, Robovský J. 2010. The Sixth Rhino: A Taxonomic Re-Assessment of the Critically Endangered Northern White Rhinoceros. *PLOS ONE* 5:e9703. DOI: 10.1371/journal.pone.0009703.

Groves CP, Kurt F. 1972. *Dicerorhinus sumatrensis*. *Mammalian Species*:1–6. DOI: 10.2307/3503818.

Groves CP, Leslie DM. 2011. *Rhinoceros sondaicus* (Perissodactyla: Rhinocerotidae). *Mammalian Species* 43:190–208. DOI: 10.2307/mammalianspecies.43.1.190.

Guérin C. 1972. Une nouvelle espèce de rhinocéros (Mammalia, Perissodactyla) à Vialette (Haute-Loire, France) et dans d'autres gisements du Villafranchien inférieur européen : *Dicerorhinus jeanvireti* n. sp. *Travaux et Documents des Laboratoires de Géologie de Lyon* 49:53–150.

Guérin C. 1980. Les Rhinocéros (Mammalia, Perissodactyla) du Miocène terminal au Pléistocène supérieur en Europe occidentale. Comparaison avec les espèces actuelles. Documents du Laboratoire de Géologie de l'Université de Lyon Thesis.

Guérin C. 1982. Les Rhinocerotidae (Mammalia, Perissodactyla) du Miocène terminal au Pleistocène supérieur d'Europe Occidentale comparés aux espèces actuelles: Tendances évolutives et relations phylogénétiques. *Geobios* 15:599–605. DOI: 10.1016/S0016-6995(82)80077-6.

Guérin C. 1989. La famille des Rhinocerotidae (Mammalia, Perissodactyla): systématique, histoire, évolution, paléoécologie. *Cranium* 6:3–14.

Guerin C. 2000. The Neogene rhinoceroses of Namibia. *Palaeontologia Africana* 36:119-138.

Guérin C. 2010. *Coelodonta antiquitatis praecursor* (Rhinocerotidae) du Pléistocène moyen final de l'Aven de Romain-la-Roche (Doubs, France). *Revue de Paléobiologie* 29:697–746.

Guérin C. 2011. Les Rhinocerotidae (Mammalia, Perissodactyla) miocènes et pliocènes des Tugen Hills (Kenya). *Estudios Geologicos* 67:333–362. DOI: 10.3989/egeol.40627.19.

Guérin C. 2012. *Anisodon grande* (Perissodactyla, Chalicotheriidae) de Sansan. In: *Mammiferes de Sansan*. Mémoires du Muséum national d'histoire naturelle. Paris, 279–315.

Guérin C, Dewolf Y, Lautridou J-P. 2003. Révision d'un site paléontologique célèbre : Saint-Prest (Chartres, France). *Geobios* 36:55–82. DOI: 10.1016/S0016-6995(02)00106-7.

Guérin C, Faure M, Argant A, Argant J, Crégut-Bonnoure É, Debard É, Delson E, Eisenmann V, Hugueney M, Limondin-Lozouet N, Martín-Suárez E, Mein P, Mourer-Chauviré C, Parenti F, Pastre J-F, Sen S, Valli A. 2004. Le gisement pliocène supérieur de Saint-Vallier (Drôme, France) : synthèse biostratigraphique et paléoécologique. *Geobios* 37:S349–S360. DOI: 10.1016/S0016-6995(04)80023-8.

Gunz P, Mitteroecker P. 2013. Semilandmarks: a method for quantifying curves and surfaces. *Hystrix, the Italian Journal of Mammalogy* 24:103–109.

Gunz P, Mitteroecker P, Bookstein FL. 2005. Semilandmarks in Three Dimensions. In: *Modern Morphometrics in Physical Anthropology*. Developments in Primatology: Progress and Prospects. Boston, MA: Slice, D. E., 73–98. DOI: 10.1007/0-387-27614-9_3.

Hadjidakis DJ, Androulakis II. 2006. Bone remodeling. *Annals of the New York Academy of Sciences* 1092:385–396.

Hallgrímsson B, Jamniczky H, Young NM, Rolian C, Parsons TE, Boughner JC, Marcucio RS. 2009. Deciphering the Palimpsest: Studying the Relationship Between Morphological Integration and Phenotypic Covariation. *Evolutionary Biology* 36:355–376. DOI: 10.1007/s11692-009-9076-5.

Hallgrímsson B, Katz DC, Aponte JD, Larson JR, Devine J, Gonzalez PN, Young NM, Roseman CC, Marcucio RS. 2019. Integration and the Developmental Genetics of Allometry. *Integrative and Comparative Biology* 59:1369–1381. DOI: 10.1093/icb/icz105.

Hallgrímsson B, Willmore K, Hall BK. 2002. Canalization, developmental stability, and morphological integration in primate limbs. *American Journal of Physical Anthropology* 119:131–158. DOI: 10.1002/ajpa.10182.

Hamilton WR. 1973. North African Lower Miocene Rhinoceroses. *Bulletin of the British Museum (Natural History), Geology* 24:349–395.

Hanot P, Herrel A, Guintard C, Cornette R. 2017. Morphological integration in the appendicular skeleton of two domestic taxa: the horse and donkey. *Proc. R. Soc. B* 284:20171241. DOI: 10.1098/rspb.2017.1241.

Hanot P, Herrel A, Guintard C, Cornette R. 2018. The impact of artificial selection on morphological integration in the appendicular skeleton of domestic horses. *Journal of Anatomy* 232:657–673. DOI: 10.1111/joa.12772.

Hanot P, Herrel A, Guintard C, Cornette R. 2019. Unravelling the hybrid vigor in domestic equids: the effect of hybridization on bone shape variation and covariation. *BMC Evolutionary Biology* 19:1–13. DOI: 10.1186/s12862-019-1520-2.

Harley EH, de Waal M, Murray S, O'Ryan C. 2016. Comparison of whole mitochondrial genome sequences of northern and southern white rhinoceroses (*Ceratotherium simum*): the conservation consequences of species definitions. *Conservation Genetics* 17:1285–1291. DOI: 10.1007/s10592-016-0861-2.

Harris MA, Steudel K. 1997. Ecological correlates of hind-limb length in the Carnivora. *Journal of Zoology* 241:381–408. DOI: 10.1111/j.1469-7998.1997.tb01966.x.

Heissig K. 1972. Paläontologische und geologische Untersuchungen im Tertiär von Pakistan – 5. Rhinocerotidae (Mammalia) aus den unteren und mittleren Siwalik-Schichten. *Abhandlungen der Bayerischen Akademie der Wissenschaften, Mathematisch-naturwissenschaftliche Klasse, München* 152:1–112.

Heissig K. 1975. Rhinocerotidae aus dem jungtertiär Anatoliens. *Geologisches Jahrbuch, Reihe B* 15:145–151.

Heissig K. 2006. Rhinocerotidae (Perissodactyla, Mammalia). *Annalen des Naturhistorischen Museums in Wien. Serie A für Mineralogie und Petrographie, Geologie und Paläontologie, Anthropologie und Prähistorie* 108:233–269.

Heissig K. 2012. Les Rhinocerotidae (Perissodactyla) de Sansan. In: *Mammiferes de Sansan*. Mémoires du Muséum national d'histoire naturelle. Paris, 317–485.

Heissig K. 2017. Revision of the European species of *Prosantorhinus* (Mammalia, Perissodactyla, Rhinocerotidae). *Fossil Imprint* 73:236–274. DOI: 10.2478/if-2017-0014.

Henderson DM. 1999. Estimating the Masses and Centers of Mass of Extinct Animals by 3-D Mathematical Slicing. *Paleobiology* 25:88–106.

Henderson DM. 2006. Burly gaits: centers of mass, stability, and the trackways of sauropod dinosaurs. *Journal of Vertebrate Paleontology* 26:907–921. DOI: 10.1671/0272-4634(2006)26[907:BGCOMS]2.0.CO;2.

Henderson K, Pantinople J, McCabe K, Richards HL, Milne N. 2017. Forelimb bone curvature in terrestrial and arboreal mammals. *PeerJ* 5:e3229. DOI: 10.7717/peerj.3229.

Hermanson JW, MacFadden BJ. 1992. Evolutionary and functional morphology of the shoulder region and stay-apparatus in fossil and extant horses (Equidae). *Journal of Vertebrate Paleontology* 12:377–386. DOI: 10.1080/02724634.1992.10011466.

Hermanson JW, Macfadden BJ. 1996. Evolutionary and functional morphology of the knee in fossil and extant horses (Equidae). *Journal of Vertebrate Paleontology* 16:349–357. DOI: 10.1080/02724634.1996.10011321.

Hildebrand M. 1974. *Analysis of vertebrate structure*. New York: John Wiley & Sons.

Hillman-Smith AKK, Groves CP. 1994. *Diceros bicornis*. *Mammalian Species*:1–8. DOI: 10.2307/3504292.

Ho J, Tumkaya T, Aryal S, Choi H, Claridge-Chang A. 2019. Moving beyond P values: data analysis with estimation graphics. *Nature Methods* 16:565–566. DOI: 10.1038/s41592-019-0470-3.

Hogervorst T, Vereecke EE. 2014. Evolution of the human hip. Part 1: the osseous framework. *Journal of Hip Preservation Surgery* 1:39–45. DOI: 10.1093/jhps/hnu013.

Holbrook LT. 1999. The Phylogeny and Classification of Tapiromorph Perissodactyls (Mammalia). *Cladistics* 15:331–350. DOI: 10.1111/j.1096-0031.1999.tb00270.x.

Holbrook LT. 2001. Comparative osteology of early Tertiary tapiromorphs (Mammalia, Perissodactyla). *Zoological Journal of the Linnean Society* 132:1–54. DOI: 10.1111/j.1096-3642.2001.tb02270.x.

Holbrook LT. 2009. Osteology of *Lophiodon* (Mammalia, Perissodactyla) and its Phylogenetic Implications. *Journal of Vertebrate Paleontology* 29:212–230. DOI: 10.1671/039.029.0117.

Holbrook LT, Lapergola J. 2011. A new genus of perissodactyl (Mammalia) from the Bridgerian of Wyoming, with comments on basal perissodactyl phylogeny. *Journal of Vertebrate Paleontology* 31:895–901. DOI: 10.1080/02724634.2011.579669.

Hone DWE, Benton MJ. 2005. The evolution of large size: how does Cope's Rule work? *Trends in Ecology & Evolution* 20:4–6. DOI: 10.1016/j.tree.2004.10.012.

Hopkins SSB. 2018. Estimation of Body Size in Fossil Mammals. In: Croft DA, Su DF, Simpson SW eds. *Methods in Paleoecology: Reconstructing Cenozoic Terrestrial Environments and Ecological Communities*. Vertebrate Paleobiology and Paleoanthropology. Cham: Springer International Publishing, 7–22. DOI: 10.1007/978-3-319-94265-0_2.

Houssaye A, Fernandez V, Billet G. 2016. Hyperspecialization in Some South American Endemic Ungulates Revealed by Long Bone Microstructure. *Journal of Mammalian Evolution* 23:221–235. DOI: 10.1007/s10914-015-9312-y.

Houssaye A, Waskow K, Hayashi S, Cornette R, Lee AH, Hutchinson JR. 2016. Biomechanical evolution of solid bones in large animals: a microanatomical investigation. *Biological Journal of the Linnean Society* 117:350–371. DOI: 10.1111/bij.12660.

Ingicco T, Bergh GD van den, Jago-on C, Bahain J-J, Chacón MG, Amano N, Forestier H, King C, Manalo K, Nomade S, Pereira A, Reyes MC, Sémah A-M, Shao Q, Voinchet P, Falguères C, Albers PCH, Lising M, Lyras G, Yurnaldi D, Rochette P, Bautista A, Vos J de. 2018. Earliest known hominin activity in the Philippines by 709 thousand years ago. *Nature* 557:233–237. DOI: 10.1038/s41586-018-0072-8.

Jame C, Tissier J, Maridet O, Becker D. 2019. Early Agenian rhinocerotids from Wischberg (Canton Bern, Switzerland) and clarification of the systematics of the genus *Diaceratherium*. *PeerJ* 7:e7517. DOI: 10.7717/peerj.7517.

Janis CM, Shoshitaishvili B, Kambic R, Figueirido B. 2012. On their knees: distal femur asymmetry in ungulates and its relationship to body size and locomotion. *Journal of Vertebrate Paleontology* 32:433–445. DOI: 10.1080/02724634.2012.635737.

Jenkins FA. 1973. The functional anatomy and evolution of the mammalian humero-ulnar articulation. *American Journal of Anatomy* 137:281–297. DOI: 10.1002/aja.1001370304.

Kappelman J. 1988. Morphology and locomotor adaptations of the bovid femur in relation to habitat. *Journal of Morphology* 198:119–130. DOI: 10.1002/jmor.1051980111.

Kelly EM, Sears KE. 2011. Reduced phenotypic covariation in marsupial limbs and the implications for mammalian evolution. *Biological Journal of the Linnean Society* 102:22–36. DOI: 10.1111/j.1095-8312.2010.01561.x.

Kennard AS. 1944. The Crayford Brickearths. *Proceedings of the Geologists' Association* 55:121-IN1. DOI: 10.1016/S0016-7878(44)80014-1.

Kingsolver JG, Pfennig DW. 2004. Individual-Level Selection as a Cause of Cope's Rule of Phyletic Size Increase. *Evolution* 58:1608–1612. DOI: 10.1111/j.0014-3820.2004.tb01740.x.

Klingenberg CP. 2008. Morphological Integration and Developmental Modularity. *Annual Review of Ecology, Evolution, and Systematics* 39:115–132. DOI: 10.1146/annurev.ecolsys.37.091305.110054.

Klingenberg CP. 2014. Studying morphological integration and modularity at multiple levels: concepts and analysis. *Philosophical Transactions of the Royal Society B: Biological Sciences* 369:20130249. DOI: 10.1098/rstb.2013.0249.

Klingenberg CP. 2016. Size, shape, and form: concepts of allometry in geometric morphometrics. *Development Genes and Evolution* 226:113–137. DOI: 10.1007/s00427-016-0539-2.

Klingenberg CP, Marugán-Lobón J. 2013. Evolutionary Covariation in Geometric Morphometric Data: Analyzing Integration, Modularity, and Allometry in a Phylogenetic Context. *Systematic Biology* 62:591–610. DOI: 10.1093/sysbio/syt025.

Kosintsev P, Mitchell KJ, Devièse T, Plicht J van der, Kuitems M, Petrova E, Tikhonov A, Higham T, Comeskey D, Turney C, Cooper A, Kolfschoten T van, Stuart AJ, Lister AM. 2018. Evolution and extinction of the giant rhinoceros *Elasmotherium sibiricum* sheds light on late Quaternary megafaunal extinctions. *Nature Ecology & Evolution*:1–8. DOI: 10.1038/s41559-018-0722-0.

Lahr MM, Wright RVS. 1996. The question of robusticity and the relationship between cranial size and shape inHomo sapiens. *Journal of Human Evolution* 31:157–191. DOI: 10.1006/jhev.1996.0056.

Lambert KL. 1971. The weight-bearing function of the fibula. A strain gauge study. *The Journal of Bone and Joint Surgery. American Volume* 53:507–513.

Langman VA, Roberts TJ, Black J, Maloiy GM, Heglund NC, Weber JM, Kram R, Taylor CR. 1995. Moving cheaply: energetics of walking in the African elephant. *Journal of Experimental Biology* 198:629–632.

Lanyon LE. 1992. Control of bone architecture by functional load bearing. *Journal of Bone and Mineral Research* 7:S369–S375. DOI: 10.1002/jbmr.5650071403.

Lanyon LE, Goodship AE, Pye CJ, MacFie JH. 1982. Mechanically adaptive bone remodelling. *Journal of Biomechanics* 15:141–154. DOI: 10.1016/0021-9290(82)90246-9.

Lanyon LE, Magee PT, Baggott DG. 1979. The relationship of functional stress and strain to the processes of bone remodelling. An experimental study on the sheep radius. *Journal of Biomechanics* 12:593–600. DOI: 10.1016/0021-9290(79)90079-4.

Larramendi A. 2016. Shoulder height, body mass and shape of proboscideans. *Acta Palaeontologica Polonica* 61:537–574.

Laurie WA, Lang EM, Groves CP. 1983. *Rhinoceros unicornis*. *Mammalian Species*:1–6. DOI: 10.2307/3504002.

Laurin M. 2004. The Evolution of Body Size, Cope's Rule and the Origin of Amniotes. *Systematic Biology* 53:594–622. DOI: 10.1080/10635150490445706.

Lawler RR. 2008. Morphological integration and natural selection in the postcranium of wild verreaux's sifaka (*Propithecus verreauxi verreauxi*). *American Journal of Physical Anthropology* 136:204–213. DOI: 10.1002/ajpa.20795.

Legendre S. 1989. Les communantés de mammifères du Paléogène (Eocène supérior et Oligocène) d'Europe Occidentale: structures, milieux et évolution. *Münchner Geowissenschaftliche Abhandlungen* Reihe A:1–110.

Lessertisseur J, Saban R. 1967. Le squelette. Squelette appendiculaire. In: *Traité de Zoologie. Tome XVI, Fascicule 1: Mammifères.* Paris: Grassé Pierre-Paul, 298–1123.

Lord E, Pathmanathan JS, Corel E, Makarenkov V, Lopez P, Bouchard F, Bhattacharya D, Antoine P-O, Le Guyader H, Lapointe F-J, Bapteste E. 2019. Introducing Trait Networks to Elucidate the Fluidity of Organismal Evolution Using Palaeontological Data. *Genome Biology and Evolution* 11:2653–2665. DOI: 10.1093/gbe/evz182.

Lu X. 2013. A juvenile skull of *Acerorhinus yuanmouensis* (Mammalia: Rhinocerotidae) from the Late Miocene hominoid fauna of the Yuanmou Basin (Yunnan, China). *Geobios* 46:539–548. DOI: 10.1016/j.geobios.2013.10.001.

Lucas SG, Emry RJ, Bayshashov BU. 1996. *Zaisanamynodon*, a Late Eocene amynodontid (Mammalia, Perissodactyla) from Kazakhstan and China. *Tertiary Research* 17:51–58.

MacFadden BJ. 1998. Tale of two Rhinos: Isotopic Ecology, Paleodiet, and Niche Differentiation of *Aphelops* and *Teloceras* from the Florida Neogene. *Paleobiology* 24:274–286.

MacFadden BJ. 2005. Diet and habitat of toxodont megaherbivores (Mammalia, Notoungulata) from the late Quaternary of South and Central America. *Quaternary Research* 64:113–124. DOI: 10.1016/j.yqres.2005.05.003.

MacLaren JA, Hulbert Jr RC, Wallace SC, Nauwelaerts S. 2018. A morphometric analysis of the forelimb in the genus *Tapirus* (Perissodactyla: Tapiridae) reveals influences of habitat, phylogeny and size through time and across geographical space. *Zoological Journal of the Linnean Society* 20:1–17.

MacLaren JA, Nauwelaerts S. 2016. A three-dimensional morphometric analysis of upper forelimb morphology in the enigmatic tapir (Perissodactyla: *Tapirus*) hints at subtle variations in locomotor ecology. *Journal of Morphology* 277:1469–1485. DOI: 10.1002/jmor.20588.

MacLaren JA, Nauwelaerts S. 2017. Interspecific variation in the tetradactyl manus of modern tapirs (Perissodactyla: *Tapirus*) exposed using geometric morphometrics. *Journal of Morphology* 278:1517–1535. DOI: 10.1002/jmor.20728.

Maddison WP, FitzJohn RG. 2015. The Unsolved Challenge to Phylogenetic Correlation Tests for Categorical Characters. *Systematic Biology* 64:127–136. DOI: 10.1093/sysbio/syu070.

Mallet C, Billet G, Houssaye A, Cornette R. 2020. A first glimpse at the influence of body mass in the morphological integration of the limb long bones: an investigation in modern rhinoceroses. *Journal of Anatomy* 237:704–726. DOI: 10.1111/joa.13232.

Mallet C, Cornette R, Billet G, Houssaye A. 2019. Interspecific variation in the limb long bones among modern rhinoceroses—extent and drivers. *PeerJ* 7:e7647. DOI: 10.7717/peerj.7647.

Mallison H, Wings O. 2014. Photogrammetry in Paleontology - A practical guide. *Journal of Paleontological Techniques*:1–31.

Marsh OC. 1884. *Dinocerata: A Monograph of an Extinct Order of Gigantic Mammals*. U.S. Government Printing Office.

Martins EP, Hansen TF. 1997. Phylogenies and the Comparative Method: A General Approach to Incorporating Phylogenetic Information into the Analysis of Interspecific Data. *The American Naturalist* 149:646–667. DOI: 10.1086/286013.

Martín-Serra A, Benson RBJ. 2019. Developmental constraints do not influence long-term phenotypic evolution of marsupial forelimbs as revealed by interspecific disparity and integration patterns. *The American Naturalist*. DOI: 10.1086/707194.

Martín-Serra A, Figueirido B, Palmqvist P. 2014. A Three-Dimensional Analysis of Morphological Evolution and Locomotor Performance of the Carnivoran Forelimb. *PLOS ONE* 9:e85574. DOI: 10.1371/journal.pone.0085574.

Martín-Serra A, Figueirido B, Pérez-Claros JA, Palmqvist P. 2015. Patterns of morphological integration in the appendicular skeleton of mammalian carnivores. *Evolution* 69:321–340. DOI: 10.1111/evo.12566.

Maynard Smith J, Savage RJG. 1956. Some locomotory adaptations in Mammals. *Zoological Journal of the Linnean Society* 42:603–622. DOI: 10.1111/j.1096-3642.1956.tb02220.x.

Mays HL, Hung C-M, Shaner P-J, Denvir J, Justice M, Yang S-F, Roth TL, Oehler DA, Fan J, Rekulapally S, Primerano DA. 2018. Genomic Analysis of Demographic History and Ecological Niche Modeling in the Endangered Sumatran Rhinoceros *Dicerorhinus sumatrensis*. *Current biology: CB* 28:70-76.e4. DOI: 10.1016/j.cub.2017.11.021.

McGhee RB, Frank AA. 1968. On the stability properties of quadruped creeping gaits. *Mathematical Biosciences* 3:331–351. DOI: 10.1016/0025-5564(68)90090-4.

McHorse BK, Biewener AA, Pierce SE. 2019. The Evolution of a Single Toe in Horses: Causes, Consequences, and the Way Forward. *Integrative and Comparative Biology* 59:638–655. DOI: 10.1093/icb/icz050.

McKinney ML. 1986. Ecological Causation of Heterochrony: A Test and Implications for Evolutionary Theory. *Paleobiology* 12:282–289.

McKinney ML, McNamara KJ. 1991. Heterochrony. In: McKinney ML, McNamara KJ eds. *Heterochrony: The Evolution of Ontogeny*. Boston, MA: Springer US, 1–12. DOI: 10.1007/978-1-4757-0773-1_1.

McNamara KJ. 2012. Heterochrony: the Evolution of Development. *Evolution: Education and Outreach* 5:203–218. DOI: 10.1007/s12052-012-0420-3.

McShea DW. 1994. Mechanisms of Large-Scale Evolutionary Trends. *Evolution* 48:1747–1763. DOI: 10.1111/j.1558-5646.1994.tb02211.x.

Mead AJ. 1999. Aspects of the systematics and paleoecologies of the middle to late Miocene North American rhinoceroses *Peraceras*, *Teleoceras*, and *Aphelops*. *ETD collection for University of Nebraska - Lincoln*:1–308.

Mead AJ. 2000. Sexual dimorphism and paleoecology in *Teleoceras*, a North American Miocene rhinoceros. *Paleobiology* 26:689–706. DOI: 10.1666/0094-8373(2000)026<0689:SDAPIT>2.0.CO;2.

Mead AJ, Wall WP. 1998. Dietary implications of jaw biomechanics in the rhinocerotoids *Hyracodon* and *Subhyracodon* from Badlands National Park, South Dakota. *National Park Service Paleontological Research* 3:23–28.

Mendoza M, Janis CM, Palmqvist P. 2006. Estimating the body mass of extinct ungulates: a study on the use of multiple regression. *Journal of Zoology* 270:90–101. DOI: 10.1111/j.1469-7998.2006.00094.x.

Ménouret B, Guérin C. 2009. *Diaceratherium massiliae* nov. sp. des argiles oligocènes de Saint-André et Saint-Henri à Marseille et de Les Milles près d'Aix-en-Provence (SE de la France), premier grand Rhinocerotidae brachypode européen. *Geobios* 42:293–327. DOI: 10.1016/j.geobios.2008.10.009.

Métais G, Sen S. 2018. The late Miocene mammals from the Konservat-Lagerstätte of Saint-Bauzile (Ardèche, France). *Comptes Rendus Palevol*. DOI: 10.1016/j.crpv.2018.05.001.

Mihlbachler MC. 2003. Demography of Late Miocene Rhinoceroses (*Teleoceras proterum* and *Aphelops malacorhinus*) from Florida: Linking Mortality and Sociality in Fossil Assemblages. *Paleobiology* 29:412–428.

Mihlbachler MC. 2005. Linking Sexual Dimorphism and Sociality in Rhinoceroses: Insights from *Teleoceras proterum* and *Aphelops malacorhinus* from the Late Miocene of Florida. *Bull. Fla. Mus. Nat. Hist* 45:495–520.

Mihlbachler MC. 2007. Sexual Dimorphism and Mortality Bias in a Small Miocene North American Rhino, *Menoceras arikarense*: Insights into the Coevolution of Sexual Dimorphism and Sociality in Rhinos. *Journal of Mammalian Evolution* 14:217–238. DOI: 10.1007/s10914-007-9048-4.

Mihlbachler MC, Lau T, Kapner D, Shockey BJ. 2014. Coevolution of the shoulder and knee in Ungulates: Implications of the evolution of locomotion and standing.

Milne N. 2016. Curved bones: An adaptation to habitual loading. *Journal of Theoretical Biology* 407:18–24. DOI: 10.1016/j.jtbi.2016.07.019.

Mitteroecker P, Gunz P, Windhager S, Schaefer K. 2013. A brief review of shape, form, and allometry in geometric morphometrics, with applications to human facial morphology. *Hystrix, the Italian Journal of Mammalogy* 24:59–66. DOI: 10.4404/hystrix-24.1-6369.

Montoya-Sanhueza G, Wilson LAB, Chinsamy A. 2019. Postnatal development of the largest subterranean mammal (*Bathyergus suillus*): Morphology, osteogenesis, and modularity of the appendicular skeleton. *Developmental Dynamics* 248:1101–1128. DOI: 10.1002/dvdy.81.

Morales JC, Melnick DJ. 1994. Molecular Systematics of the Living Rhinoceros. *Molecular Phylogenetics and Evolution* 3:128–134. DOI: 10.1006/mpev.1994.1015.

Olson EC, Miller RL. 1958. *Morphological Integration*. University of Chicago Press.

Orlando L, Leonard JA, Thenot A, Laudet V, Guerin C, Hänni C. 2003. Ancient DNA analysis reveals woolly rhino evolutionary relationships. *Molecular Phylogenetics and Evolution* 28:485–499. DOI: 10.1016/S1055-7903(03)00023-X.

Osborn HF. 1898. The extinct rhinoceroses. *Memoirs of the American Museum of Natural History* 1:75–164.

Osborn HF. 1900. The Angulation of the Limbs of Proboscidia, Dinocerata, and Other Quadrupeds, in Adaptation to Weight. *The American Naturalist* 34:89–94. DOI: 10.1086/277565.

Osborn HF. 1902. Dolichocephaly and brachycephaly in the lower mammals. *Bulletin of the American Museum of Natural History* 16:77–89.

Osborn HF. 1919. Seventeen skeletons of *Moropus*; probable habits of this animal. *Proceedings of the National Academy of Sciences* 5:250–252.

Osborn HF. 1929. *The Titanotheres of ancient Wyoming, Dakota, and Nebraska*. Government Printing Office.

Osborn HF, Wood HE. 1936. *Amynodon mongoliensis* from the Upper Eocene of Mongolia. *American Museum Novitates* 859:1–9.

Owen R. 1848. *On the Archetype and Homologies of the Vertebrate Skeleton*. London: John Van Voorst.

Oxnard CE. 1993. Bone and bones, architecture and stress, fossils and osteoporosis. *Journal of Biomechanics* 26:63–79. DOI: 10.1016/0021-9290(93)90080-X.

Panagiotopoulou O, Pataky TC, Hutchinson JR. 2019. Foot pressure distribution in White Rhinoceroses (*Ceratotherium simum*) during walking. *PeerJ* 7:e6881. DOI: 10.7717/peerj.6881.

Pandolfi L. 2016. *Persiatherium rodleri*, gen. et sp. nov. (Mammalia, Rhinocerotidae) from the upper Miocene of Maragheh (northwestern iran). *Journal of Vertebrate Paleontology* 36:e1040118. DOI: 10.1080/02724634.2015.1040118.

Pandolfi L, Boscato P, Crezzini J, Gatta M, Moroni A, Rolfo M, Tagliacozzo A. 2017a. Late Pleistocene last occurences of the narrow-nosed rhinoceros *Stephanorhinus hemitoechus* (Mammalia, Perissodactyla) in Italy. *Rivista Italiana di Paleontologia e Stratigrafia (Research In Paleontology and Stratigraphy)* 123. DOI: 10.13130/2039-4942/8300.

Pandolfi L, Cerdeño E, Codrea V, Kotsakis T. 2017b. Biogeography and chronology of the Eurasian extinct rhinoceros *Stephanorhinus etruscus* (Mammalia, Rhinocerotidae). *Comptes Rendus Palevol* 16:762–773. DOI: 10.1016/j.crpv.2017.06.004.

Pandolfi L, Codrea VA, Popescu A. 2019. *Stephanorhinus jeanvireti* (Mammalia, Rhinocerotidae) from the early Pleistocene of Colțești (southwestern Romania). *Comptes Rendus Palevol*. DOI: 10.1016/j.crpv.2019.07.004.

Pandolfi L, Fiore I, Gaeta M, Szabó P, Vennemann T, Tagliacozzo A. 2018. Rhinocerotidae (Mammalia, Perissodactyla) from the middle Pleistocene levels of Grotta Romanelli (Lecce, southern Italy). *Geobios* 51:453–468. DOI: 10.1016/j.geobios.2018.08.008.

Pandolfi L, Gasparik M, Piras P. 2015. Earliest occurrence of "*Dihoplus*" *megarhinus* (Mammalia, Rhinocerotidae) in Europe (Late Miocene, Pannonian Basin, Hungary): Palaeobiogeographical and biochronological implications. *Annales de Paléontologie* 101:325–339. DOI: 10.1016/j.annpal.2015.09.001.

Pandolfi L, Tagliacozzo A. 2015. *Stephanorhinus hemitoechus* (Mammalia, Rhinocerotidae) from the Late Pleistocene of Valle Radice (Sora, Central Italy) and re-evaluation of the morphometric variability of the species in Europe. *Geobios* 48:169–191. DOI: 10.1016/j.geobios.2015.02.002.

Pandy MG, Kumar V, Berme N, Waldron KJ. 1988. The Dynamics of Quadrupedal Locomotion. *Journal of Biomechanical Engineering* 110:230–237. DOI: 10.1115/1.3108436.

Paradis E, Blomberg SP, Bolker B, Brown J, Claude J, Cuong HS, Desper R, Didier G, Durand B, Dutheil J, Ewing J, Gascuel O, Guillerme T, Heibl C, Ives A, Jones B, Krah F, Lawson D, Lefort V, Legendre P, Lemon J, Marcon E, McCloskey R, Nylander J, Opgen-Rhein R, Popescu A-A, Royer-Carenzi M, Schliep K, Strimmer K, de Vienne D. 2018. *Ape: Analyses of Phylogenetics and Evolution*.

Paul GS. 1997. Dinosaur models: the Good, the Bad, and using them to estimate the mass of dinosaurs. In: *Dinofest International: Proceedings of a Symposium held at Arizona State University*. The Academy of Natural Sciences, Philadelphia, PA, USA: D.L.Wolberg, E.Stump & G.Rosenberg, 129–154.

Paul GS, Christiansen P. 2000. Forelimb posture in neoceratopsian dinosaurs: implications for gait and locomotion. *Paleobiology* 26:450–465. DOI: 10.1666/0094-8373(2000)026<0450:FPINDI>2.0.CO;2.

Pavlow M. 1913. Mammifères Tertiaires de la Nouvelle Russie, avec un article géologique du Prof. A.P. Pavlow – 2-e partie: *Aceratherium incisivum* Kaup, *Hipparion*, Proboscidea, Carnivora. *Nouveaux Mémoires de la Société Impériale des Naturalistes de Moscou* XVII:1–81.

Pernègre V, Tassy P. 2014. Albert Gaudry et les vertébrés fossiles du Luberon. Histoire d'une collection de référence. *Geodiversitas* 36:623–667. DOI: 10.5252/g2014n4a5.

Petti FM, Avanzini M, Belvedere M, De Gasperi M, Ferretti P, Girardi S, Remondino F, Tomasoni R. 2008. Digital 3D modelling of dinosaur footprints by photogrammetry and laser scanning techniques: integrated approach at the Coste dell'Anglone tracksite (Lower Jurassic, Southern Alps, Northern Italy). *Studi Trentini di Scienze Naturali - Acta Geologia* 83:303–315.

Pfistermüller R, Walzer C, Licka T. 2011. From Chitwan to Vienna – How do gait parameters change in a pair of Indian Rhinos (*Rhinoceros unicornis*) coming from semi-wild conditions to a European Zoo? In: *Proceedings of the 2011 International Elephant and Rhino Conservation and Research Symposium*. Rotterdam,.

Piras P, Maiorino L, Raia P, Marcolini F, Salvi D, Vignoli L, Kotsakis T. 2010. Functional and phylogenetic constraints in Rhinocerotinae craniodental morphology. *Evolutionary Ecology Research* 12:897–928.

Polly PD. 1998. Cope's Rule. *Science* 282:47–47. DOI: 10.1126/science.282.5386.47f.

Polly PD. 2007. Limbs in mammalian evolution. Chapter 15. In: *Fins into Limbs: Evolution, Development, and Transformation*. Chicago: Brian K. Hall, 245–268.

Price SA, Bininda-Emonds ORP. 2009. A comprehensive phylogeny of extant horses, rhinos and tapirs (Perissodactyla) through data combination. *Zoosystematics and Evolution* 85:277–292. DOI: 10.1002/zoos.200900005.

Prothero DR. 1998a. Hyracodontidae. In: *Evolution of Tertiary Mammals of North America: Volume 1, Terrestrial Carnivores, Ungulates, and Ungulate Like Mammals*. Cambridge University Press, 589–593.

Prothero DR. 1998b. Rhinocerotidae. In: *Evolution of Tertiary Mammals of North America: Volume 1, Terrestrial Carnivores, Ungulates, and Ungulate Like Mammals*. Cambridge: Christine M. Janis, Kathleen M. Scott, Louis L. Jacobs, 595–605.

Prothero DR. 2005. *The Evolution of North American Rhinoceroses*. Cambridge.

Prothero DR. 2013. *Rhinoceros Giants: The Paleobiology of Indricotheres*. Bloomington and Indianapolis.

Prothero DR, Manning EM. 1987. Miocene rhinoceroses from the Texas Gulf Coastal Plain. *Journal of Paleontology* 61:388–423. DOI: 10.1017/S0022336000028559.

Prothero DR, Manning EM, Hanson BC. 1986. The phylogeny of the Rhinocerotoidea (Mammalia, Perissodactyla). *Zoological Journal of the Linnean Society* 87:341–366.

Prothero DR, Schoch RM. 1989. *The evolution of perissodactyls*. New York: Oxford University Press.

Prothero DR, Sereno PC. 1982. Allometry and Paleoecology of Medial Miocene Dwarf Rhinoceroses from the Texas Gulf Coastal Plain. *Paleobiology* 8:16–30.

Qiu Z-X, Wang B-Y. 1999. *Allacerops* (Rhinoceroroidea, Perissodactyla), its discovery in China and its systematic position. *Vertebrata PalAsiatica* 37:48–61.

Qiu Z-X, Wang B-Y. 2007. Paracerathere Fossils of China. *Palaeontologia Sinica, newseries C* 29:1–396.

R Core Team. 2014. *R: a language and environment for statistical computing*. Vienna: R Foundation for Statistical Computing.

Radinsky LB. 1965. Evolution of the tapiroid skeleton from *Heptodon* to *Tapirus*. *Bulletin of the Museum of Comparative Zoology* 134:69–106.

Radinsky LB. 1966. The families of the Rhinocerotoidea (Mammalia, Perissodactyla). *Journal of Mammalogy* 47:631–639.

Radinsky LB. 1967a. *Hyrachyus*, *Chasmotherium*, and the early evolution of helaletid tapiroids. American Museum novitates ; no. 2313.

Radinsky LB. 1967b. A review of the Rhinocerotoid family Hyracodontidae (Perissodactyla). Bulletin of the AMNH ; v. 136, article 1.

Raia P, Carotenuto F, Passaro F, Fulgione D, Fortelius M. 2012. Ecological Specialization in Fossil Mammals Explains Cope's Rule. *The American Naturalist* 179:328–337. DOI: 10.1086/664081.

Randau M, Goswami A. 2018. Shape Covariation (or the Lack Thereof) Between Vertebrae and Other Skeletal Traits in Felids: The Whole is Not Always Greater than the Sum of Parts. *Evolutionary Biology* 45:1–15. DOI: 10.1007/s11692-017-9443-6.

Regnault S, Hermes R, Hildebrandt T, Hutchinson J, Weller R. 2013. Osteopathology in the feet of rhinoceroses: lesion type and distribution. *Journal of Zoo and Wildlife Medicine* 44:918–927. DOI: 10.1638/2012-0277R1.1.

Remondino F, Rizzi A, Girardi S, Petti FM, Avanzini M. 2010. 3D Ichnology—recovering digital 3D models of dinosaur footprints. *The Photogrammetric Record* 25:266–282. DOI: 10.1111/j.1477-9730.2010.00587.x.

Ren L, Miller CE, Lair R, Hutchinson JR. 2010. Integration of biomechanical compliance, leverage, and power in elephant limbs. *Proceedings of the National Academy of Sciences* 107:7078–7082. DOI: 10.1073/pnas.0911396107.

Revell LJ. 2012. phytools: an R package for phylogenetic comparative biology (and other things). *Methods in Ecology and Evolution* 3:217–223. DOI: 10.1111/j.2041-210X.2011.00169.x.

Richardson MK, Gobes SMH, Leeuwen AC van, Polman JAE, Pieau C, Sánchez-Villagra MR. 2009. Heterochrony in limb evolution: developmental mechanisms and natural selection. *Journal of Experimental Zoology Part B: Molecular and Developmental Evolution* 312B:639–664. DOI: 10.1002/jez.b.21250.

Robinet C, Remy JA, Laurent Y, Danilo L, Lihoreau F. 2015. A new genus of Lophiodontidae (Perissodactyla, Mammalia) from the early Eocene of La Borie (Southern France) and the origin of the genus *Lophiodon* Cuvier, 1822. *Geobios* 48:25–38. DOI: 10.1016/j.geobios.2014.11.003.

Robinson P. 1966. Fossil Mammalia of the Huerfano Formation, Eocene, of Colorado. *Bulletin of the Peabody Museum of Natural History, Yale Unversity* 21:1–113.

Robling AG, Castillo AB, Turner CH. 2006. Biomechanical and Molecular Regulation of Bone Remodeling. *Annual Review of Biomedical Engineering* 8:455–498. DOI: 10.1146/annurev.bioeng.8.061505.095721.

Rohlf FJ. 2001. Comparative Methods for the Analysis of Continuous Variables: Geometric Interpretations. *Evolution* 55:2143–2160. DOI: 10.1111/j.0014-3820.2001.tb00731.x.

Rohlf FJ, Corti M. 2000. Use of Two-Block Partial Least-Squares to Study Covariation in Shape. *Systematic Biology* 49:740–753. DOI: 10.1080/106351500750049806.

Rohlf FJ, Slice D. 1990. Extensions of the Procrustes Method for the Optimal Superimposition of Landmarks. *Systematic Biology* 39:40–59. DOI: 10.2307/2992207.

Roman F. 1924. Contribution à l'étude de la faune de Mammifères des Littorinenkalk (Oligocène supérieur) du bassin de Mayence. Les Rhinocéros. *Travaux et Documents des Laboratoires de Géologie de Lyon* 7:1–63.

Rookmaaker K, Antoine P-O. 2012. New maps representing the historical and recent distribution of the African species of rhinoceros: *Diceros bicornis*, *Ceratotherium simum* and *Ceratotherium cottoni*. *Pachyderm* 0:91–96.

Ross MD. 1984. The influence of gravity on structure and function of animals. *Advances in Space Research* 4:305–314. DOI: 10.1016/0273-1177(84)90575-1.

Saarinen JJ, Eronen J, Fortelius M, Seppä H, Lister AM. 2016. Patterns of diet and body mass of large ungulates from the Pleistocene of Western Europe, and their relation to vegetation. *Palaeontologia Electronica* 19:1–58.

Sanborn CC, Watkins AR. 1950. Notes on the Malay Tapir and Other Game Animals in Siam. *Journal of Mammalogy* 31:430–433. DOI: 10.2307/1375112.

Scherler L, Mennecart B, Hiard F, Becker D. 2013. Evolutionary history of hoofed mammals during the Oligocene–Miocene transition in Western Europe. *Swiss Journal of Geosciences* 106:349–369. DOI: 10.1007/s00015-013-0140-x.

Schlager S. 2017. Chapter 9 - Morpho and Rvcg – Shape Analysis in R: R-Packages for Geometric Morphometrics, Shape Analysis and Surface Manipulations. In: Zheng G, Li S, Székely G eds. *Statistical Shape and Deformation Analysis*. Academic Press, 217–256. DOI: 10.1016/B978-0-12-810493-4.00011-0.

Schlager S. 2018. *Morpho: calculations and vizualisations related to Geometric Morphometrics*.

Schliep KP. 2011. phangorn: phylogenetic analysis in R. *Bioinformatics* 27:592–593. DOI: 10.1093/bioinformatics/btq706.

Schmidt M, Fischer MS. 2009. Morphological Integration in Mammalian Limb Proportions: Dissociation Between Function and Development. *Evolution* 63:749–766. DOI: 10.1111/j.1558-5646.2008.00583.x.

Schmidt-Nielsen K. 1984. *Scaling: Why is Animal Size So Important?* Cambridge: Cambridge University Press.

Scott KM. 1990. Postcranial dimensions of ungulates as predictors of body mass. In: *Body Size in Mammalian Palaeobiology: Estimation and Biological Implications*. Cambridge University Press, 301–335.

Scott K. 2007. The ecology of the late middle Pleistocene mammoths in Britain. *Quaternary International* 169–170:125–136. DOI: 10.1016/j.quaint.2006.10.009.

Scott WB, Jepsen GL. 1941. The Mammalian Fauna of the White River Oligocene. Part V. Perissodactyla. *Transactions of the American Philosophical Society, New Series* 28:747–975.

Sears KE, Behringer RR, Rasweiler IV JJ, Niswander LA. 2007. The Evolutionary and Developmental Basis of Parallel Reduction in Mammalian Zeugopod Elements. *The American Naturalist* 169:105–117. DOI: 10.1086/510259.

Sears KE, Capellini TD, Diogo R. 2015. On the serial homology of the pectoral and pelvic girdles of tetrapods. *Evolution* 69:2543–2555. DOI: 10.1111/evo.12773.

Seilacher A. 1970. Arbeitskonzept Zur Konstruktions-Morphologie. *Lethaia* 3:393–396. DOI: 10.1111/j.1502-3931.1970.tb00830.x.

Seilacher A. 1991. Self-Organizing Mechanisms in Morphogenesis and Evolution. In: Schmidt-Kittler N, Vogel K eds. *Constructional Morphology and Evolution*. Berlin, Heidelberg: Springer, 251–271. DOI: 10.1007/978-3-642-76156-0_17.

Serio C, Raia P, Meloro C. 2020. Locomotory Adaptations in 3D Humerus Geometry of Xenarthra: Testing for Convergence. *Frontiers in Ecology and Evolution* 8. DOI: 10.3389/fevo.2020.00139.

Shockey BJ. 2001. Specialized knee joints in some extinct, endemic, South American herbivores. *Acta Palaeontologica Polonica* 46:277–288.

Sinclair WJ. 1922. Hyracodons from the Big Badlands of South Dakota. *Proceedings of the American Philosophical Society* 61:65–79.

Stanley SM. 1973. An Explanation for Cope's Rule. *Evolution* 27:1–26. DOI: 10.2307/2407115.

Stein BR, Casinos A. 1997. What is a cursorial mammal? *Journal of Zoology* 242:185–192. DOI: 10.1111/j.1469-7998.1997.tb02939.x.

Steiner CC, Ryder OA. 2011. Molecular phylogeny and evolution of the Perissodactyla. *Zoological Journal of the Linnean Society* 163:1289–1303. DOI: 10.1111/j.1096-3642.2011.00752.x.

Stilson KT, Hopkins SSB, Davis EB. 2016. Osteopathology in Rhinocerotidae from 50 Million Years to the Present. *PLOS ONE* 11:e0146221. DOI: 10.1371/journal.pone.0146221.

Streiner DL, Norman GR. 2011. Correction for Multiple Testing: Is There a Resolution? *Chest* 140:16–18. DOI: 10.1378/chest.11-0523.

Stuart AJ. 1991. Mammalian Extinctions in the Late Pleistocene of Northern Eurasia and North America. *Biological Reviews* 66:453–562. DOI: 10.1111/j.1469-185X.1991.tb01149.x.

Swenson N. 2014. *Functional and Phylogenetic Ecology in R*. New York: Springer-Verlag. DOI: 10.1007/978-1-4614-9542-0.

Takebe K, Nakagawa A, Minami H, Kanazawa H, Hirohata K. 1984. Role of the Fibula in Weight-bearing. *Clinical Orthopaedics and Related Research®* 184:289.

Talbot LM, McCulloch JSG. 1965. Weight Estimations for East African Mammals from Body Measurements. *The Journal of Wildlife Management* 29:84–89. DOI: 10.2307/3798635.

Thermo Fisher Scientific. 2018. *Avizo*.

Thompson DW. 1917. *On growth and form.*

Tissier J, Antoine P-O, Becker D. 2020. New material of *Epiaceratherium* and a new species of *Mesaceratherium* clear up the phylogeny of early Rhinocerotidae (Perissodactyla). *Royal Society Open Science* 7:200633. DOI: 10.1098/rsos.200633.

Tissier J, Becker D. 2018. Nouvelle occurrence du genre *Mesaceratherium* (Rhinocerotidae) dans l'Oligocène supérieur du Bassin molassique suisse. In: *Actes de la Société jurassienne d'Émulation*. Porrentruy: Société jurassienne d'Émulation, 57–74.

Tissier J, Becker D, Codrea V, Costeur L, Fărcaş C, Solomon A, Venczel M, Maridet O. 2018. New data on Amynodontidae (Mammalia, Perissodactyla) from Eastern Europe: Phylogenetic and palaeobiogeographic implications around the Eocene-Oligocene transition. *PLOS ONE* 13:e0193774. DOI: 10.1371/journal.pone.0193774.

Tong H, Wang F, Zheng M, Chen X. 2014. New Fossils of *Stephanorhinus kirchbergensis* and *Elasmotherium peii* from the Nihewan Basin. *Acta Anthropologica Sinica* 33:369–388.

Tougard C, Delefosse T, Hänni C, Montgelard C. 2001. Phylogenetic Relationships of the Five Extant Rhinoceros Species (Rhinocerotidae, Perissodactyla) Based on Mitochondrial Cytochrome b and 12S rRNA Genes. *Molecular Phylogenetics and Evolution* 19:34–44. DOI: 10.1006/mpev.2000.0903.

Tsubamoto T. 2014. Estimating Body Mass from the Astragalus in Mammals. *Acta Palaeontologica Polonica* 59:259–265. DOI: 10.4202/app.2011.0067.

Turner CH. 1998. Three rules for bone adaptation to mechanical stimuli. *Bone* 23:399–407. DOI: 10.1016/S8756-3282(98)00118-5.

Uyeda JC, Zenil-Ferguson R, Pennell MW. 2018. Rethinking phylogenetic comparative methods. *Systematic Biology* 67:1091–1109. DOI: 10.1093/sysbio/syy031.

Valli AMF. 2005. Taphonomy of the late Miocene mammal locality of Akkasdagı, Turkey. *Geodiversitas* 27:793–808.

Van Valen L. 1965. The Study of Morphological Integration. *Evolution* 19:347–349. DOI: 10.1111/j.1558-5646.1965.tb01725.x.

Wagner GP, Pavlicev M, Cheverud JM. 2007. The road to modularity. *Nature Reviews Genetics* 8:921–931. DOI: 10.1038/nrg2267.

Walker-Larsen J, Harder LD. 2001. Vestigial Organs as Opportunities for Functional Innovation: The Example of the Penstemon Staminode. *Evolution* 55:477–487. DOI: 10.1111/j.0014-3820.2001.tb00782.x.

Wall WP. 1982. The Genus *Amynodon* and Its Relationship to Other Members of the Amynodontidae (Perissodactyla, Rhinocerotoidea). *Journal of Paleontology* 56:434–443.

Wall WP. 1983. The Correlation between High Limb-Bone Density and Aquatic Habits in Recent Mammals. *Journal of Paleontology* 57:197–207.

Wall WP. 1998. Amynodontidae. In: *Evolution of Tertiary mammals of North America*. New York: Cambridge University Press, 583–588.

Wall WP, Heinbaugh KL. 1999. Locomotor adaptations in *Metamynodon planifrons* compared to other Amynodontids (Perissodactyla, Rhinocerotoidea). *National Parks Paleontological Research* 4:8–17.

Wall WP, Hickerson W. 1995. A biomechanical analysis of locomotion in the Oligocene rhinocerotoid, *Hyracodon*. *National Park Service Paleontological Research*:25–35.

Wang H-B, Bai B, Gao F, Huang W-C, Wang Y-Q. 2013. New eggysodontid (Mammalia, Perissodactyla) material from the Paleogene of the Guangnan Basin, Yunnan Province, China. *Vertebrata PalAsiatica* 51:305–320.

Wang H, Bai B, Meng J, Wang Y. 2016. Earliest known unequivocal rhinocerotoid sheds new light on the origin of Giant Rhinos and phylogeny of early rhinocerotoids. *Scientific Reports* 6. DOI: 10.1038/srep39607.

Wang H-B, Bai B, Meng J, Wang Y-Q. 2018. A New Species of *Forstercooperia* (Perissodactyla: Paraceratheriidae) from Northern China with a Systematic Revision of Forstercooperiines. *American Museum Novitates* 2018:1–41. DOI: 10.1206/3897.1.

Wang B, Secord R. 2020. Paleoecology of *Aphelops* and *Teleoceras* (Rhinocerotidae) through an interval of changing climate and vegetation in the Neogene of the Great Plains, central United States. *Palaeogeography, Palaeoclimatology, Palaeoecology* 542:109411. DOI: 10.1016/j.palaeo.2019.109411.

Warner SE, Pickering P, Panagiotopoulou O, Pfau T, Ren L, Hutchinson JR. 2013. Size-Related Changes in Foot Impact Mechanics in Hoofed Mammals. *PLOS ONE* 8:e54784. DOI: 10.1371/journal.pone.0054784.

Wasserstein RL, Schirm AL, Lazar NA. 2019. Moving to a World Beyond "p < 0.05." *The American Statistician* 73:1–19. DOI: 10.1080/00031305.2019.1583913.

Watson JC, Wilson AM. 2007. Muscle architecture of biceps brachii, triceps brachii and supraspinatus in the horse. *Journal of Anatomy* 210:32–40. DOI: 10.1111/j.1469-7580.2006.00669.x.

Welker F, Collins MJ, Thomas JA, Wadsley M, Brace S, Cappellini E, Turvey ST, Reguero M, Gelfo JN, Kramarz A, Burger J, Thomas-Oates J, Ashford DA, Ashton PD, Rowsell K, Porter DM, Kessler B, Fischer R, Baessmann C, Kaspar S, Olsen JV, Kiley P, Elliott JA, Kelstrup CD, Mullin V, Hofreiter M, Willerslev E, Hublin J-J, Orlando L, Barnes I, MacPhee RDE. 2015. Ancient proteins resolve the evolutionary history of Darwin/'s South American ungulates. *Nature* 522:81–84. DOI: 10.1038/nature14249.

Welker F, Smith GM, Hutson JM, Kindler L, Garcia-Moreno A, Villaluenga A, Turner E, Gaudzinski-Windheuser S. 2017. Middle Pleistocene protein sequences from the rhinoceros genus *Stephanorhinus* and the phylogeny of extant and extinct Middle/Late Pleistocene Rhinocerotidae. *PeerJ* 5:e3033. DOI: 10.7717/peerj.3033.

Wilcots D. 1992. Aspects of the Functional Morphology, Phylogeny, and Paleoecology of the North American Miocene Rhinoceros, *Aphelops*. *Master's Thesis*.

Wiley DF, Amenta N, Alcantara DA, Ghosh D, Kil YJ, Delson E, Harcourt-Smith W, Rohlf FJ, St. John K, Hamann B. 2005. Evolutionary Morphing. In: *Proceedings of IEEE Visualization 2005*. Minneapolis, Minnesota,.

Willerslev E, Gilbert MTP, Binladen J, Ho SY, Campos PF, Ratan A, Tomsho LP, da Fonseca RR, Sher A, Kuznetsova TV, Nowak-Kemp M, Roth TL, Miller W, Schuster SC. 2009. Analysis of complete mitochondrial genomes from extinct and extant rhinoceroses reveals lack of phylogenetic resolution. *BMC Evolutionary Biology* 9:1–11. DOI: 10.1186/1471-2148-9-95.

Wilson JA, Schiebout JA. 1981. Early Tertiary Vertebrate Faunas Trans-Pecos Texas: Amynodontidae.

Wood HE. 1934. Revision of the Hyrachyidae. *Bulletin of the American Museum of Natural History* 67:1-134.

World Association of Veterinary Anatomists, International Committee on Veterinary Gross Anatomical Nomenclature. 2005. *Nomina anatomica veterinaria*. Hannover; Columbia [Mo.]; Ghent; Sapporo: The Editorial Committee.

Wyman J. 1867. On Symmetry and Homology in Limbs. *Proceedings of the Boston Society of Natural History* 9:1–45.

Yalden DW. 1971. The functional morphology of the carpus in ungulate mammals. *Cells Tissues Organs* 78:461–487. DOI: 10.1159/000143609.

Young NM, Hallgrímsson B. 2005. Serial Homology and the Evolution of Mammalian Limb Covariation Structure. *Evolution* 59:2691–2704. DOI: 10.1111/j.0014-3820.2005.tb00980.x.

Young NM, Wagner GP, Hallgrímsson B. 2010. Development and the evolvability of human limbs. *Proceedings of the National Academy of Sciences* 107:3400–3405. DOI: 10.1073/pnas.0911856107.

Yuan J, Sheng G, Hou X, Shuang X, Yi J, Yang H, Lai X. 2014. Ancient DNA sequences from Coelodonta antiquitatis in China reveal its divergence and phylogeny. *Science China Earth Sciences* 57:388–396. DOI: 10.1007/s11430-013-4702-6.

Zein MSA, Fitriana YS, Kurniawan Y, Chaerani K, Sirupang M. 2019. Kajian Genetika untuk Konservasi Badak Sumatera (*Dicerorhinus sumatrensis* Gloger, 1841). *JURNAL BIOLOGI INDONESIA* 15. DOI: 10.14203/jbi.v15i1.3767.

Zelditch ML, Swiderski DL, Sheets HD, Fink WL. 2012. *Geometric morphometrics for biologists: A Primer*. Academic Press.

Zhegallo V, Kalandadze N, Shapovalov A, Bessudnova Z, Noskova N, Tesakova E. 2005. On the fossil rhinoceros *Elasmotherium* (including the collections of the Russian Academy of Sciences). *Cranium* 22:17–40.

Zschokke S, Baur B. 2002. Inbreeding, outbreeding, infant growth, and size dimorphism in captive Indian rhinoceros (*Rhinoceros unicornis*). *Canadian Journal of Zoology* 80:2014–2023. DOI: 10.1139/z02-183.

General appendices

Articles de diffusion scientifique

En parallèle de mes travaux de recherche, j'ai été amené à publier deux articles de diffusion scientifique sur le site **The Conversation**, afin de vulgariser et informer sur des avancées récentes concernant la connaissance des rhinocéros actuels ou fossiles.

Légalisation de la corne de rhinocéros, un remède pire que le mal ?

Publié le 5 novembre 2018 : https://theconversation.com/legalisation-de-la-corne-de-rhinoceros-un-remede-pire-que-le-mal-106387

C'est une décision qui a provoqué autant d'indignation que d'incompréhension. Le 29 octobre dernier, la Chine annonçait par voie de presse un assouplissement de sa législation[3] relative aux cornes de rhinocéros ainsi qu'aux os de tigres.

Si le texte stipule que l'achat, la vente, l'importation ou l'exportation de « produits dérivés » du rhinocéros et du tigre restent interdits, il signale en revanche que les cornes et ossements peuvent désormais être obtenus à partir d'animaux d'élevage, à des fins de recherche médicale ou de soins, par des hôpitaux ou soignants autorisés par le gouvernement chinois.

L'annonce, accueillie par un torrent de critiques, a notamment laissé perplexe le WWF, l'une des plus importantes organisations mondiales de protection de l'environnement, qui s'inquiète d'une réouverture[4] d'un marché pourtant jugé illégal en Chine depuis 1993.

Qu'est-il donc passé par la tête des autorités chinoises ?

Un précédent en Afrique du Sud

À y regarder de plus près, ce revirement intervient un an et demi après une décision similaire en Afrique du Sud[5], où subsistent 70 % des presque 30 000 rhinocéros blancs (Ceratotherium simum) encore en vie.

En avril 2017, un moratoire en vigueur dans le pays depuis 2009 prenait fin, réautorisant le commerce de cornes en Afrique du Sud. Une décision lourdement influencée par un certain John Hume[6], riche

[3] http://english.gov.cn/policies/latest_releases/2018/10/29/content_281476367121088.htm
[4] https://www.worldwildlife.org/press-releases/wwf-statement-on-china-s-legalization-of-domestic-trade-in-tiger-bone-and-rhino-horn
[5] https://www.nationalgeographic.com/news/2017/08/wildlife-watch-rhino-horn-south-africa-auction/
[6] https://theconversation.com/why-allowing-the-sale-of-horn-stockpiles-is-a-setback-for-rhinos-in-the-wild-82773

propriétaire terrien pouvant se targuer d'être le plus gros éleveur de rhinocéros au monde, avec 1 600 animaux.

Le calcul de Hume est simple : initialement vendus à des zoos ou des réserves, ces rhinocéros représentent désormais un moyen contrôlé de produire de la corne « d'élevage ». La corne étant composée de kératine comme nos cheveux ou nos ongles, elle peut être prélevée sans douleur et repousse au fil du temps. Ainsi, en décornant son cheptel régulièrement, Hume aurait accumulé près de 6 tonnes de corne qu'il entend vendre pour inonder le marché illégal et contrecarrer le braconnage.

Mais cette décision sud-africaine ne concerne que le marché interne au pays, quasiment inexistant, puisque l'essentiel de la corne s'échange en Asie. La récente décision chinoise semble donc répondre à celle de l'Afrique du Sud, en vue de créer peu à peu un cadre légal mondial pour réguler le trafic de corne de rhinocéros : il deviendrait alors possible aux producteurs sud-africains de vendre légalement à des consommateurs asiatiques.

Un trafic global

Hasard du calendrier, à peine deux semaines avant la décision de la Chine, était diffusé en France le documentaire Rhino dollars[7] d'Olivia Mokiejewski, montrant l'ampleur et la complexité du trafic de corne à travers une investigation saisissante[8], remontant la plupart des maillons de la chaîne.

Car loin d'être un simple problème d'écologie et de disparition des espèces, le trafic de corne – et plus généralement des produits issus d'animaux – représente le quatrième plus gros trafic mondial, derrière ceux de la drogue, des armes et des êtres humains.

En Afrique du Sud, il prospère sur les ruines de l'Apartheid, les inégalités sociales que ce système a engendrées, et sur le niveau de vie très faible d'une grande partie de la population. Un rhinocéros abattu peut rapporter au braconnier 50 à 100 fois le salaire moyen[9] : difficile de parler d'écologie quand la corne devient le seul moyen de faire vivre sa famille ! La situation précaire dans les pays limitrophes, comme au Mozambique, entretient également un afflux régulier de braconniers, tout en permettant à des parrains locaux de s'enrichir rapidement.

De l'autre côté de la planète, les consommateurs, derniers maillons de la chaîne, se rencontrent principalement au Vietnam et en Chine.

Un rôle social de premier plan

[7] https://www.youtube.com/watch?v=Idq-YV6Npys
[8] https://www.lemonde.fr/afrique/article/2018/10/25/les-rhinoceros-auront-surement-disparu-dans-une-vingtaine-d-annees_5374575_3212.html
[9] Ibid.

Vu d'Occident, il est courant d'accuser la médecine traditionnelle asiatique d'employer ce prétendu remède miracle pour tout et n'importe quoi – quand bien même aucune étude scientifique sérieuse[10] n'a jamais prouvé quelque effet que ce soit.

Si ce rôle médicinal reste important, des enquêtes sur le terrain ont également clairement montré le rôle social[11] de la corne de rhinocéros.

Symbole de réussite, elle peut servir à sceller un gros contrat ou simplement être offerte comme marque de respect à une personne importante, voire un officiel de l'État. Une tendance vietnamienne se développe même depuis quelques années, consistant à offrir de la corne à un proche se sachant condamné par un cancer : le présent indique alors que la famille a retourné ciel et terre pour offrir un ultime cadeau d'exception.

C'est d'ailleurs probablement une rumeur autour d'un prétendu homme politique miraculeusement guéri d'un cancer par la corne qui a fait s'envoler le trafic au cours de la dernière décennie. Alors que les années 2000 avaient vu un net recul du braconnage et qu'on ne dénombrait que 13 rhinocéros tués en 2007 en Afrique du Sud, le massacre a dépassé les 1 200 têtes 7 ans plus tard, soit une augmentation de 9 300 %[12]. La faute à un appel d'air créée par cette rumeur au Vietnam, amplifiée par les trafiquants eux-mêmes, prêts à tout pour faire s'envoler les prix et la demande.

C'est dans ce contexte de tensions renouvelées qu'a germé l'idée d'un commerce régulé et organisé. Mais est-ce réellement la bonne voie à prendre endiguer le massacre ?

Les sérieuses limites à la légalisation

Sans surprise, les principaux partisans d'une régulation de ce commerce sont les éleveurs de rhinocéros eux-mêmes[13], à l'image de John Hume. Persuadés que le marché se régulera de lui-même et que la nature ne peut être protégée que lorsqu'on lui attribue une valeur monétaire, ils attendent la mise en place d'un commerce légal et libéral, encadré le moins possible par les États.

Mais la grande majorité des chercheurs et écologistes se penchant sur le sujet craignent, bien au contraire, que cette possible légalisation n'aggrave la situation sur plusieurs points.

Les enquêtes de terrain[14] montrent en effet clairement que les consommateurs sont prêts à payer le double du prix pour de la corne « sauvage », convaincus qu'elle est plus efficace ou simplement parce

[10] https://www.pbs.org/wnet/nature/rhinoceros-rhino-horn-use-fact-vs-fiction/1178/
[11] https://www.sciencedaily.com/releases/2018/05/180514095509.htm
[12] https://www.savetherhino.org/rhino-info/poaching-stats/
[13] http://ltrs.org.za/wp-content/uploads/2018/09/Ecological-Economics-Rhino-2018.pdf
[14] https://www.sciencedaily.com/releases/2018/05/180514095509.htm

que le prestige associé est supérieur. La corne d'élevage aurait ainsi du mal à remplacer la corne braconnée, contrairement à ce que soutient Hume.

Pire, il est hautement probable que la légalisation permette un blanchiment massif de cornes braconnées, sauf à mettre en place des filières strictes et des systèmes de contrôle efficaces et mondialement coordonnés – systèmes qui, de l'aveu même d'un pays comme le Vietnam, paraissent utopiques à l'heure actuelle.

Tout indique également que la légalisation pourrait créer une augmentation de la demande, non seulement des consommateurs réguliers, mais également auprès d'une population moins fortunée en cas de baisse des prix.

Enfin, l'élevage des rhinocéros pourrait rapidement tourner à l'industrialisation aux dépens du bien-être des animaux, comme le montrent l'exemple des nombreuses fermes à tigre asiatiques[15], agissant sous couvert de conservation de l'espèce mais où les félins sont en réalité exploités pour leurs organes dans d'atroces conditions.

Agir sur tous les maillons de la chaîne

Dans cette situation, différentes études[16] sur la légalisation du commerce de corne tendent à montrer qu'il pourrait s'agir là de la pire des solutions. A contrario, l'endiguement du trafic doit nécessairement passer par les différents maillons de la chaîne, à commencer par l'amélioration de la situation sociale dans le sud de l'Afrique, permettant de réduire le nombre de braconniers.

Des précédents existent : par une politique de conservation impliquant les habitants au plus près, le Kenya est ainsi parvenu à faire diminuer la pression du braconnage[17] sur sa faune. Les moyens d'investigation policière, permettant d'appréhender les trafiquants locaux, doivent également être renforcés et étendus.

À l'autre bout de la chaîne, en Asie, les campagnes de sensibilisation doivent agir tant sur le plan médicinal que social, afin de faire baisser la demande, en abandonnant l'argument écologiste qui n'a quasiment aucun impact sur des consommateurs se sentant non-responsables de cette situation.

Il s'agit d'un travail de fond complexe, impliquant des centaines d'acteurs différents à l'échelle mondiale, mais qui s'avérera certainement plus efficace qu'une légalisation aux conséquences

[15] https://www.nytimes.com/2017/06/05/science/animal-farms-southeast-asia-endangered-animals.html
[16] https://www.sciencedirect.com/science/article/abs/pii/S1617138115300108
[17] https://www.savetherhino.org/africa/kenya/kenya-poaching-stats-out/

potentiellement désastreuses. La communauté internationale doit donc prendre le taureau par les cornes pour que les rhinocéros ne craignent plus pour les leurs.

Qui était *Elasmotherium*, surnommé la « licorne de Sibérie » ?

Publié le 28 février 2019 : https://theconversation.com/qui-etait-elasmotherium-surnomme-la-licorne-de-siberie-109999

Cet article a fait l'objet d'une intervention dans l'émission de vulgarisation scientifique quotidienne « La Tête au carré », produite par Mathieu Vidard sur France Inter (émission du 1er mars 2019 présentée par Daniel Fievet, en compagnie d'Aline Richard, éditrice science et technologie pour The Conversation France) : https://www.franceinter.fr/emissions/la-tete-au-carre/la-tete-au-carre-01-mars-2019).

Lorsque l'on évoque la Préhistoire et ses animaux emblématiques, les premières scènes venant immanquablement à l'esprit sont souvent peuplées de mammouths laineux, de chevaux bondissants comme sur les parois de la grotte de Lascaux, ou encore de bisons, d'aurochs, de lions ou d'ours des cavernes. Pourtant, cette période ne se résume pas aux paysages de steppes glacées du Paléolithique supérieur en Europe occidentale, et bon nombre d'autres espèces disparues, petites ou grosses, ont de quoi étonner par leur apparence, leurs dimensions ou leur mode de vie.

Tel est le cas d'*Elasmotherium*[18], un genre cousin des rhinocéros actuels et laineux, appartenant comme eux à la famille des Rhinocérotidés[19], mais bien moins connu du grand public que ses proches parents en voie d'extinction. Pourtant, cette créature ne passait certainement pas inaperçue : avec des mensurations estimées à 4,5 m de long et 2 m au garrot, pour une masse entre 4 et 5 tonnes, il faisait partie intégrante de ce que les paléontologues nomment la « mégafaune du Pléistocène »[20]. Plus gros que le rhinocéros laineux, il était en outre pourvu d'un énorme dôme frontal, interprété par la plupart des chercheurs comme le support d'une immense corne pouvant atteindre 2 m de hauteur. Ceci lui a valu le surnom de « licorne de Sibérie » – même si ses mensurations ne lui confèrent pas vraiment l'apparence du cheval cornu mythologique.

Une disparition plus tardive qu'on ne le pensait

De plus, *Elasmotherium* est un des premiers genres fossiles décrits en paléontologie, nommé dès 1808 par le naturaliste allemand Fischer[21] – avant même que ne soient scientifiquement reconnus trois des cinq espèces de rhinocéros actuels ! Malgré la découverte de plusieurs squelettes complets, il n'est pas un habitant de notre imaginaire collectif préhistorique (du moins occidental). Probablement parce qu'il vivait loin : les quelques espèces connues d'*Elasmotherium*, comme *E. sibiricum* ou *E. caucasicum*, ont été découvertes principalement en Asie centrale, en Russie du sud, en Ukraine, au Kazakhstan, en

[18] https://fr.wikipedia.org/wiki/Elasmotherium
[19] http://dico-sciences-animales.cirad.fr/liste-mots.php?fiche=23992
[20] https://fr.wikipedia.org/wiki/M%C3%A9gafaune_du_Pl%C3%A9istoc%C3%A8ne
[21] https://fr.wikipedia.org/wiki/Gotthelf_Fischer_von_Waldheim

Chine et en Mongolie. Et également parce que sa disparition est estimée à 200 000 ans avant le présent : bien trop tôt pour rencontrer les hommes et femmes de Cro-Magnon européens qui auraient pu les représenter à travers leur art pariétal ou mobilier.

Du moins cette date était-elle acceptée jusqu'à la publication d'une nouvelle étude[22] en novembre 2018 dans la revue *Nature* par Pavel Kosintsev et ses collaborateurs. Les chercheurs ont réétudié 25 spécimens d'*Elasmotherium sibiricum* présents dans plusieurs musées en Russie et au Royaume-Uni. Ils ont notamment pu utiliser le collagène encore présent dans les os pour dater les spécimens à l'aide de la technique dite « AMS » (pour « Accelerator Mass Spectroscopy »[23]), permettant un comptage extrêmement précis des isotopes de carbone 14 dans l'échantillon. Surprise : les âges obtenus placent la disparition d'*Elasmotherium* aux alentours de 39 à 36 000 ans avant le présent.

Un bond dans le temps qui le rend désormais contemporain de la transition entre *Homo neanderta-lensi*s et *Homo sapiens* en Europe. Il pourrait même avoir survécu jusqu'aux alentours de 26 000 ans si l'on s'en réfère à la découverte d'un crâne au Kazakhstan en 2016[24] : malheureusement, ce spécimen ayant été découvert dans un environnement humide difficile à analyser, la datation de ce crâne reste à nuancer, sa signature isotopique ayant pu être contaminée.

Avec cette disparition s'est éteinte une lignée pourtant vieille de plusieurs dizaines de millions d'années, prenant racine au milieu de l'Éocène : l'étude de l'équipe de Kosintsev réévalue en effet la séparation entre la sous-famille des Elasmotheriinae et celle des Rhinocerotinae (à laquelle appartiennent les rhinocéros actuels) aux alentours de 47 millions d'années. Au cours du Tertiaire, les Elasmothères ont ainsi eu le temps de se diversifier et de coloniser une bonne partie de la planète, comme le montre notamment l'étude menée sur ce groupe par Pierre-Olivier Antoine en 2002[25]. Les petites formes telles que *Bugtirhinus*, atteignant un mètre au garrot, vont progressivement donner naissance à une dizaine d'espèces différentes tout au long du Miocène, lesquelles furent découvertes en Asie centrale mais également en Afrique ou en Europe, comme *Hispanotherium*, mis au jour en Espagne et en France.

Tout au long de l'évolution de cette lignée se développe également un caractère unique chez les rhinocéros : la présence de dents à croissance continue (dite « hypsodontes »[26]), poussant durant toute la vie de l'animal et s'usant au fur et à mesure, à l'image des incisives de rongeurs. Ce trait confère aux molaires d'*Elasmotherium*, chez qui cette hypsodontie est maximale, un aspect unique composé de

[22] https://www.nature.com/articles/s41559-018-0722-0
[23] https://en.wikipedia.org/wiki/Accelerator_mass_spectrometry
[24] https://thescipub.com/abstract/10.3844/ajassp.2016.189.199
[25] http://www.rhinoresourcecenter.com/pdf_files/134/1345549394.pdf?view
[26] https://fr.wikipedia.org/wiki/Hypsodontie

lames d'émail caractéristiques, ce qui donnera d'ailleurs son nom scientifique à l'animal – du grec « elasmos » (lame) et « therion » (bête).

Refroidissement du climat

Cette caractéristique particulière a d'ailleurs peut-être causé sa perte. En effet, cette hypsodontie est considérée comme une spécialisation à la consommation de graminées très abrasifs, associée à l'ingestion involontaire des poussières et grains de sable près du sol : *Elasmotherium* passait ainsi une grande partie de son temps à brouter dans les steppes et prairies d'Asie centrale, et ses dents poussaient en permanence pour compenser une usure rapide et prononcée. Kosintsev et ses collaborateurs relient donc sa disparition à un changement climatique concomitant : un refroidissement généralisé du climat – qui mènera quelques milliers d'années plus tard au dernier maximum glaciaire[27] – aurait provoqué une fragmentation des prairies et un développement d'un environnement de toundra sèche, bien moins favorable à ce rhinocéros géant. Conjointement avec d'autres espèces, il n'aurait ainsi pas pu s'adapter à la raréfaction de sa nourriture et aurait fini par disparaître, là où ses cousins les rhinocéros laineux purent proliférer.

Une licorne… sans corne ?

Cette nouvelle date de disparation supposée rouvre le vieux débat de la rencontre potentielle entre nos ancêtres et cet animal. Si aucun reste osseux n'a jamais livré de traces irréfutables de chasse ou de prédation directe ou indirecte, un dessin énigmatique dans la grotte de Rouffignac[28] en Dordogne pose question. Sur les parois couvertes de représentations de mammouths et rhinocéros laineux figure également une étrange silhouette, comme une sorte de rhinocéros à la corne démesurée et au garrot gigantesque.

Interprété dès 1964 comme une potentielle représentation d'*Elasmotherium*, le dessin conserve pourtant ses mystères. S'il est vrai que la silhouette tranche avec la plupart des rhinocéros de l'art pariétal européen, lesquelles possèdent quasi-systématiquement leurs deux cornes emblématiques, les œuvres de Rouffignac datent néanmoins de « seulement » 13 000 ans, soit bien après la disparition supposée de l'espèce. De plus, à part la découverte au XIXe siècle d'une dent potentielle d'*Elasmotherium* dans la Somme (malheureusement perdue depuis), jamais aucun reste de l'animal n'a été identifié si loin à l'ouest de l'Europe. D'autres figurations dans la grotte de Kapova en Russie[29] ont parfois été interprétées comme des représentations d'*Elasmotherium*, là encore sans aucune certitude.

[27] https://fr.wikipedia.org/wiki/Derni%C3%A8re_p%C3%A9riode_glaciaire
[28] https://www.hominides.com/html/lieux/grotte-de-rouffignac.php
[29] https://en.wikipedia.org/wiki/Kapova_Cave

Ces interprétations s'appuient en outre sur la présence supposée d'une corne gigantesque. Or, rien ne l'indique avec certitude, car aucune corne d'*Elasmotherium* n'a jamais été retrouvée à l'état fossile ! La présence d'une corne démesurée a été supposée dès la découverte des premiers crânes, par analogie avec les rhinocéros actuels et par observation du dôme frontal proéminent. Mais l'observation des rugosités osseuses à la base des cornes sur les rhinocéros actuels ne permettent que difficilement de présager de la longueur de celle-ci. Certains auteurs russes ont ainsi proposé au milieu du XXe siècle des reconstitutions avec des cornes de taille et forme variables, parfois limitées à une simple excroissance tournée vers l'arrière, voire pas de corne du tout ! Et même s'il est difficile d'imaginer cela, tant la représentation de cet animal semble aller d'elle-même, seule la découverte d'une corne fossilisée permettrait de préciser réellement la taille et la forme de l'appendice emblématique d'*Elasmotherium*. Nous saurions alors enfin si la « licorne de Sibérie » mérite bel et bien son nom mythologique.

Travaux annexes

Lors de ces trois années de thèse, j'ai été amené à participer au travail de plusieurs étudiants de Master sur des os de rhinocéros. J'ai co-encadré les travaux de Lou Moizo (M1) concernant la variation de la forme de la patella au sein des Perissodactyla actuels et fossiles, ainsi que les travaux de Kévin Gayod (M1) portant sur la comparaison critique des différentes méthodes d'estimation de masse corporelle au sein des mammifères. Ces deux études feront l'objet de publications prochainement.

J'ai également participé au travail de Cyril Etienne (M2) concernant la variation de forme de l'astragale et du calcanéum en fonction de la masse corporelle chez les Perissodactyla actuels et fossiles. Mon implication concernait essentiellement l'échantillonnage via la numérisation d'ossements, mais j'ai également été impliqué sur la réflexion globale de l'étude et de ses résultats. Ce travail a fait l'objet d'une publication en 2020 dans *Biological Journal of the Linnean Society* dont je reproduis une version dans les pages suivantes.

Biological Journal of the Linnean Society, 2020, **XX**, 1–25. With 16 figures.

Influence of mass on tarsus shape variation: a morphometrical investigation among Rhinocerotidae (Mammalia: Perissodactyla)

CYRIL ETIENNE[1*], CHRISTOPHE MALLET[1], RAPHAËL CORNETTE[2] and ALEXANDRA HOUSSAYE[1]

[1]*UMR 7179, Mécanismes Adaptatifs et Evolution, Muséum National d'Histoire Naturelle, Centre National de la Recherche Scientifique, Paris, France*
[2]*UMR 7205, Institut de Systématique, Evolution, Biodiversité, Centre National de la Recherche Scientifique, Muséum National d'Histoire Naturelle, Sorbonne Université, Ecole Publique des Hautes Etudes, Paris, France*

Received 25 October 2019; revised 7 January 2020; accepted for publication 7 January 2020

Many tetrapod lineages show extreme increases in body mass in their evolutionary history, associated with important osteological changes. The ankle joint, essential for foot movement, is assumed to be particularly affected in this regard. We investigated the morphological adaptations of the astragalus and the calcaneus in Rhinocerotidae, and analysed them in light of a comparative analysis with other Perissodactyla. We performed 3D geometric morphometrics and correlated shape with centroid size of the bone and body mass of the species. Our results show that mass has an influence on bone shape in Rhinocerotidae and in Perissodactyla, but this is not as strong as expected. In heavy animals the astragalus has a flatter trochlea, orientated more proximally, associated with a more upright posture of the limb. The calcaneus is more robust, possibly to sustain the greater tension force exerted by the muscles during plantarflexion. Both bones show wider articular facets, providing greater cohesion and better dissipation of the loading forces. The body plan of the animals also has an influence. Short-legged Teleoceratina have a flatter astragalus than the other rhinocerotids. *Paraceratherium* has a thinner calcaneus than expected. This study clarifies adaptations to high body weight among Rhinocerotidae and calls for similar investigations in other groups with massive forms.

ADDITIONAL KEYWORDS: ankle – astragalus – calcaneus – functional morphology – high body weight – geometric morphometrics – Perissodactyla – Rhinocerotidae.

INTRODUCTION

In vertebrate locomotion, bone is a rigid organ of paramount importance. It provides support for the body as well as attachment points for the muscles, via the tendons (Hildebrand, 1982; Biewener, 1990). Bone shape varies with a diversity of factors, one of the main ones being the size of the animal (Hildebrand *et al.*, 1985; Biewener, 1989; Polly, 2008; Biewener & Patek, 2018). Evolutionary convergences are usually observed when similar selective pressures are applied to the same structure independently in different groups. Accordingly, in a given clade, an increasing body mass generally results in, for example, a more vertical orientation of the pelvis (Polly, 2008), an increasing diameter of the femur (Alexander, 1985) and micro-anatomical changes such as a thick cortical bone (Houssaye *et al.*, 2016). Postural and locomotor factors such as facultative bipedalism or cursoriality are also important factors influencing the shape of the skeleton (Hildebrand, 1982; Polly, 2008). Analysing the relationship between mass and the shape of the bones, while also considering factors such as posture and locomotion, would allow a better understanding of the way animals with different body plans adapt to an increasing mass.

Rhinocerotidae (Gray, 1821) seem to be an excellent group to study morphological variations in bone related to mass and to a varying body plan. Today

*Corresponding author. E-mail: cyril.etienne@cri-paris.org

comprising five species and four genera, rhinocerotids are found only in tropical regions (Dinerstein, 2011). They were much more diverse during the Cenozoic, appearing in the mid-Eocene and comprising more than 100 species (Cerdeño, 1998). Rhinocerotids have been found in Eurasia, Africa and North America (as far south as Panama; MacFadden, 2006), and existed in a diversity of habitats, such as cold steppes, dense forests and swamps (Prothero *et al.*, 1989; Mörs, 2002; Prothero, 2005). All of them were relatively heavy animals as compared to the average body mass of mammals (Gardezi & da Silva, 1999), ranging from ~150 kg for the lightest taxa of the Eocene to 5 tons for *Elasmotherium* (Cerdeño, 1998; Becker, 2003; Antoine, 2020). They have undergone several independent extreme increases in body mass, up to more than 2 tons, during their evolutionary history (e.g. in Rhinocerotina, Teleoceratina or Elasmotheriinae; Cerdeño, 1998). They also vary in terms of body plan: some taxa are massive and sturdy (e.g. *Coelodonta*, *Ceratotherium*), some are extremely short-legged (e.g. *Teleoceras*, *Brachypotherium*, *Prosantorhinus* in the Teleoceratina tribe), while others have been described as gracile and cursorial (e.g. *Protaceratherium*, *Hispanotherium*; Cerdeño, 1998). Rhinocerotids should therefore be a very interesting group to study variations in bone shape, and analyse its relationship with different masses and morphologies. Rhinocerotidae are part of the order Perissodactyla (Owen, 1848). The Perissodactyla today only include the five species of Rhinocerotidae, the seven species of Equidae and the four species of Tapiridae, but were far more diversified during the Cenozoic, in terms of number of both species and families (Prothero & Schoch, 1989; Fig 1). They included notably the Paraceratheriidae (sometimes considered a subfamily of Hyracodontidae, see Wang *et al.*, 2016), which included some of the heaviest land mammals that have ever lived (Prothero, 2013). Perissodactyla also included the intriguing Chalicotheriidae, among which some species (the subfamily Chalicotheriinae) were facultative bipeds with a gorilla-like stance, with very short hindlimbs, and walked on the knuckles of their forelimbs, whereas others (the Schizotheriinae) had front and hindlimbs of approximately equal length (Coombs, 1983; Semprebon *et al.*, 2011). This order therefore encompasses a great diversity in terms of mass and body plan that can be related to their bone shape, and as compared with the diversity observed among Rhinocerotidae.

Our study focuses on two bones of the tarsus: the astragalus and the calcaneus. These bones are at the junction between the hind zeugopodium and the autopodium, and are essential to the movement of the foot and consequently of the entire animal. The astragalus serves as the pivot, or fulcrum, and the calcaneus as the lever arm of the foot (Carrano, 1997). These bones have been extensively studied, from taxonomic and phylogenetic points of view (see Stains, 1959; Guérin, 1980; Missiaen *et al.*, 2006; Gladman *et al.*, 2013), but also in a morphofunctional context, with multiple studies trying to link their shape to the animal's mass (see Dagosto & Terranova, 1992; Martinez & Sudre, 1995; Tsubamoto, 2014), habitat (DeGusta & Vrba, 2003; Plummer *et al.*, 2008; Curran, 2012; Barr, 2014) and mode of locomotion (Nakatsukasa *et al.*, 1997; Panciroli *et al.*, 2017). These studies all found a link between the mass of a species and the shape both of its astragalus and of its calcaneus, generally represented by linear measurements or ratios. These studies concerned a wide variety of mammals (e.g. bovids, cervids, carnivorans and primates), but none specifically studied the relationship between mass and shape on both ankle bones in perissodactyls.

In the present study, we investigated the variation of the shape of the astragalus and calcaneus across a diversity of extant and fossil Rhinocerotidae and additional Perissodactyla. Our primary aim was to identify shape variations associated with an increase of mass. We expect that mass will have a strong influence on those bones because they are extremely important for support and movement in mammals. We expect that bones of large animals will be more robust and more resistant, with wider and flatter articular facets to help dissipate forces. We also expect that adaptations will vary according to the general body plan and mode of locomotion of the animal. We studied variations of bone shape, and tested the influence of bone size and of the mean mass of each species. We first focused on shape variations across Rhinocerotidae, and then across all Perissodactyla sampled in order to compare the variations observed among Rhinocerotidae to more diverse forms (e.g. *Paraceratherium*), and thus better interpret the drivers acting on this variation.

MATERIAL AND METHODS

Material

We studied 112 astragali and 94 calcanei belonging to 43 different species across five different families of Perissodactyla, with varying masses, morphologies or locomotor modes (Supporting Information, Appendix S1; Fig. 1). Taxa were chosen to encompass as much as possible of the variation within Rhinocerotidae. A few specimens of other families of Perissodactyla with particular characteristics (e.g. an extremely high mass for *Paraceratherium*, cursoriality for horses, shortened hindlimbs for Chalicotheriinae) were included to provide a comparison point for the shape variations observed in Rhinocerotidae. Rhinocerotidae constitute our main subsample, with 40 specimens of each bone type for living

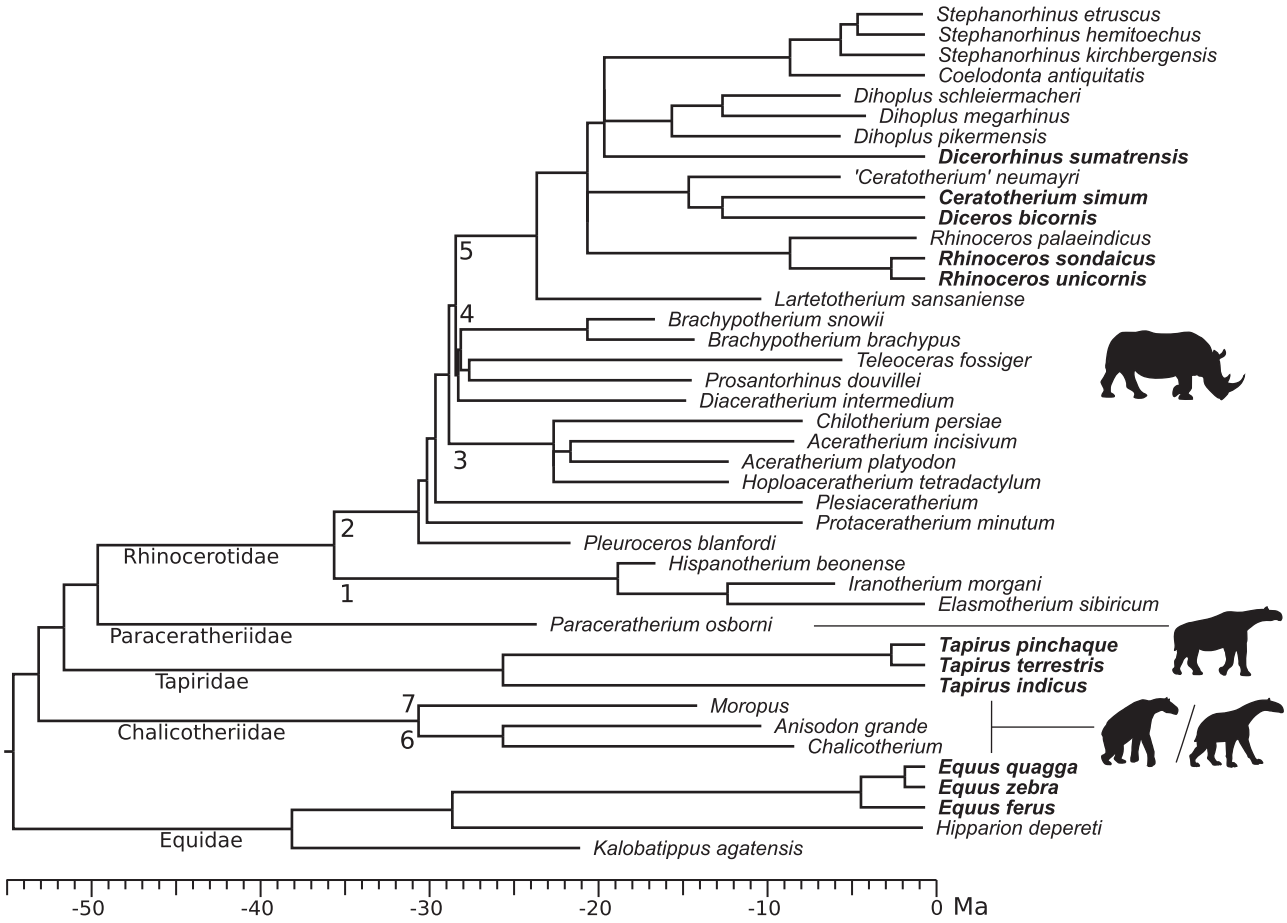

Figure 1. Composite phylogeny including the species sampled (modified from Antoine, 2002; Antoine *et al.*, 2010, 2020; Piras *et al.*, 2010; Holbrook & Lapergola, 2011; Steiner and Ryder, 2011). Occurrence dates were estimated from Antoine (1997), Piras *et al.* (2010), Antoine *et al.* (2010), Geraads *et al.* (2012), Guérin (2012) and Prothero (2013), as well as data recorded on http://fossilworks.org. 1, Elasmotheriinae; 2, Rhinocerotinae; 3, Aceratheriina; 4, Teleoceratina; 5, Rhinocerotina; 6, Schizotheriinae; 7, Chalicotheriinae. Species in bold are extant. The relationships between the five extant rhino species remain in debate; specifically the position of *Dicerorhinus sumatrensis* and its close fossil relatives is uncertain, placed either as sister taxa to *Ceratotherium* and *Diceros*, as sister taxa to *Rhinoceros*, or as sister taxa to a group comprising *Rhinoceros*, *Ceratotherium* and *Diceros* (Willerslev *et al.*, 2009; Gaudry, 2017). This phylogenetic uncertainty is here represented by a polytomy.

species. Our sample also includes 43 astragali and 31 calcanei of fossil Rhinocerotidae, including small, cursorial genera (*Protaceratherium*, *Pleuroceros*), and at least three lineages showing independent increases in body mass above 2 tons (in *Elasmotherium*, *Brachypotherium* and *Coelodonta*, plus the living *Ceratotherium* and *Rhinoceros unicornis*). We studied ten astragali and calcanei of extant Tapiridae, and eight astragali and six calcanei of Equidae. Three astragali and one calcaneus belong to *Paraceratherium* (Paraceratheriidae), and eight astragali and six calcanei belong to Chalicotheriidae. To our knowledge, all the bones belonged to adult specimens. A description of the bones, including the nomenclature used for the main anatomical features of the bones, is provided in Appendix S2.

Specimens come from the collections of the Muséum National d'Histoire Naturelle (MNHN, Paris, France), the Muséum d'Histoire Naturelle de Toulouse (MHNT, Toulouse, France), the Claude Bernard University (UCBL, Lyon, France), the Natural History Museum (NHM, London, UK), the Powell-Cotton Museum (BICPC, Birchington-on-Sea, UK), the Naturhistorisches Museum Wien (NMW, Vienna, Austria), the Zoologische Staatssammlung München (ZSM, Munich, Germany) and the Bayerische Staatssammlung für Paläontologie und Historiche Geologie (BSPHM, Munich, Germany; Supporting information, Appendix S1).

MASS ESTIMATIONS USED

Mass data were retrieved from the literature (Table 1). Methods of mass reconstructions are detailed in the references; they usually relied on regression equations and measurements on the molars or on proximal limb segments. None of them used measurements on the

Table 1. List of the masses used for the species studied here

Family	Species	Mass (kg)	Source
Rhinocerotidae	*Rhinoceros sondaicus*	1200–1500	Dinerstein (2011)
Rhinocerotidae	*Rhinoceros unicornis*	2000	Dinerstein (2011)
Rhinocerotidae	*Rhinoceros palaeindicus* †	Missing data	
Rhinocerotidae	*Diceros bicornis*	800–1300	Dinerstein (2011)
Rhinocerotidae	*Ceratotherium neumayri* †	1200	Valli (2005)
Rhinocerotidae	*Ceratotherium simum*	2300	Dinerstein (2011)
Rhinocerotidae	*Dicerorhinus sumatrensis*	600–950	Dinerstein (2011)
Rhinocerotidae	*Stephanorhinus etruscus* †	Missing data	
Rhinocerotidae	*Stephanorhinus kirchbergensis* †	1844	Saarinen *et al.* (2016)
Rhinocerotidae	*Stephanorhinus hemitoechus* †	Missing data	
Rhinocerotidae	*Coelodonta antiquitatis* †	1905	Saarinen *et al.* (2016)
Rhinocerotidae	*Dihoplus megarhinus* †	Missing data	
Rhinocerotidae	*Dihoplus schleiermacheri* †	1812	Becker (2003)
Rhinocerotidae	*Dihoplus pikermensis* †	1100	Valli (2005)
Rhinocerotidae	*Lartetotherium sansaniense* †	1204	Becker (2003)
Rhinocerotidae	*Prosantorhinus douvillei* †	Missing data	
Rhinocerotidae	*Teleoceras fossiger* †	1016	Damuth (1990)
Rhinocerotidae	*Brachypotherium brachypus* †	2327	Becker (2003)
Rhinocerotidae	*Brachypotherium snowi* †	Missing data	
Rhinocerotidae	*Aceratherium incisivum* †	1982	Becker (2003)
Rhinocerotidae	*Aceratherium platyodon* †	Missing data	
Rhinocerotidae	*Hoploaceratherium tetradactylum* †	1197	Becker (2003)
Rhinocerotidae	*Chilotherium persiae* †	Missing data	
Rhinocerotidae	*Diaceratherium intermedium* †	Missing data	
Rhinocerotidae	*Plesiaceratherium* †	Missing data	
Rhinocerotidae	*Protaceratherium minutum* †	530	Becker (2003)
Rhinocerotidae	*Pleuroceros blanfordi* †	501	Becker (2003)
Rhinocerotidae	*Victoriaceros kenyensis* †	Missing data	
Rhinocerotidae	*Hispanotherium beonense* †	Missing data	
Rhinocerotidae	*Elasmotherium sibiricum* †	4000–5000	Zhegallo *et al.* (2005)
Rhinocerotidae	*Iranotherium morgani* †	Missing data	
Paraceratheriidae †	*Paraceratherium bugtiense* †	7400	Fortelius & Kappelman (1993)
Tapiridae	*Tapirus pinchaque*	150–200	Medici (2011)
Tapiridae	*Tapirus terrestris*	220	Medici (2011)
Tapiridae	*Tapirus indicus*	280–400	Medici (2011)
Chalicotheriidae †	*Chalicotherium sp.* †	924	Costeur (2004)
Chalicotheriidae †	*Anisodon grande* †	1500	Guérin (2012)
Chalicotheriidae †	*Moropus sp.* †	1179	Damuth (1990)
Equidae	*Equus zebra*	240–380	Rubenstein (2011)
Equidae	*Equus quagga*	175–320	Rubenstein (2011)
Equidae	*Equus przewalski*	200–300	Rubenstein (2011)
Equidae	*Equus caballus*	380–600	Bongianni (1988)
Equidae	*Equus caballus* *	700–1000	Bongianni (1988)
Equidae	*Hipparion depereti* †	Missing data	
Equidae	*Kalobatippus agatensis* †	160	Jams *et al.* (1994)

†Fossil taxon.
*Two separate mass estimates were used for *Equus caballus*, one for average-sized horses and one for draught horses, given the wide morphological differences between the two.

astragalus or the calcaneus. When only a range of masses was available with no average, the mean of the minimal and maximal mass was used.

Data acquisition

The specimens were digitized using either an Artec Eva surface scanner and the Artec Studio Professional v.12.1.5.1 software (Artec 3D, 2018), or a Nikon D5500 camera (automatic mode, without flash, focal length 50 mm, aperture f/1.8) and the photogrammetry software Agisoft PhotoScan v.1.4.0 (Agisoft LLC, 2017). The 3D meshes were then exported, reduced to 60 000 faces and mirrored to have only right-side astragali and calcanei, using MeshLab v.2016.12 (Cignoni *et al.*, 2008). In two cases (astragalus of *Brachypotherium snowi* NHM-PAL-PV-M-29279 and calcaneus of *Hispanotherium beonense* MHNT-2015-0-837), the specimens were slightly damaged were curve semi-landmarks would be placed and had to be partially reconstructed using Geomagic (3D Systems, 2017).

Geometric morphometrics

Bone shape was modelled using anatomical landmarks and semi-landmarks sliding on curves (Gunz & Mitteroecker, 2013). Landmarks were all placed by the same operator (C.E.). Given that there can be marked differences in bone shape between rhinocerotids and the other perissodactyls, we split the analysis in two. Two sets of landmarks and curves were therefore defined: one for all the rhinocerotids, and another for all the perissodactyls (see Figs 2, 3; Supporting Information, Appendix S3 for descriptions of the landmarks and curves), with fewer landmarks and curves but able to encompass a broader number of taxa. The second set is mostly a subset of the first one,

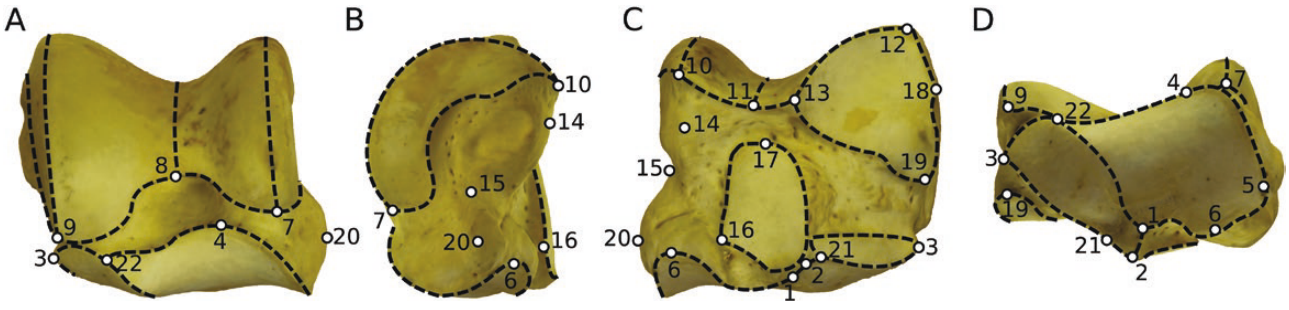

Figure 2. Representation of the landmarks and the curves placed on the astragalus of *Rhinoceros unicornis* MNHN-ZM-AC-1960-59. A, anterior; B, medial; C, posterior; and D, distal views. White dots denote the 22 anatomical landmarks, and dotted black lines the nine curves. Descriptions of the landmarks and curves are provided in Appendix S3.

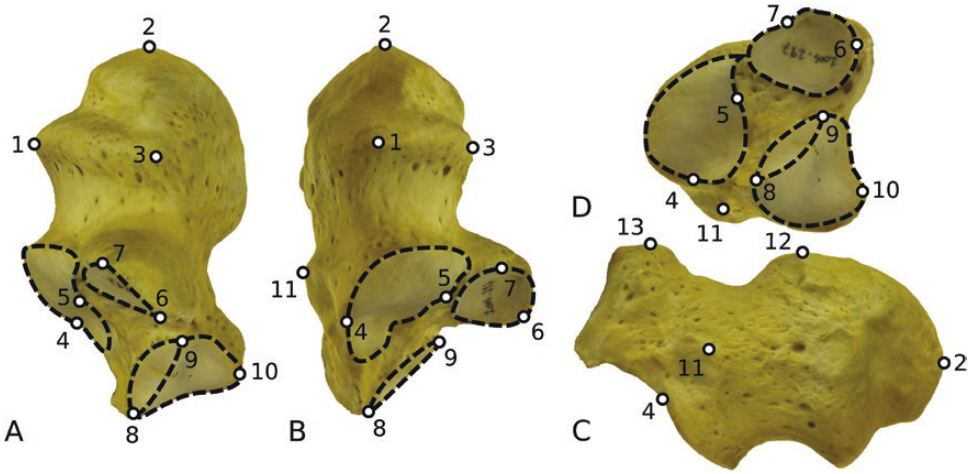

Figure 3. Representation of the landmarks and curves placed on the calcaneus of *Ceratotherium simum* MNHN-ZM-MO-2005–297. A, medial; B, anterior; C, latero-anterior; and D, distal views. White dots denote the 13 anatomical landmarks, and dotted black lines the four curves. Descriptions of the landmarks and curves are provided in Appendix S3.

so only two curves had to be redefined. Landmarks and curves were digitized on the meshes using the IDAV Landmark software package (Wiley, 2005). All the analyses and statistical tests were run using R (R Development Core Team, 2005) and RStudio (RStudio, Inc., 2018). The curves were resampled using the algorithm provided by Botton-Divet *et al.* (2016). Then, as the algorithm can result in some semi-landmarks being slightly above or below the mesh surface, the semi-landmarks were reprojected on the meshes using the closemeshKD function of the Morpho R package (Schlager *et al.*, 2018), which uses the coordinates of each semi-landmark to calculate its closest match on the surface of the mesh.

Landmarks were superimposed using a Generalized Procrustes Analysis (GPA), which translates, scales and rotates each set of landmarks to remove the information on size, position and angle, and to minimize the sum of square distances between landmark configurations (Bookstein, 1991). The curve semi-landmarks were slid along the curves to minimize the bending energy of a thin-plate-spline as described by Gunz *et al.* (2005). The bending energy is a scalar quantity that roughly represents the amount of local shape deformation between a reference set of landmarks (chosen arbitrarily among our sample). More technically, it is the integral of the squared second derivatives of the deformation (see Mitteroecker & Gunz, 2009; Gunz & Mitteroecker, 2013).

To assess the repeatability of the landmarks, and before placing the landmarks on the whole sample, we placed each landmark ten times on each of three specimens of *Diceros bicornis*, alternating between each specimen. The three specimens were assessed by sight to be the three morphologically closest. These 30 landmark sets were then superimposed using a GPA and visualized using a principal components analysis (PCA), to check that landmark error per specimen was smaller than inter-individual variation (Supporting Information, Appendix S4).

Statistical analyses

After the GPA, the aligned landmark coordinates were used in a PCA to reduce the dimensionality of our data and assess the shape variation patterns in our sample. Neighbour-joining trees were generated using a Euclidian distance matrix based on the PC-scores, in order to visualize the phenotypic similarities between each specimen or group in a multivariate manner, instead of one axis at a time, which is useful if each axis explains a small percentage of the variance. PC-scores were used instead of Procrustes coordinates to reduce the number of dimensions and thus lower the computing power required.

We tested the influence of the centroid size of each bone on its shape. Centroid size is defined as the square root of the sum of the square of the distance of each point to the centroid of the landmark set; it is most commonly used to assess the variations of shape that are due to variations of size, or allometry (Mitteroecker *et al.*, 2013; Klingenberg, 2016). Logarithms were used for the centroid size values, as recommended by Bookstein (1991) and Klingenberg (1996). Procrustes coordinates were correlated against centroid size using a multivariate regression. The allometry-free residuals from the tests were used to create allometry-free shapes for each individual, allowing analyses in which the influence of size is entirely removed (e.g. Evin *et al.*, 2011; Perrard *et al.*, 2012).

The centroid size of both bones is statistically linked to the mean mass of the species in our sample (see Supporting Information, Appendix S5; $P < 0.0001$, R^2 between 0.46 and 0.82 depending on the bone and the landmark set). The R^2 value is, however, different from 1, and therefore mass could have an influence on the shape of the bones that is independent of its centroid size. For example, two astragali or calcanei with the same centroid size belonging to species with different mean masses would exhibit divergent shapes. This was tested using a multivariate regression of the allometry-free shapes generated earlier on the logarithm of the cubic root of the mean mass of the species. Given that we could not find mass estimation for 14 sampled species, they have been removed from this analysis.

To assess the effect of shared evolutionary history of different species on the shape of the astragalus and calcaneus, the degree of phylogenetic signal in the morphological data was also assessed, using a multivariate K statistic (K-mult) based on the PC-scores. This compares the observed rate of morphological change to the expected change under Brownian motion (see Blomberg *et al.*, 2003; Adams, 2014). The phylogeny used is provided in Figure 1. The results are provided in Supporting Information, Appendix S6.

Thin plate splines were used to visualize the results of our analyses: for each set of landmarks on the calcaneus and astragalus, the mean shape generated by the GPA was mapped onto the specimen closest to the mean value. This mean-shaped model was then deformed towards the shape resulting from our analyses, for instance the shape extremes of each PCA axis.

RESULTS

Rhinocerotidae

Astragalus

Morphological variations: The neighbour-joining tree (Fig. 4) generally shows a greater morphological

proximity between members of the same species than between members of different species, which indicates that interspecific variation is generally greater than intraspecific variation. The Teleoceratina, the short-legged rhinocerotids, are clearly grouped and separated from the others, except *Diaceratherium*. Among them, *Teleoceras* has a very long branch indicating a very derived morphology for this individual. *Dicerorhinus*, *Ceratotherium simum* and *Rhinoceros* all form homogeneous groups, but *Diceros* has two specimens that are separated from the others. This might be due to them possibly either belonging to different subspecies or a different sex, but this is unknown for these specimens. All the fossil dicerorhinins (*Dihoplus*, *Stephanorhinus* and *Coelodonta*) are grouped together, but *Dicerorhinus sumatrensis* is separated from them. Aceratheriina, Elasmotheriinae, *Diaceratherium*, *Protaceratherium*, *Pleuroceros* and *Plesiaceratherium* tend to all group together, with a few exceptions. The two specimens of *Iranotherium morgani* are clearly separated from one another in the tree; this is also the case for the two *Ceratotherium neumayri* specimens. Above the tribe level, there are no clusters that seem to follow the phylogeny.

A low percentage of variance is explained by each axis of the PCA on Rhinocerotidae astragali (63.1% for the first ten axes). Only the principal components that are correlated to centroid size, or that highlight variations of shape that could be due to differences in terms of animal general body plan, are described. Thus, only PC1, PC2 and PC4 are described here. PC1 highlights differences in astragalus shape between species with different morphologies, and PC2 and PC4 are weakly but significantly correlated with centroid size. PC2 is positively correlated with centroid size ($P < 0.001$, $R^2 = 0.17$), and PC4 is negatively correlated with centroid size ($P < 0.001$, $R^2 = 0.12$). Vector representations of the deformations along the principal components are provided in Supporting Information, Appendix S7.

PC1 (14.2% of the variance, Fig. 5) strongly separates members of the short-legged Teleoceratina, on the negative side, from the other Rhinocerotidae. The axis is characterized in its negative extremity by large proximo-distal compression of the bone; a flatter and symmetrical trochlea with medio-laterally wider and lower ridges; and a trochlea with a more proximal than anterior orientation. Regarding the articular facets, at the negative side of PC1 the proximal facet with the calcaneus is distally elongate; the medial facet for the calcaneus is proximo-distally compressed, twice as broad (medio-laterally) as high (proximo-distally), and not fused to the distal facet; the distal facet for the calcaneus is medio-laterally very short; and the facet for the navicular is broader than on the positive extremity of the axis, covering most of the distal face of the astragalus.

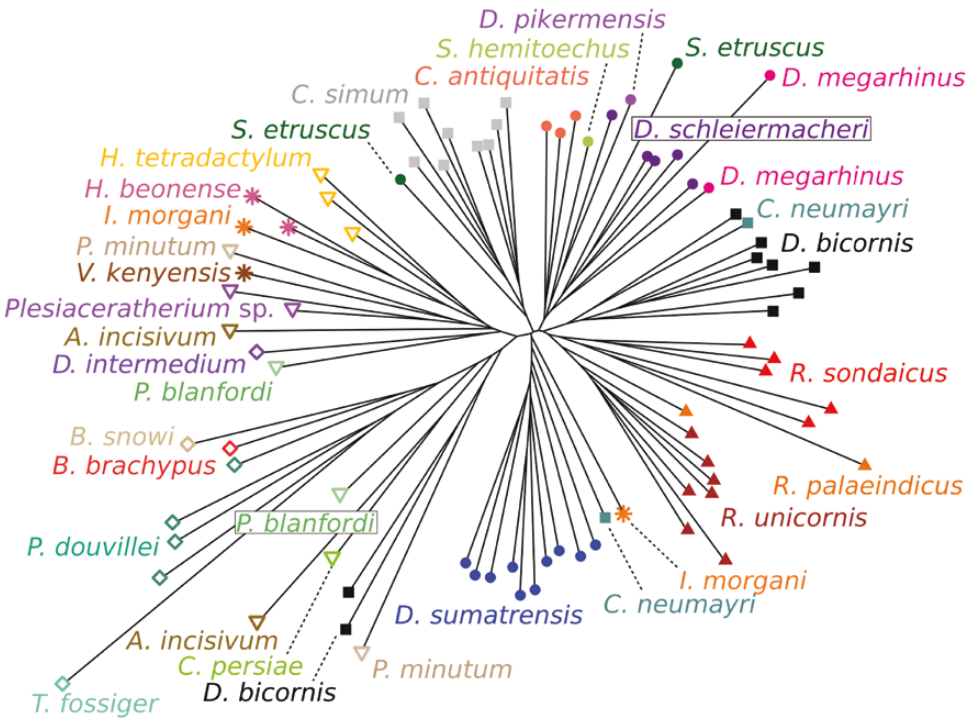

Figure 4. Neighbour-joining tree generated from a matrix of the Euclidian distance between every specimen, on the astragali of Rhinocerotidae. Legend as in Figure 5.

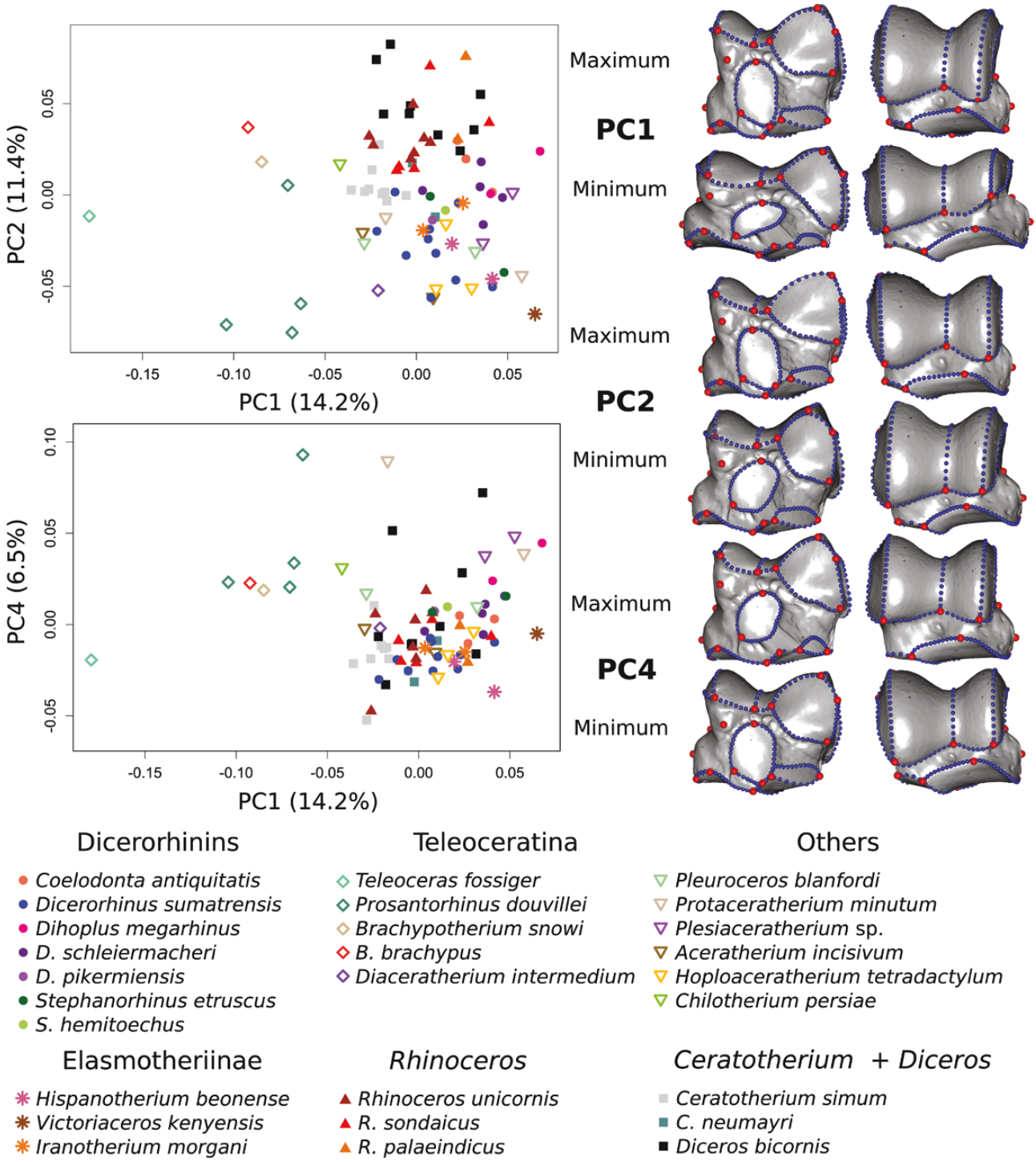

Figure 5. Results of the PCA performed on the astragalus of Rhinocerotidae. Left: repartition of the Rhinocerotidae astragali studied across PC1, PC2 and PC4. Right: thin-plate-spline deformation of a mean shape towards the maximal and minimal value of each axis. The view is first posterior then anterior. Red dots denote landmarks and blue dots denote curve semi-landmarks. Vector representations of the deformations are provided in Appendix S7A.

Along PC2 (11.4% of the variance, Fig. 5), *Diceros*, *Rhinoceros* and *Brachypotherium* are placed on the positive side, and *Dicerorhinus*, *Hoploaceratherium*, *Aceratherium*, *Hispanotherium* and *Victoriaceros* on the negative side, the other genera being scattered around the centre. Teleoceratina are spread across the

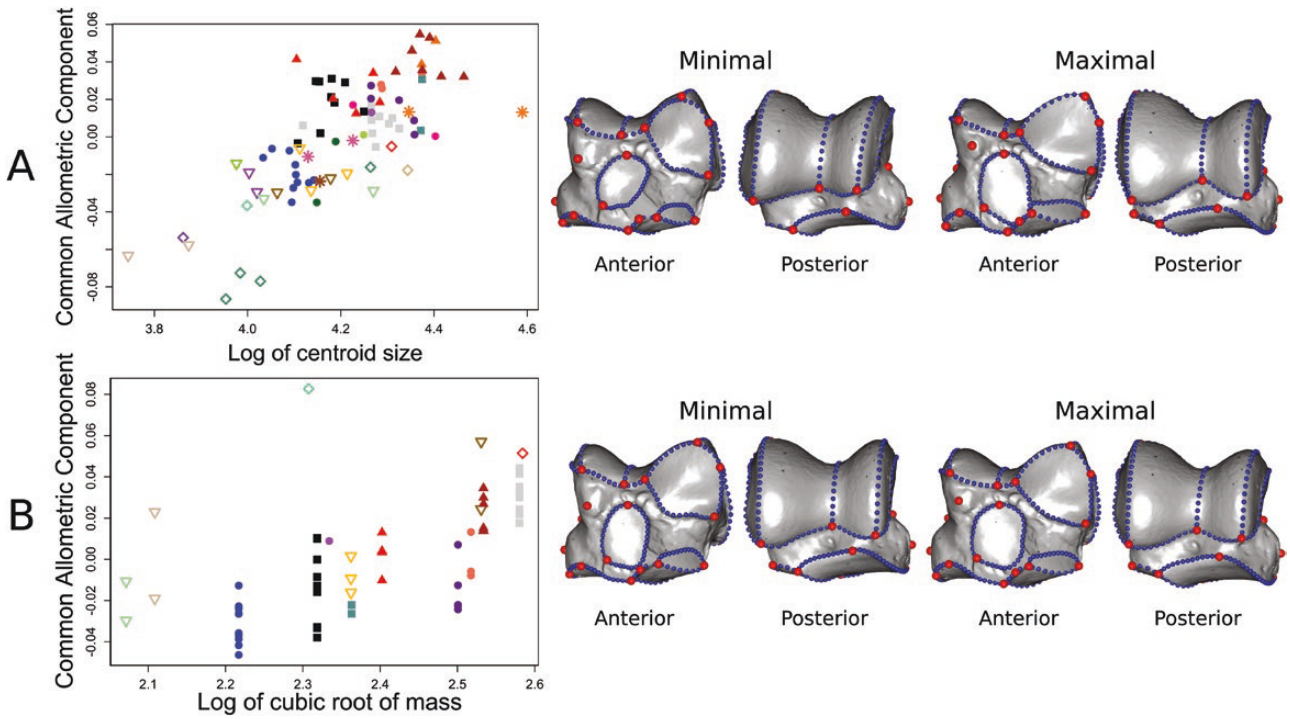

Figure 6. A, regression of the common allometric component on the logarithm of centroid size, with representations of the shapes corresponding to the theoretical maximum and minimum of allometry, on Rhinocerotidae astragali. B, regression of the common allometric component of allometry-free shapes, on the logarithm of the cubic root of the mean mass of the species, with representations of the shapes corresponding to the theoretical maximum and minimum of mass, on Rhinocerotidae astragali. Legend as in Figure 5. Vector representations are available in Appendix S7B.

whole axis. The axis is characterized at its negative extremity by a higher lateral ridge of the trochlea than observed on the positive side; a less concave distal contour of the trochlea; the pentagonal shape of the proximal facet for the calcaneus, in contrast to the medio-laterally wider triangular shape observed on the positive side; and a proximo-distal shortening of the medial facet for the calcaneus, which does not reach the distalmost point of the bone as it does on the positive side.

PC4 (6.5% of the variance, Fig. 5) shows *Protaceratherium*, *Plesiaceratherium* and *Prosantorhinus* on the positive part of the axis, and *Hispanotherium*, *Iranotherium*, *Hoploaceratherium*, *Ceratotherium*, *Dicerorhinus* and *Teleoceras* on the negative part. It is characterized at its negative extremity by a very short neck of the astragalus; a more proximal orientation of the trochlea; a distal shortening of the proximal facet for the calcaneus; and a fusion of the medial and distal facets for the calcaneus, whereas both are very well separated on the positive part of the axis.

Impact of allometry and mass: Centroid size has a significant but weak effect on the shape of the astragalus ($P < 0.01$, $R^2 = 0.04$, according to multivariate regression of the logarithm of centroid size on the Procrustes coordinates). A large astragalus (Fig. 6A) is characterized by a medio-laterally wider and triangle-shaped proximal facet with the calcaneus; medio-laterally wider and fused medial and distal facets with the calcaneus; and an articular facet with the navicular positioned less laterally offset, more directly underneath the rest of the bone.

Once the influence of centroid size is removed, there is only a weak influence of the mass of the species on the shape of the astragalus ($P < 0.05$, $R^2 = 0.03$). The shape variations are minimal: in an astragalus pertaining to a heavy species (Fig. 6B), the facets for both malleoli are enlarged, the crescent they form being wider; the proximal facet for the calcaneus is slightly more triangle-shaped; the medial facet is slightly wider medio-laterally; and the facet for the cuboid and the distal facet for the calcaneus are anteriorly extended.

Calcaneus

Morphological variations: The neighbour-joining tree based on calcaneal morphology (Fig. 7) indicates, as for the astragalus, a tendency for individuals of the

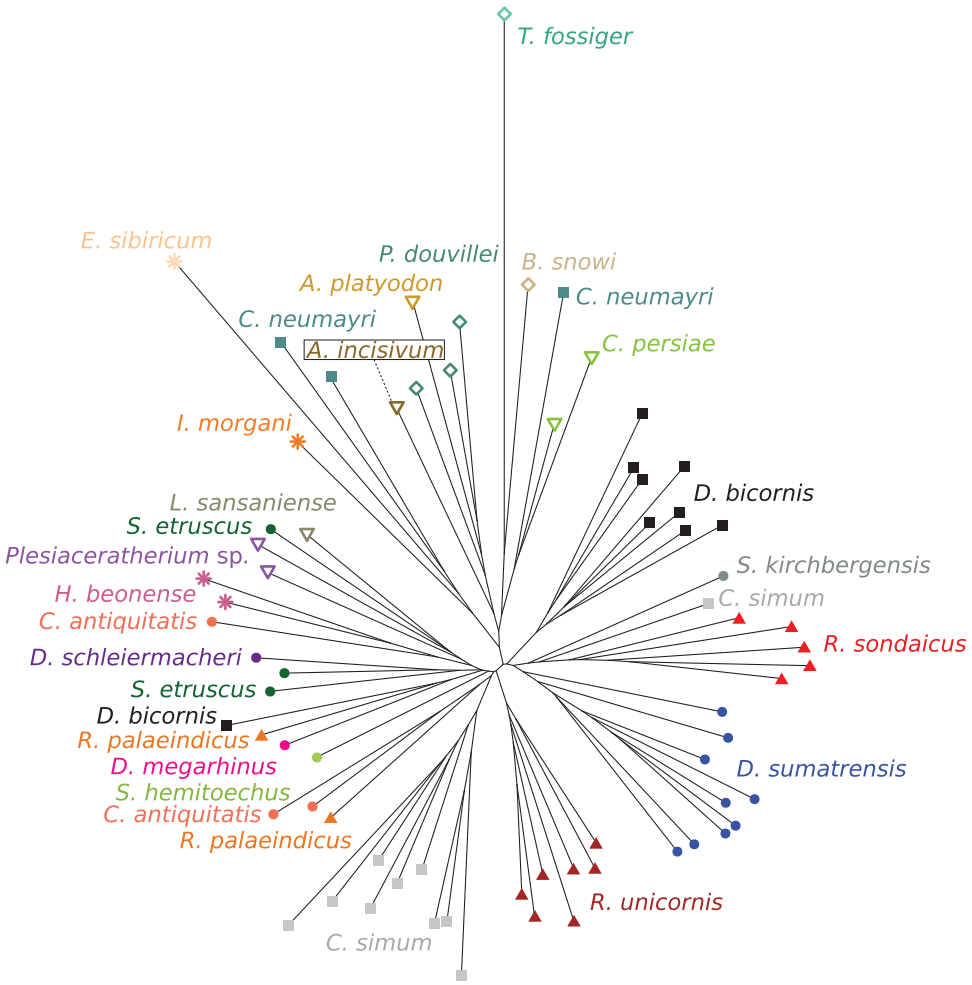

Figure 7. Neighbour-joining tree generated from a matrix of the Euclidian distance between every specimen, on the calcanei of Rhinocerotidae. Legend as in Figure 8.

same species to be grouped together. Teleoceratina are grouped with Aceratheriina, and *Teleoceras fossiger* has again the longest branch of all species. *Elasmotherium sibiricum* has also a particularly long branch. There seem to be fewer clusters of species belonging to the same higher-rank taxon than for the astragalus. Notably, the three species of the genus *Rhinoceros*, notably are scattered in the tree. *Ceratotherium neumayri* is close to *Chilotherium* and *Elasmotherium sibiricum*, and most extinct dicerorhinins are grouped with *Rhinoceros palaeindicus*, *Hispanotherium beonense* and *Plesiaceratherium*. Again, for taxa of higher rank than tribes, there are no clusters that follow the phylogeny.

As for the astragalus, a low percentage of variance is explained by each axis (66.3% for the first ten axes). Only the first two axes are described, as the first one is linked to centroid size and the second one to variations in the body plan of rhinoceroses. PC1 is weakly and negatively correlated with centroid size ($P < 0.01$, $R^2 = 0.11$).

PC1 (12.4% of the variance, Fig. 8) shows *Elasmotherium* as the genus with the most negative value, along with *Ceratotherium*, *Iranotherium* and *Lartetotherium*. *Diceros* has slightly negative values and *Rhinoceros* slightly positive values. *Dicerorhinus*, *Teleoceras* and *Brachypotherium* have the most positive values on this axis. The axis is characterized at its negative extremity by a more robust tuber calcanei; a proximal facet for the astragalus that is medio-laterally wider in its proximal half, and distally extended; a longer distal facet for the astragalus; and a larger, proximally extended facet for the cuboid whereas it is piriform (proximally reduced and distally extended) on the positive part of the axis.

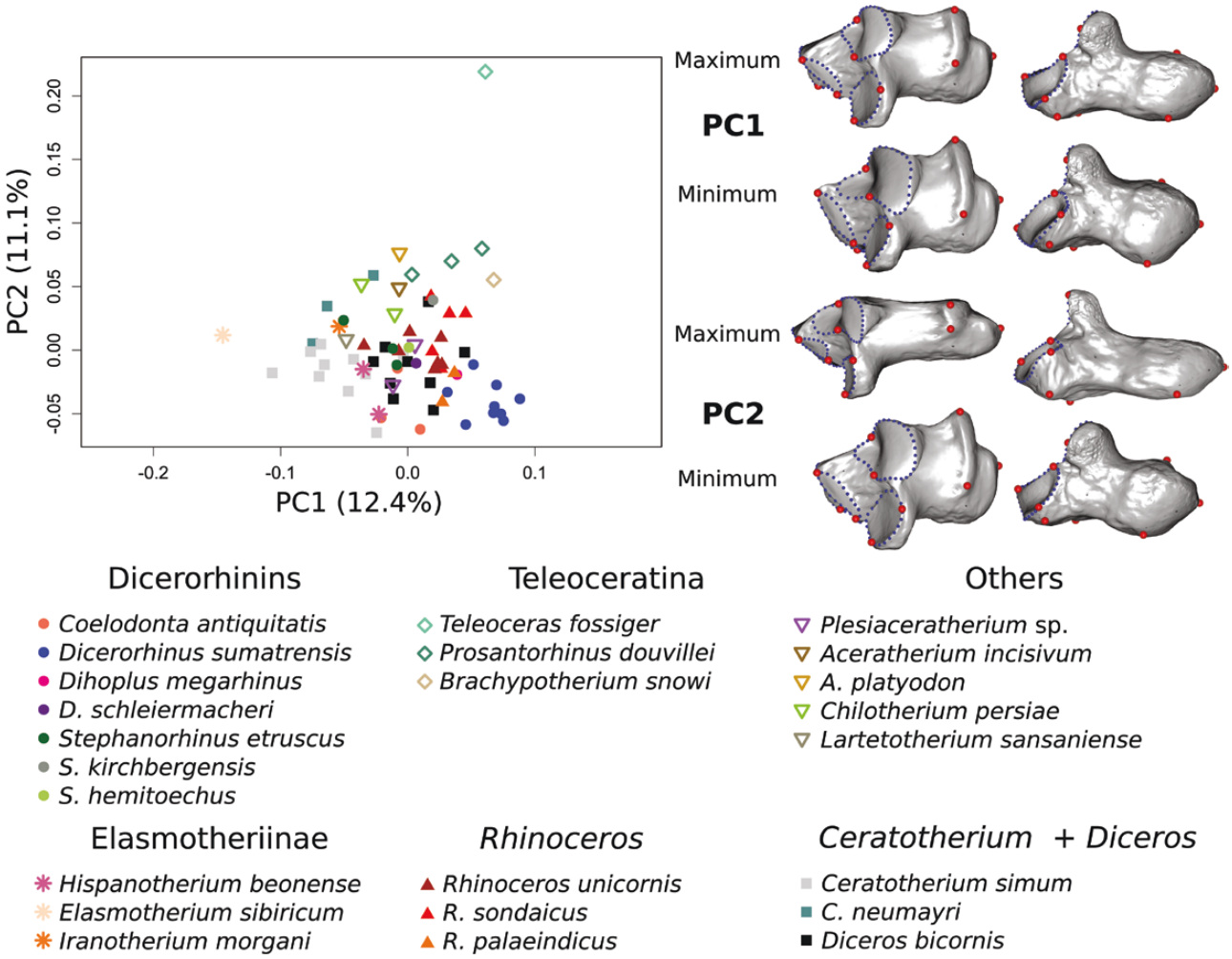

Figure 8. Results of the PCA performed on the calcanei of Rhinocerotidae. Left: repartition of the Rhinocerotidae calcanei studied across the first two PCA axes. Right: thin-plate-spline deformation of a mean shape towards the maximal and minimal values of each axis. The view is first antero-medial then postero-medial. Red dots denote landmarks and blue dots denote curve semi-landmarks. Vector representations of the deformations are provided in Appendix S7C.

PC2 (11.1%, Fig. 8) separates strongly our *Teleoceras* specimen on the negative part from the other genera. The other Teleoceratina, *Chilotherium* and *Aceratherium*, have, among the other genera, the most positive values and thus are the closest to *Teleoceras*. PC2 is characterized at its positive extremity by a more gracile tuber calcanei; a reduction of the medio-lateral width of the proximal part of the proximal facet for the astragalus; a medio-laterally wider and distally longer distal part of the proximal facet for the astragalus than on the negative extremity of the axis; a proximo-distally compressed medial facet for the astragalus (twice as wide as it is high); a much less elongated distal facet for the astragalus; and an antero-posteriorly compressed facet for the cuboid.

Impact of allometry and mass: Centroid size has a significant but weak effect on the shape of the calcaneus ($P < 0.01$, $R^2 = 0.04$; multivariate regression). A large calcaneus (Fig. 9A) has a medio-laterally wider proximal part of the proximal facet for the astragalus; a wider medial facet for the astragalus, expanding distally and merging with the distal facet for the astragalus; an elongated distal facet for the astragalus; and a sustentaculum tali orientated more distally, whereas it is orientated antero-distally in small calcanei.

Mass has a slightly stronger influence on the allometry-free shapes of the calcaneus than on those of the astragalus ($P < 0.001$, $R^2 = 0.06$). A calcaneus belonging to a heavy species (Fig. 9B) has a more robust tuber calcanei than a calcaneus belonging to a light

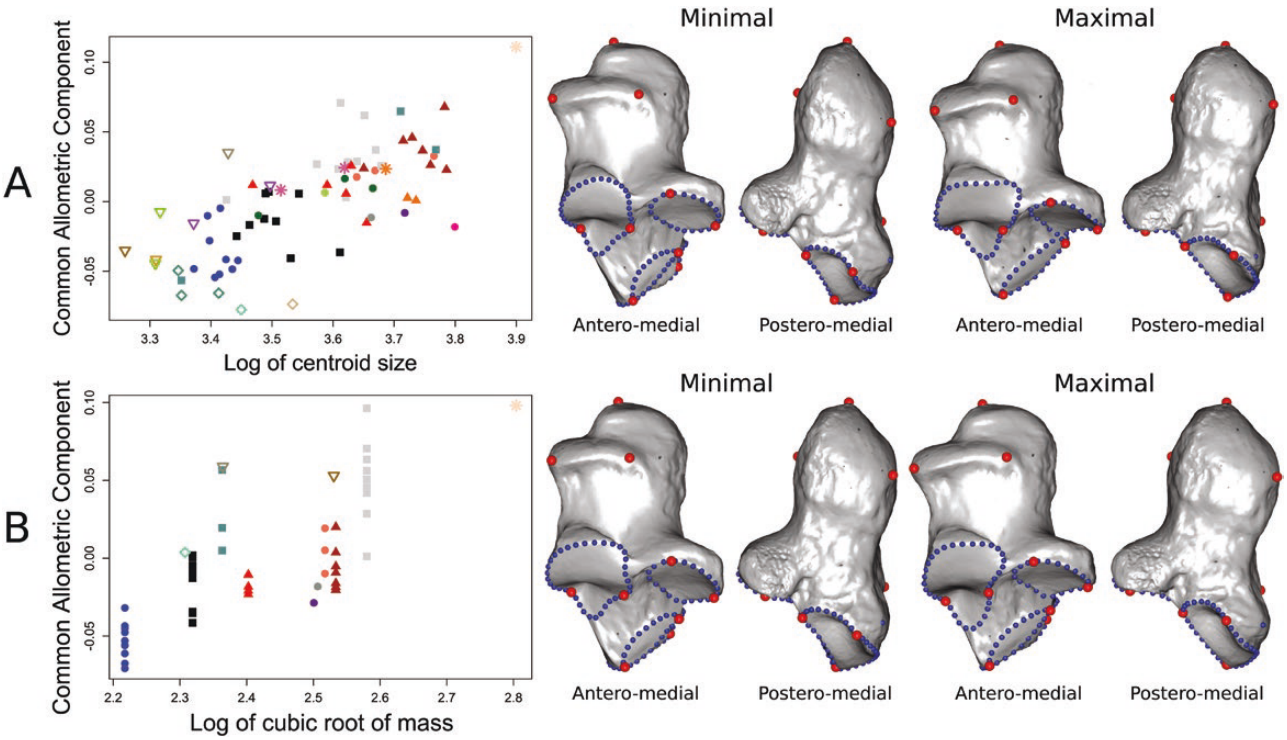

Figure 9. A, regression of the common allometric component on the logarithm of centroid size, with representations of the shapes corresponding to the theoretical maximum and minimum of allometry, on Rhinocerotidae calcanei. B, regression of the common allometric component of allometry-free shapes, on the logarithm of the cubic root of the mean mass of the species, with representations of the shapes corresponding to the theoretical maximum and minimum of mass, on Rhinocerotidae calcanei. Legend as in Figure 8. Vector representations are available in Appendix S7D.

species; the proximal facet for the astragalus is more triangular, and slightly extended medially; the distal facet for the astragalus is extended distally; and the facet for the cuboid is piriform, and wider proximally.

PERISSODACTYLA

Astragalus

The neighbour-joining tree based on astragalar morphology (Fig. 10) shows a relative clustering of the families, with some exceptions. *Moropus* is not grouped with the other chalicotheres but is closer in morphology to the Rhinocerotidae, although it has a long branch, which indicates a particular morphology. *Kalobatippus*, a three-toed anchitheriine equid from the Oligocene, has a morphology closer to tapirs and rhinocerotids than to a modern one-toed equinine or hipparionine equid. The Teleoceratina are found relatively close to *Paraceratherium*, and to a lesser extent to the Chalicotheriinae, as compared to other rhinocerotids. *Teleoceras* itself is closest to the Chalicotheriinae, sharing with them an extremely proximo-distally flattened astragalus. Families are not grouped together according to phylogenetic proximity.

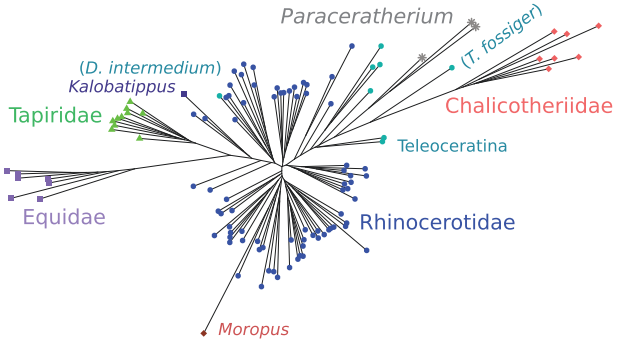

Figure 10. Neighbour-joining tree generated from a matrix of the Euclidian distance between every specimen, on the astragali of Perissodactyla. Extant species are represented as dots and extinct species as squares. Teleoceratina, *Kalobatippus* and *Moropus* belong to Rhinocerotidae, Equidae and Chalicotheriidae, respectively, but are highlighted with regard to their particular positions in the tree. Legend as in Figure 11.

The first three axes of the PCA are presented, as only those axes describe clear shape variations between the families studied, and are correlated with centroid size (PC1 and PC3, negatively: $P < 0.0001$, $R^2 = 0.28$

and $P < 0.001$, $R^2 = 0.19$ respectively; PC2, positively: $P < 0.01$, $R^2 = 0.05$). PC1 and PC3 are more strongly correlated with centroid size than on the analysis with only the Rhinocerotidae, but the R^2value remains well below 50%. The first ten axes explain 77.8% of the variance.

PC1 (37.2% of the variance, Fig. 11) separates five different groups: on the most positive part of the axis are the Equinae. Less positive are the Tapiridae, plus *Kalobatippus*. Around values of 0 are the Rhinocerotidae, except the Teleoceratina, plus *Moropus*. On the negative side are first *Paraceratherium* and the Teleoceratina, our *Teleoceras* specimen having the most negative value among them. The Chalicotheriinae have the most negative values, these being chalicotheres with very short hindlimbs. PC1 is characterized at its negative extremity by a great proximo-distal compression of the bone, twice as wide medio-laterally as high proximo-distally, whereas astragali on the positive end of the axis are approximately equal in width and height. The negative extremity of the axis is also characterized

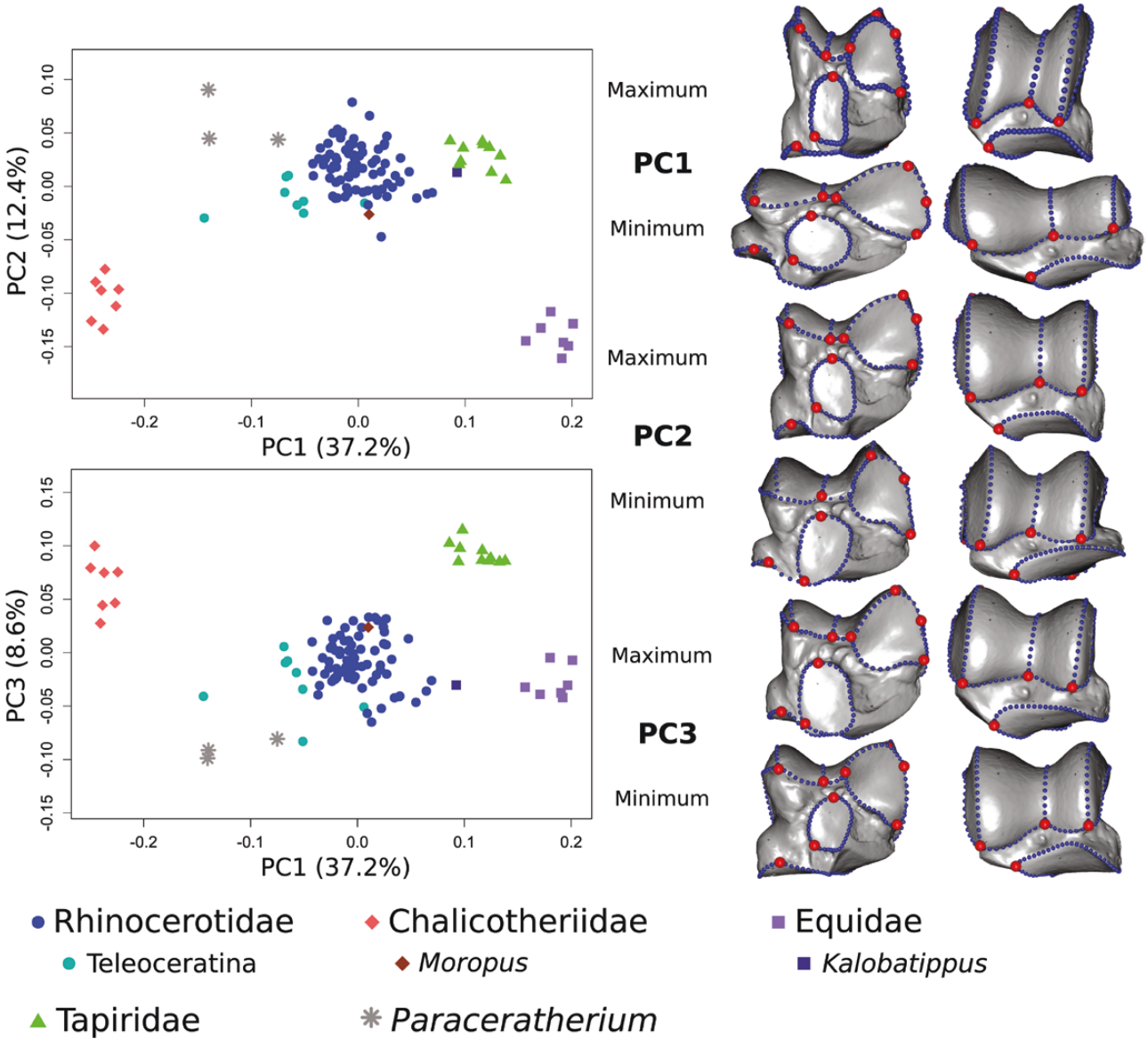

Figure 11. Results of the PCA performed on the astragalus of Perissodactyla. Left: repartition of the Perissodactyla astragali studied across the first three PCA axes. Right: thin-plate-spline deformation of a mean shape towards the maximal and minimal value of each axis. The view is first posterior then anterior. Red dots denote landmarks and blue dots denote curve semi-landmarks. Vector representations of the deformations are provided in Appendix S7E.

by a very flat trochlea with medio-laterally wide, low ridges and a shallow groove, orientated proximally, whereas the trochlea has very high ridges, a very deep groove and is orientated anteriorly on the positive end of the axis; and an extended facet for the fibular malleolus, occupying almost all of the lateral face of the astragalus. Finally, the negative part of PC1 presents a triangular and flat proximal facet for the calcaneus, whereas it is more squared and concave, with a latero-distal extension, on the positive side; a round medial facet for the calcaneus, whereas it is proximo-distally elongated on the positive end of the axis; and an overall wider and flatter facet for the navicular, positioned directly below the body of the astragalus.

PC2 (12.4% of the variance, Fig. 11) separates Equidae (except *Kalobatippus*) and Chalicotheriidae (except *Moropus*) on the negative side from the other families which have more positive values, *Paraceratherium* having the most positive values among them. Astragalar shape variations along PC2 are characterized at the negative extremity by the symmetry of the trochlea, each ridge being of similar height and width whereas the lateral ridge is relatively much wider on the positive end of the axis; the deeper groove of the trochlea; and the greater angular extent of the trochlea. The negative part of PC2 is also characterized by the round shape of the proximal facet for the calcaneus, with a latero-distal extension, whereas it is more square-shaped on the positive end of the axis; the wider medial facet for the calcaneus, positioned very distally, on the edge of the posterior face; the concavity of the lateral contour of the facet for the navicular; the great flatness of the facet for the navicular, whereas it is antero-posteriorly convex on the positive end of the axis; and its position medially offset from the centre of the bone.

On PC3 (8.6% of the variance, Fig. 11) are spread, roughly, from negative values to positive values, *Paraceratherium*, the Rhinocerotidae and Equidae, the Chalicotheriidae, and the Tapiridae, although there is generally an overlap between groups. It is characterized at its negative extremity by a slightly less symmetrical trochlea, with a wider and lower lateral ridge; a distally extended lateral ridge of the trochlea; and a smaller facet for the fibular malleolus, occupying a smaller part of the lateral face of the bone than it does on the positive end of the axis. The negative section of PC3 morphospace is also characterized by a latero-distally extended proximal facet, and a smaller medial facet for the calcaneus, which is positioned more proximally. By comparison, bones at the positive end of PC3 possess medial facets which border the distal side of the posterior face.

Impact of allometry and mass: The centroid size of the astragalus has a significant effect on its shape ($P < 0.001$ and $R^2 = 0.14$ for the astragalus, multivariate regression). A large astragalus (Fig. 12A) is characterized by an overall flat bone, twice as wide medio-laterally as high proximo-distally; medio-laterally wide and low trochlear ridges; a trochlea orientated proximally; a medio-laterally wide and triangle-shaped proximal facet for the calcaneus; a round-shaped medial facet for the calcaneus; and a wide facet for the navicular, which is flat overall and positioned below the body of the astragalus. A small astragalus is as wide as it is high, has higher trochlear ridges and a deeper trochlear groove; a more square-shaped proximal facet for the calcaneus, with a small latero-distal extension; a rectangle-shaped medial facet for the calcaneus, higher proximo-distally than wide medio-laterally; and a smaller facet for the navicular, not directly below the body of the astragalus but medially offset.

Species mass has a statistically significant but very weak effect on allometry-free astragalus shape ($P < 0.05$, $R^2 = 0.027$). An astragalus pertaining to a heavier species (Fig. 12B) has a flatter trochlea with lower ridges; a triangle-shaped proximal facet for the calcaneus; and a medial facet for the calcaneus located more laterally.

Calcaneus

The neighbour-joining tree based on calcaneus morphology (Fig. 13) also shows a relative homogeneity of the families. The closest specimen to the *Paraceratherium* specimen is *Teleoceras fossiger*. Contrary to what was observed for the astragalus, *Moropus* is grouped with the other Chalicotheriidae, although it is not as close to them as they are to each other. Again, families are not grouped following their phylogenetic relationships.

The first two axes are described, as both of them are correlated to centroid size and show clear distinctions between families. PC1 and PC2 are positively correlated with centroid size ($P < 0.001$, $R^2 = 0.27$ and $P < 0.01$, $R^2 = 0.08$, respectively). Again, PC1 is more strongly correlated with regard to size than on the analysis with Rhinocerotidae alone, but the R^2 value remains well below 0.5. The first ten axes explain 79.3% of the variance.

PC1 (31% of the variance, Fig. 14) separates (from the most negative to the most positive values): the Tapiridae, Equidae, Chalicotheriidae, and Rhinocerotidae along with *Paraceratherium*. It is characterized at its negative extremity by a far more elongate and thin tuber calcanei; a relatively smaller proximal facet for the astragalus, reduced proximally, distally and anteriorly; and a smaller facet for the cuboid, narrower because of a postero-lateral reduction.

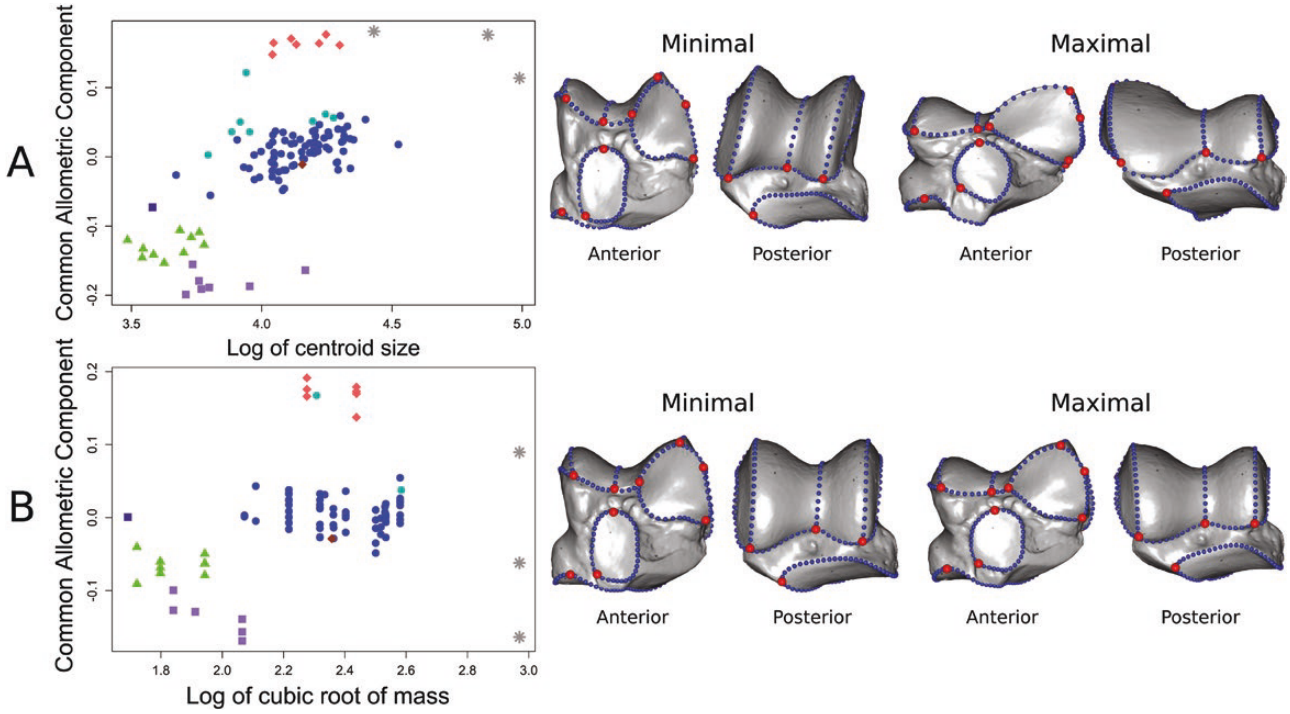

Figure 12. A, regression of the common allometric component on the logarithm of centroid size, with representations of the shapes corresponding to the theoretical maximum and minimum of allometry, on Perissodactyla astragali. B, regression of the common allometric component of allometry-free shapes, on the logarithm of the cubic root of the mean mass of the species, with representations of the shapes corresponding to the theoretical maximum and minimum of mass, on Perissodactyla astragali. Legend as in Figure 11. Vector representations are available in Appendix S7F.

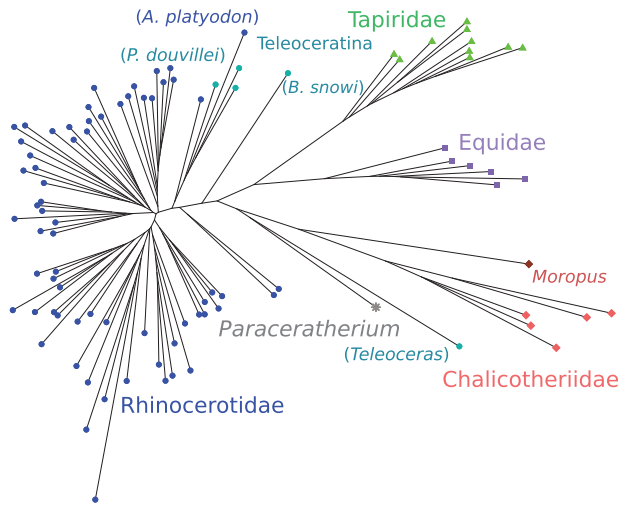

Figure 13. Neighbour-joining tree generated from a matrix of the Euclidian distance between every specimen, on the calcanei of Perissodactyla. Teleoceratina and *Moropus* belong to Rhinocerotidae and Chalicotheriidae, respectively, but are highlighted with regard to their particular positions in the tree. Legend as in Figure 14.

PC2 (16% of the variance, Fig. 14) strongly separates the Chalicotheriidae on the positive side from all the others. Our specimen of *Moropus* has a slightly less positive value than the Chalicotheriinae, and the Tapiridae have more negative values than the Equidae, Rhinocerotidae and *Paraceratherium*. The axis is characterized at its positive extremity by a more elongate and thin tuber calcanei; a head of the calcaneus that is much shorter, accounting for approximately one-third of the total length of the bone whereas on the negative end, it accounts approximately for one-half; a slightly wider, more distally orientated and much more proximally positioned facet for the cuboid, almost in contact with the proximal facet for the astragalus; a proximal facet for the astragalus that is distally very extended; and a wider medial facet for the astragalus, extended medially.

Impact of allometry and mass: The centroid size of the calcaneus has a significant influence on its shape ($P < 0.001$ and $R^2 = 0.11$, multivariate regression). A large calcaneus (Fig. 15A) is characterized by an extreme proximo-distal compression, the

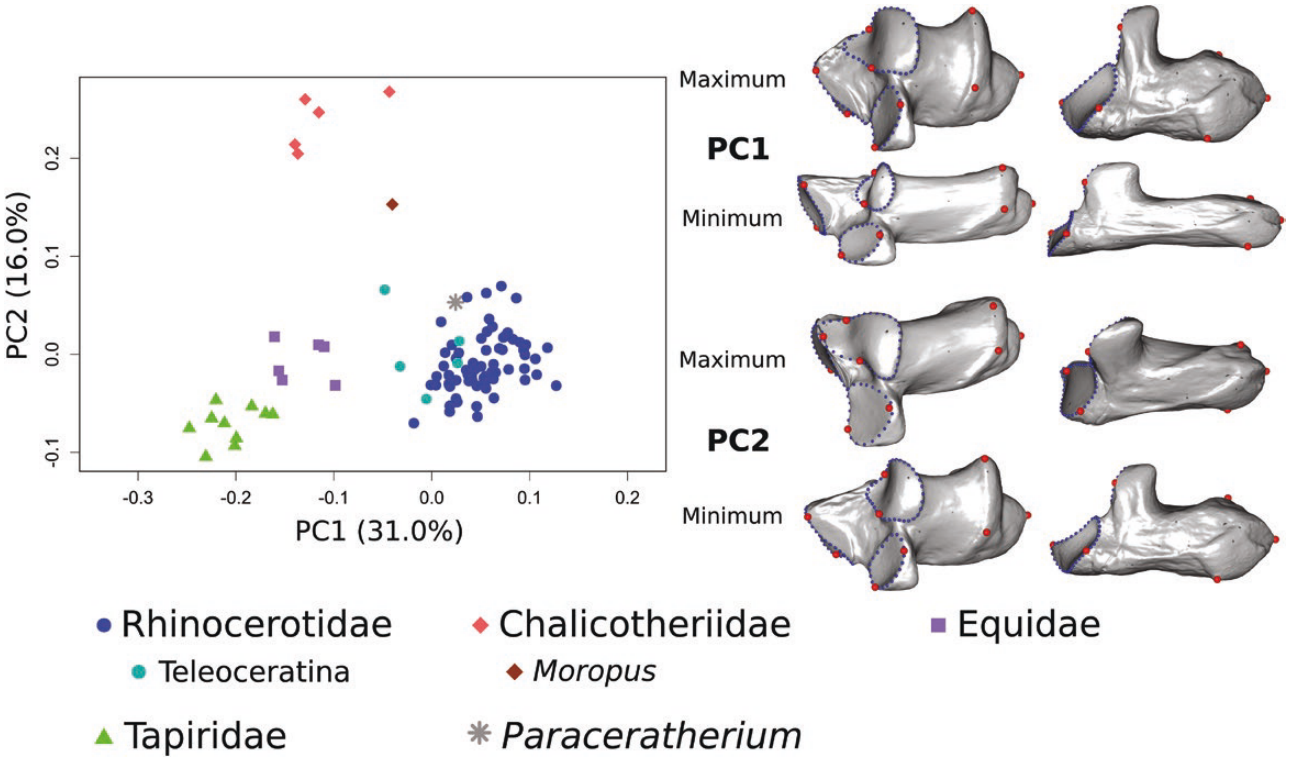

Figure 14. Results of the PCA performed on the calcaneus of Perissodactyla. Left: repartition of the Perissodactyla calcanei studied across the first two PCA axes. Right: thin-plate-spline deformation of a mean shape towards the maximal and minimal value of each axis. The view is first antero-medial then postero-medial. Red dots denote landmarks and blue dots denote curve semi-landmarks. Vector representations of the deformations are provided in Appendix S7G.

tuber calcanei being very robust; a much wider proximal facet for the astragalus, extended in all directions, especially in its proximal half; a distally orientated sustentaculum tali and medial facet for the astragalus; and a wider facet for the cuboid, triangle-shaped and latero-posteriorly extended. A small calcaneus has a very thin tuber calcanei as compared to a large calcaneus; a relatively much smaller overall proximal facet for the astragalus; an anteriorly orientated sustentaculum tali and medial facet for the astragalus; and a relatively smaller facet for the cuboid.

There is a statistically significant influence of species mass on allometry-free calcaneus shape ($P < 0.001$, $R^2 = 0.09$). Shape differences are clear (Fig. 15B), unlike those observed for the same analysis on Rhinocerotidae alone. In our sample, a calcaneus belonging to a heavier species is, on average, characterized by a stouter tuber calcanei; a wider overall proximal facet for the astragalus; a slightly wider medial facet for the astragalus, orientated distally along with the whole sustentaculum tali; and a wider facet for the cuboid, expanding more proximally.

DISCUSSION

First and foremost, it is worth noting that the percentage of variance explained by the first axes of the PCA is usually low (around 66% for the first five axes for the Perissodactyla dataset, 40% for the Rhinocerotidae dataset). The first four or five axes describe the variations between species or families, but the following axes usually distinguish one or two individuals from other specimens of the same taxon. There is indeed great intraspecific variation in the species studied, even if it remains inferior to interspecific variations (Figs 4, 7). For example, *Dicerorhinus sumatrensis* ZSM-1908-571 presents an astragalus with a wide medio-distal extension of the medial facet for the calcaneus, an extension that is absent in all the other specimens. Some specimens of *Ceratotherium simum* present a calcaneus with a fusion of the medial and distal facets for the astragalus, whereas in others they are separated by a deep groove. This could explain the low PC-scores. Indeed, if there are many different variations observed in the sample, these cannot be described on one PC

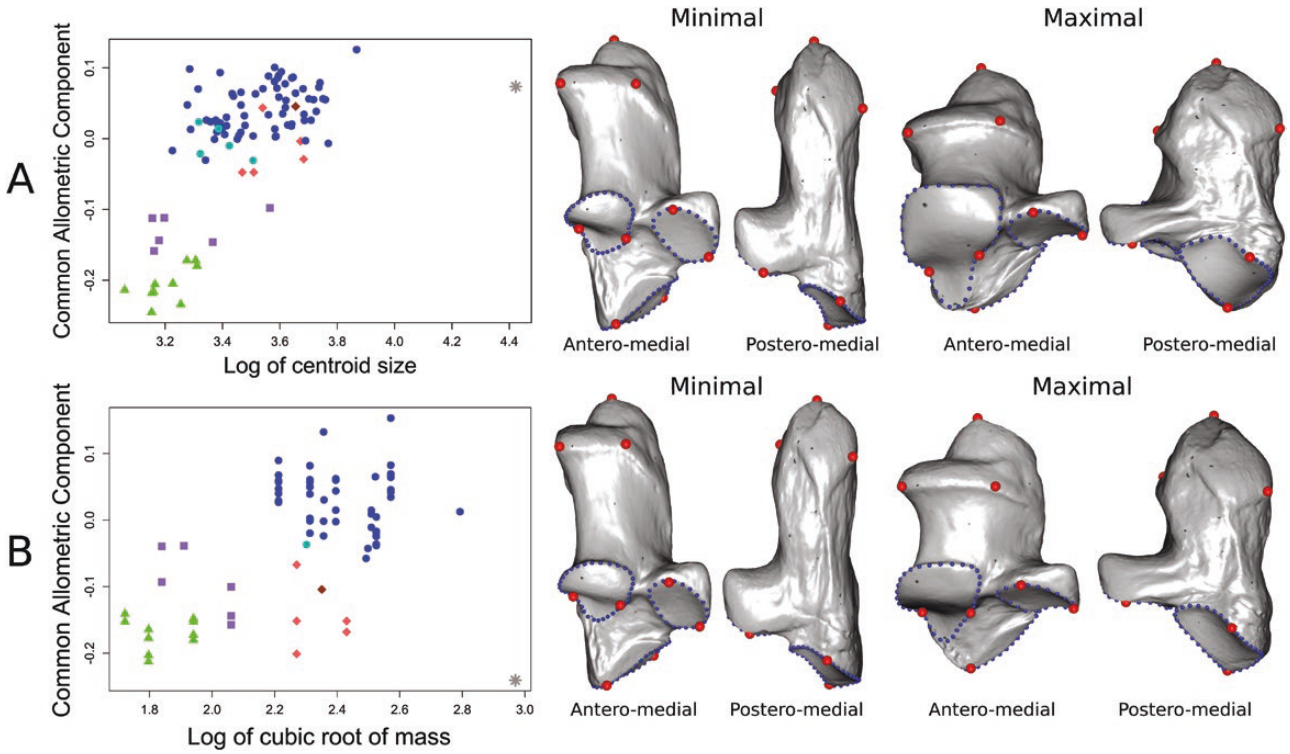

Figure 15. A, regression of the common allometric component on the logarithm of centroid size, with representations of the shape corresponding to the theoretical maximum and minimum of allometry, on Perissodactyla calcanei. B, regression of the common allometric component of allometry-free shapes, on the logarithm of the cubic root of the mean mass of the species, with representations of the shape corresponding to the theoretical maximum and minimum of mass, on Perissodactyla calcanei. Legend as in Figure 14. Vector representations are available in Appendix S7H.

alone and thus the percentage of variation explained by the first axes decreases. On the other hand, if there were a factor clearly driving a continuum of variations in all our sample, we would see a higher percentage of variance for the first axis. That factor is often size (e.g. Bonnan *et al.*, 2013; Cardini *et al.*, 2015; Knigge *et al.*, 2015); here it seems clear that size does not have a strong influence on the shape of the bones, especially in our Rhinocerotidae dataset. We have already noted qualitatively this intraspecific variability between individuals of the same species of Rhinocerotidae when digitizing the bones. It has also been observed by Guérin (1980) on various bones of the tarsus of extant rhinocerotids, by Harrison & Manning (1983) on the carpus bones of *Teleoceras*, and by Heissig (2012) on several limb bones, including the astragalus, of aceratheres. Variations in the age of the specimens, especially for individuals for which we have only an astragalus and no calcaneus or long bones associated, could account for some intraspecific variation. It is difficult to determine the age of individuals using only the astragalus, given that there is no epiphysis on this bone. Additionally, the large number of species, mostly with only one or two individuals, could also result in a greater diversity of morphological variations in our sample and thus lower the variance explained by the first axes. Finally, it appears that Rhinocerotids are a relatively conserved group in terms of the morphology of their astragalus and calcaneus. This could mean that PC scores are driven more by small, individual-specific or species-specific variations than by large-scale variations such as those linked to size or mass.

General influence of mass

The centroid size of both the astragalus and the calcaneus has an effect on their shape (Figs 6, 9). Given that the centroid size of the bone is linked to the mean mass of the species to which it belongs (Supporting Information, Appendix S5), especially on the Perissodactyla dataset, this means that mass has an influence on the shape of the bones in our sample of Perissodactyla. The percentage of variance explained by centroid size or mass, however, is lower than we originally expected. We could indeed expect mass to have a very strong influence on the shape of limb bones, explaining at least 50% of the total variance (Hildebrand *et al.*, 1985; Biewener, 1989; Campione

& Evans, 2012). It appears that, especially when studying only astragali and calcanei of rhinocerotids, which do not vary much in terms of shape, size has no overwhelming influence on the shape of the bone but is instead one factor among others (e.g. possibly habitat, phylogeny and intraspecific variations). Another study on the limb long bones of extant rhinocerotids found a relatively low influence of centroid size on the shape of the bones, although higher than observed here (R^2 between 10 and 18%; Mallet *et al.*, 2019). It is therefore possible that long bones are more affected by size than astragalus and calcaneus.

When centroid size increases, both the astragalus and the calcaneus show an increase in the size of the articular facets. Moreover, in the analysis on Rhinocerotidae alone, the distal and medial facets of each bone for the articulation with the other are fused in specimens with a high centroid size. It could be suggested that wider facets result in a more intricate association between the bones, making the talocalcaneal complex more suited to dissipate compressive forces during limb loading, during plantarflexion or during dorsiflexion of the foot (i.e. flexion or extension of the ankle). In the large astragali belonging to Perissodactyla, the trochlea is orientated proximally, directly facing the tibia and fibula, and has a lower angular extent (Fig. 12). One can assume that this orientation permits complete unfolding of the crurotarsal joint, placing the foot in the same axis as the rest of the limb. This results in a general columnar posture for the limb, as is characteristic of graviportal animals. This columnar posture would help resist twisting, bending and compression forces, and reduce the possibility of dorsiflexion of the autopodium, which would reduce maximal stride length and thus running speed (Hildebrand, 1982). *Paraceratherium* is reported to have had columnar limbs (Osborn, 1923; Prothero, 2013), and our results corroborate this, for the hind autopodium–zeugopodium at least. It can be assumed that the flatter trochlea observed in large astragali, associated with a proximo-distal compression of the bone, fulfils the same role of resistance to twisting and compression. A deeper trochlea would provide more stability for the crurotarsal joint (Polly, 2008), but lead to thinner and therefore more fragile ridges of the trochlea, unable to resist the high forces expected on the ankle of a very heavy animal. This flattening is also observed in Brontotheriidae (Osborn, 1929), Elephantidae (Csuti *et al.*, 2008) and sauropod dinosaurs (Bonnan, 2005), which supports our hypothesis.

For large calcanei belonging to Perissodactyla, beyond the increasing size of the articular surfaces, the main characteristic is that the tuber calcanei is more robust, thicker both medio-laterally and antero-posteriorly, and shorter proximo-distally compared to the total length of the calcaneus (Fig. 15). However, this is only clearly observable when studying our Perissodactyla dataset. The tuber calcanei is a lever arm for the plantarflexion of the foot; two of the muscles inserting on it are responsible for plantarflexion: the gastrocnemius and the soleus (Beddard & Treves, 1889; White & Folkens, 2005). A more robust and shorter tuber would presumably lead to a lower mechanical advantage, requiring a weaker pull from the muscles, which would be easier to resist and reduce bending stress. It could also be a consequence of the proximo-distal shortening of the foot generally observed in heavier species of our sample (Rhinocerotidae, Chalicotheriidae). An animal with an elongated foot would need a longer tuber calcaneus to keep the mechanical advantage constant; conversely, an animal with a short foot would not need a very long lever arm, assuming the mechanical advantage is indeed constant (Biewener, 1989). The correlation of the mean mass of the species on allometry-free shapes of the calcaneus corroborates this result. For two calcanei of the same size but belonging to species of different masses, the one belonging to the heaviest species will have a more robust tuber and wider articular facets (Fig. 15B). This is observable in our analysis in *Ceratotherium simum* and *Rhinoceros unicornis: C. simum* is heavier and has a slightly more robust calcaneus, but on average, the centroid size of its calcaneus is smaller than that of *R. unicornis* (Figs 5, 6). This increased robustness of the body of the calcaneus is found in other mammal families of high body mass (i.e. more than about 2 tons), such as Elephantidae (Chen & Tong, 2017), and also in fossils such as *Pyrotherium* (Shockey & Anaya Daza, 2004). Interestingly, this is not the case in Hippopotamidae, which have a rather elongate calcaneus (e.g. Fisher *et al.*, 2010: figs 6, 8). Hippopotamuses have a body plan close to Teleoceratina, with very short limbs, which also present an elongate calcaneus. Possibly the forces exerted on the calcaneus are less intense for animals with short legs; comparisons with Suidae and Amynodontidae, for example, could yield insights in this regard.

Particular cases linked to body plan and locomotion

As expected, some observed variations in bone shape appear to be linked to the diverse body plans and modes of locomotion of the taxa studied. For the astragalus, equids are characterized by the great depth of their trochlea, a common characteristic in cursorial mammals that provides stabilization of the crurotarsal joint by restricting movement to a parasagittal plan (Polly, 2008). The trochlea is also moderately deep in Rhinocerotidae (except most Teleoceratina) and

Figure 16. Anterior views of the calcanei of *Paraceratherium bugtiense* NHM-PAL-PV-M-100418 (Paraceratheriidae) and *Elasmotherium sibiricum* NHM-PAL-PV-M-12429 (Rhinocerotidae).

Tapiridae, but not in our Chalicotheriinae, animals that probably could not gallop (Coombs, 1983). Teleoceratina specimens also possess very shallow trochleas. Considering their similarity in terms of body plan with hippopotamuses, which cannot gallop (Lewison 2011), it is likely that they could not gallop either, and the shape of their astragalus is consistent with this. *Paraceratherium* and the Chalicotheriinae possess the flattest trochlea of all of our specimens, but still with clearly distinguishable ridges (Figs 11, 12), unlike elephants for instance (e.g. Scarborough *et al.*, 2016). Equids also display a greater angular extent of their trochlea, presumably allowing a greater flexion and extension of the ankle. The most cursorial species (i.e. equids and, to a lower extent, tapirs) possess, on their astragalus, curved facets for the navicular and a curved proximal facet for the calcaneus, whereas those facets are mostly flat in *Paraceratherium* and *Chalicotherium* (Fig. 11). Perhaps the curved facets help to lock the talocalcaneal and talonavicular joints and provide stability for the ankle. The flat facets of heavy species could help to dissipate the forces in the foot homogeneously and facilitate the formation of robust ridges.

A particular shape variation linked to body proportions is the proximo-distal compression of the astragalus across most of our Teleoceratina (Fig. 5). *Diaceratherium* is the only Teleoceratina from our sample having an astragalus similar to that of other rhinocerotids in this regard. Teleoceratina had extremely short, columnar limbs, like modern hippopotamuses. This compression of the astragalus could be linked to the general shortening of the limbs, each segment being proximo-distally shortened, including the basipodium. Interestingly, the astragalus is not compressed in *Diaceratherium intermedium*, a Teleoceratina that is phylogenetically the sister-group to the other Teleoceratina from our sample (Figs 1, 5). It is unclear if *D. intermedium* was short-legged like the other Teleoceratina. The species was placed in the genus *Chilotherium* for a long time, before being reassigned by Antoine *et al.* (2020). Members of the genus *Chilotherium* are characterized by having short legs (Geraads & Spassov, 2009), but no studies have been done specifically on *D. intermedium*. If this species was indeed short-legged, the shortening of the limbs would pre-date the flattening of the astragalus in our sample. The compression of the astragalus does not seem to be dependent on the size of the animal in our Teleoceratina. This condition is observed in both small (e.g. *Prosantorhinus*; <800 kg) and large (*Brachypotherium*; >2000 kg) Teleoceratina (Cerdeño, 1998; Becker, 2003). It is of note that *Paraceratherium* presents the same flattening of the astragalus as our Teleoceratina. Both groups are indeed very close regarding the morphology of their astragalus (Figs 10, 11). *Paraceratherium* is, however, very different from Teleoceratina in that it is very long-legged. It seems that different constraints, i.e. the very high mass of *Paraceratherium* and the short legs and lower mass of Teleoceratina, can produce a similar result in terms of morphology. A study incorporating Amynodontidae (rhinocerotoids with some members, such as *Metamynodon*, being short-legged like Teleoceratina; Wall, 1989), could also yield more insights on this subject. Teleoceratina astragali also differ from those of other rhinocerotids by the distal elongation of their proximal facet with the calcaneus. The facet almost reaches the distal side of the bone, whereas it reaches only halfway in other rhinocerotids (Fig. 5). The facet might need to remain relatively long in order to maintain cohesion between the astragalus and the calcaneus. Thus, when the bone is proximally reduced, the facet retains the same length and occupies relatively more space on the posterior face. *Teleoceras* is an extremely variable genus in terms of bone morphology (Harrison & Manning, 1983), a study with more individuals could thus yield insights on more subtle shape variations.

Chalicotheriinae also present a proximo-distally compressed astragalus. They differ from Teleoceratina and *Paraceratherium* in that their trochlea is orientated more anteriorly, and has a greater angular extent. This seems logical when looking at the angle

of the crurotarsal articulation: the angle is clearly superior to 90°, almost reaching a flat angle, in *Teleoceras* and *Paraceratherium*, giving the limb a columnar posture. However, it is approximatively 90° in *Chalicotherium*, whose hindlimb is far more crouched (e.g. Coombs, 1983: fig. 7B). The extremely flattened astragalus of the Chalicotheriinae is not found in *Moropus*, which shows an astragalus closer to a rhinocerotid. The trochlea in particular is deeper in *Moropus*, whereas it is shallow in *Chalicotherium* and *Anisodon*. The extreme proximo-distal compression of Chalicotheriinae astragali could be a consequence of the reduction in the length of the hind limb, with each part of the limb being reduced, just as in Teleoceratina. This shortening could also be linked to the greater mass carried by shorter hindlimbs, whereas body mass would be more evenly spread on fore- and hindlimbs if they were of equal length. It could also be a consequence of their posture. Chalicotheriinae are indeed described as bipedal browsers. It is assumed that they could adopt an erect posture on their hindlimbs and use their forelimbs to grasp branches and twigs (Zapfe, 1979; Coombs, 1983; Schulz-Kornas *et al.*, 2007). Most of their weight would therefore be supported by the hindlimbs, which would be in accordance with a stronger, flatter astragalus as observed in *Paraceratherium*. *Moropus*, and presumably the Schizotheriinae in general, have hind- and forelimbs of approximately the same length, and were postulated to use bipedal browsing less frequently (Coombs 1982, 1989). This would reduce the advantage of a flatter astragalus. Further studies are needed to confirm or refute these hypotheses, including more individuals belonging to more genera, especially for Schizotheriinae (e.g. *Ancylotherium* or *Metaschizotherium*).

Another bone presenting a shape much different from what would be expected if mass were the single driving factor is the calcaneus of *Paraceratherium*. *Paraceratherium* is by far the heaviest species of our sample, almost twice as heavy as *Elasmotherium* (Table 1). However, its calcaneus is elongated when compared to that of *Elasmotherium*, which has the most robust calcaneus (Figs 15, 16). This could be a consequence of its general body plan: *Paraceratherium* had longer legs than all the rhinocerotids. One might thus suppose that longer legs, and thus a longer autopodium as observed in *Paraceratherium* (Prothero, 2013), would lead to an elongation of the tuber calcanei to keep the mechanical advantage of the lever system of the foot constant. Antoine *et al.* (2004) have indeed observed similarities between the calcaneus of *Paraceratherium* and that of a *Giraffa*. However, Teleoceratina have very short legs and a rather elongated calcaneus as compared to other rhinocerotids (Fig. 6), and elephants have long legs but a very short calcaneus. Other individuals of *Paraceratherium* and *Elasmotherium* are needed to confirm these results, as well as smaller members of the family Paraceratheriidae (e.g. *Pappaceras* and *Juxia*; Wang, 2016). A study including other families of Rhinocerotoidea, such as the small cursorial Hyracondontidae and the short-legged Amynodontidae could provide a better understanding of the question. Ultimately, comparing heavy and stocky mammals, such as *Mixotoxodon* (Notoungulata, Meridiungulata) or *Hippopotamus amphibus* (Hippopotamidae), with heavy and slender mammals, such as *Titanotylopus* (Camelidae) or *Giraffa camelopardalis* (Giraffidae), could also help understand the adaptations in the basipodium of *Paraceratherium*. However, in these extremely disparate taxa, one must be aware of a phylogenetical signal that could mask the changes of shape linked to mass. It is unclear what gait *Paraceratherium* was capable of adopting besides walking. Paul & Christiansen (2000) have suggested it could at least attain a trot. The fact that their astragalus retains clear ridges and that their calcaneus is quite elongated, characteristics reminiscent of cursorial animals (Polly, 2008; Bassarova *et al.*, 2009), is consistent with this suggestion. Elephants possess a completely flat trochlea and a short calcaneus, and are incapable of trotting or galloping.

CONCLUSION

Overall, it appears that mass has an influence on the shape of the astragalus and calcaneus in Rhinocerotidae and in our sample of Perissodactyla. However, that influence is lower than we initially thought, especially among Rhinocerotidae alone. This suggests that Rhinocerotidae is a relatively conserved group in terms of the morphology of those bones, and that other factors, such as phylogeny or intraspecific variations, have more influence. An ecomorphological study could help to determine if habitat could have a role, but would require reliable habitat assignations for the fossil species. Nonetheless, bones belonging to heavier Rhinocerotidae present larger articular facets, presumably to help better dissipate the larger forces involved in the locomotion of heavier animals. The calcaneus is also more robust. In our sample of Perissodactyla, a stronger influence of mass is noted, with again heavier facets and stronger bones overall. We observe a flattened trochlea of the astragalus that would limit the risk of breaking, as compared to lighter animals which have a deeper trochlea with thin ridges providing stability of the crurotarsal joint. Although these features can thus be explained morphofunctionally, the phylogenetic signal is significant and could also explain variations between the families. A larger study encompassing large and

small species of Perissodactyla will be necessary to determine more specifically what drives the shape of these bones in this order. Moreover, comparisons between rhinocerotids and other perissodactyls reveal that body plan has a clear influence on the shape of the bones. Short-legged Teleoceratina display a flattened astragalus and an elongate calcaneus. Chalicotheres with short hindlimbs also display a flattened astragalus compared to chalicotheres with hindlimbs as long as their forelimbs, perhaps linked to the increased mass supported by the hindlimbs. Finally, *Paraceratherium*, which is extremely heavy and relatively long-legged compared to other rhinocerotoids, displays a flat astragalus as expected but a relatively elongate tuber calcaneus, perhaps linked to either its elongate metapodials or its phylogenetic history.

ACKNOWLEDGMENTS

This work acknowledges funding by the European Research Council and is part of the GRAVIBONE project (ERC-2016-STG-715300) allocated to A. H. We acknowledge the very helpful comments of the three reviewers, P.-O. Antoine of the University of Montpellier, J. MacLaren of the University of Liège and M. Mihlbachler of the New York Institute of Technology, and we also would like to thank J. A. Allen of the University of Southampton for editorial work. We thank the curators of all the collections where we digitized specimens: J. Lesur, C. Bens, A. Verguin and G. Billet (Muséum National d'Histoire Naturelle, Paris, France), E. Robert (Université Claude Bernard, Lyon, France), Y. Laurent (Muséum d'Histoire Naturelle de Toulouse, Toulouse, France), C. West, R. Jennings and M. Cobb (Powell-Cotton Museum, Birchington-on-Sea, UK), P. Brewer, R. Pappa and R. Portela Miguez (Natural History Museum, London, UK), A. H. van Heteren (Zoologische Staatssammlung München, Munich, Germany), G. Rößner (Bayerische Staatssammlung fur Palaöntologie und historiche Geologie, Munich, Germany), and F. Zachos, A. Bibl and U. Göhlich (Naturhistorisches Museum, Vienna, Austria).

REFERENCES

3D Systems. **2017.** *Geomagic wrap*. Rock Hill: 3D Systems.

Adams DC. 2014. A generalized K statistic for estimating phylogenetic signal from shape and other high-dimensional multivariate data. *Systematic Biology* **63:** 685–697.

Agisoft LLC. **2017.** *Agisoft PhotoScan Professional*. St Petersburg: Agisoft.

Alexander R. 1985. Body support, scaling, and allometry. In: Hildebrand M, Bramble DM, Liem KF, Wake D, eds. *Functional vertebrate morphology*. Cambridge: Belknap Press of Harvard University Press, 26–37.

Antoine PO. 1997. *Aegyrcitherium beonensis*, nouvel élasmothère (Mammalia, Perissodactyla) du gisement miocène (MN 4b) de Montréal-du-Gers (Gers, France). Position phylogénétique au sein des Elasmotheriini. *Neues Jahrbuch für Geologie und Paläontologie – Abhandlungen* **204:** 399–414.

Antoine PO. 2002. Phylogénie et évolution des Elasmotheriina (Mammalia, Rhinocerotidae). *Mémoires du Muséum national d'Histoire naturelle* **188:** 1–359.

Antoine PO. 2020. Rhinocerotids from the Siwalik faunal sequence. In: Badgley C, Pilbeam D, Morgan M, eds. *At the foot of the Himalayas: paleontology and ecosystem dynamics of the Siwalik record of Pakistan*. Baltimore: Johns Hopkins University Press (in press).

Antoine PO, **Downing KF**, **Crochet JY**, **Duranthon F**, **Flynn LJ**, **Marivaux L**, **Métais G**, **Rajpar AR**, **Roohi G. 2010.** A revision of *Aceratherium blanfordi* Lydekker, 1884 (Mammalia: Rhinocerotidae) from the Early Miocene of Pakistan: postcranials as a key. *Zoological Journal of the Linnean Society* **160:** 139–194.

Antoine PO, **Shah SMI**, **Cheema IU**, **Crochet JY**, **De Franceschi D**, **Marivaux L**, **Métais G**, **Welcomme JL. 2004.** New remains of the baluchithere *Paraceratherium bugtiense* (Pilgrim, 1910) from the Late/latest Oligocene of the Bugti hills, Balochistan, Pakistan. *Journal of Asian Earth Sciences* **24:** 71–77.

Artec 3D. **2018.** *Artec Studio Professional*. Luxembourg: Artec 3D.

Barr WA. 2014. Functional morphology of the bovid astragalus in relation to habitat: controlling phylogenetic signal in ecomorphology. *Journal of Morphology* **275:** 1201–1216.

Bassarova M, **Janis CM**, **Archer M. 2009.** The calcaneum—on the heels of marsupial locomotion. *Journal of Mammalian Evolution* **16:** 1–23.

Becker D. 2003. *Paléoécologie et paléoclimats de la Molasse du Jura (Oligo-Miocène): apport des Rhinocerotoidea (Mammalia) et des minéraux argileux*. Doctoral dissertation, Université de Fribourg.

Beddard FE, **Treves F. 1889.** On the anatomy of *Rhinoceros sumatrensis*. *Proceedings of the Zoological Society of London* **57:** 7–25.

Biewener A. 1989. Mammalian terrestrial locomotion and size. *BioScience* **39:** 776–783.

Biewener A. 1990. Biomechanics of mammalian terrestrial locomotion. *Science* **250:** 1097–1103.

Biewener A, **Patek S. 2018.** Physical and biological properties and principles. In: Biewener A, Patek S, eds. *Animal locomotion*. New York: Oxford University Press, 1–11.

Blomberg SP, **Garland T**, **Ives AR. 2003.** Testing for phylogenetic signal in comparative data: behavioral traits are more labile. *Evolution; International Journal of Organic Evolution* **57:** 717–745.

Bongianni M. 1988. *Simon & Schuster's guide to horses and ponies*. New York: Fireside.

Bonnan MF. 2005. Pes anatomy in sauropod dinosaurs: implications for functional morphology, evolution, and

phylogeny. In: Tidwell V, Carpenter K, eds. *Thunder-lizards: the sauropodomorph dinosaurs*. Bloomington: Indiana University Press, 346–380.

Bonnan MF, **Wilhite DR**, **Masters SL**, **Yates AM**, **Gardner CK**, **Aguiar A. 2013.** What lies beneath: subarticular long bone shape scaling in eutherian mammals and saurischian dinosaurs suggests different locomotor adaptations for gigantism. *PLoS One* **8:** e75216.

Bookstein FL. 1991. *Morphometric tools for landmark data: geometry and biology*. Cambridge: Cambridge University Press.

Botton-Divet L, **Cornette R**, **Fabre AC**, **Herrel A**, **Houssaye A. 2016.** Morphological analysis of long bones in semi-aquatic mustelids and their terrestrial relatives. *Integrative and Comparative Biology* **56:** 1298–1309.

Campione NE, **Evans DC. 2012.** A universal scaling relationship between body mass and proximal limb bone dimensions in quadrupedal terrestrial tetrapods. *BMC Biology* **10:** 60.

Cardini A, **Polly D**, **Dawson R**, **Milne N. 2015.** Why the long face? Kangaroos and wallabies follow the same 'rule' of cranial evolutionary allometry (CREA) as placentals. *Evolutionary Biology* **42:** 169–176.

Carrano MT. 1997. Morphological indicators of foot posture in mammals: a statistical and biomechanical analysis. *Zoological Journal of the Linnean Society* **121:** 77–104.

Cerdeño E. 1998. Diversity and evolutionary trends of the family Rhinocerotidae (Perissodactyla). *Palaeogeography, Palaeoclimatology, Palaeoecology* **141:** 13–34.

Chen X, **Tong H. 2017.** On the hindfoot bones of *Mammuthus trogontherii* from Shanshenmiaozui in Nihewan Basin, China. *Quaternary International* **445:** 50–59.

Cignoni P, **Callieri M**, **Corsini M**, **Dellepiane M**, **Ganovelli F**, **Ranzuglia G. 2008.** MeshLab: an open-source mesh processing tool. In: Proceedings of the 2008 Eurographics Italian Chapter Conference, Salerno, Italy, 129–136.

Coombs MC. 1982. Chalicotheres (Perissodactyla) as large terrestrial mammals. *Third North American Paleontological Convention, Proceedings* **I:** 99–103.

Coombs MC. 1983. Large mammalian clawed herbivores: a comparative study. *Transactions of the American Philosophical Society* **73:** 1–96.

Coombs MC. 1989. Interrelationships and diversity in the Chalicotheriidae. In: Prothero DR, Schoch RM, eds. *The evolution of perissodactyls*. New York: Oxford University Press, 321–340.

Costeur L. 2004. Cenogram analysis of the Rudabánya mammalian community: palaeoenvironmental interpretations. *Palaeontographia Italica* **90:** 303.

Csuti B, **Sargent EL**, **Bechert US. 2008.** *The elephant's foot: prevention and care of foot conditions in captive Asian and African elephants*. Ames: John Wiley & Sons.

Curran SC. 2012. Expanding ecomorphological methods: geometric morphometric analysis of Cervidae post-crania. *Journal of Archaeological Science* **39:** 1172–1182.

Dagosto M, **Terranova CJ. 1992.** Estimating the body size of Eocene primates: a comparison of results from dental and postcranial variables. *International Journal of Primatology* **13:** 307.

Damuth J. 1990. Problems in estimating body masses of archaic ungulates using dental measurements. In: Damuth J, MacFadden BJ, eds. *Body size in mammalian paleobiology: estimation and biological implications*. Cambridge: Cambridge University Press, 229–254.

DeGusta D, **Vrba E. 2003.** A method for inferring paleohabitats from the functional morphology of bovid astragali. *Journal of Archaeological Science* **30:** 1009–1022.

Dinerstein E. 2011. Family Rhinocerotidae (Rhinoceroses). In: Wilson DE, Mittermeier RA, eds. *Handbook of the mammals of the world*. Barcelona: Lynx Edicions, 144–181.

Evin A, **Horáček I**, **Hulva P. 2011.** Phenotypic diversification and island evolution of pipistrelle bats (*Pipistrellus pipistrellus* group) in the Mediterranean region inferred from geometric morphometrics and molecular phylogenetics. *Journal of Biogeography* **38:** 2091–2105.

Fisher RE, **Scott KM**, **Adrian B. 2010.** Hind limb myology of the common hippopotamus, *Hippopotamus amphibius* (Artiodactyla: Hippopotamidae). *Zoological Journal of the Linnean Society* **158:** 661–682.

Fortelius M, **Kappelman J. 1993.** The largest land mammal ever imagined. *Zoological Journal of the Linnean Society* **108:** 85–101.

Gardezi T, **da Silva J. 1999.** Diversity in relation to body size in mammals: a comparative study. *The American Naturalist* **153:** 110–123.

Gaudry M. 2017. *Molecular phylogenetics of the rhinoceros clade and evolution of UCP1 transcriptional regulatory elements across the mammalian phylogeny*. Unpublished D. Phil. Thesis, Univeristy of Manitoba.

Geraads D, **McCrossin M**, **Benefit B. 2012.** A new rhinoceros, *Victoriaceros kenyensis* gen. et sp. nov., and other Perissodactyla from the middle Miocene of Maboko, Kenya. *Journal of Mammalian Evolution* **19:** 57–75.

Geraads D, **Spassov N. 2009.** Rhinocerotidae (Mammalia) from the late Miocene of Bulgaria. *Palaeontographica Abteilung A* **287:** 99–122.

Gladman JT, **Boyer DM**, **Simons EL**, **Seiffert ER. 2013.** A calcaneus attributable to the primitive late Eocene anthropoid *Proteopithecus sylviae*: phenetic affinities and phylogenetic implications. *American Journal of Physical Anthropology* **151:** 372–397.

Gray JE. 1821. On the natural arrangement of vertebrose animals. *London Medical Repository* **15:** 296–310.

Guérin C. 1980. Les rhinocéros (Mammalia, Perissodactyla) du Miocène terminal au Pléistocène supérieur en Europe occidentale: comparaison avec les espèces actuelles. *Documents du Laboratoire de Géologie de la Faculté des Sciences de Lyon* **79:** 1–1182.

Guérin C. 2012. *Anisodon grande* (Perissodactyla, Chalicotheriidae) de Sansan. *Mémoires du Muséum national d'Histoire naturelle* **203:** 279–315.

Gunz P, **Mitteroecker P. 2013.** Semilandmarks: a method for quantifying curves and surfaces. *Hystrix, the Italian Journal of Mammalogy* **24:** 103–109.

Gunz P, **Mitteroecker P**, **Bookstein FL. 2005.** Semilandmarks in three dimensions. In: Slice D, ed. *Modern morphometrics in physical anthropology*. Boston: Springer, 73–98.

Harrison JA, **Manning EM. 1983.** Extreme carpal variability in *Teleoceras* (Rhinocerotidae, Mammalia). *Journal of Vertebrate Paleontology* **3:** 58–64.

Heissig K. 2012. Les Rhinocerotidae (Perissodactyla) de Sansan. *Mémoires du Muséum national d'Histoire naturelle* **203:** 279–315.

Hildebrand M. 1982. *Analysis of vertebrate structure*. New York: Wiley.

Hildebrand M, **Bramble DM**, **Liem KF**, **Wake D. 1985.** *Functional vertebrate morphology*. Cambridge: Belknap Press of Harvard University Press.

Holbrook LT, **Lapergola J. 2011.** A new genus of perissodactyl (Mammalia) from the Bridgerian of Wyoming, with comments on basal perissodactyl phylogeny. *Journal of Vertebrate Paleontology* **31:** 895–901.

Houssaye A, **Fernandez V**, **Billet G. 2016.** Hyperspecialization in some South American endemic ungulates revealed by long bone microstructure. *Journal of Mammalian Evolution* **23:** 221–235.

Jams CM, **Gordon IJ**, **Illius AW. 1994.** Modelling equid/ruminant competition in the fossil record. *Historical Biology* **8:** 15–29.

Klingenberg CP. 1996. Multivariate allometry. In: Marcus LF, Corti M, Loy A, Naylor GJP, Slice DE, eds. *Advances in morphometrics*. Boston: Springer, 23–49.

Klingenberg CP. 2016. Size, shape, and form: concepts of allometry in geometric morphometrics. *Development Genes and Evolution* **226:** 113–137.

Knigge RP, **Tocheri MW**, **Orr CM**, **McNulty KP. 2015.** Three-dimensional geometric morphometric analysis of talar morphology in extant gorilla taxa from highland and lowland habitats. *The Anatomical Record Advances in Integrative Anatomy and Evolutionary Biology* **298:** 277–290.

Lewison RL. 2011. Family Hippopotamidae (Hippopotamuses). In: Wilson DE, Mittermeier RA, eds. *Handbook of the mammals of the world*. Barcelona: Lynx Edicions, 308–319.

MacFadden BJ. 2006. North American Miocene land mammals from Panama. *Journal of Vertebrate Paleontology* **26:** 720–734.

Mallet C, **Cornette R**, **Billet G**, **Houssaye A. 2019.** Interspecific variation in the limb long bones among modern rhinoceroses—extent and drivers. *PeerJ* **7**:e7647.

Martinez JN, **Sudre J. 1995.** The astragalus of Paleogene artiodactyls: comparative morphology, variability and prediction of body mass. *Lethaia* **28:** 197–209.

Medici EP. 2011. Family Tapiridae (Tapirs). In: Wilson DE, Mittermeier RA, eds. *Handbook of the mammals of the world*. Barcelona: Lynx Edicions, 182–203.

Missiaen P, **Smith T**, **Guo DY**, **Bloch JI**, **Gingerich PD. 2006.** Asian gliriform origin for arctostylopid mammals. *Naturwissenschaften* **93:** 407–411.

Mitteroecker P, **Gunz P. 2009.** Advances in geometric morphometrics. *Evolutionary Biology* **36:** 235–247.

Mitteroecker P, **Gunz P**, **Windhager S**, **Schaefer K. 2013.** A brief review of shape, form, and allometry in geometric morphometrics, with applications to human facial morphology. *Hystrix, the Italian Journal of Mammalogy* **24:** 59–66.

Mörs T. 2002. Biostratigraphy and paleoecology of continental Tertiary vertebrate faunas in the Lower Rhine Embayment (NW-Germany). *Netherlands Journal of Geosciences* **81:** 177–183.

Nakatsukasa M, **Takai M**, **Setoguchi T. 1997.** Functional morphology of the postcranium and locomotor behavior of *Neosaimiri fieldsi*, a Saimiri-like Middle Miocene platyrrhine. *American Journal of Physical Anthropology* **102:** 515–544.

Osborn HF. 1923. *Baluchitherium grangeri*, a giant hornless rhinoceros from Mongolia. *American Museum Novitates* **78**.

Osborn HF. 1929. *The Titanotheres of ancient Wyoming, Dakota, and Nebraska*. Washington: Government Printing Office.

Owen R. 1848. Description of teeth and portions of jaws of two extinct Anthracotherioid quadrupeds (*Hyopotamus vectianus* and *Hyop. bovinus*) discovered by the Marchioness of Hastings in the Eocene deposits on the N.W. coast of the Isle of Wight: with an attempt to develop Cuvier's idea of the classification of pachyderms by the number of their toes. *Quarterly Journal of the Geological Society of London* **4:** 103–141.

Panciroli E, **Janis C**, **Stockdale M**, **Martín-Serra A. 2017.** Correlates between calcaneal morphology and locomotion in extant and extinct carnivorous mammals. *Journal of Morphology* **278:** 1333–1353.

Paul GS, **Christiansen P. 2000.** Forelimb posture in neoceratopsian dinosaurs: implications for gait and locomotion. *Paleobiology* **26:** 450–465.

Perrard A, **Villemant C**, **Carpenter JM**, **Baylac M. 2012.** Differences in caste dimorphism among three hornet species (Hymenoptera: Vespidae): forewing size, shape and allometry. *Journal of Evolutionary Biology* **25:** 1389–1398.

Piras P, **Maiorino L**, **Raia P**, **Marcolini F**, **Salvi D**, **Vignoli L**, **Kotsakis T. 2010.** Functional and phylogenetic constraints in Rhinocerotinae craniodental morphology. *Evolutionary Ecology Research* **12:** 897–928.

Plummer TW, **Bishop LC**, **Hertel F. 2008.** Habitat preference of extant African bovids based on astragalus morphology: operationalizing ecomorphology for palaeoenvironmental reconstruction. *Journal of Archaeological Science* **35:** 3016–3027.

Polly D. 2008. Limbs in mammalian evolution. In: Hall BK, ed. *Fins into limbs: evolution, development, and transformation.* Chicago: University of Chicago Press, 245–268.

Prothero DR. 2005. Biogeography and diversity patterns. In: *The evolution of North American rhinoceroses.* Cambridge: Cambridge University Press, 182–199.

Prothero DR. 2013. *Rhinoceros giants: the paleobiology of indricotheres*. Bloomington: Indiana University Press.

Prothero DR, **Guérin C**, **Manning E. 1989.** The history of the Rhinocerotoidea. In: Prothero DR, Schoch RM, eds. *The evolution of perissodactyls*. New York: Oxford University Press, 321–340.

Prothero DR**,** Schoch RM, **eds**. **1989.** *The evolution of perissodactyls*. New York: Oxford University Press.

R Development Core Team. **2005.** *R: a language and environment for statistical computing*. Vienna: R Foundation for Statistical Computing.

RStudio, Inc. **2018.** *RStudio*. Boston: RStudio, Inc.

Rubenstein DI. 2011. Family Equidae (Horses and relatives). In: Wilson DE, Mittermeier RA, eds. *Handbook of the mammals of the world*. Barcelona: Lynx Edicions, 106–143.

Saarinen J, **Eronen J**, **Fortelius M**, **Seppä H**, **Lister A. 2016.** Patterns of diet and body mass of large ungulates from the Pleistocene of Western Europe, and their relation to vegetation. *Palaeontologia Electronica* **19:** 1–58.

Scarborough ME, **Palombo MR**, **Chinsamy A. 2016.** Insular adaptations in the astragalus–calcaneus of Sicilian and Maltese dwarf elephants. *Quaternary International* **406:** 111–122.

Schlager S, **Jefferis G**, **Dryden I. 2018.** *Morpho: a toolbox providing methods for data-acquisition, visualisation and statistical methods related to Geometric Morphometrics and shape analysis*. Available at: https://rdrr.io/cran/Morpho/man/Morpho-package.html

Schulz-Kornas E, **Fahlke JM**, **Merceron G**, **Kaiser T. 2007.** Feeding ecology of the Chalicotheriidae (Mammalia, Perissodactyla, Ancylopoda). Results from dental micro- and mesowear analyses. *Verhandlungen des Naturwissenschaftlichen Vereins zu Hamburg* **43:** 5–32.

Semprebon GM, **Sise PJ**, **Coombs MC. 2011.** Potential bark and fruit browsing as revealed by stereomicrowear analysis of the peculiar clawed herbivores known as chalicotheres (Perissodactyla, Chalicotherioidea). *Journal of Mammalian Evolution* **18:** 33–55.

Shockey B, **Anaya Daza F. 2004.** *Pyrotherium macfaddeni*, sp nov (Late Oligocene, Bolivia) and the pedal morphology of pyrotheres. *Journal of Vertebrate Paleontology* **24:** 481–488.

Stains HJ. 1959. Use of the calcaneum in studies of taxonomy and food habits. *Journal of Mammalogy* **40:** 392–401.

Steiner CC, **Ryder OA. 2011.** Molecular phylogeny and evolution of the Perissodactyla: phylogeny of the perissodactyls. *Zoological Journal of the Linnean Society* **163:** 1289–1303.

Tsubamoto T. 2014. Estimating body mass from the astragalus in mammals. *Acta Palaeontologica Polonica* **59:** 259–265.

Valli AM. 2005. Taphonomy of the late Miocene mammal locality of Akkasdagı, Turkey. *Geodiversitas* **27:** 793–808.

Wall WP. 1989. The phylogenetic history and adaptive radiation of Amynodontidae. In: Prothero DR, Schoch RM, eds. *The evolution of perissodactyls*. New York: Oxford University Press, 341–354.

Wang H, **Bai B**, **Meng J**, **Wang Y. 2016.** Earliest known unequivocal rhinocerotoid sheds new light on the origin of giant rhinos and phylogeny of early rhinocerotoids. *Scientific Reports* **6:** 39607.

White TD, **Folkens PA. 2005.** Foot: tarsals, metatarsals, & phalanges. In: White TD, Folkens PA, eds. *The human bone manual*. San Diego: Academic Press, 287–308.

Wiley DF. 2005. *Landmark*. Davis: Institute for Data Analysis and Visualization, University of California.

Willerslev E, **Gilbert MTP**, **Binladen J**, **Ho SY**, **Campos PF**, **Ratan A**, **Tomsho LP**, **da Fonseca RR**, **Sher A**, **Kuznetsova TV**, **Nowak-Kemp M**, **Roth TL**, **Miller W**, **Schuster SC. 2009.** Analysis of complete mitochondrial genomes from extinct and extant rhinoceroses reveals lack of phylogenetic resolution. *BMC Evolutionary Biology* **9:** 95.

Zapfe H. 1979. *Chalicotherium grande (BLAINV.) aus der miozänen Spaltenfüllung von Neudorf an der March (Děvinská Nová Ves), Tschechoslowakei*. Vienna, Austria: Berger.

Zhegallo V, **Kalandadze N**, **Shapovalov A**, **Bessudnova Z**, **Noskova N**, **Tesakova E. 2005.** On the fossil rhinoceros *Elasmotherium* (including the collections of the Russian Academy of Sciences). *Cranium* **22:** 17–40.

SUPPORTING INFORMATION

Additional Supporting Information may be found in the online version of this article at the publisher's website.

Appendix S1. List of all the specimens studied.
Appendix S2. Anatomical description of the bones.
Appendix S3. Description of the landmarks and curves placed on the bones.
Appendix S4. Results of the repeatability tests.
Appendix S5. Correlation between centroid size and mean body mass.
Appendix S6. Results of the K-mult test.
Appendix S7. Vector representations of all the shape variations described.
Figure S1. Right astragalus of *Rhinoceros unicornis* MNHN-ZM-AC-1960-59, in A: anterior, B: lateral, C: posterior and D: distal views. LR: lateral ridge of the trochlea, MR: medial ridge of the trochlea, G: groove of the trochlea, Tr: trochlea, F TM: facet for the tibial malleolus, F FM: facet for the fibular malleolus, F N: facet for the navicular, F Cu: facet for the cuboid, PF C: posterior facet for the calcaneus, MF C: medial facet for the calcaneus, DF C: distal facet for the calcaneus, M T: medial tubercle, P T: posterior tubercle.
Figure S2. Right calcaneus of *Ceratotherium simum* MNHN-ZM-MO-2005–297, in A: anterior, B: medial and C: distal views. TUBER: tuber calcanei, HEAD: head of the calcaneus, ST: sustentaculum tali, RC: rostrum calcanei, GA: great apophysis, MF A: medial facet for the astragalus, PF A: proximal facet for the astragalus, DF A: distal facet for the astragalus, F Cu: facet for the cuboid, L T: lateral tubercle.
Figure S3. Results of the PCA with ten replicates of the landmarks on three different but morphologically close individuals, for each bone.

Figure S4. Regression plot of the logarithm of the centroid size of each individual against the logarithm of the cubic root of the mean mass of its species, for both bones and for both the Rhinocerotidae and the Perissodactyla datasets.

Figure S5. A, vector representations of the shape variations on PC1, PC2 and PC4 on the analysis on the astragalus of Rhinocerotidae. Posterior view. B, left: vector representations of the shape corresponding to theoretical minimum and maximum of allometry on the astragalus of Rhinocerotidae. Right: vector representations of the shape corresponding to theoretical minimum and maximum of mass on allometry-free shapes on the astragalus of Rhinocerotidae. Posterior view. C, vector representations of the shape variations on PC1 and PC2 on the analysis on the calcaneus of Rhinocerotidae. Antero-medial view. D, left: vector representations of the shape corresponding to theoretical minimum and maximum of allometry on the calcaneus of Rhinocerotidae. Right: vector representations of the shape corresponding to theoretical minimum and maximum of mass on allometry-free shapes on the calcaneus of Rhinocerotidae. Antero-medial view. E, vector representations of the shape variations on PC1, PC2 and PC3 on the analysis on the astragalus of Perissodactyla. Posterior view. F, left: vector representations of the shape corresponding to theoretical minimum and maximum of allometry on the astragalus of Perissodactyla. Right: vector representations of the shape corresponding to theoretical minimum and maximum of mass on allometry-free shapes on the astragalus of Perissodactyla. Posterior view. G, vector representations of the shape variations on PC1 and PC2 on the analysis on the calcaneus of Perissodactyla. Antero-medial view. H, left: vector representations of the shape corresponding to theoretical minimum and maximum of allometry on the calcaneus of Perissodactyla. Right: vector representations of the shape corresponding to theoretical minimum and maximum of mass on allometry-free shapes on the calcaneus of Perissodactyla. Antero-medial view.

Abstract

In terrestrial vertebrates, the shape of the limb bones is influenced, among other factors, by functional constraints, notably the need to resist loading stresses due to gravity. This led, in quadrupeds weighting hundreds of kilograms, to morphological modifications of the limb bones to avoid crushing. Such architectural modifications related to a heavy weight have been historically qualified as “graviportal”. Rhinocerotoidea are of particular interest to study the morphological changes of the limb bones related to body mass, as they are represented by five extant species and dozens of fossil genera, some being among the heaviest land mammals that ever existed. Several independent occurrences of an increase of body mass are observed in this superfamily, making it relevant to study the variation of shape in relation to weight. This work explores the shape variation of the limb long bones relatively to body mass and body proportions among Rhinocerotoidea along their evolutionary history, in order to better understand how the skeleton modifies to meet the functional requirements of a coordinated locomotion and the support of a heavy weight. To do so, I used a 3D geometric morphometrics approach to qualify and quantify the shape of the six bones composing the stylopodium and zeugopodium of a sample of modern and fossil specimens. The exploration of the long bone shape variation and covariation in relation to body mass and to the evolutionary legacy in modern rhinos has been completed by the study of numerous fossil representatives to cover a large range of weight and body proportions, taking into account the evolutionary history of the group. My work highlights an increase of bone robustness common to all heavy rhinos. The development of the insertions for powerful extensor muscles and the likely presence of passive-stay apparatuses at shoulder and knee joints in heavy rhino taxa allow to better resist flexion caused by loading forces. My results show that forelimb bones are more influenced by body mass variation than hind limb ones in Rhinocerotoidea, likely due to the different proportion of body mass that they support and to their distinct respective roles of brake and propulsion. The shape of the stylopodium bones is simultaneously related to evolutionary legacy and body mass, while that of the zeugopodium is mostly associated with the degree of brachypody (i.e. relative limb length). The fibula is the only bone showing puzzling patterns of shape variation dominated by intraspecific variations, which questions its functional role in weight bearing. The shape variation in Rhinocerotoidea carries a dual signal with uniform aspects shared by all heavy species coupled with specific features in the different taxa, corresponding to the multiplicity of limb constructions observed in the superfamily. In addition to modifications related to heavy weight, most Rhinocerotoidea retain features of running quadrupeds while displaying different ways to sustain a high mass, questioning the classical definition of graviportality mainly based on elephants. This highlights the necessity to redefine graviportality by highlighting what are the repeated features potentially linked to it in each group with independent occurrences of heavy weight.

Keyworks:

Rhinoceros; Limb bones; Body Mass; 3D Geometric Morphometrics; Functional Morphology; Morphological Integration; Graviportality; Brachypody.

Résumé

Chez les vertébrés terrestres, la forme des os des membres est influencée notamment par des contraintes fonctionnelles, comme la nécessité de résister aux contraintes de charge dues à la gravité. Ceci conduit, chez des quadrupèdes pesant plusieurs centaines de kilos, à des modifications morphologiques des os des membres pour éviter l'écrasement. De telles modifications architecturales liées à un poids élevé ont été qualifiées de "graviporteuses". Les Rhinocerotoidea présentent un intérêt particulier pour l'étude des modifications morphologiques des os des membres liées à la masse corporelle, car ils sont représentés par cinq espèces actuelles et des dizaines de genres fossiles, certains faisant partie des mammifères terrestres les plus lourds qui aient jamais existé. Plusieurs occurrences indépendantes d'augmentation de la masse corporelle sont observées dans cette superfamille, ce qui rend pertinente l'étude de la variation de la forme en fonction du poids au sein de ce groupe. Ce travail explore la variation de la forme des os longs des membres en relation avec la masse et les proportions du corps chez les Rhinocerotoidea au cours de leur histoire évolutive, afin de mieux comprendre comment le squelette se modifie pour répondre aux exigences fonctionnelles d'une locomotion coordonnée et au support d'un poids élevé. Pour ce faire, j'ai utilisé une approche de morphométrie géométrique 3D pour qualifier et quantifier la forme des six os composant le stylopode et le zeugopode. L'exploration de la variation et de la covariation de la forme des os longs par rapport à la masse corporelle et à l'héritage évolutif chez les rhinocéros modernes a été complétée par l'étude de nombreux représentants fossiles couvrant une large gamme de poids et de proportions corporelles en tenant compte de l'histoire évolutive du groupe. Mes travaux mettent en évidence une augmentation de la robustesse des os commune à tous les rhinocéros lourds. Le développement des insertions des muscles extenseurs et la présence probable de systèmes de blocage passif des articulations des épaules et des genoux chez les taxons lourds permettent de mieux résister à la flexion causée par le poids du corps. Mes résultats montrent que les os des membres antérieurs sont plus influencés par la variation de la masse corporelle que ceux des membres postérieurs, probablement en raison de la proportion différente de la masse corporelle qu'ils supportent et de leurs rôles respectifs de freinage et de propulsion. La forme des os du stylopode est liée à la fois à l'héritage évolutif et à la masse corporelle, tandis que celle du zeugopode est surtout associée au degré de brachypodie (c'est-à-dire à la longueur relative des membres). La fibula présente des patrons de variation de forme très particuliers, dominés par les variations intraspécifiques, ce qui pose la question de son rôle fonctionnel dans le support du poids. La variation de forme chez les Rhinocerotoidea est porteuse d'un double signal, avec des aspects uniformes partagés par toutes les espèces lourdes couplés à des spécificités dans les différents taxons, correspondant à la multiplicité de construction des membres observée dans la superfamille. En plus des modifications liées à une forte masse, la plupart des Rhinocerotoidea conservent des caractéristiques de quadrupède coureur tout en présentant différentes façons de soutenir une masse élevée, remettant en question la définition classique de la graviportalité principalement basée sur les éléphants. Cela souligne la nécessité de redéfinir la graviportalité en mettant en évidence les caractéristiques répétées potentiellement liées à ce phénomène dans chaque groupe présentant des occurrences indépendantes de masse élevée.

Mots-clés :

Rhinocéros ; os longs ; masse corporelle ; morphométrie géométrique 3D ; morphologie fonctionnelle ; intégration morphologique ; graviportalité ; brachypodie.